Adjoint-Based Shape Optimization Constraint by Turbulent Two-Phase Navier-Stokes Systems

Vom Promotionsausschuss der
Technischen Universität Hamburg
zur Erlangung des akademischen Grades

Doktor-Ingenieur (Dr.-Ing.)

genehmigte Dissertation

von
Niklas Kühl

aus
Rendsburg

2021

Gutachter:
1. Gutachter: Prof. Dr.-Ing. Thomas Rung
2. Gutachter: Prof. Dr. Michael Hinze
3. Gutachter: Prof. Ph.D. Rainald Löhner
4. Gutachter: Jun.-Prof. Dr. Martin Siebenborn

Tag der mündlicher Prüfung:
21. September 2021

Vorsitzender des Prüfungsausschusses:
Prof. Dr.-Ing. Otto von Estorff

Digital Object Identifier (DOI): 10.15480/882.3794
Open Researcher & Contributor ID (ORCID): 0000-0002-4229-1358

Abstract

The thesis aims to advance gradient-based optimization methods for non-parametrized shapes exposed to immiscible two-phase flows using an adjoint Reynolds-Averaged Navier-Stokes (RANS) approach. Attention is given to the trade-off between adjoint consistency and industrial process capability. The efforts can be structured into four building blocks (I-IV): Compatible fully turbulent (I) primal (physical) and (II) dual (mathematical, adjoint) relationships together with appropriate objective functional formulations (III) are analysed with curiosity and scepticism at the same time, in order to attain the required accuracy, robustness and efficiency. The geometry engine (IV), which translates the computed sensitivities into shape deformations and grid adjustments, is crucial for the efficiency of the process, the technical usability of the result, and the HPC capability. Different aspects of the simulation-driven shape optimization process are addressed. This research's common ground is to analyse potential issues in greater depth rather than to formulate ad-hoc measures. The guiding principle frequently follows the concept of "Learning from the Adjoints". It is seen that potential weaknesses displayed by an adjoint approach –e.g. when developing (continuous) analytical solutions, in conjunction with (discrete) convergence problems– are often attributable to weaknesses of the primal formulation and a twist of the research question can lead to fruitful insights.

Contributions to (I) refer to the development of an efficient engineering Cahn-Hilliard (CH) Volume-of-Fluid (VoF) branch. In line with analytical considerations for a model problem, a nonlinear Equation of State (EoS) is derived to relate an indicator function with the fluid properties. Building block (II) covers the derivation of discrete adjoint VoF formulations and the implementation of an adjoint VoF sub-cycling strategy. The suggestion of a discretely differentiable EoS, together with a novel combination of an inconsistent adjoint VoF method and the CH-VoF approach, allows for a robust and (flexible-) consistent adjoint two-phase formulation. Another major part is concerned with a continuous adjoint complement to 2D, incompressible, first-order boundary-layer equations. The findings support the heuristic neglect of the adjoint transposed convection term and offer analytical expressions for adjoint laminar boundary-layer parameters. The thesis is also concerned with improving adjoint investigations of turbulent flows using mixing-length arguments for the frozen turbulence strategy and a Law of the Wall consistent approach. An algebraic expression provides a consistent closure of the adjoint momentum equation in the logarithmic layer. Spatial decoupling of the control from the objective (III) affects the formulation of boundary conditions and reduces iterative efforts when the design surface does not cover the entire wetted surface. Additionally, an implicit surface metric approach is presented to extract the inherently smooth gradient (IV) out of the possible rough sensitivity derivative. Attention is devoted to compliance with geometrical constraints, e.g. constant volume or maximum outer dimensions. Finally, an adaptive floatation module is added to the gradient-based optimization procedure, which is not differentiated and considered frozen during the adjoint simulation. Examples included underline the capability of the *frozen floatation* approach and provide partially drastically improved ship hull shapes. It is demonstrated that fixed floatation can lead to optimization losses when the final shape is released.

Almost without exception, applications relate to maritime two-phase flows at the industrial level. Some of them are conducted even in full-scale. They refer to a Kriso container ship, a generic submarine, a double-ended ferry, and an offshore-supply vessel.

Acknowledgements

The dissertation is based on results from my time as a research assistant at the Institute of Fluid Dynamics and Ship Theory (FDS) at the Hamburg University of Technology (TUHH).

It seems like yesterday that I attended (purely out of interest) the lecture "Turbulent Flows" by Prof. Dr.-Ing. Thomas Rung, towards the end of my student days at the TUHH. Back then, I had almost no clue about the so-called "adjoint world", which T. Rung offered me to enter as a member of his team. I want to express my deepest gratitude for the trust placed in me from the first day on, especially during the initially stormy times, in which the headwind seemed to increase rather than decrease. I have always appreciated the balance between challenge and support during the opportunity to acquire as well as execute research projects with partners from academia and industry. I thoroughly enjoyed the countless hours of conversations on all kinds of theoretical, practical, and methodological issues, as well as the many topics beyond. During the very heartfelt and touching speech after the defense of this thesis, I was literally speechless.

Furthermore, I would like to thank the other examiners of this thesis. Prof. Dr. Michael Hinze has a decisive influence on this work through his mathematical consulting. In addition, I am thankful for his assistance in preparing the proposal for the research project on which this thesis is based. The advice of Jun.-Prof. Dr. Martin Siebenborn led my initially circumstantial shape optimization process based on "sensitivity smoothing in space" to a compact yet robust approach. I thank Prof. Ph.D. Rainald Löhner for his invitation to work with him in the USA, and I am sad that I had to abandon the stay abruptly due to the COVID-19 pandemic. In addition, I would like to thank Prof. Dr.-Ing. Otto von Estorff for chairing the examination committee.

I look back with pleasure on an educational time with older colleagues like Torben Mühlbach and Dr.-Ing. Svenja Schubert, and I look forward to observing and accompanying newer colleagues like Peter Marvin Müller and Georgios Bletsos.

Last but not least, I thank my parents for their continuous support during my studies and Beke for her patience with me and my time-consuming research, but especially for everything beyond.

Contents

Nomenclature

Lower-case Latin

a^*	Coefficient for boundary-layer estimation or wave amplitude
b	Double well potential or coefficient for boundary-layer estimation
$c, \hat{c}^*$	Concentration or drag/friction coefficient, adjoint concentration, adjoint drag/friction/sensitivity coefficient
d_i^*	Displacement field or distance between two cell centers
e_α	Unit vector in α-direction
$f, \hat{f}$	Aggregation function for local mass transfer or stream function, adjoint stream function
f_i^*	Force
$g, \hat{g}, g_\mathrm{i}^*, \hat{g}_\mathrm{i}^*$	Help function within a similarity transformation, adjoint help function, gravitational acceleration or shape gradient, adjoint shape gradient
h^*	Generic spatial discrete increment
j_i^*	Volume diffusion flux
$k^*, \hat{k}^*$	Turbulent kinetic energy or wave number, adjoint turbulent kinetic energy
l^*	Mixing length
m	Equation of state
n^*, n_i	Normal direction, normal vector
$p^*, \hat{p}^*$	Pressure, adjoint pressure
$q^*, \hat{q}^*$	General source or local free surface sharpness indicator, general adjoint source
$r, \hat{r}$	Local convective sensor, adjoint local convective sensor
r_i	Force direction
$s^*, \hat{s}^*$	General source, general adjoint source
s_i^*	Sensitivity derivative
t^*, t_i	Tangential direction or traction or time, tangential vector
u_i^*	Control
$v_\mathrm{i}^*, \hat{v}_\mathrm{i}^*$	Velocity, adjoint velocity
w^*	Distance to nearest wall
x_i^*	Spatial position
y, x_2	Non-dimensional distance to nearest wall

Upper-case Latin

$\dot{m}^*$	Mass flux
$\dot{V}^*$	Volume flux
Oh	Ohnesorge number
St	Strouhal number
We	Weber number

$\tilde{M}$	Mobility Scaling
$A^{*\mathrm{w}}, A$	Water plane area, system matrix
B^*	Boundary conditions
$C^*, C, \hat{C}^*, \mathrm{Ca}, \mathrm{Co}$	Coefficient or curvature, reference concentration, reference adjoint concentration, Cahn number, Courant number
D, D^*_{ik}	Diffusion, geometric interpolation matrix
E^*, Eu	Free energy, Euler number
F^*, F, Fn	Heave force, face, Froude number
H^*	Height
I^*	Moment of inertia
J^*	Objective functional
L^*	Reference length or Lagrangian
M^*	Mobility or trim moment
$P, P^*, \hat{P}^*, \mathrm{Pe}, \mathrm{Pr}$	Cell center or production, reference pressure, reference adjoint pressure, Peclet number, Prandtl number
Q	Global free surface sharpness measure
R, R^*, Re	Reduction, residual or radius, Reynolds number
$S^*, S^*_{\mathrm{ik}}, \hat{S}_{\mathrm{ik}}$	Source, shear rate tensor, adjoint shear rate tensor
T^*	Reference time or transformation or time
$V^*, \hat{V}^*$	Volume or reference velocity or design velocity, reference adjoint velocity

Lower-case Greek

α	Step size or geometric coefficient or concentration shifting constant
$\delta^*, \hat{\delta}^*$	Boundary-layer thickness or variation, adjoint boundary-layer thickness
δ_{ik}	Kronecker delta
ϵ_{ijk}	Levi-Civita-Symbol
$\eta, \hat{\eta}$	Similarity variable, adjoint similarity variable
γ^*	Transition length
$\hat{\varphi}^*$	General adjoint field quantity
κ	Kármán constant
λ^*	Wave length or interpolation factor
μ^*	Dynamic Viscosity
ν^*	Kinematic Viscosity
ω^*	Specific dissipation rate or relaxation factor
$\psi^*, \hat{\psi}$	Chemical potential or stream function, adjoint stream function
ρ^*	Density
$\sigma^*, \sigma^*_{\mathrm{i}}, \hat{\sigma}_{\mathrm{i}}$	Surface tension, surface force, adjoint surface force
$\tau^*, \hat{\tau}^*, \tau^*_{\mathrm{ik}}, \hat{\tau}^*_{\mathrm{ik}}$	Shear stress or design time, adjoint shear stress, shear stress tensor, adjoint shear stress tensor
θ	Angle between flow and free surface or phase angle or non-dimensional temperature
ε^*	Dissipation rate or discrete control perturbation
φ^*	General field quantity or angle between flow and free surface
ξ	Amplification factor

Upper-case Greek

Δ^*	Outer boundary-layer position or increment (e.g. time slice)
Γ^*	Area
Ω^*	Volume

Superscripts

a, adj, A	Fluid a, adjoint, Fluid A
b, B	Fluid b, Fluid B or neighbour
BL	Boundary-layer
C, CH, CO	Convective, consistent, chord, channel, Couette
D	Design or displacement downwind or diffusive
eff, E	Effective, external
F	Face, frozen
g	Geometric
H	Hydrostatic
I	Inlet or internal
l	Laminar, local
m, M, mod	Material law, mass or outer iteration, modeled
O	Objective or pressure outlet
phys, pri, p, P, PP	Physical, primal, p-Laplacian exponent, cell center, perpendicular
S, ST	Symmetry, surface tension
t, tar	Turbulent, target
U	Upwind
vD	van-Driest
W	Wall

Subscripts

τ	Shear stress
99	99% boundary-layer thickness
D	Displacement
E	Energy
f, F	Friction
H	Height
i, j, k, l, m	Cartesian coordinates
L	Length
M	Momentum
n	Normal
t	Tangential
w, W	Wall

Operations

$\Delta^* f = \underline{\nabla}^* \cdot \underline{\nabla}^* f$	Laplacian of scalar field f
$\lvert(\cdot)\rvert$	Absolute value
$\lvert\lvert(\cdot)\rvert\rvert$	Euclidean norm
$\mathrm{D}\,(\cdot)/\mathrm{D}\,t^*$	Conservative derivative
$\mathrm{d}\,(\cdot)/\mathrm{d}\,t^*$	Substantial (a.k.a. material) derivative

$\max(\cdot)$	Maximum value
$\underline{\min}(\cdot)$	Minimum value
$\overline{(\cdot)}$	Mean
$\underline{\nabla}^* f$	Gradient of scalar field f
$\underline{\nabla}^* \cdot \underline{f}$	Divergence of vector field $\underline{f}$

Abbreviations

1D, 2D and 3D	One-, Two- and Three-Dimensional
AD	Automatic Differentiation (Algorithmic Differentiation)
AIAA	American Institute of Aeronautics and Astronautics
ALE	Arbitrary Lagrangian Eulerian (Formulation)
ATC	Adjoint Transpose Convection
BE	Backward Euler
BiCG	Biconjugate Gradient
BRICS	Blended Reconstructed Interface Capturing Scheme
BVM	Boussinesq Viscosity Model
CA	Continuous Adjoint
CAD	Computer-Aided Design
CBC	Convective Boundedness Criterion
CDS	Central Differencing Scheme
CFD	Computational Fluid Dynamics
CG	Conjugate Gradient
CH	Cahn-Hilliard
CICSAM	Compressive Interface Capturing Scheme for Arbitrary Meshes
CV	Control Volume
DA	Discrete Adjoint
DARPA	Defense Advanced Research Projects Agency
DC	Deferred Correction
DDS	Downwind Differencing Scheme
DEF	Double Ended Ferry
DES	Deteched Eddy Simulation
DNS	Direct Numerical Simulation
EoS	Equation of State
FD	Finite-Differencing
FDM	Finite-Difference Method
FreSCo+	Free Surface Code (in-house RANS code)
FS	Full Scale
FV	Finite-Volume
FVM	Finite-Volume Method
HC	Hyper-C
HPC	High Performance Computing
HR	High-Reynolds
HRIC	High-Resolution Interface Capturing
ITTL	Implicit Three Time Level
KCS	Kriso Container Ship
LB	Laplace Beltrami

LDDS	Linear Downwind Differencing Scheme
LES	Large Eddy Simulation
LIVRA	Least Squares Volume-of-Fluid Interface Reconstruction Algorithm
LoW	Law of the Wall
LR	Low-Reynolds
LUDS	Linear Upwind Differencing Scheme
MDO	Multidisciplinary Design Optimization
MPI	Message Passing Interface
MS	Model Scale
MUSCL	Monotone Upstream-Centered Schemes for Conservation Laws
NACA	National Advisory Committee for Aeronautics
NVD	Normalized Variable Diagram
ODE	Ordinary Differential Equation
OSV	Offshore Supply Vessel
PDE	Partial Differential Equation
PETSC	Portable, Extensible Toolkit for Scientific Computation
PLIC	Piecewise Linear Interface Reconstruction
QDICK	Quadratic Downwind Interpolation of Convective Kinematics
QUICK	Quadratic Upwind Interpolation of Convective Kinematics
RA	Reynolds-Averaging
RANS	Reynolds-Averaged NavierStokes
RTT	Reynolds Transport Theorem
SIMadPLE	Semi-Implicit Method for adjoint Pressure-Linked Equations
SIMPLE	Semi-Implicit Method for Pressure-Linked Equations
SLIC	Simple Line Interface Calculation
SP	Steklov Poincaré
SST	Shear Stress Transport
TKE	Turbulent Kinetic Energy
TVD	Total Variation Dimishing
UDS	Upwind Differencing Scheme
UQ	Ultimate-Quickest
V&V	Verification & Validation
VoF	Volume-of-Fluid
ZPG	Zero Pressure Gradient

1 Scientific Aims and Motivation

International shipping is responsible for the transport of around 90% of the global trade. The dominant role of shipping is attributable to the low fuel consumption per tonne-km of transported cargo. However, the mere magnitude of around 45-50 thousand operating merchant vessels puts environmental and economic aspects of shipping more and more into the focus of optimization efforts. The seaborne pollution and approximately 50% of the direct operating costs for shipping are related to fuel consumption, which is governed by the vessel's resistance. The latter is primarily controlled (approximately 75%) by steady hydrodynamic contributions, i.e. the wave drag in calm water and the friction drag along the wetted surface. Therefore, reducing these drag contributions –even by a few per mille– is highly appreciated from commercial and environmental perspectives.

Different routes to reduce the drag of a ship or, generally speaking, improve an engineering design exist. Traditional approaches largely refer to existing knowledge and experience, supplemented by either experimental or computational validation strategies. While time-to-market intervals of new products are nowadays subject to drastic reductions, the requested design changes associated with their optimization or their adjustment to the development of new markets are often beyond the limits of well-proven technology. This dilemma indicates a pressing need to revise existing processes and implement simulation-based optimization alternatives. This thesis addresses the ambition for a simulation-driven optimization process. It is concerned with developing a holistic, robust and efficient computational shape optimization framework dedicated to the hydrodynamic optimization of ship hulls at Froude- and Reynolds numbers of practical interest. The related challenges are comprehensive. They are associated with high Reynolds number turbulent flow and the characteristics of the two-phase flow of immiscible fluids, which feature a virtually discontinuous property change across the free surface. Moreover, meaningful shape updates for approximately $\mathcal{O}(10^5)$ discrete surface points must obey a variety of practical and manufacturing restrictions, and the hydrodynamic performance of the vessel is altered by possible floatation.

The industrial focus of the research manifests itself in the pursued holistic approach. This suggests to employ a reduced interface, intertwined optimization procedure with high-performance computing capabilities using parallel applications on spatially partitioned grids. The scope of the procedure includes the validation and optimization of the hydrodynamic performance, as well as the update of the design and its discrete representation over a sequence of several dozen design cycles that might involve large localized deviations from the initial design. Adjoint methods will be used in a Computer Aided Design (CAD)-free (also known as (a.k.a.) node-based), gradient-based optimization environment to capture frequently employed technical objectives, e.g. minimal wave and friction drag or a minimized surface elevation. The node-based, CAD-free strategy supports the efficient optimization of consecutive design updates in combination with a mesh morphing procedure that does not require to adjust the parallel algorithm during the optimization

procedure and benefits from comparably simple restart features. At the same time it resolves the shape optimization potentials at the level of the numerical grid.

The goal of the thesis is to advance gradient-based optimization methods for CAD-free and thus non-parametrized shapes exposed to immiscible two-phase flows using an adjoint Reynolds-Averaged Navier-Stokes (RANS) approach. Attention is given to the trade-off between adjoint consistency and industrial process capability. The efforts can be structured into four building blocks (I-IV), which the author believes are indispensable for an industrialized fluid dynamic optimization process: Compatible fully turbulent (I) primal (physical) and (II) dual (mathematical, adjoint) relationships together with appropriate objective functional formulations (III) are analysed with curiosity and skepticism at the same time, in order to attain the required accuracy, robustness and efficiency. Moreover, the geometry engine (IV), which translates the computed sensitivities into shape deformations and grid adjustments, is crucial for the efficiency of the process, the technical usability of the result, as well as the High-Performance-Computing (HPC) capability. The first building block seems controversial, since an enforced primal flow description is usually considered to be the starting point of the adjoint formulation. However, as displayed in this research, inconsistencies between the primal and the dual description might point to deficiencies of the primal flow model. A relevant example refers to accurate yet efficient two-phase flow models including their interface treatment in continuous and discrete space, where the adjoint perspective provides guidelines for appropriate primal flow models. Aiming to improve optimizations of industrial applications, an efficient algebraic adjoint turbulence treatment, robustness enhancing alternatives to spatially separate the control from a force objective, as well as advanced techniques to drive the CAD-free shape and mesh deformation for partially wetted shapes subjected to manufacturing constraints are also put into the focus of this thesis. Applications are devoted to three industrial hulls with different missions, i.e. a container vessel, an offshore supply vessel and a double-ended ferry, supplemented by a generic submarine hull. Moreover, results are reported for several theoretical and computational investigations of fundamental flows of interest, e.g. boundary-layer flows and homogeneous shear flows. Findings and suggested approaches are transferable to other engineering applications, e.g. the design of near-shore operating renewable energy devices harvesting ocean waves in the surge zone close to a free surface.

The initial sections of this chapter provide a brief discussion on the state-of-the-art of the primal two-phase flow model (I), the adjoint Computational Fluid Dynamics (CFD) models for two-phase flows (II) and the geometry engine (IV) which comprises both the shape description in discrete and continuous space as well as the discrete mesh update. These summaries motivate the major research questions addressed in the thesis. The final section outlines the detailed contributions of the present thesis.

1.1 Maritime Computational Fluid Dynamics

Many two-phase flows are characterized by immiscible fluids that feature negligible compressibility. A prominent example refers to maritime free surface flows. Technical applications of such flows are often subjected to large interface deformations, e.g. breaking waves, and the accurate simulation of these flows requires a computational model that conserves the mass of each phase whilst preserving a sharp interface. These requirements still pose a challenge in mesh-based computational fluid dynamics.

Engineering two-phase flow simulations mostly refer to either of two interface-capturing methods, cf. Ferziger and Peric [2012]: Namely the Level-Set approach of Osher and Sethian [1988] and the Volume-of-Fluid (VoF) method proposed by Hirt and Nichols [1981], which both reconstruct the free surface from an indicator function. The Level-Set method introduced by Osher and Sethian [1988] or Sussman [1994] and Sussman et al. [1998] utilizes a signed distance function to characterize the interface by the zero-value iso-surface. The continuous distribution of the signed distance simplifies a higher-order discretization of the related transport equation and the geometry of the interface can be determined with improved accuracy. A drawback of the standard Level-Set method is that it does not guarantee mass conservation. Olsson and Kreiss [2005] as well as Olsson et al. [2007] proposed a mass conservative Level-Set approach based on a smeared Heaviside function which follows a similar idea compared to the diffuse (VoF) interface approach herein. Two-phase applications of the VoF method suggested by Noh and Woodward [1976] and later refined by Hirt and Nichols [1981] usually employ a scalar volume concentration of a foreground phase to identify the fluid state of each cell. The method is conservative and capable to predict merging and rupturing of free surfaces. For immiscible fluids, any mixing of both phases is undesired but numerically difficult to avoid. Different strategies are conceivable to improve interface compression: Geometric reconstruction schemes, e.g. Simple Line Interface Calculation (SLIC, Noh and Woodward [1976]), Piecewise-Linear Interface Calculation (PLIC, Hirt and Nichols [1981]) or Least Squares Volume-of-Fluid Interface Reconstruction Algorithm (LVIRA, Pilliod Jr. and Puckett [2004]) and dedicated downwind-biased advection schemes, e.g. the Compressive Interface Capturing Scheme for Arbitrary Meshes (CICSAM, Ubbink and Issa [1999]), High Resolution Interface Capturing (HRIC, Muzaferija and Peric [1999]) or Blended Reconstructed Interface Capturing Scheme (BRICS, Wackers et al. [2011]). Geometric reconstruction schemes are afflicted with a considerable algorithmic complexity which reduces their popularity. Dedicated advection schemes are slightly heuristic but fairly simple to implement. They maintain an approximately sharp interface subject to sufficiently small time steps. On the downside, they require transient simulations even when applying implicit numerical schemes to steady state problems, e.g. the calm-water resistance of steady cruising ships. To further improve the interface compression, some authors have proposed to add an artificial compression or anti-diffusion term, e.g. So et al. [2011], Heyns et al. [2013]. These methods rely on heuristic compression factors and improve the compressiveness at the expense of a reduced numerical stability.

If surface tension effects are negligible, VoF models using dedicated advection schemes are deemed to be a good compromise between efficiency, accuracy and conservation properties. An alternative, much less common approach refers to diffuse interface models, often labeled Cahn-Hilliard (CH) models, e.g. Cahn and Hilliard [1958]. Here, the (ideally) sharp interface of the continuous phase is replaced by a (thin) layer where the fluids mix. The approach is able to mimic phase separation and thus promises resharpening features which are attractive for engineering simulations. Although the neglect of surface tension is an acceptable assumption in many engineering problems, it appears that the CH approach incorporates surface tension in a natural way and no additional model, e.g. the Continuum Method of Brackbill et al. [1992] or Lafaurie et al. [1994], is required. There exists a variety of different CH approaches for two fluids, e.g. models governed by fluids with matched densities (labeled as Model H, cf. Hohenberg and Halperin [1977]), identical viscosities (Boussinesq Fluid, cf. Jacqmin [1999]) or so-called thermodynamically consis-

tent systems (e.g. Lowengrub and Truskinovsky [1998], Abels et al. [2012]), just to name a few. The thermodynamically consistent approach has received attention for energetic reasons, in particular if an inherent divergence-free velocity field is sought. Examples refer to Khanwale et al. [2020a,b], who recently employed an octree-based mesh refinement approach to an adaptive finite-element discretization of the energy-stable formulation to study canonical test cases like Rayleigh-Taylor instabilities or rising bubbles. In addition to the different CH variants, several strategies for their coupling with the momentum and continuity equations have been suggested. Further distinctions refer to balancing either the mass or the volume fluxes between both phases (Lowengrub and Truskinovsky [1998], Ding et al. [2007]), the considered baseline conservation equations (Abels et al. [2012], Ding et al. [2007]), and the introduction of modifications to ensure thermodynamic consistency (Lowengrub and Truskinovsky [1998], Abels et al. [2012]).

The VoF scheme offers a closed system of Partial Differential Equations (PDEs), but entails an evolved heuristic parametrization of the employed approximations. Examples refer to the influences of the Courant number or the flow direction on the reconstruction of face values. On the contrary, three additional parameters occur in the CH method, which however have a more rigorous physical significance. The first and second parameter correspond to the transition length or interface thickness as well as the surface tension coefficient. The third parameter refers to the mobility that governs the strength of the phase separation process. Combining the CH model with the Navier-Stokes equations, essentially results in an augmented VoF formulation, labeled CH-VoF in this thesis. This inheres a nonlinear, diffusive right-hand side (r.h.s.) of order four, which is zero outside the interface region. The nonlinear character of the CH-VoF model is beneficial. It supports a) an accurate computation of surface tension effects when the interface is adequately resolved and b) the use of stable, upwind-biased advective approximations in under-resolved flow simulations. Whilst the former is often deemed insignificant for industrial applications, the latter promises substantial efficiency improvements. Furthermore, CH-strategies offer clear benefits for a robust adjoint formulation.

1.2 Adjoint Computational Fluid Dynamics

In the context of local fluid dynamic optimization, the adjoint analysis aims at the efficient computation of derivative information for an integral objective functional with respect to (w.r.t.) a general control function, cf. Pironneau [1974], Jameson [1988, 1995], Jameson et al. [1998], Giles and Pierce [1997, 2000] and Giannakoglou and Papadimitriou [2008]. In continuous space, the dual or adjoint flow state can be interpreted as a co-state and always follows from the underlying primal PDE governed model that describes the flow physics. However, the appropriate formulation of boundary conditions and the adequate discretization is often not intuitively clear in a PDE-based, continuous adjoint (CA) framework, cf. Soto and Löhner [2001, 2004], Othmer [2008, 2014], Zymaris et al. [2010], Springer and Urban [2015], Kröger et al. [2018] and Kapellos et al. [2019]. Hence, the development of numerical CA strategies clearly lags behind the primal progress which has motivated the development of discrete adjoint (DA) approaches using automatic differentiation to synchronize the primal and dual development states, e.g. Griewank [1989], Griewank and Walther [2000], Nadarajah and Jameson [2000], Nadarajah [2003], Giles et al. [2003], Dwight and Brézillon [2006], Mader et al. [2008], Gauger et al. [2008]. The DA approach

passes over the adjoint PDE and directly bridges the discrete linearized primal flow into a consistent discrete dual approach, cf. a comprehensive discussion in Giles and Pierce [1997, 2000], the lecture series by Vassberg and Jameson [2006a,b] or a review and classification of Martins and Hwang [2013].

Despite the various merits and drawbacks of the DA vs. the CA method (cf. Peter and Dwight [2010] or Griewank and Walther [2008]), the CA approach is unique for its invaluable contribution to a physical or computational understanding (cf. Bletsos et al. [2021]) and will therefore be the method of choice in the present thesis. Among many others, two major topics in the field of adjoint fluid mechanics are considered in this thesis, referring to the treatment of adjoint turbulence and adjoint two-phase flow. Supplementary contributions will be made with regards to appropriate adjoint discretizations.

Adjoint Turbulence Treatment

Modelling equations for the turbulent closure already appear comparatively complex on the primal side. The latter is underlined by an unfavorable algorithmic complexity that frequently contains possibly non-differentiable expressions and variable couplings, even on the level of coefficients (Menter [1994], Yakhot et al. [1992]) making it inconvenient for a continuous adjoint approach in practical applications. This has motivated the neglect of adjoint turbulence models in line with the frozen turbulence approach, cf. Dwight and Brézillon [2006], Othmer [2008], Stück [2012]. However, the influence of the variation of the turbulence parameters is an open discussion (Marta and Shankaran [2013], Dwight and Brézillon [2006]) which is a comprehensible reason why discrete adjoint approaches using automatic differentiation have been derived that aim at a synchronization of the primal and dual turbulent development states, cf. Nielsen et al. [2004, 2010], Nielsen and Diskin [2013]. The development of the continuous adjoint method w.r.t. adjoint turbulence modelling initially started with the derivation of adjoint one-equation closures (Zymaris et al. [2009], Bueno-Orovio et al. [2012], Bagheri and Da Ronch [2020]) followed by the complete linearization of prominent statistical closures, e.g. an adjoint $k-\varepsilon$ (Papoutsis-Kiachagias et al. [2015], Zymaris et al. [2010]) and $k-\omega$ (Kavvadias et al. [2015a], Hartmann et al. [2011], Manservisi and Menghini [2016a,b]) model. All previously mentioned contributions share the idea of deriving adjoint turbulence modelling equations. Optimizations of complex engineering flows using fully consistent, differentiated turbulence transport models are –as mentioned– however rare, cf. Karpouzas et al. [2016], Papoutsis-Kiachagias and Giannakoglou [2016]. Primal turbulence transport models inhere multiple nonlinearities and inter-parameter couplings, that significantly hamper the robustness and the efficiency of a consistent adjoint framework and hinder their routinely utilization in engineering applications. On the other hand, the continuous adjoint framework gives access to dedicated adjoint turbulence modelling at a lower level of adjoint consistency.

Adjoint Two-Phase Flow

Although a few publications on hydrodynamic optimization can be found, a holistic view on adjoint shape optimization in free surface-flows is scarce. Ragab [2001a,b] developed a design framework for the optimization of surface ships and submarines operating near a free surface based on potential flow methods. The optimization is performed for wave resistance objectives, but also for inverse approaches to reach a prescribed pressure dis-

tribution and wave pattern. Söding [2001a,b,c] employed the adjoint complement of a potential flow solver to reduce the resistance of merchant vessels. Soto and Löhner [2001] and Soto et al. [2004] applied an adjoint Euler-flow solver to reduce the resistance of a container vessel using a frozen free surface approach. An adjoint Euler-flow method that incorporates an interface-tracking approach was used by Martinelli and Jameson [2007] to reduce the wave resistance of an academic Wigley hull. The challenges associated with the concentration transport in VoF schemes have motivated the restriction of the previous research to either simplified VoF schemes (Springer [2014], Springer and Urban [2015]), Level-Set-based strategies (Palacios et al. [2012, 2013]) or diffusive interface schemes (Garcke et al. [2019], Hinze and Kahle [2011]) in interface capturing approaches. The primal VoF approach transports the discontinuous flow properties along with the free surface. In previous work related to shocks, similar differentiability problems were treated with shift differentiability (Ulbrich [2002, 2003]) or the application of an artificial viscosity with the purpose of filtering out physical solutions, cf. Giles and Ulbrich [2010]. Synthetic viscosities have also been used for error estimation in transient shallow-water flows as reported by Beckers et al. [2019]. Moreover, the above-mentioned compressive approximations of the primal convective kinematics are based on heuristic, nonlinear expressions, which are cumbersome to translate into an adjoint context. Palacios et al. [2012, 2013] thus opted for an adjoint Level-Set Euler-flow solver that is applied to 2D and 3D obstacles in free surface channel flows. Springer and Urban [2015] developed an adjoint VoF Navier-Stokes solver to identify the floatation position of ships, but neglected some of the adjoint coupling terms and compromised on the duality of the approximation. Their main objective referred to the equilibrium of the trim moment at steady state.

1.3 Geometry Engines used by Adjoint Shape Optimizer

The discrete representation of the actual continuous shape derivative is provided by an adjoint solver and can therefore be interpreted as the sensitivity of all n^{CFD} discrete CFD-related surface points. The possibly rough shape sensitivity derivative is frequently embedded in a deterministic gradient-based shape optimization process in three ways that refer to either

a) parameterized shape descriptions from a CAD-framework of the CFD surrounding design process. Their integral nature allows for a continuous, inherently smooth shape control with known tangential and thus geodetic connectivity. Hence, potentially noisy shapes due to high-frequency modes on CFD-discretization level can be effectively suppressed. On the downside, the design space is –possibly severely– limited a priori by the initial parameterization, therefore perhaps hides further optimization potential and different CAD models may result in different optimal shapes. For complex engineering flows, the CAD parameter space of size $10 \leq n^{\mathrm{CAD}} \leq 100$ is confronted by a CFD (surface grid) space of approximately $10^3 \leq n^{\mathrm{CFD}} \leq 10^6$ surface elements. The drawback can be partially circumvented by an over-parameterization (Agarwal et al. [2018]) or partially-parametric approaches (Harries et al. [2019]). Furthermore, the adjoint-based shape derivative along the discrete CFD representation requires a transformation into the discrete CAD parameter framework, which is frequently done by differentiating the parameterization in line with the chain rule, e.g. Yu et al. [2011], Xu et al. [2014]. In a complex, industrial shape description,

the Jacobian of this CAD-CFD relationship may not be explicitly available due to black-box-like CAD software, which introduces further work in terms of numerical CAD-CFD differentiation. Compliance of dimensions between CAD and CFD parameters is not guaranteed which probably hinders the interpretation of parameter sensitivities. A survey of parameterization approaches is offered by Samareh [1999, 2001] and Nadarajah et al. [2007]. If the relation between CAD-parameters and volume grid is not available, a re-meshing of the fluid domain might be necessary after each geometry update. This procedure usually discards previous primal/adjoint field solutions and forces a restart of both simulations from scratch. While the re-meshing can be automated, the lack of restart capabilities can become prohibitively expensive.

b) a coupling of mesh node updates using either local shape functions, e.g. FE-type functions (Soto et al. [2002, 2004]), or global shape functions like Hicks-Henne approaches (Hicks and Henne [1978]), Bezier-Bernstein polynomials (Kavvadias et al. [2015b]) or Free-Form Deformation techniques (Sederberg and Parry [1986], Ronzheimer [2005], Duvigneau [2006]). Although less pronounced in the case of a sufficient number of control points, the merits and drawbacks of the global shape function approach coincide with those of the CAD parameterizations of the previous item.

c) a shape optimization in the design space of the discrete CFD surface that allows to access local features and shape optima on the level of the discrete CFD resolution. The "raw" adjoint shape derivatives suffer from a few well-known weaknesses, e.g. they only describe the normal deformation but do not provide tangential information and the shape derivatives are not necessarily smooth. These deficiencies yield rough/noisy shape updates (cf. Stück and Rung [2011], Kröger and Rung [2015]) and lead to distorted near-wall meshes which in turn hamper the preservation of numerical accuracy during the optimization procedure, e.g. Stavropoulou et al. [2014] and Bletzinger [2014]. As a consequence, the adjoint shape derivatives have to be regularized to obtain meaningful technical shape updates as initially proposed by Jameson and Vassberg [2000] and Vassberg and Jameson [2006a,b] in terms of an implicit, continuous smoothing operator based on an extended definition of the inner product, frequently labeled Sobolev-gradient. In general, the habitat of the shape gradient –surface- vs. volume-based– depends on the underlying surface metric. Prominent examples refer to Laplace-Beltrami (LB) or Steklov-Poincar (SP) type metrics, e.g. Schulz and Siebenborn [2016]. Applying the smoothing operation on the surface leads to the LB operator and a related surface metric. For computational reasons, the practice is often performed in an explicit manner, cf. Bletzinger [2014]. The explicitly filtered gradient, e.g. by using consistent kernel functions (Kröger and Rung [2015]), marks a first-order approximation to the implicit Sobolev-gradient, cf. Stück and Rung [2011]. The LB approach exclusively operates in the tangent space of the controlled shape. Once a regularized deformation field is available along the design boundary, a subsequent mesh deformation equation transports the surface-based gradient information into the interior field in terms of, e.g. spring analogies or based on an additional Laplacian PDE together with prescribed boundary deformations, cf. Löhner and Yang [1996], Crumpton and Giles [1997], Jasak and Tuković [2006]. The SP approach refers to a novel strategy on an industrial level that employs an elliptic volume-based formulation where smoothed results are subsequently projected

on the boundary. The approach essentially tries to combine the 2D shape update in continuous space with the 3D mesh update using the discrete CFD mesh sensitivities, cf. Schulz and Siebenborn [2016], Haubner et al. [2021]. The approach exclusively operates in the fluid domain and is thus attractive for its compatibility with a CFD solver environment. The use of standardized solution routines (assembling, solving, etc.) supplied by the flow solver, usually scrutinized for scaling performance on HPC clusters, represents the benefit of the SP approach. Once the volume-based representation of the shape gradient is available, it can be readily used to manipulate the volume mesh as part of a gradient-based optimization procedure. Since no further operations are necessary, the volume-based SP approach is preferred and extended to geometrically constraint shape updates in this thesis. Whether LB or SP is employed, the shape deformation directly manipulates the volume mesh based on the previously determined inherently smooth shape gradient. Hence, an adjustment of the geometry is done while preserving the grid topology that allows a restart based on previous field solutions. In the context of a steepest gradient descent approach together with comparably small step sizes, the solutions are usually nearby and a speedup in total computational time of about an order of magnitude is realistic for the applications in this thesis.

All approaches might need to transfer the final geometry into the CAD-framework of the CFD surrounding design process in an industrial environment. Hence, whether a), b) or c) is employed depends on the underlying geometry infrastructure which is probably balanced by the user.

1.4 Starting Point and Contributions of the Thesis

The thesis is based on two previous works of Stück [2012] and Kröger [2016]. The former suggested a hybrid method based on elements of the continuous and discrete adjoint method. Starting from a closed continuous derivation of the single-phase adjoint equations for incompressible fluids (integration by parts), the corresponding discrete adjoint operators (summation by parts) were developed. The modular approach allows a flexible process for adjoint investigations of a wide variety of engineering flows. The hybrid adjoint strategy is used to derive the adjoint complement to compressive primal flux approximation schemes in this thesis. Furthermore, explicit sensitivity filtering techniques were presented in the context of gradient preconditioning methods to finally gain a detailed insight into the optimization problem from the perspective of the objective. The baton was taken over by Kröger [2016] and two essential features were added to the process chain. First, an adjoint two-phase solver based on the VoF method was supplemented. Although VoF approaches to immiscible two-phase flows are inherently unsteady, the adjoint two-phase system was developed around the converged steady primal flow. The variation of the locally variable phase dependent material properties generates various additional source/sink-like terms, which finally results in a tightly coupled system of the adjoint momentum, concentration and continuity equations. The consistency of the approach was compromised by the introduction of a heuristic adjoint diffusion term that was necessary to stabilize the numerical procedure. The latter serves as a starting point of present theoretical investigations into duality conflicts and related conclusions for the primal two-phase flow model as well as

the discrete adjoint approach. In addition, a sensitivity regularization method which extended the "gradient preconditioning" using compactly supported, inherently smooth and consistent kernel-based strategies has been presented. The approach gives access to the description of a surface tangential direction of shape node position updates, which proved to be process stabilizing and profitable to perform CAD-free optimizations over many ten design cycles. The explicit nature of the filter approach results in cumbersome impositions of geometric constraints which –if employed inexperienced– impedes the mesh-morphing procedure. An alternative shape morphing approach is proposed in this work, that is mainly distinguished by its generic volume-based formulation.

Contributions of the Thesis

Based on the previously described state-of-the-art, different aspects of the simulation-driven shape optimization process were addressed. A common ground of this research was to analyse potential issues in greater depth rather than to formulate adhoc measures. The guiding principle frequently followed the concept of "Learning from the Adjoints". It is seen that potential weaknesses displayed by an adjoint approach –e.g. when developing (continuous) analytical solutions, in conjunction with (discrete) convergence problems, or enhanced iterative efforts– are often attributable to weaknesses of the primal formulation, and a twist of the research question can lead to fruitful insights.

I Primal Two-Phase Flow Model

Observations during previous research of Kröger [2016] reveal severe robustness issues of adjoint sharp-interface VoF methods, particularly when applied to large Reynolds- and Froude number marine engineering problems. Similar issues were reported for shallow-water models by Beckers et al. [2019]. Heuristic adhoc measures to regularize the adjoint solution refer to breaking the duality by introducing a parameterized diffusion operator to the adjoint concentration equation, cf. Kröger et al. [2018]. In the spirit of "Learning from the Adjoint", such measures suggest to introduce a consistent change to the primal model along the route of diffuse interface models that support phase separation. Chapter 2 of this thesis reports the derivation of a mass-conservative diffuse interface model that combines ideas of a Cahn-Hilliard (CH) approach (cf. Hinze and Kahle [2011], Abels et al. [2012]) with the classical VoF framework and is labeled CH-VoF herein. This strategy leads to a consistent primal/dual approach (cf. II). The most relevant contributions of this work refer to:

I.1 Derivation and implementation of a CH-VoF scheme.

Different from most other strategies, the present CH-VoF framework supports mass-conservative phase relations and results in a weakly compressible formulation. The formulation complies with a generic shear flow example that is used to analyse the adjoint formulations (cf. II).

I.2 Formulation and validation of an efficient engineering CH-VoF branch.

In general, the CH-VoF method is capable to resolve the interface physics. In engineering studies, the interface physics are beyond the interest and not resolved. Therefore, the under-resolved interface physics are replaced by a subgrid-model for a

mobility parameter. The scheme offers resharpening capabilities, i.e. an initially diffuse interface is sharpened rather than blurred when the solution is advanced, which is attractive for engineering simulations that mostly suffer from successive interface blurring.

Due to the sharp interface representation, the CH-VoF approach makes the use of compressive convection schemes obsolete and supports the use of upwind biased approximations of convective kinematics. As opposed to compressive VoF schemes that ground on downwind-biased schemes, the approach supports steady computations and is not restricted to small Courant numbers in pseudo-time, if constructed appropriately.

I.3 Formulation of an equation of state for the fluid properties.

In line with analytical considerations for a model problem, a nonlinear Equation of State (EoS) is derived to relate the indicator function (a.k.a. concentration) with the fluid properties. As a result, minimal blurs of the concentration in immiscible flows are bypassed and the resulting system is virtually insensitive of the spatial resolution in marine engineering CFD setups.

I.4 Validation for marine engineering and geophysical flows.

A secondary advantage of the model is that it incorporates surface tension in a natural way when interface physics are resolved and no additional model is required, e.g. the Continuum Method of Brackbill et al. [1992] and Lafaurie et al. [1994]. Hence the CH-VoF is successfully applied to both gravity and capillary driven wave fields reported by Prosperetti [1981], cf. Cha. 2.

Results of the primal two-phase modelling efforts were published in Kühl et al. [2021a].

II Adjoint Discretization and Flow Modelling

A substantial portion of the thesis analyses the coupled primal and adjoint VoF model. A systematic derivation of (discrete) dual VoF formulations is a first contribution of the thesis. Supplementary, a closed analytical solution to a model problem is presented, which displays that the adjoint part seems to be ill-posed. As a remedy, an additional diffusive concentration term is introduced to the adjoint concentration equation along the route suggested by Kröger et al. [2018]. The heuristic modification violates the dual consistency but strongly regularizes the solution of the adjoint system. The term can be connected to a primal companion of the CH-VoF formulation to resolve duality conflicts in line with "Learning from the Adjoints" as previously described. The following novel aspects of adjoint two-phase modelling are reported:

II.1 Derivation of discrete adjoint VoF Formulations.

Immiscible fluids are modeled by discontinuous primal densities and viscosities across an (ideally) sharp interface. This usually requires compressive, downwind-biased, nonlinear approximations of primal convective fluxes. The thesis derives the corresponding adjoint schemes for the first time. Attention is restricted to two prominent compressive schemes, namely the High Resolution Interface Capturing Scheme

(HRIC) and the Compressive Interface Capturing Scheme for Arbitrary Meshes (CICSAM). Along the route suggested by Stück and Rung [2013], the derivation starts from the discrete primal approach and uses summation by parts to derive the corresponding adjoint formulation, which can subsequently be interpreted in a continuous sense. It is seen that the dual schemes rigorously mirror the primal Normalized-Variable-Diagram (NVD) stencils.

II.2 Formulation and implementation of an adjoint-VoF sub-cycling strategy.

In steady applications, the primal and dual procedures are advanced in pseudo-time and the integration of the dual approach is performed around the converged primal field. An adjoint sub-cycling strategy is introduced to ensure compliance of the primal and dual integration. Therefore, the adjoint system experiences the same time step (Courant number) restrictions as the primal system, is independent of the primal time horizon and forms a robust as well as an a priori stable solution process.

II.3 A novel combination of the inconsistent adjoint VoF method with the CH-VoF approach.

Combining the CH-VoF efforts with their adjoint complement allows for a robust and (flexible-) consistent adjoint two-phase formulation.

II.4 Formulation of a discretely differentiable equation of state.

In contrast to a linear EoS, which returns a constant derivative with respect to the observed concentration, nonlinear alternatives reveal an intensified local contribution along the interfacial region that weakens noticeably towards the bulk phases. In the sharp interface limit, the employed sigmoid (e.g. hyperbolic tangent) EoS turns into a Heaviside function and the adjoint system experiences an abrupt (Dirac) impulse along the interface. From a discrete perspective, the adjoint system conceptually pushes the phase transition regime below the grid resolution which in turn reproduces a frozen-concentration approach since the discrete system is unable to resolve each local adjoint concentration source. Therefore the primal sharpening (I.4) is reversed in adjoint mode.

The derivation of the adjoint two-phase discretization (II.1/2) is published in Kühl et al. [2021b].

Another major part of the thesis is concerned with a continuous adjoint complement to 2D, incompressible, first-order boundary-layer (b.-l.) equations. The topic is detailed in Cha. 4 and was inspired by the debate on the discretization and the importance of adjoint transpose convective terms (ATC), which arise due to the nonlinearity of the primal convective linear momentum transport. The ATC terms might disappear for compressible flows, cf. Soto and Löhner [2004], but are also frequently neglected in incompressible simulations due to their detrimental influence on the numerical robustness, e.g. Othmer [2008], Springer and Urban [2015] and Karpouzas et al. [2016]. The aim here is to analyse a simple yet relevant flow situation which supports a statement on the relevance of the ATC term. Novel contributions refer to:

II.5 Derivation of adjoint b.-l. equations.

It is demonstrated that the adjoint b.-l. equations can be derived in two ways, either following a *first simplify then derive* or a *first derive and then simplify* strategy. The simplification step comprises the classical b.-l. approximation and the derivation step transfers the primal flow equation into a companion adjoint equation. Both approaches lead to the same result, which underlines their formal correctness.

II.6 Derivation of an adjoint Blasius equation.

The analyses of the coupled primal/adjoint b.-l. framework leads to similarity parameters, which turn the PDE problem into a boundary value problem described by a set of Ordinary-Differential-Equations (ODE) and –for the first time– support the formulation of an adjoint complement to the classical Blasius equation.

II.7 Study of the adjoint transpose convection.

It is demonstrated that the ATC term, which is often debated in the literature, vanishes for a self-similar, laminar b.-l. flow. This finding supports the heuristic neglect of the term used by many authors of CA optimization studies in case of complex engineering shear flows.

II.8 Analytical expressions for adjoint laminar b.-l. parameters.

A formalism is derived which provides analytical expressions of an adjoint b.-l. thickness, wall shear stress, skin friction and drag coefficient as well as the shape sensitivity expression for a shear driven drag objective.

Related material on adjoint approaches to laminar b.-l. flows is published in Kühl et al. [2021d].

Next to the analysis of laminar b.-l. flows, the thesis is also concerned with improving adjoint investigations of turbulent flows (cf. Cha. 4). Engineering turbulence treatment usually refers to Reynolds-averaged strategies and mostly employs Boussinesq-viscosity models (BVM) based on differential transport equations for one or two turbulence parameters, cf. Wilcox [1998]. The influence of the variation of the turbulence parameters is an open discussion (Marta and Shankaran [2013]) and optimizations of complex engineering flows using fully consistent, differentiated turbulence transport models are rare (Papoutsis-Kiachagias and Giannakoglou [2016]) due to the significant increase of complexity. The present strategy focuses on the near-wall flow model which is crucial to the sensitivity prediction. In contrast to former studies, attention is restricted to algebraic adjoint strategies, irrespective of the primal turbulence model. The starting point of the attempt is an analysis of a simple unidirectional shear flow using Prandtl's mixing-length hypothesis (Prandtl [1925], Pope [2001]), which is the foundation of virtually all wall function-based RANS boundary-layer descriptions. Related novel aspects refer to:

II.9 Adjoint turbulent near-wall flow.

Using mixing-length arguments, a unified algebraic adjoint momentum equation is derived for the frozen turbulence strategy and a Law of the Wall (LoW) consistent (differentiated) approach. The algebraic character is a direct consequence of the frequently employed assumption that all primal flow properties algebraically scale with the friction velocity in the logarithmic layer. It is compatible with wall function assumptions for prominent BVM, which ground on the mixing-length hypothesis.

II.10 Adjoint Law of the Wall.

An adjoint momentum LoW is derived which resembles its primal counterpart in many aspects.

II.11 Algebraic adjoint turbulence model.

A simple algebraic expression provides a consistent closure of the adjoint momentum equation in the logarithmic layer. This might also serve as a closure approximation for more general adjoint flows, whilst still using standard one- or two-equation Boussinesq-viscosity models for the primal flow. Results obtained by the LoW-consistent algebraic closure come at no extra cost and indicate an acceleration of the optimization process as well as improved optimal solutions. A hidden benefit of the suggested LoW-consistent approach refers to the enhanced stability of the numerical framework due to the augmented viscosity.

Related material on the adjoint LoW is available in Kühl et al. [2021c].

III Objective Functional Formulation

The adjoint equations connect the physical/primal flow description with the objective functional and the control, e.g. the shape description. The adjoint equations are thus objective dependent. This impedes a canonical coding of the continuous adjoint method and sometimes makes the formulation of boundary conditions a delicate issue. Hence, different objectives yield different adjoint problems which refer to different mathematical and computational models. Whereas this property is usually deemed undesirable, it can also serve as an opportunity, if the line of thought is reversed in line with "Learning from the Adjoints": Can one formulate an alternative adjoint problem, which is computationally more efficient and provides the same physical answer? A related example is analysed in Cha. 3, which covers the material of another contribution of the thesis.

III.1 Direct vs. indirect objective functional formulation.

Two objective functional formulations related to Newton's law for external flows are investigated by either directly observing the boundary forces or (indirectly) concluding on the forces from an observation of the momentum loss in the far field. It is seen that both strategies are fully equivalent from an optimization point of view, but can attain different efficiencies. The spatial decoupling of the control from the objective affects the formulation of boundary conditions and reduces the iterative efforts when the design surface does not cover the entire wetted surface, which is often the case in practical applications.

Results for the comparison of the direct vs. indirect objective functional formulation for external flows were published in Kühl et al. [2019].

IV Geometry Modelling

Since the local shape optimizations in this work are characterized by a steepest (gradient) descent procedure, a suitable approximation of the shape gradient has to be chosen after the successful determination of the shape sensitivity (derivative). The thesis discusses techniques to obtain a descent direction from the available shape sensitivity. This crucial

part of a robust, industrialized, node-based optimization procedure depends on the choice of the considered surface metric. Prominent examples refer to Laplace-Beltrami (LB) or Steklov-Poincar (SP) type metrics, cf. Schulz and Siebenborn [2016]. The LB approach exclusively operates in the tangent space of the shape components released for design and the SP approach leads to a domain formulation, where results are projected on the boundary and the update of the entire volume mesh is implicitly obtained concurrent to the shape update. The possibility to use standardized routines supplied by the flow solver (assembling, solving, etc.), which are usually optimized for HPC, favors the SP approach. The innovative features of the thesis refer to:

IV.1 An implicit SP approach is presented which acts on sensitivity level only, and offers inherently smooth shapes. Attention is devoted to the compliance with geometrical constraints, as, e.g., constant volume, maximum outer dimensions or a plane transom.

The approach is generalized based on a p-Laplace approach. A co-authored contribution is available in Müller et al. [2021].

V Complex Marine Engineering Applications

Almost without exception, all practical applications relate to maritime two-phase flows at industrial level, some of them are conducted even in full-scale. A change in the flow due to the change in shape has an influence on the floating position. The innovations as compared to the state-of-the-art consist in:

V.1 Shape optimization of free floating vessels.

An adaptive floatation module is added to the gradient-based optimization procedure. The floating model is not differentiated and considered frozen during the adjoint simulation. Thus, each new shape undergoes an adaptation of its floating position during the primal run.

Various studies with / without free floatation during the optimization are discussed. Examples included underline the capability of the *frozen floatation* approach and provide partially drastically improved ship hull shapes. It is also demonstrated that fixed floatation can lead to drastic optimization losses when the final shape is released.

The presented applications refer to a Kriso container ship (KCS), a generic submarine (DARPA), a double-ended ferry (DEF) and an offshore-supply vessel (OSV).

A.1 One considered ship hull refers to the KCS in model scale at Fn = 0.26 and Re = 1.4×10^7. The test case was part of several international workshops that focused on the assessment of hydrodynamic simulation procedures (e.g. Larsson et al. [2013]) and offers a large body of numerical and experimental reference data. The investigated initial configuration refers to experimental calm-water studies conducted by Kim et al. [2001] and was previously computed under the aegis of the Gothenburg 2010 workshop (cf. Larsson et al. [2013]). The test case is mainly investigated for validation purposes of the primal two-phase solver.

A.2 The generic DARPA (Defense Advanced Research Projects Agency) SUBOFF geometry is studied without appendages as described by Groves et al. [1989]. This

test case is commonly used during studies that focus on, e.g. the propulsion and manoeuvring of submarines that operate deeply submerged or in the vicinity of the free surface, cf. Wang et al. [2020], Daum et al. [2017], Chase and Carrica [2013]. When operating close to the free surface, the wave field induced by the interaction of the dynamic pressure field with the free surface is unfavorable in terms of wave resistance as well as the signature of the submarine.

A.3 The DEF is to be optimized such that the final shape has a symmetrical bow and stern so that forward and reverse ferry travel is equivalent from a fluid mechanical perspective, i.e. the same forces act on the ferry for both cruises which should ensure the same maneuverability. The application area of ferries often refers to coastal or inland waterways. Hence, a compact hull design should be maintained, making the test case attractive for the verification of geometric constraints.

A.4 The final application refers to an OSV in both model- and full-scale, where the hull length is small compared to the cruising speed. As a consequence, the supply vessel operates at comparably large Froude numbers ($\mathrm{Fn} > 0.3$) and therefore experiences high wave resistances based on, e.g., braking waves. A modification of the latter might trigger a change of the floatation and therefore the OSV represents a competitive test case for the presented adjoint-based two-phase shape optimization framework under free floatation. The geometry features a transom which allows for geometrical constraints based on a robust mesh deformation process.

Outline of the Thesis

The remainder of the thesis is organized as follows: The two main chapters 2 and 4 refer to the primal and adjoint turbulent two-phase systems, starting with the primal consideration. Each of the two chapters is consistently divided into four sections that refer to 1) a continuous derivation, 2) the subsequent numerical discretization followed by 3) a verification of the implementation and 4) a validation of the respective approach. Chapter 3 between the two main discussions refers to fundamental aspects of non-parameterized shape optimization under state constraints. Chapter 5 applies the previously presented approaches to several two-phase engineering flows. The final Chapter 6 provides conclusions and outlines future research. To keep the presentation concise and precise, parts of the derivations have been moved to the appendix. Within the thesis, Einsteins summation convention is used for lower-case Latin subscripts, vectors as well as tensors are defined with reference to Cartesian coordinates and dimensional variables are consistently marked with an asterisk.

2 Primal Flow

Maritime two-phase flows are characterized by immiscible fluids that feature negligible compressibility. Technical applications of such flows are often subjected to large interface deformations, e.g. breaking waves. The accurate simulation of these flows requires a computational model that conserves the mass of each phase whilst preserving a sharp interface. These requirements still pose a challenge in mesh-based computational fluid dynamics.

This second chapter describes all aspects of the primal two-phase flow. Emphasis is given to marine engineering flows consisting of two virtually immiscible fluid phases – more precisely air and water – which are deemed incompressible. The flow model consists of non-dispersed, separate fluids which are observed in an Eulerian framework. Furthermore, no-slip is assumed between the fluid phases along the interface and therefore the participating fluids share the same velocity field.

The remainder of this chapter is structured as follows: The first section is devoted to the mathematical model of the primal two-phase flow. The second section addresses the discretization of the related governing equations using a second-order accurate finite volume procedure. The third section outlines the verification of the discrete primal flow procedure against generic test cases which feature analytical or generalized solutions on simplified scenarios. The last section reports on the validation of the discrete primal flow procedure for more complex applications.

2.1 Primal Two-Phase Flow Model

The derivation of the mathematical model originates from the conservation of a general quantity φ^* under the influence of a velocity field v_k^*. Using Reynolds Transport Theorem (RTT), also known as the Leibnitz integration rule, the temporal change of φ^* in a control mass with volume $\Omega^{*\mathrm{M}}$, which is advected by the velocity v_k^* under the influence of a source $S^{*\varphi}$, translates into an integral expression over a spatially fixed Eulerian control volume $\Omega^{*\mathrm{V}}$ occupied by the control mass

$$\frac{\mathrm{d}}{\mathrm{d}\,t^*}\int_{\Omega^{*\mathrm{M}}}\varphi^*\mathrm{d}\Omega^* - S^{*\varphi} = 0 \qquad \overset{\mathrm{RTT}}{\rightarrow} \qquad \int_{\Omega^{*\mathrm{V}}}\left[\frac{\partial\varphi^*}{\partial\,t^*} + \frac{\partial\,v_\mathrm{k}^*\varphi^*}{\partial\,x_\mathrm{k}^*} - s^{*\varphi}\right]\mathrm{d}\Omega^* = 0\,. \tag{2.1}$$

This relation represents the Eulerian formalism where $s^{*\varphi}$ refers to a volume specific (intensive) counter part of the quantity-dependent (extensive) Eulerian source term $S^{*\varphi}$. These sources cover multiple origins, in particular also contributions from diffusive transport. Relation (2.1) is deemed to hold for arbitrary control volumes, which yields a strong/differential form of the RTT for continuously differentiable fields

$$\frac{\partial\,\varphi^*}{\partial\,t^*} + v_\mathrm{k}^*\frac{\partial\,\varphi^*}{\partial\,x_\mathrm{k}^*} = \frac{\mathrm{d}\,\varphi^*}{\mathrm{d}\,t^*} = s^{*\varphi} - \frac{\partial\,v_\mathrm{k}^*}{\partial\,x_\mathrm{k}^*}\,\varphi^*. \tag{2.2}$$

The text occasionally employs $\mathrm{D}\,\varphi^*/\mathrm{D}\,t^* := \mathrm{d}\,\varphi^*/\mathrm{d}\,t^* + \varphi^*(\partial v_\mathrm{k}^*/\partial\, x_\mathrm{k}^*)$. Both abbreviations are equivalent for a solenoidal velocity field, i.e. $\partial\, v_\mathrm{k}^*/\partial\, x_\mathrm{k}^* = 0$.

2.1.1 Conservation of Mass

The conservation of mass follows from the general transport equation (2.2) by employing $\varphi^* = \rho^*$, which formally yields

$$\frac{\partial\, \rho^*}{\partial\, t^*} + \frac{\partial\, v_\mathrm{k}^*\, \rho^*}{\partial\, x_\mathrm{k}^*} = s^{*\rho}\,. \tag{2.3}$$

If the mass is conserved, as is the usual approach for single-phase flows, this requires $s^{*\rho} = 0$. The two-phase flow consists of two parts which refer to fluid A and fluid B. The respective specie densities add up to the fluid density, i.e. $\rho^* = \rho^{*\mathrm{A}} + \rho^{*\mathrm{B}}$ and the mass conservation for the species is governed by

$$\frac{\partial\, \rho^{*\mathrm{A}}}{\partial\, t^*} + \frac{\partial\, v_\mathrm{k}^* \rho^{*\mathrm{A}}}{\partial\, x_\mathrm{k}^*} = s^{*\rho,\mathrm{A}} \qquad \text{and} \qquad \frac{\partial\, \rho^{*\mathrm{B}}}{\partial\, t^*} + \frac{\partial\, v_\mathrm{k}^*\, \rho^{*\mathrm{B}}}{\partial\, x_\mathrm{k}^*} = s^{*\rho,\mathrm{B}}\,. \tag{2.4}$$

Relation (2.4) allows for a mass transfer between fluid A and fluid B and their sum provides the r.h.s. of (2.3), i.e. $s^{*\rho} = s^{*\rho,\mathrm{A}} + s^{*\rho,\mathrm{B}}$. Mind that conserving the global mass yields $s^{*\rho,\mathrm{A}} = -s^{*\rho,\mathrm{B}}$. Referring to marine engineering applications, both fluids are expected to be incompressible and virtually immiscible. As outlined below, the local fluid density ρ^* is attached to an indicator or concentration function c using an equation of state. The EoS extracts the density field from the concentration function and the bulk densities of the participating fluids.

2.1.2 Density Equation of State

The density equation of state does not follow from a rigid physical relation and gives room for additional modelling assumptions. A foreground phase concentration $c \in [c^\mathrm{a}, c^\mathrm{b}]$ is used as a measure of phase and fluid properties. The concentration ranges from a foreground state (c^a) to a background state (c^b). In this work, the two reference states are defined by $c^\mathrm{a} = 1$ as well as $c^\mathrm{b} = 0$. The choice is arbitrary but appropriate for the purpose of comparison with the well established VoF approach, cf. Hirt and Nichols [1981]. With this choice, the concentration value relates to the filling level or volume concentration of the foreground phase fluid.

A density equation of state $m^\rho(c)$ is introduced that extracts the specie density from a concentration field c and the given bulk densities $\rho^{*\mathrm{a}}$ (e.g., air density) and $\rho^{*\mathrm{b}}$ (e.g., water density), which are considered invariable

$$\rho^{*\mathrm{A}} = m^\rho\, \rho^{*\mathrm{a}} \qquad \text{and} \qquad \rho^{*\mathrm{B}} = (1 - m^\rho)\, \rho^{*\mathrm{b}}\,. \tag{2.5}$$

This yields

$$\rho^* = m^\rho \rho^{*\mathrm{a}} + (1 - m^\rho)\, \rho^{*\mathrm{b}} \qquad \text{or} \qquad \rho^* = m^\rho \rho^{*\Delta} + \rho^{*\mathrm{b}}, \tag{2.6}$$

where $\rho^{*\Delta} = \rho^{*\mathrm{a}} - \rho^{*\mathrm{b}}$ marks the difference of the bulk densities. Assuming $c^\mathrm{a} > c^\mathrm{b}$ and $\rho^{*\mathrm{a}} < \rho^{*\mathrm{b}}$, some basic requirements for the construction of the EoS relation m^ρ considered in this thesis read:

1. Exclusion of non-physical density states, e.g. $\rho^* < \rho^{*\mathrm{a}}$ and $\rho^* > \rho^{*\mathrm{b}}$. This shares ideas with the boundedness requirement frequently used for the interpolation of convective kinematics which is ensured by $0 \leq m^\rho \leq 1$.

2. Recovering the single-phase in the respective limit state. This requires $m^\rho(c^\mathrm{a}) = 0$ as well as $m^\rho(c^\mathrm{b}) = 1$ based on (2.6).

3. A positive slope $\partial\, m^\rho / \partial\, c \geq 0$ to preserve a continuous shift between the two fluids (monotonicity).

4. Point symmetry around the interfacial region at $(c^\mathrm{a}+c^\mathrm{b})/2$ should represent the fluid interface combined with $m^\rho((c^\mathrm{a}+c^\mathrm{b})/2) = 0.5$.

Note that these requirements also ensure $\int m^\rho \,\mathrm{d}c = (c^\mathrm{a} + c^\mathrm{b})/2 = 1/2$. The standard density EoS corresponds to a simple linear interpolation between the limit states

$$m^{\rho,1} = \begin{cases} 0 & \text{if } c < c^\mathrm{a} \\ 1 & \text{if } c > c^\mathrm{b} \\ c & \text{otherwise} \end{cases} . \tag{2.7}$$

A more advanced nonlinear alternative follows the rule of a hyperbolic tangent

$$m^{\rho,2} = \frac{1}{2}\left[\tanh\left(\frac{2c - c^\mathrm{a} - c^\mathrm{b}}{\gamma^{\mathrm{m},\rho}\,(c^\mathrm{a} - c^\mathrm{b})}\right) + 1\right]. \tag{2.8}$$

A third alternative refers to a truncated linearization of the the hyperbolic tangent approach around $(c^\mathrm{a} + c^\mathrm{b})/2$

$$m^{\rho,3} = \begin{cases} 0 & \text{if } c < \frac{1}{2}\left[(1-\gamma^{\mathrm{m},\rho})\,c^\mathrm{a} + (1+\gamma^{\mathrm{m},\rho})\,c^\mathrm{b}\right] \\ 1 & \text{if } c > \frac{1}{2}\left[(1+\gamma^{\mathrm{m},\rho})\,c^\mathrm{a} + (1-\gamma^{\mathrm{m},\rho})\,c^\mathrm{b}\right] \\ \frac{2\,c+(\gamma^{\mathrm{m},\rho}-1)c^\mathrm{a}-(\gamma^{\mathrm{m},\rho}+1)c^\mathrm{b}}{2\gamma^{\mathrm{m},\rho}\left(c^\mathrm{a}-c^\mathrm{b}\right)} & \text{otherwise} \end{cases} . \tag{2.9}$$

The three EoS relations are depicted in Fig. 2.1 (a). The graphs are supplemented by three unsuitable suggestions, that either induce negative densities due to $m^\rho < 0$, blur the density field due to vanishing $\partial\, m^\rho / \partial\, c$, or violate the equal mass distribution due to $\int m^\rho dc \neq 0.5$.

Both more advanced EoS suggestions employ a user specified thickness $\gamma^{\mathrm{m},\rho}$ of the transition region. Generally, the hyperbolic approach reaches the limit states only asymptotically. In this regard, an upper bound for the transition length is estimated numerically by $\gamma^{\mathrm{m},\rho} \leq 0.3$ to limit the error w.r.t. the pure phase below 0.1%, see Fig. 2.1 (b). Moreover, the linearized hyperbolic strategy $m^{\rho,2}$ requires $\gamma^{\mathrm{m},\rho} \leq 1.0$. Since small values are prone to generate artificial staircase effects in the employed Finite-Volume approximation, typical values for the transition length employed by the linearized hyperbolic scheme refer to $0.5 \leq \gamma^{\mathrm{m},\rho} \leq 0.8$.

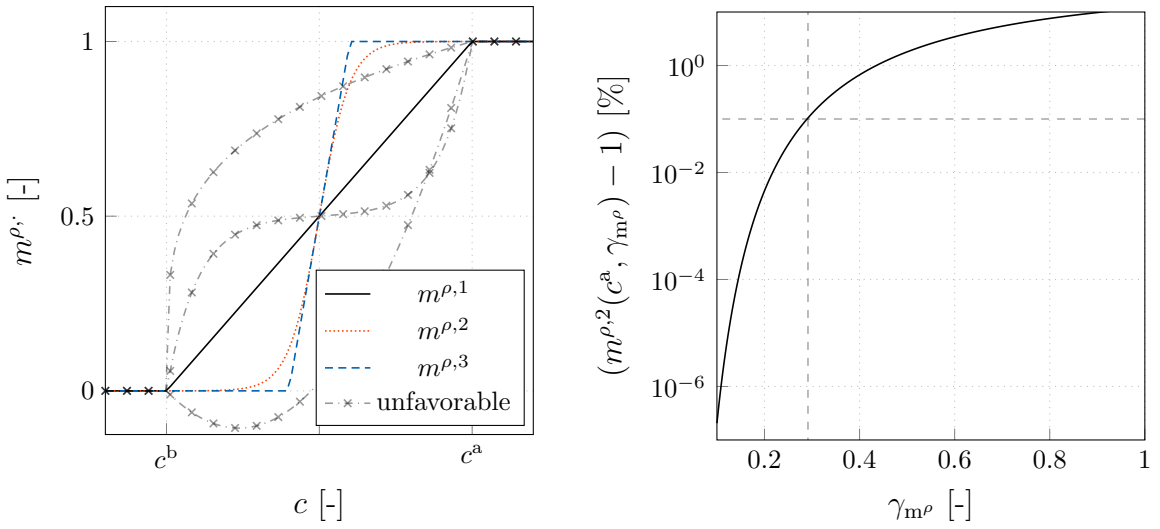

(a) (b)

Figure 2.1: Density interpolation: (a) Different linear and nonlinear density interpolations as well as (b) the relative error w.r.t. no mixture in the limit case $m^{\rho,2}(c^{\mathrm{a}}) \stackrel{!}{=} 1$ for a varying interface thickness $\gamma^{\mathrm{m},\rho}$.

Mass vs. Volume Conservation

Introducing the density interpolation (2.6) into the governing equations (2.4) for the specie densities and additionally considering constant bulk densities $\rho^{*\mathrm{a}}$ as well as $\rho^{*\mathrm{b}}$ yields

$$\frac{\partial m^\rho}{\partial c}\frac{\mathrm{d}c}{\mathrm{d}t^*} + \frac{\partial v_{\mathrm{k}}^*}{\partial x_{\mathrm{k}}^*} m^\rho = \frac{s^{*\rho,\mathrm{A}}}{\rho^{*\mathrm{a}}} \qquad \text{and} \qquad -\frac{\partial m^\rho}{\partial c}\frac{\mathrm{d}c}{\mathrm{d}t^*} + \frac{\partial v_{\mathrm{k}}^*}{\partial x_{\mathrm{k}}^*}\left[1 - m^\rho\right] = \frac{s^{*\rho,\mathrm{B}}}{\rho^{*\mathrm{b}}}\,. \tag{2.10}$$

Summing up both relations (2.10) allows to describe the velocity divergence as a function of the volume diffusion fluxes $j_{\mathrm{k}}^{*\mathrm{A}}$ and $j_{\mathrm{k}}^{*\mathrm{B}}$, viz.

$$\frac{\partial v_{\mathrm{k}}^*}{\partial x_{\mathrm{k}}^*} = \frac{s^{*\rho,\mathrm{A}}}{\rho^{*\mathrm{a}}} + \frac{s^{*\rho,\mathrm{B}}}{\rho^{*\mathrm{b}}} = \frac{\partial}{\partial x_{\mathrm{k}}^*}\left[j_{\mathrm{k}}^{*\mathrm{A}} + j_{\mathrm{k}}^{*\mathrm{B}}\right]. \tag{2.11}$$

Two options associated with different velocity definitions are conceivable: A mass conservative approach ($s^{*\rho,\mathrm{A}} = -s^{*\rho,\mathrm{B}}$) and a volume conservative approach ($j_{\mathrm{k}}^{*\mathrm{A}} = -j_{\mathrm{k}}^{*\mathrm{B}}$). Most authors opt for a volume conservative approach and employ a volume-averaged velocity field. In this case, mass is only globally conserved, provided that the interfacial regions do not intersect with the domain boundaries (Ding et al. [2007]), which might be difficult for, e.g., traveling waves. An advantage might refer to a convenient zero velocity divergence. On the contrary, assuming a mass conservative approach by means of $s^{*\rho} = s^{*\rho,\mathrm{A}} + s^{*\rho,\mathrm{B}} = 0$, one has to account for divergence effects of the observed mass-averaged velocity field.

In marine engineering applications, the interface is generally thin – particularly in the sharp interface limit, where both options are identical – and the preference is related to the employed numerical method. The present thesis refers to the mass conservative formulation. In that regard, the velocity divergence is expressed from the continuity equation

(2.3) using $s^{*\rho} = 0$

$$\frac{\partial v_{\mathrm{k}}^*}{\partial x_{\mathrm{k}}^*} = f^{\rho} \frac{\mathrm{d}\, c}{\mathrm{d}\, t^*} \qquad \text{with} \qquad f^{\rho} = \frac{-\rho^{*\Delta}}{\rho^*} \frac{\partial\, m^{\rho}}{\partial\, c} \,. \tag{2.12}$$

A divergence free velocity field is only obtained from $\mathrm{d}\, c/\mathrm{d}\, t^* = 0$, $\rho^{*\Delta} = 0$ or $\partial\, m^{\rho}/\partial\, c = 0$. Referring to the above given requirements on the EoS relation m^{ρ}, the latter might occur at the boundary zone of the phase transition regime, but is not valid in the center. As will be shown in the subsequent Sec. 2.1.4, $\mathrm{d}\, c/\mathrm{d}\, t^* = 0$ is inherently true for a classical VoF scheme but not necessarily true for other concentration transport models.

2.1.3 Viscosity Equation of State

Analogue to the density EoS $m^{\rho}(c)$ described in Sec. 2.1.2, the molecular viscosity employs a similar EoS $m^{\mu}(c)$

$$\mu^* = m^{\mu} \mu^{*\mathrm{a}} + [1 - m^{\mu}]\, \mu^{*\mathrm{b}} \qquad \text{or} \qquad \mu^* = m^{\mu} \left[\mu^{*\Delta}\right] + \mu^{*\mathrm{b}} \tag{2.13}$$

based on the bulk viscosities $\mu^{*\mathrm{a}}$ and $\mu^{*\mathrm{b}}$ (e.g., air and water), where $\mu^{*\Delta} = \mu^{*\mathrm{a}} - \mu^{*\mathrm{b}}$ denotes the difference of the bulk viscosities which are deemed constant. Basic considerations on the definition of $m^{\mu}(c)$ mentioned in Sec. 2.1.2 also apply here. Though this is not necessary, the present thesis assigns $m^{\mu} = m^{\rho}$.

2.1.4 Concentration Transport

Engineering two-phase flow simulations mostly refer to either of two interface-capturing methods (Ferziger and Peric [2012]), namely the Level-Set method (Osher and Sethian [1988]) and the Volume-of-Fluid (VoF) approach (Hirt and Nichols [1981]), which both reconstruct the free surface from an indicator or concentration function.

The Level-Set method introduced by Osher and Sethian [1988] or Sussman [1994] and Sussman et al. [1998] utilizes a signed distance function to characterize the interface by the zero-value iso surface. The continuous distribution of the signed distance simplifies a higher-order discretization of the related transport equation, and the geometry of the interface can be determined with improved accuracy. A drawback of the standard Level-Set method is that it does not guarantee mass conservation. Olsson and Kreiss [2005] as well as Olsson et al. [2007] proposed a mass conservative Level-Set approach based on a smeared Heaviside function which follows a similar idea as the diffuse interface approach herein. Two-phase applications of the VoF method suggested by Noh and Woodward [1976] and later refined by Hirt and Nichols [1981] usually employ a scalar volume concentration of a foreground phase to identify the fluid state of each cell. The method is conservative and capable to predict merging and rupturing of free surfaces. For immiscible fluids, any mixing of both phases is undesired but numerically difficult to avoid. Different strategies are conceivable to improve interface compression: Geometric reconstruction schemes and dedicated downwind-biased advection schemes, cf. Sec. 2.2.7. If surface tension effects are negligible, VoF models using dedicated advection schemes are deemed a good compromise between efficiency, accuracy and conservation properties. An alternative, much less common approach refers to diffuse interface models, often labeled Cahn-Hilliard (CH) models (Cahn and Hilliard [1958]). Here, the (ideally sharp) interface is replaced by a

(thin) layer where the fluids mix. The approach is able to mimic phase separation and thus promises resharpening features which are attractive for engineering simulations. Although the neglect of surface tension is an acceptable assumption in many engineering problems, it appears that the CH approach incorporates surface tension in a natural way and no additional model, e.g., the Continuum Method (Brackbill et al. [1992], Lafaurie et al. [1994]), is required.

All strategies identify the interface between the fluids from an indicator or concentration function and thereby facilitate the determination of material properties using the EoS described in Sec. 2.1.2. The evolution of the concentration c follows from an additional transport equation. The non-dimensionality of c underlines that different interpretations are permissible, referring, e.g., to a volume or mass concentration. Two options will be discussed herein, i.e. the classical Volume-of-Fluid (VoF) and the Cahn-Hilliard (CH) approach. The concentration field has been limited in terms of the maximum (c^{a}) and minimum (c^{b}) possible values in the previous subsection. These limits do not have to agree for both approaches. While the limits in the VoF case appear clear due to its association with the volume fraction covered by a foreground phase, the CH approach basically allows a variety of choices.

Volume-of-Fluid Method

The VoF approach associates the concentration c^V to the volume fraction of the total volume V^* occupied by the foreground fluid A, i.e. $c^V = V^{*\mathrm{A}}/V^*$. The respective volume concentration of the background fluid B follows from the compatibility relation that all concentrations should sum up to unity, viz. $V^{*\mathrm{B}}/V^* = (V^* - V^{*\mathrm{A}})/V^* = 1 - c^V$. As mentioned above, the general relation of ρ^* w.r.t. c, e.g. (2.6) and (2.7), suggests limit values of the concentration of $c^{\mathrm{a}} = 1$ and $c^{\mathrm{b}} = 0$.

Alternatively, the identification can be performed on mass concentration level. A definition of the mass concentration might read $V^{*\mathrm{A}}\rho^{*\mathrm{A}}/(V^*\rho^*) = c^{\mathrm{M}}$. The compatibility condition again yields a measure for the second mass concentration, viz. $V^{*\mathrm{B}}\rho^{*\mathrm{B}}/(V^*\rho^*) = (V^*\rho^* - V^{*\mathrm{A}}\rho^{*\mathrm{A}})/(V^*\rho^*) = 1 - c^{\mathrm{M}}$. Both definitions can be substituted by a compact form as $c^{\mathrm{M}} = c^{\mathrm{V}}\rho^{*a}/\rho^*$.

The superscript M/V is dropped in the remainder and the thesis simply adheres to the volume concentration. Moreover, it is assumed that the material derivative $\mathrm{d}c/\mathrm{d}t^*$ of the concentration vanishes in line with the immiscibility assumption of the two fluids which conserves the material properties, e.g. what once was water will never become air and vice versa, viz.

$$\frac{\partial c}{\partial t^*} + v^*_{\mathrm{k}}\frac{\partial c}{\partial x^*_{\mathrm{k}}} = 0\,. \tag{2.14}$$

As outlined above, the VoF relation (2.14) enforces a zero divergence of the velocity field, c.f. (2.12), which thus yields a numerically preferred, conservative formulation of the concentration transport

$$\frac{\partial c}{\partial t^*} + \frac{\partial\, v^*_{\mathrm{k}} c}{\partial x^*_{\mathrm{k}}} = 0. \tag{2.15}$$

It should be noted that the interpretation of c can be transferred to a discrete – e.g. Finite-Volume based – conception as originally proposed by Hirt and Nichols [1981]. Scaling down the control volume size towards the infinitesimal limit, a binary and thus sharp

representation is expected in the absence of any interfacial physics. This agrees with the immiscible fluids assumption which strictly speaking restricts the admissible concentration value to the limit values. In practice, however, (leading) errors in the numerical approximation yield intermediate values and the identification of the interface usually follows from $c = (c^{\mathrm{a}} + c^{\mathrm{b}})/2 = 0.5$.

Diffuse Interface Method

This paragraph briefly describes the diffusive interface model for isothermal two-phase flows as originally described in a landmark paper by Cahn and Hilliard [1958] and later elucidated by Jacqmin [1999]. The present approach refers to a classical CH-model and is based upon the free energy E^* of the interface Γ^* between two isothermal fluid phases

$$E^* = \int e^* \, \mathrm{d}\Gamma^* = \int \left[C^{*\mathrm{a}} \, b\,(c) + \frac{C^{*\mathrm{b}}}{2} \left| \frac{\partial\, c}{\partial\, x_{\mathrm{k}}^*} \right|^2 \right] \mathrm{d}\Gamma^* \,. \tag{2.16}$$

The coefficients $C^{*\mathrm{a}}$[Pa] and $C^{*\mathrm{b}}$[N] can be determined from the interface thickness γ^*[m] and surface tension $\sigma^{*\mathrm{a,b}}$[N/m] between the two fluids, as outlined below. The first term of e^* refers to the bulk energy density and aims to separate the fluids. The second term represents the gradient energy which widens the interface. To model separated (immiscible) fluids, a fourth-order polynomial, labeled "double well potential", is often used to describe the bulk energy density, i.e. $b\,(c) = (c - c^{\mathrm{a}})^2 \left(c - c^{\mathrm{b}}\right)^2$. To maintain compatibility with the VoF approach and to harmonize the implementation of both methods, the roots are chosen in line with the VoF method (cf. Fig. 2.2 (a)), viz.

$$b\,(c) = (c - 1)^2 \; c^2. \tag{2.17}$$

In equilibrium conditions, E^* is minimized w.r.t. c. Using variational calculus this relates to the root of a chemical potential ψ^* for the equilibrium state of plane interfaces (i.e. $\psi^* = 0$)

$$\psi^* = \frac{\delta\, E^*}{\delta\, c} = C^{*\mathrm{a}} \frac{\partial\, b}{\partial\, c} - C^{*\mathrm{b}} \frac{\partial^2 c}{\partial x_{\mathrm{k}}^{*2}} \qquad \rightarrow \qquad C^{*\mathrm{a}} \frac{\partial\, b}{\partial\, c} = C^{*\mathrm{b}} \frac{\mathrm{d}^2\, c}{\mathrm{d}\, n^{*2}} \,, \tag{2.18}$$

where $n^* = x_{\mathrm{k}}^* \, n_{\mathrm{k}}$ represents the interface normal direction. Substituting (2.17) into (2.18), one obtains a hyperbolic tangent concentration profile. This also renders a relation between the coefficients $C^{*\mathrm{a}}$ and $C^{*\mathrm{b}}$ as well as an interface thickness γ^*, viz.

$$c\,(n^*) = \frac{1}{2} \left[\tanh\left(\frac{2\, n^*}{\gamma^*} \right) + 1 \right] \qquad \text{with} \qquad \gamma^* = \sqrt{\frac{8\, C^{*\mathrm{b}}}{C^{*\mathrm{a}}}} \,. \tag{2.19}$$

Similarly, surface tension forces can be related to the concentration. Jacqmin [1999] outlined, that the convective rate of change of the free energy widens or compresses the interface. The term reads $\delta\, E^* / \delta\, c\,(v_{\mathrm{k}}^* \, \partial\, c / \partial\, x_{\mathrm{k}}^*) = \psi^* \, (v_{\mathrm{k}}^* \, \partial\, c / \partial\, x_{\mathrm{k}}^*)$ and should be balanced by the power $f_{\mathrm{k}}^{*\mathrm{ST}} \, v_{\mathrm{k}}^*$ of the surface tension force $f_{\mathrm{k}}^{*\mathrm{ST}}$. This immediately reveals the surface tension force used herein

$$f_{\mathrm{k}}^{*\mathrm{ST}} = \psi^* \, \frac{\partial\, c}{\partial\, x_{\mathrm{k}}^*} \,. \tag{2.20}$$

Some authors rearrange this definition into an apparent pressure term and a term involving the chemical potential gradient $f_{\mathrm{k}}^{*\mathrm{ST}} = \partial(\psi^* c)/\partial x_{\mathrm{k}}^* - c\,\partial\psi^*/\partial x_{\mathrm{k}}^*$, e.g. Song et al. [2019]. The strategy is also partially followed in this work, in which the apparent pressure is incorporated into a pressure correction scheme. Similarly, other authors employ the relation

$$\psi^* \frac{\partial c}{\partial x_{\mathrm{k}}^*} - \left[C^{*\mathrm{a}} \frac{\partial b}{\partial x_{\mathrm{k}}^*} + \frac{C^{*\mathrm{b}}}{2} \frac{\partial}{\partial x_{\mathrm{k}}^*} \left(\frac{\partial c}{\partial x_{\mathrm{k}}^*} \right)^2 \right] = -\frac{\partial}{\partial x_{\mathrm{k}}^*} \left[C^{*\mathrm{b}} \frac{\partial c}{\partial x_{\mathrm{k}}^*} \frac{\partial c}{\partial x_{\mathrm{k}}^*} \right] \tag{2.21}$$

to express the surface tension force by the divergence of a surface tension stress $-C^{*\mathrm{b}}\,(\partial c/\partial x_{\mathrm{k}}^*)(\partial c/\partial x_{\mathrm{k}}^*)$ and the gradient of a related apparent pressure $C^{*\mathrm{a}}\,b + 0.5\,C^{*\mathrm{b}}(\partial c/\partial x_{\mathrm{k}}^*)^2$, cf. Lowengrub and Truskinovsky [1998] and Abels et al. [2012]. Expression (2.21) associates vanishing surface tension effects with $C^{*\mathrm{b}} = 0$. Jacqmin [1999] also deduced a link between the surface tension and $C^{*\mathrm{a}}$, $C^{*\mathrm{b}}$ for a plane interface

$$\sigma^{*\mathrm{a,b}} = C^{*\mathrm{b}} \int_{-\infty}^{\infty} \left[\frac{\partial c}{\partial n^*} \right]^2 \mathrm{d}\, n^*. \tag{2.22}$$

Substituting (2.19) into (2.22) yields

$$\sigma^{*\mathrm{a,b}} = \sqrt{\frac{C^{*\mathrm{a}}\, C^{*\mathrm{b}}}{18}}. \tag{2.23}$$

Once γ^* and $\sigma^{*\mathrm{a,b}}$ have been chosen, both CH coefficients can be determined from the plane interface relations (2.19, 2.23)

$$C^{*\mathrm{a}} = 12 \frac{\sigma^{*\mathrm{a,b}}}{\gamma^*} \qquad \text{and} \qquad C^{*\mathrm{b}} = \frac{3}{2} \sigma^{*\mathrm{a,b}}\, \gamma^*. \tag{2.24}$$

Similar to the VoF method, the concentration field of the CH method is governed by an additional transport equation that models the mass transfer between the participating fluids. The approach of Lowengrub and Truskinovsky [1998] is adopted, which refers to the transport of a foreground fluid mass concentration $c^{\mathrm{M}} = c\,\rho^{*\mathrm{a}}/\rho^*$

$$\rho^* \frac{\mathrm{d}\, c^{\mathrm{M}}}{\mathrm{d}\, t^*} = \frac{\partial}{\partial x_{\mathrm{k}}^*} \left[M^{*\mathrm{M}} \frac{\partial \psi^*}{\partial x_{\mathrm{k}}^*} \right]. \tag{2.25}$$

Equation (2.25) employs a mass-based mobility parameter $M^{*\mathrm{M}}$ to control the strength of the phase separation process. Using the continuity relation (2.3) leads to

$$\frac{\partial\, \rho^*\, c^{\mathrm{M}}}{\partial\, t^*} + \frac{\partial\, \rho^*\, v_{\mathrm{k}}^*\, c^{\mathrm{M}}}{\partial\, x_{\mathrm{k}}^*} = \frac{\partial}{\partial\, x_{\mathrm{k}}^*} \left[M^{*\mathrm{M}} \frac{\partial\, \psi^*}{\partial\, x_{\mathrm{k}}^*} \right]. \tag{2.26}$$

The desired conservative volume concentration-based transport equation follows from (2.26) and $\rho^*\, c^{\mathrm{M}} = \rho^{*\mathrm{a}}\, c$ and $M^{*\mathrm{M}} = \rho^{*\mathrm{a}}\, M^*$

$$\frac{\partial c}{\partial t^*} + \frac{\partial\, v_{\mathrm{k}}^* c}{\partial x_{\mathrm{k}}^*} = \frac{\partial}{\partial x_{\mathrm{k}}^*} \left[M^* \frac{\partial \psi^*}{\partial x_{\mathrm{k}}^*} \right]. \tag{2.27}$$

Equation (2.27) agrees with the VoF counterpart (2.15) except for the non-zero r.h.s. of order four and is referred to as CH-VoF in the remainder. The mobility parameter

M^* of dimension $\mathrm{m^3s/kg}$ [$\hat{=}\ \nu/\mathrm{Pa}$] refers to a free parameter in line with its mass-based companion and will be explored for under-resolved flows in Sec. 2.2.9. The conservative CH-Eqn. (2.27) can be rewritten

$$\frac{\mathrm{d}\,c}{\mathrm{d}\,t^*} = \frac{\partial}{\partial\, x_\mathrm{k}^*}\left[M^*\frac{\partial\,\psi^*}{\partial\, x_\mathrm{k}^*}\right] - c\frac{\partial\, v_\mathrm{k}^*}{\partial\, x_\mathrm{k}^*} \tag{2.28}$$

Thereby Eqn. (2.28) helps to express the divergence relation (2.12)

$$\frac{\mathrm{d}\,c}{\mathrm{d}\,t^*} = \frac{1}{1+f^\rho\, c}\,\frac{\partial}{\partial x_\mathrm{k}^*}\left[M^*\frac{\partial\psi^*}{\partial x_\mathrm{k}^*}\right] \qquad \text{and} \qquad \frac{\partial v_\mathrm{k}^*}{\partial x_\mathrm{k}^*} = \frac{f^\rho}{1+f^\rho\, c}\,\frac{\partial}{\partial x_\mathrm{k}^*}\left[M^*\frac{\partial\psi^*}{\partial x_\mathrm{k}^*}\right], \tag{2.29}$$

where $\psi^* = C^{*\mathrm{a}}b' - C^{*\mathrm{b}}(\partial^2\, c/\partial x_\mathrm{k}^{*2})$ is non-zero along the interfacial region only. Note that f^ρ is virtually zero everywhere in combination with the nonlinear density EoS (2.12) in the sharp interface limit, which is why the divergence of the velocity field vanishes almost everywhere.

2.1.5 Conservation of Momentum

The conservation of linear momentum follows from the general conservation equation by employing $\varphi^* = \rho^* v_\mathrm{i}^*$ and $s^{*\rho\,\mathrm{v_i}} = \sigma_\mathrm{i}^* - f_\mathrm{i}^{*\mathrm{V}}$, where σ_i^* and $f_\mathrm{i}^{*\mathrm{V}}$ represent a generalized surface and volume force, respectively. For the applications herein they read

$$\sigma_\mathrm{i}^* = \frac{\partial\tau_{ik}^*}{\partial\, x_\mathrm{k}^*} = \frac{\partial}{\partial\, x_\mathrm{k}^*}\left[2\,\mu^*\, S_\mathrm{ik}^* - \left[\frac{2}{3}\,\mu^*\,\frac{\partial\, v_\mathrm{m}^*}{\partial\, x_\mathrm{m}^*} + p^*\right]\delta_\mathrm{ik}\right] \quad \text{and} \quad f_\mathrm{i}^{*\mathrm{V}} = \rho^*\, g_\mathrm{i}^* + \psi^*\frac{\partial\, c}{\partial\, x_\mathrm{i}^*}. \tag{2.30}$$

Here $S_\mathrm{ik}^* = 0.5\,(\partial\, v_\mathrm{i}^*/\partial\, x_\mathrm{k}^* + \partial\, v_\mathrm{k}^*/\partial\, x_\mathrm{i}^*)$, δ_ik and g_i^* represent the components of the strain rate tensor, the Kronecker delta as well as the gravitational acceleration vector. A symmetric strain tensor inherently satisfies the balance of angular momentum. An application of Eqn. (2.2) results in

$$\begin{aligned}\frac{\partial\,\rho^*\, v_\mathrm{i}^*}{\partial\, t^*} + \frac{\partial\, v_\mathrm{k}^*\,\rho^*\, v_\mathrm{i}^*}{\partial\, x_\mathrm{k}^*} = s^{*\rho\,\mathrm{v_i}} = \frac{\partial}{\partial\, x_\mathrm{k}^*}\left[2\,\mu^*\, S_\mathrm{ik}^* - \left[\frac{2}{3}\,\mu^*\frac{\partial\, v_\mathrm{l}^*}{\partial\, x_\mathrm{l}^*} + p^*\right]\delta_\mathrm{ik}\right] \\ + \rho^*\, g_\mathrm{i}^* + \psi^*\frac{\partial\, c}{\partial\, x_\mathrm{i}^*}\,.\end{aligned} \tag{2.31}$$

Application of the mass conservation allows the isolation of a substantial part of the left-hand side (l.h.s.) as well as a substitute for the velocity divergence (2.29) on the r.h.s., viz.

$$\begin{aligned}\rho^*\left[\frac{\partial\, v_\mathrm{i}^*}{\partial\, t^*} + v_\mathrm{k}^*\frac{\partial\, v_\mathrm{i}^*}{\partial\, x_\mathrm{k}^*}\right] = \frac{\partial}{\partial\, x_\mathrm{k}^*}\left[2\,\mu^*\, S_\mathrm{ik}^* - \left(\frac{2}{3}\,\mu^*\frac{f^\rho}{1+f^\rho\, c}\,\frac{\partial}{\partial x_\mathrm{l}^*}\left[M^*\frac{\partial\,\psi^*}{\partial\, x_\mathrm{l}^*}\right] + p^*\right)\delta_\mathrm{ik}\right] \\ + \rho^*\, g_\mathrm{i}^* + \psi^*\frac{\partial c}{\partial x_\mathrm{i}^*}.\end{aligned} \tag{2.32}$$

2.1.6 Turbulence Modeling

The applications in this work refer almost without exception to either fairly low ($\mathrm{Re} < 10^2$) or high ($\mathrm{Re} > 10^7$) Reynolds numbers. The high Reynolds number flows are characterized

by turbulent motion which span a wide range of spatial-temporal scales. The spatial resolution requirements for turbulent flows increases nonlinearly with the Reynolds number, and time resolved simulations are required even when the flow field is statistically steady. For the high Reynolds number, turbulent flow simulations, scale resolving Large/Detached Eddy Simulations (LES, DES) or even Direct Numerical Simulations (DNS) approaches are therefore deemed prohibitively expensive.

This thesis employs a classical, statistically averaged variable concept, which is also known as Reynolds-averaging (RA), cf. Reynolds [1895], of flow variables and is convenient for engineering applications. Thereby field quantities are conceptually subdivided into their mean value $\bar{\varphi}^*$ and a fluctuating, turbulent portion $\varphi^{*\prime}$, viz. $\varphi^* = \bar{\varphi}^* + \varphi^{*\prime}$, and attention is restricted to the governing equations for the statistically averaged field quantities. However, turbulent fluctuations of the concentration are neglected in this thesis and the bulk densities of the participating fluids are deemed constant in line with the hypothesis of Morkovin [1962], as usual in low speed and low (turbulent) Mach number flows. Moreover, the applications in this thesis exclusively correspond to statistically steady flows, which is why the influence of time is not further discussed.

Following the conventional incompressible Reynolds-averaging Navier-Stokes (RANS) concept, the averaging of the transport Eqn. (2.2) reads

$$\begin{aligned}\frac{\mathrm{D}\,\varphi^*}{\mathrm{D}\,t^*} = 0 \quad \overset{\mathrm{RA}}{\rightarrow} \quad \overline{\frac{\partial\,(\bar{\varphi}^* + \varphi^{*\prime})}{\partial\,t}} + \overline{\frac{\partial\,(\bar{v}_\mathrm{k}^* + v_\mathrm{k}^{*\prime})\,(\bar{\varphi}^* + \varphi^{*\prime})}{\partial\,x_\mathrm{k}^*}} &= \frac{\partial \bar{\varphi}^*}{\partial\,t^*} + \frac{\partial\,\bar{v}_\mathrm{k}^*\,\bar{\varphi}^*}{\partial\,x_\mathrm{k}^*} + \overline{\frac{\partial\,v_\mathrm{k}^{*\prime}\,\varphi^{*\prime}}{\partial\,x_\mathrm{k}^*}} \\ &= \frac{\mathrm{D}\,\bar{\varphi}^*}{\mathrm{D}\,t^*} + \overline{\frac{\partial\,v_\mathrm{k}^{*\prime}\,\varphi^{*\prime}}{\partial\,x_\mathrm{k}^*}}. \end{aligned} \tag{2.33}$$

All linear terms in the governing balance Eqn. (2.12), (2.28) as well as (2.32) are simply reformulated for the respective averaged quantities and only the nonlinear convective momentum transport ($\varphi' \rightarrow (\rho^*\,v_\mathrm{i}^*)' = \rho^*\,v_\mathrm{i}^{*\prime} \neq 0$) introduces additional unknowns. The latter form the Reynolds-Stress tensor that consists of six additional unknowns. In this thesis, they are modeled based on the incompressible Boussinesq Viscosity Model (BVM) that relates the deviatoric part of the Reynolds-stress tensor to the mean strain rate, viz.

$$\begin{aligned}-\frac{\partial}{\partial\,x_\mathrm{k}^*}\left[\rho^*\,\overline{v_\mathrm{i}^{\prime *}\,v_\mathrm{k}^{\prime *}}\right] = \frac{\partial}{\partial\,x_\mathrm{k}^*}\left[\mu^{*\mathrm{t}}\left(\frac{\partial\,\bar{v}_\mathrm{i}^*}{\partial\,x_\mathrm{k}^*} + \frac{\partial\,\bar{v}_\mathrm{k}^*}{\partial\,x_\mathrm{i}^*}\right) - p^{*\mathrm{t}}\delta_\mathrm{ik}\right] \quad &\text{with} \quad p^{*\mathrm{t}} = \frac{2}{3}\,\rho^*\,k^* \\ &\text{and} \quad k^* = \frac{1}{2}\overline{v_\mathrm{i}^{*\prime}\,v_\mathrm{i}^{*\prime}}, \end{aligned} \tag{2.34}$$

where $\mu^{*\mathrm{t}}$ and k^* refer to the turbulent (eddy) viscosity and kinetic energy (TKE), respectively. While the former extends the molecular viscosity to an effective viscosity, e.g. $\mu^{*\mathrm{eff}} = \mu^* + \mu^{*\mathrm{t}}$, the latter contributes to an effective pressure, viz. $p^{*\mathrm{eff}} = p^* + (2/3)\,\rho^*\,k^*$.

A turbulence closure model is needed to model $\mu^{*\mathrm{t}}$ and k^*. The work at hand employs two prominent two-equation closures, namely the $k^* - \varepsilon^*$ model proposed by Jones and Launder [1972] as well as a Wilcox [1998] $k^* - \omega^*$ model and related variations suggested by Menter [1994]. Supplementary, turbulent boundary-layer flows are investigated in an adjoint context using a comparably simple algebraic turbulence model based on Prandtl's mixing-length hypothesis, cf. Prandtl [1925]. In the remainder of the thesis, the over-bar notation used to denote averaged quantities is omitted to improve the readability.

Algebraic Turbulence Model

Zero-equation or algebraic models use exclusively algebraic closure relations. Their formulation is related to modelling zero pressure gradient boundary-layer flows under the exclusive influence of a single Reynolds shear-stress. Due to the focus on the shear-stress, the influence of the turbulent kinetic energy k^* in (2.34) as well as the isotropic part of the BVM are neglected. The approach followed in here is based on the mixing-length hypothesis of Prandtl [1925], e.g. $\mu^{*\mathrm{t}} = \rho^* \, (l^{*\mathrm{m}})^2 \, \mathrm{d}v_i^*/\mathrm{d}x_k^*$, which grounds on the definition of a mixing length $l^{*\mathrm{m}}$ and serves as basis for the universal Law of the Wall (LoW) and associated wall boundary conditions used for more complex wall bounded flow simulations, cf. Sec. 2.3.3.

The combination of the mixing length hypothesis with a Van Driest [1956] damping function f^{vD} allows a continuous and thus differentiable definition of the turbulent viscosity when traversing from the very near-wall region (where $\mu^{*\mathrm{t}}/\mu^* \to 0$), frequently labeled viscous sub layer, over the buffer layer into the logarithmic logarithmic layer, where $\mu^*/\mu^{*\mathrm{t}} \to 0$, viz.

$$\mu^{*\mathrm{t}} = \rho^* \, \left(l^{*\mathrm{m}} f^{\mathrm{vD}}\right)^2 \, \frac{\mathrm{d}\, v_{\mathrm{i}}^*}{\mathrm{d}\, x_{\mathrm{k}}^*} \, t_{\mathrm{i}} \, n_{\mathrm{k}} \quad \text{with} \quad l^{*\mathrm{m}} = \kappa \, w^* \quad \text{and} \quad f^{\mathrm{vD}} = 1 - \mathrm{e}^{\frac{-y^+}{A^+}} \, . \tag{2.35}$$

Here w^* and y^+ represent the dimensional and non-dimensional normal distance to the nearest wall, respectively. $A^+ = 27$ as well as $\kappa = 0.4$ refer to additional scalar model constants and t_{i} $[n_{\mathrm{k}}]$ account for the near-wall streamwise [normal] direction that will be elucidated in Sec. 2.3.3.

Two-Equation Turbulence Modeling

More sophisticated two-equation BVM frequently share the idea of expressing the turbulent viscosity via the product between the TKE and a turbulent time scale T^*, e.g.

$$\mu^{*\mathrm{t}} = \rho^* \, C^{\mu} k^* T^* = \rho^* \, C^{\mu} \, \frac{k^{*2}}{\varepsilon^*} = \rho^* \, \frac{k^*}{\omega^*} \tag{2.36}$$

where $T^* = k^*/\varepsilon^*$ and $T^* = 1/(C^{\mu}\omega^*)$ represent two popular choices to define a turbulent time scale using either the dissipation rate ε^* or the specific dissipation rate ω^* of the TKE, respectively. $C^{\mu} = 0.09$ refers to an empirical value. Note that (2.36) allows to express each quantity by the other, viz. $\varepsilon^* = C^{\mu} \, k^* \, \omega^*$.

The conservation of the turbulent quantities is generally ensured by employing (2.2) based on $\varphi^* = \rho^* \, q^*$ and $s^{*\mathrm{q}} = \mathrm{D}^{*\mathrm{q}} + \mathrm{P}^{*\mathrm{q}} - \mathrm{R}^{*\mathrm{q}}$ where q^* refers to the turbulent quantity of interest, e.g. $q^* = k^*$ $(q^* = \varepsilon^*)$ $[\, q^* = \omega^*]$ if the turbulent kinetic energy (TKE dissipation rate) [specific TKE dissipation rate] is considered and $\mathrm{D}^{*\mathrm{q}}$, $\mathrm{P}^{*\mathrm{q}}$ as well as $\mathrm{R}^{*\mathrm{q}}$ refer to its diffusion, production and reduction, respectively, viz.

$$\begin{aligned} \frac{\mathrm{D}\, q^*}{\mathrm{D}t^*} = \frac{\partial \rho^* \, q^*}{\partial t^*} + \frac{\partial \, v_{\mathrm{k}}^* \, \rho^* \, q^*}{\partial \, x_{\mathrm{k}}^*} = s^{*\mathrm{q}} \qquad \overset{(2.3)}{\rightarrow} \qquad & \frac{\mathrm{d}\, q^*}{\mathrm{d}\, t^*} = \rho^* \left[\frac{\partial \, q^*}{\partial t^*} + v_{\mathrm{k}}^* \frac{\partial \, q^*}{\partial \, x_{\mathrm{k}}^*} \right] \\ & = \mathrm{D}^{*\mathrm{q}} + \mathrm{P}^{*\mathrm{q}} - \mathrm{R}^{*\mathrm{q}} \, . \end{aligned} \tag{2.37}$$

The conservation of TKE k^* follows from

$$\mathrm{D}^{*\mathrm{k}} = \frac{\partial}{\partial \, x_{\mathrm{k}}^*} \left[\left(\mu^* + \frac{\mu^{*\mathrm{t}}}{C^{\mathrm{k},2}} \right) \frac{\partial \, k^*}{\partial \, x_{\mathrm{k}}^*} \right] , \quad \mathrm{P}^{*\mathrm{k}} = 2 \, \mu^{*\mathrm{t}} \, S_{\mathrm{ik}}^* \, S_{\mathrm{ik}}^* \quad \text{and} \quad \mathrm{R}^{*\mathrm{k}} = \rho^* \, C^{*k,1}, \tag{2.38}$$

where the closure specific abbreviations $C^{*k,1} = \varepsilon^*$, $C^{\mathrm{k},2} = \sigma^{k,\varepsilon}$ [$C^{*k,1} = C^{\mu}\, k^*\, \omega^*$, $C^{k,2} = \sigma^{k,\omega}$] are introduced that depend on the underlying $k^* - \varepsilon^*$ [$k^* - \omega^*$] model. Besides, the balance of TKE dissipation ε^* is modeled via

$$\mathrm{D}^{*\varepsilon} = \frac{\partial}{\partial\, x_{\mathrm{k}}^*}\left[\left(\mu^* + \frac{\mu^{*\mathrm{t}}}{\sigma^{\varepsilon}}\right)\frac{\partial\, \varepsilon^*}{\partial\, x_{\mathrm{k}}^*}\right], \quad \mathrm{P}^{*\varepsilon} = C^{\varepsilon,1}\frac{\varepsilon^*}{k^*}\,\mathrm{P}^{*\mathrm{k}} \quad \text{and} \quad \mathrm{R}^{*\varepsilon} = C^{\varepsilon,2}\,\rho^*\,\frac{\varepsilon^{*2}}{k^*}\,, \tag{2.39}$$

and the conservation of the specific TKE dissipation rate ω^* follows from

$$\mathrm{D}^{*\omega} = \frac{\partial}{\partial x_{\mathrm{k}}^*}\left[\left(\mu^* + \frac{\mu^{*\mathrm{t}}}{\sigma^{\omega}}\right)\frac{\partial\, \omega^*}{\partial\, x_{\mathrm{k}}^*}\right], \quad \mathrm{P}^{*\omega} = C^{\omega,1}\,\frac{\omega^*}{k^*}\,P^{*\mathrm{k}} \quad \text{and} \quad \mathrm{R}^{*\omega} = C^{\omega,2}\,\rho^*\,\omega^{*2}\,. \tag{2.40}$$

The model specific closure coefficients read:

$$q^* = \varepsilon^*: \qquad C^{\varepsilon,1} = 1.44 \qquad C^{\varepsilon,2} = 1.91 \qquad \sigma^{k,\varepsilon} = 1.0 \qquad \sigma^{\varepsilon} = 1.3 \tag{2.41}$$

$$q^* = \omega^*: \qquad C^{\omega,1} = \frac{5}{9} \qquad C^{\omega,2} = 0.075 \qquad \sigma^{k,\omega} = 2.0 \qquad \sigma^{\omega} = 2.0\,. \tag{2.42}$$

Both turbulence models have different pros and cons and therefore their specific range of application. Further details on both models can be found in Wilcox [1998]. The shear stress transport (SST) model developed by Menter [1994] and Menter et al. [2003] is also employed in this thesis. The model attempts to combine the advantages of the two models by distinguishing zonally between an inner (near-wall) $k^* - \omega^*$ formulation and an outer $k^* - \varepsilon^*$ formulation. The approach also accounts for the Bradshaw hypothesis to model non-equilibrium situations. The hypothesis refers to the observation of Bradshaw et al. [1967] that the Boussinesq hypothesis might fail in non-equilibrium, who inferred that this is due to the employed stress-strain relation rather than an inadequacy of the BVM concept. A detailed description of the complete model can be found in Menter [1994]. The model also gained attention for two-phase maritime applications, cf. Larsson et al. [2003], Zhang [2010], Gatin et al. [2015], Shen et al. [2015], Daum et al. [2017].

2.1.7 Two-Phase Reynolds-Averaged Navier-Stokes System

The governing equations of the previous sections are summarized in a compact form for the sake of clarity. They form the incompressible Cahn-Hilliard Volume-of-Fluid Reynolds-

Averaged Navier-Stokes (CH-VoF RANS) equations

$$\mathrm{R}^{*\mathrm{p}} = \frac{\partial v_\mathrm{k}^*}{\partial x_\mathrm{k}^*} - \frac{f^\rho}{1+f^\rho\,c}\frac{\partial}{\partial\, x_\mathrm{k}^*}\left[M^*\frac{\partial\,\psi^*}{\partial\, x_\mathrm{k}^*}\right] = 0 \tag{2.43}$$

$$\mathrm{R}^{*\mathrm{c}} = \frac{\mathrm{d}\,c}{\mathrm{d}\,t^*} - \frac{1}{1+f^\rho\,c}\frac{\partial}{\partial\, x_\mathrm{k}^*}\left[M^*\frac{\partial\,\psi^*}{\partial\, x_\mathrm{k}^*}\right] = 0 \tag{2.44}$$

$$\begin{aligned}\mathrm{R}_\mathrm{i}^{*\mathrm{v_i}} =& \rho^*\frac{\mathrm{d}\,v_\mathrm{i}^*}{\mathrm{d}\,t^*} + \frac{\partial}{\partial\, x_\mathrm{k}^*}\left[p^{*\mathrm{eff}}\,\delta_\mathrm{ij} - 2\,\mu^{*\mathrm{eff}}\,S_\mathrm{ij}^*\right] - \rho^*\,g_\mathrm{i}^* \\ &+ \frac{2}{3}\frac{\partial}{\partial\, x_\mathrm{i}^*}\left[\mu^*\,\frac{f^\rho}{1+f^\rho\,c}\frac{\partial}{\partial\, x_\mathrm{k}^*}\left[M^*\frac{\partial\,\psi^*}{\partial\, x_\mathrm{k}^*}\right]\right] - \psi^*\,\frac{\partial\,c}{\partial\, x_\mathrm{i}^*} = 0\end{aligned} \tag{2.45}$$

$$\mathrm{R}^{*\mathrm{k}} = \rho^*\frac{\mathrm{d}\,k^*}{\mathrm{d}\,t^*} - \frac{\partial}{\partial\, x_\mathrm{k}^*}\left[\left(\mu^* + \frac{\mu^{*\mathrm{t}}}{C^{k,2}}\right)\frac{\partial\,k^*}{\partial\, x_\mathrm{k}^*}\right] - P^{k^*} + \rho^*\,C^{k,1^*} = 0 \tag{2.46}$$

$$\mathrm{R}^{*\varepsilon} = \rho^*\frac{\mathrm{d}\,\varepsilon^*}{\mathrm{d}\,t^*} - \frac{\partial}{\partial\, x_\mathrm{k}^*}\left[\left(\mu^* + \frac{\mu^{*\mathrm{t}}}{\sigma^\varepsilon}\right)\frac{\partial\,\varepsilon^*}{\partial\, x_\mathrm{k}^*}\right] - C^{\varepsilon,1}\,\frac{\varepsilon^*}{k^*}\,P^{k^*} + C^{\varepsilon,2}\,\rho^*\,\frac{\varepsilon^{*2}}{k^*} = 0 \tag{2.47}$$

$$\mathrm{R}^{*\omega} = \rho^*\frac{\mathrm{d}\,\omega^*}{\mathrm{d}\,t^*} - \frac{\partial}{\partial\, x_\mathrm{k}^*}\left[\left(\mu^* + \frac{\mu^{*\mathrm{t}}}{\sigma^\omega}\right)\frac{\partial\,\omega^*}{\partial\, x_\mathrm{k}^*}\right] - C^{\omega,1}\,\frac{\omega^*}{k^*}\,\mathrm{P}^{*\mathrm{k}} + C^{\omega,2}\,\rho^*\,\omega^{*2} = 0\,. \tag{2.48}$$

where $\mu^{*\mathrm{eff}} = \mu^* + \mu^{*\mathrm{t}}$ and $p^{*\mathrm{eff}} = p^* + p^{*\mathrm{t}}$ represent effective viscosity and pressure, respectively. It should be noted that Eqns. (2.43)-(2.48) describe fully turbulent, statistically averaged ($p^{*\mathrm{t}} \to (2/3)\,\rho^*\,k^*$, $\mu^{*\mathrm{t}} \to \rho^*\,C^\mu\,k^{*2}/\varepsilon^*$) or laminar ($p^{*\mathrm{t}} \to 0$, $\mu^{*\mathrm{t}} \to 0$) flows. Laminar flow studies skip (2.46) as well as (2.47) or (2.48) and ignore $\mu^{*\mathrm{t}}$ and $p^{*\mathrm{t}}$. In conjunction with VoF, a solenoidal velocity field is recovered due to the neglect of diffusive mass transfer, viz. $\psi^*, M^* \to 0$.

Non-Dimensional Governing Equations support the discussion of influences and assist the verification. Assuming a spatially constant mobility M^*, the non-conservative concentration, mass and momentum equations read

$$\mathrm{R}^\mathrm{c} = \frac{1}{\mathrm{St}}\frac{\partial\,c}{\partial\,t} + v_\mathrm{k}\frac{\partial\,c}{\partial\,x_\mathrm{k}} = \frac{1}{\mathrm{Pe}}\frac{\partial^2}{\partial\,x_\mathrm{k}^2}\left[12\frac{\partial\,b}{\partial\,c} - \frac{3\,\mathrm{Ca}^2}{2}\frac{\partial^2\,c}{\partial\,x_\mathrm{m}^2}\right]\left(\frac{1}{1+f^\rho\,c}\right) \tag{2.49}$$

$$\mathrm{R}^\mathrm{p} = \frac{\partial\,v_\mathrm{k}}{\partial\,x_\mathrm{k}} = \frac{1}{\mathrm{Pe}}\frac{f^\rho}{1+f^\rho\,c}\frac{\partial^2\,\psi}{\partial\,x_\mathrm{k}^2} \tag{2.50}$$

$$\begin{aligned}\mathrm{R}_\mathrm{i}^{\mathrm{v_i}} = \rho\left[\frac{1}{\mathrm{St}}\frac{\partial\,v_\mathrm{i}}{\partial\,t} + v_\mathrm{k}\frac{\partial\,v_\mathrm{i}}{\partial\,x_\mathrm{k}}\right] + \frac{\partial}{\partial\,x_\mathrm{k}}\left[\mathrm{Eu}\,p^{\mathrm{eff}}\,\delta_\mathrm{ij} - \frac{2}{\mathrm{Re}}\,\mu^{\mathrm{eff}}\,S_\mathrm{ij}\right] - \frac{1}{\mathrm{Fn}^2}\,\rho\,g_\mathrm{i} \\ = \frac{1}{\mathrm{We}}\,\psi\,\frac{\partial c}{\partial x_\mathrm{i}} - \frac{2}{3}\frac{1}{\mathrm{Re}}\frac{\partial}{\partial\,x_\mathrm{i}}\left[\frac{\mu}{\mathrm{Pe}}\frac{f^\rho}{1+f^\rho\,c}\frac{\partial^2\,\psi}{\partial\,x_\mathrm{i}^2}\right],\end{aligned} \tag{2.51}$$

where contributions from interface resolving CH formulations are consistently placed on the r.h.s. . The Reynolds- and Froude number definitions always refer to the density $\rho^{*\mathrm{b}}$ and the viscosity $\mu^{*\mathrm{b}}$, unless it is stated otherwise. The momentum Eqn. (2.51) inheres two source terms which are not related to the velocity and display a well-known pairing in hydrostatic conditions ($\mathrm{Fn} \to 0$), e.g. $p + \rho\,g_\mathrm{k}\,x_\mathrm{k}$. Hence typical choices for the reference pressure are $\mathrm{P}^* = \rho^{*\mathrm{b}}\mathrm{V}^{*2}$ (i.e. $\mathrm{Eu} = 1$; hydrodynamics) or $\mathrm{P}^* = \rho^{*\mathrm{b}}\mathrm{G}^*\mathrm{L}^*$ (i.e. $\mathrm{Eu} = \mathrm{Fn}^{-2}$; hydrostatics). By way of example, the relationship between a dimensional quantity, a reference value and a non-dimensional quantity reads $v_\mathrm{i}^* = V^* v_\mathrm{i}$. The dimensionless

parameters are defined by

$$\mathrm{St} = \frac{\mathrm{T}^* \, \mathrm{V}^*}{\mathrm{L}^*} \text{ (Strouhal)} \quad \mathrm{Eu} = \frac{\mathrm{P}^*}{\rho^{*\mathrm{b}} \, \mathrm{V}^{*2}} \text{ (Euler)} \quad \mathrm{Re} = \frac{\rho^{*\mathrm{b}} \, \mathrm{V}^* \, \mathrm{L}^*}{\mu^{*\mathrm{b}}} \text{ (Reynolds)}$$
$$\mathrm{Fn} = \frac{\mathrm{V}^*}{\sqrt{G^* \, \mathrm{L}^*}} \text{ (Froude)} \quad \mathrm{Pe} = \frac{\mathrm{V}^* \, \mathrm{L}^* \, \gamma^*}{\mathrm{M}^* \, \sigma^{*\mathrm{a,b}}} \text{ (Peclet)} \quad \mathrm{Ca} = \frac{\gamma^*}{\mathrm{L}^*} \text{ (Cahn)} \qquad \text{and}$$
$$\mathrm{We} = \frac{\rho^{*\mathrm{b}} \, \mathrm{V}^{*2} \, \gamma^*}{\sigma^{*\mathrm{a,b}}} \text{ (Weber).} \tag{2.52}$$

The quantities utilized for the non-dimensionalization are given in Tab. 2.1. Local discrete similarity parameters employ $\mathrm{L}^* = |\Delta x_\mathrm{i}^*|$, $\mathrm{T}^* = \Delta \, t^*$ and $\mathrm{V}^* = |v_\mathrm{i}^*|$ etc.. It should be pointed out that the transition length γ^* can be small compared to a local grid spacing $\Delta \, x_\mathrm{i}^*$, resulting in small (discrete) Cahn numbers, which supports the neglect of the second term on the r.h.s. of (2.49) in an under-resolved sharp interface limit.

field quantity	x_i^*	v_i^*	g_i^*	p^*	t^*	ρ^*	μ^*	c	ψ^*
reference value	L^*	V^*	G^*	P^*	T^*	$\rho^{\mathrm{b}*}$	$\mu^{\mathrm{b}*}$	1	$\sigma^{*\mathrm{a,b}}/\gamma^*$

Table 2.1: Quantities for the non-dimensionalization of the governing equations.

2.1.8 Under-Resolved Interfacial Flow

This section briefly discusses means to model the mobility parameter M^* in flows where the interface thickness γ^* is hardly resolved by the numerical grid and the surface tension influence is neglected due to the coarse resolution of the interface. As outlined in Sec. 2.1.4, $C^{*\mathrm{b}} = 0$ in the absence of surface tension and the concentration equation (2.27) simplifies to

$$\frac{\partial \, c}{\partial \, t^*} + \frac{\partial \, v_\mathrm{k}^* \, c}{\partial x_\mathrm{k}^*} = \frac{\partial}{\partial \, x_\mathrm{k}^*} \left[M^* \frac{\partial}{\partial \, x_\mathrm{k}^*} \left(C^{*\mathrm{a}} \frac{\partial \, b}{\partial \, c} \right) \right] . \tag{2.53}$$

Using $\partial \, b / \partial x_\mathrm{k}^* = (\partial \, c / \partial x_\mathrm{k}^*) \, \partial \, b / \partial \, c$ together with the definition of the double well potential b from Eqn. (2.17) yields

$$\frac{\partial}{\partial \, x_\mathrm{k}^*} \left[M^* \frac{\partial}{\partial \, x_\mathrm{k}^*} \left(C^{*\mathrm{a}} \frac{\partial \, b}{\partial \, c} \right) \right] = \frac{\partial}{\partial \, x_\mathrm{k}^*} \left[\left(M^* \, C^{*\mathrm{a}} \, \frac{\partial^2 \, b}{\partial \, c^2} \right) \frac{\partial \, c}{\partial \, x_\mathrm{k}^*} \right] = \frac{\partial}{\partial x_\mathrm{k}^*} \left[\nu^{*\mathrm{c}} \, \frac{\partial \, c}{\partial \, x_\mathrm{k}^*} \right] , \tag{2.54}$$

where $\nu^{*\mathrm{c}} = C^{*\mathrm{a}} \, M^* b'' = 2 \, C^{*\mathrm{a}} \, M^* (6 \, c^2 - 6 \, c + 1)$ resembles a nonlinear apparent viscosity. Depending on the concentration value, (2.54) acts locally diffusive ($\nu^{*\mathrm{c}} \geq 0$) or compressive ($\nu^{*\mathrm{c}} < 0$). As outlined in Fig. 2.2, the apparent viscosity in (2.54) vanishes at $c = 0.5(1 \pm 1/\sqrt{3})$ and is negative over approximately 58% of the transition region. Aiming at a closure for the mobility parameter in under-resolved simulations, the mobility is separated into a physical and a modeled part, i.e.

$$M^* = M^{*\mathrm{phys}} + M^{*\mathrm{mod}}. \tag{2.55}$$

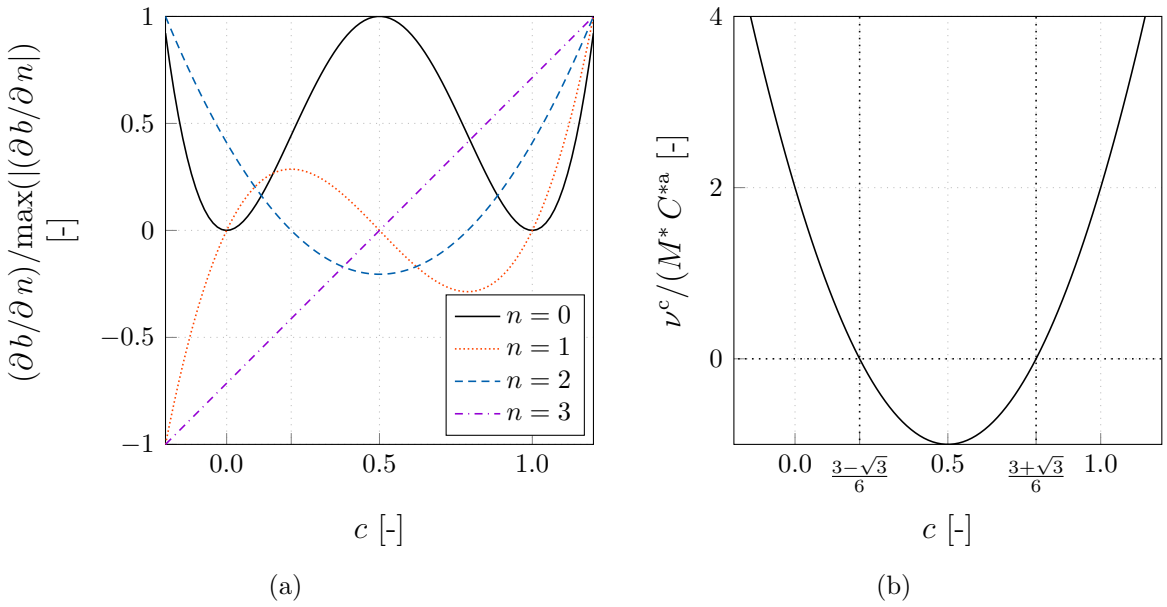

Figure 2.2: Double well potential: (a) Normalized fourth-order polynomial b as well as its first three (normalized) derivatives and (b) the apparent viscosity based b'' with indicated roots.

The physical part is usually assigned to fairly small values, e.g. $M^{*\mathrm{phys}} << 1 \times 10^{-15}\,\mathrm{m^3 s/kg}$, cf. Jacqmin [2000] or Magaletti et al. [2013]. Jacqmin [1999] reports that the mobility typically scales with the transition length $M^* \propto \gamma^{*n}$, where n varies between $1 \leq n \leq 2$. Moreover, a recent publication of Magaletti et al. [2013] suggests $n = 2$ and thus $\mathrm{Pe} \sim \mathrm{Ca}^{-1}$ or $\gamma^* \sim \sqrt{\sigma^{*\mathrm{a,b}} M^*/V^*}$. Most engineering settings are therefore unable to sufficiently resolve the transition length and the numerical contribution $M^{*\mathrm{mod}}$ is considered to be dominant. Sec. 2.2.9 proposes an approach to estimate the homogeneous mobility parameter based on leading errors of the approximation of the convective concentration transport.

Under-Resolved Equation System

A divergence-free primal velocity field is achieved if a) the VoF approach is used, b) both participating fluids feature the same bulk density or c) a nonlinear EoS is employed, cf. Eqn. (2.12). Hence, under-resolved CH-VoF studies consistently employ f^ρ or $We \to 0$ that further simplifies the primal conservation of mass, momentum and concentration. The resulting subsystem of equations forms the relevant set of PDEs which serves as the basis for all adjoint studies, viz.

$$\mathrm{R}^{*\mathrm{p}} = \frac{\partial v_\mathrm{k}^*}{\partial x_\mathrm{k}^*} = 0 \tag{2.56}$$

$$\mathrm{R}^{*\mathrm{c}} = \frac{\partial c}{\partial t^*} + \frac{\partial v_\mathrm{k}^* c}{\partial x_\mathrm{k}^*} - \frac{\partial}{\partial x_\mathrm{k}^*}\left[\nu^{*\mathrm{c}} \frac{\partial c}{\partial x_\mathrm{k}^*}\right] = 0 \tag{2.57}$$

$$\mathrm{R}_\mathrm{i}^{*\mathrm{v_i}} = \rho^*\left[\frac{\partial v_\mathrm{i}^*}{\partial t^*} + v_\mathrm{k}^* \frac{\partial v_\mathrm{i}^*}{\partial x_\mathrm{k}^*}\right] + \frac{\partial}{\partial x_\mathrm{k}^*}\left[p^{*\mathrm{eff}}\,\delta_\mathrm{ij} - 2\,\mu^{*\mathrm{eff}}\,S_\mathrm{ij}^*\right] - \rho^*\,g_\mathrm{i}^* = 0\,. \tag{2.58}$$

Their boundary conditions in Tab. 2.2 close (2.56)-(2.58). Constant values of the pressure gradient typically follow from hydrostatic contributions of an extended pressure, viz. $p^{*\mathrm{eff}} \rightarrow p^* + \rho^* \, x^*_\mathrm{k} \, g^*_\mathrm{k}$ and thus $\partial p^{*\mathrm{eff}} / \partial x^*_\mathrm{i} \rightarrow \partial p^* / \partial x^*_\mathrm{i} + \rho^* \, g^*_\mathrm{i}$. In all cases, inlet, symmetry and slip-wall boundaries are perpendicular to the gravity vector and no hydrostatic boundary contributions occur.

boundary type	v^*_i	p^*	c
inlet	$v^*_\mathrm{i} = v^{*\mathrm{in}}_\mathrm{i}$	$\frac{\partial p^*}{\partial n^*} = 0$	$c = c^\mathrm{in}$
outlet	$\frac{\partial v^*_\mathrm{i}}{\partial n^*} = 0$	$p^* = \rho^* \, g^*_\mathrm{k} \, x^*_\mathrm{k}$	$\frac{\partial c}{\partial n^*} = 0$
symmetry	$v^*_\mathrm{i} \, n_\mathrm{i} = 0, \; \frac{\partial \, v^*_\mathrm{i}}{\partial \, n^*} t_\mathrm{i}$	$\frac{\partial p^*}{\partial n^*} = 0$	$\frac{\partial c}{\partial n^*} = 0$
wall (slip)	$v^*_\mathrm{i} \, n_\mathrm{i} = 0, \; \frac{\partial \, v^*_\mathrm{i}}{\partial \, n^*} t_\mathrm{i}$	$\frac{\partial p^*}{\partial n^*} = 0$	$\frac{\partial c}{\partial n^*} = 0$
wall (no-slip)	$v^*_\mathrm{i} = v^{*\mathrm{w}}_\mathrm{i}$	$\frac{\partial p^*}{\partial n^*} = \rho^* \, g^*_\mathrm{k} \, n^*_\mathrm{k}$	$\frac{\partial c}{\partial n^*} = 0$

Table 2.2: Boundary conditions for the primal equations, where t_i [n_i] refer to the local boundary tangential [normal] vector.

2.2 Discrete Primal Two-Phase Flow

The closely coupled Eqns. (2.43)-(2.48) are discretized and approximated in space and time to obtain a numerical solution. This section describes the baseline procedure as introduced in Rung et al. [2009], briefly summarizes the discretization and outlines the numerical approximation based upon a second-order accurate Finite-Volume method (FVM).

All primal flow discretization concepts will be reused in Sec. 4.2 for the discretization of the adjoint flow. Mind that the primal/dual system shares the same Euclidean space and time horizon in possibly reversed mode. This motivates a more detailed insight to the discretization of individual expressions in Sec. 2.2 and 4.2 based on a generic transport equation.

2.2.1 Baseline Procedure

After spatial discretization of (2.43)-(2.48), a coupled system of NP equations is obtained after a suitable finite approximation for each field quantity $n^{\varphi} = [1, ..., \mathrm{N}^{\varphi}]$ with $\mathrm{N}^{\varphi} = 5$ [$\mathrm{N}^{\varphi} = 7$] if a laminar [turbulent] flow is considered. The discrete field variables are algorithmically linked via a sequential procedure, in which the individual equation systems are solved in a fixed sequence, cf. Alg. 1. The latter is implemented by means of *outer-iterations* that are performed until all –or only a selected subset of equations– are converged below a prescribed tolerance $\mathrm{R}^{*\varphi,\min}$ or a maximum number of outer iterations $\mathrm{N}^{\mathrm{out,max}}$ is reached.

Potential cross-coupling lags and employs values of the last outer iteration for the respective system variable(s), which also applies to the application of boundary conditions, cf. Sec. 2.2.8. The iterative solution procedure of the algebraic system of each outer iteration employs the Portable, Extensible Toolkit for Scientific Computation (PETSc, cf. Balay et al. [2019]) library that distinguishes between solvers for symmetric (e.g. Conjugate Gradient, CG) and asymmetric (e.g. Biconjugate Gradient, BiCG) matrices which in turn follow from the basic physical characteristics of the underlying equation. Their iterative counter refers to so-called *inner-iterations* and a termination criterion employs either a prescribed convergence tolerance or a maximum number of inner-iterations. The described sequential iteration technique is modularized and the algorithm changes only slightly if additional field equations are added. Several modules are implemented generically and invoked in a modular fashion in line with a generic transport equation, cf. Sec. 2.2.6.

The outer iterations are embedded in a time loop $n^{\mathrm{T}} = [1, ..., \mathrm{N}^{\mathrm{T}}]$ if the system is advanced in time, cf. Alg. 1. Hence, the simulated time horizon $t^* = [t^{\mathrm{start}*}, t^{\mathrm{end}*}]$ is discretized into NT equally distributed time slices $\Delta t^* = t^*(n^{\mathrm{T}})$ where $n^{\mathrm{T}} = [1, ..., \mathrm{N}^{\mathrm{T}}]$ represents the actual time step. The discrete time step size Δt^* usually follows from an a priori known, user defined value that fixes the total number of time steps NT. For steady applications, the time progresses in a pseudo-time and resembles an additional relaxation. Despite the steady nature of all applications in this thesis, the integration in pseudo-time is unavoidable for VoF procedures. The adjoint-based studied cost functionals are free of temporal expressions and their adjoint systems are linearized around the temporally converged primal state.

Algorithm 1: Schematic overview of the sequential primal solution procedure based on outer-iterations embedded in an optional temporal loop.

```
while n^T ≤ N^T do
    while (n^out ≤ N^out,max) or (R^*φ ≤ R^*φ,min) do
        approximate linearized momentum equations
        approximate pressure correction equation
        approximate linearized turbulence equations
        approximate linearized concentration equation
```

2.2.2 Spatial Discretization

The spatial domain is discretized by NP contiguous control volumes (CV) or cells of individual size $\Delta\Omega^{*\mathrm{P}}$, where $P \in [1, NP]$ denotes to the cell center. The control volumes are of arbitrary polyhedral shape and form an unstructured numerical grid. In principle, the control volumes could move and deform over time along the route of an Arbitrary Langrangian-Eulerian approach (Völkner et al. [2017], Schubert and Rung [2019], Schubert [2019], Luo-Theilen and Rung [2017, 2019], Theilen [2020]), which is however not meaningful for steady or quasi steady problems in the focus of this study. A collocated variable arrangement is employed, hence, all transported quantities are stored in the cell center. Variable values at other locations have to be reconstructed using the geometry and topology information outlined below.

Geometrical and Topological Relations

Next to the cell centered values of the dependent variables, the employed FV approximation requires the values at the center F of the faces between two control volumes. The numerical grid and the face-based data structure involves NF faces separating the cells from each other and the exterior domain. The definition of the face oriented vectors connecting the relevant positions reads

$$d_{\mathrm{i}}^{*\mathrm{F}} = \tilde{d}_{\mathrm{i}}^{*\mathrm{F}} + \bar{d}_{\mathrm{i}}^{*\mathrm{F}} \qquad \text{with} \qquad \tilde{d}_{\mathrm{i}}^{*\mathrm{F}} = x_{\mathrm{i}}^{*\mathrm{F}} x_{\mathrm{i}}^{*\mathrm{P}} \qquad \text{and} \qquad \bar{d}_{\mathrm{i}}^{*\mathrm{F}} = x_{\mathrm{i}}^{*\mathrm{NB}} x_{\mathrm{i}}^{*\mathrm{F}} \,. \tag{2.59}$$

The considered domain is enclosed by NΓ degenerated boundary cells as depicted Fig. 2.3 (b), which have no volume and a midpoint coordinate that coincides with the center of the adjacent face, viz. $\bar{d}_{\mathrm{i}}^{*\mathrm{F}} = 0 \rightarrow d_{\mathrm{i}}^{*\mathrm{B}} = \tilde{d}_{\mathrm{i}}^{*\mathrm{F}}$. Figure 2.3 (a) displays an arrangement of two adjacent interior control volumes and (b) the analogue boundary situation. The local approximations are constructed from values extracted at the cell center P, the face centers F separating the control volume around P from the neighboring control volumes and the centers of the neighboring control volume denoted by NB (or B). They employ the cell size $\Delta\Omega^{*\mathrm{P}}$ as well as the area $\Delta\Gamma^{*\mathrm{F}}$ and the respective area vector $\Delta\Gamma_{\mathrm{i}}^{*\mathrm{F}} = \Delta\Gamma^{*\mathrm{F}}\, n_{\mathrm{i}}$ of all cell adjacent faces where n_{i} represents the local face normal. Some crucial aspects for the approximation are: a) The connecting vector $d_{\mathrm{i}}^{*\mathrm{F}}$ between two face adjacent cell centers does not necessarily pierce through the face center F and sometimes does not even pierce through the face at all, b) the connecting vector $d_{\mathrm{i}}^{*\mathrm{F}}$ is not necessarily co-linear to the face normal n_{i} and c) faces are not necessarily centered between the center of the neighboring cell.

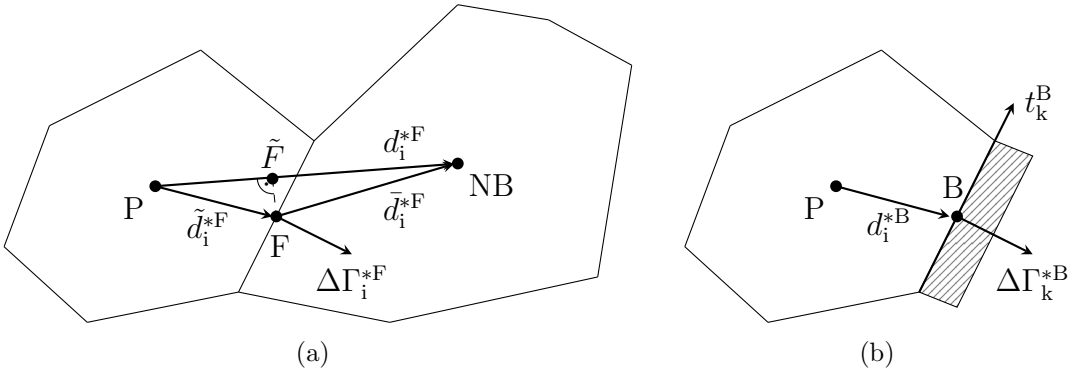

Figure 2.3: Schematic representation of a Finite-Volume arrangement (a) in the field and (b) along the boundary.

Reconstruction of Face Values

Face values are obtained by interpolating adjacent cell-centered values linearly to an intermediate location $\tilde{\mathrm{F}}$ along the connecting line. As displayed in Fig. 2.3 (a), the intermediate point is located perpendicular above the location of the face center F and the interpolation is second-order accurate, viz.

$$\varphi^{*\mathrm{F}} = \underbrace{\left(1-\lambda^{\mathrm{F}}\right)\varphi^{*\mathrm{P}} + \lambda^{\mathrm{F}}\,\varphi^{*\mathrm{NP}}}_{\text{interp.}} + \underbrace{\left(x_{\mathrm{i}}^{*\mathrm{F}} - x_{\mathrm{i}}^{*\tilde{\mathrm{F}}}\right)\left.\frac{\partial\,\varphi^{*}}{\partial\,x_{\mathrm{i}}^{*}}\right|^{\tilde{\mathrm{F}}}}_{\text{extrap.}} + O(h^{*\,2})$$

$$\text{with} \qquad \lambda^{\mathrm{F}} = \frac{\Delta\Gamma_{\mathrm{i}}^{*\mathrm{F}}\left(x_{\mathrm{i}}^{*\mathrm{F}} - x_{\mathrm{i}}^{*\mathrm{P}}\right)}{\left[\Delta\Gamma_{\mathrm{k}}^{*}\,d_{\mathrm{k}}^{*}\right]^{\mathrm{F}}}\,. \tag{2.60}$$

Since, this intermediate point $\tilde{\mathrm{F}}$ does not necessarily coincide with the face center F, a subsequent explicit non-orthogonality correction is optionally added. The explicit correction can be regarded as an extrapolation that ensures second-order accuracy even on unstructured grids. The required gradient in the intermediate point $\tilde{\mathrm{F}}$ follows from a second-order accurate linear interpolation

$$\left.\frac{\partial\,\varphi^{*}}{\partial\,x_{\mathrm{i}}^{*}}\right|^{\tilde{\mathrm{F}}} = \left(1-\lambda^{\mathrm{F}}\right)\left.\frac{\partial\,\varphi^{*}}{\partial\,x_{\mathrm{i}}^{*}}\right|^{\mathrm{P}} + \lambda^{\mathrm{F}}\left.\frac{\partial\,\varphi^{*}}{\partial\,x_{\mathrm{i}}^{*}}\right|^{\mathrm{NB}} + O(h^{*\,2})\,. \tag{2.61}$$

The majority of field variables and gradients are interpolated based on Eqn. (2.60).

Many flows considered in this work –and most engineering flows– are characterized by large Reynolds numbers and thus convection dominates. The interpolation of face values to approximate the convective fluxes is therefore crucial and will be discussed in greater detail below. Moreover, the interpolation of face values is especially relevant from a hybrid continuous/discrete adjoint perspective.

2.2.3 Spatial Approximation

The governing Eqns. (2.43)-(2.48) can be expressed in a generic residual expression for a conserved quantity φ^*, viz.

$$\mathrm{R}^{*\varphi} = \frac{\partial \varphi^*}{\partial t^*} + \frac{\partial v_\mathrm{k}^* \varphi^*}{\partial x_\mathrm{k}^*} - \frac{\partial}{\partial x_\mathrm{k}^*}\left(\mu^{*\varphi}\frac{\partial \varphi^*}{\partial x_\mathrm{k}^*}\right) - q^{*\varphi} = 0\,. \tag{2.62}$$

The individual terms of (2.62) refer to *temporal*, *convective* and *diffusive* transport as well as external *sources* from left to right, respectively. Mind that the last two contributions refer to $s^{*\varphi}$ in Eqn. (2.1). Using the FV method, the equation is treated in a weak form for each CV, e.g.

$$\begin{aligned}\int_{\Delta\Omega^*(P)} \mathrm{R}^{*\varphi}\mathrm{d}\Omega^* = &\int_{\Delta\Omega^*(P)} \left[\frac{\partial \varphi^*}{\partial t^*} - q^{*\varphi}\right]\mathrm{d}\Omega^* \\ &+ \oint_{\Gamma^*(\Delta\Omega^*(P))} \left[v_\mathrm{k}^*\varphi^* - \left(\mu^{*\varphi}\frac{\partial \varphi^*}{\partial x_\mathrm{k}^*}\right)\right] n_\mathrm{k}\,\mathrm{d}\Gamma^* = 0\,,\end{aligned} \tag{2.63}$$

where the Gauss-theorem has been applied to the integral over the convective and diffusive terms. Spatial approximations are required to determine volume and surface integrals, as well as the spatial gradients at the cell faces. All spatial integrals are approximated based on the second-order accurate mid-point rule as described below. Spatial gradients refer to second-order central differencing schemes (CDS).

Volume Integrals

The approximation of volume integrals by the midpoint rule yields:

$$\int_{\Delta\Omega^*(P)} \psi^*\,\mathrm{d}\Omega^* = [\psi^*\,\Delta\Omega^*]^\mathrm{P} + O(h^{*\,2}). \tag{2.64}$$

For the example of the generic transport equation (2.63), one obtains

$$\int_{\Delta\Omega^*(P)} \left[\frac{\partial \varphi^*}{\partial t^*} - q^{*\varphi}\right]\mathrm{d}\Omega^* = \left[\frac{\partial \varphi^*}{\partial t^*} - q^{*\varphi}\right]^\mathrm{P} \Delta\Omega^{*\mathrm{P}} + O(h^{*\,2})\,. \tag{2.65}$$

Surface Integrals

The closed surface integral is fractioned into integrals over the individual faces F between P and its neighbors NB. The face integrals are again approximated using the midpoint rule, viz.

$$\oint_{\Gamma^*(\Delta\Omega^*(\mathrm{P}))} \psi^*\,\mathrm{d}\Gamma_\mathrm{k}^* = \sum_{\mathrm{F(P)}} \int_{\Gamma^*(\mathrm{F})} \psi^*\,\mathrm{d}\Gamma_\mathrm{k}^* = \sum_{\mathrm{F(P)}} [\psi^*\,\Delta\Gamma_\mathrm{k}^*]^\mathrm{F} + O(h^{*\,2})\,. \tag{2.66}$$

For the example of the generic transport equation (2.63), one obtains

$$\oint_{\Gamma^*(\Delta\Omega^*(\mathrm{P}))} \left[v_\mathrm{k}^*\varphi^* - \left(\mu^{*\varphi}\frac{\partial \varphi^*}{\partial x_\mathrm{k}^*}\right)\right]\mathrm{d}\Gamma_\mathrm{k}^* = \sum_{\mathrm{F(P)}} \left[v_\mathrm{k}^*\varphi^* - \left(\mu^{*\varphi}\frac{\partial \varphi^*}{\partial x_\mathrm{k}^*}\right)\right]^\mathrm{F} \Delta\Gamma_k^{*\mathrm{F}} + O(h^{*\,2})\,. \tag{2.67}$$

The convective and diffusive fluxes have to be evaluated at the face center. The evaluation of the face centered viscosities (diffusivities) $\mu^{*\varphi}$ follows the procedure outlined in (2.60). The same procedure is employed to predict the face velocity v_{k}^{*} of the convective term. The face value of the transported variable φ^{*} is usually reconstructed with a specific rule on a case by case basis, cf. Sec. 2.2.6. The approximation of spatial gradients at the cell centers is outlined below and subsequently interpolated to the face center also using (2.60).

Spatial Gradients

The numerical procedure requires approximations of spatial gradients at various positions of the code. The discrete approximation of a gradient at the cell center is either computed from a fully conservative approach, using integration by parts –a.k.a. Gauss's Theorem–, or from a non-conservative –but more robust– weighted Least-Square method.

Gaussian Approaches follow from an integral formulation of spatial gradients using the second-order formulae (2.64) and (2.66), viz.

$$\left.\begin{array}{lll} (1) & \int_{\Delta\Omega^{*(\mathrm{P})}} \frac{\partial\varphi^{*}}{\partial x_{\mathrm{k}}^{*}}\,\mathrm{d}\Omega^{*} & \approx \left[\frac{\partial\varphi^{*}}{\partial x_{\mathrm{k}}^{*}}\,\Delta\Omega^{*}\right]^{\mathrm{P}} \\ (2) & \int_{\Delta\Omega^{*(\mathrm{P})}} \frac{\partial\varphi^{*}}{\partial x_{\mathrm{k}}^{*}}\,\mathrm{d}\Omega^{*} = \sum_{\mathrm{F(P)}} \int_{\Gamma^{*(\mathrm{F})}} \varphi^{*}\,\mathrm{d}\Gamma^{*} & \approx \sum_{\mathrm{F(P)}} \left[\varphi^{*}\,\Delta\Gamma_{\mathrm{k}}^{*}\right]^{\mathrm{F}} \end{array}\right\} \overset{1=\ddots}{\rightarrow}$$

$$\overset{\ddots=2}{\rightarrow} \qquad \left.\frac{\partial\varphi^{*}}{\partial x_{\mathrm{k}}^{*}}\right|^{\mathrm{P}} = \frac{1}{\Delta\Omega^{*\mathrm{P}}} \sum_{\mathrm{F(P)}} \left[\varphi^{*}\,\Delta\Gamma_{\mathrm{k}}^{*}\right]^{\mathrm{F}} + O(h^{*\,2})\,. \tag{2.68}$$

Face values are linearly interpolated from the adjacent cell-centered values, cf. Sec. 2.2.2.

Least-Squares Approaches follow from a first-order Taylor series expansion of the face-centered value for each face per cell, viz. $\varphi^{*\mathrm{NB}} \approx \varphi^{*\mathrm{P}} + d_{\mathrm{i}}^{*\mathrm{F}}[\partial\varphi^{*}/\partial x_{\mathrm{i}}^{*}]^{\mathrm{P}} + O(h^{*})$ that can be rearranged to compute for the desired gradient. The relation is over-determined since the number of adjacent cells always exceeds the dimension. Hence, a regression is applied based on the symmetric matrix D_{ik}^{*P} that regularizes the expression in the Least-Squares sense and agrees with second-order central differences on regular grids

$$\varphi^{*\mathrm{F}} \approx \varphi^{*\mathrm{P}} + d_{\mathrm{i}}^{*\mathrm{F}} \left.\frac{\partial\varphi^{*}}{\partial x_{\mathrm{i}}^{*}}\right|^{\mathrm{P}} \quad \rightarrow \quad \left.\frac{\partial\varphi^{*}}{\partial x_{\mathrm{i}}^{*}}\right|^{\mathrm{P}} \approx D_{\mathrm{ik}}^{*-1,P} \sum_{\mathrm{F(P)}} \left[\frac{d_{\mathrm{k}}^{*}}{||d_{\mathrm{m}}^{*}||}\right]^{\mathrm{F}} \left[\varphi^{\mathrm{F}^{*}} - \varphi^{\mathrm{P}^{*}}\right]$$

$$\text{with} \qquad D_{\mathrm{ki}}^{*P} = \sum_{\mathrm{F(P)}} \left[\frac{d_{\mathrm{k}}^{*}\,d_{\mathrm{i}}^{*}}{||d_{\mathrm{m}}^{*}||}\right]^{\mathrm{F}}\,. \tag{2.69}$$

Equation (2.69) is preconditioned by the reciprocal cell center distance $||d_{\mathrm{m}}^{*}||$ to counteract issues caused by distorted grids. The approach is not conservative but improves the accuracy and stability for unfavorable –e.g. highly skewed– cells.

2.2.4 Temporal Discretization

In general the temporal discretization involves variable time step sizes which are fed into implicit two and three time layer approximations. The applications of this thesis refer to steady problems. Time stepping is thus restricted to converge the primal (and adjoint)

flow field in pseudo-time to steady state using constant time step sizes. Necessary for the study of the discrete adjoint system, a continuous time integral is discretized as follows

$$\int \varphi^* \, \mathrm{d}t^* \qquad \overset{\text{discretize}}{\rightarrow} \qquad \sum_{\mathrm{T}} \int_{\Delta \mathrm{t}^*(\mathrm{T})} \varphi^* \, \mathrm{d}t^* \, . \tag{2.70}$$

2.2.5 Temporal Approximation

Temporal Integrals

Analogous to the spatial integration, time integrals employ the midpoint rule, viz.

$$\int_{\Delta \mathrm{t}^*(\mathrm{T})} \varphi^* \, \mathrm{d}t^* = \left[\varphi^* \, \Delta t^*\right]^{\mathrm{T}} + O(\Delta t^{*2}) \, . \tag{2.71}$$

The evaluation of time integrals solely occurs during the theoretical derivation of the adjoint system.

Temporal Derivatives

Temporal changes are approximated either by a first-order implicit backward Euler (BE) method or a second-order accurate implicit three time level approach (ITTL). The former discretizes a continuous quantity φ^* based on temporal information from the actual time instance (T) as well as the previous (T-1), viz.

$$\frac{\partial \, \varphi^*}{\partial \, t^*} = \frac{\varphi^{*\mathrm{T}} - \varphi^{*\mathrm{T}-1}}{\Delta t^*} + O(\Delta t^*) \tag{2.72}$$

and refers to the method of choice when the intermediate solution of a pseudo-transient simulation is not of interest, e.g. the total ship resistance in calm water where $\partial \, \varphi^* / \partial \, t^*|_{t^{*\mathrm{end}}} \rightarrow 0$. Such quasi-steady simulations frequently employ a non-constant, adaptive time step procedure that hooks up on the local Courant number distribution where typical values are between $0.2 \leq \mathrm{Co} \leq 0.4$. If the temporal behavior of the simulated system is relevant, an additional previous time step (T-2) is considered to the approximation. The resulting second-order accurate ITTL stencil reads

$$\frac{\partial \, \varphi^*}{\partial \, t^*} = \frac{3\varphi^{*\mathrm{T}} - 4 \, \varphi^{*\mathrm{T}-1} + \varphi^{*\mathrm{T}-2}}{2 \, \Delta t^*} + O(\Delta t^{*2}) \tag{2.73}$$

based on a constant time step size.

2.2.6 Algebraic Equation System

The employed FV approximation of (2.63) yields a discrete system of size $\mathrm{NP} \times \mathrm{NP}$, where each line corresponds to a particular CV-balance

$$A^{*\varphi,\mathrm{P}} \varphi^{*\mathrm{P}} - \sum_{\mathrm{NB(P)}} A^{*\varphi,\mathrm{NB}} \varphi^{*\mathrm{NB}} = S^{*\varphi,\mathrm{P}} \, . \tag{2.74}$$

Each discrete quantity also varies in time as well as per outer-iteration, e.g. strictly speaking the general quantity and source term reads $\varphi^{*\mathrm{P,M,T}}$ and $S^{*\varphi,\mathrm{P,M,T}}$ at the discrete

cell center P, the outer iteration M as well as the discrete time step T. For reasons of readability, the last two incremented indices (M,T) are suppressed if not needed, viz. $\varphi^{*\mathrm{P}} \equiv \varphi^{*\mathrm{P,M,T}}$ and $S^{*\varphi,\mathrm{P}} \equiv S^{*\varphi,\mathrm{P,M,T}}$. The preceding part of this section presents the discrete translation of the individual terms in (2.63) which contribute to (2.74).

The resulting system matrix should render two properties to support a stable solution process and physically realistic solutions. To maintain bounded solutions, one requires positive coefficients $A^{*P}, A^{*NB} > 0$. At the same time, the diagonal dominance of the matrix is required to support the iterative solution procedure, e.g. $A^{*P} \geq \sum A^{*NB}$. Once the discrete relation is assembled, an under-relaxation is employed

$$A^{*\varphi,\mathrm{P}} \rightarrow \frac{A^{*\varphi,\mathrm{P}}}{\omega^{\varphi}} \qquad \text{and} \qquad S^{*\varphi,\mathrm{P}} \leftarrow \frac{(1-\omega^{\varphi})\, A^{*\varphi,\mathrm{P}}}{\omega^{\varphi}} \tilde{\varphi}^{*\mathrm{P}}\,, \tag{2.75}$$

where $\tilde{\varphi}^{*\mathrm{P}}$ follows from the previous outer iteration. The relaxation supports the diagonal dominance. Related parameters are case specific, but typical values refer to, e.g., $\omega^{\mathrm{vi}} = 0.6$, $\omega^{\mathrm{k}} = 0.4$ and $\omega^{\mathrm{c}} = 0.4$. The approximation of the fluid dynamic pressure is tailored to employ $\omega^{\mathrm{p}} = 1.0$. Relaxation of the effective pressure is realized within the actual velocity-pressure coupling routine and usually employs $\tilde{\omega}^{\mathrm{p}} = 0.2$.

Transient Contributions using the implicit BE approximation (2.72) together with the integration rule (2.64) result in the following contributions to the main diagonal and the r.h.s.

$$A^{*\mathrm{P,T}} \leftarrow \frac{\Delta\, \Omega^{*\mathrm{P}}}{\Delta t^{*}} \qquad \text{and} \qquad S^{*\varphi,\mathrm{P,T}} \leftarrow \frac{\Delta\, \Omega^{*\mathrm{P}}}{\Delta t^{*}}\, \varphi^{*\mathrm{P,T-1}}\,. \tag{2.76}$$

Similarly, the second-order accurate ITTL (2.73) and the integration rule (2.64) return the following contributions to (2.74)

$$A^{*\varphi,\mathrm{P,T}} \leftarrow \frac{3}{2}\frac{\Delta\, \Omega^{*\mathrm{P}}}{\Delta t^{*}} \qquad \text{and} \qquad S^{*\varphi,\mathrm{P,T}} \leftarrow \frac{\Delta \Omega^{*\mathrm{P}}}{\Delta t^{*}} \left[2\,\varphi^{*\mathrm{P,T-1}} - \frac{1}{2}\varphi^{*\mathrm{P,T-2}}\right]. \tag{2.77}$$

Convective Contributions are characterized by their directional information transport. Following the approximation of surface integrals (2.67), the convective flux is fractioned into

$$\sum_{\mathrm{F(P)}} [v^{*}_{\mathrm{k}}\, \varphi^{*}\, \Delta\Gamma^{*}_{\mathrm{k}}]^{\mathrm{F}} = \sum_{\mathrm{F(P)}} \dot{V}^{*\mathrm{F}}\, \varphi^{*\mathrm{F}} \tag{2.78}$$

where $\dot{V}^{*\mathrm{F}} = v^{*\mathrm{F}}_{\mathrm{k}}\, \Delta\Gamma^{*\mathrm{F}}_{\mathrm{k}}$ represents the volume flux across the face F, and the velocity $v^{*\mathrm{F}}_{\mathrm{k}}$ is interpolated linearly in line with Eqn. (2.60). To account for the directional information transport, upwind biased formulae are employed to approximate $\varphi^{*\mathrm{F}}$. To this end, $\varphi^{*\mathrm{F}}$ is split into a sum of an implicit and an explicit term, e.g.

$$\sum_{\mathrm{F(P)}} [v^{*}_{\mathrm{k}}\, \varphi^{*}\, \Delta\Gamma^{*}_{\mathrm{k}}]^{\mathrm{F}} = \sum_{\mathrm{F(P)}} \dot{V}^{*\mathrm{F}}\, \varphi^{*\mathrm{F}} \rightarrow \sum_{\mathrm{F(P)}} \dot{V}^{*\mathrm{F}} \left[\varphi^{*\mathrm{U}} + \mathrm{DC}^{*\mathrm{C},\varphi,\mathrm{F}}\right]. \tag{2.79}$$

A simple, first-order accurate upwind differencing scheme (UDS) is implicitly considered to retain the desired properties of the matrix coefficients, viz.

$$\dot{V}^{*\mathrm{F}}\varphi^{*\mathrm{U}} := \max\left(\dot{V}^{*\mathrm{F}}, 0\right)\, \varphi^{*\mathrm{P}} + \min\left(\dot{V}^{*\mathrm{F}}, 0\right)\, \varphi^{*\mathrm{NB}}\,. \tag{2.80}$$

The second term of (2.79) refers to a convective (upper index C) Deferred Correction (DC) contribution, which is explicitly considered on the r.h.s and computed from values of the previous iteration. The latter optionally accounts for high-order contributions as a supplement to the UDS part, viz.

$$\dot{V}^{*\mathrm{F}}\,\mathrm{DC}^{*\mathrm{C},\varphi,\mathrm{F}} = \frac{\dot{V}^{*\mathrm{F}}}{4}\left[(1+\kappa)\left(\varphi^{*\mathrm{D}}-\varphi^{*\mathrm{U}}\right)+(1-\kappa)\left(\varphi^{*\mathrm{U}}-\varphi^{*\mathrm{UU}}\right)\right]. \tag{2.81}$$

Equation (2.81) offers a generic way to account for various baseline convection schemes based on the constant $\kappa \in [-1,1]$. The preferred choice in this thesis is the third-order Quadratic Upwind Interpolation of Convective Kinematics (QUICK) scheme of Leonard [1979] which refers to $\kappa = 0.5$. Other popular schemes supported by (2.81) are the central differencing (CDS, $\kappa = 1$) and linear upwind differencing (LUDS, $\kappa = -1$) schemes. On unstructured grids, the $\varphi^{*\mathrm{UU}}$ value is not explicitly available and reconstructed with second-order accurate central differences, viz. $\varphi^{*\mathrm{UU}} \approx \varphi^{*\mathrm{D}} - 2\,d_{\mathrm{i}}^{*\mathrm{F}}(\partial\,\varphi^{*\mathrm{U}}/\partial\,x_{\mathrm{i}}^{*})$, cf. Fig. 2.4. Though this restricts the attainable reconstruction accuracy, it does not additionally harm the spatial order of accuracy for this term due to the upstream second-order accurate numerical integration.

In line with *Godunov's Theorem*, only first-order schemes can be monotone (bounded) and avoid the generation of new extreme values, cf. Godunov [1954, 1959]. Therefore nonlinear elements are introduced to (2.81) to avoid the generation and amplification of extremes. Van Leer [1979] presented a popular Monotonic Upstream Scheme for Conservation Laws (MUSCL) that scrambles the nonlinearities into a damping function ψ based on a local sensor r, e.g.

$$\dot{V}^{*\mathrm{F}}\,\mathrm{DC}^{*\mathrm{C},\varphi,\mathrm{F}} = \frac{\dot{V}^{*\mathrm{F}}}{4}\left[(1+\kappa)\left(\varphi^{*\mathrm{D}}-\varphi^{*\mathrm{U}}\right)\psi\left(r\right)+(1-\kappa)\left(\varphi^{*\mathrm{U}}-\varphi^{*\mathrm{UU}}\right)\psi\left(\frac{1}{r}\right)\right]$$
$$\text{and} \qquad r = \frac{\varphi^{*\mathrm{U}}-\varphi^{*\mathrm{UU}}}{\varphi^{*\mathrm{D}}-\varphi^{*\mathrm{U}}}. \tag{2.82}$$

Harten [1997] motivated the so-called total variation diminishing (TVD) scheme which accounts for monotonicity preservation by locally decreasing the approximation order. Many other approaches exist that, e.g., restrict ψ, c.f. Lien and Leschziner [1994a,b]. Related discussions frequently employ a Normalized Variable Diagramm (NVD), and the implementation of dedicated NVD schemes follows the same strategy compared to the TVD methods. A major contribution of this work is concerned with adjoint NVD schemes dedicated to the convective transport of the concentration c in conjunction with VoF approaches and are considered separately in Sec. 2.2.7. A detailed overview of primal / adjoint TVD schemes can be found in Stück [2012]. The nonlinear TVD/NVD functions are particularly unpleasant w.r.t. their corresponding adjoint operators as they produce unfavorable derivatives. Hence, the function ψ is usually kept frozen and thus not considered in the adjoint calculus, cf. Stück [2012], Stück and Rung [2013], Kröger [2016], Kröger et al. [2018], Manzke [2018].

The convective contributions to (2.74) read:

$$A^{*\varphi,\mathrm{P}} \leftarrow \sum_{\mathrm{F(P)}} -\min\left(\dot{V}^{*\mathrm{F}},0\right), \quad A^{*\varphi,\mathrm{NB}} \leftarrow -\min\left(\dot{V}^{*\mathrm{F}},0\right), \quad S^{*\varphi,\mathrm{P}} \leftarrow -\sum_{\mathrm{F(P)}} \dot{V}^{*\mathrm{F}}\mathrm{DC}^{*\mathrm{C},\varphi,\mathrm{F}}. \tag{2.83}$$

A word of caution should be noted regarding the main diagonal contribution. The latter employs $\sum_{F(P)} -\min(\dot{V}^{*\mathrm{F}}, 0) = \sum_{F(P)} \max(\dot{V}^{*\mathrm{F}}, 0)$ which is strictly speaking only true for a converged (mass conservative) state, but supports the dominance of the matrix diagonal and the iterative procedure. Mind that the volume flux is a function of the velocity, and a Picard linearization is employed within the iterative solution procedure, cf. Alg. 1. For the transport of density-weighted field quantities, e.g. the linear momentum $\varphi_{\mathrm{i}}^{*} = \rho^{*}\, v_{\mathrm{i}}^{*}$, the volume flux is replaced by a mass flux, viz. $\dot{V}^{*\mathrm{F}} \rightarrow \dot{m}^{*\mathrm{F}} = [\rho^{*}\, v_{\mathrm{k}}^{*}\, \Delta\Gamma_{\mathrm{k}}^{*}]^{\mathrm{F}}$.

Diffusive Contributions follow from an unbiased information transport. The discrete representation of the diffusive flux in (2.67) is also fractioned into an implicit part and an explicit deferred correction

$$\sum_{\mathrm{F(P)}} \left[\mu^{*\varphi} \frac{\partial\, \varphi^{*}}{\partial\, x_{\mathrm{k}}^{*}}\, \Delta\Gamma_{\mathrm{k}}^{*} \right]^{\mathrm{F}} \rightarrow \sum_{\mathrm{F(P)}} [\mu^{*\varphi}\, \Delta\Gamma^{*}]^{\mathrm{F}} \left[\frac{\varphi^{*\mathrm{NB}} - \varphi^{*\mathrm{P}}}{||d_{\mathrm{k}}^{\mathrm{F}^{*}}||\, \alpha^{\mathrm{n}}} + \mathrm{DC}^{*\mathrm{D},\varphi,\mathrm{F}} \right] , \tag{2.84}$$

where $\mathrm{DC}^{*\mathrm{D},\varphi,\mathrm{F}}$ represents a diffusive (superscript D) deferred correction contribution. The coefficient $\alpha = [d_{\mathrm{i}}\, n_{\mathrm{i}} / ||d_{\mathrm{k}}^{*}||]^{\mathrm{F}}$ optionally accounts for unfavorable face-to-normal arrangements and employed exponents refer to $\mathrm{n} = 1$ for the assembly of the pressure correction equation and $\mathrm{n} = 0$ in all other cases. A CDS resembling, implicit approximation accounts for the unbiased information transport, viz. $\partial\, \varphi^{*\mathrm{F}} / \partial\, x_{\mathrm{i}}^{*} \approx (\varphi^{*\mathrm{NP}} - \varphi^{*\mathrm{P}}) / ||d_{\mathrm{k}}^{\mathrm{F}^{*}}||$, supports the diagonal dominance and maintains positive coefficients. The explicit DC contribution accounts for possible non-orthogonality

$$\mathrm{DC}^{*\mathrm{D},\varphi,\mathrm{F}} = \left[\mu^{*\varphi} \frac{\Delta\Gamma^{*}}{||d_{\mathrm{i}}^{*}||} \frac{\partial\, \varphi^{*}}{\partial\, x_{\mathrm{k}}^{*}} \left(\frac{d_{\mathrm{k}}^{*}}{\alpha^{\mathrm{n}}} - n_{\mathrm{k}}\, ||d_{\mathrm{i}}^{*}|| \right) \right]^{\mathrm{F}} , \tag{2.85}$$

where the face gradient is determined by (2.60). The explicit $\mathrm{DC}^{*\mathrm{D},\varphi,\mathrm{F}}$ contribution tends to zero if the computational grid is perfectly orthogonal ($[d_{\mathrm{k}}^{*} / ||d_{\mathrm{i}}^{*}|| - n_{\mathrm{k}}]^{\mathrm{F}} \rightarrow 0$). The diffusive contribution to (2.74) reads

$$A^{*\varphi,\mathrm{P}} \leftarrow \sum_{\mathrm{F(P)}} \left[\mu^{*\varphi} \frac{\Delta\Gamma^{*}}{||d_{\mathrm{k}}^{*}|| \alpha^{\mathrm{n}}} \right]^{\mathrm{F}} , \quad A^{*\varphi,\mathrm{NB}} \leftarrow \left[\mu^{*\varphi} \frac{\Delta\Gamma^{*}}{||d_{\mathrm{k}}^{*}|| \alpha^{\mathrm{n}}} \right]^{*\mathrm{F}} \quad \text{and} \quad S^{*\varphi,\mathrm{P}} \leftarrow -\sum_{\mathrm{F(P)}} \mathrm{DC}^{*\mathrm{D},\varphi,\mathrm{F}} . \tag{2.86}$$

Sources and Sinks are considered as explicit contributions to the r.h.s. using the midpoint rule (2.64)

$$S^{*\varphi,\mathrm{P}} \leftarrow [q^{*\varphi}\, \Delta\Omega^{*}]^{\mathrm{P}} . \tag{2.87}$$

The explicit contributions to the r.h.s. differ strongly from the respective conserved quantities, e.g. $q^{*\mathrm{v_i},\mathrm{P}} = f_{\mathrm{i}}^{*\mathrm{ST},\mathrm{P}}$ if surface tension contributions are added to the momentum balance.

Pressure Determination

The pressure-velocity coupling follows a modified version of the Semi-Implicit Method for Pressure-Linked Equations (SIMPLE) pressure correction algorithm, originally proposed

by Patankar and Spalding [1972]. At first, a velocity distribution $\tilde{v}_\mathrm{i}^*$ is determined from the discretized momentum equation using an estimated pressure $\tilde{p}^*$. Usually, these velocities do not satisfy the discrete continuity equation and the resulting discrete continuity defect of each CV, e.g. $\sum_{\mathrm{F(P)}}[\tilde{v}_\mathrm{i}^*\Gamma_\mathrm{i}^*]^\mathrm{F} - [s^{*\mathrm{p}}\Delta\Omega^*]^\mathrm{P}$, is used to compute a correction of the estimated pressure in an iterative procedure, e.g. $\tilde{p}^{*P} \leftarrow p'^{*P}$. A combination of the discretized momentum (in reduced form) and continuity yields the inherently discrete pressure correction equation, cf. Ferziger and Peric [2012], which shares features with the pressure Poisson equation, cf. Chorin [1968]. Analogous to Yakubov et al. [2015], the pressure correction scheme employed herein accounts for velocity divergence sources that are of relevance for the CH-VoF model, cf. (2.43). The algebraic pressure correction scheme features only discretized diffusive fluxes and r.h.s contributions. The former are assembled in line with Eqn. (2.84) using $\mu^{*\mathrm{p,P}} = [\Delta\Omega^*/A^{*\mathrm{v_i}}]^\mathrm{P}$ and respective face values follow from a linear interpolation. The r.h.s. inheres contributions from the non-solenoidal velocity field as well as further CH-related sources, viz.

$$S^{*\mathrm{p}',\mathrm{P}} \leftarrow \left[\frac{\mathrm{d}c}{\mathrm{d}t^*}\Delta\Omega^*\right]^\mathrm{P} + \sum_{\mathrm{F(P)}}\left[\tilde{v}_\mathrm{i}^*\Delta\Gamma_\mathrm{i}^*\right]^\mathrm{F} . \tag{2.88}$$

Mind that the first r.h.s. contribution a priori vanishes for the VoF scheme and the converged pressure field should globally support zero velocity divergence. The pressure update involves an under-relaxation $\tilde{p}^{*P} \leftarrow \tilde{\omega}^{\mathrm{p}'}p'^{*P}$ that usually employs $\tilde{\omega}^{\mathrm{p}'} = 0.2$. The odd-even decoupling problem of the co-located variable arrangement is suppressed with a fourth-order artificial dissipation term on the r.h.s of the continuity equation along a route outlined by Rhie and Chow [1983]. The latter also considers contributions from gravity and surface tension in order to strengthen the iterative procedure.

2.2.7 Compressive Interface Capturing Schemes

The majority of practical applications employ a VoF-based interface capturing scheme. In conjunction with two-phase flows, the method poses for predicting sharp interfaces. Different strategies are conceivable to improve interface compression: Geometric reconstruction schemes, e.g. SLIC (Noh and Woodward [1976]), PLIC (Hirt and Nichols [1981]) or LVIRA (Pilliod Jr. and Puckett [2004]), and dedicated downwind-biased advection schemes, e.g. CICSAM (Ubbink and Issa [1999]), HRIC (Muzaferija and Peric [1999]) or BRICS (Wackers et al. [2011]). Geometric reconstruction schemes are afflicted with a considerable algorithmic complexity which reduces their popularity. Dedicated advection schemes are slightly heuristic but fairly simple to implement. They maintain an approximately sharp interface subject to sufficiently small time steps. On the downside, they require transient implicit simulations even for steady state problems, e.g., the calm-water resistance of steady cruising ships. To further improve the interface compression, some authors have proposed to add an artificial compression or anti-diffusion term, e.g., So et al. [2011], Heyns et al. [2013]. These methods rely on heuristic compression factors and improve the compressiveness at the expense of a reduced numerical stability. As outlined at the beginning of Sec. 2.1.4, VoF models using dedicated advection schemes are considered to offer a reasonable compromise between efficiency, accuracy and conservation properties.

A classical starting point for the derivation of prominent interface capturing schemes is the NVD, first proposed by Leonard [1991]. In line with Fig. 2.4, the general challenge

reads: How to interpolate the (on cell level) discrete non-dimensional field value (e.g. $c^{\mathrm{U}} = 1$ and $c^{\mathrm{D}} = 0$) on the face F in between, so that during the numerical simulation a) the transported field quantity is bounded and b) the interface remains sharp. While a) results in the Convective Boundedness Criterion (CBC) (e.g. $c^{\mathrm{U}} \geq c^{\mathrm{F}} \geq c^{\mathrm{D}}$), b) is a matter of the diffusive/compressive character of the underlying numerical approximation. Thus, a normalization based on all relevant cell quantities around F is introduced, viz.

$$c_{\mathrm{n}} = \frac{c - c^{\mathrm{UU}}}{c^{\mathrm{D}} - c^{\mathrm{UU}}} \qquad \rightarrow \qquad c_{\mathrm{n}}^{\mathrm{D}} = 1, \qquad c_{\mathrm{n}}^{\mathrm{UU}} = 0 \qquad \text{and} \qquad c_{\mathrm{n}}^{\mathrm{D}} \geq c_{\mathrm{n}}^{\mathrm{U}} \geq c_{\mathrm{n}}^{\mathrm{UU}} \,. \tag{2.89}$$

A mirrored strategy will be used later for the normalization of the adjoint face value $\hat{c}_{\mathrm{n}}$ around the face F. The general dependence of $c^{\mathrm{F}}(c^{\mathrm{UU}}, c^{\mathrm{U}}, c^{\mathrm{D}})$ reduces to $c_{\mathrm{n}}^{\mathrm{F}}(c_{\mathrm{n}}^{\mathrm{U}})$ in the normalized setting for the primal variable. Explicit implementations inhere an additional dependence on the face Courant number Co^{F}, cf. Leonard [1991]. The relation is depicted in Fig. 2.5 for three bounded baseline schemes, e.g. Upwind (UDS), Central (CDS) and Downwind (DDS) Differencing Scheme. The regime between CDS and UDS [DDS] is prone to be diffusive [compressive]. Thus, modern interface capturing schemes try to stay as long as possible in the compressive regime and fall back to an upwind biased scheme when the discrete local setting is insufficient. Two prominent examples for such compressive approximations refer to (a) the High Resolution Interface Capturing Scheme (HRIC) of Muzaferija and Peric [1999] and (b) the Compressive Interface Capturing Scheme for Arbitrary Meshes (CICSAM) of Ubbink and Issa [1999] which are investigated in the upcoming passage.

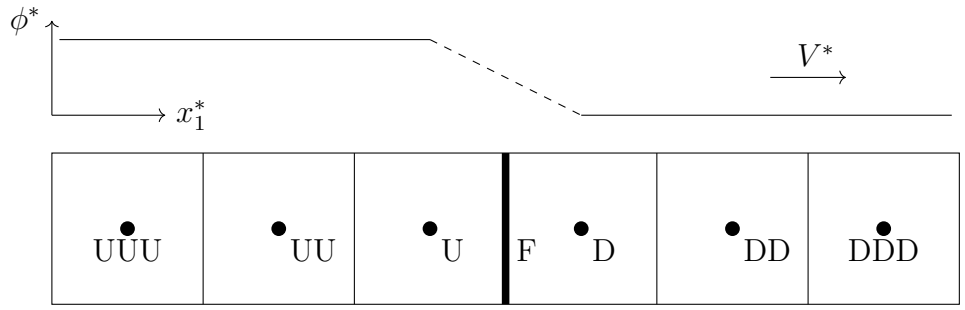

Figure 2.4: Schematic one-dimensional view of the interpolation of primal field quantities ϕ^* on the face F from the adjacent cells located upstream (U) or downstream (D) of F under the flow field V^*.

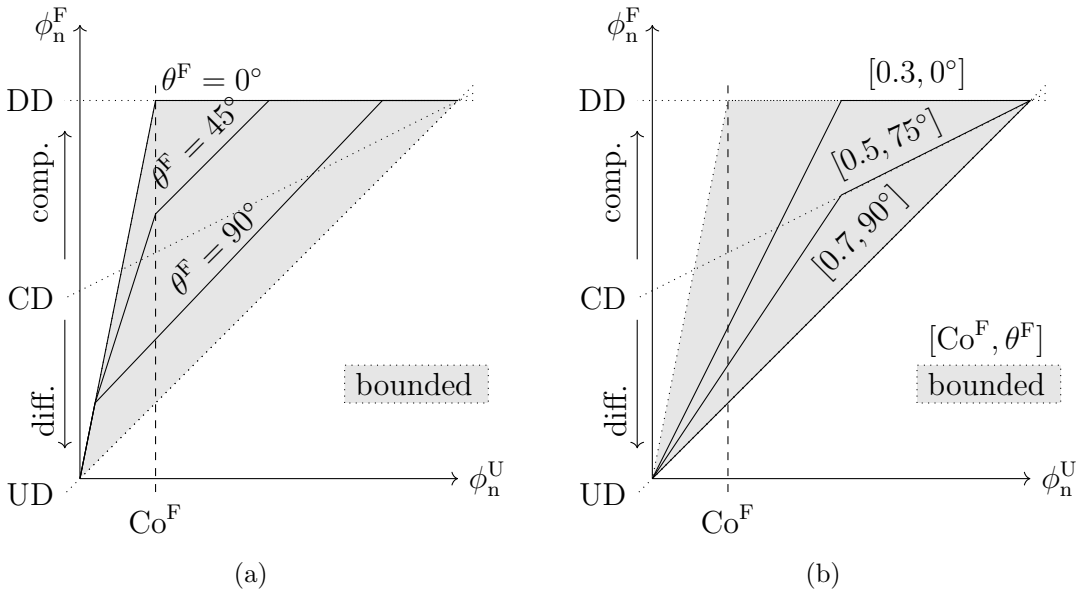

Figure 2.5: Sketch of the Normalized Variable Diagram (NVD) for two compressive convection schemes: (a) Compressive Interface Capturing Scheme for Arbitrary Meshes (CICSAM) and (b) High Resolution Interface Capturing Scheme (HRIC).

High Resolution Interface Capturing (HRIC)

The normalized face value c_n^F is basically determined in three consecutive steps. In compact notation they read:

$$c_n^F = \begin{cases} c_n^{F,2} & : Co^F < Co_l^F \\ c_n^U + \left(c_n^{F,2} - c_n^U\right) \frac{Co_u^F - Co^F}{Co_u^F - Co_l^F} & : Co_l^F \leq Co^F \leq Co_u^F \\ c_n^U & : Co^F > Co_u^F \end{cases},$$

$$\text{with} \qquad c_n^{F,2} = \gamma^F c_n^{F,3} + \left(1 - \gamma^F\right) c_n^U,$$

$$\text{and} \qquad c_n^{F,3} = \begin{cases} 2c_n^U & : c_n^U \in [0, 0.5] \\ 1 & : c_n^U \in [0.5, 1] \\ c_n^U & : c_n^U \notin [0, 1] \end{cases}, \tag{2.90}$$

where three additional quantities enter the approximation to ensure a stable coefficient matrix while preserving a positive main diagonal via the definition of an upper (lower) Courant number Co_u^F (Co_l^F). Frequently employed values are $Co_l^F = 0.3$ and $Co_u^F = 0.7$. The third quantity considers the alignment of the flow with the free surface normal $\gamma^F = \sqrt{|\cos(\theta^F)|}$ where θ^F represents the angle between the free surface normal and the flow direction. Mind that slightly different HRIC formulations exist, e.g. Park et al. [2009].

Compressive Interface Capturing Scheme for Arbitrary Meshes (CICSAM)

The normalized face value c_n^F within the CICSAM procedure is determined via a blending between the Hyper-C (HC) and the Ultimate-Quickest (UQ) scheme. The latter is inspired

by a QUICK approach for the face value. A compact notation reads:

$$
\begin{aligned}
c_{\mathrm{n}}^{\mathrm{F}} &= \gamma^{\mathrm{F}} c_{\mathrm{n}}^{\mathrm{F,HC}} + (1-\gamma^{\mathrm{F}}) c_{\mathrm{n}}^{\mathrm{F,UQ}} \\
&\text{with} \qquad c_{\mathrm{n}}^{\mathrm{F,HC}} = \begin{cases} \min\left(1, \frac{c_{\mathrm{n}}^{\mathrm{U}}}{\mathrm{Co}^{\mathrm{F}}}\right) & : 0 \le c_{\mathrm{n}}^{\mathrm{U}} \le 1 \\ c_{\mathrm{n}}^{\mathrm{U}} & : c_{\mathrm{n}}^{\mathrm{U}} \notin [0,1] \end{cases} \\
&\text{and} \qquad c_{\mathrm{n}}^{\mathrm{F,UQ}} = \begin{cases} \min\left(c_{\mathrm{n}}^{\mathrm{F,HC}}, \frac{8\mathrm{Co}^{\mathrm{F}} c_{\mathrm{n}}^{\mathrm{U}} + \left(1-\mathrm{Co}^{\mathrm{F}}\right)\left(6c_{\mathrm{n}}^{\mathrm{U}}+3\right)}{8}\right) & : 0 \le c_{\mathrm{n}}^{\mathrm{U}} \le 1 \\ c_{\mathrm{n}}^{\mathrm{U}} & : c_{\mathrm{n}}^{\mathrm{U}} \notin [0,1] \end{cases} .
\end{aligned} \tag{2.91}
$$

Again, a blending factor is introduced that accounts for the free surface to flow alignment, viz. $\gamma^{\mathrm{F}} = \min((1+\cos(2\,\theta^{\mathrm{F}}))/2, 1)$ where θ^{F} represents the relation between interface normal and the vector connecting adjacent cells. Again, it should be noted that this is only one of many formulations. Whether HC or UQ is used, CICSAM falls back to pure UDS for inadequate situations.

2.2.8 Boundary Conditions

Boundary conditions serve to separate the examined region from the environment. The boundary conditions summarized in Tab. 2.2 are mathematically grouped into conditions of either Dirichlet or Neumann type that provide either a fixed boundary value or gradient, respectively, viz.

$$
\varphi^{*\mathrm{B}} = \text{const.} \qquad \text{and} \qquad \left.\frac{\partial\,\varphi^*}{\partial\,n^*}\right|^{*\mathrm{B}} \approx \frac{\varphi^{*\mathrm{P}} - \varphi^{*\mathrm{B}}}{||d_{\mathrm{i}}^{*\mathrm{B}}||} = \text{const.}\,. \tag{2.92}
$$

Optionally, combinations of Neumann and Dirichlet conditions might occur (Robin conditions), but are not relevant in this study. From an engineering point of view, the boundary conditions employed in the present thesis can be divided into four categories, e.g. inlet (I), prescribed pressure outlet (O), wall (W) and symmetry (S) boundaries. To support the analysis, vectors and tensors are commonly distinguished into tangential and normal components, e.g. $[t_{\mathrm{i}}^* = v_{\mathrm{i}}^* - (v_{\mathrm{k}}^*\,n_{\mathrm{k}})\,n_{\mathrm{i}}]$ in tangential direction and $[(v_{\mathrm{k}}^*\,n_{\mathrm{k}})n_{\mathrm{i}}]$ in the direction of the normal. Splitting the boundary forces into normal and tangential traction denoted by $t_{\mathrm{i}} = t_{\mathrm{i}}^*/\|t_{\mathrm{i}}^*\|$and n_{i} and additionally assuming negligible curvature, one obtains

$$
\sigma_{\mathrm{i}}^{*B} = \left[\mu^{*\mathrm{v_i}}\left(\frac{\partial v_t^*}{\partial n^*} + \frac{\partial v_n^*}{\partial t^*}\right)\right]^B t_{\mathrm{i}} + \left[2\mu^{*\mathrm{v_i}}\frac{\partial v_n^*}{\partial n^*} - p^*\right]^B n_{\mathrm{i}}\,. \tag{2.93}
$$

Along the inlet, the velocity vector, the turbulence parameters and the concentration field are prescribed. In all considered cases, the inlet normal is perpendicular to the gravity vector. Since the bulk fluids are deemed incompressible, which virtually also holds for the composed flow, the pressure cannot be specified along the inlet and zero normal pressure gradients are imposed. On the contrary, the hydrostatic pressure is prescribed along the outlet boundary and vanishing normal gradients are assumed for all other field values. Along the symmetry planes, scalar field values (p^*, c, k^*, ε^*, ω^*) are also subjected to zero normal gradients. The normal component of the velocity is suppressed along the symmetry plane and the tangential velocity components are extrapolated with zero-order accuracy

from the field onto the symmetry plane. Therefore, the tangential force in (2.93) vanishes and only the normal force component remains

$$\sigma_{\mathrm{i}}^{*\mathrm{S}} = \left[2\,\mu^{*\mathrm{v_i}} \frac{\partial\, v_n^*}{\partial\, n^*} - p^* \right] n_{\mathrm{i}}\,. \tag{2.94}$$

The pressure is extrapolated with zero-order accuracy. Along slip walls, all variables except for turbulence quantities comply with the symmetry conditions. In particular, the tangential force again vanishes. Turbulence variables are subjected to no-slip wall conditions, as described below. No slip wall conditions are more evolved. As regards the momentum equations, a free-cutting concept is employed along the no slip wall that replaces the free forces acting on the wetted body by a closure model, while assuming identical velocity of wall and fluid as well as negligible curvature. Due to the prescribed wall velocity, the wall effective pressure is extrapolated with first-order accuracy from the field to the wall. The corresponding wall force involves viscous shear and pressure components, e.g.

$$\sigma_{\mathrm{i}}^{*\mathrm{W}} = \mu^{*\mathrm{v_i}} \frac{\partial\, v_t^*}{\partial\, n^*} t_{\mathrm{i}} - p^*\, n_{\mathrm{i}}\,. \tag{2.95}$$

Appropriate models to close the viscous wall shear either refer to a unidirectional laminar shear or logarithmic wall function related prescription of turbulent shear forces. Both relate to the wall tangential projection of the velocity in the wall adjacent CV and only differ in the value of $\mu^{*\mathrm{W}}$. The turbulence energy k^* follows a zero normal gradient condition, which is asymptotically compatible to both the low-Re and the wall function approaches, cf. Wilcox [1998]. Using the same asymptotic approach, the wall adjacent field values of the energy dissipation ε^* and the specific energy dissipation ω^* can be prescribed using the wall normal distance and the TKE value adjacent to the wall. As outlined below, these boundary conditions result in a manipulation of the convective and the diffusive boundary flux, cf. Fig. 2.3 (b), along the face of the boundary adjacent interior control volume.

Convective fluxes follow from (2.78) and (2.83). They involve an implicit first-order UDS approximation which reveals

$$A^{*\varphi,\mathrm{P}} \leftarrow -\min\left(\dot{V}^{*\mathrm{B}}, 0\right)\,. \tag{2.96}$$

One only needs to distinguish whether, as well as in which direction (in vs. out) a convective transport occurs.

- **Inlet** conditions refer to an inflow velocity $v_{\mathrm{k}}^{*\mathrm{I}}$ pointing into the domain as well as the boundary adjacent CV and therefore a negative volume flux $\dot{V}^{*B} = v_{\mathrm{k}}^{*I} \Delta\Gamma_{\mathrm{k}}^{*B}$ enters (2.96).
- **Prescribed pressure outlet** conditions are characterized by zero entries to the coefficient matrix, due to the outward directed positive flux $\dot{V}^{*\mathrm{B}}$.
- **Symmetry** and **no-slip / slip wall** boundary conditions prohibit a convective flux over the boundary via $\dot{V}^{*\mathrm{B}} = 0$. Since the convective flux is suppressed along the boundary, no convective contributions to the r.h.s or the coefficient matrix occurs for this face.

Diffusive fluxes follow from (2.86), viz.

$$A^{*\varphi,\mathrm{P}} \leftarrow \left[\frac{\mu^{*\varphi}\Delta\Gamma^*}{||d_\mathrm{k}^*||\alpha^\mathrm{n}}\right]^\mathrm{B} \qquad \text{and} \qquad S^{*\varphi,\mathrm{P}} \leftarrow \left[\frac{\mu^{*\varphi}\,\Delta\Gamma^*}{||d_\mathrm{k}^*||\alpha^n}\right]^\mathrm{B} \varphi^{*\mathrm{B}}\,. \tag{2.97}$$

- **Inlet** boundaries are characterized by Dirichlet conditions for all transport quantities except the pressure. Due to the zero gradient pressure condition, diffusive contributions (2.97) are suppressed for the pressure, which provides an implicit condition. The diffusive flux of all other variables follows from (2.97) based on the given inlet $\varphi^{*\mathrm{B}} = \varphi^{*\mathrm{I}}$ quantities from Tab. 2.2. If the momentum equations are assembled, further explicit contributions are added to supplement the complete strain rate tensor. Similarly, the pressure is extrapolated with zero-order to the boundary to complete the normal force on this face.

- **Prescribed pressure outlet** boundary conditions swap the former relation and employ zero gradients for all quantities ($\partial\,\varphi^{*\mathrm{B}}/\partial n^* = 0$) except the effective pressure. Since $\varphi^{*\mathrm{B}} = \varphi^{*\mathrm{P}}$ eliminates the sum of all contributions to (2.97), these contributions are simply not considered for $\varphi^* \neq p^*$. The effective pressure is assigned to a hydrostatic Dirichlet condition along the outlet, e.g. $p^{*\mathrm{B}} = p^{*\mathrm{O}} = [\rho^*\, g_\mathrm{k}^*\, x_\mathrm{k}^*]$, and this value enters (2.97).

- **Symmetry** and **slip-wall** boundary conditions do suppress the wall normal gradient of the scalar properties. Hence all contributions to (2.97) are simply suppressed for $\varphi^* = c, p^*$ along a slip wall and $\varphi^* = c, p^*, k^*, \omega^*, \varepsilon^*$ along symmetry planes. Moreover, no shear stress is transmitted, due to the symmetry $\partial v_\mathrm{t}^*/\partial n^* = 0$ as well as the no-penetration condition $\partial v_\mathrm{n}^*/\partial t^* = 0$ and considered forces reduce to $[2\mu^{*v_\mathrm{i}}(\partial v_n^*/\partial n^*) - p^*]^B\, n_\mathrm{i}$, cf. Eqn. (2.93) and (2.94), which requires to extrapolate the pressure as well as to consider a source for the momentum equations

$$A^{*\mathrm{v_i},\mathrm{P}} \leftarrow 0 \qquad \text{and} \qquad S^{*\mathrm{v_i},\mathrm{P}} \leftarrow \left[\frac{\mu^{*v_\mathrm{i}}\,\Delta\Gamma}{||d_\mathrm{k}^*||\alpha^n}\right]^\mathrm{B} 2\left[(v_\mathrm{k}^{*B} - v_\mathrm{k}^{*P})n_\mathrm{k}^\mathrm{B}\right] n_\mathrm{i}^\mathrm{B}\,. \tag{2.98}$$

  A symmetry plane always employs $v_\mathrm{i}^{*\mathrm{B}} = v_\mathrm{i}^{*\mathrm{S}} = 0$.

- **No-Slip Wall** boundary conditions suppress the wall normal gradient of $\varphi^* = c, k^*$ and the effective pressure is interpolated with first-order accuracy to capture hydrostatic effects, viz. $\partial p^{*\mathrm{eff}}/\partial n^* = \rho^*\, g_\mathrm{i}^*\, n_\mathrm{i}$. A zero wall normal gradient is imposed on $\varphi^* = k^*$, cf. reasoning above, and the remaining turbulent quantities $\varphi^* = \omega^*, \epsilon^*$ are prescribed based on the wall normal distance combined with the TKE value in the first interior cell, cf. Wilcox [1998]. Viscous shear and pressure forces acting on a wall follow from (2.95), viz. $\mu^{*\mathrm{v_i}}\partial v_t^*/\partial n^* t_\mathrm{i} - p^*\, n_\mathrm{i}$. They require to extrapolate the pressure and yield the following changes to the discrete momentum equation

$$A^{*\mathrm{v_i},\mathrm{P}} \leftarrow 0 \qquad \text{and} \qquad S^{*\mathrm{v_i},\mathrm{P}} \leftarrow \left[\frac{\mu^{*v_\mathrm{i}}\,\Delta\Gamma}{||d_\mathrm{k}^*||\alpha^n}\right]^\mathrm{B} \left[(v_\mathrm{k}^{*B} - v_\mathrm{k}^{*P})t_\mathrm{k}^\mathrm{B}\right] t_\mathrm{i}^\mathrm{B}\,. \tag{2.99}$$

  Aiming at a more implicit strategy, the above given approach is replaced by

$$A^{*\mathrm{v_i},\mathrm{P}} \leftarrow \left[\frac{\mu^{*v_\mathrm{i}}\,\Delta\Gamma}{||d_\mathrm{k}^*||\alpha^n}\right]^\mathrm{B} \quad \text{and} \quad S^{*\mathrm{v_i},\mathrm{P}} \leftarrow \left[\frac{\mu^{*v_\mathrm{i}}\,\Delta\Gamma}{||d_\mathrm{k}^*||\alpha^n}\right]^\mathrm{B} \left(\left[(v_\mathrm{k}^{*B} - v_\mathrm{k}^{*P})t_\mathrm{k}^\mathrm{B}\right] t_\mathrm{i}^\mathrm{B} + v_\mathrm{i}^{*P}\right)\,. \tag{2.100}$$

All studies in this thesis refer to non-moving walls, hence $v_{\mathrm{i}}^{*\mathrm{B}} = v_{\mathrm{i}}^{*\mathrm{W}} = 0$. The approach is generic and allows for the manipulation of the actual wall shear, e.g. in line with the universal LoW for momentum boundary-layers, cf. Sec. 2.3.3.

2.2.9 Homogeneous Mobility Model

The sign-change of the apparent viscosity resembles a compressive approximation of the convective term, which switches from UDS to DDS approximations along the interface, and thus from positive to negative (apparent) viscosities, to keep the interface sharp, cf. Sec. 2.2.7. The formulation of $M^{*\mathrm{mod}}$ in (2.55) is based on the interface blurring introduced by upwind-biased convective schemes. An estimation of the tensorial numerical diffusion at a cell face returned by a first-order upwind scheme might read

$$\nu_{\mathrm{ik}}^{*\mathrm{UDS,F}} = \left(\lambda \Delta x_{\mathrm{k}}^{*}\, v_{\mathrm{i}}^{*}\right)^{\mathrm{F}} . \tag{2.101}$$

Depending on the time discretization scheme, the related error might be extended into the estimate of the mobility parameter by a modified equation analysis. For the example of a first-order implicit time discretization, the modified equation analysis suggests a simple supplement of a Courant number term, e.g. $\nu_{\mathrm{ik}}^{*\mathrm{UDS,F}} \leftarrow \nu_{\mathrm{ik}}^{*\mathrm{UDS,F}}\, \mathrm{Co}_{\mathrm{ik}}^{\mathrm{F}}$. The estimate (2.101) is spatially and temporally variable. Spatially volatile mobility distributions are deemed to obstruct the robustness of the procedure. Hence, a homogenized approach estimates the mobility based on the maximum norm of the matrix valued numerical diffusion

$$M^{*\mathrm{mod}} = \frac{\tilde{M}}{C^{*\mathrm{a}} \left| \left\{ n^{\mathrm{F}} : \Delta x_{\mathrm{i}}^{*} \frac{\partial c}{\partial x_{\mathrm{i}}^{*}}^{\mathrm{F}} \geq \Delta \mathrm{c} \right\} \right|} \sum_{\mathrm{F}}^{\mathrm{NF}} \begin{cases} \max\limits_{\mathrm{i,k}} \left(\left| \lambda\, \Delta x_{\mathrm{k}}^{*}\, v_{\mathrm{i}}^{*} \right| \right)^{\mathrm{F}} & \text{if } \Delta x_{\mathrm{i}}^{*} \frac{\partial c}{\partial x_{\mathrm{i}}^{*}}^{\mathrm{F}} \geq \Delta \mathrm{c} \,, \\ 0 & \text{otherwise} \end{cases} . \tag{2.102}$$

Note that the field is filtered to extract the interface region, e.g. only faces with a projected concentration gradient above $\Delta \mathrm{c} = 10^{-3}$ are considered.

2.2.10 Stability of the Approximation

The numerical approximation of the considered set of transport Eqns. (2.43)-(2.48) is stable if reasonably chosen, e.g. physically inspired finite approximations are applied combined with a sufficient under-relaxation. This is especially evident if the DC contributions of convective and diffusive transport are neglected, cf. Eqns. (2.79) and (2.84). The main diagonal entry of the steady transport equation reads

$$A^{*\varphi,\mathrm{P}} \leftarrow \sum_{\mathrm{F(P)}} \left[-\min\left(\dot{V}^{*}, 0 \right) + \frac{\mu^{*\varphi}\, \Delta \Gamma^{*}}{||d_{\mathrm{k}}^{*}|| \alpha^{\mathrm{n}}} \right]^{\mathrm{F}} \tag{2.103}$$

and is inherently greater than zero if the diffusivity $\mu^{*\varphi} \geq 0$ is positive. Since convection schemes in particular are prone to introduce numerical diffusion, a main challenge refers to the transportation of a non-diffusive and thus sharp concentration field based on a given velocity field. Two initially different trade-offs are accepted w.r.t. approximation stability, which end up in similar characteristic in line with Eqn. (2.103).

1. The classical VoF method neglects diffusive contributions within the approximation ($\mu^{*\mathrm{c}} = 0$). Instead, the approximation direction of the convective term switches from UDS to DDS which in turn changes the numerical leading error from a diffusive to a compressive character, cf. Fig. 2.5. The resulting violation of the physical consistency finally provides a negative contribution to the main diagonals and impedes the numerical stability which will be further outlined in the following.

2. The CH-VoF approach continues with physically consistent approximations of the convective concentration transport. However, the diffusivity is not necessarily zero, cf. Eqn. (2.54) as well as Fig. 2.2, and even becomes negative over approximately 58% of the concentration spectrum, which reflects the compressive interface physics of the diffusive formulation. From a numerical point of view, the partially negative diffusion constant can be translated into the numerical leading error of the downwind approximation inherent to VoF and therefore similarly impedes the stability of the approximation in case of an unfortunate choice of the mobility parameter.

Hence, the pseudo-temporal VoF process can therefore be translated locally into a steady CH-VoF approach. An essential advantage of the latter is the possibility to neglect the integration in pseudo-time which shows a measurable gain in convergence speed. In the following, the stability problems of VoF and CH-VoF will be discussed in more detail. During the approximation of the primal VoF equation, the main diagonal coefficient of the system matrix is affected if the approximation of the convective term switches locally from UDS to DDS. Using the BE discretization of $\mathrm{d}\,c/\mathrm{d}\,t^* = 0$ yields the following main diagonal entry for an upwind or downwind interpolation of c^{F}, viz.

$$\left[\frac{c^{*\mathrm{P,T}} - c^{*\mathrm{P,T-1}}}{\Delta t^*}\right]\Delta\Omega^{*\mathrm{P}} + \sum_{\mathrm{F(P)}}\left[\dot{V}\,c\right]^{\mathrm{F,T}} = 0$$

$$\rightarrow \qquad A^{*\mathrm{c,P,T}} = \frac{\Delta\Omega^{*\mathrm{P}}}{\Delta t^*} + \sum_{\mathrm{F(P)}}\begin{cases}\max\left(\dot{V}^{*\mathrm{F,T}}, 0\right) & : \mathrm{UDS} \\ \min\left(\dot{V}^{*\mathrm{F,T}}, 0\right) & : \mathrm{DDS}\end{cases}. \tag{2.104}$$

Mind that the UDS implementation usually refers to the convergent state, e.g. $\max\left(\dot{V}^{*\mathrm{F,T}}, 0\right) = -\min\left(\dot{V}^{*\mathrm{F,T}}, 0\right)$, cf. Eqn. (2.83). In order to preserve diagonal dominance and avoid a zero crossing introduced by DDS, the time step Δt^* must be chosen carefully to comply with $\Delta t^*\,\dot{V}^{*\mathrm{F,T}}/\Delta\Omega^{*\mathrm{P}} = \mathrm{Co} < 1/2$, or even lower in 3D flows (e.g. $\mathrm{Co} \leq 0.3$). Since this time step dependency originates from the concentration equation only, sub-cycling strategies can be employed to increase the efficiency of the temporal integration (cf. Ubbink and Issa [1999], Manzke et al. [2012]). Basically, sub-cycling slows the simulation within admissible Courant number bounds and subdivides the temporal integration based on an invalid (too large) time step into several valid (smaller) sub time steps as exemplary sketched in Alg. (2). Special attention should be paid on (un)synchronization as well as in-between gradient computation, cf. Manzke [2018] for a detailed discussion.

The CH-VoF Eqn. (2.54) is studied using a discrete von-Neumann stability analysis. Assuming a one-dimensional grid with spacing Δx^* as well as a constant flow velocity V^* and mobility M^*, the latter yields the following amplification factor:

$$\xi = \frac{\xi^{m+1}}{\xi^m} = \frac{1 + \mathrm{Co}^{\mathrm{diff}}\frac{C^{*\mathrm{b}}}{C^{*\mathrm{a}}\Delta x^2}\left[4\cos^2(\theta) - 8\cos(\theta) + 5\right]}{1 + \mathrm{Co}\left[1 - \cos(\theta) + i\sin(\theta)\right] + 2\mathrm{Co}^{\mathrm{diff}}b''\left[1 - \cos(\theta)\right]} \tag{2.105}$$

Algorithm 2: Schematic overview of the sequential primal solution procedure based on sub-cycling within each outer-iteration loop.

```
while n^T ≤ N^T do
    while (n^out ≤ N^out,max) or (R^φ ≤ R^φ,min) do
        approximate linearized momentum equations
        approximate pressure correction equation
        approximate linearized turbulence equations
        Δt* = Δt*/N
        for sub-cycle=1,N do
            approximate linearized concentration equation
        Δt* = Δt* N
```

where $\mathrm{Co}^{\mathrm{diff}} = \Delta t^* \, M^* / \Delta x^{*2}$ represents the diffusive analogue to the convective Courant number $\mathrm{Co} = \mathrm{Co}^{\mathrm{conv}} = \Delta t^* \, M^* / \Delta x^*$ and $b'' = 12c^2 - 12c + 2$. Here i and m represent the imaginary unit ($i^2 = -1$) and an iteration counter. The parameter $\theta = \beta \Delta x$ with $\cos(\beta \, \Delta x) = 1/2 \left(e^{-J \beta \, \Delta x} + e^{J \beta \, \Delta x} \right)$ represents the phase angle. The system can be thought of as unconditional stable if $\xi \leq 1$. With attention restricted to the under-resolved situation ($C^{*\mathrm{a}} = 1 \, \mathrm{Pa}$, $C^{*\mathrm{b}} = 0 \, \mathrm{N}$), one obtains

$$\begin{aligned} \xi = \frac{\xi^{m+1}}{\xi^m} &= \frac{1}{1 + \left(\mathrm{Co} + 2\mathrm{Co}^{\mathrm{diff}} b'' \right) \left[1 - \cos(\theta) \right] + i \, \mathrm{Co} \sin(\theta)} \\ &= \frac{1 + \left(\mathrm{Co} + 2\mathrm{Co}^{\mathrm{diff}} b'' \right) \left[1 - \cos(\theta) \right]}{\left(1 + \left(\mathrm{Co} + 2\mathrm{Co}^{\mathrm{diff}} b'' \right) \left[1 - \cos(\theta) \right] \right)^2 + \left(\mathrm{Co} \sin(\theta) \right)^2} \\ &\quad - i \frac{\mathrm{Co} \sin(\theta)}{\left(1 + \left(\mathrm{Co} + 2\mathrm{Co}^{\mathrm{diff}} b'' \right) \left[1 - \cos(\theta) \right] \right)^2 + \left(\mathrm{Co} \sin(\theta) \right)^2}. \end{aligned} \tag{2.106}$$

Confining the interest to the real term in (2.106), the system is stable for the pure phases ($c_0 = 0$, $c_0 = 1$). Along the phase transition regime $c = 0.5$ the stability limits are estimated by

$$\tilde{M} \leq 1 \qquad \text{and} \qquad \tilde{M} \geq \left[1 + \frac{2}{\mathrm{Co} \left[1 - \cos(\theta) \right]} \right]. \tag{2.107}$$

Figure 2.6 depicts the amplification factor for three different Courant numbers ($\mathrm{Co} = 0.1$, $\mathrm{Co} = 1$, $\mathrm{Co} = 10$) and five different exemplary phase angles as a function of the non-dimensional mobility parameter $\tilde{M}$. Approaching the steady state limit, the analysis only excludes $\tilde{M} = 1$. In case of $\theta \to 0$, the branch $\tilde{M} \leq 1$ might be a safer recommendation. Therefore $\tilde{M} = 0.1$ is used for all applications displayed in Sec. 2.3 and 2.4, for which no stability problems are observed. If alternative convection schemes are used, the 1st-order upwind based analysis still provides reliable estimates.

2.2.11 Modeling of Floatation

The present study also considers an adjustment of the trim and sinkage of ship hulls during the pseudo-temporal integration. The floating geometry is initialized in its resting position

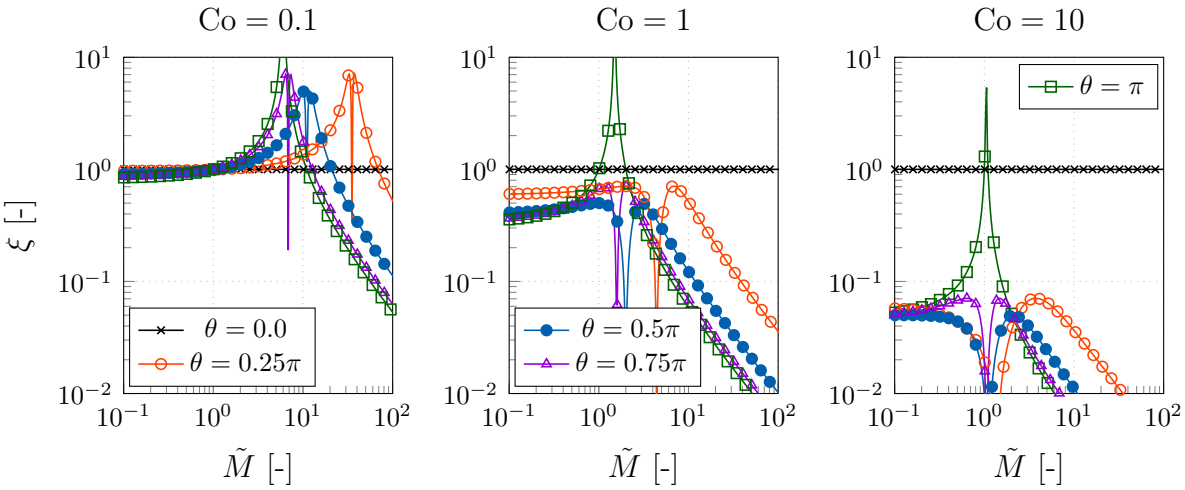

Figure 2.6: Amplification factor of a one-dimensional CH system over the mobility factor $\tilde{M}$ for different phase angles θ and convective Courant numbers, e.g. Co = 0.1 (left), Co = 1 (middle) and Co = 10 (right).

based on prescribed hydrostatic data. This refers to an initial displacement $V^{*\mathrm{ini}}$, center of gravity $x_{\mathrm{j}}^{*\mathrm{g}}$ and rotation center $x_{\mathrm{j}}^{*\mathrm{r}}$.

Once the flow around the hull develops and the forces deviate from the initial hydrostatic values, the floatation is corrected. To this end, the surface grid of the hull, which refers to the interior domain boundary, is rigidly displaced and rotated while all exterior boundaries are kept fixed. An estimation of the of trim and sinkage errors w.r.t. the prescribed hydrostatic data follows from the net heave force $F^{*\mathrm{H}}$ and trim moment $M^{*\mathrm{T}}$, viz.

$$\Delta S^* = \frac{F^{*\mathrm{H}}}{\rho^{*\mathrm{b}}\,|g_{\mathrm{k}}^*|\,A^{*\mathrm{w}}} \qquad \text{and} \qquad \Delta T^* = \frac{M^{*\mathrm{T}}}{\rho^{*\mathrm{b}}\,|g_{\mathrm{k}}^*|\,I^{*\mathrm{w}}} \tag{2.108}$$

where $A^{*\mathrm{w}}$, $I^{*\mathrm{w}}$ and $\rho^{*\mathrm{b}}$ represent the water-plane area, its moment of inertia around the rotating axis and the density of the heavier (background) fluid, respectively, cf. Yang and Löhner [2002]. The trim increment ΔT^* is not to be confused with the time increment Δt^* from Sec. 2.2.4. The net heave force and trim moment follow from the fluid flow induced forces along all hydrostatic boundaries plus additional hydrostatic data, viz.

$$\begin{aligned} F^{*\mathrm{H}} &= \frac{g_{\mathrm{i}}^*}{|g_{\mathrm{k}}^*|}\left[\int_{\Gamma^{*\mathrm{H}}} f_{\mathrm{i}}^*\,\mathrm{d}\Gamma^* + V^{*\mathrm{ini}}\,\rho^{*\mathrm{b}}\,g_{\mathrm{i}}^*\right] \qquad \text{and} \\ M^{*\mathrm{T}} &= \frac{\epsilon_{\mathrm{ijk}}\,g_{\mathrm{j}}^*\,V_{\mathrm{k}}^*}{|\epsilon_{\mathrm{ijk}}\,g_{\mathrm{j}}^*\,V_{\mathrm{k}}^*|}\left[\int_{\Gamma^{*\mathrm{H}}} \epsilon_{\mathrm{ilm}}\left[x_{\mathrm{l}}^* - x_{\mathrm{l}}^{*\mathrm{r}}\right] f_{\mathrm{m}}^*\,\mathrm{d}\Gamma^* + V^{*\mathrm{ini}}\,\rho^{*\mathrm{b}}\epsilon_{\mathrm{ilm}}\left[x_{\mathrm{l}}^{*\mathrm{g}} - x_{\mathrm{l}}^{*\mathrm{r}}\right] g_{\mathrm{m}}^*\right] \end{aligned} \tag{2.109}$$

where $f_{\mathrm{i}}^* = \left[2\,\mu^{*\mathrm{eff}}\,S_{\mathrm{ik}}^* - p^{*\mathrm{eff}}\,\delta_{\mathrm{ik}}\right] n_{\mathrm{k}}$ and V_{k}^* represent the effective fluid dynamic forces as well as the bulk velocity, respectively. Here ϵ_{ijk} refers to the Levi-Civita-Symbol used to compute an outer vector product. Only the gravity parallel [gravity-bulk-velocity orthogonal] part of the acting forces [moments] is considered. In the absence of flow, only hydrostatic forces remain and the sinkage relation is directly fulfilled, e.g. $F^{*\mathrm{H}} = 0$ and thus $\Delta S^* = 0$ for an appropriate $V^{*\mathrm{ini}}$.

Once the forces on the hull converge, the actual hydrostatic error is evaluated according to Eqn. (2.108). Subsequently, the trim and sinkage corrections are combined and relaxed

in terms of a rigid body motion based on a displacement field $d_{\mathrm{i}}^{*\mathrm{h}}$ along the hydrostatic boundaries

$$d_{\mathrm{i}}^{*\mathrm{h}} = \left[\Delta S^{*}\,\delta_{\mathrm{i}3} + \Delta T^{*}\,R_{\mathrm{i}2}\right]\omega^{\mathrm{h}} \tag{2.110}$$

where $R_{\mathrm{i}2}$ refers to a rotation matrix around the trim/x_2^*-axis and the gravity is supposed to act in negative x_3^* direction. Robust floatation adjustments refer to $0.2 \leq \omega^{\mathrm{h}} \leq 0.6$. The interior boundary deformation and the fixed exterior boundaries serve as Dirichlet conditions for a mesh morphing routine which computes the new cell centers from a FV approximation of

$$\frac{\partial}{\partial x_{\mathrm{k}}^{*}}\left[\mu^{*\mathrm{d_i}}\frac{\partial d_{\mathrm{i}}^{*}}{\partial x_{\mathrm{k}}^{*}}\right] = 0 \quad \text{in} \quad \Omega^{*} \qquad \text{with} \qquad \begin{cases} d_{\mathrm{i}}^{*} = d_{\mathrm{i}}^{*\mathrm{h}} & \text{on} \quad \Gamma^{*} \cap \Gamma^{*\mathrm{H}} \\ d_{\mathrm{i}}^{*} = 0 & \text{on} \quad \Gamma^{*} \end{cases} . \tag{2.111}$$

The diffusivity refers to the inverse (non zero) distance to the nearest wall, which avoids a grid distortion in the vicinity of the hull. A subsequent deformation of the cell vertices follows from an averaged interpolation of all vertex-adjacent centers $N^{\mathrm{P(V)}}$, viz.

$$d_{\mathrm{i}}^{*\mathrm{V}} = \frac{1}{N^{\mathrm{P(V)}}}\sum_{\mathrm{P}=1}^{N^{\mathrm{P(V)}}}\left[d_{\mathrm{i}}^{*\mathrm{P}} + \frac{\partial\, d_{\mathrm{i}}^{*\mathrm{P}}}{\partial\, x_{\mathrm{k}}^{*}}\left(x_{\mathrm{k}}^{*\mathrm{V}} - x_{\mathrm{k}}^{*\mathrm{P}}\right)\right] . \tag{2.112}$$

After the update of the grid, the geometric quantities are recalculated for each CV. Because topological relationships remain unaltered, the simulation is continued by a simple restart from the previous outer iteration.

2.3 Primal Flow Verification

After the governing equations have been derived and subsequently discretized, the discrete numerical model is verified. The latter is typically achieved on the basis of (non-trivial) analytical or even generalized solutions and is commonly referred to as verification. This thesis follows the definition of the American Institute of Aeronautics and Astronautics (AIAA [1998]), in which verification and validation (V&V) are defined as follows

- *Verification* is the process of determining if a computational simulation accurately represents the conceptual model, but no claim is made of the relationship of the simulation to the real world.

- *Validation* is the process of determining if a computational simulation represents the real world.

A significant part of this work is concerned with adjoint fluid mechanics. An important aspect arises in this context, since solutions of a primal verification study typically give rise to an adjoint companion. The validation of the adjoint framework, especially w.r.t. real world problems, is slightly delicate and will be explored in more detail in Sec. 4.3 and 4.4. The considered verification studies involve laminar and turbulent single- and two-phase flows. Emphasis is given to plane shear flow cases, i.e. boundary-layers and Couette flows, which also serve the verification of the adjoint system in Sec. 4.3.

2.3.1 Laminar (Blasius) Boundary-Layer Equation

Two-dimensional equations for the laminar single-phase momentum b.-l. in the x_1^*-x_2^*-plane can be derived in two consecutive steps. First, the governing Eqns. (2.56)-(2.58) are non-dimensionalized with the reference quantities given in Tab. 2.3. The laminar governing

primal quantity/operator	v_1^*	v_2^*	p^*	$\partial\phi^*/\partial x_1^*$	$\partial\phi^*/\partial x_2^*$
reference value	V_1^*	V_2^*	P^*	L	δ^*

Table 2.3: Reference quantities of the 2D governing primal b.-l. equations.

equations are divided by density and considered to be free of gravitational forces. In line with the non-dimensionalization in Sec. 2.1.7, an exemplary relationship between a dimensional term, its reference values and non-dimensional quantities reads $v_2^*\,\partial v_1^*/\partial x_2^* = (V_2^* V_1^*/\delta^*)\,(v_2 \partial v_1/\partial x_2)$. Subsequently, a scaling analysis is performed, where it is assumed that the spatial extent in streamwise x_1^*-direction is significantly larger than the extent in the direction of the wall normal x_2^*, viz. $L^* \gg \delta^*$. The assumption is in line with a flat plate of semi-infinite length L^* ($\rightarrow \infty$) in the x_1^* direction under a homogeneous steady inflow V_1^*, cf. Fig. 2.7. The continuity Eqn. (2.43) reveals an order of magnitude scaling of the normal velocity, viz. $V_2^* \propto V_1^* \delta^*/L^*$. The complete scaling analysis is performed in

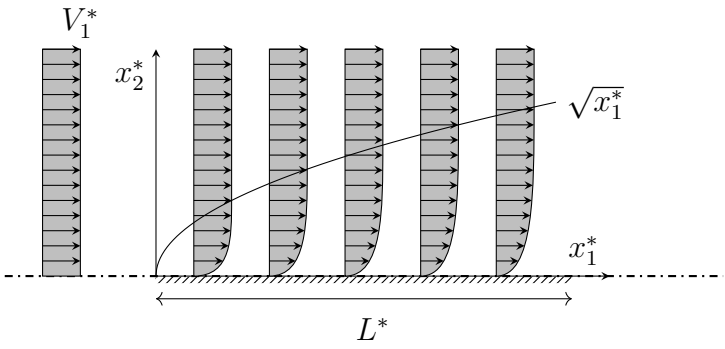

Figure 2.7: Illustration of the (forward) primal V_1 flow over a flat finite plate in the x_1^*-x_2^* plane.

App. A.1 and only the resulting b.-l. equations are given below, i.e.

$$\mathrm{R}_1^{\mathrm{v,BL}^*}: v_1^* \frac{\partial v_1^*}{\partial x_1^*} + v_2^* \frac{\partial v_1^*}{\partial x_2^*} + \frac{1}{\rho^*}\frac{\partial p^*}{\partial x_1^*} - \nu^* \frac{\partial^2 v_1^*}{\partial {x_2}^{2^*}} = 0 \tag{2.113}$$

$$\mathrm{R}_2^{\mathrm{v,BL}^*}: \frac{1}{\rho^*}\frac{\partial p^*}{\partial x_2^*} = 0 \tag{2.114}$$

$$\mathrm{R}^{\mathrm{p,BL}^*}: -\frac{\partial v_1^*}{\partial x_1^*} - \frac{\partial v_2^*}{\partial x_2^*} = 0. \tag{2.115}$$

The traditional strategy to obtain generalized solutions for (2.113)-(2.115) aims to downgrade the coupled PDEs to ODEs along a route outlined by Blasius [1907]. The latter is achieved based on a) a prior coordinate transformation, which requires suitable similarity coordinates, to b) simplify the corresponding equations.

The primal b.-l. flow is anticipated to be a function of the plate normal and tangential coordinate, viz. $v_1^*/V_1^* = g(\eta)$ with $\eta = x_2^*/\delta^*(x_1^*)$, where g and δ^* represent a (so far) unknown function as well as a measure for the b.-l. thickness. Thus, one can directly compute the spatial velocity gradients, e.g. $\partial v_1^*/\partial x_1^* = -V_1^* g'(x_2^*/\delta^{2^*})(\partial\delta^*/\partial x_1^*)$ with $g' = \mathrm{d}g/\mathrm{d}\eta$. An integration of Eqn. (2.113) along the wall normal coordinate from the wall to the b.-l. edge reads

$$2\int_0^{\delta^*} v_1^* \frac{\partial v_1^*}{\partial x_1^*}\mathrm{d}x_2^* + \int_0^{\delta^*} v_2^* \frac{\partial v_1^*}{\partial x_2^*}\mathrm{d}x_2^* - \int_0^{\delta^*} \nu^* \frac{\partial^2 v_1^*}{\partial {x_2^*}^{2^*}}\mathrm{d}x_2^* = 0. \tag{2.116}$$

Applying the continuity equation ($\partial\, v_2^*/\partial\, x_2^* = -\partial\, v_1^*/\partial\, x_1^*$) together with the new definition of the plate tangential velocity allows the elimination of the plate normal velocity, i.e.

$$-2{V_1}^{2^*}\int_0^{\delta^*} g g' \frac{x_2^*}{\delta^{2^*}}\frac{\partial\delta^*}{\partial x_1^*}\mathrm{d}x_2^* + {V_1}^{2^*}\int_0^{\delta^*} g' \frac{x_2^*}{\delta^{2^*}}\frac{\partial\delta^*}{\partial x_1^*}\mathrm{d}x_2^* - \nu^* V_1^* g' \frac{1}{\delta^*}\Big|_0^{\delta^*} = 0. \tag{2.117}$$

Substituting $\eta = x_2^*/\delta^*$ ($\mathrm{d}x_2^* = \delta^*\mathrm{d}\eta = \mathrm{d}(x_2^*/\delta^*)$) offers an ODE for δ^*, viz.

$$[B - 2A]\frac{\partial\delta^*}{\partial x_1^*}\delta^* = \frac{\nu^*}{V_1^*}C, \tag{2.118}$$

where all integrals are condensed to the parameters A and B

$$A = \int_0^1 g g' \eta\,\mathrm{d}\eta\,, \qquad B = \int_0^1 g'\eta\,\mathrm{d}\eta\,, \quad \text{and} \quad C = g'(1) - g'(0). \tag{2.119}$$

Equation (2.118) can be solved w.r.t. δ^*, which yields

$$\delta^* = \sqrt{\frac{2C}{b\,[B-2A]}}\sqrt{\frac{\nu^*\,[a^*+bx_1^*]}{V_1^*}} \qquad \rightarrow \qquad \delta^* \propto \sqrt{\frac{\nu^*\,[a^*+bx_1^*]}{V_1^*}}\,. \tag{2.120}$$

The last expression supports an estimation of the boundary-layer thickness and offers a suitable choice for the similarity variable $\eta = x_2^*\sqrt{V_1^*/[\nu^*(a^*+bx_1^*)]}$. It should be pointed out that classical b.-l. thickness measures employ $a^*=0$ and $b=1$, which is basically due to the chosen origin and direction of the coordinate system. The origin is usually located at the upstream edge of the plate – in line with the origin of the primal b.-l. – pointing downstream in x_1^*. However, motivated by the adjoint analysis performed in Sec. 4.3.1, the more general expression is retained to adjust to the reversal of the b.-l. from a downstream origin in the adjoint mode. Using the similarity variable η, a scalar stream function ψ^* can be defined, that inherently satisfies the continuity expression (2.115), e.g. $v_1^* = \partial\psi^*/\partial x_2^*$, $v_2^* = -\partial\psi^*/\partial x_1^*$, and offers access to the plate tangential velocity, viz.

$$\psi^* = \int_0^{x_2^*} v_1^*\mathrm{d}x_2^* = \int_{\eta(0)}^{\eta(x_2^*)} g(\eta)V_1^*\delta\mathrm{d}\eta = \sqrt{\nu^*\,[a+bx_1^*]\,V_1^*}\underbrace{\int_0^{\eta} g\mathrm{d}\eta}_{f(\eta)}\,. \tag{2.121}$$

All primal b.-l. terms can be expressed in terms of f and η, e.g. $\partial^2 v_1^*/\partial x_2^{*2} = V_1^{*2}/[\nu(a^*+bx_1^*)]f'''$, as summarized in App. A.3. Assuming a homogeneous pressure field, the substitutions of all terms of Eqn. (2.113) yields the well known Blasius equation for a laminar flat plate b.-l. flow

$$R_1^{\mathrm{BL}^*} \qquad \rightarrow \qquad -2f''' - bff'' = 0. \tag{2.122}$$

The Blasius equation is numerically approximated based on a shooting method. An exemplary ©Matlab code is available in the respective repository, cf. Kühl [2020]. The primal procedure tries to hit the boundary value $f'_\infty = 1$ for $\eta \rightarrow \infty$ with prescribed wall values $f_0 = 0$ and $f'_0 = 0$. The boundary value problem is controlled by f''_0 at the wall and iterated to convergence until the value f'_∞ falls below a numerical limit of $(f'_\infty - 1) < 10^{-08}$. The result is depicted in Fig. 2.8, where $a^*=0$ and $b=1$ were assumed. The displayed numerical results perfectly match with available data from the literature, e.g. Blasius [1907], Schlichting and Gersten [2006]. The most interesting aspect is the availability of a companion adjoint Blasius solution which is outlined in Sec. 4.3.1.

Estimation of Interface Thickness and Wall Shear Stress

For known values of the Blasius solution, various b.-l. quantities can be derived, e.g. the b.-l. thickness or the shear stress distribution. This also applies to the adjoint counterparts as shown in Sec. 4.3.1. Assigning the primal b.-l. thickness to $v_1^*/V_1^* = 0.99$, yields a value of $\eta_{99} \rightarrow 4.91 \approx 5$ in line with Fig. 2.8, viz.

$$\delta_{99}^* \approx 5\sqrt{\frac{\nu^*(a^*+bx_1^*)}{V_1^*}} \qquad \text{or} \qquad \frac{\delta_{99}^*}{(a^*+bx_1^*)} \approx \frac{5}{\sqrt{\mathrm{Re}_{(a^*+bx_1^*)}}}. \tag{2.123}$$

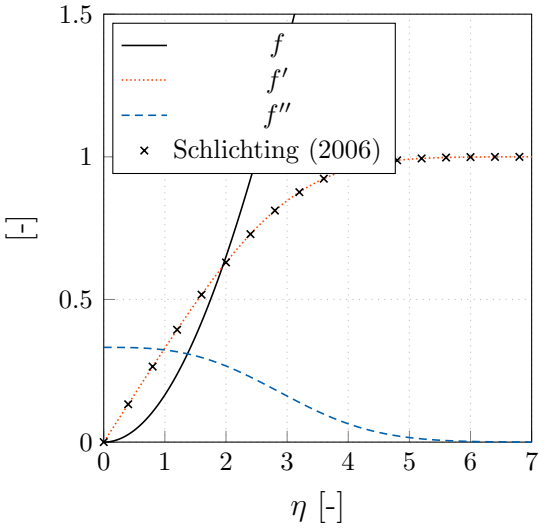

Figure 2.8: Results of a shooting method for the primal Blasius equation.

Several primal b.-l. thickness measures exist, e.g. the displacement (δ_D), momentum (δ_M) and energy (δ_E) thickness, which follow from the relation $\mathrm{d}x_2^* = \delta^* \,\mathrm{d}\eta$

$$V_1^* \delta_\mathrm{D} = \int_0^\infty \left[V_1^* - v_1^*\right] \mathrm{d}x_2^* \qquad \rightarrow \quad \delta_\mathrm{D} = \int_0^\infty \left[1 - f'\right] \mathrm{d}x_2^*$$
$$\approx 1.7208 \sqrt{\frac{\nu^*(a^* + bx_1^*)}{V_1^*}}\,, \tag{2.124}$$

$$\rho^* V_1^{2^*} \delta_\mathrm{M} = \rho \int_0^\infty v_1^* \left[V_1^* - v_1^*\right] \mathrm{d}x_2^* \qquad \rightarrow \quad \delta_\mathrm{M} = \int_0^\infty f' \left[1 - f'\right] \mathrm{d}x_2^*$$
$$\approx 0.6641 \sqrt{\frac{\nu^*(a^* + bx_1^*)}{V_1^*}}\,, \tag{2.125}$$

$$\rho^* V_1^{3^*} \delta_\mathrm{E} = \rho^* \int_0^\infty v_1^* \left[V_1^{2^*} - v_1^{2^*}\right] \mathrm{d}x_2^* \quad \rightarrow \quad \delta_\mathrm{E} = \int_0^\infty f' \left[1 - f'^2\right] \mathrm{d}x_2^*$$
$$\approx 1.0444 \sqrt{\frac{\nu^*(a^* + bx_1^*)}{V_1^*}}\,. \tag{2.126}$$

Additionally, the Blasius solution offers insight into the shear stress acting on the plate

$$\tau_\mathrm{w}^* = \mu^* \left.\frac{\partial v_1^*}{\partial x_2^*}\right|_{\mathrm{x}_2^*=0} = \mu^* V_1^* \sqrt{\frac{V_1^*}{\nu^*(a^* + bx_1^*)}} f_\mathrm{w}''$$
$$\rightarrow \qquad \tau_\mathrm{w}^* \approx 0.3321\, \mu^*\, V_1^* \sqrt{\frac{V_1^*}{\nu^*(a^* + bx_1^*)}}\,. \tag{2.127}$$

The shear is usually non-dimensionalized with a dynamic pressure ($p_\infty^* = \rho^* V_1^{2^*}/2$) to obtain skin-friction coefficients, i.e.

$$c_\mathrm{f} = \frac{\tau_\mathrm{w}^*}{\frac{1}{2}\rho^* V_1^{2^*}} = \frac{2 f_\mathrm{w}''}{\sqrt{\mathrm{Re}_{\mathrm{a+bx_1}}}} \qquad \rightarrow \qquad c_\mathrm{f} \approx \frac{0.6642}{\sqrt{\mathrm{Re}_{\mathrm{a+bx_1}}}}\,. \tag{2.128}$$

Moreover, known shear-stress distributions allow the integration of a total shear force acting on the plate

$$F_{\mathrm{s}}^{*} = \int_{\Gamma^{*}} \tau_{\mathrm{w}}^{*} \mathrm{d}\Gamma_{\mathrm{w}}^{*} = t^{*} \int_{0}^{\mathrm{L}^{*}} \mu^{*} \left.\frac{\partial v_1^{*}}{\partial x_2^{*}}\right|_{\mathrm{x}_2^{*}=0} \mathrm{d}x_1^{*} = 2 f_{\mathrm{w}}'' \, t^{*} \, V_1^{*} \sqrt{\mu^{*} \rho^{*} V_1^{*}} \frac{\sqrt{a^{*} + bL^{*}} - \sqrt{a^{*}}}{b}$$

$$\rightarrow \quad F_{\mathrm{s}}^{*} \approx 0.664 \, t^{*} \, V_1^{*} \sqrt{\mu^{*} \rho^{*} V_1^{*}} \frac{\sqrt{a^{*} + bL^{*}} - \sqrt{a^{*}}}{b} \,, \tag{2.129}$$

where t^{*} corresponds to the lateral expansion of the plate. As expected, the choice of the coordinate system has no influence on the force, since $F_{\mathrm{s}}^{*}(a^{*}=0, b=1) = F_{\mathrm{s}}^{*}(a^{*}=L^{*}, b=-1) = 2 f_{\mathrm{w}}'' \, t^{*} \sqrt{\mu^{*} \rho^{*} L^{*} V_1^{3^{*}}}$. One can compute the primal drag coefficient either from an integration of Eqn. (2.128) or from dividing Eqn. (2.129) by the dynamic pressure and the wetted surface ($L^{*} \, t^{*}$), viz.

$$c_{\mathrm{d}} = \frac{F_{\mathrm{s}}^{*}}{p_{\infty}^{*} t^{*} L^{*}} = \frac{1}{L^{*}} \int_{0}^{\mathrm{L}^{*}} c_{\mathrm{f}} \, \mathrm{d}x_1^{*} = \frac{4 f_{\mathrm{w}}''}{\sqrt{Re_{\mathrm{L}}}} \frac{\sqrt{a^{*} + bL^{*}} - \sqrt{a^{*}}}{b\sqrt{L^{*}}}$$

$$\rightarrow \qquad c_{\mathrm{d}} \approx \frac{1.3284}{\sqrt{Re_{\mathrm{L}}}} \frac{\sqrt{a^{*} + bL^{*}} - \sqrt{a^{*}}}{b\sqrt{L^{*}}} \,. \tag{2.130}$$

Verification

The Navier-Stokes procedure is firstly verified for the b.-l. flow over a finite-length flat plate, cf. Figs. 2.7 and 2.9. Numerical results are compared with the results obtained from the shooting methods for the Blasius equation. The discretized two-dimensional domain has a length of $3L$ and a height of L, where L denotes the plate length. The inlet and top boundaries are located one length away from the origin of the coordinate system. The latter is located in the leading edge of the plate. The velocity is prescribed at the inlet, a slip wall is used along the top boundary, and symmetry conditions are employed along the bottom before and after the plate. A constant pressure is imposed at the outlet and the convective term for primal momentum is approximated using the QUICK scheme. To ensure the independence of the objective functional with respect to spatial discretization, a grid study was conducted. The considered five grids are all symmetric with respect to the mid-plate at $x_1^{*}/L^{*} = 1/2$, and the grid spacing in horizontal and vertical direction was successively halved between two consecutive grids. Figure 2.10 depicts the evolution of the drag coefficient c_{d} over the grid refinement levelindicated by the number of control volumes n^{fv} for an exemplary flow at $\mathrm{Re_L} = 10^4$. Based on the grid convergence studies, all results shown hereafter were obtained for the finest grid level that consists of approximately 28.000 control volumes. The plate is discretized with 160 surface elements in streamwise direction and the boundary-layers were typically resolved by more than 50 control volumes. Since the investigated Reynolds numbers vary by two orders of magnitude, the plate normal resolution was adjusted to ensure $y^{+} = x_2^{+} = \mathcal{O}(10^{-1})$ in all cases.

Figure 2.10 compares the predicted results for drag coefficient c_{d} (center) and 99%-b.-l. thickness δ_{99}^{*} at $x_1^{*}/L^{*} = 3/4$ (right) against the Blasius results based on a measure that employs $a^{*} = 0$ and $b = 1$. Quantitatively, the resistance coefficient [interface thickness] obtained from a Blasius solution is slightly overestimated [underestimated] by the Navier-Stokes procedure for small Reynolds numbers, whereby the qualitative behavior is still in fair agreement. Supplementary to the comparison of integral parameters depicted by Fig.

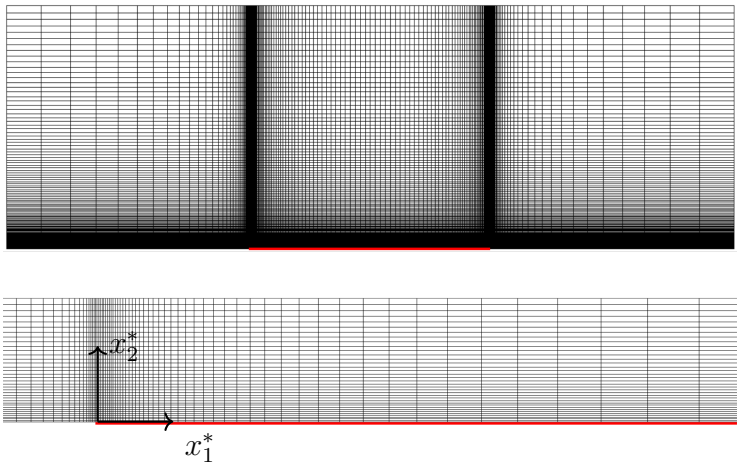

Figure 2.9: Employed structured grid for the flat plate flow. Complete domain (top) and refined region around the leading edge where the origin of the coordinate system is located (bottom). The plate is indicated by red lines.

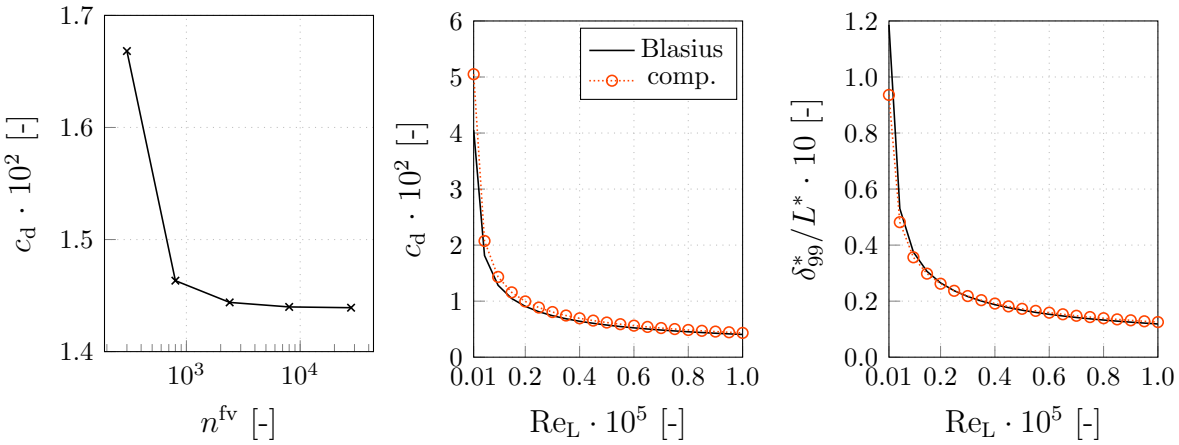

Figure 2.10: Predicted integral parameters for the primal flat plate flow. Evolution of the drag coefficient c_d over the grid refinement level – indicated by the amount of control volumes – n_fv (left), comparison of drag coefficients (center) as well as b.-l. thicknesses (δ_{99}^*; right) at $x_1^*/L^* = 3/4$ for a range of Reynolds numbers predicted by the Blasius and the Navier-Stokes procedures.

2.10, local results were examined. Results displayed in the present thesis are confined to $\mathrm{Re_L} = 10^4$. Figure 2.11 compares the normalized tangential v_1^*/V_1^* (left) and normal v_2^*/V_1^* (center) velocity profile against the similarity solution for a range of locations. While the tangential velocity fits almost perfectly with the Blasius solution, the normal component deviates significantly from the expected solution when the b.-l. approaches the trailing edge. This phenomenon is attributed to the abrupt change of the boundary condition for the examined finite-length plate, cf. Fig. 2.9, and the ability of trailing-edge information to propagate upstream in a Navier-Stokes framework. As also shown in Fig. 2.11, pronounced deviations from Blasius solutions occur for the local skin-friction coefficient c_f at the trailing edge and approximately 20% upstream.

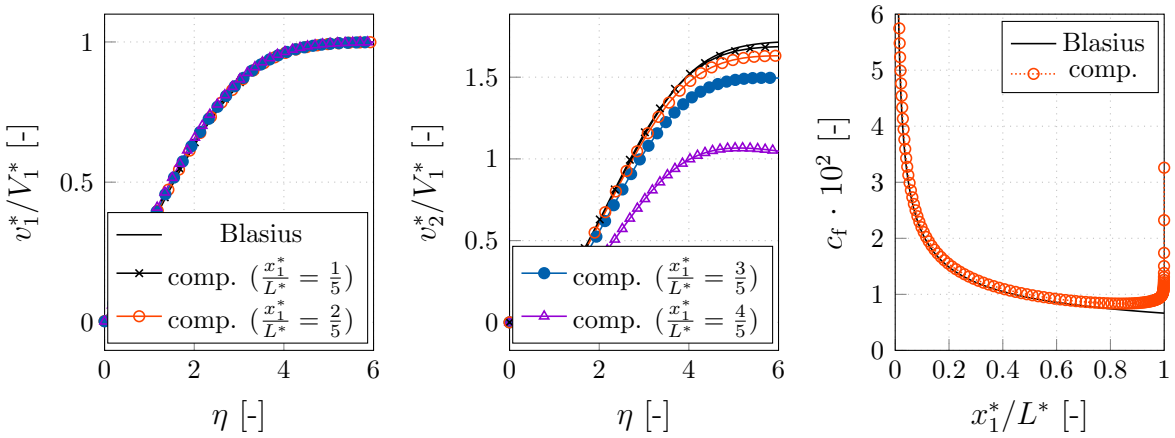

Figure 2.11: Comparison of Blasius and Navier-Stokes results for the primal flow over a flat plate at $\mathrm{Re_L} = 10^4$. Tangential velocity (v_1^*/V_1^*) against f' (left) and normal velocity (v_2^*/V_1^*) against $f'\eta - f$ (center) at four different locations. Skin-friction coefficient c_f against $0.664/\mathrm{Re}_{x_1}$ based on $a^* = 0$ and $b = 1$ (right).

2.3.2 Two-Phase Plane Couette-Flow

The implementation of the sharp and diffusive two-phase systems is verified for a planar Couette flow under the influence of inclined gravity, wherefore non-dimensional analytical solutions are constructed and compared with the numerical results. Figure 2.12 (left) illustrates the considered test case and the employed numerical grid (right) which involves 50×200 control volumes. The channel height refers to H^*. The lower half of the channel is filled with a dense background fluid and the free surface follows along a horizontal line $x_2^*/H^* = 1/2$, where the origin of the coordinate system is located at the bottom wall. The latter is at rest and the top wall moves with $v_1^*/V_1^{*\mathrm{top}} = 1$ along the horizontal direction. Field values are non-dimensionalized with the reference quantities, $V^* = V_1^{*\mathrm{top}}$, $L^* = H^*$ and $P^* = \rho_\mathrm{b}^* \, ||g_\mathrm{i}^*|| \, H^*$ in line with the non-dimensional equation system (2.49)-(2.51). The

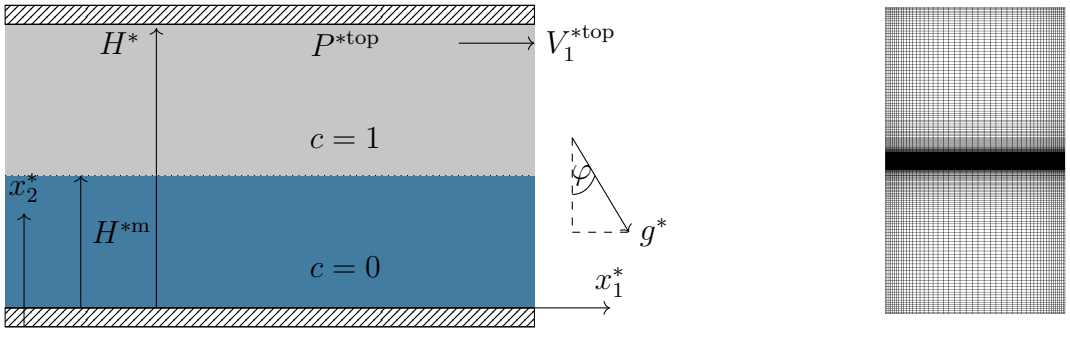

Figure 2.12: (a) Setup of the planar Couette flow verification case and (b) employed computational grid.

velocity is assumed to be unidirectional, i.e. $v_1(x_2)$, and in a fully developed, laminar, steady state. Moreover, the concentration field is also considered steady and homogeneous

in the primary direction (x_1). The interface normal between the two immiscible fluids is directed orthogonal to the wall boundaries and a body-force with variable angle of attack acts on the flow ($g_1^* = \sin(\varphi)g^*$, $g_2^* = \cos(\varphi)g^*$). Again, the flow is of particular interest due to the availability of analytical solutions for both the primal and the adjoint flow field.

Verification against Analytical Sharp Interface Solutions (VoF) are obtained by assuming an abrupt change of the fluid properties across the interface from the foreground to the background fluid. Hence, interfacial physics are neglected based on $M^* = 0$ and $\psi^* = 0$ but the gravitational vector has a variable direction of attack. The mixture fraction displays a jump at the interface and the non-dimensional primal governing equations shrink as follows

$$\mathrm{R}_1^{\mathrm{v,CO}} : \rho\, v_2 \frac{\partial\, v_1}{\partial x_2} - \frac{1}{\mathrm{Re}} \frac{\partial}{\partial x_2}\left[\mu \frac{\partial v_1}{\partial x_2}\right] - \frac{1}{\mathrm{Fn}^2}\rho\, g_1 \qquad = 0 \tag{2.131}$$

$$\mathrm{R}_2^{\mathrm{v,CO}} : \rho\, v_2 \frac{\partial\, v_2}{\partial x_2} - \frac{1}{\mathrm{Re}} \frac{\partial}{\partial x_2}\left[\mu \frac{\partial v_2}{\partial x_2}\right] + \mathrm{Eu}\frac{\partial p}{\partial x_2} - \frac{1}{\mathrm{Fn}^2}\rho\, g_2 = 0 \tag{2.132}$$

$$\mathrm{R}^{\mathrm{p,CO}} : \frac{\partial v_2}{\partial x_2} \qquad = 0 \tag{2.133}$$

$$\mathrm{R}^{\mathrm{c,CO}} : v_2 \frac{\partial\, c}{\partial x_2} \qquad = 0\,. \tag{2.134}$$

The analytical solution to the flow is integrated to

$$0 \leq x_2 < \frac{1}{2} : \begin{cases} v_1 & = \frac{1}{\mu_\mathrm{b}}\left(\frac{1}{2}T_\mathrm{b}{x_2}^2 + C_{1\mathrm{b}}x_2 + C_{2\mathrm{b}}\right) \\ p & = K_\mathrm{b}x_2 + C_{3\mathrm{b}} \\ v_2 & = 0 \\ c & = 0 \end{cases} \tag{2.135}$$

$$\frac{1}{2} < x_2 \leq 1 : \begin{cases} v_1 & = \frac{1}{\mu_\mathrm{a}}\left(\frac{1}{2}T_\mathrm{a}{x_2}^2 + C_{1\mathrm{a}}x_2 + C_{2\mathrm{a}}\right) \\ p & = K_\mathrm{a}x_2 + C_{3\mathrm{a}} \\ v_2 & = 0 \\ c & = 1\,, \end{cases} \tag{2.136}$$

with the following integration constants

$$C_{1\mathrm{a}} = \frac{\mu_\mathrm{a}\left[\frac{1}{4}T_\mathrm{b} - \frac{1}{2}T_\mathrm{a} + 2\right] - \frac{3}{4}T_\mathrm{a}}{1+\mu_\mathrm{a}},\quad C_{2\mathrm{a}} = \mu_a - \frac{1}{2}T_\mathrm{a} - C_{1\mathrm{a}},\quad C_{3\mathrm{a}} = -K_\mathrm{a} \tag{2.137}$$

$$C_{1\mathrm{b}} = \frac{1}{2}\left(T_\mathrm{a} - T_\mathrm{b}\right) + C_{1\mathrm{a}}, \qquad C_{2\mathrm{b}} = 0 \qquad C_{3\mathrm{b}} = -\frac{1}{2}\left(K_\mathrm{a} + K_\mathrm{b}\right) \tag{2.138}$$

and abbreviations

$$T_\mathrm{a} = -\frac{\mathrm{Re_H}}{\mathrm{Fn}^2}\rho_\mathrm{a} g_1, \qquad K_\mathrm{a} = \frac{1}{\mathrm{Fn}^2\mathrm{Eu}}\rho_\mathrm{a} g_2 \tag{2.139}$$

$$T_\mathrm{b} = -\frac{\mathrm{Re_H}}{\mathrm{Fn}^2}\rho_\mathrm{b} g_1, \qquad K_\mathrm{b} = \frac{1}{\mathrm{Fn}^2\mathrm{Eu}}\rho_\mathrm{b} g_2\,. \tag{2.140}$$

This solution follows from Dirichlet conditions for the concentration and velocities along the top as well as the bottom wall ($v_1(1) = c(0) = 1,\ v_1(0) = c(1) = 0$). Additionally,

a prescribed top-wall pressure ($p(1) = 0$) is employed. The planar two-phase Couette flow illustrated by Fig. 2.12 is solved with periodic boundary conditions for Reynolds and Froude numbers of $\mathrm{Re_H} = 100$ and $\mathrm{Fn} = 5$. The required non-dimensional density (viscosity) ratios are assigned to exemplary values of $\rho_\mathrm{a} = \rho_\mathrm{a}^*/\rho_\mathrm{b}^* = 1/4$ ($\mu_\mathrm{a} = \mu_\mathrm{a}^*/\mu_\mathrm{b}^* = 1/4$), $\rho_\mathrm{a} = 1$ ($\mu_\mathrm{a} = 1$) as well as $\rho_\mathrm{a} = 4$ ($\mu_\mathrm{a} = 4$) and therefore range from a lighter and less viscous to a heavier and more viscous upper fluid. Convective primal momentum fluxes are discretized using a UDS whereas diffusion employs a CDS. The approximation of convective concentration transport is realized with the HRIC approach. A comparison of the analytical primal solutions (2.135, 2.136) with the numerical results for a gravity angle of $\varphi = 10°$ is displayed in Fig. 2.13. The numerical implementation resolves the ideally

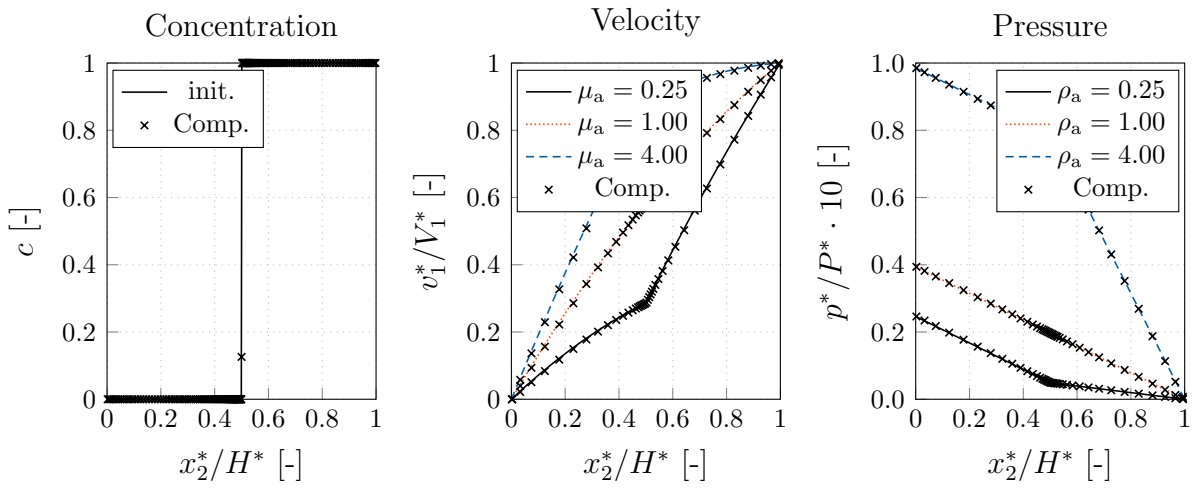

Figure 2.13: Plane Couette flow case ($\mathrm{Re_H} = 100$, $\mathrm{Fn_H} = 5$). Comparison of analytical solutions with primal VoF results for the concentration (left), the velocity (center) and the pressure (right) in a plane Couette flow at a Froude and Reynolds number of $\mathrm{Re_H} = 100$ and $\mathrm{Fn} = 5$ using a density (viscosity) ratios of $\rho_\mathrm{a} = \rho_\mathrm{a}^*/\rho_\mathrm{b}^* = 1/4$ ($\mu_\mathrm{a} = \mu_\mathrm{a}^*/\mu_\mathrm{b}^* = 1/4$), $\rho_\mathrm{a} = 1$ ($\mu_\mathrm{a} = 1$) and $\rho_\mathrm{a} = 4$ ($\mu_\mathrm{a} = 4$) under a gravity angle of $\varphi = 10°$.

sharp interface between both fluid phases within 2-4 cells, which is a common observation for VoF procedures that employ compressive approximations for the convective term.

Verification against Analytical Diffuse Interface Solutions (CH-VoF) are obtained by resolving the interfacial region while fixing the gravitational vector to be in line with the interface normal, e.g. $x_\mathrm{i}\, g_\mathrm{i} = 0$ and $\varphi = 0°$. Hence, the complexity is shifted from the streamwise momentum equation –that no longer experiences gravitation– to the concentration equation. The latter has a non-trivial solution now which directly couples into both momentum equations due to the extraction of fluid properties based on c. The sim-

plification of Eqns. (2.51)-(2.49) results in

$$\mathrm{R}_1^{\mathrm{v,CO}} : \rho\, v_2 \frac{\partial\, v_1}{\partial x_2} - \frac{1}{\mathrm{Re}} \frac{\partial}{\partial x_2} \left[\mu \frac{\partial v_1}{\partial x_2} \right] - \frac{1}{\mathrm{Fn}^2} \rho\, g_1 \qquad = 0 \tag{2.141}$$

$$\mathrm{R}_2^{\mathrm{v,CO}} : \rho\, v_2 \frac{\partial\, v_2}{\partial x_2} - \frac{1}{\mathrm{Re}} \frac{\partial}{\partial x_2} \left[\mu \frac{\partial v_2}{\partial x_2} \right] + \mathrm{Eu} \frac{\partial p}{\partial x_2} - \frac{1}{\mathrm{Fn}^2} \rho\, g_2 = 0 \tag{2.142}$$

$$\mathrm{R}^{\mathrm{p,CO}} : \frac{\partial v_2}{\partial x_2} \qquad = 0 \tag{2.143}$$

$$\mathrm{R}^{\mathrm{c,CO}} : v_2 \frac{\partial\, c}{\partial x_2} + \frac{1}{\mathrm{Pe}} \frac{\partial^2}{\partial {x_2}^2} \left[4c^3 - 6c^2 + 2c - \mathrm{Ca}_{\mathrm{H}}^2 \frac{\partial^2 c}{\partial {x_2}^2} \right] = 0\,. \tag{2.144}$$

Using the linear EoS (2.7) allows an integration of (2.141)-(2.144) and results in the following analytical solution

$$v_1 = \frac{4\; x_2 + \mathrm{Ca_H}\; (\mu_\mathrm{a} - 1) \log \left[\frac{\mu_\mathrm{a}+1+(1-\mu_\mathrm{a})\; \tanh\left(\mathrm{Ca_H}^{-1}\right)}{\mu_\mathrm{a}+1-(1-\mu_\mathrm{a})\; \tanh\left(\mathrm{Ca_H^{-1}}\left(2x_2^{-}1\right)\right)} \frac{\tanh\left(\mathrm{Ca_H^{-1}}(2x_2-1)\right)+1}{1-\tanh\left(\mathrm{Ca_H^{-1}}\right)} \right]}{4 + \mathrm{Ca_H}\;\; (\mu^\mathrm{a} - 1) \log \left[\frac{\mu_\mathrm{a}+1+(1-\mu_\mathrm{a})\; \tanh\left(\mathrm{Ca_H^{-1}}\right)}{\mu_\mathrm{a}+1-(1-\mu_\mathrm{a})\; \tanh\left(\mathrm{Ca_H^{-1}}\right)} \frac{\tanh\left(\mathrm{Ca_H^{-1}}\right)+1}{1-\tanh\left(\mathrm{Ca_H^{-1}}\right)} \right]} \tag{2.145}$$

$$p = \frac{1}{\mathrm{Eu}\; \mathrm{Fn_H^2}} \left[\rho_\mathrm{a}\,(1 - x_2) + \frac{\mathrm{Ca_H}\,\rho_\Delta}{4} \log \left(\frac{\tanh\left(\mathrm{Ca_H}^{-1}\,(x_2 - 1)\right) + 1}{\tanh\left(\mathrm{Ca_H^{-1}}\right) + 1} \right) \right] \tag{2.146}$$

$$v_2 = 0 \tag{2.147}$$

$$c = \frac{1}{2} \left[\tanh\left(\mathrm{Ca_H^{-1}}\,(2x_2 - 1)\right) + 1 \right]. \tag{2.148}$$

Similar to the sharp interface consideration, the solution follows from Dirichlet conditions for the concentration and velocities along the top as well as the bottom wall ($v_1(1) = c(0) = 1,\; v_1(0) = c(1) = 0$). A prescribed top-wall pressure ($p(1) = 0$) is employed. Thanks to the mass balance, the solution is independent from the Peclet number and thus also from the mobility parameter M^*. Computational results for the CH-VoF system follow the above VoF configuration and the mobility is assigned to a value that results in $\mathrm{Pe} = 10^5$. Predictive results are compared with analytical solutions for a range of Cahn numbers (Ca=0.2, 0.1, 0.02), viscosity ratios ($\mu_\mathrm{a} = 0.25, 1, 4$) and density ratios ($\rho_\mathrm{a} = 0.25, 1, 4$) along with exemplary flow conditions of $\mathrm{Re_H} = 100$, $\mathrm{Fn_H} = 0.5$ and $\mathrm{Eu} = 4$. Numerical results extracted along the center vertical line are displayed in Fig. 2.14. The left graph compares analytical and computed concentration profiles for three different Cahn numbers. A comparison of results obtained for different fluid properties at $\mathrm{Ca_H}$=0.1 is displayed in the other two graphs of the figure. All comparisons reveal an excellent predictive agreement with the analytical solutions (2.145)-(2.148).

2.3.3 Universal Law of the Wall for Turbulent Flows

The discussion on the third verification example is confined to single-phase, turbulent plane wall flows, using a local orthogonal coordinate system as illustrated in Fig. 2.15, where x_2^* denotes the wall normal coordinate or distance and x_1^* refers to the wall tangential direction. The flow field is considered to be fully developed and assumed as uni-directional, i.e. $v_1^*(x_2^*)$ in the vicinity of the wall. A key element of the concept - which is crucial for

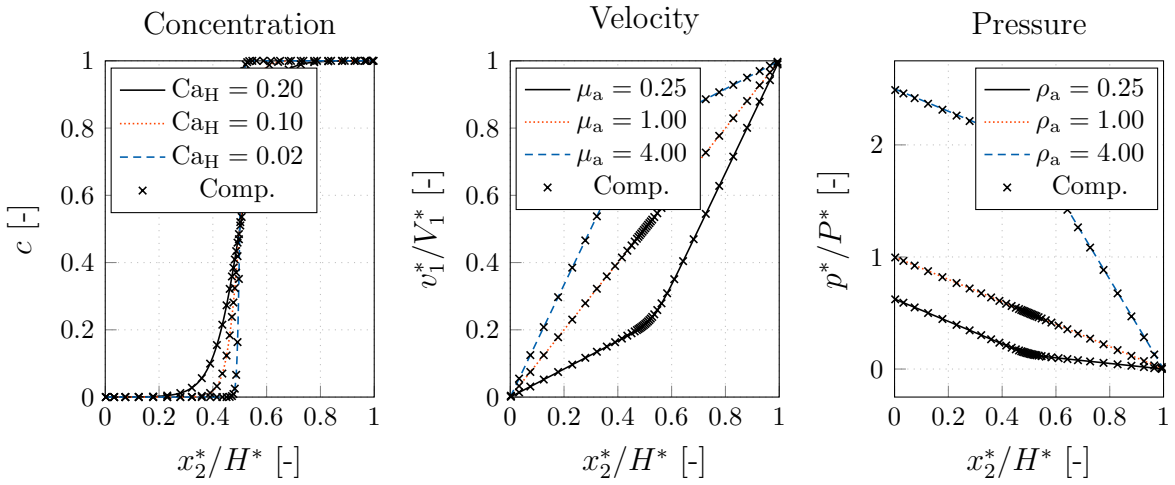

Figure 2.14: Comparison of numerical CH-VoF and analytical results for the planar Couette flow example at $\mathrm{Re_H} = 100$, $\mathrm{Fn_H} = 0.5$, $\mathrm{Eu} = 4$ and $\mathrm{Pe} = 1 \times 10^5$. Left: Concentration profiles for different Cahn numbers; Middle: Velocity profiles for different viscosity ratios ($\mathrm{Ca_H}$=0.1); Right: Pressure profiles for different density ratios ($\mathrm{Ca_H}$=0.1).

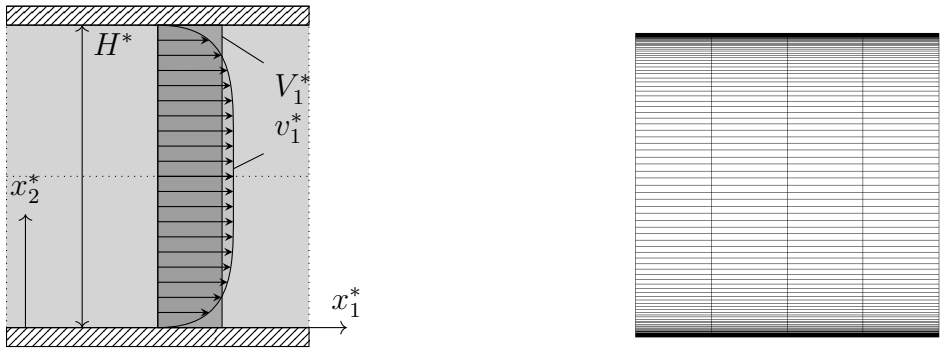

(a) (b)

Figure 2.15: Investigated turbulent channel flow. Sketch of the considered geometry (a) and computational grid (b) for an exemplary Reynolds number of $\mathrm{Re_H} = 10^7$.

the formulation of boundary conditions for turbulent wall flows – is the constant shear stress hypothesis. The latter assumes $\tau^{*\mathrm{eff}} = \text{const.}$, for the inner region of a wall b.-l. $x_2^*/\Delta^* << 1$, where $x_2^* = \Delta^*$ denotes the outer edge of the b.-l. . The simple relation substitutes the momentum equation above the wall and supports the derivation of the primal –and later also for the adjoint– LoW, viz.

$$\mathrm{R}_1^{\mathrm{v,CH}^*}: \qquad \frac{\mathrm{d}\tau^{*\mathrm{eff}}}{\mathrm{d}x_2^*} = \frac{\mathrm{d}}{\mathrm{d}x_2^*}\left[\mu^{*\mathrm{eff}}\frac{\mathrm{d}v_1^*}{\mathrm{d}x_2^*}\right] = 0\,. \tag{2.149}$$

The validity of (2.149) improves with increasing boundary-layer thickness which increases with Reynolds number, cf. Pope [2001], Wilcox [1998]. Mind that despite the particular turbulence model employed to determine $\mu^{*\mathrm{t}}$, e.g. the $k^* - \epsilon^*$, $k^* - \omega^*$ or $\nu^{*\mathrm{t}}$ formulation (e.g. Wilcox [1998], Spalart and Allmaras [1992]), their values usually comply with the

mixing length hypothesis in the logarithmic layer, i.e. $\mu^{*\mathrm{t}} = \rho^* (\kappa\, x_2^*)^2\, \mathrm{d}v_1^*/\mathrm{d}x_2^*$, where $(\kappa\, x_2^*)$ denotes the mixing length and κ is the von-Karman constant.

According to its units, the constant stress $\tau^{*\mathrm{eff}}$ is anticipated to be proportional to the square of a friction velocity $V_{1,\tau}^*$, viz. $\tau^{*\mathrm{eff}} := \rho^*\, {V_{1,\tau}^2}^* = \text{const.}$. The two-layer model assumes a vanishing turbulent stress in the immediate vicinity of the turbulence damping wall ($\mu^{*\mathrm{t}}/\mu^* \to 0$), frequently labeled as viscous sub-layer, and the opposite behavior beyond a certain wall normal distance, i.e. the logarithmic-layer, where $\mu^*/\mu^{*\mathrm{t}} \to 0$. Using $\nu^* = \mu^*/\rho^*$ and $\nu^{*\mathrm{t}} = \mu^{*\mathrm{t}}/\rho^*$, Eqn. (2.149) is usually integrated separately for both limit cases

$$x_2^* < \tilde{x_2}^* : \qquad {V_{1,\tau}^2}^* = \nu^* \frac{\mathrm{d}v_1^*}{\mathrm{d}x_2^*} \qquad \to \qquad v_1^* = \frac{{V_{1,\tau}^2}^*}{\nu} x_2^* + C_1^* \tag{2.150}$$

$$x_2^* \geq \tilde{x_2}^* : \qquad {V_{1,\tau}^2}^* = (\kappa x_2^*)^2 \left|\frac{\mathrm{d}v_1^*}{\mathrm{d}x_2^*}\right| \frac{\mathrm{d}v_1^*}{\mathrm{d}x_2^*} \qquad \to \qquad v_1^* = \frac{V_{1,\tau}^*}{\kappa} \ln(x_2^*) + C_2^* \,, \tag{2.151}$$

where $\tilde{x_2}^*$ represents the (theoretical) intersection of the sub- and the logarithmic-layer solution. The use of a no-slip condition along the wall, i.e. at $x_2^* = 0$, returns $u_{\mathrm{w}}^* = C_1^* = 0$. The integration constant C_2^* is chosen so that the desired transition point is realized and thereby hinges on the choice of κ. Using non-dimensional parameters, i.e. $x_2^+ = V_{1,\tau}^* x_2^*/\nu^*$ and $v_1^+ := v_1^*/V_{1,\tau}^*$ yields a more compact form of the LoW, viz.

$$v_1^+ = \begin{cases} x_2^+ & \text{for } x_2^+ < \tilde{x_2}^+ \\ \frac{1}{\kappa} \ln\left(x_2^+\right) + B & \text{for } x_2^+ \geq \tilde{x_2}^+ \end{cases}, \tag{2.152}$$

where the constant C_2^* is turned into a non-dimensional constant B. Frequently used parameter combinations refer to $\kappa = 0.4$ and $B = 5$ to match $\tilde{x}_2^+ \approx 11$. In reality the transition from the near-wall to the logarithmic-layer solution spreads over a small region labeled as buffer-layer.

Verification

The computational studies are performed for turbulent flows at Reynolds numbers between $10^6 \leq \mathrm{Re_H} \leq 10^8$ based on the channel height H^*, the bulk velocity V_1^* and the kinematic fluid viscosity ν^*. A simple, fully developed 2D channel flow is considered, cf. Fig. 2.15 (a). Periodic boundary conditions are employed for the velocity between the inlet and the outlet. A no-slip condition is used along the top and bottom boundaries in conjunction with low-Re and high-Re grids. The numerical grids consist of 4×250 Finite-Volumes and the wall normal resolutions reach down to $x_2^+ = \mathcal{O}(10^{-1})$ for the low-Re cases and $x_2^+ \approx 50$ for the high-Re cases, cf. Fig. 2.15 (b). The low-Re study aims to verify the predictive agreement with the LoW (2.152) when the turbulent closure refers to a mixing-length model supplemented by a van-Driest damping function, cf. Eqn. (2.35). The approach is also chosen for later adjoint LoW studies, cf. Sec. 4.3.3. Results obtained from a high-Re formulation employ a $k^* - \epsilon^*$ closure. Figure 2.16 depicts the results obtained for the low- and high-Re studies. For all three investigated Reynolds numbers, the results are in remarkably fair predictive agreement with the respective LoW (2.152). All low-Re results feature a narrow buffer-layer region triggered by the employed van-Driest term.

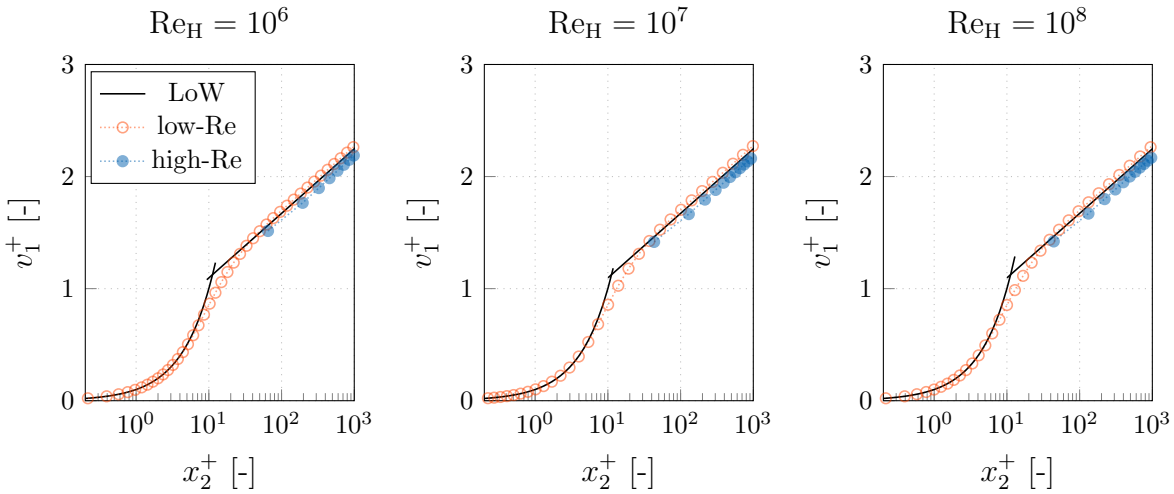

Figure 2.16: Turbulent channel flow (Low- and High-Reynolds formulation): Predicted primal results based on a low- and high-Reynolds formulation for Reynolds numbers between $10^6 \leq \mathrm{Re_H} \leq 10^8$ increasing from left to right.

2.4 Primal Flow Validation

After the successful verification of the implementation, more complex situations are investigated for validation purposes. Hence, whereas the previous section aimed to demonstrate that the *equations are solved correctly*, this section investigates if the *correct equations are solved* by means of several 1D, 2D and 3D studies where experimental or analytical solutions are available.

2.4.1 Stationary Bubble

The influence of the surface tension model is verified by computing the transition from an initial non-equilibrium (rectangular) bubble into an equilibrium (circular) bubble. The example is restricted to advancing a 2D flow field without gravitational effects ($\mathrm{Fn} = \infty$) in pseudo-time. As outlined in Fig. 2.17, a lighter foreground phase ($\rho^{*\mathrm{a}}/\rho^{*\mathrm{b}} = 1/100$) rectangle with an edge length of $L^* = 0.005\,\mathrm{m}$ is initially embedded into a heavier phase, such that the surface tension directs the shape of the interface towards a circle. Equal viscosities are employed for both fluids. Due to the symmetrical arrangement, only one quarter of the bubble is simulated on a homogeneous isotropic grid. Symmetry conditions are placed along the two main axes and the outer boundaries of the domain. Second-order approximations are conducted for transient (ITTL) and convective (QUICK) terms. The grid employs 550×550 control volumes to cover the quartered domain of $L^* \times L^*$. The Cahn number based on the initial edge length L^* reads $\mathrm{Ca_L} = 0.02$ and the transition is resolved by 11 control volumes. In line with an assumed unit Reynolds number, the reference velocity is defined as $V^* = \mu^{*\mathrm{b}}/(\rho^{*\mathrm{b}}\ L^*)$. The mobility and the surface tension are chosen to end up with Peclet and Weber numbers of $\mathrm{Pe_L} = 4 \times 10^4$ and $\mathrm{We} = 800$ respectively.

As observed in Fig. 2.17 (a), the rectangular bubble deforms into a circle over time. In addition the figure indicates the temporary velocity vectors which decay in time. In the final state, the pressure difference between the bubble center and a far outside location reads $\Delta p^* = 2.0\,\mathrm{Pa}$, which matches the result of the 2D Young-Laplace law, i.e. $\Delta p^* = \sigma^{*\mathrm{a,b}}/R^*$, and also indicates the correct prediction of the final bubble radius $R^* = L^*/\sqrt{\pi}$. To underline the correct pressure approximation, the same situation is simulated with an increased transition length for three different surface tension values $\sigma^{*\mathrm{a,b}} = 0.5, 0.25, 0.0625$ [N/m] at $\mathrm{Ca_L} = 0.1$, $\mathrm{Pe_L} = 200[N/m]/\sigma^{*\mathrm{a,b}}$, $\mathrm{We} = 4[N/m]/\sigma^{*\mathrm{a,b}}$. Figure 2.17 (b) shows the resulting pressure distributions over a radial coordinate which reveal a fair agreement with theoretical results.

2.4.2 Standing Waves

The second example deals with the decay of standing waves which are initialized according to Fig. 2.18 (a). It should be assessed, if the shear driven energy exchange between the two fluids is captured correctly in both, the capillary and the gravity regime under the influence of vertical gravitational acceleration g_2^*. Numerical results are compared with analytical solutions of Prosperetti [1981], which exist for identical kinematic viscosities ($\mu^{*\mathrm{a}}/\rho^{*\mathrm{a}} = \mu^{*\mathrm{b}}/\rho^{*\mathrm{b}}$) in the linear (laminar) flow regime. A comprehensive overview and derivation is offered by Akervik and Vartdal [2016]. The initial wave length complies with a unit wave number ($k^* = 2\,\pi/\lambda^* = 1\,\mathrm{m}$) and the initial wave amplitude corresponds to

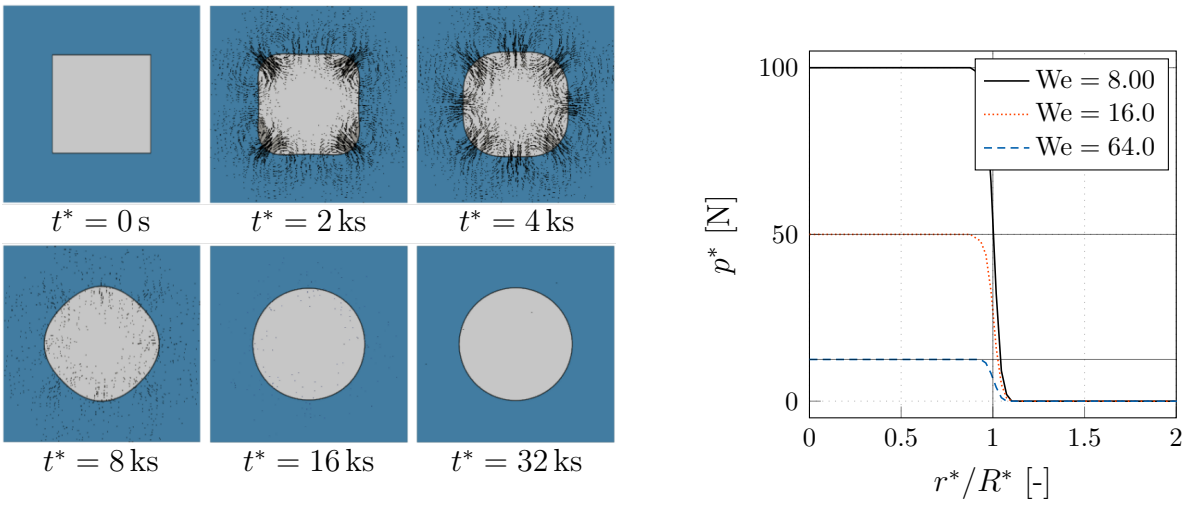

(a) (b)

Figure 2.17: (a) Evolution of shape and velocity fields for the surface tension driven transition from an initially rectangular to a round bubble (ks refers to 10^3 seconds) and (b) computed pressure distribution along a radial slice that originates in the center of a bubble with radius $R^* = L^*/\sqrt{\pi}$ for different surface tension coefficients $\sigma^{*\mathrm{a,b}} = 0.5, 0.25, 0.0625$ [N/m] at $\mathrm{Ca_L} = 0.1$, $\mathrm{Pe_L} = 200[N/m]/\sigma^{*\mathrm{a,b}}$ and $\mathrm{We} = 4[N/m]/\sigma^{*\mathrm{a,b}}$. Grey horizontal lines in (b) indicate the expected interior pressure obtained by the Young-Laplace law.

$a^* = 0.01\,\lambda^*$. The reference velocities refer to $V^* = \sqrt{|g_2^*|\,\lambda^*}$ and $V^* = \sqrt{\sigma^{*\mathrm{a,b}}/(\lambda^*\,\rho^{*\mathrm{b}})}$ for the gravity and the capillary case, respectively. The extent of the 2D computational domain depicted in Fig. 2.18 (b) reads $\lambda^* \times \lambda^*$. A locally refined grid with approximately 250.000 isotropic control volumes is employed. The resolution of the free surface region refers to $\Delta x_1^* = \Delta x_2^* = \lambda^*/4000$. The time step is assigned to $\Delta t^* = \lambda^*/(4000V^*)$ which is sufficient to ensure Courant numbers below $\mathrm{Co} < 0.1$. Symmetry [no-slip] conditions are used along constant x_1^* [x_2^*] boundaries of the domain and second-order approximations are conducted for transient (ITTL) and convective (QUICK) terms.

For the gravity wave, surface tension influences are neglected and the density ratio and Reynolds number read $\rho^{*\mathrm{a}}/\rho^{*\mathrm{b}} = 1/100$ and $\mathrm{Re} = V^*\lambda^*/\nu^{*\mathrm{b}} = 1000$. The CH-VoF simulations are based on the mobility estimation described in Sec. 2.2.9 and the nonlinear EoS ($\tilde{M} = 0.1$, $\gamma^{\mathrm{m},\rho} = 0.4$). Figure 2.19 (top) displays the evolution of the free surface elevation at the horizontal left end ($x_1^*/\lambda^* = 0$) predicted by CH-VoF and VoF next to the analytical solution of Prosperetti [1981]. In comparison to the linear theory, the top figure reveals a slightly stronger wave damping and a minor phase shift returned by the CH-VoF approach for the gravity case, which outperforms the present VoF method. The latter is a consequence of the resharpening character of the CH-VoF approach, which is scrutinized in next subsection.

For the capillary case, the density and viscosity ratios read $\rho^{*\mathrm{a}}/\rho^{*\mathrm{b}} = 1/100$ and $\mu^{*\mathrm{a}}/\mu^{*\mathrm{b}} = 1/10$, respectively, the interface thickness is resolved by 10 vertical cells and follows from a Cahn number of $\mathrm{Ca}_\lambda = \gamma^*/\lambda^* = 1/400$. The Ohnesorge number adjusts the surface tension force σ^* and reads $\mathrm{Oh} = \mu^{*\mathrm{b}}/\sqrt{(\sigma^{*\mathrm{a,b}}\lambda\rho^{*\mathrm{b}})} = 1/100$. The mobility parameter is prescribed

in accordance with a Peclet number of $\mathrm{Pe}_\lambda = 2 \cdot 10^{10}$ together with the linear EoS. Conclusions drawn for the capillary case are similar to the gravity case, as indicated by Fig. 2.19 (bottom), which compares the evolution of the wave amplitude at the horizontal left end ($x_1^*/\lambda^* = 0$) predicted by the present CH-VoF with the analytical solution of Prosperetti [1981].

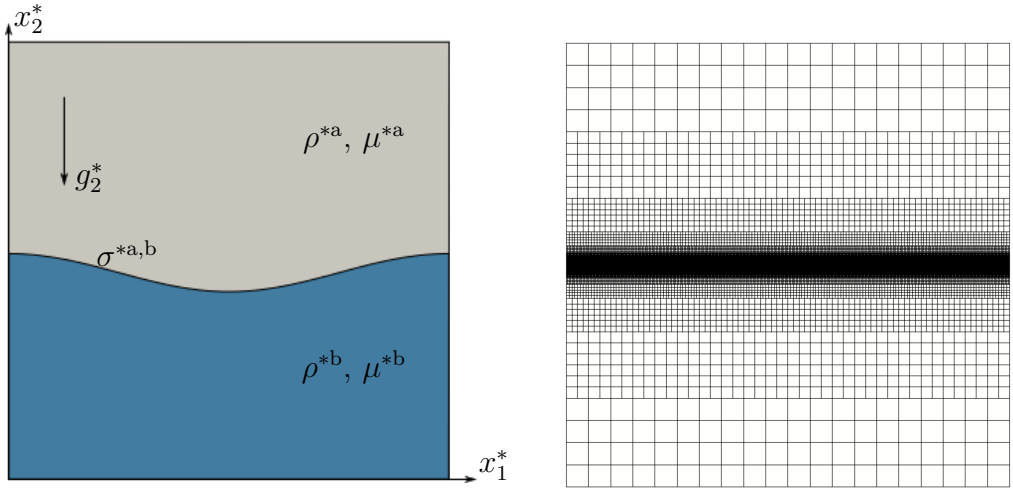

Figure 2.18: (a) Initial setup of the standing wave case (scaled for visualization purposes) and (b) employed computational grid.

2.4.3 Resharpening Capability

An illustrative 1D example is used to demonstrate the resharpening capability of the nonlinear density (2.6) and viscosity (2.13) EoS. A free surface is transported by a prescribed flow field on the grid depicted in Fig. 2.20 (a). The horizontal flow field is directed from left to right with a constant velocity of $V^* = v_1^* = 1\,\mathrm{m/s}$, and only the concentration equation (2.27) is computed. The employed grid is homogeneous ($\lambda = 0.5$) and features $\Delta x_1^* = 10^{-3}\mathrm{m}$ and $\Delta x_2^* = 1\mathrm{m}$. The simulation is initialized with a sharp interface along a vertical line at the center location $x_1^* = 1\mathrm{m}$. Figure 2.20 (b) displays a partly blurred interface from one CH simulation with $\tilde{M} = 0.1$ and $\mathrm{Co} = 1$ after $t^* = 5\,\mathrm{s}$. The corresponding density field obtained from the nonlinear equation of state using $\gamma^{\mathrm{m},\rho} = 0.1$ is displayed in Fig. 2.20 (c). Although the concentration field is slightly blurred, the resulting density and viscosity fields are sharp.

Subsequently, an additional 2D example refers to a circle of radius $r^*/L^* = 0.15$ that is initially placed at $x_\mathrm{i}^*/L^* = [0.5, 0.75]^\mathrm{T}$ in a square of unit length ($L^* = 1\,\mathrm{m}$) as described in Rider and Kothe [1998]. In this frequently employed validation example, the free surface is advected under a spatial deforming velocity field $v_1^* = -\partial\psi^*/\partial x_2^*$, $v_2^* = \partial\psi^*/\partial x_1^*$ where $\psi^* = \sin^2(x_1^*\,\pi)\sin^2(x_2^*\,,\pi)/\pi$ defines the stream function. Above all, it should be shown that the proposed approach allows for Courant numbers $\mathcal{O}(1)$ and has resharpening capabilities also under complex and large interface deformations. Therefore, a comparatively fine numerical grid with $\Delta x_\mathrm{i}^*/L^* = 1/400$ is used combined with $\Delta t^* = \mathrm{Co}\,\Delta x_\mathrm{i}^*/V^*$ and $\mathrm{Co} = 2$ as well as $V^* = 1\,\mathrm{m/s}$ in accordance to the maximum value from the stream

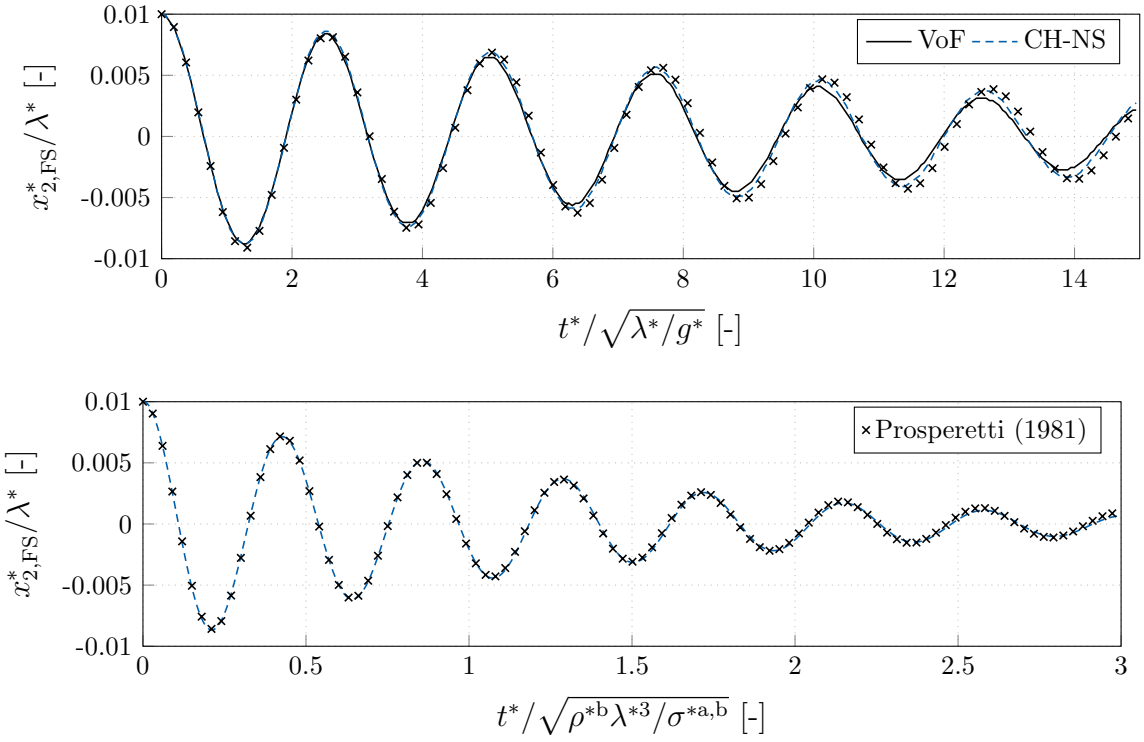

Figure 2.19: Comparison of the analytical (symbols) and numerical time evolution for the wave elevation at the left boundary ($x^*_1/\lambda^* = 0$) obtained for the gravity (top) and the capillary (bottom) case.

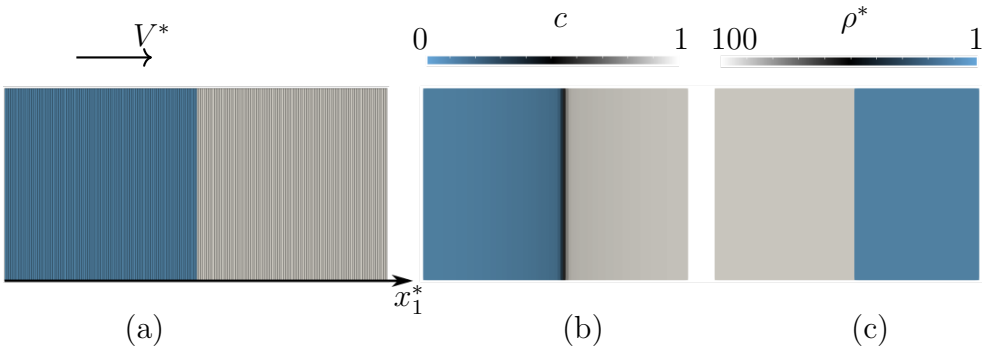

Figure 2.20: (a) Computational grid with initial conditions for a 1D concentration advection, (b) slightly blurred interface predicted by a CH-VoF simulation using $\tilde{M} = 0.1$ and $\mathrm{Co} = 1$ after $t^* = 5\,\mathrm{s}$ and (c) corresponding density field returned by the nonlinear equation of state ($\gamma^{\mathrm{m},\rho} = 0.05$).

function definition. Symmetry boundary conditions are used and second-order approximations are conducted for transient (ITTL) and convective (QUICK) terms. Results are assessed by means of the predicted interface sharpness and the spatial progression of the interface over time. A local sharpness indicator quantity q is used to judge the interface quality as suggested in Manzke [2018]. The latter employs the computed con-

centration gradient at an interfacial face and multiplies this with twice the grid-spacing, i.e. $q^{-1} = 2\Delta x_\mathrm{i}^* \, (\partial c / \partial x_\mathrm{i}^*)_{(c=0.5)}$. In the present example, an interfacial face is a face that is adjacent by one cell featuring $c < 0.5$ and one cell featuring $c > 0.5$. A perfectly sharp interface results in $q = 1$, acceptable interfaces follow from $q < 3$ and a global reference is determined by the arithmetic average of all local sharpness indicators q, labeled Q.

Three CH-VoF simulations are performed. Two simulations refer to temporally constant mobility parameter values $\tilde{M} = 1$ and $\tilde{M} = 0.01$, which should feature measurable differences on the predicted sharpness. In the third case, $\tilde{M}$ switches between the two constant values, i.e. $\tilde{M}(1\,\mathrm{s} \leq t^* \leq 2\,\mathrm{s}) = 0.01$ and $\tilde{M}(t^* < 1\,\mathrm{s}, 2\,\mathrm{s} < t^*) = 1$. The evolution of the advected concentration over time is displayed in Fig. 2.21 (a) for the switching mobility parameter case. In the first and last third of the simulation the interface remains basically sharp, which is no longer the case for the time $1\,\mathrm{s} \leq t^* \leq 2\,\mathrm{s}$ where the lower choice of $\tilde{M}$ is not able to overcome the numerical diffusion. The visible temporary blurring is also displayed by the sharpness indicator in Fig. 2.21 (b) (bottom) that underlines the (on-the-fly) resharpening capability and the competent predictive performance of the CH-VoF in comparison to VoF schemes (HRIC; Co = 0.2).

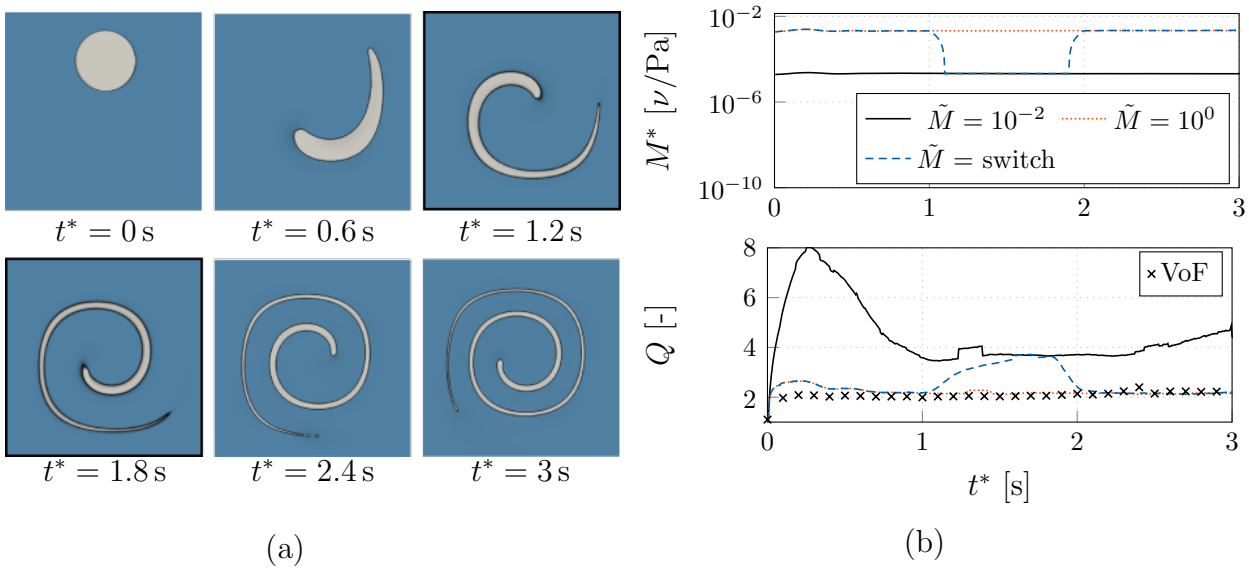

Figure 2.21: Time evolution of (a) the concentration contour for a prescribed mobility of $\tilde{M} = 1$ that is reduced to $\tilde{M} = 0.01$ between $1\,\mathrm{s} \leq t^* \leq 2\,\mathrm{s}$ and (b) mobility M^* (top) and global sharpness indicator Q (bottom) over the simulation time for different under-resolved CH-VoF simulations at Co = 2.

2.4.4 Hydrofoil

The next example refers to the wave pattern downstream of a submerged NACA0012 hydrofoil at 5° incidence in accordance with experimental data of Duncan [1981, 1983], cf. Fig. 2.22 (a). The chord length to submergence ratio at the leading edge of the foil reads $L^{*\mathrm{c}}/L^* = 7/9$. The study is performed for a turbulent flow at $\mathrm{Re} = V^* \, L^{*\mathrm{c}}/\nu^{*\mathrm{b}} = 144\,855$ and $\mathrm{Fn} = V^*/\sqrt{G^* L^*} = 0.567$, based on the gravitational acceleration $G^* = |g_2^*|$, the inflow velocity $V^* = |v_1^*|$ and the kinematic viscosity of the water $\nu^{*\mathrm{b}}$. The two-

dimensional domain has a length and height of $75\,L^{*\mathrm{c}}$ and $25\,L^{*\mathrm{c}}$, where the inlet and bottom boundaries are located 10 chord-lengths away from the origin. A dimensionless wave length of $\lambda = \lambda^*/L^* = 2\,\pi\,\mathrm{Fn}^2 = 2.0193$ is expected.

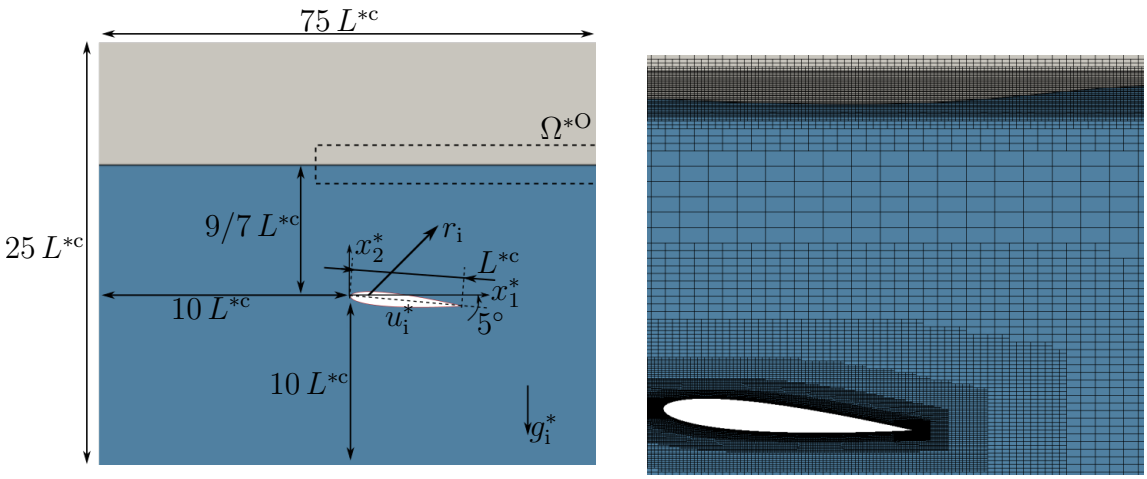

(a) (b)

Figure 2.22: Submerged hydrofoil case ($\mathrm{Re_L} = 144\,855$, $\mathrm{Fn} = 0.567$): (a) Schematic drawing of the initial configuration and (b) unstructured numerical grid around the foil and the free surface.

The utilized unstructured numerical grid is displayed in Fig. 2.22 (b) and consists of approximately 150 000 control volumes. The fully turbulent simulations employ a wall-function-based $k^* - \omega^*$ SST model and all convective terms are approximated using the QUICK scheme. At the inlet, velocity and concentration values are prescribed, slip walls are used along the top and bottom boundaries and a hydrostatic pressure boundary is employed along the outlet. The wall normal distance of the first grid layer reads $y^+ = x_2^+ \approx 30.0$ and the free surface refinement employs approximately $\Delta x_1^*/\lambda^* = 1/100$ cells in the longitudinal as well as $\Delta x_2^*/\lambda^* = 1/400$ cells in the normal direction. The VoF approach is integrated in pseudo-time with a time step size of $\Delta t^* = \Delta x_2^*/V^*$ Co together with $\mathrm{Co} = 0.1$. The CH-VoF results are obtained from a steady state approach.

The study neglects surface tension due to an under-resolved interface thickness and employs both the linear (2.7) as well as the nonlinear EoS, $\gamma^{\mathrm{m},\rho} = \gamma^{\mathrm{m},\mu} = 0.6$. The surface tension force is neglected in the momentum equation and the concentration equation utilizes $C_2^* = 0\,\mathrm{N}$ and $C_1^* = 1\,\mathrm{Pa}$. Figure 2.23(a) shows the wave elevation for two CH-VoF simulations with the same modeled mobility parameter ($\tilde{M} = 0.1$) but different EoS next to the result of a VoF simulation. The nonlinear EoS outperforms the linear version and drives the CH-VoF approach closer to the experimental data as well as to the VoF result. Similar to the results displayed in Fig. 2.20, the linear model provides slightly blurred density fields which translate into a reduction of the wave amplitude. Figure 2.23 (b) tracks the drag force coefficient over the simulation time $t^{*\mathrm{sim}}$ for the VoF and the nonlinear CH-VoF simulations. The predicted drag differs about 0.4% and a speed up of approximately one order of magnitude is achieved through the Courant number independent CH-VoF approach.

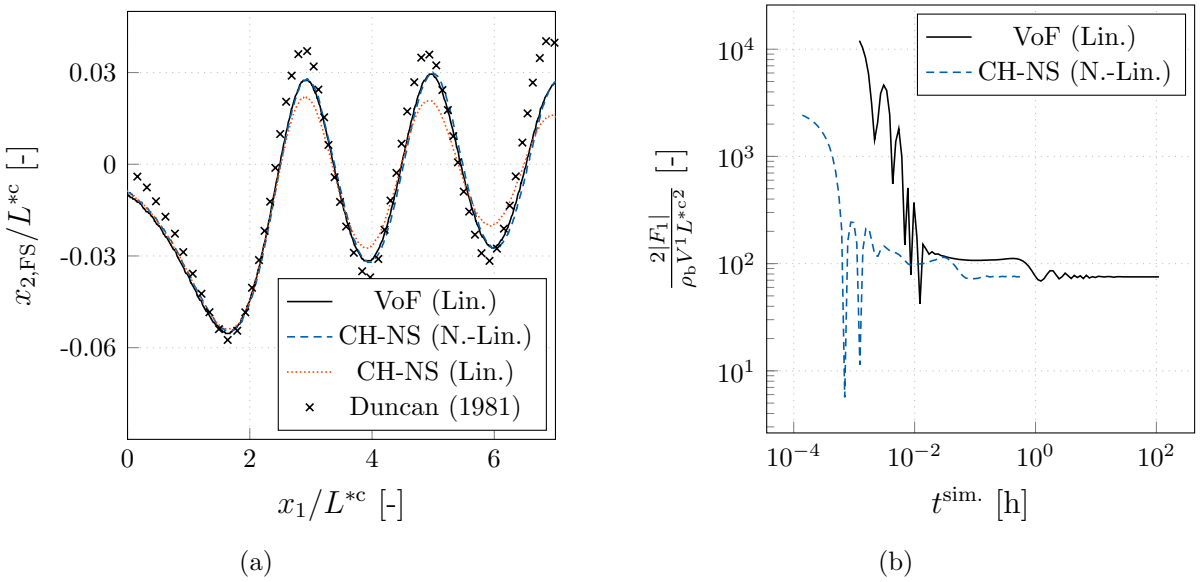

Figure 2.23: Submerged hydrofoil case ($\mathrm{Re_L} = 144\,855$, $\mathrm{Fn} = 0.567$): Comparison of predicted normalized (a) wave elevation and (b) drag force over wall-clock time.

2.4.5 Flow around a Kriso Container Ship

The final validation case refers to the fully turbulent flow around an unappended Kriso container ship hull (KCS). Experimental resistance data and wave fields are published by Kim et al. [2001] for a 1:31.6 scale model and a large amount of comparative numerical data exists, e.g. Larsson et al. [2003], Kröger et al. [2018], Kröger [2016], Manzke et al. [2012], Banks et al. [2010]. The distance between aft and front perpendiculars of the hull model serves as a reference length $L^* = 7.2786\,\mathrm{m}$ ($= L^{*\mathrm{pp}}$). Other reference values refer to the gravity acceleration $G^* = |g_3^*|$, the inflow velocity magnitude $V = |v_1^*|$ and the kinematic viscosity of the water $\nu^{*\mathrm{b}}$. The model scale investigations refer to Reynolds- and Froude numbers of $\mathrm{Re} = V^*\,L^*/\nu^{*\mathrm{b}} = 1.4 \times 10^7$ and $\mathrm{Fn} = V^*/\sqrt{G^*\,L^*} = 0.26$. The hull is fixed at the full scale static draught with zero trim and the motion and propulsion of the ship are suppressed during the simulation and the experiments.

The numerical grid consists of approximately 14.6 million unstructured hexahedral cells. The domains extends over $5\,L^*$, $1.75\,L^*$, $2.5\,L^*$ in longitudinal (x_1^*), lateral (x_2^*) and vertical (x_3^*) direction. Due to symmetry, only half of the flow field is simulated. The inlet is located upstream at $x_1^*/L^{*\mathrm{pp}} = 3$ and the free surface is initialized at $x_3^*/L^{*\mathrm{pp}} = 1.75$ over the lower boundary of the domain. The surface of the hull is discretized with approximately 300,000 surface elements. The wall normal resolution of the hull refers to a dimensionless wall distances of $30 \leq y^+ = x_2^+ \leq 100$ and justifies the use of wall functions. The vertical resolution of the free surface region is constant throughout the domain and attempts to resolve the expected wave amplitude of $5 \cdot 10^{-4} L^{*\mathrm{pp}}$ by hundred cells in the immediate vicinity of the hull. The tangential resolution of the free surface is refined within a Kelvin-Wedge to capture the resulting wave pattern. Based on the current Froude number, a dimensionless wavelength of $\lambda^*/L^{*\mathrm{pp}} = 2\,\pi\,\mathrm{Fn}^2 = 0.4247$ is expected, which is approximated with roughly 100 cells. Figure 2.24 indicates the different refinement levels for the near and the far field.

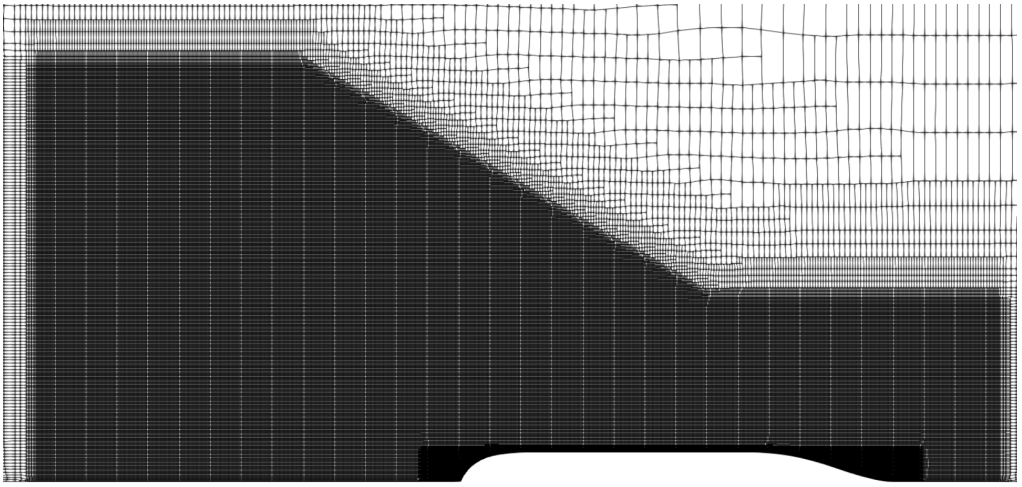

Figure 2.24: Kriso container ship case ($\mathrm{Re} = 1.4 \cdot 10^7$ and $\mathrm{Fn} = 0.26$): Illustration of the employed computational mesh along the still water plane in the vicinity of the vessel hull.

At the inlet, outlet, outer and lower boundaries, Dirichlet values for velocity and concentration are specified, while the pressure is extrapolated. A reverse situation is given at the top face which corresponds to a pressure boundary. Symmetry and wall boundary conditions are declared along the mid-ship plane as well as the hull. Turbulence is modeled by a high-Re $k^* - \epsilon^*$ model. Convective momentum transport is realized by a QUICK scheme. Similar to the 2D case, data obtained from CH-VoF simulation is compared with VoF results. CH-VoF calculations refer again to steady simulations using $\tilde{M} = 0.1$ and the nonlinear EoS. VoF calculations employ time stepping based on $\Delta t^* = \Delta x^*_{3,\mathrm{FS}}/V^*$ Co, where the Courant number is assigned to $\mathrm{Co} = 0.3$ and $\Delta x^*_{3,\mathrm{FS}}$ denotes the vertical resolution of the free surface. All simulations are performed until the integrated forces on the hull converge.

Figure 2.25 depicts the evolution of total resistance over the wall-clock time. The predicted total drag force coefficient is normalized with the static wetted surface of 9.5121 m^2 and converges to $c_\mathrm{d} = 3.68 \times 10^{-3}$ and $c_\mathrm{d} = 3.66 \times 10^{-3}$ for the CH-VoF and the VoF simulation. Both values differ by only 0.5% and compare favorable with the experimental value $c_\mathrm{d} = 3.56 \times 10^{-3}$ – subject to the influence of other aspects, e.g. turbulence modelling. However, the CH-VoF approach clearly outperforms the VoF simulation with respect to computational time, while introducing only minor additional wave damping, cf. Fig. 2.26. The wave elevation ($x^*_{\mathrm{FS},3}/L^{*\mathrm{pp}}$) measured at three different lateral planes through the free surface, i.e. $x^*_2/L^{*\mathrm{pp}} = 0.0741$, $x^*_2/L^{*\mathrm{pp}} = 0.1509$ and $x^*_2/L^{*\mathrm{pp}} = 00.4224$, is compared with experimental data in Fig. 2.27. The predictive discrepancy is generally small and the nonlinear CH-VoF tends to provide slightly larger amplitudes. Mind that the nonlinear EoS 2.9 leads to a significant sharpening of the density field, as illustrated by Fig. 2.28.

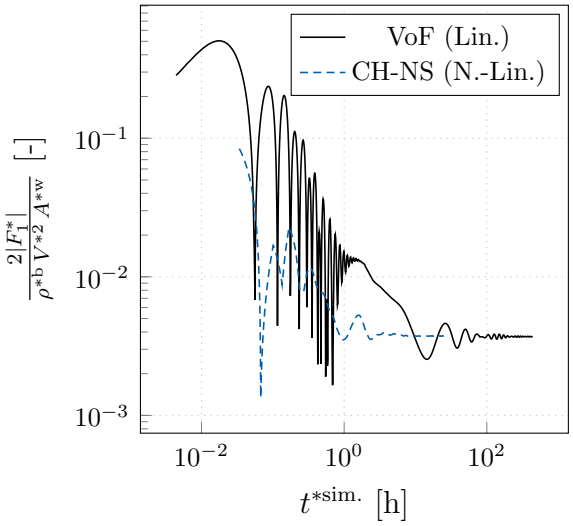

Figure 2.25: Kriso container ship case ($\text{Re} = 1.4 \cdot 10^7$ and $\text{Fn} = 0.26$): Evolution of the predicted drag force over the wall-clock simulation time for the VoF and CH-VoF simulation.

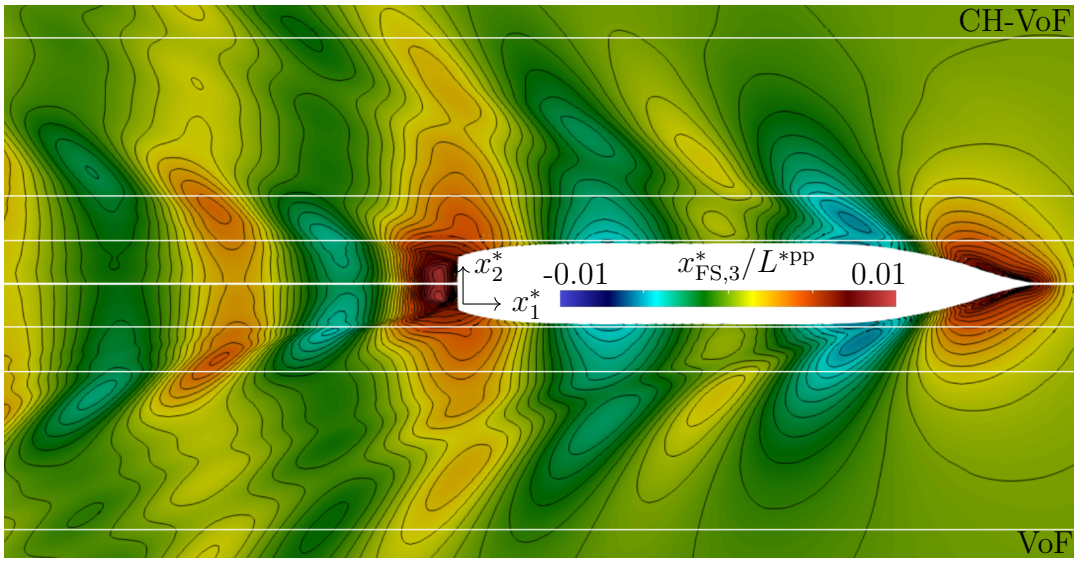

Figure 2.26: Kriso container ship case ($\text{Re} = 1.4 \cdot 10^7$ and $\text{Fn} = 0.26$): Comparison of predicted wave field obtained by the VoF (bottom) and CH-VoF (top) approach. White horizontal lines indicate evaluation planes used for the wave cuts displayed in Fig. 2.27.

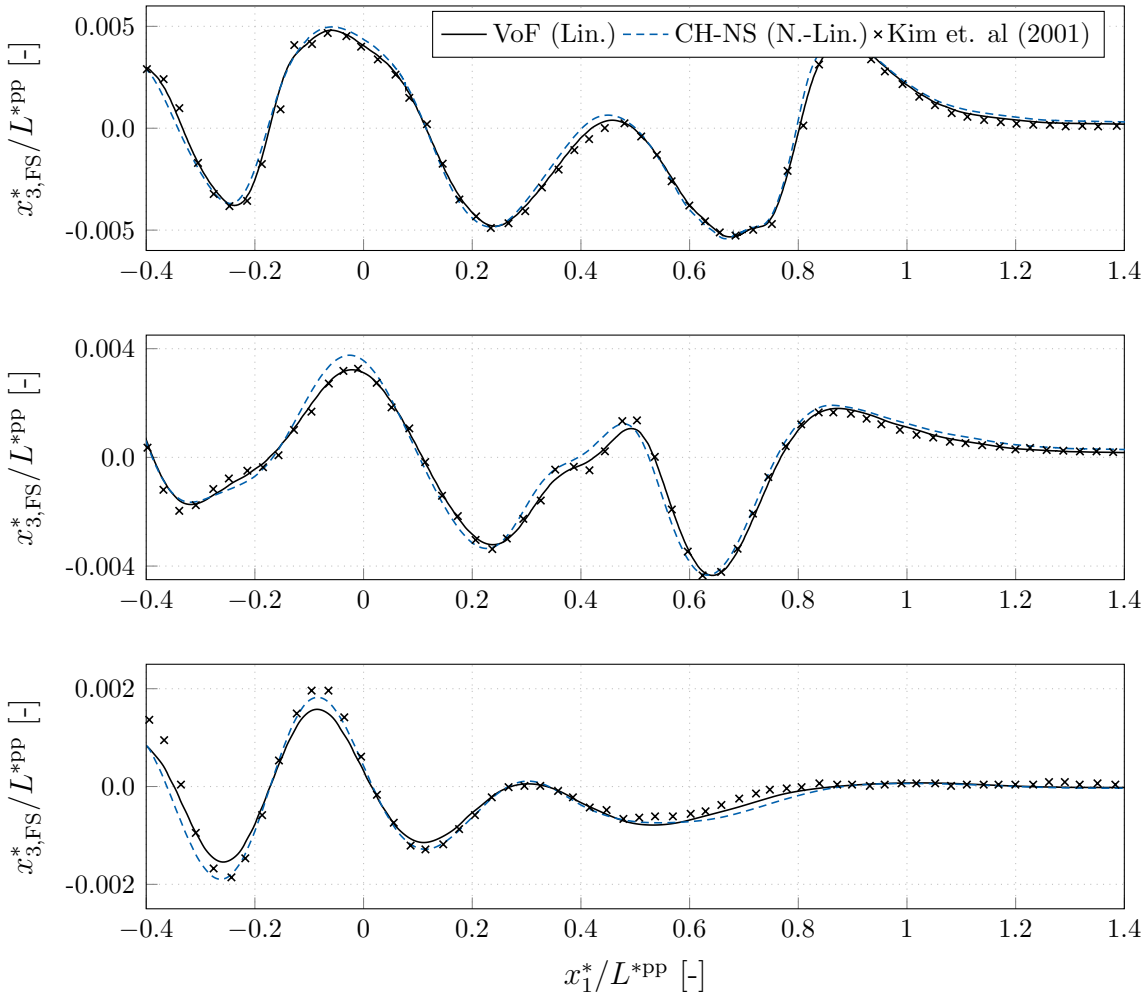

Figure 2.27: Kriso container ship case ($\mathrm{Re} = 1.4 \cdot 10^7$ and $\mathrm{Fn} = 0.26$): Comparison of measured and predicted wave elevation in 3 lateral planes, i.e. close to the hull at (a) $x_2^*/L^{*\mathrm{pp}} = 0.0741$, (b) at $x_2^*/L^{*\mathrm{pp}} = 0.1509$ and at a remote position (c) $x_2^*/L^{*\mathrm{pp}} = 0.4224$.

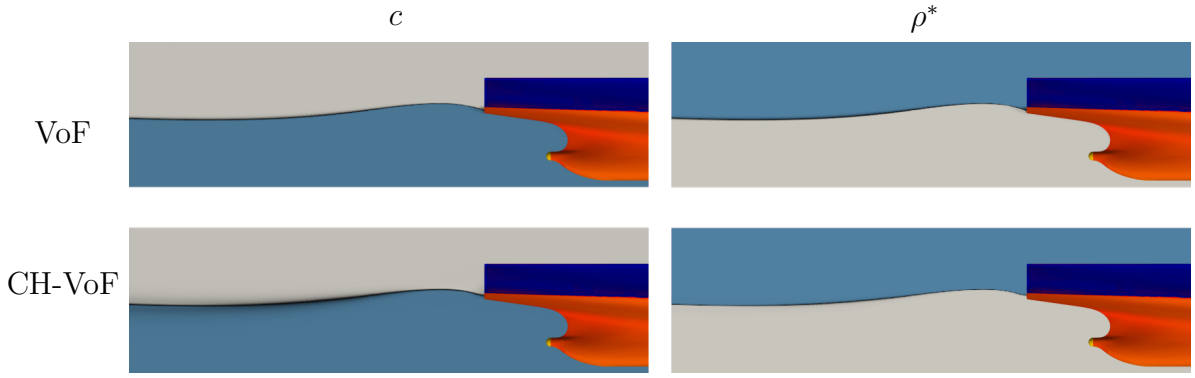

Figure 2.28: Kriso container ship case ($\mathrm{Re} = 1.4 \cdot 10^7$ and $\mathrm{Fn} = 0.26$): Concentration (left) and density field (right) obtained from a VoF with linear EoS (top) and a CH-VoF with nonlinear EoS (bottom).

3 Local Shape Optimization under State and Geometrical Constraints

In the previous chapter, the governing equations for describing maritime turbulent engineering flows were derived and discussed. Besides, a discrete FV-approximation of the equations was presented, verified and validated. Therefore, it is assumed that the discrete representation of the continuous balance equations provides an acceptable way to evaluate marine engineering devices' performance.

The third chapter deals with possibilities to improve the performance using shape modifications. Two optimization strategies have been established in the engineering context, typically referred to as global (gradient-free, stochastic) and local (gradient-based, deterministic) methods. Prominent global methods are evolutionary algorithms, which rely on population-based, evolutionary optimization strategies to explore the entire design space, cf. Back [1996], Giannakoglou [2002], Thévenin and Janiga [2008], Deb [2011]. They aim at global optima and can consider multi-criteria optimizations to determine, e.g. Pareto fronts of non-dominating solutions. The evaluation software (PDE solver) can conveniently be invoked as a black box. A disadvantage of global optimization methods is the considerable computational effort due to the relatively large number of required performance evaluations. The number of evaluations scales nonlinearly with the number of design variables, which theoretically tends to infinity in parameter-free shape optimization. Therefore, parameter-free shape optimizations based on gradient-free approaches become prohibitively expensive in complex engineering flows. On the contrary, local optimization methods start at a defined position in the design space and rely on local gradient information to advance the design. Thus, they operate close to an existing initial/previous design, cf. Luenberger et al. [1984], Löhner [2008], Thévenin and Janiga [2008], Mohammadi and Pironneau [2010] and seek for a local optimum. The required descent information poses a challenge since the employed PDE solver usually does not provide derivative information. Therefore, a black box approach can be used in rare cases only and –dependent on the design space size– specially tailored tools for the derivative approximation are needed.

This chapter first describes prominent methods for obtaining derivative or sensitivity information for shape optimization problems. Thereupon, the cost functionals investigated in this thesis are presented and discussed w.r.t. their formulation. After a presentation of the material derivative concept, the determination of shape derivatives is addressed in the context of a general shape calculus. Subsequently, techniques are presented to account for geometrical constraints and how to extract the shape gradient from the shape derivative. The chapter concludes by presenting the overall employed optimization procedure in terms of a gradient-based steepest descent approach.

3.1 Generic Shape Optimization Problem

A shape-design performance is measured via a scalar cost functional J^* in terms of a fluid mechanically motivated objective that depends on the flow state vector $\underline{\varphi}^*$ from Cha. 2. The objective shall be optimized by modifying a control vector $\underline{u}^*$, represented by either all or only parts of the walled flow boundary. A valid physical state requirement provides the following generic constraint shape optimization problem

$$\text{min.} \quad J(\underline{\varphi}^*(\underline{u}^*), \underline{u}^*) \qquad \text{s.t.} \qquad \underline{\mathrm{R}}^{*\varphi}(\underline{\varphi}^*(\underline{u}^*), \underline{u}^*) = 0\,, \tag{3.1}$$

where the cost functional can be either surface-based (e.g., total drag) or volume-based (e.g., prescribed wave field). The state is described by a –usually nonlinear– PDE $\underline{\mathrm{R}}^{*\varphi}$ that is valid in the entire domain and closed by boundary conditions $\underline{\mathrm{B}}^{*\varphi}$. A typical process chain to classify the actual design performance and determine its position in the design space proceeds in the following three steps, viz.

1. Define/modify the control $\underline{u}^*$.
2. Estimate the state $\underline{\varphi}^*(\underline{u}^*)$ via the approximation of $\underline{\mathrm{R}}^{*\varphi}(\underline{\varphi}^*(\underline{u}^*), \underline{u}^*) = 0$.
3. Evaluate the objective $J(\underline{\varphi}^*(\underline{u}^*), \underline{u}^*)$.

In this work, local optimization strategies are pursued, and the concept of sensitivity analysis is discussed in the following. Existing approaches to determine the sensitivity of J^* w.r.t. the control $\underline{u}$ –that describes the design boundary $\Gamma^{*\mathrm{D}}$– can be divided into direct (Jacobian) or indirect (adjoint, Lagrangian) methods. Direct approaches apply the sequence above in forward mode by perturbing the control $\delta\underline{u}^*$ (sender) to finally estimate the variation of the objective δJ^* (receiver) w.r.t. to the control, i.e. $\delta J^*/\delta\underline{u}^*$. Indirect, adjoint procedures reverse the procedural flow of direct approaches by swapping the sender-receiver relation.

3.1.1 Sensitivity Analysis

In constrained optimization, the term sensitivity refers to the response of the cost functional due to a perturbation in the control parameter. For illustrative purposes, this subsection exclusively considers discrete relationships, e.g. it is assumed that both the design as well as the state space are finite dimensional. Hence, a scalar objective J^* is controlled by N^α control parameters (u^*_α) and depends on N^β states (φ^*_β) that follow from N^γ state equations $(\mathrm{R}^{*\varphi}_\gamma)$. In the following, Einstein's summation convention is extended in the sense that a summation is performed from $1, ..., N^{(\cdot)}$ over double-occurring indices. A linear response of $J^*(\varphi^*_\beta(u^*_\alpha), u^*_\alpha)$ yields the following sensitivity expression

$$\frac{\delta\, J^*}{\delta\, u^*_\alpha} = \frac{\partial\, J^*}{\partial\, u^*_\alpha} + \frac{\partial\, J^*}{\partial\, \varphi^*_\beta}\frac{\delta\, \varphi^*_\beta}{\delta\, u^*_\alpha}\,. \tag{3.2}$$

The partial derivatives in (3.2) can be determined straight-forward. However, the implicit dependence of the cost functional over the state on the control results in an additional contribution. The latter is frequently referred to as state derivative $\delta\,\varphi^*_\beta/\delta\,u^*_\alpha$ and accounts for a change in the state due to a change in the control. The determination of the state derivative is the challenging task of a local optimization.

Finite-Difference Method

The Finite-Difference Method (FDM) traverses the previously mentioned evaluation chain in forwarding mode individually for each control parameter. A value ϵ^* successively perturbs the latter so that a second-order accurate central difference formula can be employed

$$\frac{\delta\, J^*}{\delta\, u^*_\alpha} = \frac{J^*(u^*_\alpha + \epsilon^*\, e_\alpha) - J^*(u^*_\alpha - \epsilon^*\, e_\alpha)}{2\,\epsilon^*} + O(\epsilon^{*2})\,, \tag{3.3}$$

where e_α refers to a unit vector in α-direction. In principle, discrete stencils of first or even higher-order are conceivable, but all FD studies in this work are formed based on (3.3). The FD approach has two crucial drawbacks in the context of shape optimization. 1) The number of functional evaluations and, therefore, repetitive forward runs scale directly with the design space's size. 2) The size of the discrete disturbance ϵ^* is usually unknown and possibly differs for each control parameter. ϵ^* is limited downward by numerics (e.g. regarding round-off errors due to subtractive cancellation) and upward by physics due to possible nonlinearities. The latter is circumvented in the following, direct approach. The FD method's fundamental advantages are the independence from a state (PDE) solver and a straight-forward parallelization.

Direct (Jacobian) Method

The direct (Jacobian) approach is based on the solution of the linearized equations of state, where $\mathrm{R}^{*\varphi}_\gamma = 0$ ($\delta\mathrm{R}^{*\varphi}_\gamma = 0$) must be satisfied at all N^γ discrete evaluation positions (e.g. all CV's from Sec. 2.2), viz.

$$\frac{\delta\, \mathrm{R}^{*\varphi}_\gamma}{\delta\, u^*_\alpha} = \frac{\partial\, \mathrm{R}^{*\varphi}_\gamma}{\partial\, u^*_\alpha} + \frac{\partial\, \mathrm{R}^{*\varphi}_\gamma}{\partial\, \varphi^*_\beta}\frac{\delta\, \varphi^*_\beta}{\delta\, u^*_\alpha} = 0\,. \tag{3.4}$$

Analogous to the FDM, all control parameters are successively perturbed and (3.4) is solved for the state derivative $\delta\, \varphi^*_\beta / \delta\, u^*_\alpha$. Subsequently, the latter can be used for sensitivity analysis for any cost functional using (3.2). The method has similar advantages and disadvantages as the FDM. It also scales with the number of control parameters as the process chain is traversed in forwarding mode. Although a linearized PDE solver is necessary, the disturbance size can be estimated more optimistically since the system response is linear by definition.

Indirect (Adjoint, Lagrangian) Method

The constrained optimization problem is transformed into an unconstrained companion where the PDE constraint is linearly attached to the actual cost functional

$$L^*(\varphi^*_\beta(u^*_\alpha), \hat{\varphi}^*_\gamma, u^*_\alpha) = J^*(\varphi^*_\beta(u^*_\alpha), u^*_\alpha) + \hat{\varphi}^*_\gamma\, \mathrm{R}^{*\varphi}_\gamma(\varphi^*_\beta(u^*_\alpha), u^*_\alpha)\,. \tag{3.5}$$

The Lagrange multipliers $\hat{\varphi}^*_\gamma$ are usually labeled adjoint or dual variables and do not depend on the state or the control. L^* is frequently denoted as an extended cost functional and, strictly speaking, equals J^* due to the residual character of $\mathrm{R}^{*\varphi}$. Hence, J^* and L^* have identical dimensions and a variation of the latter allows for a combination of the variation

of the objective (3.2) as well as the state equation (3.4), viz.

$$\delta L^* = \delta J^* + \hat{\varphi}^*_\gamma \, \delta \mathrm{R}^{*\varphi}_\gamma \quad \overset{(3.2)+(3.4)}{\rightarrow} \quad \frac{\delta \, L^*}{\delta \, u^*_\alpha} = \frac{\partial \, J^*}{\partial \, u^*_\alpha} + \hat{\varphi}^*_\gamma \frac{\partial \, \mathrm{R}^{*\varphi}_\gamma}{\partial \, u^*_\alpha} + \frac{\delta \, \varphi^*_\beta}{\delta \, u^*_\alpha} \underbrace{\left[\frac{\partial \, J^*}{\partial \, \varphi^*_\beta} + \hat{\varphi}^*_\gamma \frac{\partial \, \mathrm{R}^{*\varphi}_\gamma}{\partial \, \varphi^*_\beta} \right]}_{\mathrm{R}^{*\hat{\varphi}}_\gamma} . \tag{3.6}$$

A solution of the adjoint equation $\mathrm{R}^{*\hat{\varphi}}_\gamma = 0$ provides the adjoint variables $\hat{\varphi}^*_\gamma$, which can subsequently be used to determine the influence of a control perturbation on the Lagrangian and thus also on J^*. The indirect character bypasses the state derivative's evaluation, and the sensitivity can be determined independently of the size of the design space. However, the cost functional now appears in the adjoint equation and thereby influences $\hat{\varphi}^*_\gamma$. Hence, the adjoint method scales with the number of objective functionals. In contrast to the former, the Lagrangian approach is the only technique without any discrete perturbation evaluation and, therefore, able to offer a continuous sensitivity derivative of unparameterized shapes. The Lagrangian approach runs through the process chain in reverse order, hence swaps the sender-receiver relation and evaluates all conceivable perturbed shapes simultaneously – for one particular objective.

In the context of unparameterized shape optimization, the design space size tends to infinity ($N^\alpha \rightarrow \infty$), which makes direct approaches obsolete. Although engineering-related applications are frequently examined discretely, the remainder of this chapter focuses on a continuous interpretation.

3.2 Objective Functional

Three fluid mechanically motivated cost functionals are investigated in this thesis. They exclusively refer to external flow objectives either of surface- or volume-based character. The former balance the momentum flux across the domain boundaries and attempt to minimize the respective momentum loss, which is physically equivalent to the reactive force on the fluid flow exposed geometry. It will be shown that a suitable formulation of the force objective can simplify the desired shape derivative. An alternative objective aims at minimizing the deviation of the current concentration field c w.r.t. a given target concentration distribution c^{tar}. This functional speaks exclusively through the concentration and is used for quality control of the associated adjoint concentration equation. A typical application of the inverse concentration functional refers to minimising the wave deflection of a free surface.

Force Objectives

The objective functional refers to the component of the flow-induced forces acting on the body in the direction r_{i}. The force can be determined in two different ways, referred to as interior a) and exterior b) strategy.

a) Referring to Fig. 3.1 (a), the projected force can be determined by integrating the stress components along the body surface and then projecting them into the direction

Figure 3.1: Evaluation of forces acting on a cylinder: (a) interior evaluation using surface stresses ($\Gamma^{*O} \equiv \Gamma^{*D}$) and (b) exterior evaluation balancing the fluxes ($\Gamma^{*D} \cap \Gamma^{*O} = \emptyset$). Integration areas are indicated by dashed lines that also hint on the habitat of the surface objective $J^{*\Gamma}$.

of the objective force component

$$J^{*\Gamma,I} = \int_{\Gamma^{*O}} \left[p^{*\text{eff}}\, \delta_{ik} - 2\, \mu^{*\text{eff}}\, S^*_{ik} \right] n_k\, r_i \, \mathrm{d}\Gamma^* \,. \tag{3.7}$$

b) The force objective can also be examined by the momentum loss inside the computational domain, cf. Fig. 3.1 (b). The latter is reformulated via integration by parts and evaluated along the far-field boundaries, namely

$$J^{*\Gamma,E} = -\int_{\Gamma^{*O}} \left[v^*_i\, \rho^*\, v^*_k + p^{*\text{eff}}\, \delta_{ik} - 2\, \mu^{*\text{eff}}\, S^*_{ik} \right] n_k\, r_i \, \mathrm{d}\Gamma^* \,. \tag{3.8}$$

Inverse Concentration Objective

The inverse concentration objective aims at minimizing the deviation of the current concentration field c w.r.t. a given target concentration distribution c^{tar}

$$J^{*\Omega} = \int_{\Omega^{*O}} \frac{1}{2} \left[c - c^{\text{tar}} \right]^2 \mathrm{d}\Omega^* \,. \tag{3.9}$$

The deviation is measured in the least-square sense over a prescribed spatial region Ω^{*O}.

3.3 Constraint Shape Derivatives

The cost functionals of the previous section are controlled via parts of the walled flow domain. Fundamental relationships of fluid mechanical shape optimization are considered in the following, and the control is consistently considered as a vector-valued boundary coordinate u^*_i from now on. Hence, an arbitrary shape Γ^* is described by an infinite number of surface points u^*_i. Note that only the normal component of a surface perturbation influences a shape derivative, viz. $\delta u^*_i = \delta u^*\, n_i = \delta n^*\, n_i = \delta n^*_i$ or $\delta n^* = \delta u^*_i\, n_i$, also known as the structure theorem of Hadamard-Zolésio, cf. Hadamard [1968], Delfour and Zolésio [2011].

Two approaches to obtain and interpret a shape derivative are presented below. The first is based on a compareable intuitive engineering approach and follows the concept of material derivative. Subsequently, a somewhat more general approach based on the general shape calculus is discussed.

Concept of Material Derivative

A disturbance δu_{i}^* is applied at any point along the surface of an *Old Shape* u_{i}^* resulting in a *New Shape* $\tilde{u}_{\mathrm{i}}^* = u_{\mathrm{i}}^* + \delta n_{\mathrm{i}}^*$. The applied disturbance induces a change in the state $\delta\varphi^*$ which in turn yields a *New State* $\tilde{\varphi}^* = \varphi^* + \delta\varphi^*$ due to the *New Shape*. In line with Soto and Löhner [2004], Othmer [2008], Schmidt and Schulz [2009], Stück [2012], the latter can be approximated to second-order, viz.

$$\tilde{\varphi}^*(\tilde{u}_{\mathrm{i}}^*) = \varphi^* + \left[\delta + \delta n^* \frac{\partial}{\partial\, n^*}\right] \varphi^* + O(\delta n^{*2})\,. \tag{3.10}$$

To obtain a shape sensitivity, a quantification of the *New State* due to a *New Shape* is of interest. While direct methods explicitly evaluate the *New State* due to (each) *New Shape*, the indirect adjoint approach allows the desired quantification of the *New State* on the *Old Shape*, since the variation of the flow state is not explicitly evaluated, cf. Sec. 3.1.1. Accordingly, both direct and indirect methods evaluate the bracketed expression in (3.10)

$$\left[\delta + \delta n^* \frac{\partial}{\partial\, n^*}\right] \qquad \rightarrow \qquad \left[\delta^{\mathrm{l}} + \delta^{\mathrm{c}} + \delta^{\mathrm{g}}\right] \tag{3.11}$$

which is frequently denoted as a material derivative in terms of *local* (δ^{l}) as well as *convective* and –possibly– *geometric* ($\delta n^*(\partial/\partial\, n^*)$) contributions, i.e. $\delta^{\mathrm{l}} + \delta^{\mathrm{c}} + \delta^{\mathrm{g}}$. A *local* perturbation follows from a local change in the state, a *convective* change accounts for a surface-normal displacements and a *geometrical* variation considers potential changes of the surface area and orientation, cf. Stück [2012]. Note that the surface perturbation δn^* is zero everywhere except along the design boundaries $\Gamma^{*\mathrm{D}}$ which likewise holds for *convective* and *geometric* contributions. However, *local* variations have to be evaluated everywhere.

Expression (3.11) resembles the non-conservative, substantial derivative from Cha. 2, cf. Eqn. (2.2). In this analogy, the disturbance has velocity character, as discussed in the upcoming section. The outlined control perturbation based on the distinction between old/new shape/state allows the systematic application of the material derivative approach to the objective functional (δJ^*), its PDE constraints ($\delta \mathrm{R}^{*\varphi}$), and their boundary conditions ($\delta \mathrm{B}^{*\varphi}$). The former and the latter are relevant for this thesis and therefore performed in Sec. 3.4. Local variations of the field equations are efficiently circumvented via an adjoint strategy. First, an alternative approach to determining shape derivatives is presented, which follows the mathematically more rigorous concept of shape calculus.

Shape Calculus

The transformation T^* from an initial towards an alternative shape – e.g. for optimization purposes – can generally be performed in a design-time τ^*, viz.

$$\Gamma^{*\tau} := \{T^{*\tau}(u_{\mathrm{i}}^{*0}) : u_{\mathrm{i}}^{*0} \in \Gamma^{*0}, \tau^* \geq 0\} \qquad \text{with} \qquad T^{*0}(u_{\mathrm{i}}^{*0}) = u_{\mathrm{i}}^{*0}\,. \tag{3.12}$$

Compared to the physical time t^*, the design-time is a parent or superior quantity. The design-temporal change of all surface coordinates can be described via the so-called speed method:

$$\frac{\mathrm{d}u_\mathrm{i}^{*\tau}}{\mathrm{d}\tau^*} = V_\mathrm{i}^{*\tau}\left(u_\mathrm{i}^{*\tau}\right) \qquad \text{with} \qquad \tau^* \geq 0\,, \tag{3.13}$$

where the velocity field $V_\mathrm{i}^{*\tau}$ is often denoted as design velocity, which therefore defines the units of $V_\mathrm{i}^{*\tau}$ and τ^*. The mapping T^* in Eqn. (3.12) can be interpreted as a forward integration following the gradient $G_\mathrm{i}^{*\tau}$ in design time:

$$T^{*\tau}(u_\mathrm{i}^{*0}) := u_\mathrm{i}^{*0} + \tau^* G_\mathrm{i}^{*\tau} = u_\mathrm{i}^{*\tau} \qquad \text{with} \qquad \tau^* \geq 0, \tag{3.14}$$

frequently labeled as perturbation of identity which is equivalent to the speed method for first-order calculus, cf. Schmidt et al. [2013]. Combining Eqns. (3.13) and (3.14) yields $\mathrm{d}\,T^{*\tau}/\mathrm{d}\,\tau^* = G_\mathrm{i}^{*\tau} = \mathrm{d}\,u_\mathrm{i}^{*\tau}/\mathrm{d}\tau^* = V_\mathrm{i}^{*\tau}$. The aim is now to connect the design velocity with derivative information of a volume $J^{*\Omega}$ or surface $J^{*\Gamma}$ cost functional (cf. Eqn. (3.1) and Sec. 3.2). The shape derivative based on the introduced design velocity is obtained by Hadamard's boundary variation method for volume and surface integrals, cf. App. B.2 and Hadamard [1968], Delfour and Zolésio [2011], Delfour and Zolésio [2011], Sokolowski and Zolésio [1992], Allaire et al. [2021]. The determination of a shape derivative is individual and must be determined anew for each cost functional and state constraint. Hence, the following discussion is not exhaustive and aims at building a bridge towards the previous section.

In line with Allaire et al. [2021], a Lagrangian approach is employed

$$L^*\left(\varphi^*(u_\mathrm{i}^{*\tau}), \hat{\varphi}^*, u_\mathrm{i}^{*\tau}\right) = J^*\left(\varphi^*(u_\mathrm{i}^{*\tau}), u_\mathrm{i}^{*\tau}\right) + \int \hat{\varphi}^*\,\mathrm{R}^{*\varphi}\left(\varphi^*(u_\mathrm{i}^{*\tau}), u_\mathrm{i}^{*\tau}\right)\,\mathrm{d}\Omega^*\,, \tag{3.15}$$

where $\mathrm{R}^{*\varphi}$ contains the general residual of the physics to be fulfilled and $\hat{\varphi}^*$ represents the associated adjoint variable that does not depend on the state and the design time, cf. its discrete analogue (3.5). The derivation of the shape sensitivity employs first-order optimality conditions to ensure the independence of (3.15) w.r.t. the primal and adjoint state. Subsequently, descent information can be obtained from remaining variational contributions. An exemplary laminar single-phase discussion is sketched in App. B.3 for the boundary-based force objectives (3.7)-(3.8) without particularly addressing the adjoint flow. The latter is intensively considered in the upcoming Cha. 4. The following shape derivative rule frequently appears (cf. Allaire et al. [2021]) and is therefore interpreted as a generalized total shape derivative expression, viz.

$$\frac{\mathrm{d}}{\mathrm{d}\tau^*} L^*\left(\varphi^*(u_\mathrm{i}^{*\tau}), \hat{\varphi}^*, u_\mathrm{i}^{*\tau}\right)\Big|_{\tau^*=0} = \int_{\Gamma^{*\mathrm{D}}} \underbrace{\left[\!\left[s^* \right]\!\right]}_{\delta^\mathrm{l}} V_\mathrm{k}^{*0}\, n_\mathrm{k}\,\mathrm{d}\Gamma^* + \int_{\Gamma^{*\mathrm{D}}\cap\Gamma^{*\mathrm{O}}} \underbrace{\left[\!\left[\kappa^*\, j^{*\Gamma} \right]\!\right]}_{\delta^\mathrm{c}+\delta^\mathrm{g}} V_\mathrm{k}^{*0}\, n_\mathrm{k}\,\mathrm{d}\Gamma^*\,, \tag{3.16}$$

where the three parts are denoted as *local*, *convective* and *geometric* derivative, respectively, cf. Schmidt [2010], Stück [2012], Schmidt et al. [2013]. The *local* component refers to the adjoint-based shape sensitivity derivative and typically inheres the inner product between primal and adjoint gradient normal to the controlled wall, i.e. $s^* = \delta^\mathrm{l} j^{*\Gamma} =$

$-(\partial\hat{\varphi}^*\partial n^*)(\partial\varphi^*/\partial n^*)$, cf. Allaire et al. [2021]. *Convective* and *geometric* changes are combined in a mean curvature expression, cf. Eqn. (B.6). The applied shape calculus allows the specification of boundary conditions for the design velocity $V_{\mathrm{k}}^{*\tau}$ at $\tau^* = 0$. A natural choice refers to $V_{\mathrm{k}}^{*0} = 0$ along $\Gamma^*\backslash\Gamma^{*\mathrm{D}}$. Note that $j^{*\Gamma} = 0$ along $\Gamma^*\backslash\Gamma^{*\mathrm{O}}$ so that a distinction between the habitat of the objective functional $\Gamma^{*\mathrm{O}}$ and the control $\Gamma^{*\mathrm{D}}$ is necessary: both the *convective* as well as the *geometric* contribution need to be evaluated along the intersected area $\Gamma^{*\mathrm{D}} \cap \Gamma^{*\mathrm{O}} \neq \emptyset$. The crucial point now is: the complexity of the objective functional derivative expression is reduced by decoupling control and objective surfaces, as *geometric* as well as *convective* contributions to the total shape derivative disappear due to the unperturbed control, and only the *local* contribution remains. Section 3.4 outlines differences between an internal and external force evaluation approach from an adjoint perspective, which leads to a simplification of the total shape derivative (3.16).

3.4 Variation of Objectives and Boundary Conditions

This section applies the introduced shape-variational calculus to all considered objective functionals from Sec. 3.2 ($\delta J^* = (\delta^{\mathrm{l}} + \delta^{\mathrm{c}} + \delta^{\mathrm{g}})J^*$) as well as the boundary conditions ($\delta B^{*\Gamma,\mathrm{I}} = (\delta^{\mathrm{l}} + \delta^{\mathrm{c}} + \delta^{\mathrm{g}})B^*$) from Tab. 2.2.

Force Objectives

As proposed in Sec. 3.2, force objectives can be determined in two different ways, either following an a) interior or b) exterior strategy.

a) In this classical example, the design surface coincides with the objective surface. This requires the evaluation of the complete variation, i.e. $\delta J^{*\Gamma,\mathrm{I}} = (\delta^{\mathrm{l}} + \delta^{\mathrm{c}} + \delta^{\mathrm{g}})J^{*\Gamma,\mathrm{I}}$.

The *local* change of the force objective functional follows from a variation

$$\delta^{\mathrm{l}} J^{*\Gamma,\mathrm{I}} = \int_{\Gamma^{*\mathrm{O}}} \left[\delta p^{*\mathrm{eff}}\,\delta_{\mathrm{ij}} - 2\left[\delta\mu^{*\mathrm{eff}}\,S_{\mathrm{ik}}^* + \mu^{*\mathrm{eff}}\,\delta S_{\mathrm{ik}}^*\right]\right] n_{\mathrm{k}}\, r_{\mathrm{i}}\,\mathrm{d}\Gamma^* \,. \tag{3.17}$$

The effective quantities include turbulent contributions. Fluid properties are explicitly expressed in terms of the primal concentration field (cf. (2.6) and (2.13)). As a consequence, the variation of density and viscosity translates into a variation of the concentration, e.g. $\delta\rho^* = \rho^{*\Delta}\delta c$ and $\delta\mu^* = \mu^{*\Delta}\delta c$ which will be further discussed in Sec. 4.1.3.

The *convective* contribution follows directly from the hydrostatic contribution of the effective pressure, i.e. $p^{*\mathrm{g}} = \rho^*\, g_{\mathrm{k}}^*\, x_{\mathrm{k}}^*$. An illustrative example refers to a steady, laminar, single-phase flow of an incompressible fluid around a cylinder under gravity's influence. The convective change triggers gravitational contributions, viz.

$$\begin{aligned}\delta^c J^{*\Gamma,\mathrm{I}} = \int_{\Gamma^{*\mathrm{D}}\cap\Gamma^{*\mathrm{O}}} \frac{\partial\, j^{*\Gamma,\mathrm{I}}}{\partial\, n^*} V_{\mathrm{k}}^0\, n_{\mathrm{k}}\,\mathrm{d}\Gamma^* &= \int_{\Gamma^{*\mathrm{D}}\cap\Gamma^{*\mathrm{O}}} \frac{\partial(\rho^*\, g_{\mathrm{k}}^*\, x_{\mathrm{k}}^*\, n_{\mathrm{i}}\, r_{\mathrm{i}})}{\partial x_{\mathrm{m}}^*} n_{\mathrm{m}}\, V_{\mathrm{k}}^0\, n_{\mathrm{k}}\,\mathrm{d}\Gamma^* \\ &= \int_{\Gamma^{*\mathrm{D}}\cap\Gamma^{*\mathrm{O}}} \left[\rho^*\, g_{\mathrm{k}}^*\, r_{\mathrm{k}} + C^*\,(\varphi^*)\right] V_{\mathrm{k}}^0\, n_{\mathrm{k}}\,\mathrm{d}\Gamma \,. \end{aligned} \tag{3.18}$$

The employed operations are further expanded in App. C. Two contributions arise: a constant one that is active if and only if the force direction sees gravity (i.e., $g_{\mathrm{k}}^*\, r_{\mathrm{k}} \neq 0$)

as well as locally varying contributions $C^*(\varphi^*)$. The latter can be parametrized through polar coordinates for a simple cylindrical example and is mainly zero due to the symmetric cylinder setting. Interestingly, if the normal design velocity is approximated via a perturbation constant ($V_{\mathrm{k}}^{*0}\, n_{\mathrm{k}} \approx \epsilon^*$), its magnitude cancels out as demonstrated by the local FD results, viz.

$$\begin{aligned}
\delta^{\mathrm{c}}_{u=\tilde{\mathrm{u}}} J^{*\Gamma,\mathrm{I}} &= \frac{J^*\left(\tilde{u}_{\mathrm{i}}^* + \epsilon^* n_{\mathrm{i}}\right) - J^*\left(\tilde{u}_{\mathrm{i}}^* - \epsilon^* n_{\mathrm{i}}\right)}{2\,\epsilon^*} \\
&= \frac{1}{2\,\epsilon^*}\Bigg[\int_{\Gamma^{*\mathrm{D}\tau}\cap\Gamma^{*\mathrm{O}}} \epsilon^*\left[\rho^*\, g_{\mathrm{k}}^*\, r_{\mathrm{k}} + C^*\left(\varphi^*\right)\right]\mathrm{d}\Gamma^* \\
&\qquad - \int_{\Gamma^{*\mathrm{D}\tau}\cap\Gamma^{*\mathrm{O}}} (-\epsilon^*)\left[\rho^*\, g_{\mathrm{k}}^*\, r_{\mathrm{k}} + C^*\left(\varphi^*\right)\right]\mathrm{d}\Gamma^*\Bigg] \\
&= \rho^*\, g_{\mathrm{k}}^*\, r_{\mathrm{k}} + \int_{\Gamma^{*\mathrm{D}\tau}\cap\Gamma^{*\mathrm{O}}} C^*\left(\varphi^*\right)\mathrm{d}\Gamma^*\,. \qquad (3.19)
\end{aligned}$$

The *geometric* contribution accounts for the tangential change of the surface normal. In case of a circular cylinder, this leads to a constant that is scrambled with the angular contributions from the convective contribution ($C^*(\varphi^*) \rightarrow \tilde{C}(\varphi^*)^*$) and the complete derivative of the objective reads

$$\delta J^{*\Gamma,\mathrm{I}} = \left(\delta^{\mathrm{c}} + \delta^{\mathrm{g}} + \delta^{\mathrm{l}}\right) J^{*\Gamma,\mathrm{I}} = \int_{\Gamma_{\mathrm{O}}\cap\Gamma_{\mathrm{D}}} \left(\rho^*\, g_{\mathrm{k}}^* r_{\mathrm{k}} + \tilde{C}\left(\varphi^*\right)\right)\mathrm{d}\Gamma + \delta^{\mathrm{l}} J^{*\Gamma,\mathrm{I}}\,. \qquad (3.20)$$

Note that convective contributions depend on primal physics and may disappear, which is not the case for geometric components. The latter can be interpreted as curvatures immanent to industrial applications as formally encountered in the general shape derivative Eqn. (3.16).

b) Due to the decoupling of control and objective, *convective* as well as *geometric* contributions are zero ($(\delta^{\mathrm{c}} + \delta^{\mathrm{g}})J^{*\Gamma,\mathrm{E}} = 0$) and only *local* contributions remain, viz.

$$\begin{aligned}
\delta J^{*\Gamma,\mathrm{E}} = \delta^{\mathrm{l}} J^{*\Gamma,\mathrm{E}} = -\int_{\Gamma^{*\mathrm{O}}} &\left[\delta v_{\mathrm{i}}^*\, \rho^*\, v_{\mathrm{k}}^* + v_{\mathrm{i}}^*\, \delta\rho^*\, v_{\mathrm{k}}^* + v_{\mathrm{i}}^*\, \rho^*\, \delta v_{\mathrm{k}}^*\right. \qquad (3.21) \\
&\left. + \delta p^{*\mathrm{eff}}\, \delta_{\mathrm{ik}} - 2\left[\delta\mu^{*\mathrm{eff}}\, S_{\mathrm{ik}}^* + \mu^{*\mathrm{eff}}\, \delta S_{\mathrm{ik}}^*\right]\right] n_{\mathrm{k}}\, r_{\mathrm{i}}\, \mathrm{d}\Gamma^*\,. \qquad (3.22)
\end{aligned}$$

As will be shown in the upcoming Cha. 4, there is more than one answer in the sense of the adjoint approach to the same question since the adjoint velocity experiences non-zero Dirichlet boundary conditions along regions with a predefined cost functional. While in the interior case a) a non-zero adjoint velocity sticks to the body to be optimized, this is precisely the other way around in the exterior case b). The variable form of appearance resembles the transport theorem formulated in an Arbitrary Lagrangian-Eulerian (ALE) frame of reference. Formulation a) corresponds to a moving grid approach, whereas b) is similar to an Eulerian description. Besides, the external formulation always results in smooth boundary conditions along the obstacle walls, even if only parts of a shape are released for design, which improves the numerical solution behavior.

Inverse Concentration Objective

As long as the objective area $\Omega^{*\mathrm{O}}$ does not touch the controlled boundary, *convective* and *geometric* variation contributions disappear and only *local* variations remain, viz.

$$\delta J^{*\Omega} = \delta^{\mathrm{l}} J^{*\Omega} = \int_{\Omega^{*\mathrm{O}}} \delta c \left[c - c^{\mathrm{tar}} \right] \mathrm{d}\Omega^* \,. \tag{3.23}$$

Boundary Conditions

The material derivative $(\delta + \delta n^* (\partial / \partial n^*)$ is applied to generic boundary conditions of Dirichlet ($\mathrm{D}^{*\varphi}$) and Neumann ($\mathrm{N}^{*\varphi}$) type. The argumentation assumes that the boundary conditions of the *Old State* on the *Old Shape* must be equal to those of the *New State* on the *New Shape*, viz. $(\cdot)|^{\mathrm{old}} = (\cdot)|^{\mathrm{new}}$. The control perturbation ($\delta n^* = 0$) and thus the variational contributions disappear along all boundaries that do not belong to the design surface, i.e. $\Gamma^* \cap \Gamma^{*\mathrm{D}} = \emptyset$. However, if the respective boundary is subjected to control, the variations need to be further expanded, viz.

$$\delta\varphi^* = 0 \qquad \text{or} \qquad \frac{\partial\,(\delta\varphi^*)}{\partial\, n^*} = 0 \qquad \text{on} \qquad \Gamma^* \tag{3.24}$$

$$\delta\varphi^* = -\delta n^* \frac{\partial\,\varphi^*}{\partial\, n^*} \qquad \text{or} \qquad \frac{\partial\,(\delta\varphi^*)}{\partial\, n^*} = -\delta n^* \frac{\partial}{\partial\, n^*} \left[\frac{\partial\,\varphi^*}{\partial\, n^*} \right] \qquad \text{on} \qquad \Gamma^* \cap \Gamma^{*\mathrm{D}} \,. \tag{3.25}$$

A variation of the primal boundary conditions from Tab. 2.2 according to (3.24)-(3.25) is listed in Tab. 3.1. Due to the concept of material derivative, local contributions disappear along almost all boundaries. In line with Eqns. (3.24)-(3.25), the following variations of primal velocity and concentration can be developed along controlled no-slip boundaries

$$\delta v_{\mathrm{i}}^* = -\delta n^* \frac{\partial\, v_{\mathrm{i}}^*}{\partial\, n^*} \qquad \text{and} \qquad \frac{\partial \delta c}{\partial\, n^*} = -\delta n^* \frac{\partial}{\partial\, n^*} \left[\frac{\partial\, c}{\partial\, n^*} \right] = 0 \,. \tag{3.26}$$

The variation of the effective pressure gradient condition $\partial\, p^* / \partial\, n^* = \rho^*\, g_{\mathrm{k}}^*\, n_{\mathrm{k}}$ is further expanded

$$\frac{\partial \delta p^*}{\partial\, n^*} = -\delta n^* \frac{\partial}{\partial\, n^*} \left[\rho^*\, g_{\mathrm{k}}^*\, n_{\mathrm{k}} \right] = -\delta n^* \frac{\partial\, \rho^*}{\partial\, c} \frac{\partial\, c}{\partial\, n^*} \rho^*\, g_{\mathrm{k}}^*\, n_{\mathrm{k}} = 0 \,. \tag{3.27}$$

and likewise vanishes due to a zero gradient condition for the concentration. The variations of the primal boundary conditions are collected in Tab. 3.1. They will be reused to derive the adjoint boundary conditions in Sec. 4.1.6.

3.5 Shape Gradient Approximation for Non-Parameterized Shapes

Shape optimization procedures in the discrete CFD surface's design space allow access to local features and shape optima on the level of the discrete CFD resolution. However, the "raw" adjoint shape derivatives suffer from a few well-known weaknesses, e.g. they only describe the normal deformation (cf. Sec. 3.3) but do not provide tangential information and the shape derivatives are not necessarily smooth. These deficiencies yield rough/noisy

boundary type	δv_i^*	δp^*	δc
inlet	$\delta v_\mathrm{i}^* = 0$	$\frac{\partial\,\delta p^*}{\partial\,n^*} = 0$	$\delta c = 0$
outlet	$\frac{\partial\,\delta v_\mathrm{i}^*}{\partial\,n^*} = 0$	$\delta p^* = 0$	$\frac{\partial\,\delta c}{\partial\,n^*} = 0$
symmetry	$\delta v_\mathrm{i}^*\,n_\mathrm{i} = 0,\ \frac{\partial\,\delta v_\mathrm{i}^*}{\partial\,n^*} t_\mathrm{i} = 0$	$\frac{\partial\,\delta p^*}{\partial\,n^*} = 0$	$\frac{\partial\,\delta c}{\partial\,n^*} = 0$
wall (slip)	$\delta v_\mathrm{i}^*\,n_\mathrm{i} = 0,\ \frac{\partial\,\delta v_\mathrm{i}^*}{\partial\,n^*} t_\mathrm{i} = 0$	$\frac{\partial\,\delta p^*}{\partial\,n^*} = 0$	$\frac{\partial\,\delta c}{\partial\,n^*} = 0$
wall (no-slip, $\Gamma^* \not\subset \Gamma^{*\mathrm{D}}$)	$\delta v_\mathrm{i}^* = 0$	$\frac{\partial\,\delta p^*}{\partial\,n^*} = 0$	$\frac{\partial\,\delta c}{\partial\,n^*} = 0$
wall (no-slip, $\Gamma^* \subset \Gamma^{*\mathrm{D}}$)	$\delta v_\mathrm{i}^* = -\delta n^* \frac{\partial\,v_\mathrm{i}^*}{\partial\,n^*}$	$\frac{\partial\,\delta p^*}{\partial\,n^*} = 0$	$\frac{\partial\,\delta c}{\partial\,n^*} = 0$

Table 3.1: Variations of the primal boundary conditions where t_i [n_i] refers to the local boundary tangential [normal] and $\delta n^* = \delta u_\mathrm{k}^*\,n_\mathrm{k}$.

shape updates (cf. Stück and Rung [2011], Kröger and Rung [2015]) and lead to distorted near-wall meshes which in turn hamper the preservation of numerical accuracy during the optimization procedure, e.g. Stavropoulou et al. [2014] and Bletzinger [2014]. As a consequence, the adjoint shape derivatives have to be regularized to obtain meaningful technical shape updates as initially proposed by Jameson and Vassberg [2000] and Vassberg and Jameson [2006a,b] in terms of an implicit, continuous smoothing operator based on an extended definition of the inner product, frequently labeled "Sobolev-gradient". In the following, g_i^* denotes the shape gradient. In general, the shape gradient habitat –surface- vs. volume-based– depends on the underlying surface metric. Prominent examples refer to Laplace-Beltrami (LB) or Steklov-Poincar (SP) type metrics, e.g. Schulz and Siebenborn [2016].

3.5.1 Laplace-Beltrami

Applying the smoothing operation along the design boundary $\Gamma^{*\mathrm{D}}$ leads to the LB equation with a source term corresponding to the shape sensitivity $s_\mathrm{i}^* = s^*\,n_\mathrm{i}$, viz.

$$\tilde{g}_\mathrm{i}^* - \mu^{*\tilde{\mathrm{g}}_\mathrm{i}2}\Delta^{*\Gamma}\tilde{g}_\mathrm{i}^* = g_\mathrm{i}^* - \mu^{*\tilde{\mathrm{g}}_\mathrm{i}2}\left[\frac{\partial^2\,\tilde{g}_\mathrm{i}^*}{\partial\,x_\mathrm{k}^{*2}} - n_\mathrm{k}\frac{\partial^2\,\tilde{g}_\mathrm{i}^*}{\partial\,x_\mathrm{k}^*\,\partial\,x_\mathrm{l}^*}n_\mathrm{l}\right] = s_\mathrm{i}^* \qquad \text{on} \qquad \Gamma^* \cap \Gamma^{*\mathrm{D}}\,, \quad (3.28)$$

where the LB operator operator is introduced as the tangential Laplacian, i.e. $\Delta^{*\Gamma} = \Delta^* - \Delta_\mathrm{n}^*$, cf. App. B.1. For dimensional reasons, the LB Eqn. (3.28) inheres a diffusivity $\mu^{*\tilde{\mathrm{g}}_\mathrm{i}}$ that corresponds to a squared length which allows for an adjustment of the gradient smoothness and influences the search direction. Note that the gradient equals the sensitivity derivative in the limiting case of $\mu^{*\tilde{\mathrm{g}}_\mathrm{i}} \to 0$. The LB Eqn. (3.28) is defined along the walled domain boundary and therefore requires a tailored two-dimensional approximation infrastructure. Classical CFD solvers may reach their limits since standardized solution routines (assembling, solving, etc.) are not necessarily available. As a consequence, Eqn. (3.28) is often approximated explicitly, cf. Bletzinger [2014]. The explicitly filtered gradient, e.g. by using consistent kernel functions (Kröger and Rung [2015]), marks a first-order approximation to the implicit Sobolev-gradient, cf. Stück and Rung [2011]. Note that potentially expensive manipulations of the smoothing operation are necessary if the geometry contains, e.g., symmetry constraints. Once the boundary-based shape gradient is available along $\Gamma^{*\mathrm{D}}$, a subsequent mesh deformation equation transports the surface-based gradient

information into the interior field in terms of, e.g. spring analogies or based on an additional Laplacian PDE together with prescribed boundary deformations, cf. Löhner and Yang [1996], Crumpton and Giles [1997], Jasak and Tuković [2006].

In line with the modelling of floatation, cf. Sec. 2.2.11 and Eqn. (2.111), the shape gradient $\tilde{g}_{\mathrm{i}}^{*}$ enters the boundary conditions of the following Laplacian PDE

$$\frac{\partial}{\partial x_{\mathrm{k}}^{*}}\left[\mu^{*\mathrm{g_i}}\frac{\partial g_{\mathrm{i}}^{*}}{\partial x_{\mathrm{k}}^{*}}\right]=0 \quad \text{in} \quad \Omega^{*} \qquad \text{with} \qquad \begin{cases} g_{\mathrm{i}}^{*}=\tilde{g}_{\mathrm{i}}^{*} & \text{on} \quad \Gamma^{*}\cap\Gamma^{*\mathrm{D}} \\ g_{\mathrm{i}}^{*}=0 & \text{on} \quad \Gamma^{*} \end{cases}. \tag{3.29}$$

The diffusivity $\mu^{*\mathrm{g_i}}$ refers to the inverse (non zero) distance to the nearest wall, which suppresses distortion of the grid in the vicinity of the design wall, cf. (2.111).

3.5.2 Steklov-Poincaré

The SP approach refers to a novel strategy on an industrial level that employs an elliptic volume-based formulation where smoothed results are subsequently projected on the boundary. Unlike the previous smoothing operations along the design boundary, the SP procedure essentially tries to combine the 2D shape update in continuous space with the 3D mesh update using the discrete CFD mesh sensitivities, cf. Schulz and Siebenborn [2016], Haubner et al. [2021]. The approach exclusively operates in the fluid domain and is thus attractive due to its compatibility with a CFD solver environment. The use of standard HPC-capable solution routines (assembling, solving, etc.) supplied by the flow solver represents a major benefit of the SP procedure.

The SP-approach resembles Eqn. (3.29) based on a manipulation of the boundary condition along the controlled boundary $\Gamma^{*\mathrm{D}}$, viz.

$$\frac{\partial}{\partial x_{\mathrm{k}}^{*}}\left[\mu^{*\mathrm{g_i}}\frac{\partial g_{\mathrm{i}}^{*}}{\partial x_{\mathrm{k}}^{*}}\right]=0 \quad \text{in} \quad \Omega^{*} \qquad \text{with} \qquad \begin{cases} \frac{\partial g_{\mathrm{i}}^{*}}{\partial n^{*}}=s^{*}\,n_{\mathrm{i}} & \text{on} \quad \Gamma^{*}\cap\Gamma^{*\mathrm{D}} \\ g_{\mathrm{i}}^{*}\,n_{\mathrm{i}}=0,\ \frac{\partial g_{\mathrm{i}}^{*}}{\partial n^{*}}t_{\mathrm{i}}=0 & \text{on} \quad \Gamma^{*\mathrm{Symm}} \\ g_{\mathrm{i}}^{*}=0 & \text{on} \quad \Gamma^{*} \end{cases}, \tag{3.30}$$

where the Dirichlet condition of the LB-metric translates into a Neumann condition that directly employs the sensitivity derivative, cf. Schulz and Siebenborn [2016], Haubner et al. [2021]. Accordingly, the gradient units in (3.30) differ from those in (3.29), which translates to a different employed step size within a steepest descent approach.

Note that no additional boundary-based operations are necessary and the number of equations to be solved decreases compared with the LB approach. Moreover, modifications of the boundary conditions listed in (3.30) support an intuitive introduction of additional geometric constraints. Examples included in the application chapter of this thesis refer to fixed intersection lines along a symmetry plane via $g_{\mathrm{i}}^{*}=0$ on $\Gamma^{*\mathrm{Symm}}$, or the realization of a mandatory flat ship transom obtained by $g_{\mathrm{i}}^{*}\,n_{\mathrm{i}}=0$ along $\Gamma^{*\tilde{\mathrm{D}}}$. In contrast to the LB metric, the SP approach involves only a single user-defined parameter, i.e. the diffusivity $\mu^{*\mathrm{g_i}}$ used in (3.30). In this thesis, the diffusivity refers to the inverse (non zero) distance to the nearest wall in line with (2.111)) and (3.29). More sophisticated SP approaches employ a nonlinear viscosity, e.g. $\mu^{*\mathrm{g_i}}=[(\partial\, g_{\mathrm{i}}^{*}/\partial\, x_{\mathrm{k}}^{*})(\partial\, g_{\mathrm{i}}^{*}/\partial\, x_{\mathrm{k}}^{*})]^{(p-2)/2}$ in terms of a p-Laplacian approach, cf. Müller et al. [2021].

The SP-approach is the preferred approach of this thesis. A step in the steepest descent direction is performed once the volume-based shape gradient is available, cf. Sec. 3.7. Prior to this, other technical constraints are incorporated into the process.

3.6 Geometrical Constraints

Geometrical constraints are frequently divided into global (integral) and local criteria, and their implementation in the node-based shape optimization framework is presented in this section.

3.6.1 Local Constraints

Local constraints restrict the motion of the shape in Euclidean space, and refer to, e.g., restricted main dimensions or curvature constraints. Examples refer to a maximum length and width or a plane transom of a ship. The constraints result in local expressions that frequently inhere large spatial gradients.

Various strategies are conceivable to meet local constraints, e.g. all geometrical constraints can be incorporated on equation level to determine the field gradient, cf. Eqns. (3.29)-(3.30), which also applies to the subsequent global constraints. However, this essentially resembles a sub-optimization problem and –for performance reasons– requires the availability of a suitable, i.e. Newton-type solver. Alternatively, so-called augmented Lagrangian methods relax geometrical constraints via the introduction of additional Lagrangian multipliers, cf. Allaire et al. [2004], Andreani et al. [2008], Allaire et al. [2021], Müller et al. [2021]. The latter serve as additional process parameters and usually result in an increased number of optimization cycles, especially if several geometrical constraints should be considered simultaneously. Moreover, the designs often do not perfectly adhere to the permissible design space during the optimization, cf. Allaire et al. [2004], Müller et al. [2021]. The procedure essentially augments the actual flow sensitivity, is modularizable and intuitively to use. An exemplary geometric inequality constraint refers to a maximum control-coordinate $\tilde{u}_{\mathrm{i}}^*$ in x_{i}-direction. The general optimization problem (3.1) is augmented

$$\min J^*(\varphi^*(u_{\mathrm{i}}^*), u_{\mathrm{i}}^*) \qquad \text{s.t.} \qquad \mathrm{R}^{*\varphi}(\varphi^*(u_{\mathrm{i}}^*)) = 0 \qquad \text{and} \qquad u_{\mathrm{i}}^* - \tilde{u}_{\mathrm{i}}^* \leq 0\,, \tag{3.31}$$

and the sensitivity of the shape w.r.t. the flow $s^*\, n_{\mathrm{i}}$ is assumed to be available. As long as the shape remains below the upper control bound, the constraint is inherently fulfilled. However, if the shape moves beyond the boundary, an additional geometric sensitivity $s_{\mathrm{i}}^{*\mathrm{u}}$ is added to the flow sensitivity. Note that the latter was the reason for moving beyond the maximum coordinate, viz.

$$s^*\, n_{\mathrm{i}} \leftarrow \alpha^{*\mathrm{u_i}}\, s_{\mathrm{i}}^{*\mathrm{u}} \qquad \text{with} \qquad s_{\mathrm{i}}^{*\mathrm{u}} = \begin{cases} 0 & : u_{\mathrm{i}}^* - \tilde{u}_{\mathrm{i}}^* \leq 0 \\ \tilde{u}_{\mathrm{i}}^* - u_{\mathrm{i}}^* & : u_{\mathrm{i}}^* - \tilde{u}_{\mathrm{i}}^* > 0 \end{cases}. \tag{3.32}$$

Compliance of the dimensions and scaling of the geometric constraint is ensured by the constant $\alpha^{*\mathrm{u_i}}$. A natural choice of the scaling refers to the inverse step size of the employed steepest descent approach.

3.6.2 Global Constraints

Global constraints require the preservation of integral quantities such as, e.g., constant displaced water, a maximum wetted surface or a fixed center of gravity. The former is of particular importance in this work since the optimizations often try to eliminate the

surface and thereby the obstacle. Explicit LB approaches project the boundary-based gradient into the penalty-free space

$$g_{\mathrm{i}}^{*} \leftarrow \alpha^{*\mathrm{g_i}}\, n_{\mathrm{i}} \qquad \text{with} \qquad \alpha^{*\mathrm{g_i}} = -\frac{\int_{\Gamma^{*\mathrm{W}}} g_{\mathrm{i}}^{*}\, n_{\mathrm{i}}\, \mathrm{d}\Gamma}{\int_{\Gamma^{*\mathrm{W}}} 1\, \mathrm{d}\Gamma}\,, \tag{3.33}$$

whereby, e.g., only the wetted boundary $\Gamma^{*\mathrm{W}}$ is considered. The projection (3.33) can be applied on sensitivity level if the explicit filtering refers to consistent kernel functions, c.f. Kröger and Rung [2015], Löhner [2008]. Once available, the projected gradient is plugged into the field deformation Eqn. (3.29). In contrast, implicit SP procedures solve an additional field equation

$$\frac{\partial}{\partial x_{\mathrm{k}}^{*}}\left[\mu^{*\hat{\mathrm{g}}_{\mathrm{i}}}\frac{\partial \hat{g}_{\mathrm{i}}^{*}}{\partial x_{\mathrm{k}}^{*}}\right] = 0 \quad \text{in} \quad \Omega^{*} \qquad \text{with} \qquad \begin{cases} \frac{\partial\, \hat{g}_{\mathrm{i}}*}{\partial\, n^{*}} = n_{\mathrm{i}} & \text{on} \quad \Gamma^{*} \cap \Gamma^{*\mathrm{D}} \\ \hat{g}_{\mathrm{i}}^{*}\, n_{\mathrm{i}} = 0, \frac{\partial\, \hat{g}_{\mathrm{i}}^{*}}{\partial\, n^{*}} t_{\mathrm{i}} = 0 & \text{on} \quad \Gamma^{*\mathrm{Symm}} \\ \hat{g}_{\mathrm{i}}^{*} = 0 & \text{on} \quad \Gamma^{*} \end{cases} \tag{3.34}$$

that allows for an analogous treatment of local geometric boundary conditions as, e.g. plane surfaces or fixed main slices. The explicit normal vector dependence of (3.33) is incorporated implicitly as Neumann condition in (3.34). The approach shares ideas of a sub-optimization optimization problem that aims minimizing the squared integral of the deformation flux through the wetted part of the shape constraint by the SP field deformation Eqn. (3.30), viz. $J^{*\Gamma,\mathrm{D}} = \left[\int_{\Gamma^{*\mathrm{W}}} d_{\mathrm{i}}^{*}\, n_{\mathrm{i}}\, \mathrm{d}\Gamma^{*}\right]^{2}$. After an approximation of (3.34), a superposition of g_{i}^{*} and $\hat{g}_{\mathrm{i}}^{*}$ yields a conservative volume-based shape gradient, viz.

$$g_{\mathrm{i}}^{*} \leftarrow \alpha^{*\mathrm{g_i}}\, \hat{g}_{\mathrm{i}}^{*} \qquad \text{with} \qquad \alpha^{*\mathrm{g_i}} = -\frac{\int_{\Gamma^{*\mathrm{W}}} g_{\mathrm{i}}^{*}\, n_{\mathrm{i}}\, \mathrm{d}\Gamma}{\int_{\Gamma^{*\mathrm{W}}} \hat{g}_{\mathrm{i}}^{*}\, n_{\mathrm{i}}\, \mathrm{d}\Gamma}\,. \tag{3.35}$$

The explicit LB approach is used for validation purposes in Sec. 4.4. All applications in Cha. 5 employ the SP approach, i.e. approximate (3.30) as well as (3.34). Their implementation follows the generic transport equation concept from Sec. 2.2.

3.7 Optimization Procedure

After all engineering constraints are incorporated, either locally on sensitivity level or globally within the shape gradient, a descent procedure is employed to minimize the cost functional. For this purpose, the volume-based representation of the shape gradient is multiplied by a sufficiently small step size $d_{\mathrm{i}}^{*} = -\alpha^{*\mathrm{d_i}}\, g_{\mathrm{i}}^{*}$ that a) ensures compliance of dimensions between the LB [SP] shape gradient $[g_{\mathrm{i}}^{*}] = [J^{*}]/(\mathrm{m}^3\,\mathrm{s})$ $[[g_{\mathrm{i}}^{*}] = [J^{*}]/(\mathrm{m}^2\,\mathrm{s})]$ and the deformation field $[d_{\mathrm{i}}^{*}] = \mathrm{m}$, i.e. $[\alpha^{*\mathrm{d_i}}] = (\mathrm{m}^4\,\mathrm{s})/[J^{*}]$ $[[\alpha^{*\mathrm{d_i}}] = (\mathrm{m}^3\,\mathrm{s})/[J^{*}]]$ and b) serves as an optimization step in the direction of steepest descent. The step size remains constant over the optimization process and is frequently estimated based on a maximum initial displacement, i.e. $\alpha^{*\mathrm{d_i}} = d_{\mathrm{i}}^{*\max}/\max(g_{\mathrm{i}}^{*})$. Typical values for this maximum displacement refer to $1/10000 \leq d_{\mathrm{i}}^{*\max}/L^{*} \leq 1/1000$, where L^{*} denotes to a reference length of the underlying geometry, e.g. the ship length. Subsequent deformation of the cell vertices follows from an averaged interpolation of all vertex-adjacent centers $N^{\mathrm{P(V)}}$ in line with (2.112). After the update of the grid, geometric quantities are recalculated for each CV. Topological relationships remain unaltered and the simulation is continued by a restart

from the previous optimization step to evaluate the new objective functional value. Due to the employed steepest descent approach and comparably small step sizes, field solutions of two consecutive shapes are usually nearby. Compared to a simulation from scratch, a speedup in total computational time of about an order of magnitude is realistic for this thesis's applications. The optimization loop is terminated if a maximum number of optimization cycles N^{O} is reached or if the relative cost functional decrease w.r.t. the initial shape falls below $\epsilon^{\mathrm{J}}[\%]$ during an optimization step, cf. Alg. 3.

Algorithm 3: Schematic representation of the employed gradient descent procedure, where N^{O}, $\alpha^{*\mathrm{d_i}}$, ϵ^{J}, and $J^{*\mathrm{ini}}$ denote the maximum optimization iteration, a user-defined step size, the objective convergence criterion, and the initial ($n^{\mathrm{opt}} = 1$) cost functional value, respectively.

```
define: α^{*d_i}, N^O and ε^J
n^opt = 1
while (n^opt ≤ N^O) do
    approximate primal two-phase system, cf. (2.43)-(2.48)
    evaluate cost functional J* from Sec. 3.2
    if (n^opt > 1) and (J* − J^{*ini})/J^{*ini} · 100 ≤ ε^J) then
        terminate
    else
        approximate adjoint two-phase system, cf. (4.16)-(4.18)
        compute shape (sensitivity) derivative w.r.t. the fluid flow s*, cf. (4.44),
         (4.58) and (4.64)
        employ local geometric constraint(s) and manipulate shape derivative, e.g.
         (3.32)
        approximate shape gradient, e.g. (3.28)-(3.29) or (3.30)
        employ global geometric constraint(s) and manipulate the shape gradient,
         e.g. (3.33) or (3.34)
        define displacement field: d_i^* = −α^{*d_i} g_i^*
        perform a domain (shape) update (2.112)
    n^opt ← +1
```

4 Adjoint Flow

As illustrated in the previous chapter, an adjoint analysis represents -perhaps- the only feasible procedure to determine the sensitivity derivative of a cost functional subjected to turbulent two-phase flow w.r.t. non-parameterized shapes. An adjoint system always follows the primal model, depends on the underlying cost functional, and is thus difficult to generalize.

The fourth chapter is devoted to describing all aspects of the discrete adjoint flow model. Emphasis is put on a compromise between consistency, effort and robustness. Focus is put to the near-wall region, which is crucial to shape optimization. Starting from a closed continuous derivation of the two-phase adjoint equations for incompressible bulk fluids (integration by parts), the corresponding discrete adjoint operators (summation by parts) are developed.

The chapter is structured as follows: The first section derives the continuous adjoint complement to all primal conservation relations for an under-resolved two-phase system (2.56)-(2.58). The second section presents the adjoint discretization for a generic adjoint transport equation. The third section outlines a detailed verification of the discrete adjoint implementation against all verification cases already discussed in Sec. 2.3. The chapter concludes with a validation of the adjoint formulation.

4.1 Adjoint Two-Phase Flow Model

The governing equations of the primal flow follow from general conservation laws. Initially, they are comparatively universal and leave the user room for subsequent additional modelling assumptions or simplifications. A suitable example for this refers to the conservation of mass: Starting from $\mathrm{D}\,\rho^*/\mathrm{D}\,t^* = 0$ finally leads to $\partial v_\mathrm{i}^*/\partial x_\mathrm{i}^* = 0$ if, e.g., $\mathrm{d}\,c/\mathrm{d}\,t^* = 0$ applies. Two ways – which must agree – are conceivable to obtain the consistent continuous adjoint system to the simplified primal flow model. The general (non-simplified) primal model is firstly differentiated and subsequently simplified, a procedure which is denoted by a *derive-and-simplify* strategy. Alternatively, the adjoint derivation can already start at the primal simplification, which corresponds to a *simplify-and-derive* strategy. If desired, the latter can use the primal simplifications in a backward fashion to arrive at the consistent, continuous adjoint system of the non-simplified primal model. In general, the *simplify-and-derive* approach is employed to arrive at the continuous adjoint complement to the under-resolved two-phase RANS system. A brief discussion of the corresponding *derive-and-simplify* case is provided in App. D.1. Moreover, selected verification cases displayed in Sec. 4.3 pursue both strategies.

Starting Point

The general cost functional from (3.1) is augmented by the simplified primal under-resolved two-phase RANS system (2.56)-(2.58) that yields the following Lagrangian

$$L^* = J^* + \int\int \left[\hat{p}^*\,\mathrm{R}^{*\mathrm{p}} + \hat{c}^*\,\mathrm{R}^{*\mathrm{c}} + \hat{v}_\mathrm{i}^*\,\mathrm{R}^{*\mathrm{v_i}}\right] \mathrm{d}\Omega^*\,\mathrm{d}t^*\,, \tag{4.1}$$

where $\hat{p}^*$, $\hat{c}^*$ and $\hat{v}_\mathrm{i}^*$ refer to adjoint pressure, adjoint concentration and adjoint velocity components, respectively, cf. (3.15). The units of adjoint pressure and adjoint concentration are equal $[\hat{p}^*] = [\hat{c}^*] = [J^*]\,1/\mathrm{m}^3$. The unit of the adjoint velocity is $[\hat{v}_i^*] = [J^*]\,1/(\mathrm{N\,s})$.

It is assumed that the adjoint influence of turbulence modelling aspects is minor, which justifies the frequently employed frozen turbulence assumption, cf. Dwight and Brézillon [2006], Othmer [2008], Stück [2012], Stück and Rung [2013]. An attempt to scrutinize this assumption and improve the adjoint treatment of modeled turbulence is discussed at the end of this chapter. Here, the logarithmic region of a canonical turbulent shear flow is analysed, and LoW consistent adjoint formulations are derived which only involve an algebraic modification. Mind that the wall flow is the most critical region for most engineering applications.

The current work focuses on quasi-steady primal flows, and the objectives are free of temporal expressions. In this context, quasi-steady means that a temporal derivative initially appears in the equations but loses its significance over the temporal forward integration process and finally disappears. Hence, the unsteady term vanishes for the converged primal solution, and the primal time history is physically meaningless. Therefore, all adjoint time steps are linearized around the same converged primal flow field. However, the time-dependent adjoint terms are initially retained during the derivation and optionally serve to stabilize the adjoint solution process in a pseudo-time integration. An expansion of (4.1) provides the relevant Lagrangian for this section, viz.

$$\begin{aligned} L^* = {} & \int_{\Gamma^\mathrm{O}} j^{*\Gamma}\,\mathrm{d}\Gamma^* + \int_{\Omega^\mathrm{O}} j^{*\Omega}\,\mathrm{d}\Omega^* \\ & + \int\int \hat{p}^* \left[- \frac{\partial\, v_\mathrm{k}^*}{\partial\, x_\mathrm{k}^*}\right] + \hat{c}^* \left[\frac{\partial\, c}{\partial\, t^*} + v_\mathrm{k}^* \frac{\partial\, c}{\partial\, x_\mathrm{k}^*} - \frac{\partial}{\partial\, x_\mathrm{k}^*}\left[\nu^{*\mathrm{c}} \frac{\partial\, c}{\partial\, x_\mathrm{k}^*}\right]\right] \\ & \quad + \hat{v}_\mathrm{i}^* \left[\rho^* \left[\frac{\partial\, v_\mathrm{i}^*}{\partial\, t^*} + v_\mathrm{k}^* \frac{\partial\, v_\mathrm{i}^*}{\partial\, x_\mathrm{k}^*}\right] + \frac{\partial}{\partial\, x_\mathrm{k}^*}\left[p^{*\mathrm{eff}}\,\delta_\mathrm{ik} - 2\,\mu^{*\mathrm{eff}}\,S_\mathrm{ik}^*\right] - \rho^*\,g_\mathrm{i}^*\right] \mathrm{d}\Omega^*\,\mathrm{d}t^*\,. \end{aligned} \tag{4.2}$$

All primal balance equations assume a solenoidal velocity field. As already discussed at the end of Sec. 2.1.7, this follows if a) the VoF approach is employed ($\nu^{*\mathrm{c}} = 0$), b) both participating fluids feature the same bulk density $\rho^{*\Delta} = 0$ or c) a nonlinear EoS is used ($f^\rho \to 0$), cf. Eqn. (2.12).

First-order optimality conditions demand the derivatives of the Lagrangian to disappear in all relevant directions at the optimal point, which leads to the adjoint system of equations (Heners et al. [2017]) and, in the end, allows the definition of a sensitivity rule along the design surface. In the following, the necessary functional derivatives in the direction of the pressure, concentration, and velocity are determined and subsequently summarized. A differentiation of the highly nonlinear EoS (2.12) would introduce robustness issues, in particular for an insufficient interface resolution. Since the EoS is only active in a thin interface region, which is generally not resolved in engineering flow simulations, the differentiation of the EoS is modified.

For reasons of clarity, the primal boundary conditions will be considered later when deriving the adjoint boundary conditions.

4.1.1 Pressure Variation

Mass conservation has been reformulated into a volume-conservation, which is used to determine the effective fluid dynamic pressure. A derivative of (4.2) in the direction of the fluid dynamic pressure p^* reads

$$\delta_{\mathrm{p}} L^* \cdot \delta p^* = \int_{\Gamma^{*\mathrm{o}}} \frac{\partial\, j^{*\Gamma}}{\partial\, p^*} \delta p^* \,\mathrm{d}\Gamma^* + \int_{\Omega^{*\mathrm{o}}} \frac{\partial\, j^{*\Omega}}{\partial\, p^*} \delta p^* \,\mathrm{d}\Omega^* + \int\int \hat{v}_{\mathrm{i}}^* \left[\frac{\partial\, \delta p^*}{\partial\, x_{\mathrm{i}}^*} \right] \mathrm{d}\Omega^* \mathrm{d}t^* \quad \stackrel{!}{=} 0 \quad \forall\, \delta p^* \,. \tag{4.3}$$

Mind that the derivative in the effective pressure direction $p^{*\mathrm{eff}}$ is deliberately not determined, and the related influence of an adjoint turbulence treatment is discussed later. Isolation of all pressure variations yields

$$\begin{aligned} \delta_{\mathrm{p}} L^* \cdot \delta p^* = & \int_{\Gamma^{*\mathrm{o}}} \frac{\partial\, j^{*\Gamma}}{\partial\, p^*} \delta p^* \,\mathrm{d}\Gamma^* + \int_{\Omega^{*\mathrm{o}}} \frac{\partial\, j^{*\Omega}}{\partial\, p^* *} \delta p^* \,\mathrm{d}\Omega^* \\ & + \int\int \delta p^* \, \hat{v}_{\mathrm{i}}^* n_{\mathrm{i}} \,\mathrm{d}\Gamma^* \mathrm{d}t^* + \int\int \delta p^* \left[- \frac{\partial\, \hat{v}_{\mathrm{i}}^*}{\partial\, x_{\mathrm{i}}^*} \right] \mathrm{d}\Omega^* \mathrm{d}t^* \quad \stackrel{!}{=} 0 \quad \forall\, \delta p^* \,. \end{aligned} \tag{4.4}$$

A divergence-free adjoint velocity field is obtained as long as the volume-based objective functional does not depend on the pressure, which is the case for all considered objectives in this thesis, cf. Sec. 3.2.

4.1.2 Concentration Variation

The local density $\rho^* = \rho^*(c)$ and viscosity $\mu^* = \mu^*(c)$ are expressed in terms of the primal concentration field using the EoS (2.6) and (2.13), respectively. Hence, the derivative in the concentration direction appears to be much more extensive since several implicit dependencies arise, viz.

$$\begin{aligned} \delta_{\mathrm{c}} L^* \cdot \delta c = & \int_{\Gamma^{*\mathrm{o}}} \frac{\partial\, j^{*\Gamma}}{\partial\, c} \delta c \,\mathrm{d}\Gamma^* + \int_{\Omega^{*\mathrm{o}}} \frac{\partial\, j^{*\Omega}}{\partial\, c} \delta c \,\mathrm{d}\Omega^* \\ & + \int\int \hat{c}^* \left[\frac{\partial\, \delta c}{\partial\, t^*} + v_{\mathrm{k}}^* \frac{\partial\, \delta c}{\partial\, x_{\mathrm{k}}^*} - \frac{\partial}{\partial\, x_{\mathrm{k}}^*} \left[\nu^{*\mathrm{c}\prime} \, \delta c \, \frac{\partial\, c}{\partial\, x_{\mathrm{k}}^*} + \nu^{*\mathrm{c}} \frac{\partial\, \delta c}{\partial\, x_{\mathrm{k}}^*} \right] \right] \\ & \quad + \hat{v}_{\mathrm{i}}^* \left[\left[\frac{\partial\, v_{\mathrm{i}}^*}{\partial\, t^*} + v_{\mathrm{k}}^* \frac{\partial\, v_{\mathrm{i}}^*}{\partial\, x_{\mathrm{k}}^*} \right] \rho^{*\Delta} \, m^{\rho\prime} \, \delta c \right. \\ & \qquad + \frac{\partial}{\partial\, x_{\mathrm{k}}^*} \left[\frac{2}{3} k^* \, \rho^{*\Delta} \, m^{\rho\prime} \, \delta c \, \delta_{\mathrm{ik}} - 2 \left[\mu^{*\Delta} \, m^{\mu\prime} \, \delta c + \frac{\partial\, \mu^{*\mathrm{t}}}{\partial\, \rho^*} \rho^{*\Delta} \, m^{\rho\prime} \, \delta c \right] S_{\mathrm{ik}} \right] \\ & \qquad \left. - \rho^{*\Delta} \, m^{\rho\prime} \, \delta c \, g_{\mathrm{i}}^* \right] \mathrm{d}\Omega^* \mathrm{d}t^* \quad \stackrel{!}{=} 0 \quad \forall\, \delta c \,, \end{aligned} \tag{4.5}$$

where $\nu^{*\mathrm{c}\prime} = \partial\, \nu^{*\mathrm{c}} / \partial\, c$, $m^{\rho\prime} = \partial\, m^{\rho} / \partial\, c$ and $m^{\mu\prime} = \partial\, m^{\mu} / \partial\, c$ refer to the first derivative of the apparent viscosity and density as well as viscosity EoS, respectively. The terms will be discussed in more detail below. One part of the variation of the dynamic turbulent

viscosity follows from its partial derivative w.r.t. the density after applying the chain rule, viz. $\delta_\mathrm{c}\mu^{*\mathrm{t}} \cdot \delta c = (\partial\,\mu^{*\mathrm{t}}/\partial\,\rho^*)(\partial\,\rho^*/\partial\; m^\rho)(\partial\, m^\rho/\partial\, c)\delta c$, cf. Eqn. (2.36). The isolation of all concentration variations yields

$$
\begin{aligned}
\delta_\mathrm{c} L^* \cdot \delta c = & \int \delta c\, \hat{c}^*\, \mathrm{d}\Omega^* \Big|_{\mathrm{t}^0}^{\mathrm{t}^\mathrm{E}} + \int_{\Gamma^{*\mathrm{O}}} \frac{\partial\, j^{*\Gamma}}{\partial\, c} \delta c\, \mathrm{d}\Gamma^* + \int_{\Omega^{*\mathrm{O}}} \frac{\partial\, j^{*\Omega}}{\partial\, c} \delta c\, \mathrm{d}\Omega^* \\
& + \int\int \delta c \Bigg[\hat{c}^*\, v_\mathrm{k}^*\, n_\mathrm{k} - \hat{c}^*\, \nu^{*\mathrm{c}\prime} \frac{\partial\, c}{\partial\, n} + \nu^{*\mathrm{c}} \frac{\partial\, \hat{c}^*}{\partial\, n} + \hat{v}_\mathrm{i}^* \left[\frac{2}{3} k^*\, n_\mathrm{i} - 2\, \frac{\partial\, \mu^{*\mathrm{t}}}{\partial\, \rho^*} S_\mathrm{ik}\, n_\mathrm{k} \right] \rho^{*\Delta} m^{\rho\prime} \\
& \qquad - \hat{v}_\mathrm{i}^*\, 2\, S_\mathrm{ik}\, n_\mathrm{k}\, \mu^{*\Delta} m^{\mu\prime} \Bigg] \\
& \qquad - \frac{\partial\, \delta c}{\partial\, n} \left[\hat{c}^*\, \nu^{*\mathrm{c}} \right] \mathrm{d}\Gamma^*\, \mathrm{d}t^* \\
& + \int\int \delta c \Bigg[- \frac{\partial\, \hat{c}^*}{\partial\, t^*} - \frac{\partial\, v_\mathrm{k}^*\, \hat{c}^*}{\partial\, x_\mathrm{k}^*} + \nu^{*\mathrm{c}\prime} \frac{\partial\, \hat{c}^*}{\partial\, x_\mathrm{k}^*} \frac{\partial\, c}{\partial\, x_\mathrm{k}^*} - \frac{\partial}{\partial\, x_\mathrm{k}^*} \left[\nu^{*\mathrm{c}} \frac{\partial\, \hat{c}^*}{\partial\, x_\mathrm{k}^*} \right] \\
& \qquad + \rho^{*\Delta} m^{\rho\prime} \left[\hat{v}_\mathrm{i}^* \frac{\partial\, v_\mathrm{i}^*}{\partial\, t^*} + \hat{v}_\mathrm{i}^*\, v_\mathrm{k}^* \frac{\partial\, v_\mathrm{i}^*}{\partial\, x_\mathrm{k}^*} - \frac{2}{3} k^* \frac{\partial\, \hat{v}_\mathrm{i}^*}{\partial\, x_\mathrm{i}^*} - \hat{v}_\mathrm{i}^*\, g_\mathrm{i}^* + \frac{\partial\, \mu^{*\mathrm{t}}}{\partial\, \rho^*} S_\mathrm{ik} \frac{\partial\, \hat{v}_\mathrm{i}^*}{\partial\, x_\mathrm{k}^*} \right] \\
& \qquad + \mu^{*\Delta} m^{\mu\prime} \left[2\, S_\mathrm{ik} \frac{\partial\, \hat{v}_\mathrm{i}^*}{\partial\, x_\mathrm{k}^*} \right] \Bigg] \mathrm{d}\Omega^* \mathrm{d}t^* \quad \stackrel{!}{=} 0 \quad \forall\, \delta c\,.
\end{aligned}
\tag{4.6}
$$

Two terms that scale with the difference of the bulk densities $\rho^{*\Delta}$ vanish: The adjoint velocity field is solenoidal, cf. (4.4), which reveals $2/3\, k^*(\partial\, \hat{v}_\mathrm{i}^*/\partial\, x_\mathrm{i}^*) \to 0$. Additionally, a temporally converged primal field is assumed so that $(\partial\, v_\mathrm{i}^*/\partial\, t^*) \to 0$.

The third term of the volume integral in (4.6) deserves further explanation. The term scales with the $\nu^{*\mathrm{c}\prime}$ and is multiplied by the gradient of the primal concentration which disappears in the bulk phases. The introduction of diffusivity within the primal system offers a) a desired diffusion operator (cf. Sec. 4.3.2) as well as b) a second contribution from the nonlinearity of the CH diffusivity, cf. (2.54). The former a) inheres a free mobility parameter that follows from a resolution-based estimation (2.102). The latter b) is associated with the first [third] derivative of $\nu^{*\mathrm{c}}$ [b] and follows from the variation of the primal apparent concentration viscosity. The third derivative reads $b''' = 24\, c - 12(c^\mathrm{a} + c^\mathrm{b}) = 24\, c - 12$. This corresponds to a linear increase in the concentration spectrum, which features the boundary values $b(c^\mathrm{b}) = 12(c^\mathrm{b} - c^\mathrm{a}) = -12$ and $b(c^\mathrm{a}) = 12(c^\mathrm{a} - c^\mathrm{b}) = 12$ in the bulk phases, and has a root at $c = (c^\mathrm{a} + c^\mathrm{b})/2 = 0.5$, cf. Fig. 2.2. Hence, the third term of (4.6) vanishes everywhere, except along $0 < c < 0.5$ and $0.5 < c < 1$. The remaining variation contribution of the third term is neglected due to the insufficient resolution in order not to compromise the numerical robustness.

4.1.3 Density Variation

All derivatives of material properties enter the adjoint concentration equation with the respective differences of the bulk properties $\rho^{*\Delta}$ and $\mu^{*\Delta}$, which are multiplied by the derivative of their respective EoS, cf. (4.5)-(4.6). A straightforward differentiation of the density EoS (2.6) reads

$$
\delta\rho^* = \frac{\partial\, \rho^*}{\partial\, m^\rho} \frac{\partial\, m^\rho}{\partial\, c} \delta c = \rho^{*\Delta} \frac{\partial\, m^\rho}{\partial c} \delta c\,. \tag{4.7}
$$

Each proposed nonlinear EoS hides the $\rho^{*\Delta}$-terms everywhere in the field except along the free surface. They narrow the interpolation regime and yield an increased slope around the critical point $c = 0.5$. All EoS formulations agree from an integral perspective, e.g. $\int m^\rho \,\mathrm{d}c = (c^\mathrm{a} + c^\mathrm{b})/2 = 1/2$. Accordingly, also the first derivative of the employed EoS results in the same integral value if integration is applied over the complete concentration spectrum (cf. Fig. 2.1), viz.

$$\int_{c^\mathrm{b}}^{c^\mathrm{a}} m^{\rho,(\cdot)} \,\mathrm{d}c = \frac{1}{2}\left[c^{\mathrm{a}2} - c^{\mathrm{b}2}\right] \qquad \text{and} \qquad \int_{c^\mathrm{b}}^{c^\mathrm{a}} m^{\rho,(\cdot)\prime} \,\mathrm{d}c = \left[m^{(\cdot)}\right]_{c^\mathrm{b}}^{c^\mathrm{a}} = \left[c^\mathrm{a} - c^\mathrm{b}\right] . \tag{4.8}$$

where $m^{\rho,(\cdot)}$ either refers to the linear (2.7), hyperbolic (2.8) or its linearized (2.9) EoS, respectively. Whereas the linear EoS offers a constant derivative, its nonlinear alternatives reveal an intensified local contribution along the interfacial region that weakens noticeably towards the bulk phases. If the hyperbolic tangent or any sigmoid alternative turns into a Heaviside function, the adjoint system experiences an abrupt (Dirac) impulse along the interface based on the density relevant source terms in (4.6). However, the integral impact does not change and exactly matches that of a linear approach. A discrete perspective reveals a vulnerability: The adjoint system conceptually pushes the phase transition below the grid resolution for this work's applications. Hence, a nonlinear, sharpness promoting EoS would finally reproduce a *frozen-concentration* approach since the discrete system will not sufficiently resolve each local adjoint concentration source. This is in line with later validation studies of the adjoint system against FD and was also observed by Veelken [2020]. Consequently, the actual sharpening is reversed in adjoint mode by a substitution $c \to \tilde{c} = \gamma^{\mathrm{m},\rho} c + (1 - \gamma^{\mathrm{m},\rho})/2$, as indicated in Fig. 4.1. A subsequent linearization of the hyperbolic term followed by an asymptotic reduction $\tilde{c}(\gamma^{\mathrm{m},\rho} \to 0) = 1/2$ towards the limit case of a vanishing sharpening thickness finally yields

$$\delta\rho^* = \frac{\partial\,\rho^*}{\partial\,m^\rho}\frac{\partial\,m^\rho}{\partial\,\tilde{c}}\frac{\partial\,\tilde{c}}{\partial\,c}\delta c = \rho^{*\Delta}\frac{1}{\gamma^{\mathrm{m},\rho}}\left[1 - \underbrace{\tanh\left(\frac{2\,\tilde{c}-1}{\gamma^{\mathrm{m},\rho}}\right)^2}_{\overset{\text{lin.}}{\to}\ [(2\,\tilde{c}-1)/\gamma^{\mathrm{m},\rho}]^2}\right]\frac{\partial\,\tilde{c}}{\partial\,c}\delta c = \rho^{*\Delta}\delta c \tag{4.9}$$

in combination with $\partial\,\tilde{c}/\partial\,c = \gamma^{\mathrm{m},\rho}$.

4.1.4 Viscosity Variation

The present thesis assigns $m^\mu = m^\rho$ and the derivative of the molecular viscosity EoS is reversed analogously to (4.9), viz.

$$\delta\mu^* = \mu^{*\Delta}\delta c\,, \tag{4.10}$$

so that the previous EoS derivatives are unified and therefore not considered in the following.

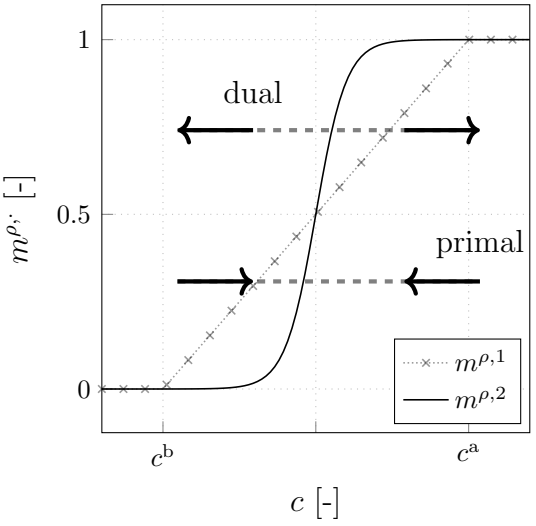

Figure 4.1: Adjoint density interpolation schemes reverse the primal sharpening via a substitution $c \to \tilde{c} = \gamma^{\mathrm{m},\rho} c + (1 - \gamma^{\mathrm{m},\rho})/2$ followed by an asymptotic reduction $\gamma^{\mathrm{m},\rho} \to 0$.

4.1.5 Velocity Variation

A derivative of the Lagrangian (4.1) in velocity direction reads

$$\begin{aligned}
\delta_{\mathrm{v_i}} L^* \cdot \delta v_{\mathrm{i}}^* = & \int_{\Gamma^{*\mathrm{O}}} \frac{\partial\, j^{*\Gamma}}{\partial\, v_{\mathrm{i}}^*} \delta v_{\mathrm{i}}^* \,\mathrm{d}\Gamma^* + \int_{\Omega^{*\mathrm{O}}} \frac{\partial\, j^{*\Omega}}{\partial\, v_{\mathrm{i}}^*} \delta v_{\mathrm{i}}^* \,\mathrm{d}\Omega^* \\
& + \int\int \hat{p} \left[- \frac{\partial\, \delta v_{\mathrm{i}}^*}{\partial\, x_{\mathrm{i}}^*} \right] + \hat{c}^* \left[(\delta v_{\mathrm{k}})^* \frac{\partial\, c}{\partial\, x_{\mathrm{k}}^*} \right] \\
& \quad + \hat{v}_{\mathrm{i}}^* \left[\rho^* \left[\frac{\partial\, \delta v_{\mathrm{i}}^*}{\partial\, t^*} + (\delta v_{\mathrm{k}})^* \frac{\partial\, v_{\mathrm{i}}^*}{\partial\, x_{\mathrm{k}}^*} + v_{\mathrm{k}}^* \frac{\partial\, \delta v_{\mathrm{i}}^*}{\partial\, x_{\mathrm{k}}^*} \right] \right. \\
& \qquad \left. - \frac{\partial}{\partial\, x_{\mathrm{k}}^*} \left[2\mu^{*\mathrm{eff}} \, (\delta S_{\mathrm{ik}})^* \right] \right] \mathrm{d}\Omega^* \mathrm{d}t^* \quad \stackrel{!}{=} 0 \quad \forall\, \delta v_{\mathrm{i}}^* \,,
\end{aligned} \tag{4.11}$$

where $\delta S_{\mathrm{ik}}^* = \partial\, \delta v_{\mathrm{i}}^* / \partial\, x_{\mathrm{k}}^* + \partial\, \delta v_{\mathrm{k}}^* / \partial\, x_{\mathrm{i}}^*$ represents the varied strain rate tensor. The isolation of all velocity variations yields the field equations for the adjoint velocity, viz.

$$\begin{aligned}
\delta_{\mathrm{v_i}} L^* \cdot \delta v_{\mathrm{i}}^* = & \int \delta v_{\mathrm{i}}^* \, \rho^* \, \hat{v}_{\mathrm{i}}^* \,\mathrm{d}\Omega^* \Big|_{\mathrm{t^0}}^{\mathrm{t^E}} + \int_{\Gamma^{*\mathrm{O}}} \frac{\partial\, j^{*\Gamma}}{\partial\, v_{\mathrm{i}}^*} \delta v_{\mathrm{i}}^* \,\mathrm{d}\Gamma^* + \int_{\Omega^{*\mathrm{O}}} \frac{\partial\, j^{*\Omega}}{\partial\, v_{\mathrm{i}}^*} \delta v_{\mathrm{i}}^* \,\mathrm{d}\Omega^* \\
& + \int\int \delta v_{\mathrm{i}}^* \left[v_{\mathrm{k}}^* \, \rho^* \, \hat{v}_{\mathrm{i}}^* \, n_{\mathrm{k}} + 2\mu^{*\mathrm{eff}} \hat{S}_{\mathrm{ik}}^* \, n_{\mathrm{k}} - \hat{p} \, n_{\mathrm{i}} \right] - \delta S_{\mathrm{ik}}^* \left[2\mu^{*\mathrm{eff}} \, \hat{v}_{\mathrm{i}}^* \, n_{\mathrm{k}} \right] \mathrm{d}\Gamma^* \mathrm{d}t^* \\
& + \int\int \delta v_{\mathrm{i}}^* \left[- \frac{\partial\, \hat{v}_{\mathrm{i}}^* \, \rho^*}{\partial\, t^*} - \frac{\partial\, v_{\mathrm{k}}^* \, \rho^* \, \hat{v}_{\mathrm{i}}^*}{\partial\, x_{\mathrm{k}}^*} + \frac{\partial\, \hat{p}^*}{\partial\, x_{\mathrm{i}}^*} - \frac{\partial}{\partial\, x_{\mathrm{k}}^*} \left[2\mu^{*\mathrm{eff}} \hat{S}_{\mathrm{ik}}^* \right] \right. \\
& \qquad \left. + \hat{c}^* \frac{\partial\, c}{\partial\, x_{\mathrm{i}}^*} + \rho^* \, \hat{v}_{\mathrm{k}}^* \frac{\partial\, v_{\mathrm{k}}^*}{\partial\, x_{\mathrm{i}}^*} \right] \mathrm{d}\Omega^* \mathrm{d}t^* \quad \stackrel{!}{=} 0 \quad \forall\, \delta v_{\mathrm{i}}^* \,.
\end{aligned} \tag{4.12}$$

The convective momentum and concentration changes result in additional variational velocity contributions, which explicitly enter the adjoint velocity equation in terms of advective sources. The former is frequently denoted as Adjoint Transpose Convection (ATC)

and will be further investigated in Sec. 4.3.1. The latter introduces the adjoint two-phase information to the adjoint velocity field and neglecting this contribution essentially resembles a frozen concentration approach. Due to the frozen turbulence assumption, the convective contributions of k^* and ω^* or ε^* are neglected. With a positive adjoint pressure gradient on the l.h.s., the adjoint velocity equation closely resembles its primal companion. The parabolic operators reverse their sign due to integration by parts, and an application of the primal mass conservation (cf. Sec. 2.1.1) allows their reformulation, viz. $-\mathrm{D}(\rho^*\,\hat{v}_\mathrm{i}^*)/\mathrm{D}\,t^* = -\rho^*(\mathrm{d}\,\hat{v}_\mathrm{i}^*/\mathrm{d}\,t^*)$.

4.1.6 Adjoint Two-Phase Reynolds-Averaged Navier-Stokes System

All functional derivatives including volume integrals are summarized in a compact form

$$
\begin{aligned}
\delta_\mathrm{p} L^{*\Omega}\cdot\delta p^* &= \int_{\Omega^{*\mathrm{O}}} \frac{\partial\, j^{*\Omega}}{\partial\, p^*}\delta p^*\,\mathrm{d}\Omega^* + \int\int \delta p^*\Big[-\frac{\partial\,\hat{v}_\mathrm{i}^*}{\partial\, x_\mathrm{i}^*}\Big]\mathrm{d}\Omega^*\mathrm{d}t^* \\
&\stackrel{!}{=} 0 \quad \forall\,\delta p^* \qquad (4.13)\\
\delta_\mathrm{c} L^{*\Omega}\cdot\delta c &= \int_{\Omega^{*\mathrm{O}}} \frac{\partial\, j^{*\Omega}}{\partial\, c}\delta c\,\mathrm{d}\Omega^* + \int\int \delta c\Big[-\frac{\mathrm{d}\,\hat{c}^*}{\mathrm{d}\,t^*} \\
&\qquad - \rho^{*\Delta}\Big[\hat{v}_\mathrm{i}^*\,g_\mathrm{i}^* - \hat{v}_\mathrm{i}^*\,v_\mathrm{k}^*\frac{\partial\, v_\mathrm{i}^*}{\partial\, x_\mathrm{k}^*} - \frac{\partial\,\mu^{*\mathrm{t}}}{\partial\,\rho^*}S_\mathrm{ik}^*\frac{\partial\,\hat{v}_\mathrm{i}^*}{\partial\, x_\mathrm{k}^*}\Big] \\
&\qquad + \mu^{*\Delta}\Big[2\,S_\mathrm{ik}\frac{\partial\,\hat{v}_\mathrm{i}^*}{\partial\, x_\mathrm{k}^*}\Big] - \frac{\partial}{\partial\, x_\mathrm{k}^*}\Big[\nu^{*\mathrm{c}}\frac{\partial\,\hat{c}^*}{\partial\, x_\mathrm{k}^*}\Big]\Big]\mathrm{d}\Omega^*\mathrm{d}t^* \\
&\stackrel{!}{=} 0 \quad \forall\,\delta c \qquad (4.14)\\
\delta_{\mathrm{v_i}} L^{*\Omega}\cdot\delta v_\mathrm{i}^* &= \int_{\Omega^{*\mathrm{O}}} \frac{\partial\, j^{*\Omega}}{\partial\, v_\mathrm{i}^*}\delta v_\mathrm{i}^*\,\mathrm{d}\Omega^* + \int\int \delta v_\mathrm{i}^*\Big[-\rho^*\frac{\mathrm{d}\,\hat{v}_\mathrm{i}^*}{\mathrm{d}\,t^*} + \frac{\partial}{\partial\, x_\mathrm{k}^*}\Big[\hat{p}^*\delta_\mathrm{ik} - \mu^{*\mathrm{eff}}\hat{S}_\mathrm{ik}^*\Big] \\
&\qquad + \hat{c}^*\frac{\partial\, c}{\partial\, x_\mathrm{i}^*} + \hat{v}_\mathrm{k}^*\,\rho^*\frac{\partial\, v_\mathrm{k}^*}{\partial\, x_\mathrm{i}^*}\Big]\mathrm{d}\Omega^*\mathrm{d}t^* \\
&\stackrel{!}{=} 0 \quad \forall\,\delta v_\mathrm{i}^*\,, \qquad (4.15)
\end{aligned}
$$

where the superscript (Ω) indicates the volumetric part of the differentiated Lagrangian. The integration limits of the spatial cost functional are conceptually extended to the entire volume. Contributions of the cost functional are active in areas of $\Omega^{*\mathrm{O}} \cap \Omega^* \neq \emptyset$ only. Assuming temporal independence of the cost functional allows a combination of both integrants in each differentiated direction. Demanding first-order optimality conditions

finally yields the adjoint field equations, viz.

$$\mathrm{R}^{*\hat{\mathrm{p}}} = -\frac{\partial \hat{v}_\mathrm{k}^*}{\partial x_\mathrm{k}^*} + \frac{\partial\, j^{*\Omega}}{\partial\, p^*} = 0 \tag{4.16}$$

$$\begin{aligned}\mathrm{R}^{*\hat{\mathrm{c}}} = &-\frac{\partial\, \hat{c}}{\partial\, t^*} - v_\mathrm{k}^* \frac{\partial\, \hat{c}^*}{\partial\, x_\mathrm{k}^*} - \rho^{*\Delta}\left[\hat{v}_\mathrm{i}^*\, g_\mathrm{i}^* - \hat{v}_\mathrm{i}^*\, v_\mathrm{k}^* \frac{\partial\, v_\mathrm{i}^*}{\partial\, x_\mathrm{k}^*} - \frac{\partial\, \mu^{*\mathrm{t}}}{\partial\, \rho^*} S_\mathrm{ik}^* \frac{\partial\, \hat{v}_\mathrm{i}^*}{\partial\, x_\mathrm{k}^*}\right] \\ &+ \mu^{*\Delta}\left[2\, S_\mathrm{ik} \frac{\partial\, \hat{v}_\mathrm{i}^*}{\partial\, x_\mathrm{k}^*}\right] + \frac{\partial\, j^{*\Omega}}{\partial\, c} = \frac{\partial}{\partial\, x_\mathrm{k}^*}\left[\nu^{*\mathrm{c}} \frac{\partial\, \hat{c}^*}{\partial\, x_\mathrm{k}^*}\right]\end{aligned} \tag{4.17}$$

$$\begin{aligned}\mathrm{R}_\mathrm{i}^{*\hat{\mathrm{v}}_\mathrm{i}} = &-\rho^*\left[\frac{\partial\, \hat{v}_\mathrm{i}^*}{\partial\, t^*} + v_\mathrm{k}^* \frac{\partial\, \hat{v}_\mathrm{i}^*}{\partial\, x_\mathrm{k}^*}\right] + \frac{\partial}{\partial\, x_\mathrm{k}^*}\left[\hat{p}^*\, \delta_\mathrm{ik} - 2\, \mu^{*\mathrm{eff}}\, \hat{S}_\mathrm{ik}^*\right] \\ &+ \hat{c}^* \frac{\partial\, c}{\partial\, x_\mathrm{i}^*} + \rho^*\, \hat{v}_\mathrm{k}^* \frac{\partial\, v_\mathrm{k}^*}{\partial\, x_\mathrm{i}^*} + \frac{\partial\, j^{*\Omega}}{\partial\, v_\mathrm{i}^*} = 0\,.\end{aligned} \tag{4.18}$$

The adjoint equations are similar to their primal companions. However, additional advection and cross-coupling terms occur. Above all, the adjoint concentration equation contains significantly more terms that scale with the two fluids' density or viscosity difference. The term on the r.h.s. of (4.17) is of particular importance since this additional diffusivity bridges the gap between an adjoint sharp vs. an under-resolved diffusive interface formulation. The latter is illustrated utilizing a plane Couette flow example discussed in Sec. 4.3.2.

Interpretation of Primal vs. Dual Time Horizon

Originating from integration by parts, the adjoint time integration is inverted, e.g. declining w.r.t. the physical time. The latter is why the complete primal solution has to be stored during the (forward) integration to be available to the adjoint solver for its subsequent (backward) integration. Several memory-reduced methods such as one-shot (piggy-bag) methods (Gherman and Schulz [2005], Kuruvila et al. [1994], Özkaya and Gauger [2009]) for pseudo-time stepping simulations or check-pointing approaches (Giering and Kaminski [1998], Griewank and Walther [2000], Hinze and Sternberg [2005], Hinze et al. [2006]) were suggested. They reduce the memory requirements at the expense of enhanced (partially rerunning) computing efforts, cf. Kapellos et al. [2019]. The formulation of the present adjoint problem is pseudo-time dependent. Although the primal flow problem is formerly unsteady, the steady state in terms of, e.g. the wave field at $t^* \to \infty$ ($\Delta t^* \to \infty$) is sought.

4.1.7 Boundary Conditions

The adjoint boundary conditions result from the boundary integrals of Eqns. (4.4), (4.6), (4.12) which likewise have to disappear for all variations (cf. Tab. 4.1). They are summa-

rized in a compact form, viz.

$$\begin{aligned}
\delta_{\mathrm{P}} L^{*\Gamma} \cdot \delta p^* &= \delta_{\mathrm{P}} J^{*\Gamma} \cdot \delta p^* + \int\int \delta p^*\, \hat{v}_{\mathrm{i}}^* n_{\mathrm{i}}\, \mathrm{d}\Gamma^* \mathrm{d}t^* \\
&\stackrel{!}{=} 0 \quad \forall\, \delta p^* \qquad (4.19) \\
\delta_{\mathrm{c}} L^{*\Gamma} \cdot \delta c &= \delta_{\mathrm{c}} J^{*\Gamma} \cdot \delta c + \int\int \delta c \Big[\hat{c}^*\, v_{\mathrm{k}}^*\, n_{\mathrm{k}} + \nu^{*\mathrm{c}} \frac{\partial\, \hat{c}^*}{\partial\, n} \\
&\qquad - \hat{v}_{\mathrm{i}}^*\, 2\, S_{\mathrm{ik}}\, n_{\mathrm{k}}\, \mu^{*\Delta} \\
&\qquad + \hat{v}_{\mathrm{i}}^* \Big[\frac{2}{3} k^*\, n_{\mathrm{i}} - 2\, \frac{\partial\, \mu^{*\mathrm{t}}}{\partial\, \rho^*} S_{\mathrm{ik}}\, n_{\mathrm{k}} \Big] \rho^{*\Delta} \Big] \\
&\qquad - \frac{\partial\, \delta c}{\partial\, n} \Big[\hat{c}^*\, \nu^{*\mathrm{c}} \Big] \mathrm{d}\Gamma^*\, \mathrm{d}t^* \\
&\stackrel{!}{=} 0 \quad \forall\, \delta c \qquad (4.20) \\
\delta_{\mathrm{v_i}} L^{*\Gamma} \cdot \delta v_{\mathrm{i}}^* &= \delta_{\mathrm{v_i}} J^{*\Gamma} \cdot \delta v_{\mathrm{i}}^* + \int\int \delta v_{\mathrm{i}}^* \Big[v_{\mathrm{k}}^*\, \rho^*\, \hat{v}_{\mathrm{i}}^*\, n_{\mathrm{k}} + 2\, \mu^{*\mathrm{eff}} \hat{S}_{\mathrm{ik}}^*\, n_{\mathrm{k}} - \hat{p}\, n_{\mathrm{i}} \Big] \\
&\qquad - \delta S_{\mathrm{ik}}^* \Big[2\, \hat{v}_{\mathrm{i}}^*\, \mu^{*\mathrm{eff}}\, n_{\mathrm{k}} \Big] \mathrm{d}\Gamma^* \mathrm{d}t^* \\
&\stackrel{!}{=} 0 \quad \forall\, \delta v_{\mathrm{i}}^*\,, \qquad (4.21)
\end{aligned}$$

where the superscript (Γ) indicates the boundary part of the differentiated Lagrangian. The adjoint boundary conditions follow from the first-order optimality conditions for the boundary Lagrangian and also consider the variation of primal boundary conditions denoted in Tab. 3.1. The respective companions of the primal boundary conditions are denoted below. Separate formulations are employed to describe conditions for boundaries which contain cost functional contributions.

- Along the **Inlet**, both the primal velocity and the concentration field are fixed and their variations $\delta v_{\mathrm{i}}^* = 0$ and $\delta c = 0$ vanish, cf. Sec. 3.4. The pressure is extrapolated with zero gradient, hence $\partial \delta p^* / \partial n^* = 0$. Inserting these relations in (4.19)-(4.21) yields the remaining parts of the derivatives of the Lagrangian along the inlet

$$\begin{aligned}
\delta_{\mathrm{p}} L^{*\Gamma} \cdot \delta p^* &= \int\int_{\Gamma^{*\mathrm{in}}} \delta p^* \quad \Big[\hat{v}_{\mathrm{i}}^*\, n_{\mathrm{i}} \Big] \mathrm{d}\Gamma^* \mathrm{d}t^* \quad \stackrel{!}{=} 0 \quad \forall\, \delta p^* \qquad (4.22) \\
\delta_{\mathrm{c}} L^{*\Gamma} \cdot \delta c &= \int\int_{\Gamma^{*\mathrm{in}}} \frac{\partial\, \delta c}{\partial\, x_{\mathrm{k}}^*} \quad \Big[- \hat{c}^*\, \nu^{*\mathrm{c}}\, n_{\mathrm{k}} \Big] \mathrm{d}\Gamma^*\, \mathrm{d}t^* \quad \stackrel{!}{=} 0 \quad \forall\, \delta c \qquad (4.23) \\
\delta_{\mathrm{v_i}} L^{*\Gamma} \cdot \delta v_{\mathrm{i}}^* &= \int\int_{\Gamma^{*\mathrm{in}}} (\delta S_{\mathrm{ik}})^* \Big[- \hat{v}_{\mathrm{i}}^*\, 2\, \mu^{*\mathrm{eff}}\, n_{\mathrm{k}} \Big] \mathrm{d}\Gamma^* \mathrm{d}t^* \quad \stackrel{!}{=} 0 \quad \forall\, \delta v_{\mathrm{i}}^*\,. \qquad (4.24)
\end{aligned}$$

  According to (4.22) and (4.24), first-order optimality conditions demand a zero adjoint velocity $\hat{v}_{\mathrm{i}}^* = 0$. A condition results for the CH-VoF adjoint concentration only ($\nu^{*\mathrm{c}} \neq 0$) and requires a vanishing Dirichlet value $\hat{c}^* = 0$. VoF methods neglect the apparent concentration viscosity ($\nu^{*\mathrm{c}} = 0$) and therefore support any boundary condition. In the present work, the same Dirichlet condition is prescribed for the VoF and the CH-VoF formulation for consistency reasons. The adjoint pressure does not appear explicitly in the derivatives. In line with the primal formulation, a zero gradient is employed.

Further variational contributions arise if the external force functional is active, cf. (3.22), viz. $\delta J^{*\Gamma,\mathrm{E}} = [2\mu^{*\mathrm{eff}}\,\delta S^*_{\mathrm{ik}}\,n_{\mathrm{k}} - \delta p^*\,n_{\mathrm{i}}]r_{\mathrm{i}}$ and the derivatives for the force-objective based Lagrangian are augmented

$$\delta_{\mathrm{p}} L^{*\Gamma,\mathrm{E}}\cdot\delta p^* = \int\int_{\Gamma^{*\mathrm{in}}} \delta p^* \quad \left[\left[\hat{v}_{\mathrm{i}} - r_{\mathrm{i}}\right] n_{\mathrm{i}}\right] \mathrm{d}\Gamma^* \mathrm{d}t^* \qquad \stackrel{!}{=} 0 \quad \forall\,\delta p^* \tag{4.25}$$

$$\delta_{\mathrm{c}} L^{*\Gamma,\mathrm{E}}\cdot\delta c = \int\int_{\Gamma^{*\mathrm{in}}} \frac{\partial\,\delta c}{\partial\,x^*_{\mathrm{k}}} \quad \left[-\hat{c}^*\,\nu^{*\mathrm{c}}\,n_{\mathrm{k}}\right] \mathrm{d}\Gamma^*\,\mathrm{d}t^* \qquad \stackrel{!}{=} 0 \quad \forall\,\delta c \tag{4.26}$$

$$\delta_{\mathrm{v_i}} L^{*\Gamma,\mathrm{E}}\cdot\delta v^*_{\mathrm{i}} = \int\int_{\Gamma^{*\mathrm{in}}} (\delta S_{\mathrm{ik}})^* \left[-\left[\hat{v}_{\mathrm{i}} - r_{\mathrm{i}}\right] 2\,\mu^{*\mathrm{eff}}\,n_{\mathrm{k}}\right] \mathrm{d}\Gamma^* \mathrm{d}t^* \qquad \stackrel{!}{=} 0 \quad \forall\,\delta v^*_{\mathrm{i}}\,. \tag{4.27}$$

Therefore, the adjoint velocity is modified w.r.t. the (non-dimensional) force direction to be minimized, viz. $\hat{v}_{\mathrm{i}} = r_{\mathrm{i}}$. Boundary conditions for adjoint pressure and concentration are not affected.

- A hydrostatic pressure is prescribed along the **Outlet**. As a consequence, its variation $\delta p^* = 0$ is zero which directly fulfills the derivative of the boundary-based Lagrangian in pressure direction (4.19). All other quantities are extrapolated with zero gradients, e.g. $\partial\,\delta v^*_{\mathrm{i}}/\partial n^* = 0$ and $\partial\,\delta c/\partial n^* = 0$. An outlet far away from a fluid flow exposed geometry motivates the neglect of $S^*_{\mathrm{ik}} \to 0$ ($\delta S^*_{\mathrm{ik}} = 0$) and thus also $k^* \to 0$. As a consequence, the boundary-based Lagrangian simplifies to

$$\begin{aligned}\delta_{\mathrm{c}} L^{*\Gamma}\cdot\delta c &= \int\int_{\Gamma^{*\mathrm{out}}} \delta c \left[\hat{c}^*\,v^*_{\mathrm{k}}\,n_{\mathrm{k}} + \nu^{*\mathrm{c}}\frac{\partial\,\hat{c}^*}{\partial\,n^*}\right] \mathrm{d}\Gamma^*\mathrm{d}t^* \\ &\stackrel{!}{=} 0 \quad \forall\,\delta c \end{aligned} \tag{4.28}$$

$$\begin{aligned}\delta_{\mathrm{v_i}} L^{*\Gamma}\cdot\delta v^*_{\mathrm{i}} &= \int\int_{\Gamma^{*\mathrm{out}}} \delta v^*_{\mathrm{i}} \left[v^*_{\mathrm{k}}\,\rho^*\,\hat{v}^*_{\mathrm{i}}\,n_{\mathrm{k}} + \mu^{*\mathrm{eff}}\,\hat{S}^*_{\mathrm{ik}}\,n_{\mathrm{k}} - \hat{p}^*\,n_{\mathrm{i}}\right] \mathrm{d}\Gamma^*\mathrm{d}t^* \\ &\stackrel{!}{=} 0 \quad \forall\,\delta v^*_{\mathrm{i}}\,. \end{aligned} \tag{4.29}$$

The adjoint velocity and the adjoint pressure are coupled via relation (4.29). In line with the primal formulation, a zero gradient is employed for the adjoint velocity ($\partial\,\hat{v}^*_{\mathrm{i}}/\partial\,n^* = 0$) and the adjoint pressure is explicitly fixed via a Dirichlet condition to

$$\hat{p}^{*\mathrm{out}} = \left[v^*_{\mathrm{k}}\,\rho^*\,\hat{v}^*_{\mathrm{i}} + \mu^{*\mathrm{eff}}\,\hat{S}^*_{\mathrm{ik}}\,n_{\mathrm{k}}\right]\,n_{\mathrm{i}}\,. \tag{4.30}$$

VoF approaches follow from $\nu^{*\mathrm{c}} = 0$ which gives rise to a zero adjoint concentration value, i.e. $\hat{c}^* = 0$, from (4.28). For the CH-VoF case, it is assumed that the ratio of convective to diffusive concentration transport along the outlet justifies the neglect of the latter and also $\hat{c}^* = 0$ is employed.

In line with the inlet boundary, further variational contributions arise if the external force functional is active, viz. $\delta J^{*\Gamma,\mathrm{E}} = -[\delta v^*_{\mathrm{i}}\,\rho^*\,v^*_{\mathrm{k}} + v^*_{\mathrm{i}}(\rho^{*\Delta}\,\delta c\,v^*_{\mathrm{k}} + \rho^*\,\delta v^*_{\mathrm{k}})]n_{\mathrm{k}}\,r_{\mathrm{i}}$, cf.

(3.22). Hence, both remaining derivatives can be simplified to

$$\delta_{\mathrm{c}} L^{*\Gamma,\mathrm{E}} \cdot \delta c = \int\int_{\Gamma^{*\mathrm{out}}} \delta c \left[\hat{c}^* \, v_{\mathrm{k}}^* \, n_{\mathrm{k}} + \nu^{*\mathrm{c}} \frac{\partial \, \hat{c}^*}{\partial \, n^*} - \rho^{*\Delta} \, v_{\mathrm{k}}^* \, v_{\mathrm{i}}^* \, n_{\mathrm{k}} \, r_{\mathrm{i}} \right] \mathrm{d}\Gamma^* \mathrm{d}t^*$$
$$\stackrel{!}{=} 0 \quad \forall \, \delta c \tag{4.31}$$

$$\delta_{\mathrm{v_i}} L^{*\Gamma,\mathrm{E}} \cdot \delta v_{\mathrm{i}}^* = \int\int_{\Gamma^{*\mathrm{out}}} \delta v_{\mathrm{i}}^* \left[v_{\mathrm{k}}^* \, \rho^* \, (\hat{v}_{\mathrm{i}} \, n_{\mathrm{k}} - n_{\mathrm{k}} \, r_{\mathrm{i}} - n_{\mathrm{i}} \, r_{\mathrm{k}}) + \mu^{*\mathrm{eff}} \hat{S}_{\mathrm{ik}}^* \, n_{\mathrm{k}} - \hat{p}^* \, n_{\mathrm{i}} \right] \mathrm{d}\Gamma^* \mathrm{d}t^*$$
$$\stackrel{!}{=} 0 \quad \forall \, \delta v_{\mathrm{i}}^* \, . \tag{4.32}$$

The adjoint concentration experiences a contribution from the variation of the convective momentum transport and the adjoint pressure-velocity relationship picks up the direction of the force to be minimized, viz.

$$\hat{c}^{*\mathrm{out,E}} = \frac{\rho^{*\Delta} \, v_{\mathrm{k}}^* \, v_{\mathrm{i}}^* \, n_{\mathrm{k}} \, r_{\mathrm{i}}}{v_{\mathrm{m}}^* \, n_{\mathrm{m}}} \qquad \text{and}$$
$$\hat{p}^{*\mathrm{out,E}} = \left[v_{\mathrm{k}}^* \, \rho^* \, (\hat{v}_{\mathrm{i}} \, n_{\mathrm{k}} - n_{\mathrm{k}} \, r_{\mathrm{i}} - n_{\mathrm{i}} \, r_{\mathrm{k}}) + \mu^{*\mathrm{eff}} \hat{S}_{\mathrm{ik}}^* \, n_{\mathrm{k}} \right] n_{\mathrm{i}} \, . \tag{4.33}$$

- **Symmetry Planes** and **Slip Walls** experience zero normal gradients for primal pressure as well as primal concentration, viz. $\partial \, \delta p^* / \partial \, n^* = 0$ and $\partial \, \delta c / \partial \, n^* = 0$. The velocity field has a zero Dirichlet normal as well as zero Neumann tangential component, e.g., $\delta v_{\mathrm{i}}^* \, n_{\mathrm{i}} = 0$ and $(\partial \, \delta v_{\mathrm{i}}^* / \partial \, n^*) t_{\mathrm{i}} = 0$. The respective derivatives of the boundary-based Lagrangian simplify to

$$\delta_{\mathrm{p}} L^{*\Gamma} \cdot \delta p^* = \int\int_{\Gamma^{*\mathrm{symm}}} \delta p^* \left[\hat{v}_{\mathrm{i}}^* n_{\mathrm{i}} \right] \mathrm{d}\Gamma^* \mathrm{d}t^* \stackrel{!}{=} 0 \quad \forall \, \delta p^* \tag{4.34}$$

$$\delta_{\mathrm{c}} L^{*\Gamma} \cdot \delta c = \int\int_{\Gamma^{*\mathrm{symm}}} \delta c \left[\nu^{*\mathrm{c}} \frac{\partial \, \hat{c}^*}{\partial \, n^*} \right] \mathrm{d}\Gamma^* \mathrm{d}t^* \stackrel{!}{=} 0 \quad \forall \, \delta c \tag{4.35}$$

$$\delta_{\mathrm{v_i}} L^{*\Gamma} \cdot \delta v_{\mathrm{i}}^* = \int\int_{\Gamma^{*\mathrm{symm}}} \mu^{*\mathrm{eff}} \left[\delta v_{\mathrm{i}}^* \hat{S}_{\mathrm{ik}}^* - (\delta S_{\mathrm{ik}})^* \, \hat{v}_{\mathrm{i}}^* \, n_{\mathrm{k}} \right] \mathrm{d}\Gamma^* \mathrm{d}t^* \stackrel{!}{=} 0 \quad \forall \, \delta v_{\mathrm{i}}^* \, . \tag{4.36}$$

The adjoint velocity field experiences the same distinction compared to the primal field, i.e. no adjoint flux normal to the symmetry plane ($\hat{v}_{\mathrm{i}}^* \, n_{\mathrm{i}} = 0$) and no normal gradient of its tangential component, viz. $(\partial \, \hat{v}_{\mathrm{i}}^* / \partial \, n^*) t_{\mathrm{i}}$. The latter follows from a decomposition into wall normal and wall tangential components of the remaining parts of Eqn. (4.36). A zero gradient condition is employed for the adjoint pressure and concentration.

- Along **No-Slip Walls**, zero normal gradients are prescribed for (effective) primal pressure as well as primal concentration, viz. $\partial \, \delta p^* / \partial \, n^* = 0$ and $\partial \, \delta c / \partial \, n^* = 0$, and

the boundary-based Lagrangian takes the following simplified form

$$\begin{aligned}
\delta_{\mathrm{p}} L^{*\Gamma} \cdot \delta p^* &= \int\int_{\Gamma^{*\mathrm{wall}}} \delta p^* \left[\hat{v}_{\mathrm{i}}^* \, n_{\mathrm{i}} \right] \mathrm{d}\Gamma^* \mathrm{d}t^* \\
&\stackrel{!}{=} 0 \quad \forall \, \delta p^* \qquad (4.37) \\
\delta_{\mathrm{c}} L^{*\Gamma} \cdot \delta c &= \int\int_{\Gamma^{*\mathrm{wall}}} \delta c \, \left[\nu^{*\mathrm{c}} \frac{\partial \, \hat{c}^*}{\partial \, n^*} - \hat{v}_{\mathrm{i}}^* \, 2 \, S_{\mathrm{ik}} \, n_{\mathrm{k}} \, \mu^{*\Delta} \right. \\
&\qquad \left. + \hat{v}_{\mathrm{i}}^* \, 2 \, \frac{\partial \, \mu^{*\mathrm{t}}}{\partial \, \rho^*} S_{\mathrm{ik}} \, n_{\mathrm{k}} \, \rho^{*\Delta} \right] \mathrm{d}\Gamma^* \mathrm{d}t^* \\
&\stackrel{!}{=} 0 \quad \forall \, \delta c \qquad (4.38) \\
\delta_{\mathrm{v_i}} L^{*\Gamma} \cdot \delta v_{\mathrm{i}}^* &= \int\int_{\Gamma^{*\mathrm{wall}}} \delta v_{\mathrm{i}}^* \left[\mu^{*\mathrm{eff}} \hat{S}_{\mathrm{ik}}^* \, n_{\mathrm{k}} - \hat{p} \, n_{\mathrm{i}} \right] - \delta S_{\mathrm{ik}}^* \left[\hat{v}_{\mathrm{i}}^* \, 2 \, \hat{v}_{\mathrm{i}}^* \, \mu^{*\mathrm{eff}} \, n_{\mathrm{k}} \right] \mathrm{d}\Gamma^* \mathrm{d}t^* \\
&\stackrel{!}{=} 0 \quad \forall \, \delta v_{\mathrm{i}}^* \, . \qquad (4.39)
\end{aligned}$$

Therefore, the adjoint velocity is simply zero ($\hat{v}_{\mathrm{i}}^* = 0$) and the concentration variation requires a zero adjoint concentration gradient $\partial \, \hat{c}^* / \partial \, n^* = 0$. Following the primal model, the adjoint pressure gradient is likewise set to zero, i.e. $\partial \, \hat{p}^* / \partial \, n^* = 0$.

Further variational contributions occur if an internal force objective is active along a no-slip wall, viz. $\delta J^{*\Gamma,\mathrm{I}} = [\delta p^* \, \delta_{\mathrm{ik}} - 2 \delta \mu^{*\mathrm{eff}} \, S_{\mathrm{ik}}^* - 2 \mu^{*\mathrm{eff}} \, \delta S_{\mathrm{ik}}^*] n_{\mathrm{k}} \, r_{\mathrm{i}}$, cf. (3.17), which augment (4.37)-(4.39) towards

$$\begin{aligned}
\delta_{\mathrm{p}} L^{*\Gamma,\mathrm{I}} \cdot \delta p^* &= \int\int_{\Gamma^{*\mathrm{wall}}} \delta p^* \left[\left[\hat{v}_{\mathrm{i}} + r_{\mathrm{i}} \right] n_{\mathrm{i}} \right] \mathrm{d}\Gamma^* \mathrm{d}t^* \\
&\stackrel{!}{=} 0 \quad \forall \, \delta p^* \qquad (4.40) \\
\delta_{\mathrm{c}} L^{*\Gamma,\mathrm{I}} \cdot \delta c &= \int\int_{\Gamma^{*\mathrm{wall}}} \delta c \, \left[\nu^{*\mathrm{c}} \frac{\partial \, \hat{c}^*}{\partial \, n^*} - \left[\hat{v}_{\mathrm{i}} + r_{\mathrm{i}} \right] 2 \, S_{\mathrm{ik}} \, n_{\mathrm{k}} \, \mu^{*\Delta} \right. \\
&\qquad \left. + \left[\hat{v}_{\mathrm{i}} + r_{\mathrm{i}} \right] 2 \, \frac{\partial \, \mu^{*\mathrm{t}}}{\partial \, \rho^*} S_{\mathrm{ik}} \, n_{\mathrm{k}} \, \rho^{*\Delta} \right] \mathrm{d}\Gamma^* \mathrm{d}t^* \\
&\stackrel{!}{=} 0 \quad \forall \, \delta c \qquad (4.41) \\
\delta_{\mathrm{v_i}} L^{*\Gamma,\mathrm{I}} \cdot \delta v_{\mathrm{i}}^* &= \int\int_{\Gamma^{*\mathrm{wall}}} \delta v_{\mathrm{i}}^* \left[\mu^{*\mathrm{eff}} \hat{S}_{\mathrm{ik}}^* \, n_{\mathrm{k}} - \hat{p} \, n_{\mathrm{i}} \right] - \delta S_{\mathrm{ik}}^* \left[\left[\hat{v}_{\mathrm{i}}^* + r_{\mathrm{i}} \right] 2 \, \hat{v}_{\mathrm{i}}^* \, \mu^{*\mathrm{eff}} \, n_{\mathrm{k}} \right] \mathrm{d}\Gamma^* \mathrm{d}t^* \\
&\stackrel{!}{=} 0 \quad \forall \, \delta v_{\mathrm{i}}^* \, . \qquad (4.42)
\end{aligned}$$

The –now dimensionless– adjoint velocity reads $\hat{v}_{\mathrm{i}} = -r_{\mathrm{i}}$ and boundary conditions for adjoint concentration and pressure are not affected.

If the actual no-slip wall is not released for design, the variation of the velocity vanishes ($\delta v_{\mathrm{i}}^* = 0$) and all optimality conditions are satisfied. However, if the wall is to be controlled, further contributions arise that have been discussed in Sec. 3.4, e.g. a linear development of the flow reveals $\delta v_{\mathrm{i}}^* = -\delta u^* (\partial \, v_{\mathrm{i}}^* / \partial \, n^*)$ where $\delta u^* = \delta n^* = \delta x_{\mathrm{k}}^* \, n_{\mathrm{k}}$ along Γ^{D}, cf. (3.26). Since all respective optimality conditions are satisfied, sensitivity information can only be obtained from the final optimality condition in terms of a derivative of the Lagrangian in the direction of the control, i.e.

$$\delta_{\mathrm{u}} L^* \cdot \delta u^* = \int\int_{\Gamma^{*\mathrm{D}}} \frac{\partial \, v_{\mathrm{i}}^*}{\partial \, n^*} \delta u^* \left[\hat{p} \, n_{\mathrm{i}} - \mu^{*\mathrm{eff}} \hat{S}_{\mathrm{ik}}^* \, n_{\mathrm{k}} \right] \mathrm{d}\Gamma^* \mathrm{d}t^* \quad \stackrel{!}{=} 0 \quad \forall \, \delta u^* \, . \qquad (4.43)$$

boundary type	$\hat{v}_\mathrm{i}^*$	$\hat{p}^*$	$\hat{c}^*$
inlet	$\hat{v}_\mathrm{i}^* = 0$	$\frac{\partial \hat{p}^*}{\partial n^*} = 0$	$\hat{c}^* = 0$
outlet	$\frac{\partial \hat{v}_\mathrm{i}^*}{\partial n^*} = 0$	$\hat{p}^* = \hat{p}^{*\mathrm{out}}$	$\hat{c}^* = 0$
symmetry	$\hat{v}_\mathrm{i}^* \, n_\mathrm{i} = 0$, $\frac{\partial \hat{v}_\mathrm{i}^*}{\partial n^*} t_\mathrm{i} = 0$	$\frac{\partial \hat{p}^*}{\partial n^*} = 0$	$\frac{\partial \hat{c}^*}{\partial n^*} = 0$
wall (slip)	$\hat{v}_\mathrm{i}^* \, n_\mathrm{i} = 0$, $\frac{\partial \hat{v}_\mathrm{i}^*}{\partial n^*} t_\mathrm{i} = 0$	$\frac{\partial \hat{p}^*}{\partial n^*} = 0$	$\frac{\partial \hat{c}^*}{\partial n^*} = 0$
wall (no-slip)	$\hat{v}_\mathrm{i}^* = 0$	$\frac{\partial \hat{p}^*}{\partial n^*} = 0$	$\frac{\partial \hat{c}^*}{\partial n^*} = 0$
inlet ($\Gamma \subset \Gamma^{\mathrm{O,E}}$)	$\hat{v}_\mathrm{i} = r_\mathrm{i}$	$\frac{\partial \hat{p}^*}{\partial n^*} = 0$	$\hat{c}^* = 0$
outlet ($\Gamma \subset \Gamma^{\mathrm{O,E}}$)	$\frac{\partial \hat{v}_\mathrm{i}^*}{\partial n^*} = 0$	$\hat{p}^* = \hat{p}^{*\mathrm{out,E}}$	$\hat{c}^* = \hat{c}^{*\mathrm{out,E}}$
wall (no-slip, $\Gamma \subset \Gamma^{\mathrm{O,I}}$)	$\hat{v}_\mathrm{i} = -r_\mathrm{i}$	$\frac{\partial \hat{p}^*}{\partial n^*} = 0$	$\frac{\partial \hat{c}^*}{\partial n^*} = 0$

Table 4.1: Boundary conditions for the adjoint equations where t_i [n_i] refer to the local boundary tangential [normal]. The first five lines refer to the general boundary conditions in the absence of any active boundary-based cost functional.

The latter gives rise to the desired shape sensitivity derivative s^*, which follows from $(\partial \, v_\mathrm{i}^* / \partial \, n^*) \, n_\mathrm{i} = 0$ and reads

$$\delta_\mathrm{u} L^* = \int \int_{\Gamma^{*\mathrm{D}}} \mu^{*\mathrm{eff}} \frac{\partial \, v_\mathrm{i}^*}{\partial \, n^*} \left[- \frac{\partial \, \hat{v}_\mathrm{i}^*}{\partial \, n^*} \right] \mathrm{d}\Gamma^* \mathrm{d}t^* \qquad \rightarrow \qquad s^* = - \mu^{*\mathrm{eff}} \frac{\partial \, v_\mathrm{i}^*}{\partial \, n^*} \frac{\partial \, \hat{v}_\mathrm{i}^*}{\partial \, n^*} \, . \quad (4.44)$$

The relation will be further explored below in terms of a wall function-based turbulent flow description.

All adjoint boundary conditions are summarized in Tab. 4.1. Mind that adjoint flow turbulence has been neglected, but the subsequent Sec. 4.1.8 is concerned with an adjoint LoW. It is assumed, that a consistent adjoint treatment close to design boundaries is of particular importance. Therefore, the study analyses the adjoint complement to a simple unidirectional turbulent shear, which is the foundation of virtually all wall function-based primal boundary conditions using a classical mixing-length hypothesis, cf. Prandtl [1925], Pope [2001]. Note that the vast majority of primal boundary condition implementations resembles this generic flow model and assumes negligible curvature to split the boundary forces into normal and tangential traction, cf. Sec. 2.2.8. The following study sugests a similar strategy for the adjoint velocity boundary condition and complies with all adjoint velocity boundary conditions outlined in Tab. 4.1.

4.1.8 Adjoint Treatment of Flow Turbulence

In this thesis, primal flow turbulence modeling refers to Reynolds-averaging strategies (cf. Sec. 2.1.6) and employs BVM based on differential transport equations for two turbulence parameters. The influence of the variation of the turbulence parameters is an open discussion (Marta and Shankaran [2013]), and optimizations of complex engineering flow using entirely consistent, differentiated turbulence transport models are rare (Papoutsis-Kiachagias and Giannakoglou [2016], Kapellos et al. [2019]) due to the significant increase of complexity. Primal turbulence transport models inhere multiple nonlinearities and inter-parameter couplings that significantly hamper the robustness and the efficiency of a consistent adjoint framework and hinder their utilization in engineering applications.

The continuous adjoint framework gives access to dedicated adjoint turbulence modelling at a lower level of adjoint consistency. One research question of the present effort is to investigate the potential of an algebraic adjoint turbulence treatment that offers the algorithmic benefits of a frozen turbulence approach. In contrast to former studies, the present effort originates from analysing the adjoint complement to a simple unidirectional turbulent shear flow. This canonical flow is the foundation of virtually all wall function-based boundary conditions and grounds on the mixing-length hypothesis, cf. Prandtl [1925], Pope [2001]. With attention given to a plane 2D b.-l., e.g. the lower half of a channel illustrated in Fig. 2.15 of Sec. 2.3.3, an unconstrained optimization problem for the drag functional (3.7) reads

$$\min \quad J^* = -\mu^{*\mathrm{eff}} \frac{\mathrm{d}\, v_1^*}{\mathrm{d}\, x_2^*}\bigg|_{\mathrm{W}} \quad \text{s.t.} \quad \mathrm{R}_1^{*\mathrm{v,CH}} = 0 \quad \rightarrow \quad L^* = J^* - \int \hat{v}_1\, \mathrm{R}_1^{*\mathrm{v,CH}}\, \mathrm{d}x_2^*\,, \tag{4.45}$$

where the index $(\cdot)_{\mathrm{W}}$ denotes a wall value. The integral in streamwise (x_1^*) direction has been neglected, since the channel is assumed to be fully developed and only the wall normal direction (x_2^*) is of relevance. The adjoint velocity is dimensionless for the considered drag objective. Using $\rho^*\,\nu^* = \mu^*$ together with a constant density ρ^*, the total variation of the Lagrangian yields

$$\delta L^* = -(\delta\nu^{\mathrm{eff}})^* \frac{\mathrm{d}\, v_1^*}{\mathrm{d}\, x_2^*}\bigg|_{W} - \nu^{*\mathrm{eff}} \frac{\mathrm{d}\, \delta v_1^*}{\mathrm{d}\, x_2^*}\bigg|_{W} - \int \hat{v}_1 \left[\frac{\mathrm{d}}{\mathrm{d}\, x_2^*}\left[(\delta\nu^{*\mathrm{eff}})^* \frac{\mathrm{d}\, v_1^*}{\mathrm{d}\, x_2^*} + \nu^{*\mathrm{eff}} \frac{\mathrm{d}\delta v_1^*}{\mathrm{d}\, x_2^*}\right]\right] \mathrm{d}x_2^*\,. \tag{4.46}$$

The frozen turbulence assumption neglects the variation of the turbulent viscosity, i.e. $\delta\nu^{*\mathrm{t}} = 0 \rightarrow \delta\nu^{*\mathrm{eff}} = 0$. An isolation of δv_1^* allows the formulation of first-order optimality conditions, viz.

$$\begin{aligned}\delta_{\mathrm{v}_1} L^* \cdot \delta v_1^* = -\nu^{*\mathrm{eff}} \frac{\mathrm{d}\, \delta v_1^*}{\mathrm{d}\, x_2^*}\bigg|_{W} &- \left[\nu^{*\mathrm{eff}} \left(\hat{v}_1 \frac{\mathrm{d}\, \delta v_1^*}{\mathrm{d}\, x_2^*} - \frac{\mathrm{d}\, \hat{v}_1}{\mathrm{d}\, x_2^*} \delta v_1^*\right)\right]_w^{\Delta} \\ &- \int \delta v_1^* \left[\frac{\mathrm{d}}{\mathrm{d}\, x_2^*}\left[\nu^{*\mathrm{eff}} \frac{\mathrm{d}\, \hat{v}_1}{\mathrm{d}\, x_2^*}\right]\right] \mathrm{d}\, x_2^* \qquad \overset{!}{=} 0 \qquad \forall\, \delta v_1^*\,. \end{aligned} \tag{4.47}$$

Here, $x_2^* = \Delta^*$ marks the position of the outer boundary. The adjoint equation to (2.149) follows from the integral expression in (4.47) and reads

$$\hat{\mathrm{R}}_1^{*\mathrm{v,CH,F}}: \qquad \frac{\mathrm{d}}{\mathrm{d}\, x_2^*}\left[(\nu^* + \nu^{*\mathrm{t}}) \frac{\mathrm{d}\, \hat{v}_1}{\mathrm{d}\, x_2^*}\right] = 0\,. \tag{4.48}$$

The superscript (F) indicates the reference to the frozen turbulence assumption. The boundary conditions along the wall as well as the outer boundary arise from the remaining terms, viz.

$$x_2^* = \Delta^*: \quad \left[\hat{v}_1 \frac{\mathrm{d}\, \delta v_1^*}{\mathrm{d}\, x_2^*} - \frac{\mathrm{d}\, \hat{v}_1}{\mathrm{d}\, x_2^*} \delta v_1^*\right] \quad \text{with} \quad \delta\left(\frac{\mathrm{d}\, v_1^*}{\mathrm{d}\, x_2^*}\right) = \frac{\mathrm{d}\, \delta v_1^*}{\mathrm{d}\, x_2^*} = 0 \qquad \rightarrow \quad \frac{\mathrm{d}\, \hat{v}_1}{\mathrm{d}\, x_2^*}\bigg|_{\Delta} = 0 \tag{4.49}$$

$$x_2^* = 0: \quad \left[(1 + \hat{v}_1) \frac{\mathrm{d}\, \delta v_1^*}{\mathrm{d}\, x_2^*} - \frac{\mathrm{d}\, \hat{v}_1}{\mathrm{d}\, x_2^*} \delta v_1^*\right] \quad \text{with} \quad \delta v_1^* = 0 \qquad \rightarrow \quad \hat{v}_1\big|_{\mathrm{W}} = -1\,. \tag{4.50}$$

Following the general derivation from above, the adjoint velocity is simply zero at the wall for other cost functionals.

A consistent approach also considers the variation of the turbulent viscosity as suggested by the mixing length hypothesis. As outlined in Sec. 2.1.6, the turbulent viscosity exclusively depends on the tangential mean velocity next to the wall distance, and the related variation reads $\delta\nu^{*\mathrm{t}} = (\kappa x_2^*)^2\,(\mathrm{d}\,\delta v_1^*/\mathrm{d}\,x_2^*)$. The latter augments (4.47) towards a consistent total variation

$$\delta_{\mathrm{v}_1} L^* \cdot \delta v_1^* = -(\nu^{*\mathrm{eff}} + \nu^{*\mathrm{t}}) \frac{\mathrm{d}\,\delta v_1^*}{\mathrm{d}\,x_2^*}\bigg|_W - \left[(\nu^{*\mathrm{eff}} + \nu^{*\mathrm{t}}) \left(\hat{v}_1 \frac{\mathrm{d}\,\delta v_1^*}{\mathrm{d}\,x_2^*} - \frac{\mathrm{d}\,\hat{v}_1}{\mathrm{d}\,x_2^*}\delta v_1^*\right)\right]_w^\Delta - \int \delta v_1^* \left[\frac{\mathrm{d}}{\mathrm{d}\,x_2^*}\left[(\nu^{*\mathrm{eff}} + \nu^{*\mathrm{t}}) \frac{\mathrm{d}\,\hat{v}_1}{\mathrm{d}\,x_2^*}\right]\right] \mathrm{d}x_2^* \quad \overset{!}{=} 0 \quad \forall\,\delta v_1^*. \tag{4.51}$$

Interestingly, (4.51) resembles (4.47) by doubling the turbulent contribution. Hence, the consistent adjoint to (2.149) reads

$$\hat{\mathrm{R}}_1^{*\mathrm{v,CH,C}}: \qquad \frac{\mathrm{d}}{\mathrm{d}\,x_2^*}\left[\left(\nu^* + 2\,\nu^{*\mathrm{t}}\right) \frac{\mathrm{d}\,\hat{v}_1}{\mathrm{d}\,x_2^*}\right] = 0. \tag{4.52}$$

The superscript (C) serves to separate the adjoint formulation based on the consistent algebraic closure model from the frozen turbulence framework. Necessary boundary conditions follow again from the boundary parts in (4.51) and agree with Eqns. (4.49)-(4.50).

A sensitivity rule of the objective w.r.t. a general control variable depends on the definition as well as on the nature of the control. For example the relation $\delta v_1^* = 0$ (4.50) along the channel wall holds as long as the wall is not subjected to control, cf. (3.24). However, if the wall is examined for its optimization potential, further variational contributions follow from the concept of material derivative (3.11) and are available based on a linear development of the local flow w.r.t. a perturbation in wall normal direction $\delta v_1^* = -(\mathrm{d}\,v_1^*/\mathrm{d}\,x_2^*)\delta x_2^*$, cf. Sec. 3.2. The latter yields a shape sensitivity derivative expression

$$\delta_{\mathrm{u}} L^* \cdot \delta u^* = -(\nu^* + \beta\,\nu^{*\mathrm{t}}) \frac{\mathrm{d}\,\hat{v}_1}{\mathrm{d}\,x_2^*} \frac{\mathrm{d}\,v_1^*}{\mathrm{d}\,x_2^*} (\delta u)^* \qquad \overset{!}{=} 0 \qquad \forall\,\delta u^*$$

$$\rightarrow \qquad \delta_{\mathrm{u}} L^* = -(\nu^* + \beta\,\nu^{*\mathrm{t}}) \frac{\mathrm{d}\,\hat{v}_1}{\mathrm{d}\,x_2^*}\bigg|_W \frac{\mathrm{d}\,v_1^*}{\mathrm{d}\,x_2^*}\bigg|_{\mathrm{W}}. \tag{4.53}$$

The coefficient $\beta = 1$ [$\beta = 2$] accounts for a frozen [consistent] algebraic formulation and $\beta = 1$ is in line with the general shape sensitivity (4.44). The simple algebraic manipulation of the adjoint turbulent viscosity also supports more general primal BVM.

Adjoint Two-Equation Wall Functions

The study refers to the baseline $k^* - \varepsilon^*$ model from Sec. 2.1.6, c.f. Jones and Launder [1972]. The employed wall boundary conditions are of significance. In line with Sec. 2.2.8, they refer to standard approaches and employ prescribed shear stress and pressure loads on the wall face of the wall-adjacent elements to close the primal momentum equations. Zero wall normal gradients for the TKE k^* and a prescribed near-wall value of the energy dissipation ε^*, including the assurance of the local turbulence equilibrium $P^{*\mathrm{k}} = \varepsilon^*$ in the wall-adjacent cell, serve to close the primal turbulence model equations, cf. Wilcox [1998].

The study resembles the investigation from before by directly imposing either the primal low-Re or the high-Re formulation. Again, an exemplary objective refers to the fluid flow-induced shear force in an internal formulation, cf. Sec. 3.2. The algorithmic structure for the low- and the high-Re situation is identical. The only difference refers to assigned specific values for the wall shear in line with either of the two solutions (2.152). The near-wall value of ϵ^* accommodates to the low- ($\epsilon^* = 2\,\nu^* k^*/x_2^{*2}$) or the high-Re situation ($\epsilon^* = V_{1,\tau}^{*3}/(\kappa x_2^*) = (\sqrt{C^\mu} k^*)^{3/2}/(\kappa x_2^*)$), cf. Sec. 4.2.6. As regards the adjoint approach, only the adjoint momentum is considered. The wall value $\hat{v}_1^*$ does not differ for the low- and the high-Re situation. However, when attention is given to high-Re simulations, the resolution of $\hat{v}_1^*$ in the very near-wall region is deemed computationally expensive and it is more convenient to follow the same implementation strategy as for the primal flow.

Employing a low-Re approach, one frequently imposes

$$k^* = 0\,, \quad \epsilon^* = 2\nu^* \frac{k^*}{x_2^{*2}} \quad \rightarrow \quad \nu^{*\mathrm{t}} = 0 \tag{4.54}$$

for the turbulent quantities in the very near-wall regime. This again allows for the construction of a Lagrangian, viz.

$$L^* = -\left[\nu^* \frac{\mathrm{d}\, v_1^*}{\mathrm{d}\, x_2^*}\right]_{\mathrm{W}} - \int \left[\hat{v}_1 \frac{\mathrm{d}}{\mathrm{d}\, x_2^*}\left[\nu^* \left(\frac{\mathrm{d}\, v_1^*}{\mathrm{d}\, x_2^*}\right)\right] - \hat{k}^*\,[k^*] - \hat{\epsilon}^* \left[\epsilon - 2\nu^* \frac{k^*}{x_2^{*2}}\right]\right] \mathrm{d}\, x_2^*\,. \tag{4.55}$$

A variation is performed in App. D.2 and reveals the following relations at the inner and outer b.-l. position, viz.

$$x_2^* = \Delta: \quad \left[\hat{v}_1 \frac{\mathrm{d}(\delta v_1)}{\mathrm{d}\, x_2^*} - \frac{\mathrm{d}\hat{v}_1}{\mathrm{d}\, x_2^*}\delta v_1^*\right] \quad \text{with} \quad \delta\left(\frac{\mathrm{d}\, v_1^*}{\mathrm{d}\, x_2^*}\right) = \frac{\mathrm{d}(\delta v_1)}{\mathrm{d}\, x_2^*} = 0 \quad \rightarrow \quad \left.\frac{\mathrm{d}\hat{v}_1}{\mathrm{d}\, x_2^*}\right|_{\Delta} = 0 \tag{4.56}$$

$$x_2^* = 0: \quad \left[(1+\hat{v}_1) \frac{\mathrm{d}(\delta v_1)}{\mathrm{d}\, x_2^*} - \frac{\mathrm{d}\hat{v}_1}{\mathrm{d}\, x_2^*}\delta v_1^*\right] \quad \text{with} \quad \delta v_1 = 0 \quad \rightarrow \quad \hat{v}_1\big|_{\mathrm{W}} = -1\,. \tag{4.57}$$

This again confirms the findings of Eqns. (4.49)-(4.50). Eqn. (4.57) is fulfilled if either

$$\delta v_1^* = 0 \qquad \text{or} \qquad \delta v_1^* = -\frac{\mathrm{d}\, v_1^*}{\mathrm{d}\, x_2^*}(\delta u)^* \qquad \rightarrow \qquad \delta_{\mathrm{u}} L^{*\mathrm{LR}} = -\nu^* \left.\frac{\mathrm{d}\hat{v}_1}{\mathrm{d}\, x_2^*}\right|_{\mathrm{W}} \left.\frac{\mathrm{d}\, v_1^*}{\mathrm{d}\, x_2^*}\right|_{\mathrm{W}} \tag{4.58}$$

holds that allows for a low-Re (LR) shape derivative expression (cf. Eqn. (4.53)) if a linear development of the local flow w.r.t. a perturbation in wall normal direction is applied.

Employing a high-Re $k^* - \epsilon^*$ formulation, one frequently imposes

$$k^* = \frac{V_{1\tau}^{*2}}{\sqrt{C^\mu}}\,, \qquad \epsilon^* = \frac{V_{1\tau}^{*3}}{\kappa\, x_2^*} \quad \rightarrow \quad \nu^{*\mathrm{t}} = C^\mu \frac{k^{*2}}{\epsilon^*} = V_{1\tau}^* \kappa\, x_2^* = (\kappa\, x_2^*)^2 \frac{\mathrm{d}\, v_1^*}{\mathrm{d}\, x_2^*}. \tag{4.59}$$

Hence, a possible Lagrangian, that is valid within the logarithmic layer [within in the first cell] from a continuous [discrete] perspective, reads

$$L^* = -\left[V_{1\tau}(\kappa\, x_2^*) \frac{\mathrm{d}\, v_1^*}{\mathrm{d}\, x_2^*}\right]_{\mathrm{W}} - \int \left[\hat{v}_1 \frac{\mathrm{d}}{\mathrm{d}\, x_2^*}\left[(\kappa\, x_2^*)^2 \left[\frac{\mathrm{d}\, v_1^*}{\mathrm{d}\, x_2^*}\right]^2\right] - \hat{k}^* \left[k^* - \frac{V_{1\tau}^{*2}}{\sqrt{C^\mu}}\right] - \hat{\epsilon}\left[\epsilon - \frac{V_{1\tau}^3}{\kappa\, x_2^*}\right]\right] \mathrm{d}\, x_2^*\,. \tag{4.60}$$

Substituting $\epsilon^* = V_{1\tau}^{*3}/(\kappa\, x_2^*) = (k^*\sqrt{C^\mu})^{3/2}/(\kappa\, x_2^*)$ as well as $(\kappa\, x_2^*)\mathrm{d}\, v_1^*/\mathrm{d}\, x_2^* = V_{1\tau}^* = (k^*\sqrt{C^\mu})^{1/2}$, one ends up with

$$L^* = -\left[V_{1\tau}^*(\kappa\, x_2^*)\frac{\mathrm{d}\, v_1^*}{\mathrm{d}\, x_2^*}\right]_{\mathrm{W}} - \int \left[\hat{v}_1 \frac{\mathrm{d}}{\mathrm{d}\, x_2^*}\left[(\kappa\, x_2^*)\left[\frac{\mathrm{d}\, v_1^*}{\mathrm{d}\, x_2^*}\right]\cdot(k^*\sqrt{C^\mu})^{1/2}\right]\right.$$
$$\left. - \hat{k}^*\left[k^* - \frac{V_{1\tau}^{*2}}{\sqrt{C^\mu}}\right] - \hat{\epsilon}^*\left[\epsilon^* - \frac{(k^*\sqrt{C^\mu})^{3/2}}{\kappa\, x_2^*}\right]\right]\mathrm{d}\, x_2^*\,. \quad (4.61)$$

A variation is performed in App. D.3. The results can be collected in a compact form and subsequently eliminated. The respective contributions at the inner and outer b.-l. position read

$$x_2^* = \Delta^*: \quad (\delta k)^*\frac{\sqrt{C^\mu}}{2}\frac{(\kappa\, x_2^*)}{V_{1\tau}^*}\frac{\mathrm{d}\, v_1^*}{\mathrm{d}\, x_2^*}\hat{v}_1 - \frac{\mathrm{d}\delta v_1^*}{\mathrm{d}\, x_2^*}V_{1\tau}^*(\kappa\, x_2^*)\hat{v}_1$$
$$+ \delta v_1^*\left[2(\kappa\, x_2^*)V_{1\tau}^*\frac{\mathrm{d}\hat{v}_1}{\mathrm{d}\, x_2^*}\right] \overset{!}{=} 0 \quad \forall\,(\delta k, \delta v_1)^*$$
$$\text{with} \quad (\delta k)^* = 0 \quad \text{and} \quad \frac{\mathrm{d}\delta v_1^*}{\mathrm{d}\, x_2^*} = 0 \quad \rightarrow \quad \left.\frac{\mathrm{d}\hat{v}_1}{\mathrm{d}\, x_2^*}\right|_{\Delta} = 0 \quad (4.62)$$

$$x_2^* = 0: \quad (\delta k)^*\left[\frac{\sqrt{C^\mu}}{2}\frac{(\kappa\, x_2^*)}{V_{1\tau}^*}\frac{\mathrm{d}\, v_1^*}{\mathrm{d}\, x_2^*}\left[1+\hat{v}_1\right]\right] - \frac{\mathrm{d}\delta v_1^*}{\mathrm{d}\, x_2^*}\left[V_{1\tau}^*(\kappa\, x_2^*)\left[1+\hat{v}_1\right]\right]$$
$$+ \delta v_1^*\left[2(\kappa\, x_2^*)V_{1\tau}^*\frac{\mathrm{d}\hat{v}_1}{\mathrm{d}\, x_2^*}\right] \overset{!}{=} 0 \quad \forall\,(\delta k, \delta v_1)^*$$
$$\text{with} \quad (\delta k)^* = 0 \quad \text{and} \quad \delta v_1^* = 0 \quad \rightarrow \quad \hat{v}_1\big|_{\mathrm{W}} = -1\,. \quad (4.63)$$

Similar to the low-Re formulation, the relation is again fulfilled if either

$$\delta v_1^* = 0 \qquad \text{or} \qquad \delta v_1^* = -\frac{\mathrm{d}\, v_1^*}{\mathrm{d}\, x_2^*}(\delta u)^* \qquad \rightarrow \qquad \delta_{\mathrm{u}} L^{*\mathrm{HR}} = -2(\kappa\, x_2^*)V_{1\tau}^*\left.\frac{\mathrm{d}\hat{v}_1}{\mathrm{d}\, x_2^*}\right|_{\mathrm{W}}\left.\frac{\mathrm{d}\, v_1^*}{\mathrm{d}\, x_2^*}\right|_{\mathrm{W}}$$
$$= -2\nu^{*\mathrm{t}}\left.\frac{\mathrm{d}\hat{v}_1}{\mathrm{d}\, x_2^*}\right|_{\mathrm{W}}\left.\frac{\mathrm{d}\, v_1^*}{\mathrm{d}\, x_2^*}\right|_{\mathrm{W}} \quad (4.64)$$

holds that allows for a high-Re (HR) shape derivative expression based on twice the turbulent viscosity (cf. Eqn. (4.53)). This is beneficial from a discrete perspective, since in line with the primal implementation, robust stress conditions that prescribe $\hat{\tau}^{*\mathrm{eff}}$ and $\hat{p}^*$ (cf. Sec. 4.2.6) instead of a simple Dirichlet condition $\hat{v}_1(x_2 = 0) = \hat{v}_1^{\mathrm{W}}$ can be employed. The latter requires the derivation of an adjoint complement to the universal LoW (4.171), which is outlined in Sec. 4.3.3.

One can conclude that there is no need for adjoint turbulent transport equations in the range of validity of the adjoint LoW, if the above-presented wall function-based two-equation closure is employed. An exception refers to volumetric objectives that explicitly depend on turbulent quantities and – of course – the wake regime of the b.-l. or other more complex wall-detached zones of interest. Nonetheless, the benefit can be substantial and comes at a negligible cost, which is particularly appreciated. The reason is attributed to the algebraic scaling of all mean flow and turbulence parameters with the friction velocity $V_{1,\tau}^*$ within the logarithmic layer. It should be noted that the adjoint equations possibly experience twice the primal turbulent viscosity since $\beta = 2$ [$\beta = 1$] is chosen in the

consistent [frozen] case. Since the suggested approach is only consistent in the sub-layer and the logarithmic region, it can only be hypothesized that the consistency improves compared to the frozen turbulence approach for other applications. However, shape optimization problems are by definition interested in the primal / adjoint near-wall flow. Hence a consistent adjoint formulation is particularly relevant in this region. Using a two-equation model, the consistency is restricted to the momentum equation and assumes the eddy-viscosity distribution to agree with the mixing-length results, e.g. $2\,\mu^{*\mathrm{eff}}\,\hat{S}^{*}_{\mathrm{ik}} \rightarrow 2\,(\mu^{*} + \beta\,\mu^{*\mathrm{t}})\,\hat{S}^{*}_{\mathrm{ik}}$ in (4.18). Moreover, the robustness of the adjoint numerical procedure benefits from an augmented viscosity.

4.1.9 Adjoint Non-Dimensional Governing Equations

For a more detailed analysis, the adjoint Eqns. (4.16)-(4.18) are non-dimensionalized. The employed reference quantities as well as the resulting non-dimensional field quantities follow the primal approach and are given in Tab. 2.1. The non-dimensional set of adjoint equations belonging to the general functional (3.1) reads:

$$\mathrm{R}^{\hat{\mathrm{p}}} : -\frac{\partial \hat{v}_{\mathrm{i}}}{\partial x_{\mathrm{i}}} + \left[\frac{J^{*}\,L^{*}}{\hat{V}^{*}\,P^{*}}\right]\frac{\partial j_{\Omega}}{\partial p} = 0 \qquad (4.65)$$

$$\begin{aligned}\mathrm{R}^{\hat{\mathrm{c}}} : &-\frac{1}{\mathrm{St}}\frac{\partial \hat{c}}{\partial t} - v_{\mathrm{k}}\frac{\partial \hat{c}}{\partial x_{\mathrm{k}}} - \left[\frac{C^{*}}{V^{*}}\right]\frac{\nu^{\mathrm{c}}}{\mathrm{Re}}\frac{\partial^{2}\,\hat{c}}{\partial\, x_{\mathrm{k}}^{2}} \\ &- \left[\frac{V^{*}\hat{V}^{*}}{C^{*}}\right]\left[\frac{\rho_{\Delta}}{\mathrm{Fn}^{2}}\hat{v}_{\mathrm{i}}\,g_{\mathrm{i}} - \rho_{\Delta}\hat{v}_{\mathrm{i}}v_{\mathrm{k}}\frac{\partial v_{\mathrm{i}}}{\partial x_{\mathrm{k}}} - \frac{1}{\mathrm{Re}}\left[\frac{\partial\,\mu^{\mathrm{t}}}{\partial\,\rho}\rho^{\Delta} + 2\,\mu_{\Delta}\right]S_{\mathrm{ik}}\frac{\partial \hat{v}_{\mathrm{i}}}{\partial x_{\mathrm{k}}}\right] \\ &+ \left[\frac{J^{*}\,L^{*}}{\rho_{\mathrm{b}}^{*}\,V^{*}\,C^{*}}\right]\frac{\partial j_{\Omega}}{\partial c} = 0 \qquad (4.66)\end{aligned}$$

$$\begin{aligned}\mathrm{R}_{\mathrm{i}}^{\hat{\mathrm{v}}_{\mathrm{i}}} : &-\frac{\rho}{\mathrm{St}}\frac{\partial \hat{v}_{\mathrm{i}}}{\partial t} - \rho v_{\mathrm{k}}\frac{\partial \hat{v}_{\mathrm{i}}}{\partial x_{\mathrm{k}}} - \frac{\partial}{\partial x_{\mathrm{k}}}\left[\frac{2(\mu+\beta\mu^{\mathrm{eff}})}{\mathrm{Re}}\hat{S}_{\mathrm{ik}}\right] \\ &+ \left[\frac{C^{*}}{V^{*}\,\hat{V}^{*}}\right]\left[\frac{\partial \hat{p}}{\partial x_{\mathrm{i}}} + \hat{c}\frac{\partial c}{\partial x_{\mathrm{i}}}\right] + \rho\hat{v}_{\mathrm{k}}\frac{\partial v_{\mathrm{k}}}{\partial x_{\mathrm{i}}} + \left[\frac{J^{*}\rho_{\mathrm{b}}^{*}\hat{V}^{*}}{L^{*}}\right]\frac{\partial j_{\Omega}}{\partial v_{\mathrm{i}}} = 0\,, \qquad (4.67)\end{aligned}$$

based on the same reference quantities for adjoint pressure and adjoint concentration, i.e. $\hat{P}^{*} = \hat{C}^{*} = \rho^{*\mathrm{b}}\,C$, as well as $[\nu^{\mathrm{c}}] = [\nu]$. One can observe that the adjoint system generally displays a stronger coupling and seems challenging to solve due to the locally volatile characteristics. Two source terms that do not depend on $\hat{v}_{\mathrm{i}}$ occur in the adjoint momentum Eqn. (4.67), where the sum $\hat{p}+c\,\hat{c}$ forms an adjoint hydrostatic pairing. The sum could also be condensed into an effective adjoint pressure along the route of the frequently employed scrambling of pressure and turbulent kinetic energy for BVM. However, this would require a vanishing concentration gradient $\partial\,c/\partial\,x_{\mathrm{i}} = 0$. The adjoint concentration Eqn. (4.66) has a strong similarity to the primal momentum equation and contains Froude-, Reynolds-, and Strouhal number terms. As opposed to the primal and adjoint momentum equations, the Reynolds number contribution is not linked to the transported property in the case of VoF ($\nu^{c} = 0$). Hence three terms acting as pure source terms appear in Eqn. (4.66): An augmented convection term, a Reynolds- and a Froude number term. However, the adjoint concentration equation does not feature a hydrostatic correspondence or pairing of variables since the velocity scaling differs for all three source terms. The missing links to the transported property and pairing options are the origin of an ill-posed nature of

Eqn. (4.66) if the adjoint VoF approach ($\nu^c = 0$) is considered. The issue scales with the property differences between the two fluids.

Sharp Interface (VoF) Consideration

During previous research of Kröger [2016], observations reveal severe robustness issues of adjoint sharp-interface VoF methods, mainly when applied to large Reynolds- and Froude number marine engineering problems. Similar issues were reported for shallow-water models by Beckers et al. [2019]. Heuristic ad hoc measures to regularize the adjoint solution refer to breaking the duality by introducing a parameterized diffusion operator to the adjoint concentration equation, cf. Kröger et al. [2018]. The ill-posed nature of the problem is related to the grossly simplified inter-phase physics of the VoF procedure.

Combining the CH-VoF efforts with their adjoint complement allows for a robust and flexible consistent adjoint two-phase formulation. Although a primal (forward) integration may employ a compressive VoF approach, the adjoint (backward) simulation is free to use an under-resolved CH-VoF method. Note that both methods already lead to nearly identical results in primal mode, cf. Sec. 2.3 and 2.4. Adjoint CH-VoF studies frequently employ a spatially constant (positive) diffusivity that follows from the roughly estimated under-resolved primal flows. This represents a, albeit small, break in dual consistency since the consistent CH-VoF viscosity is spatially variable and strictly speaking becomes negative along the phase transition regime. When attention is directed to practical marine engineering applications, the computational effort associated with time stepping of compressive primal approximations is substantial. As outlined above, the related effort is anticipated to increase for the respective adjoint system. Therefore, means to reduce this effort whilst still retaining reliable sensitivity information are appreciated.

4.2 Discrete Adjoint Two-Phase Flow

In line with their primal companion, the closely coupled Eqns. (4.16)-(4.18) are discretized and approximated to obtain a numerical solution. The numerical procedure follows the baseline procedure from Sec. 2.2 and re-uses roughly 80% of the code infrastructure. This section outlines the main procedural differences and describes a consistent approximation based upon the already introduced second-order accurate FVM. In contrast to the former section regarding the continuous derivation of the two-phase adjoint equations for incompressible fluids (integration by parts), this section derives the corresponding discrete adjoint operators (summation by parts) for generic routines assembled implicitly on the l.h.s., so that finally, a consistent hybrid discrete-continuous adjoint simulation process is available.

4.2.1 Baseline Procedure

The adjoint procedure resembles a (backward) restart case based on the fully-converged, cell-centered, primal (forward) values. A coupled system of NP adjoint equations is obtained after a suitable finite approximation for each adjoint field quantity. In line with the primal procedure, the discrete adjoint variables are algorithmically linked via a sequential procedure, in which the individual equation systems are solved in a fixed sequence, cf. Alg. 4. Potential cross-coupling lags and employs values of the last outer iteration for the respective adjoint system, which also applies to the application of adjoint boundary conditions, cf. Sec. 4.2.6. The continuous adjoint system has been linearized around the temporally converged primal state and the integration in pseudo-time in Alg. 4 resembles an additional relaxation. In principle, steady primal simulations can be followed by unsteady adjoint runs or vice versa. Termination criteria for maximum outer iterations $N^{\mathrm{out,max}}$ or maximum time steps N^{T} do not have to agree for the primal and adjoint simulations.

The adjoint procedure uses the same spatial (cf. Sec. 2.2.2) and temporal (cf. Sec. 2.2.4) discretization. However, the respective approximations differ in some cases, which is the focus of Sec. 4.2.

Algorithm 4: Schematic overview of the sequential adjoint (backward) solution procedure based on a restart of the primal (forward) integration.

```
while n^T ≤ N^T do
    while (n^out ≤ N^out,max) or (R^φ ≤ R^φ,min) do
        approximate linearized momentum equations
        approximate pressure correction equation
        approximate linearized turbulence equations
        approximate linearized concentration equation
while n^T ≤ N^T do
    while (n^out ≤ N^out,max) or (R^φ̂ ≤ R^φ̂,min) do
        approximate adjoint momentum equations
        approximate adjoint pressure correction equation
        approximate adjoint concentration equation
```

4.2.2 Spatial Approximation

The governing adjoint Eqns. (4.16)-(4.18) can be expressed in a generic residual expression for a conserved adjoint quantity $\hat{\varphi}^*$, viz.

$$\mathrm{R}^{*\hat{\varphi}} = -\frac{\partial\,\hat{\varphi}^*}{\partial\,t^*} - \frac{\partial\,v_\mathrm{k}^*\,\hat{\varphi}^*}{\partial\,x_\mathrm{k}^*} - \frac{\partial}{\partial\,x_\mathrm{k}^*}\left(\mu^{*\hat{\varphi}}\frac{\partial\,\hat{\varphi}^*}{\partial\,x_\mathrm{k}^*}\right) - q^{*\hat{\varphi}} = 0\,. \tag{4.68}$$

In contrast to the primal counterpart (2.63), the signs of the parabolic operators have changed. Using the FV method, the equation is treated in a weak form for each CV

$$\begin{aligned}\int_{\Delta\Omega^*(\mathrm{P})} \mathrm{R}^{*\hat{\varphi}}\,\mathrm{d}\Omega^* = &\int_{\Delta\Omega^*(\mathrm{P})}\left[-\frac{\partial\,\hat{\varphi}^*}{\partial\,t^*} - q^{*\hat{\varphi}}\right]\mathrm{d}\Omega^* \\ &+ \oint_{\Gamma^*(\Delta\Omega^*(\mathrm{P}))}\left[-v_\mathrm{k}^*\,\hat{\varphi}^* - \left(\mu^{*\hat{\varphi}}\frac{\partial\,\hat{\varphi}^*}{\partial\,x_\mathrm{k}^*}\right)\right] n_\mathrm{k}\,\mathrm{d}\Gamma^* = 0\,.\end{aligned} \tag{4.69}$$

All spatial integrals are approximated based on the second-order accurate mid-point rule and spatial gradients follow from second-order CDS as described in Sec. 2.2.3. However, the interpolation of face values is crucial to the integration of fluxes and will be discussed in Sec. 4.2.4 and 4.2.5.

4.2.3 Temporal Approximation

Temporal integrals over adjoint quantities solely occur during the theoretical derivation of the adjoint system and follow the primal procedure, cf. Eqn. (2.71). Temporal derivatives in terms of an implicit BE approximation follow from the spatial and temporal approximation of the first-order accurate primal BE stencil for each control volume P (cf. Eqn. (2.64) and (2.72)) based on a constant time step size

$$\begin{aligned}L^* &= ... + \int\int \hat{\varphi}^*\frac{\partial\,\varphi^*}{\partial\,t^*}\,\mathrm{d}\Omega^*\,\mathrm{d}t^* + ... \\ &\rightarrow \qquad L^* \approx ... + \sum_\mathrm{T}\sum_\mathrm{P}\left[\hat{\varphi}^{*\mathrm{T}}\frac{\varphi^{*\mathrm{T}} - \varphi^{*\mathrm{T}-1}}{\Delta t^*}\Delta\Omega^*\right]^\mathrm{P}\Delta t^* + ... \end{aligned} \tag{4.70}$$

In line with the spatial discretization of the primal quantity φ^*, its corresponding Lagrangian multiplier $\hat{\varphi}^*$ is approximated as a cell-centered quantity with second-order accuracy also. To clarify the summation by parts character, three intermediate time slices are further investigated, viz.

$$\begin{aligned}L^* \approx ... &+ \sum_\mathrm{P}\left[\hat{\varphi}^{*\mathrm{T}-1}\left[\varphi^{*\mathrm{T}-1} - \varphi^{*\mathrm{T}-2}\right]\Delta\Omega^*\right]^\mathrm{P} \\ &+ \sum_\mathrm{P}\left[\hat{\varphi}^{*\mathrm{T}}\quad\left[\varphi^{*\mathrm{T}}\quad - \varphi^{*\mathrm{T}-1}\right]\Delta\Omega^*\right]^\mathrm{P} \\ &+ \sum_\mathrm{P}\left[\hat{\varphi}^{*\mathrm{T}+1}\left[\varphi^{*\mathrm{T}+1} - \varphi^{*\mathrm{T}}\quad\right]\Delta\Omega^*\right]^\mathrm{P} + ...\,,\end{aligned} \tag{4.71}$$

where the temporal increment Δt^* cancels due to the employed temporal integration. A variation of L^* and a subsequent isolation of all time-variations yields

$$\begin{aligned}\delta_\varphi L^* \cdot \delta\varphi^* \approx ... &- \sum_{\mathrm{P}} \left[\delta\varphi^{*\mathrm{T}-1} \left[\hat{\varphi}^{*\mathrm{T}} \quad - \hat{\varphi}^{*\mathrm{T}-1} \right] \Delta\Omega^* \right]^{\mathrm{P}} \\ &- \sum_{\mathrm{P}} \left[\delta\varphi^{*\mathrm{T}} \quad \left[\hat{\varphi}^{*\mathrm{T}+1} - \hat{\varphi}^{*\mathrm{T}} \quad \right] \Delta\Omega^* \right]^{\mathrm{P}} \\ &- \sum_{\mathrm{P}} \left[\delta\varphi^{*\mathrm{T}+1} \left[\hat{\varphi}^{*\mathrm{T}+2} - \hat{\varphi}^{*\mathrm{T}+1} \right] \Delta\Omega^* \right]^{\mathrm{P}} - ... \qquad \stackrel{!}{=} 0 \qquad \forall\, \delta\varphi^{*(\cdot)} \,. \end{aligned} \tag{4.72}$$

This allows to rewrite (4.70) and thus reach the adjoint BE stencil from the central line

$$\begin{aligned}\delta_\varphi L^* \cdot \delta\varphi^* &= ... - \int \int \delta\varphi^* \frac{\partial\, \hat{\varphi}}{\partial\, t^*} \,\mathrm{d}\Omega^* \,\mathrm{d}t + ... \\ \rightarrow \quad \delta_\varphi L^* \cdot \delta\varphi^* &\approx ... - \sum_{\mathrm{T}} \sum_{\mathrm{P}} \left[\delta\varphi^{*\mathrm{T}} \frac{\hat{\varphi}^{*\mathrm{T}+1} - \hat{\varphi}^{*\mathrm{T}}}{\Delta t^*} \Delta\Omega^* \right]^{\mathrm{P}} \Delta t^* + ... \,. \end{aligned} \tag{4.73}$$

In line with its primal companion, the adjoint BE approximation is first-order accurate. The procedure works analogously for the ITTL approach, but is not applied in the context of this thesis.

4.2.4 Adjoint Algebraic Equation System

The employed FV approximation of (4.69) yields a discrete system of size NP × NP, where each line corresponds to a particular CV-balance

$$A^{*\hat{\varphi},\mathrm{P}} \hat{\varphi}^{*\mathrm{P}} - \sum_{\mathrm{NB(P)}} A^{*\hat{\varphi},\mathrm{NB}} \hat{\varphi}^{*\mathrm{NB}} = S^{*\hat{\varphi},\mathrm{P}} \,. \tag{4.74}$$

Each discrete quantity also varies in time (T) as well as per outer-iteration (M). For reasons of readability, the last two incremented indices (M,T) are suppressed if not needed, viz. $\hat{\varphi}^{*\mathrm{P}} \equiv \hat{\varphi}^{*\mathrm{P,M,T}}$ and $S^{*\hat{\varphi},\mathrm{P}} \equiv S^{*\hat{\varphi},\mathrm{P,M,T}}$. The preceding part of this section presents the discrete translation of the individual terms in (4.69) which contribute to (4.74). The resulting adjoint system matrix should render the same properties as its primal companion to support a stable solution process and physically realistic solutions, i.e. positive coefficients $A^{*P}, A^{*NB} > 0$ and a diagonal dominance of the matrix $A^{*P} \geq \sum A^{*NB}$. Once the discrete relation is assembled, an under-relaxation is employed

$$A^{*\hat{\varphi},\mathrm{P}} \rightarrow \frac{A^{*\hat{\varphi},\mathrm{P}}}{\omega^{\hat{\varphi}}} \qquad \text{and} \qquad S^{*\hat{\varphi},\mathrm{P}} \leftarrow \frac{\left(1-\omega^{\hat{\varphi}}\right) A^{*\hat{\varphi},\mathrm{P}}}{\omega^{\hat{\varphi}}} \tilde{\hat{\varphi}}^{*\mathrm{P}} \,, \tag{4.75}$$

where $\tilde{\hat{\varphi}}^{*\mathrm{P}}$ follows from the previous outer iteration. Related parameters are case specific and usually employ half of the primal relaxation values due to the stronger coupling of the adjoint system and the related challenges for a segregated procedure. Hence, typical values refer to, e.g., $\omega^{\hat{\mathrm{v}}_\mathrm{i}} = 0.3$ and $\omega^{\hat{\mathrm{c}}} = 0.1$. In line with its primal companion, the approximation of the adjoint pressure is tailored to employ $\omega^{\hat{\mathrm{p}}} = 1.0$ and its relaxation is realized within the actual adjoint velocity-pressure coupling routine that usually employs $\tilde{\omega}^{\hat{\mathrm{p}}} = 0.1$.

Transient Contributions based on the implicit adjoint BE approximation (4.73) result in the following contributions to the main diagonal and the r.h.s.

$$A^{*\hat{\varphi},\mathrm{P},\mathrm{T}} \leftarrow \frac{\Delta\,\Omega^{*\mathrm{P}}}{\Delta t^*} \qquad \text{and} \qquad S^{*\hat{\varphi},\mathrm{P},\mathrm{T}} \leftarrow \frac{\Delta\,\Omega^{*\mathrm{P}}}{\Delta t^*}\,\hat{\varphi}^{*\mathrm{P},\mathrm{T}+1}\,. \tag{4.76}$$

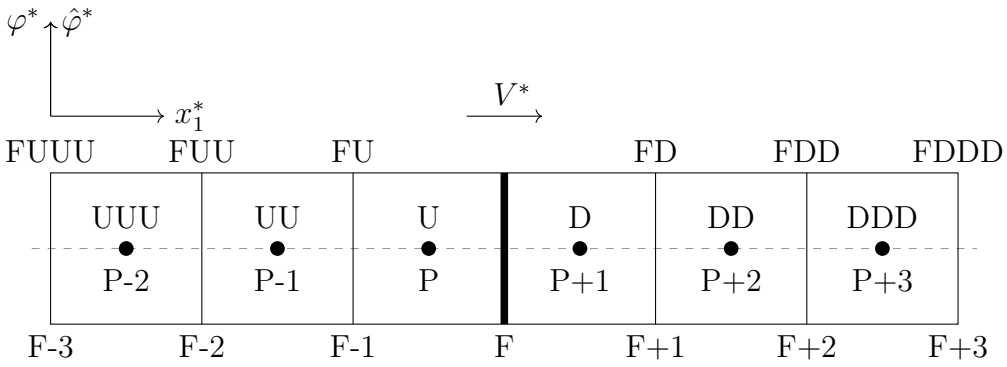

Figure 4.2: Schematic one-dimensional sketch for the approximation of biased ($[..., \mathrm{UU}, \mathrm{U}, \mathrm{D}, ...]$-based) and unbiased ($[..., \mathrm{P}-1, \mathrm{P}, \mathrm{P}+1, ...]$-based) adjoint operators.

Convective Contributions of adjoint quantities are characterized by their directional information transport in reversed mode compared to the primal velocity field. Following the primal approximation, the convective flux is formulated in terms of a volume flux across the face F times the transported field quantity on the face. Upwind biased formulae are employed that account for the directional information transport and the discrete Lagrangian based on (2.79) reads

$$\begin{aligned} L^* &= ... + \int\int \hat{\varphi}^* \frac{\partial\, v_{\mathrm{k}}^*\, \varphi^*}{\partial\, x_{\mathrm{k}}^*} \mathrm{d}\Omega^*\, \mathrm{d}t^* + ... \\ &\rightarrow \qquad L^* \approx ... + \sum_{\mathrm{T}} \sum_{\mathrm{P}} \hat{\varphi}^{*\mathrm{P}} \sum_{\mathrm{F(P)}} \dot{V}^{*\mathrm{F}} \left[\varphi^{*\mathrm{U}} + \mathrm{DC}^{*\mathrm{C},\varphi,\mathrm{F}}\right] \Delta t^* + ... \,. \end{aligned} \tag{4.77}$$

A first-order accurate UDS $\dot{V}^{*\mathrm{F}}\varphi^{*\mathrm{U}} := \max(\dot{V}^{*\mathrm{F}}, 0)\,\varphi^{*\mathrm{P}} + \min(\dot{V}^{*\mathrm{F}}, 0)\,\varphi^{*\mathrm{NB}}$ is implicitly considered followed by an explicit DC that accounts for high-order contributions. An expansion of the implicit UDS contribution around the cell P in Fig. 4.2 for one exclusive time step T reads

$$\begin{aligned} L^* \approx ... &+ \hat{\varphi}^{*\mathrm{UU}} \left[\dot{V}^{*\mathrm{FU}}\varphi^{*\mathrm{UU}} - \dot{V}^{*\mathrm{FUU}}\varphi^{*\mathrm{UUU}}\right] \\ &+ \hat{\varphi}^{*\mathrm{U}} \left[\dot{V}^{*\mathrm{F}}\ \varphi^{*\mathrm{U}}\ - \dot{V}^{*\mathrm{FU}}\ \varphi^{*\mathrm{UU}}\right] \\ &+ \hat{\varphi}^{*\mathrm{D}} \left[\dot{V}^{*\mathrm{FD}}\varphi^{*\mathrm{D}}\ - \dot{V}^{*\mathrm{F}}\ \varphi^{*\mathrm{U}}\right] + ... \end{aligned} \tag{4.78}$$

and allows for a variation of the generic transport variable as well as the volume flux. Whereas the former offers a discrete approximation strategy for the convective transport

of $\hat{\varphi}^*$, the latter yields the advective ATC contribution immanent to the adjoint momentum balance. The variation of the transported quantity in (4.78) allows for a re-ordered expression that finally offers the discrete adjoint approximation scheme, viz.

$$\begin{aligned}\delta_\varphi L^* \cdot \delta\varphi^* \approx \ldots & -\delta\varphi^{*\mathrm{UU}} \left[-\dot{V}^{*\mathrm{FUU}} \hat{\varphi}^{*\mathrm{UU}} + \dot{V}^{*\mathrm{FU}} \hat{\varphi}^{*\mathrm{U}} \right] \\ & -\delta\varphi^{*\mathrm{U}} \left[-\dot{V}^{*\mathrm{FU}} \hat{\varphi}^{*\mathrm{U}} + \dot{V}^{*\mathrm{F}} \hat{\varphi}^{*\mathrm{D}} \right] \\ & -\delta\varphi^{*\mathrm{D}} \left[-\dot{V}^{*\mathrm{F}} \hat{\varphi}^{*\mathrm{D}} + \dot{V}^{*\mathrm{FD}} \hat{\varphi}^{*\mathrm{DD}} \right] - \ldots \quad \stackrel{!}{=} 0 \qquad \forall\, \delta\varphi^{*(\cdot)} \,. \end{aligned} \tag{4.79}$$

An intermediate step employs the local continuity equation, i.e. $\sum_{F(P)} -\min(\dot{V}^{*\mathrm{F}}, 0) = \sum_{F(P)} \max(\dot{V}^{*\mathrm{F}}, 0)$, cf. word of caution below (2.83). A color marking indicates the mirrored character of the rearrangement. First-order optimality conditions finally yield the adjoint approximation, i.e. the central line corresponds to the following DDS approximation

$$\dot{V}^{*\mathrm{F}} \hat{\varphi}^{*\mathrm{D}} := \min\left(\dot{V}^{*\mathrm{F}}, 0\right) \hat{\varphi}^{*\mathrm{P}} + \max\left(\dot{V}^{*\mathrm{F}}, 0\right) \hat{\varphi}^{*\mathrm{NB}} \,. \tag{4.80}$$

The adjoint complement to primal high-order contributions follows the same principle and is analogously incorporated into a DC term, so that the rearranged variation of the Lagrangian finally reads

$$\begin{aligned} \delta_\varphi L^* \cdot \delta\varphi^* &= \ldots - \int\int \delta\varphi^* \left[\frac{\partial\, v_{\mathrm{k}}^*\, \hat{\varphi}^*}{\partial\, x_{\mathrm{k}}^*} \right] \mathrm{d}\Omega^*\, \mathrm{d}t^* + \ldots \\ \rightarrow \quad \delta_\varphi L^* \cdot \delta\varphi^* &\approx \ldots - \sum_{\mathrm{T}} \sum_{\mathrm{P}} \delta\varphi^{*\mathrm{P}} \sum_{\mathrm{F(P)}} \dot{V}^{\mathrm{F}} \left[\hat{\varphi}^{*\mathrm{D}} + \mathrm{DC}^{*\mathrm{C},\hat{\varphi},\mathrm{F}} \right] \Delta t^* + \ldots \,. \end{aligned} \tag{4.81}$$

The DC contribution optionally accounts for high-order contributions as a supplement to the DDS part. Stück [2012] presented an adjoint MUSCL-scheme that scrambles the nonlinearities into a damping function ψ based on a local (dual) sensor $\hat{r}$, viz.

$$\begin{aligned} \dot{V}^{*\mathrm{F}}\, \mathrm{DC}^{*\mathrm{C},\hat{\varphi},\mathrm{F}} &= \frac{\dot{V}^{*\mathrm{F}}}{4} \left[(1+\kappa) \left(\hat{\varphi}^{*\mathrm{U}} - \hat{\varphi}^{*\mathrm{D}} \right) \psi\left(\hat{r}\right) + (1-\kappa) \left(\hat{\varphi}^{*\mathrm{D}} - \hat{\varphi}^{*\mathrm{DD}} \right) \psi\left(\frac{1}{\hat{r}}\right) \right] \\ & \qquad \text{and} \qquad \hat{r} = \frac{\hat{\varphi}^{*\mathrm{D}} - \hat{\varphi}^{*\mathrm{DD}}}{\hat{\varphi}^{*\mathrm{U}} - \hat{\varphi}^{*\mathrm{D}}} \,. \end{aligned} \tag{4.82}$$

Equation (4.82) reveals a mirrored approximation compared to its primal complement (2.82) and offers a generic way to account for various baseline adjoint convection schemes based on the constant $\kappa \in [-1, 1]$. The preferred choice in this thesis is the third-order Quadratic Downwind Interpolation of Convective Kinematics (QDICK) scheme which refers to $\kappa = 0.5$. Other popular schemes supported by (4.82) are the self adjoint central differencing ($\kappa = 1$) scheme as well as the Linear Downwind Differencing ($\kappa = -1$) scheme (LDDS). On unstructured grids, the $\hat{\varphi}^{*\mathrm{DD}}$ value is not explicitly available and reconstructed with second-order accurate central differences, viz. $\hat{\varphi}^{*\mathrm{DD}} \approx \hat{\varphi}^{*\mathrm{U}} - 2\, d_{\mathrm{i}}^{*\mathrm{F}} (\partial\, \hat{\varphi}^{*\mathrm{D}} / \partial\, x_{\mathrm{i}}^*)$, cf. Fig. 2.4. The nonlinear TVD/NVD functions are particularly unpleasant w.r.t. their corresponding adjoint operators as they produce unfavorable derivatives and potential

nonlinearities. As a consequence, they are not differentiated in the adjoint calculus and considered to be frozen, cf. Stück [2012], Stück and Rung [2013], Kröger [2016], Kröger et al. [2018], Manzke [2018]. A major contribution of this work is concerned with adjoint NVD schemes dedicated to the convective transport of the concentration c in conjunction with VoF approaches. The derivation is presented separately in Sec. 4.2.5.

The convective contributions to (4.74) read

$$A^{*\hat{\varphi},\mathrm{P}} \leftarrow \sum_{\mathrm{F(P)}} \max\left(\dot{V}^{*\mathrm{F}},0\right), \quad A^{*\hat{\varphi},\mathrm{NB}} \leftarrow \max\left(\dot{V}^{*\mathrm{F}},0\right), \quad S^{*\hat{\varphi},\mathrm{P}} \leftarrow -\sum_{\mathrm{F(P)}} \dot{V}^{*\mathrm{F}} \mathrm{DC}^{*\mathrm{C},\hat{\varphi},\mathrm{F}}, \tag{4.83}$$

where all high-order contributions are implemented explicitly. For the transport of density-weighted adjoint field quantities, e.g. the linear adjoint momentum $\hat{\varphi}_\mathrm{i}^* = \rho^*\,\hat{v}_\mathrm{i}^*$, the volume flux is replaced by a mass flux, viz. $\dot{V}^{*\mathrm{F}} \rightarrow \dot{m}^{*\mathrm{F}} = [\rho^*\, v_\mathrm{k}^*\, \Delta\Gamma_\mathrm{k}^*]^\mathrm{F}$.

Diffusive Contributions follow from an unbiased information transport in primal mode that has been fractioned into an implicit part and an explicit deferred correction, cf. (2.84). The corresponding discrete Laplacian reads

$$\begin{aligned} L^* &= \ldots + \int\int \hat{\varphi}^* \frac{\partial}{\partial\, x_\mathrm{k}^*}\left[\mu^{*\varphi}\frac{\partial\,\varphi^*}{\partial\, x_\mathrm{k}^*}\right] \mathrm{d}\Omega^*\,\mathrm{d}t^* + \ldots \\ \rightarrow\quad L^* &\approx \ldots + \sum_\mathrm{T}\sum_\mathrm{P}\hat{\varphi}^{*\mathrm{P}} \sum_{\mathrm{F(P)}} [\mu^{*\varphi}\,\Delta\Gamma^*]^\mathrm{F}\left[\frac{\varphi^{*\mathrm{NP}}-\varphi^{*\mathrm{P}}}{||d_\mathrm{k}^{\mathrm{F}*}||\,\alpha^\mathrm{n}} + \mathrm{DC}^{*\mathrm{D},\varphi,\mathrm{F}}\right]\Delta t^{*\mathrm{T}} + \ldots . \end{aligned} \tag{4.84}$$

The implicit part of (4.84) is expanded on the 1D-grid depicted in Fig. 4.2 for one exclusive time step, viz.

$$\begin{aligned} L^* \approx \ldots &+\hat{\varphi}^{*\mathrm{P}-1}\left[\left[\frac{\mu^{*\varphi}\Delta\Gamma}{||d_\mathrm{k}||\,\alpha^\mathrm{n}}\right]^{\mathrm{F}-1}\left[\varphi^{*\mathrm{P}} - \varphi^{*\mathrm{P}-1}\right] + \left[\frac{\mu^{*\varphi}\Delta\Gamma}{||d_\mathrm{k}||\,\alpha^\mathrm{n}}\right]^{\mathrm{F}-2}\left[\varphi^{*\mathrm{P}-2} - \varphi^{*\mathrm{P}-1}\right]\right] \\ &+\hat{\varphi}^{*\mathrm{P}}\left[\left[\frac{\mu^{*\varphi}\Delta\Gamma}{||d_\mathrm{k}||\,\alpha^\mathrm{n}}\right]^{\mathrm{F}}\left[\varphi^{*\mathrm{P}+1} - \varphi^{*\mathrm{P}}\right] + \left[\frac{\mu^{*\varphi}\Delta\Gamma}{||d_\mathrm{k}||\,\alpha^\mathrm{n}}\right]^{\mathrm{F}-1}\left[\varphi^{*\mathrm{P}-1} - \varphi^{*\mathrm{P}}\right]\right] \\ &+\hat{\varphi}^{*\mathrm{P}+1}\left[\left[\frac{\mu^{*\varphi}\Delta\Gamma}{||d_\mathrm{k}||\,\alpha^\mathrm{n}}\right]^{\mathrm{F}+1}\left[\varphi^{*\mathrm{P}+2} - \varphi^{*\mathrm{P}+1}\right] + \left[\frac{\mu^{*\varphi}\Delta\Gamma}{||d_\mathrm{k}||\,\alpha^\mathrm{n}}\right]^{\mathrm{F}}\left[\varphi^{*\mathrm{P}} - \varphi^{*\mathrm{P}+1}\right]\right] + \ldots . \end{aligned} \tag{4.85}$$

A variation of (4.85) followed by an isolation of all discrete variations reveals

$$\begin{aligned} \delta_\varphi L^*\cdot\delta\varphi^* \approx \ldots &+\delta\varphi^{*\mathrm{P}-2}\left[\left[\frac{\mu^{*\varphi}\Delta\Gamma}{||d_\mathrm{k}\,\alpha^\mathrm{n}||}\right]^{\mathrm{F}-1}\left[\hat{\varphi}^{*\mathrm{P}} - \hat{\varphi}^{*\mathrm{P}-1}\right] + \left[\frac{\mu^{*\varphi}\Delta\Gamma}{||d_\mathrm{k}\,\alpha^\mathrm{n}||}\right]^{\mathrm{F}-2}\left[\hat{\varphi}^{*\mathrm{P}-2} - \hat{\varphi}^{*\mathrm{P}-1}\right]\right] \\ &+\delta\varphi^{*\mathrm{P}}\left[\left[\frac{\mu^{*\varphi}\Delta\Gamma}{||d_\mathrm{k}\,\alpha^\mathrm{n}||}\right]^{\mathrm{F}}\left[\hat{\varphi}^{*\mathrm{P}+1} - \hat{\varphi}^{*\mathrm{P}}\right] + \left[\frac{\mu^{*\varphi}\Delta\Gamma}{||d_\mathrm{k}\,\alpha^\mathrm{n}||}\right]^{\mathrm{F}-1}\left[\hat{\varphi}^{*\mathrm{P}-1} - \hat{\varphi}^{*\mathrm{P}}\right]\right] \\ &+\delta\varphi^{*\mathrm{P}+1}\left[\left[\frac{\mu^{*\varphi}\Delta\Gamma}{||d_\mathrm{k}\,\alpha^\mathrm{n}||}\right]^{\mathrm{F}+1}\left[\hat{\varphi}^{*\mathrm{P}+2} - \hat{\varphi}^{*\mathrm{P}+1}\right] + \left[\frac{\mu^{*\varphi}\Delta\Gamma}{||d_\mathrm{k}\,\alpha^\mathrm{n}||}\right]^{\mathrm{F}}\left[\hat{\varphi}^{*\mathrm{P}} - \hat{\varphi}^{*\mathrm{P}+1}\right]\right] + \ldots \\ &\stackrel{!}{=} 0 \qquad \forall\,\delta\varphi^{*(\cdot)}\,. \end{aligned} \tag{4.86}$$

A color marking indicates the symmetrical character of the rearrangement. First-order optimality conditions finally yield the adjoint approximation. Due to the self adjoint nature of diffusion, (4.86) resembles its primal (CDS) complement. Together with $\mu^{*\varphi} \rightarrow \mu^{*\hat{\varphi}}$, the discrete Lagrangian reads

$$\begin{aligned} \delta_\varphi L^* \cdot \delta\varphi^* &= ... + \int\int \delta\varphi^* \left[\frac{\partial}{\partial\, x_\mathrm{k}^*} \left[\mu^{*\hat{\varphi}} \frac{\partial\, \hat{\varphi}^*}{\partial\, x_\mathrm{k}^*} \right] \right] \mathrm{d}\Omega^* \, \mathrm{d}t^* + ... \\ \rightarrow \quad \delta_\varphi L^* \cdot \delta\varphi^* &\approx ... + \sum_\mathrm{T} \sum_\mathrm{P} \delta\varphi^{*\mathrm{P}} \sum_{\mathrm{F(P)}} \left[\mu^{*\hat{\varphi}}\, \Delta\Gamma^* \right]^\mathrm{F} \left[\frac{\hat{\varphi}^{*\mathrm{NP}} - \hat{\varphi}^{*\mathrm{P}}}{||d_\mathrm{k}^{\mathrm{F}*}||\, \alpha^\mathrm{n}} + \mathrm{DC}^{*\mathrm{D},\varphi,\mathrm{F}} \right] \Delta t^{*\mathrm{T}} + ... \,, \end{aligned} \tag{4.87}$$

and the following diffusive contributions to (4.74) are

$$A^{*\hat{\varphi},\mathrm{P}} \leftarrow \sum_{\mathrm{F(P)}} \left[\mu^{*\hat{\varphi}} \frac{\Delta\Gamma^*}{||d_\mathrm{k}^*|| \alpha^\mathrm{n}} \right]^\mathrm{F} , \quad A^{*\hat{\varphi},\mathrm{NB}} \leftarrow \left[\mu^{*\hat{\varphi}} \frac{\Delta\Gamma^*}{||d_\mathrm{k}^*|| \alpha^\mathrm{n}} \right]^{*\mathrm{F}} \quad \text{and} \quad S^{*\hat{\varphi},\mathrm{P}} \leftarrow - \sum_{\mathrm{F(P)}} \mathrm{DC}^{*\mathrm{D},\hat{\varphi},\mathrm{F}} . \tag{4.88}$$

Although not symmetric on non-equidistant, unstructured grids, the primal non-orthogonality correction is reused in adjoint mode. Note that the DC contribution tends to zero for perfectly orthogonal grids.

Sources and Sinks are considered as explicit contributions to the r.h.s. using the midpoint rule (2.64). A consistent implementation follows the hybrid adjoint strategy from before and can be generalized to

$$S^{*\hat{\varphi},\mathrm{P}} \leftarrow \left[q^{*\hat{\varphi}}\, \Delta\Omega^* \right]^\mathrm{P} . \tag{4.89}$$

The explicit contributions to the r.h.s. differ strongly from the respective considered equation, e.g., $q^{*\hat{\mathrm{v}}_\mathrm{i},\mathrm{P}} = -[\hat{c}^*(\partial\, c/\partial\, x_\mathrm{i}^*)]^\mathrm{P}$ introduces the adjoint two-phase information into the adjoint momentum balance. The expression is almost zero in the complete field except a small regime along the interfacial region. Hence, this formulation is comparably robust and thus the preferred choice. Mind that the product of primal and adjoint concentration introduces the two-phase information to the adjoint velocity field, which in turn enters the sensitivity derivative (4.44). A robust and consistent approximation of this term is crucial, since a neglection resembles a frozen concentration approach. As already discussed in Sec. 2.1.4, the interpolation of fluid data from the concentration distribution does not follow from a physical conservation equation but rather represents a basic modeling assumption. Due to the vivid character of the concentration field, a manipulation possibility of the adjoint momentum source arises. Adding a constant value to the primal concentration gradient, viz. $\partial\,(c - \alpha^\mathrm{c})/\partial\, x_\mathrm{i}^* = \partial\, c/\partial\, x_\mathrm{i}^*$, followed by integration by parts shifts the gradient from the primal field to its adjoint companion. In line with the hybrid adjoint strategy, one ends up with the following approximation

$$S^{*\hat{\mathrm{v}}_\mathrm{i},\mathrm{P}} \leftarrow \left[(c - \alpha^\mathrm{c}) \frac{\partial \hat{c}^*}{\partial x_\mathrm{i}^*} \Delta\Omega^* \right]^\mathrm{P} \tag{4.90}$$

which, however, features further boundary fluxes. Thus, it is possible to shift the active region of the adjoint concentration within the adjoint momentum equation via a formal

re-definition of $c^{\mathrm{a}} \rightarrow c^{\mathrm{a}} - \alpha^{\mathrm{c}}$ and $c^{\mathrm{b}} \rightarrow c^{\mathrm{b}} + \alpha^{\mathrm{c}}$. Reasonable values refer to $\alpha^{\mathrm{c}} = 0$ ($\alpha^{\mathrm{c}} = 1$) to activate the term in the foreground (background) phase a (b). To obtain a consistent dual formulation, the four source/sink terms on the r.h.s. of the adjoint concentration equation experience a sign change as well, since $c^{\Delta} = c^{\mathrm{a}} - c^{\mathrm{b}} = 1 \rightarrow -1 = c^{\mathrm{a}} - c^{\mathrm{b}} - 2\alpha^{\mathrm{c}} = c^{\Delta}$, cf. Eqn. (2.6). However, Eqn. (4.90) refers to an unpreferred advective formulation and is employed for V&V purposes only.

Pressure Determination

The adjoint pressure-velocity coupling follows a modified version of the SIMPLE pressure correction algorithm, referred to a Semi-Implicit Method for adjoint Pressure-Linked Equations (SIMadPLE). At first, an adjoint velocity distribution $\tilde{\hat{v}}_{\mathrm{i}}^{*}$ is determined from the discretized adjoint momentum equations using an estimated adjoint pressure $\tilde{\hat{p}}^{*}$. Usually, these adjoint velocities do not satisfy the discrete adjoint continuity equation and the resulting discrete adjoint continuity defect of each CV, e.g., $\sum_{\mathrm{F(P)}} [\tilde{\hat{v}}_{\mathrm{i}}^{*} \Gamma_{\mathrm{i}}^{*}]^{\mathrm{F}} - [s^{*\hat{\mathrm{p}}} \Delta\Omega^{*}]^{\mathrm{P}}$, is used to compute a correction of the estimated adjoint pressure in an iterative procedure, e.g., $\tilde{\hat{p}}^{*P} \leftarrow \hat{p}'^{*P}$. A combination of the discretized adjoint momentum (in reduced form) and adjoint continuity yields the inherently discrete adjoint pressure correction equation. The algebraic adjoint pressure correction scheme features only discretized diffusive fluxes and r.h.s contributions. The former are assembled in line with Eqn. (4.84) using $\mu^{*\hat{\mathrm{p}},\mathrm{P}} = \left[\Delta\Omega^{*}/A^{*\hat{\mathrm{v}}_{\mathrm{i}}}\right]^{\mathrm{P}}$ and respective face values follow from a linear interpolation. The r.h.s. inheres the actual continuity defect, viz.

$$S^{*\hat{\mathrm{p}}',\mathrm{P}} \leftarrow \sum_{\mathrm{F(P)}} \left[\tilde{\hat{v}}_{\mathrm{i}}^{*} \Delta\Gamma_{\mathrm{i}}^{*}\right]^{\mathrm{F}} . \tag{4.91}$$

The adjoint pressure update involves an under-relaxation $\tilde{\hat{p}}^{*P} \leftarrow \tilde{\omega}^{\hat{\mathrm{p}}'} \hat{p}'^{*P}$ that usually employs $\tilde{\omega}^{\hat{\mathrm{p}}'} = 0.1$. In line with the primal procedure, the odd-even decoupling problem of the co-located variable arrangement is suppressed with a fourth-order artificial dissipation term on the r.h.s of the continuity equation, cf. Rhie and Chow [1983].

4.2.5 Adjoint Compressive Interface Capturing Schemes

In Sec. 2.2.7, two prominent primal compressive convection schemes were introduced based on the NVD diagram, cf. Fig. 2.5. The adjoint consideration starts with the normalization based on all relevant cell quantities around F, viz.

$$\hat{c}_{\mathrm{n}} = \frac{\hat{c}^{*} - \hat{c}^{*\mathrm{DD}}}{\hat{c}^{*\mathrm{U}} - \hat{c}^{*\mathrm{DD}}} \qquad \rightarrow \qquad \hat{c}_{\mathrm{n}}^{\mathrm{U}} = 1, \qquad \hat{c}_{\mathrm{n}}^{\mathrm{DD}} = 0 \qquad \text{and} \qquad \hat{c}_{\mathrm{n}}^{\mathrm{U}} \geq \hat{c}_{\mathrm{n}}^{\mathrm{D}} \geq \hat{c}_{\mathrm{n}}^{\mathrm{DD}} , \tag{4.92}$$

where a mirrored normalization of the adjoint face value $\hat{c}_{\mathrm{n}}$ around the face F is anticipated. The discussion originates in the discrete analogue to the continuous Lagrangian for the transported property c, viz.

$$\begin{aligned} L^{*} &= ... + \int\int \hat{c}^{*} v_{\mathrm{k}}^{*} \frac{\partial c}{\partial x_{\mathrm{k}}^{*}} \, \mathrm{d}\Omega^{*} \, \mathrm{d}t^{*} + ... \\ &\rightarrow \qquad L^{*} \approx ... + \sum_{\mathrm{T}} \sum_{\mathrm{P}} \hat{c}^{*\mathrm{P}} \sum_{\mathrm{F(P)}} \dot{V}^{*\mathrm{F}} \left[c^{*\mathrm{U}} + \mathrm{DC}^{*\mathrm{C,c,F}}\right] \Delta t^{*} + ... \end{aligned} \tag{4.93}$$

The investigated approaches differ in the approximation of $c^{\mathrm{F}} = c^{*\mathrm{U}} + \mathrm{DC}^{*\mathrm{C,c,F}}$ only. This will be explored in more detail below.

Adjoint High Resolution Interface Capturing (adHRIC)

The continuous adjoint system is derived for quasi steady cases or simulations over an integration within a pseudo-time. Thus, after the primal integration until convergence, the discrete Courant number distribution as well as concentration distribution are known. Based on the primal HRIC scheme (2.90), one can clearly decide how the value of each face in Eqn. (4.93) is approximated. Algorithmically, one needs to decide between three situations: 1) pure UDS, 2) pure DDS or 3) an interpolation between both based on Co^{F}.

Therefore, the derivation of the adjoint HRIC scheme needs to be done for all scenarios in the last case distinction within the primal procedure (2.90), viz. $c_{\mathrm{n}}^{\mathrm{F},3} = 2c_{\mathrm{n}}^{\mathrm{U}}$, $c_{\mathrm{n}}^{\mathrm{F},3} = 1$ as well as $c_{\mathrm{n}}^{\mathrm{F},3} = c_{\mathrm{n}}^{\mathrm{U}}$. As already shown, a primal UDS yields an adjoint DDS schemes. The relation can be inverted directly. Hence, only the adjoint to $c_{\mathrm{n}}^{\mathrm{F},3} = 2c_{\mathrm{n}}^{\mathrm{U}}$ is derived exemplary. Based on Eqn. (2.89), the expression can be casted to $c^{\mathrm{F},3} = 2c^{\mathrm{U}} - c^{\mathrm{UU}}$ and the discrete Lagrangian (4.93) is expanded for the control volumes UU, U, D and DD (cf. Fig. 4.2) at one exclusive time step, viz.

$$\begin{aligned} L^* \approx \ldots &+ \hat{c}^{*\mathrm{UU}}\big[\dot{V}^{*\mathrm{F}-1}\big(2c^{UU} - c^{\mathrm{UUU}}\big) - \dot{V}^{*\mathrm{F}-2}\big(2c^{UUU} - c^{\mathrm{UUUU}}\big)\big] \\ &+ \hat{c}^{*\mathrm{U}}\ \big[\dot{V}^{*\mathrm{F}}\ \ \big(2c^{U} - c^{\mathrm{UU}}\ \big) - \dot{V}^{*\mathrm{F}-1}\big(2c^{UU} - c^{\mathrm{UUU}}\ \big)\big] \\ &+ \hat{c}^{*\mathrm{D}}\ \big[\dot{V}^{*\mathrm{F}+1}\big(2c^{D} - c^{\mathrm{U}}\ \big) - \dot{V}^{*\mathrm{F}}\ \ \big(2c^{U} - c^{\mathrm{UU}}\ \big)\big] \\ &+ \hat{c}^{*\mathrm{DD}}\big[\dot{V}^{*\mathrm{F}+2}\big(2c^{DD} - c^{\mathrm{D}}\ \big) - \dot{V}^{*\mathrm{F}+1}\big(2c^{D} - c^{\mathrm{U}}\ \big)\big] + \ldots . \end{aligned} \tag{4.94}$$

A derivative of L^* in concentration direction and a subsequent isolation of all variations resembles the summation by parts characteristics. First-order optimality conditions finally yield the adjoint face value, viz.

$$\begin{aligned} \delta_{\mathrm{c}} L^* \cdot \delta c^{(\cdot)} \approx \ldots &- \delta c^{UU}\ \ \big[\dot{V}^{*\mathrm{F}-1}\big(2\hat{c}^{*U} - \hat{c}^{*\mathrm{D}}\ \big) - \dot{V}^{*\mathrm{F}-2}\big(2\hat{c}^{*UU} - \hat{c}^{*\mathrm{U}}\ \big)\big] \\ &- \delta c^{U}\ \ \big[\dot{V}^{*\mathrm{F}}\ \ \big(2\hat{c}^{*D} - \hat{c}^{*\mathrm{DD}}\ \big) - \dot{V}^{*\mathrm{F}-1}\big(2\hat{c}^{*U} - \hat{c}^{*\mathrm{D}}\ \big)\big] \\ &- \delta c^{D}\ \ \big[\dot{V}^{*\mathrm{F}+1}\big(2\hat{c}^{*DD} - \hat{c}^{*\mathrm{DDD}}\ \big) - \dot{V}^{*\mathrm{F}}\ \ \big(2\hat{c}^{*D} - \hat{c}^{*\mathrm{DD}}\ \big)\big] \\ &- \delta c^{DD}\ \ \big[\dot{V}^{*\mathrm{F}+2}\big(2\hat{c}^{*DDD} - \hat{c}^{*\mathrm{DDDD}}\big) - \dot{V}^{*\mathrm{F}+1}\big(2\hat{c}^{*DD} - \hat{c}^{*\mathrm{DDD}}\big)\big] + \ldots \\ \overset{!}{=} 0 \qquad &\forall\, \delta c^{(\cdot)} . \end{aligned} \tag{4.95}$$

The adjoint face value interpolation results in mirroring the primal stencil. For the unknown face value within the adjoint HRIC scheme in Fig. 4.3, i.e. the first inner bracket in Eqn. (4.95), one ends up with $\hat{c}^{*\mathrm{F}} = 2\hat{c}^{*\mathrm{D}} - \hat{c}^{*\mathrm{DD}}$ or $\hat{c}_{\mathrm{n}}^{\mathrm{F}} = 2\hat{c}_{\mathrm{n}}^{\mathrm{D}}$ after applying the adjoint

normalization from Eqn. (4.92). Finally, the adjoint HRIC scheme to Eqn. (2.90) reads

$$\hat{c}_{\mathrm{n}}^{\mathrm{F}} = \begin{cases} \hat{c}_{\mathrm{n}}^{\mathrm{F},2} & : \mathrm{Co}^{\mathrm{F}} < \mathrm{Co}_{\mathrm{l}}^{\mathrm{F}} \\ \hat{c}_{\mathrm{n}}^{\mathrm{D}} + \left(\hat{c}_{\mathrm{n}}^{\mathrm{F},2} - \hat{c}_{\mathrm{n}}^{\mathrm{D}}\right) \frac{\mathrm{Co}_{\mathrm{u}}^{\mathrm{F}} - \mathrm{Co}^{\mathrm{F}}}{\mathrm{Co}_{\mathrm{u}}^{\mathrm{F}} - \mathrm{Co}_{\mathrm{l}}^{\mathrm{F}}} & : \mathrm{Co}_{\mathrm{l}}^{\mathrm{F}} \leq \mathrm{Co}^{\mathrm{F}} \leq \mathrm{Co}_{\mathrm{u}}^{\mathrm{F}} \\ \hat{c}_{\mathrm{n}}^{\mathrm{D}} & : \mathrm{Co}^{\mathrm{F}} > \mathrm{Co}_{\mathrm{u}}^{\mathrm{F}} \end{cases},$$

$$\text{with} \quad \hat{c}_{\mathrm{n}}^{\mathrm{F},2} = \gamma^{\mathrm{F}} \hat{c}_{\mathrm{n}}^{\mathrm{F},3} + \left(1 - \gamma^{\mathrm{F}}\right) \hat{c}_{\mathrm{n}}^{\mathrm{D}},$$

$$\text{and} \quad \hat{c}_{\mathrm{n}}^{\mathrm{F},3} = \begin{cases} 2\hat{c}_{\mathrm{n}}^{\mathrm{D}} & : \hat{c}_{\mathrm{n}}^{\mathrm{D}} \in [0, 0.5] \\ 1 & : \hat{c}_{\mathrm{n}}^{\mathrm{D}} \in [0.5, 1] \\ \hat{c}_{\mathrm{n}}^{\mathrm{D}} & : \hat{c}_{\mathrm{n}}^{\mathrm{D}} \notin [0, 1] \end{cases}, \tag{4.96}$$

where all upwind approximations are switched to downwind and vice versa.

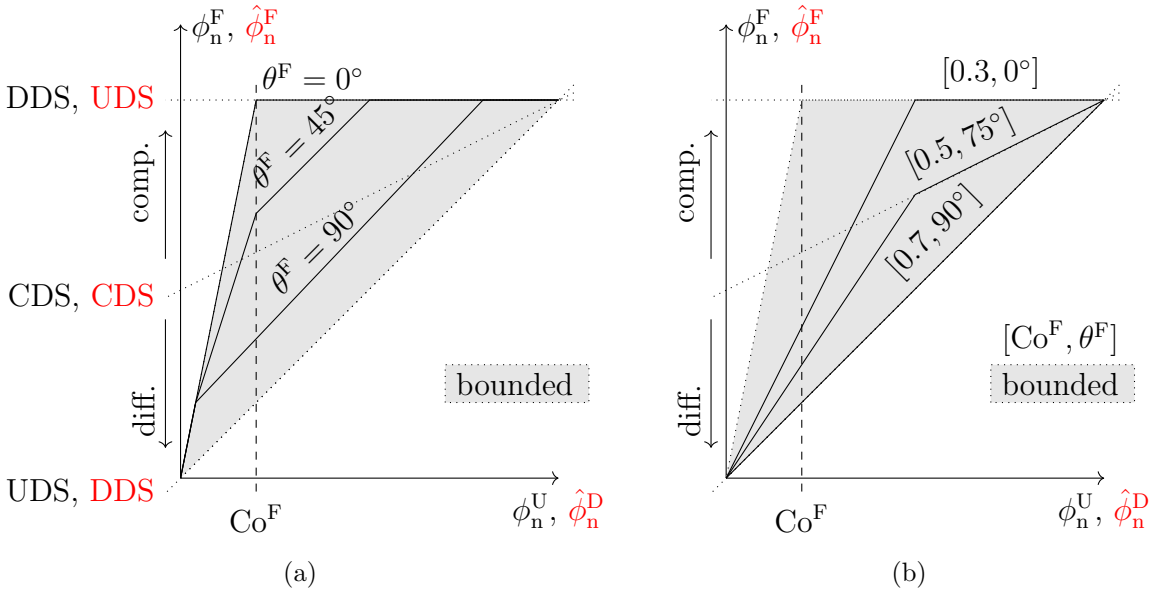

Figure 4.3: Sketch of the Normalized Variable Diagram (NVD) for two compressive convection schemes: (a) Compressive Interface Capturing Scheme for Arbitrary Meshes (CICSAM) and (b) High Resolution Interface Capturing Scheme (HRIC) as well as their adjoint analogue (red).

Adjoint Compressive Interface Capturing Scheme for Arbitrary Meshes (adCICSAM)

The normalized face value $c_{\mathrm{n}}^{\mathrm{F}}$ within the CICSAM procedure is determined via a blending between the HC and the UQ scheme, cf. Sec. 2.2.7. If HC is active, the first case switches between DDS ($c_{\mathrm{n}}^{\mathrm{F,HC}} = 1$) and UDS ($c_{\mathrm{n}}^{\mathrm{F,HC}} = c_{\mathrm{n}}^{\mathrm{U}}/\mathrm{Co}^{\mathrm{F}}$). Thus, the adjoint to HC reads ($\hat{c}_{\mathrm{n}}^{\mathrm{F,HC}} = 1$) or ($\hat{c}_{\mathrm{n}}^{\mathrm{F,HC}} = \hat{c}_{\mathrm{n}}^{\mathrm{D}}/\mathrm{Co}^{\mathrm{F}}$). The delicate term refers to the first QUICK-like case within the UQ scenario. A denormalization offers $c^{\mathrm{F}} = [\mathrm{Co}^{\mathrm{F}} + 3]\, c^{\mathrm{U}}/4 + [\mathrm{Co}^{\mathrm{F}} - 1]\, c^{\mathrm{UU}}/8 + [1 - \mathrm{Co}^{\mathrm{F}}]\, 3c^{\mathrm{D}}/8$ or $c^{\mathrm{F}} = 3/8\, c^{\mathrm{D}} + 3/4\, c^{\mathrm{U}} - 1/8\, c^{\mathrm{UU}}$ for $\mathrm{Co}^{\mathrm{F}} \to 0$ and $c^{\mathrm{F}} = c^{\mathrm{U}}$ for $\mathrm{Co}^{\mathrm{F}} \to 1$. Again, the discrete Lagrangian (4.93) is constructed for the control volumes UU, U, D and

DD for one exemplary time step, cf. Fig. 4.3,

$$\begin{aligned} L^* = .. &+ \hat{c}^{*\mathrm{UU}}\big[\dot{V}^{\mathrm{F}-1}\big(r\,c^{\mathrm{UU}} + s\,c^{\mathrm{UUU}} + t\,c^{\mathrm{U}} \quad\big) - \dot{V}^{\mathrm{F}-2}\big(r\,c^{\mathrm{UUU}} + s\,c^{\mathrm{UUUU}} + t\,c^{\mathrm{UU}}\big)\big] \\ &+ \hat{c}^{*\mathrm{U}} \ \big[\dot{V}^{\mathrm{F}} \ \ \big(r\,c^{\mathrm{U}} \ + s\,c^{\mathrm{UU}} \ + t\,c^{\mathrm{D}} \ \big) - \dot{V}^{\mathrm{F}-1}\big(r\,c^{\mathrm{UU}} \ + s\,c^{\mathrm{UUU}} \ + t\,c^{\mathrm{U}} \ \big)\big] \\ &+ \hat{c}^{*\mathrm{D}} \ \big[\dot{V}^{\mathrm{F}+1}\big(r\,c^{\mathrm{D}} \ + s\,c^{\mathrm{U}} \ + t\,c^{\mathrm{DD}} \big) - \dot{V}^{\mathrm{F}} \ \ \big(r\,c^{\mathrm{U}} \ + s\,c^{\mathrm{UU}} \ + t\,c^{\mathrm{D}} \ \big)\big] \\ &+ \hat{c}^{*\mathrm{DD}}\big[\dot{V}^{\mathrm{F}+2}\big(r\,c^{\mathrm{DD}} + s\,c^{\mathrm{D}} \ + t\,c^{\mathrm{DDD}}\big) - \dot{V}^{\mathrm{F}+1}\big(r\,c^{\mathrm{D}} \ + s\,c^{\mathrm{U}} \ + t\,c^{\mathrm{DD}}\big)\big] + \ldots . \end{aligned} \tag{4.97}$$

Here the coefficients $r = [\mathrm{Co}^{\mathrm{F}} + 3]/4$, $s = [\mathrm{Co}^{\mathrm{F}} - 1]/8$ and $t = 3[1 - \mathrm{Co}^{\mathrm{F}}]/8$ are defined to shorten the notation. In line with the adjoint HRIC derivation, a variation of L^* and a subsequent isolation of all variations yields

$$\begin{aligned} &\delta_{\mathrm{c}} L^* \cdot \ \delta c^{(\cdot)} = \ldots \\ &- \delta c^{\mathrm{UU}}\big[\dot{V}^{\mathrm{F}-1}\big(r\,\hat{c}^{*\mathrm{U}} \ + s\,\hat{c}^{*\mathrm{D}} \ + t\,\hat{c}^{*\mathrm{UU}}\big) - \dot{V}^{\mathrm{F}-2}\big(r\,\hat{c}^{*\mathrm{UU}} + s\,\hat{c}^{*\mathrm{U}} \ + t\,\hat{c}^{*\mathrm{UUU}}\big)\big] \\ &- \delta c^{\mathrm{U}} \ \big[\dot{V}^{\mathrm{F}} \ \ \big(r\,\hat{c}^{*\mathrm{D}} \ + s\,\hat{c}^{*\mathrm{DD}} \ + t\,\hat{c}^{*\mathrm{U}} \ \big) - \dot{V}^{\mathrm{F}-1}\big(r\,\hat{c}^{*\mathrm{U}} \ + s\,\hat{c}^{*\mathrm{D}} \ + t\,\hat{c}^{*\mathrm{UU}} \ \big)\big] \\ &- \delta c^{\mathrm{D}} \ \big[\dot{V}^{\mathrm{F}+1}\big(r\,\hat{c}^{*\mathrm{DD}} \ + s\,\hat{c}^{*\mathrm{DDD}} \ + t\,\hat{c}^{*\mathrm{D}} \ \big) - \dot{V}^{\mathrm{F}} \ \ \big(r\,\hat{c}^{*\mathrm{D}} \ + s\,\hat{c}^{*\mathrm{DD}} \ + t\,\hat{c}^{*\mathrm{U}} \ \big)\big] \\ &- \delta c^{\mathrm{DD}}\big[\dot{V}^{\mathrm{F}+2}\big(r\,\hat{c}^{*\mathrm{DDD}} \ + s\,\hat{c}^{*\mathrm{DDDD}} + t\,\hat{c}^{*\mathrm{DD}}\big) - \dot{V}^{\mathrm{F}+1}\big(r\,\hat{c}^{*\mathrm{DD}} + s\,\hat{c}^{*\mathrm{DDD}} + t\,\hat{c}^{*\mathrm{D}} \ \big)\big] \\ &\qquad - \ldots \stackrel{!}{=} 0 \qquad\qquad \forall\, \delta c^{(\cdot)} . \end{aligned} \tag{4.98}$$

For the unknown face value in Fig. 4.3 within the adjoint CICSAM scheme, i.e. the first inner bracket in Eqn. (4.98), one obtains $\hat{c}^{*\mathrm{F}} = r\,\hat{c}^{*\mathrm{D}} + s\,\hat{c}^{*\mathrm{DD}} + t\,\hat{c}^{*\mathrm{U}}$ or $\hat{c}^{\mathrm{F}}_{\mathrm{n}} = 8\mathrm{Co}^{\mathrm{F}}\hat{c}^{\mathrm{D}}_{\mathrm{n}} + (1 - \mathrm{Co}^{\mathrm{F}})(6\hat{c}^{\mathrm{D}}_{\mathrm{n}} + 3)$ after applying the adjoint normalization from Eqn. (4.92) where $r + s + t = 1$ is used. Thus, an adjoint formulation to the CICSAM scheme of Eqn. (2.91) reads

$$\begin{aligned} \hat{c}^{\mathrm{F}}_{\mathrm{n}} &= \gamma^{\mathrm{F}}\hat{c}^{\mathrm{F,HC}}_{\mathrm{n}} + (1 - \gamma^{\mathrm{F}})\hat{c}^{\mathrm{F,UQ}}_{\mathrm{n}} \\ &\text{with} \qquad \hat{c}^{\mathrm{F,HC}}_{\mathrm{n}} = \begin{cases} \min\left(1, \frac{\hat{c}^{\mathrm{D}}_{\mathrm{n}}}{\mathrm{Co}^{\mathrm{F}}}\right) & : 0 \le \hat{c}^{\mathrm{D}}_{\mathrm{n}} \le 1 \\ \hat{c}^{\mathrm{D}}_{\mathrm{n}} & : \hat{c}^{\mathrm{D}}_{\mathrm{n}} \notin [0,1] \end{cases} \\ &\text{and} \qquad \hat{c}^{\mathrm{F,UQ}}_{\mathrm{n}} = \begin{cases} \min\left(\hat{c}^{\mathrm{F,HC}}_{\mathrm{n}}, \frac{8\mathrm{Co}^{\mathrm{F}}\hat{c}^{\mathrm{D}}_{\mathrm{n}} + \left(1 - \mathrm{Co}^{\mathrm{F}}\right)\left(6\hat{c}^{\mathrm{D}}_{\mathrm{n}} + 3\right)}{8}\right) & : 0 \le \hat{c}^{\mathrm{D}}_{\mathrm{n}} \le 1 \\ \hat{c}^{\mathrm{D}}_{\mathrm{n}} & : \hat{c}^{\mathrm{D}}_{\mathrm{n}} \notin [0,1] \end{cases} . \end{aligned} \tag{4.99}$$

Again, downwind and upwind are rigorously exchanged.

A Note on Additional Variational Contributions

Eqns. (2.90) as well as (2.91) inhere several implicit dependencies on the flow field, e.g. via the local Courant number or the free surface orientation. These relationships adjust the NVD evaluations and are kept frozen during the above mentioned derivation of the adjoint HRIC and CICSAM schemes. This strategy was previously also used for the formulation of an adjoint complement to higher-order convection schemes, e.g., TVD schemes, cf. Stück and Rung [2013].

The implementation of the resulting mirrored HRIC/CICSAM approximations of the adjoint convective concentration transport resembles the proposed DC strategy of the

primal companion schemes, i.e. $\mathrm{DC}^{*\mathrm{C},\hat{\mathrm{c}},\mathrm{F}}$ for each face value, viz.

$$\begin{aligned}\delta_{\mathrm{c}} L^* \cdot \delta c = \ldots - \int\int \delta c \left[v_{\mathrm{k}}^* \frac{\partial \hat{c}^*}{\partial x_{\mathrm{k}}^*} \right] \mathrm{d}\Omega^* \, \mathrm{d}t^* + \ldots \\ \rightarrow \quad \delta_{\mathrm{c}} L^* \cdot \delta c \approx \ldots - \sum_{\mathrm{T}} \sum_{\mathrm{P}} \delta c^{*\mathrm{P}} \sum_{\mathrm{F(P)}} \dot{V}^{*\mathrm{F}} \left[\hat{c}^{*\mathrm{D}} + \mathrm{DC}^{*\mathrm{C},\hat{\mathrm{c}},\mathrm{F}} \right] \Delta t^* + \ldots . \end{aligned} \tag{4.100}$$

Note that the adjoint concentration equation has little in common with its primal counterpart, e.g. several source terms occur, which results in further pseudo-time step requirements.

4.2.6 Adjoint Boundary Conditions

The adjoint boundary conditions summarized in Tab. 4.1 are mathematically grouped into conditions of either Dirichlet or Neumann type that provide either a fixed boundary value or gradient, respectively, viz.

$$\hat{\varphi}^{*\mathrm{B}} = \text{const.} \qquad \text{and} \qquad \left. \frac{\partial \hat{\varphi}^*}{\partial n^*} \right|^{*\mathrm{B}} \approx \frac{\hat{\varphi}^{*\mathrm{P}} - \hat{\varphi}^{*\mathrm{B}}}{||d_{\mathrm{i}}^{*\mathrm{B}}||} = \text{const.} . \tag{4.101}$$

Analogous to the primal discussion, vectors and tensors are distinguished into tangential and normal components, e.g. $[\hat{t}_{\mathrm{i}}^* = \hat{v}_{\mathrm{i}}^* - (\hat{v}_{\mathrm{k}}^* \, n_{\mathrm{k}}) \, n_{\mathrm{i}}]$ in tangential direction and $[(\hat{v}_{\mathrm{k}}^* \, n_{\mathrm{k}}) n_{\mathrm{i}}]$ in the direction of the normal. Since the adjoint momentum equation strongly resembles the primal counterpart, a free-cutting analogy is again employed. Splitting the adjoint boundary forces into tangential and normal adjoint traction denoted by $t_{\mathrm{i}} = \hat{t}_{\mathrm{i}}^* / \|\hat{t}_{\mathrm{i}}^*\|$ as well as n_{i} and additionally assuming negligible curvature, one obtains

$$\hat{\sigma}_{\mathrm{i}}^{*B} = \left[\mu^{*\hat{\mathrm{v}}_{\mathrm{i}}} \left(\frac{\partial \hat{v}_t^*}{\partial n^*} + \frac{\partial \hat{v}_n^*}{\partial t^*} \right) \right]^B t_{\mathrm{i}} + \left[2 \mu^{*\hat{\mathrm{v}}_{\mathrm{i}}} \frac{\partial \hat{v}_n^*}{\partial n^*} - \hat{p}^* \right]^B n_{\mathrm{i}} . \tag{4.102}$$

Along the inlet, the adjoint velocity vector and the adjoint concentration field are prescribed. A zero normal gradient is assumed for the adjoint pressure. Along the symmetry planes and slip walls, scalar field values ($\hat{p}^*$, $\hat{c}^*$) are also subjected to zero normal gradients. The normal component of the adjoint velocity is suppressed and the tangential adjoint velocity components are extrapolated with zero-order accuracy from the field onto the symmetry plane. Therefore, the tangential adjoint force in (4.102) vanishes and only the normal component remains,

$$\hat{\sigma}_{\mathrm{i}}^{*\mathrm{S}} = \left[2 \, \mu^{*\hat{\mathrm{v}}_{\mathrm{i}}} \frac{\partial \hat{v}_n^*}{\partial n^*} - \hat{p}^* \right] n_{\mathrm{i}} . \tag{4.103}$$

The adjoint pressure is extrapolated with zero-order accuracy. No slip wall conditions employ a free-cutting concept that replaces the adjoint free forces acting on the wetted body by an adjoint closure model, while assuming negligible local wall curvature. Due to the prescribed adjoint wall velocity, the adjoint pressure is extrapolated with zero-order accuracy from the field to the wall. The corresponding adjoint wall force involves adjoint shear and adjoint pressure components, i.e.

$$\hat{\sigma}_{\mathrm{i}}^{*\mathrm{W}} = \mu^{*\hat{\mathrm{v}}_{\mathrm{i}}} \frac{\partial \hat{v}_t^*}{\partial n^*} t_{\mathrm{i}} - \hat{p}^* \, n_{\mathrm{i}} . \tag{4.104}$$

Appropriate models to close the adjoint wall shear, i.e. the effective viscosity $\mu^{*\hat{\mathrm{v}}_\mathrm{i}}$, either refer to adjoint complements to unidirectional shear flows, applicable in the laminar or turbulent low-Re studies, or an adjoint wall function strategy valid for high-Re turbulent flow studies. Both relate to the wall tangential projection of the adjoint velocity in the wall adjacent CV and only differ in the value of $\mu^{*\hat{\mathrm{v}}_\mathrm{i}}$, cf. Eqn. (4.52), which simplifies the implementation. As outlined below and in line with the primal procedure, these boundary conditions result in a manipulation of the convective and the diffusive boundary flux, cf. Fig. 2.3 (b), along the face of the boundary adjacent interior control volume.

Convective fluxes follow from (4.81) as well as (4.83) and consequently reverse their primal implementation (2.96). They involve an implicit first-order DDS approximation which reveals

$$A^{*\hat{\varphi},\mathrm{P}} \leftarrow \max\left(\dot{V}^{*\mathrm{B}}, 0\right) . \tag{4.105}$$

One only needs to distinguish whether, as well as in which direction (inflow vs. outflow) a convective adjoint transport occurs.

- **Inlet** conditions refer to an outflow ($-v_\mathrm{k}^{*\mathrm{I}}$) of the domain as well as the boundary adjacent CV and therefore a positive volume flux $\dot{V}^{*B} = v_\mathrm{k}^{*\mathrm{I}} \Delta\Gamma_\mathrm{k}^{*\mathrm{B}}$ enters (4.105).
- **Prescribed pressure outlet** conditions are characterized by zero entries to the coefficient matrix, due to the inward directed negative flux $\dot{V}^{*\mathrm{B}}$.
- **Symmetry** and **no-slip / slip wall** boundary conditions suppress a convective transport over the boundary via $\dot{V}^{*\mathrm{B}} = 0$. Since the convective flux is suppressed along the boundary, no convective contributions to the r.h.s. or the coefficient matrix occur for this face.

Diffusive fluxes follow from (4.88) and resemble their primal complement (2.97) due to the self-adjoint nature, viz.

$$A^{*\hat{\varphi},\mathrm{P}} \leftarrow \left[\frac{\mu^{*\hat{\varphi}} \Delta\Gamma^*}{||d_\mathrm{k}^*|| \alpha^\mathrm{n}}\right]^\mathrm{B} \qquad \text{and} \qquad S^{*\hat{\varphi},\mathrm{P}} \leftarrow \left[\frac{\mu^{*\hat{\varphi}} \Delta\Gamma^*}{||d_\mathrm{k}^*|| \alpha^n}\right]^\mathrm{B} \hat{\varphi}^{*\mathrm{B}} . \tag{4.106}$$

- **Inlet** boundaries are characterized by Dirichlet conditions for all adjoint quantities except the adjoint pressure. Due to the zero gradient adjoint pressure condition, diffusive contributions (4.106) are suppressed, which provides an implicit condition. The diffusive flux of all other adjoint variables follows from (4.106) based on the given inlet $\hat{\varphi}^{*\mathrm{B}} = \hat{\varphi}^{*\mathrm{I}}$ quantities from Tab. 4.1. If the adjoint momentum equations are assembled, further explicit contributions are added to supplement the complete adjoint strain rate tensor. Similarly, the adjoint pressure is extrapolated with zero-order to the boundary to complete the normal adjoint force on this face.
- **Prescribed pressure outlet** boundary conditions employ zero gradients for the adjoint velocity ($\partial\, \hat{v}_\mathrm{i}^{*\mathrm{B}} / \partial\, n^* = 0$). These contributions are not considered for $\hat{\varphi}^* \neq \hat{p}^*, \hat{c}^*$, since $\hat{\varphi}^{*\mathrm{B}} = \hat{\varphi}^{*\mathrm{P}}$ eliminates the sum of all contributions to (4.106). The adjoint pressure and concentration are assigned to constant Dirichlet conditions along the outlet, e.g. $\hat{p}^{*\mathrm{B}} = \hat{p}^{*\mathrm{out}}$ and $\hat{c}^{*\mathrm{B}} = \hat{c}^{*\mathrm{out}}$, which enter (4.106).

- **Symmetry** and **slip-wall** boundary conditions do suppress the wall normal gradient of the scalar properties. Hence, all contributions to (4.106) are suppressed for $\hat{\varphi}^* = \hat{c}^*, \hat{p}^*$. Moreover, no adjoint shear stress is transmitted due to the symmetry $\partial\,\hat{v}_\mathrm{t}^*/\partial\,n^* = 0$ as well as the no-penetration condition $\partial\,\hat{v}_\mathrm{n}^*/\partial\,t^* = 0$ and considered adjoint forces reduce to $\left[2\mu^{*\hat{v}_\mathrm{i}}(\partial\,\hat{v}_n^*/\partial\,n^*) - \hat{p}^*\right]^B n_\mathrm{i}$, cf. Eqns. (4.102) and (4.103), which requires to extrapolate the adjoint pressure as well as to consider a source for the adjoint momentum equations, viz.

$$A^{*\hat{\mathrm{v}}_\mathrm{i},\mathrm{P}} \leftarrow 0 \qquad \text{and} \qquad S^{*\hat{\mathrm{v}}_\mathrm{i},\mathrm{P}} \leftarrow \left[\frac{\mu^{*\hat{v}_\mathrm{i}}\,\Delta\Gamma}{||d_\mathrm{k}^*||\alpha^n}\right]^\mathrm{B} 2\left[(\hat{v}_\mathrm{k}^{*B} - \hat{v}_\mathrm{k}^{*P})n_\mathrm{k}^\mathrm{B}\right] n_\mathrm{i}^\mathrm{B}\,. \tag{4.107}$$

  A symmetry plane always employs $\hat{v}_\mathrm{i}^{*\mathrm{B}} = \hat{v}_\mathrm{i}^{*\mathrm{S}} = 0$.

- **No-Slip Wall** boundary conditions suppress the wall normal gradient of adjoint pressure as well as adjoint concentration and contributions to (4.106) are again suppressed for $\hat{\varphi}^* = \hat{c}^*, \hat{p}^*$. Adjoint viscous shear and pressure forces acting on a wall follow from (4.104), viz. $\mu^{*\hat{\mathrm{v}}_\mathrm{i}}\partial\,\hat{v}_t^*/\partial\,n^* t_\mathrm{i} - \hat{p}^*\,n_\mathrm{i}$. They require to extrapolate the pressure and yield the following changes to the discrete adjoint momentum equations

$$A^{*\hat{\mathrm{v}}_\mathrm{i},\mathrm{P}} \leftarrow \left[\frac{\mu^{*\hat{v}_\mathrm{i}}\,\Delta\Gamma}{||d_\mathrm{k}^*||\alpha^n}\right]^\mathrm{B} \quad \text{and} \quad S^{*\hat{\mathrm{v}}_\mathrm{i},\mathrm{P}} \leftarrow \left[\frac{\mu^{*\hat{v}_\mathrm{i}}\,\Delta\Gamma}{||d_\mathrm{k}^*||\alpha^n}\right]^\mathrm{B} \left(\left[(\hat{v}_\mathrm{k}^{*B} - \hat{v}_\mathrm{k}^{*P})t_\mathrm{k}^\mathrm{B}\right] t_\mathrm{i}^\mathrm{B} + \hat{v}_\mathrm{i}^{*P}\right)\,. \tag{4.108}$$

  Note that adjoint studies often involve moving walls, e.g. $\hat{v}_\mathrm{i}^\mathrm{B} = \hat{v}_\mathrm{i}^\mathrm{W} = -r_\mathrm{i}$, cf. Tab 4.1. The approach is generic and allows for the manipulation of the actual wall shear in line with the adjoint complement to the universal LoW for momentum, cf. Sec. 4.1.7 and 4.3.3.

4.2.7 Stability of the Adjoint Approximation

During the approximation of the primal VoF equation, its main diagonal coefficient of the system matrix is affected if the approximation of the convective term switches locally from UDS to DDS. Using a first-order BE discretization of $\mathrm{D}\,c/\mathrm{D}\,t^* = 0$ yields the main diagonal entry for upwind and downwind interpolation of c^F from Eqn. (2.104). The primal time step size must be chosen to comply with a sufficiently small Courant number in-order to preserve diagonal dominance. The primal time step dependence can be efficiently circumvented if a sub-cycling strategy is employed to the temporal forward integration, cf. Ubbink and Issa [1999], Manzke et al. [2012] or Sec. 2.2.10. In adjoint mode, the compressive convection schemes switch from DDS to UDS along the critical interfacial region. A closer look at the main diagonal coefficient of $-\mathrm{D}\,\hat{c}^*/\mathrm{D}t^* = 0$ reveals a similar observation compared to the primal discretization,

$$-\left[\frac{\hat{c}^{*\mathrm{P},\mathrm{T}+1} - \hat{c}^{*\mathrm{P},\mathrm{T}}}{\Delta t^*}\right]\Delta\Omega^* - \sum_{\mathrm{F(P)}} \dot{V}^{*\mathrm{F},\mathrm{T}}\hat{c}^{*\mathrm{F},\mathrm{T}} = 0$$

$$\rightarrow \qquad A^{*\hat{\mathrm{c}},\mathrm{P},\mathrm{T}} = \frac{\Delta\Omega^*}{\Delta t^*} - \sum_{\mathrm{F(P)}} \begin{cases} \min\left(\dot{V}^{*\mathrm{F},\mathrm{T}}, 0\right) & : \mathrm{DDS} \\ \max\left(\dot{V}^{*\mathrm{F},\mathrm{T}}, 0\right) & : \mathrm{UDS} \end{cases}. \tag{4.109}$$

Mind that the r.h.s. of Eqn. (4.17) is not zero and inheres several source/sink terms which are independent of $\hat{c}^*$. In contrast to downwinding during the primal integration, an upwind interpolation of the adjoint face value $\hat{c}^{*\mathrm{F}}$ weakens the main diagonal. Thus, the adjoint backward integration facilitates a sub-cycling procedure for the dual concentration equation also, as schematically coded in Alg. (5). Basically, the primal/dual time step sizes as well as the number of sub-cycles do not have to match. Nevertheless, coincidence of time step size and sub-cycles yield an adjoint simulation that is always UDS-stable at cells and faces that are primal DDS-stable. Time accuracy is not required from the intermediate temporary solutions of the primal/dual flow fields which in turn greatly simplifies the approach. Time stepping can thus be interpreted as a relaxation during the numerical integration and is solely used to ensure/improve the stability of the segregated algorithm. Moreover, no formal consistency demands arise w.r.t. discretization and evaluation of the primal/dual unsteady terms, e.g., different time step stencils and sizes are valid. Algorithmically, however, the adjoint solver should know the primal Courant number distribution in order to consistently invert the primal NVD board, e.g., switch from UDS to DDS and vice versa.

When attention is directed to practical marine engineering applications, the computational effort associated with time stepping of compressive primal approximations is substantial. The stability criteria for the adjoint CH-VoF system are similar due to a slightly negative apparent viscosity along the phase transition regime, cf. Sec. 2.2.10. However, since various additional coupling terms are on the r.h.s. of the adjoint concentration equation, significantly smaller pseudo-time steps and relaxation parameters are usually employed. As a consequence, adjoint CH-VoF studies frequently employ a spatially constant (positive) diffusivity that follows from the estimated primal under-resolved flow model.

The complete discrete procedure to obtain the adjoint-based shape derivative is documented in Alg. 5.

Algorithm 5: (Pseudo) temporal integration of the primal and adjoint two-phase system based on a sub-cycling approach for the computation of the shape derivative (4.58) or (4.64).

while $n^{\mathrm{T}} \leq \mathrm{N}^{\mathrm{T}}$ **do**
  while $(n^{\mathrm{out}} \leq \mathrm{N}^{\mathrm{out,max}})$ *or* $(\mathrm{R}^{\varphi} \leq \mathrm{R}^{\varphi,\mathrm{min}})$ **do**
    approximate linearized momentum equations
    approximate pressure correction equation
    approximate linearized turbulence equations
    $\Delta t^* = \Delta t^*/N$
    for *sub-cycle=1,N* **do**
      approximate linearized concentration equation
    $\Delta t^* = \Delta t^* N$
while $n^{\mathrm{T}} \leq \mathrm{N}^{\mathrm{T}}$ **do**
  while $(n^{\mathrm{out}} \leq \mathrm{N}^{\mathrm{out,max}})$ *or* $(\mathrm{R}^{\hat{\varphi}} \leq \mathrm{R}^{\hat{\varphi},\mathrm{min}})$ **do**
    approximate adjoint momentum equations
    approximate adjoint pressure correction equation
    $\Delta t^* = \Delta t^*/N$
    for *adSub-cycle=1,N* **do**
      approximate adjoint concentration equation
    $\Delta t^* = \Delta t^* N$
compute shape derivative (4.58) or (4.64)

4.3 Adjoint Flow Verification

After the adjoint equations have been derived and subsequently discretized, the discrete adjoint numerical model is verified. This is done based on the three test cases already studied for primal verification purposes, cf. Sec. 2.3. Regarding the definition of V&V, this thesis follows the route suggested by the AIAA as sketched at the beginning of Sec. 2.3. The discrete approximation of a continuous adjoint equation can be likewise verified utilising, e.g., analytical or generalized solutions. However, the connection between an adjoint result and the real world might be questionable, which is why the definition of V&V is rephrased in adjoint mode, and each approach tries to answer if

- Verification: *the adjoint equations are solved correctly.* As indicated before, this can be checked on the basis of analytical or generalized solutions.
- Validation: *the correct adjoint equations are solved.* Since the fundamental motivation of the underlying adjoint investigations refers to a derivative determination of an objective functional w.r.t. a shape, the question of the derived adjoint equations' correctness can be validated against alternative methods for the shape derivative estimation. Prominent alternatives are the direct methods from Sec. 3.1.1 that examine the agreement of the shape derivative integrand s^*, cf. Eqns. (4.44), (4.58) and (4.64). Such approaches are referred to as a local validation. Alternatively, the adjoint-based shape derivative can also be validated globally by comparing the integrated sensitivity derivative or even performing complete optimization studies of possibly divergent adjoint formulations under identical optimization conditions. In any case, a descent direction should be obtained when a minimum is sought.

To verify the adjoint implementation against simplified or generalized solutions, such benchmark problems and their solutions must first be derived. This in turn is associated with a small validation exercise: Since the physical relationships on the primal side are often comparatively complex, adjoint benchmark problems and their continuous adjoint solutions can be derived pursuing different approaches, i.e. the *simplify-and-derive* or the *derive-and-simplify* approach. An agreement between both results should reveal formal correctness.

4.3.1 Adjoint Laminar (Blasius) Boundary-Layer Equation

The adjoint b.-l. equations can be derived in two ways, following either a *derive-and-simplify* or a *simplify-and-derive* strategy. In both cases the derivation step starts with the definition of a surface- [volume-] based objective functional j^Γ $[j^\Omega]$ that allows for the construction of an augmented objective as already done at the beginning of Cha. 4. Following the *derive-and-simplify* route, one first obtains the adjoint Eqns. (4.16)-(4.18). Assuming a single-phase flow, the adjoint equations resemble their primal companion augmented by an additional cross coupling term, frequently labeled as ATC, due to the nonlinearity of the primal convective momentum transport. The term might disappear for compressible flows, cf. Soto and Löhner [2004]. Nevertheless, the ATC terms are frequently also neglected in incompressible formulations due to the related impairment of the numerical robustness, e.g., Springer and Urban [2015], Othmer [2008]. Some authors raise a *mathematical* argument based on the approximation order, viz. $\delta[v_\mathrm{k}^* \, (\partial \, v_\mathrm{i}^* / \partial \, x_\mathrm{k}^*)] =$

adjoint quantity/operator	$\hat{v}_1^*$	$\hat{v}_2^*$	$\hat{p}^*$	$\partial\,\hat{\phi}^*/\partial\,x_1^*$	$\partial\,\hat{\phi}^*/\partial\,x_2^*$
reference value	$\hat{V}_1^*$	$\hat{V}_2^*$	$\hat{P}^*$	L^*	$\hat{\delta}^*$

Table 4.2: Reference quantities of the 2D governing adjoint b.-l. equations.

$\delta v_{\mathrm{k}}^*\,(\partial\,v_{\mathrm{i}}^*/\partial\,x_{\mathrm{k}}^*) + v_{\mathrm{k}}^*\,(\partial\,\delta v_{\mathrm{i}}^*/\partial\,x_{\mathrm{k}}^*) \approx \mathcal{O}(\delta v_{\mathrm{k}}^*) + \mathcal{O}(\partial\,\delta v_{\mathrm{i}}^*/\partial\,x_{\mathrm{k}}^*)$, to justify the neglect of the ATC, cf. Anderson and Bonhaus [1999], Elliott and Peraire [1997], Othmer [2008]. The present thesis provides another indicator for the *physically* justifiable neglect of this term.

Similar to the primal problem, the adjoint single-phase system (4.16)-(4.18) is analyzed w.r.t. the spatial scale/order of magnitude in a non-dimensional setting. The corresponding reference quantities follow from Tab. 4.2. One can define a scaling of the x_2^*-derivative of an adjoint quantity with $\hat{\delta}^*$, viz. $v_2^*\partial\,\hat{v}_1^*/\partial\,x_2^* = (V_2^*\,\hat{V}_1^*/\hat{\delta}^*)\,(v_2(\partial\,\hat{v}_1/\partial x_2))$. The scaling analysis of Eqns. (4.16)-(4.18) is performed in App. A.2 for an objective that does not depend on the primal pressure, e.g. $\partial\,j^{*\Omega}/\partial p^* = 0$, yielding:

$$\mathrm{R}_1^{*\hat{\mathrm{v}},\mathrm{BL}} : -v_1^*\frac{\partial\,\hat{v}_1^*}{\partial\,x_1^*} - v_2^*\frac{\partial\,\hat{v}_1^*}{\partial\,x_2^*} + \hat{v}_1^*\frac{\partial\,v_1^*}{\partial\,x_1^*} + \frac{\partial\,\hat{p}^*}{\partial\,x_1^*} - \nu^*\frac{\partial^2\,\hat{v}_1^*}{\partial\,{x_2}^{*2}} = -\frac{\partial\,j^{*\Omega}}{\partial\,v_1^*} \tag{4.110}$$

$$\mathrm{R}_2^{*\hat{\mathrm{v}},\mathrm{BL}} : \hat{v}_1^*\frac{\partial v_1^*}{\partial\,x_2^*} + \frac{\partial\,\hat{p}^*}{\partial\,x_2^*} = -\frac{\partial\,j^{*\Omega}}{\partial\,v_2^*} \tag{4.111}$$

$$\mathrm{R}^{*\hat{\mathrm{p}},\mathrm{BL}} : -\left(\frac{1}{\rho^*}\frac{\partial\,\hat{v}_1^*}{\partial\,x_1^*} + \frac{1}{\rho^*}\frac{\partial\,\hat{v}_2^*}{\partial\,x_2^*}\right) = 0\,. \tag{4.112}$$

Alternatively, Eqns. (4.110)-(4.112) can also be derived in a *simplify-and-derive* approach. Figure 4.4 depicts the two different routes to the benchmark problem. The *simplify-and-derive* approach starts with a Lagrangian based on the primal b.-l. equations (2.113)-(2.115) , viz.

$$\begin{aligned} L^* = &\int_{\Gamma^*} j^{*\Gamma}\,\mathrm{d}\Gamma^* + \int_{\Gamma^{*\mathrm{wall}}} \hat{v}_{\mathrm{i}}^*\,v_{\mathrm{i}}^* + \hat{p}^*\frac{\partial\,p^*}{\partial\,n^*}\mathrm{d}\Gamma^* + \int_{\Omega^{*\mathrm{O}}} j^{*\Omega}\,\mathrm{d}\Omega^* \\ &+ \int_{\Omega^*} \hat{v}_1^*\left[v_1^*\frac{\partial\,v_1^*}{\partial\,x_1^*} + v_2^*\frac{\partial\,v_1^*}{\partial\,x_2^*} + \frac{\partial\,p^*}{\partial\,x_1^*}\frac{1}{\rho^*} - \nu^*\frac{\partial^2\,v_1^*}{\partial\,{x_2}^{*2}}\right] \\ &\quad + \hat{v}_2^*\left[\frac{\partial\,p^*}{\partial\,x_2^*}\frac{1}{\rho^*}\right] + \hat{p}^*\left[\frac{\partial\,v_1^*}{\partial\,x_1^*} + \frac{\partial\,v_2^*}{\partial\,x_2^*}\right]\mathrm{d}\Omega^*\,. \end{aligned} \tag{4.113}$$

Again, first-order optimality conditions force vanishing derivatives of the Lagrangian in all dependent directions ($\delta_{\mathrm{v_i}}L^*\cdot\delta v_{\mathrm{i}}^* = \delta_{\mathrm{v_1}}L^*\cdot\delta v_1^* + \delta_{\mathrm{v_2}}L^*\cdot\delta v_2^* = 0\ \forall\,(\delta v_1^*, \delta v_2^*)$, $\delta_{\mathrm{p}}L^*\cdot\delta p^* =$

$0\ \forall \delta p^*$), i.e.

$$
\begin{aligned}
\delta_{\mathrm{v}_1} L^* \cdot \delta v_1^* + \delta_{\mathrm{v}_2} L^* \cdot \delta v_2^* = & \int_{\Gamma^{*\mathrm{wall}}} \hat{v}_1^*\, \delta v_1^* + \hat{v}_2^*\, \delta v_2^* \mathrm{d}\Gamma^* \\
& + \int_{\Gamma^*} \delta v_1^* \left[\frac{\partial\, j^{*\Gamma}}{\partial\, v_1^*} + \hat{v}_1^* \frac{\partial\, v_1^*}{\partial\, x_1^*} + \hat{v}_1^*\, v_1^*\, n_1 + \hat{v}_1^*\, v_2^*\, n_2 - \hat{p}^*\, n_2 + \nu^* \frac{\partial\, \hat{v}_1^*}{\partial\, x_2^*} n_2 \right] \\
& \quad - \nu^* \left(\hat{v}_1^* \frac{\partial\, (\delta v_1^*)}{\partial\, x_2^*} n_2 \right) \\
& \quad + \delta v_2^* \left[\frac{\partial\, j^{*\Gamma}}{\partial\, v_2^*} - \hat{p}^*\, n_2 \right] \mathrm{d}\Gamma^* \\
& + \int_{\Omega^*} \delta v_1^* \left[\hat{v}_1^* \frac{\partial\, v_1^*}{\partial\, x_1^*} - \frac{\partial\, \hat{v}_1^*\, v_1^*}{\partial\, x_1^*} - \frac{\partial\, \hat{v}_1^*\, v_2^*}{\partial\, x_2^*} - \nu^* \frac{\partial^2\, \hat{v}_1^*}{\partial\, {x_2^*}^2} - \frac{\partial\, \hat{p}^*}{\partial\, x_1^*} + \frac{\partial\, j^{*\Omega}}{\partial\, v_1^*} \right] \\
& \quad + \delta v_2^* \left[\hat{v}_1^* \frac{\partial\, v_1^*}{\partial\, x_2^*} - \frac{\partial\, \hat{p}^*}{\partial\, x_2^*} + \frac{\partial\, j^{*\Omega}}{\partial\, v_2^*} \right] \mathrm{d}\Omega^* \\
& \stackrel{!}{=} 0 \qquad \forall\, (\delta v_1^*, \delta v_2^*) \qquad (4.114)
\end{aligned}
$$

$$
\begin{aligned}
\delta_{\mathrm{p}} L^* \cdot \delta p^* = & \int_{\Gamma^{*\mathrm{wall}}} \hat{p}^* \frac{\partial\, (\delta p^*)}{\partial n^*} \mathrm{d}\Gamma^* \\
& + \int_{\Gamma^*} \delta p^* \left[\frac{\partial\, j^{*\Gamma}}{\partial\, p^*} + \hat{v}_1^*\, n_1 \frac{1}{\rho^*} + \hat{v}_2^*\, n_2 \frac{1}{\rho^*} \right] \mathrm{d}\Gamma^* \\
& + \int_{\Omega^*} \delta p^* \left[- \frac{\partial\, \hat{v}_1^*}{\partial\, x_1^*} \frac{1}{\rho^*} - \frac{\partial\, \hat{v}_2^*}{\partial\, x_2^*} \frac{1}{\rho^*} \right] \mathrm{d}\Omega^* \\
& \stackrel{!}{=} 0 \qquad \forall \delta p^*. \qquad (4.115)
\end{aligned}
$$

The adjoint b.-l. equations as well as their boundary conditions are obtained from Eqns. (4.114)-(4.115).

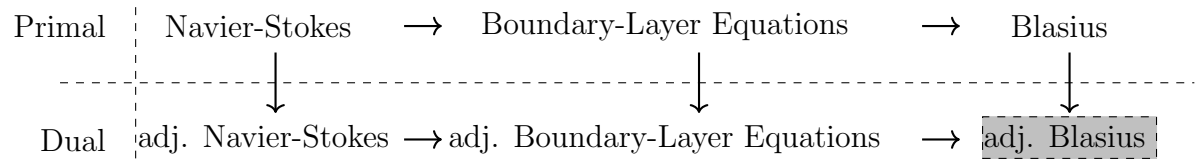

Figure 4.4: Schematic derivation-flow of adjoint counterparts to known primal simplifications for near-wall flow physics towards the desired adjoint Blasius equation (dark grey).

The adjoint b.-l. quantities are convected by the primal flow and a similar behavior of the adjoint field and a scalar field is anticipated, e.g. a temperature field, although the latter usually does not have to fulfill a continuity equation. The interpretation of the adjoint flow is non-intuitive due to the influence of the objective functional, e.g. volume-based objectives possibly introduce a non-divergence free adjoint velocity field. Therefore the present investigations are confined to boundary-based objectives. In line with the primal flow from Sec. 2.3.1, one starts with the similarity variable and assumes the adjoint mean flow to depend on the plate normal and tangential coordinate, viz. $\hat{v}_1^*/\hat{V}_1^* = \hat{g}(\hat{\eta})$ with $\hat{\eta} = x_2^*/\hat{\delta}^*(x_1^*)$ where $\hat{g}$ and $\hat{\delta}^*$ represent the adjoint complement of g and δ^*. Again, one can

directly compute all required spatial derivatives, e.g. $\partial\,\hat{v}_1^*/\partial x_1^* = -\hat{V}_1^*\hat{g}'(x_2^*/\hat{\delta}^{*2})(\partial\,\hat{\delta}^*/\partial\,x_1^*)$ with $\hat{g}' = \mathrm{d}\,\hat{g}/\mathrm{d}\hat{\eta}$. An integration of (4.110) between the wall and the adjoint b.-l. edge while assuming adjoint ZPG along the wall normal coordinate reads

$$-\int_0^{\hat{\delta}^*} v_1^*\frac{\partial\,\hat{v}_1^*}{\partial\,x_1^*}\,\mathrm{d}x_2^* - \int_0^{\hat{\delta}^*} v_2^*\frac{\partial\,\hat{v}_1^*}{\partial\,x_2^*}\,\mathrm{d}x_2^* - \int_0^{\hat{\delta}^*} \nu^*\frac{\partial^2\,\hat{v}_1^*}{\partial\,x_2^{*2}}\,\mathrm{d}x_2^* = -\int_0^{\hat{\delta}^*} \hat{v}_1^*\frac{\partial\,v_1^*}{\partial\,x_1^*}\,\mathrm{d}x_2^*\,. \tag{4.116}$$

Here the additional term on the r.h.s. corresponds to the ATC term originating from the nonlinear convection. Applying the primal continuity equation ($\partial\,v_2^*/\partial\,x_2^* = -\partial\,v_{1^*}/\partial\,x_1^*$) interestingly cancels the ATC term, viz.

$$-\int_0^{\hat{\delta}^*} v_1^*\frac{\partial\,\hat{v}_1^*}{\partial\,x_1^*}\,\mathrm{d}x_2^* + \hat{V}_1^*\int_0^{\hat{\delta}^*}\frac{\partial\,v_1^*}{\partial\,x_1^*}\,\mathrm{d}x_2^* - \int_0^{\hat{\delta}^*}\hat{v}_1^*\frac{\partial\,v_1^*}{\partial\,x_1^*}\,\mathrm{d}x_2^* - \nu^*\frac{\partial\,\hat{v}_1^*}{\partial\,x_2^*}\bigg|_0^{\hat{\delta}^*} = -\int_0^{\hat{\delta}^*}\hat{v}_1^*\frac{\partial\,v_1^*}{\partial\,x_1^*}\,\mathrm{d}x_2^*\,. \tag{4.117}$$

Combining the primal tangential velocity ($v_1^*/V_1^* = g(\eta)$) and its (anticipated) adjoint complement yields

$$\frac{\partial\,\hat{\delta}^*}{\partial\,x_1^*}\int_0^1 g\hat{g}'\hat{\eta}\,\mathrm{d}\hat{\eta} - \frac{\partial\,\delta^*}{\partial\,x_1^*}\int_0^{\delta^*/\hat{\delta}^*} g'\eta\,\mathrm{d}\eta - \frac{\nu^*}{V_1^*}\hat{g}'\frac{1}{\hat{\delta}^*}\bigg|_0^1 = 0. \tag{4.118}$$

Substituting $\hat{\eta} = x_2^*/\hat{\delta}^*$ ($\mathrm{d}x_2^* = \hat{\delta}^*\mathrm{d}\hat{\eta} = \hat{\delta}^*\mathrm{d}(x_2^*/\hat{\delta}^*)$) offers an ODE for $\hat{\delta}^*$ that inheres the primal b.-l. thickness measure

$$\left[\hat{A}\frac{\partial\,\hat{\delta}^*}{\partial x_1^*} - \hat{B}^*\frac{\partial\,\delta^*}{\partial\,x_1^*}\right]\hat{\delta}^* = \frac{\nu^*}{V_1^*}\hat{C}. \tag{4.119}$$

Again, all integrals are condensed into coefficients, viz.

$$\hat{A} = \int_0^1 g\hat{g}'\hat{\eta}\,\mathrm{d}\hat{\eta}\,, \qquad \hat{B} = \int_0^{\delta/\hat{\delta}} g'\eta\,\mathrm{d}\eta \quad \text{and} \quad \hat{C} = \hat{g}'(1) - \hat{g}'(0). \tag{4.120}$$

Thanks to the available primal δ^*, one can reformulate Eqn. (4.119), viz.

$$C_1\frac{\partial\,\hat{\delta}^*}{\partial\,x_1^*}\hat{\delta}^* - C_2^*\frac{\hat{\delta}^*}{\sqrt{a^* + bx_1^*}} = C_3^*\,, \tag{4.121}$$

where $C_1 = \hat{A}$, $C_2^* = \hat{B}(b/2)\sqrt{2C/(b[A-2B])}\sqrt{\nu^*/V_1^*}$ and $C_3^* = \hat{C}\nu^*/V_1^*$ are introduced to keep the notation compact. Thus, one can solve Eqn. (4.121) w.r.t. $\hat{\delta}$,

$$\hat{\delta}^* = -\frac{2C_3^*}{C_2^* + \sqrt{C_2^{*2} + 2\,b\,C_1C_3^*}}\sqrt{a^* + b\,x_1^*} \tag{4.122}$$

and quantify an adjoint b.-l. thickness by the expression

$$\hat{\delta}^* = -\frac{C_3^*}{C_2^*}\frac{b\hat{B}}{C_2^* + \sqrt{C_2^{*2} + 2\,b\,C_1C_3^*}}\underbrace{\sqrt{\frac{2C}{b\,[B-2\,A]}}\sqrt{\frac{\nu^*(a^* + b\,x_1^*)}{V_1^*}}}_{\delta^*}$$

$$\rightarrow \qquad \hat{\delta}^* \propto \delta^* \propto \sqrt{\frac{\nu^*(a^* + b\,x_1^*)}{V_1^*}}, \tag{4.123}$$

which is somehow proportional to the primal b.-l. thickness. Finally, one can define an adjoint similarity variable that equals the primal one, viz.

$$\hat{\eta} = \frac{x_2^*}{\hat{\delta}^*} \propto x_2^* \sqrt{\frac{V_1^*}{\nu^*(a^* + b\, x_1^*)}} = \frac{x_2^*}{\delta^*} = \eta. \tag{4.124}$$

A challenge in the interpretation of the adjoint results follows from the inverted convection characteristics of the adjoint flow field. To describe the primal b.-l. velocity, the origin of the coordinate system is typically positioned at the plate origin ($a^* = 0$, $b = 1$). However, a reasonable measurement based on the plate end is obtained for the adjoint system ($a^* = L^*$, $b = -1$). The latter motivates the negative sign in Eqn. (4.123) and indicates a formal issue for the numerical verification of the approach: Physically, the plate is assumed to extent infinitely in streamwise direction. For an adjoint approach, this is numerically uncomfortable.

Analogous to the primal derivation, an adjoint velocity field is sought that satisfies Eqns. (4.110)-(4.112) where the primal flow field is already known. Again, one has to satisfy a continuity equation. Hence an adjoint stream function $\hat{\psi}^*$ is defined that inherently complies with (4.112), e.g., $\hat{v}_1^* = \partial\,\hat{\psi}^*/\partial\, x_2^*$, $\hat{v}_2^* = -\partial\,\hat{\psi}^*/\partial\, x_1^*$, and offers access to the wall tangential adjoint velocity, viz.

$$\hat{\psi}^* = \int_0^{x_2^*} \hat{v}_1^*\, \mathrm{d}x_2^* = \int_{\hat{\eta}(0)}^{\hat{\eta}(x_2^*)} \hat{g}(\hat{\eta}) \hat{V}_1^* \hat{\delta}^*\, \mathrm{d}\hat{\eta} = \sqrt{\frac{\nu^*\,[a^* + b\, x_1^*]\,\hat{V}_1^{*2}}{V_1^*}} \underbrace{\int_0^{\hat{\eta}} \hat{g}\, \mathrm{d}\hat{\eta}}_{\hat{f}(\hat{\eta})}. \tag{4.125}$$

All adjoint b.-l. expressions can be computed from $\hat{f}$ and $\hat{\eta}$, e.g. $\partial\,\hat{v}_1^{*2}/\partial\, x_2^{*2} = \hat{V}_1^*\, V_1^*/[\nu^*(a^* + b\, x_1^*)]\hat{f}'''$. Details of the similarity transformations are provided in App. A.3. The streamwise adjoint b.-l. equation (4.110) reduces to

$$b\,[\hat{\eta} - \eta]\, f' \hat{f}'' + b f \hat{f}'' - 2\hat{f}''' = b f'' \hat{f}' \eta\,. \tag{4.126}$$

In combination with (4.124), the adjoint complement to the Blasius equation arises

$$\mathrm{R}_1^{*\hat{\mathrm{v}},\mathrm{BL}} \quad \rightarrow \quad -2\hat{f}''' + b\hat{f}'' f = b\hat{f}' f''\eta\,, \tag{4.127}$$

$$\mathrm{R}_2^{*\hat{\mathrm{v}},\mathrm{BL}} \quad \rightarrow \quad \hat{f}' f'' = 0\,. \tag{4.128}$$

The first [second] equation corresponds to the generalized tangential [normal] adjoint b.-l. equation. Interestingly, the normal adjoint momentum balance (4.128) cancels the ATC term in the corresponding tangential direction (4.127). The result is therefore similar to their primal counterpart with an inverted sign in front of the nonlinearity originating from the inverted convection characteristics. Note that the advective fluxes vanish for the investigated self-similar b.-l. flow. This conclusion supports the heuristic neglect of the term used by many authors of continuous adjoint optimization studies into complex engineering shear flows.

To pursue the *simplify-and-derive* strategy, one typically first inserts the primal simplification. As a result, however, the streamwise adjoint Blasius equation (4.127) cannot be retrieved directly from a variation of (2.122), due to the (x_1^*-nonlinear) η-based coordinate transformation inherent to the initial simplification step. A way out avoids the similarity

transformation and declares the x_2^*-derivative of the adjoint stream function $\hat{\psi}_{x_2}^* = \partial\,\hat{\psi}/\partial\,x_2^*$ as a Lagrange multiplier. The latter represents an educated guess, which follows from the previous discussions of the thesis, viz.

$$L^* = ... + \int_{\mathrm{x}_1^*}\int_{\mathrm{x}_2^*} \hat{v}_1^*\,\mathrm{R}_1^{*\mathrm{v,BL}}\,\mathrm{d}x_2^*\,\mathrm{d}x_1^*$$

$$\rightarrow \qquad L^* = ... + \int_{\mathrm{x}_1^*}\int_{\mathrm{x}_2^*} \hat{\psi}_{x_2}^*\left[\psi_{x_2}^*\psi_{x_2,x_1}^* - \psi_{x_1}^*\psi_{x_2,x_2}^* + \nu^*\,\psi_{x_2,x_2,x_2}^*\right]\mathrm{d}x_2^*\,\mathrm{d}x_1^*. \quad (4.129)$$

Using first-order optimality conditions, the adjoint equations can be derived from the stream function-based formulation (4.129) using integration by parts in Euclidean (Cartesian) space

$$\delta_{\psi_{(x_2)}}L^*\cdot\delta(\psi_{x_2}^*) = ... + \int_{\mathrm{x}_1^*}\int_{\mathrm{x}_2^*}\delta\left(\psi_{x_2}^*\right)\left[\hat{\psi}_{x_2}^*\psi_{x_2,x_1}^* - \left(\hat{\psi}_{x_2}^*\psi_{x_2}^*\right)_{x_1}\right.$$
$$\left. - \left(\hat{\psi}_{x_2}^*\psi_{x_1}^*\right)_{x_2} + \nu^*\,\hat{\psi}_{x_2,x_2,x_2}^*\right]\mathrm{d}\,x_2^*\,\mathrm{d}x_1^*\,, \quad (4.130)$$

$$\delta_{\psi_{(x_1)}}L^*\cdot\delta(\psi_{x_1}^*) = ... - \int_{\mathrm{x}_1^*}\int_{\mathrm{x}_2^*}\delta\left(\psi_{x_1}^*\right)\left[\hat{\psi}_{x_2}^*\psi_{x_2,x_2}^*\right]\mathrm{d}x_2^*\,\mathrm{d}x_1^*\,. \quad (4.131)$$

Subsequently a similarity transformation is imposed based on available primal and adjoint similarity relations, viz.

$$\delta_{f'}L^*\cdot\delta(f') = ... + \int_{\mathrm{x}_1^*}\int_{\eta}\delta(f')\left[-b\hat{f}'f''\eta + b\hat{f}''f - 2\hat{f}'''\right]\mathrm{d}\eta\sqrt{\frac{V_1^{*3}\hat{V}_1^{*2}\nu^*}{a^* + b\,x_1^*}}\mathrm{d}x_1^*$$
$$\stackrel{!}{=} 0 \qquad \forall\,\delta(f') \quad (4.132)$$

$$\delta_{f'\eta-f}L^*\cdot\delta(f'\eta - f) = ... + \int_{\mathrm{x}_1^*}\int_{\eta}\delta(f'\eta - f)\left[\hat{f}'f''\right]\mathrm{d}\eta\sqrt{\frac{V_1^{*3}\hat{V}_1^{*2}\nu^*}{a^* + b\,x_1^*}}\mathrm{d}x_1^*$$
$$\stackrel{!}{=} 0 \qquad \forall\,\delta(f'\eta - f). \quad (4.133)$$

The expressions in the square brackets correspond to the plate tangential and normal adjoint Blasius equations (4.127)-(4.128). The first terms in the respective brackets contain the first derivative $\hat{f}'$ and originate from the variation of the convection $((\delta v_{\mathrm{k}}^*)\,\partial\,v_1^*/\partial\,x_{\mathrm{k}}^*)$. These terms result in the ATC contribution to the adjoint Blasius equations. The term that inheres the second derivative $\hat{f}''$ follows from the perturbed convected primal momentum $(v_{\mathrm{k}}^*\,\partial(\delta v_1^*)/\partial\,x_{\mathrm{k}}^*)$ and switches sign due to integration by parts. The diffusion term refers to the third term in (4.132) and enters the equation analogous to the primal counterpart with a third derivative. Its self-adjoint character is underlined by its consistent sign in the adjoint and primal equations.

In line with its primal companion, the adjoint Blasius equation is numerically approximated based on a shooting method. An exemplary ©Matlab code is available at Kühl [2020]. The adjoint solution employs stored discrete values of the primal procedure. It uses the same discretization of the generalized similarity variable η as the primal system together with a similar shooting approach to compute the adjoint Blasius solution. Using $a^* = L^*$ and $b = -1$, the method aims at hitting the value $\hat{f}'_\infty = 1$ for $\eta \rightarrow \infty$ with

prescribed wall values $\hat{f}_0 = 0$ and $\hat{f}'_0 = 0$ but variable $\hat{f}''_0$ for $\eta = 0$. Similar to the primal flow, the adjoint boundary value problem is iterated to convergence until $(\hat{f}' - 1) < 10^{-8}$ is reached. The numerical results are shown by the right graph of Fig. 4.5 for two simulations that either consider or neglect the ATC term. In case of neglecting ATC, the procedure resembles the primal results. As it will be shown in the next section, the latter is expected from analytical studies. In case with ATC, the convergence of $\hat{f}'_\infty$ is shifted outwards by one order of magnitude in η and results in an increased b.-l. thickness.

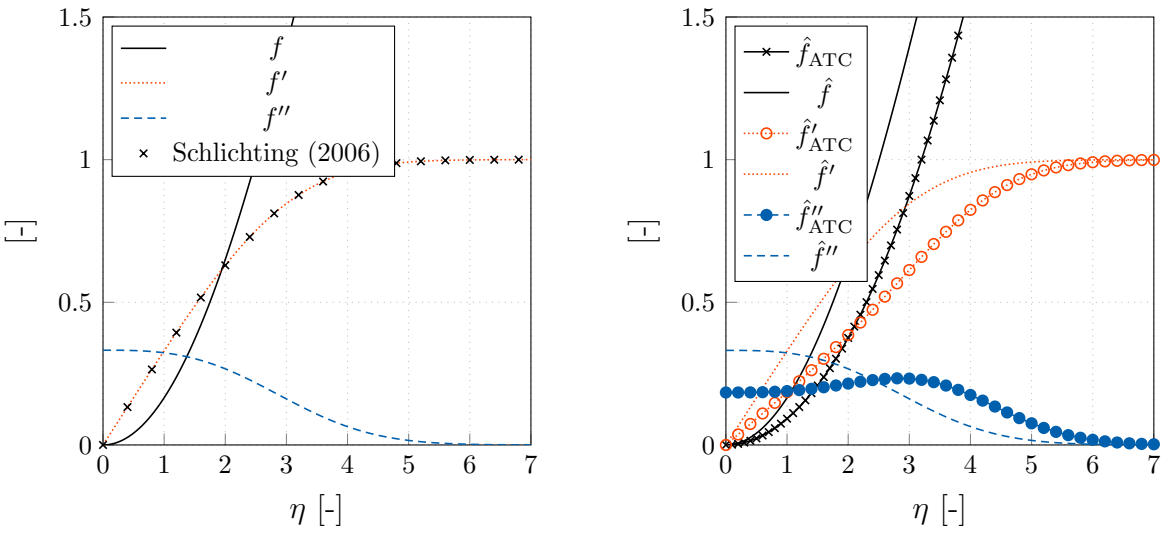

Figure 4.5: Results of a shooting method for (a) the primal and (b) the adjoint Blasius equation. Marked lines in (b) indicate adjoint results considering the adjoint transpose convection (ATC) term.

Analytical Investigation of the Adjoint Blasius Equation

Using the similarity transformation introduced above, the adjoint b.-l. Eqns. (4.110)-(4.112) were successfully transformed from PDEs into ODEs. In the absence of volume objectives that depend on the fluid velocity and pressure, Eqns. (4.127)-(4.128) are generally valid which is the case in this thesis. The derivation of the continuous adjoint equations reveals the use of Dirichlet conditions for the adjoint velocity along no-slip walls (cf. Tab. 4.1). The latter follows from the objective of interest, which, however, can occur in different forms depending on the underlying objective functional.

In the following, either a linear dependence of the cost functional w.r.t. pressure or no functional is assumed along the plate. An illustrative example refers to the evaluation of flow induced forces on the considered plate, where two options to introduce this objective are conceivable that refer to an interior or exterior formulation, cf. Sec. 3.2. Despite their differences, both formulations employ the similarity transformation to derive a generalized velocity profile, and one can define a normalized adjoint tangential velocity profile by

$$\hat{f}' = \frac{\hat{v}_1^*}{\hat{V}_1^*} \qquad \rightarrow \qquad \hat{f}' = \frac{\hat{v}_1^* - \hat{V}_1^{*\mathrm{W}}}{\hat{V}_1^{*\infty} - \hat{V}_1^{*\mathrm{W}}} \,. \tag{4.134}$$

Equation (4.134) reminds of the Blasius solution for a thermal b.-l., e.g. $-2\Theta''-\mathrm{Pr}f\Theta'=0$, where $\Theta=(T^*-T^{*\mathrm{W}})/(T^{*\infty}-T^{*\mathrm{W}})$ is a non-dimensional temperature and T^* as well as Pr represent the temperature and Prandtl number.

Influence of Adjoint Transposed Convection: Inserting the normal adjoint Blasius equation (4.128) into its tangential companion yields the adjoint Blasius Eqn. (4.127) without ATC on the r.h.s. . Choosing a b.-l. measure based on $a^*=0$ and $b=1$, one can incorporate the primal Blasius expression ($f=-2f'''/f''$) into the adjoint counterpart and conclude

$$\frac{f'''}{f''}=-\frac{\hat{f}'''}{\hat{f}''}. \tag{4.135}$$

Note that expression (4.135) agrees with an analogue relationship of the thermal b.-l., viz.

$$\frac{f'''}{f''}=\frac{1}{\mathrm{Pr}}\frac{\Theta''}{\Theta'}\,, \tag{4.136}$$

for a negative unit Prandtl number $\mathrm{Pr}=-1$, which underlines the reverse flow direction of adjoint systems. Separation of variables allows for a solution for $\hat{f}'$ as well as Θ,

$$\hat{f}'=C_1\int_0^\eta\frac{1}{f''}\mathrm{d}\eta+C_2 \qquad \text{and} \qquad \Theta=C_3\int_0^\eta\left(f''\right)^{\mathrm{Pr}}\mathrm{d}\eta+C_4\,. \tag{4.137}$$

Unfortunately, the negative unit Prandtl number of the adjoint system introduces a singularity in (4.137), since $f''\to 0$ for $\eta\to\infty$ holds for the primal system as shown in Fig. 4.5. The singularity can only be circumvented with an appropriate measure for the adjoint b.-l., viz. $a^*=L^*$ and $b=-1$. The integration constants of the adjoint velocity profile follow from the boundary conditions for $\hat{f}'(\eta\to 0)=0$ as well as $\hat{f}'(\eta\to\infty)=1$ and yield

$$C_1=\int_0^\infty f''\mathrm{d}\eta \qquad \text{and} \qquad C_2=0\,. \tag{4.138}$$

The final solution reads

$$\hat{f}'=\frac{\int_0^\eta f''\mathrm{d}\eta}{\int_0^\infty f''\mathrm{d}\eta} \qquad \rightarrow \qquad \hat{f}'=\frac{f'}{f'\left(\infty\right)-f'\left(0\right)}=f'. \tag{4.139}$$

Hence, the generalized adjoint velocity profile equals its primal counterpart when ATC is suppressed.

Estimation of Adjoint Interface Thickness and Wall Shear Stress: For known values of the Blasius solution, various statements about, e.g., b.-l. thickness or shear stress distribution can be derived that also apply to the adjoint counterparts. Assigning the primal b.-l. thickness to $v_1^*/V_1^*=0.99$, yields a value of $\eta_{99}\to 4.91\approx 5$ in line with Fig. 4.5 and Eqn. (4.124). The numerical and analytical results of the previous sections reveal the same b.-l. thickness for primal and adjoint flow, viz. $\hat{\delta}_{99}^*=\delta_{99}^*$ in case of no ATC. However, if the additional r.h.s. term is incorporated, one ends up with approximately $\hat{\eta}_{99}^*\to 5.9424\approx 6$, cf. Fig. 4.5, and thus

$$\hat{\delta}_{99}^*\approx 6\sqrt{\frac{\nu^*(a^*+b\,x_1^*)}{V_1^*}} \qquad \text{or} \qquad \frac{\hat{\delta}_{99}^*}{(a^*+b\,x_1^*)}\approx\frac{6}{\sqrt{\mathrm{Re}_{(\mathrm{a+b\,x_1})}}}. \tag{4.140}$$

In the remainder of this subsection, the estimated adjoint Blasius values refer to the formulation including ATC, and the notation $(\cdot)_\mathrm{W}$ indicates an evaluation along the wall at $\eta = 0$. Mind that neglecting the ATC yields strong similarities between the primal and the dual Blasius solutions, e.g. $\hat{f}''_\mathrm{W} = f''_\mathrm{W}$. Several primal b.-l. thickness measures exist, e.g. the displacement ($\delta^{*\mathrm{D}}$), momentum ($\delta^{*\mathrm{M}}$) and energy ($\delta^{*\mathrm{E}}$) thickness, which follow from the relation $\mathrm{d}x_2^* = \delta^* \, \mathrm{d}\eta$, cf. Eqns. (2.124)-(2.126). Similar expressions can be derived for the adjoint b.-l., viz.

$$\hat{V}_1^* \hat{\delta}^{*\mathrm{D}} = \int_0^\infty \left[\hat{V}_1^* - \hat{v}_1^*\right] \mathrm{d}x_2^* \qquad \rightarrow \quad \hat{\delta}^{*\mathrm{D}} = \int_0^1 \left[1 - \hat{f}'\right] \mathrm{d}x_2^* \approx 2.5336 \sqrt{\frac{\nu^*(a^* + b\, x_1^*)}{V_1^*}}\,, \tag{4.141}$$

$$\rho^* \, \hat{V}_1^{*2} \hat{\delta}^{*\mathrm{M}} = \rho^* \int_0^\infty \hat{v}_1^* \left[\hat{V}_1^* - \hat{v}_1^*\right] \mathrm{d}x_2^* \qquad \rightarrow \quad \hat{\delta}^{*\mathrm{M}} = \int_0^1 \hat{f}' \left[1 - \hat{f}'\right] \mathrm{d}x_2^* \approx 0.8430 \sqrt{\frac{\nu^*(a^* + b\, x_1^*)}{V_1^*}}\,, \tag{4.142}$$

$$\rho^* \hat{V}_1^{*3} \hat{\delta}^{*\mathrm{E}} = \rho^* \int_0^\infty \hat{v}_1^* \left[\hat{V}_1^{*2} - \hat{v}_1^{*2}\right] \mathrm{d}x_2^* \quad \rightarrow \quad \hat{\delta}^{*\mathrm{E}} = \int_0^1 \hat{f}' \left[1 - \hat{f}'^{,2}\right] \mathrm{d}x_2^* \approx 1.2830 \sqrt{\frac{\nu^*(a^* + b\, x_1^*)}{V_1^*}}\,. \tag{4.143}$$

The relations between primal and adjoint b.-l. thicknesses read

$$\frac{\delta^*_{99}}{\hat{\delta}^*_{99}} \approx 0.8263, \qquad \frac{\delta^{*\mathrm{D}}}{\hat{\delta}^{*\mathrm{D}}} \approx 0.6792, \qquad \frac{\delta^{*\mathrm{M}}}{\hat{\delta}^{*\mathrm{M}}} \approx 0.7878, \quad \text{and} \quad \frac{\delta^{*\mathrm{E}}}{\hat{\delta}^{*\mathrm{E}}} \approx 0.8140\,. \tag{4.144}$$

Additionally, the generalized Blasius solution offers insight into the adjoint shear stress acting on the plate

$$\hat{\tau}^*_\mathrm{W} = \mu^* \frac{\partial\, \hat{v}_1^*}{\partial x_2^*}\bigg|_{\mathrm{x}_2^*=0} = \mu^* \hat{V}_1^* \sqrt{\frac{V_1^*}{\nu^*(a^* + b\, x_1^*)}}\, \hat{f}''_\mathrm{W} \quad \rightarrow \quad \hat{\tau}^*_\mathrm{W} \approx 0.1845\, \mu^* \, \hat{V}_1^* \sqrt{\frac{V_1^*}{\nu^*(a^* + b\, x_1^*)}}. \tag{4.145}$$

The resulting dual shear is significantly smaller compared to the primal one, e.g. $\tau^*_\mathrm{W}/\hat{\tau}^*_\mathrm{W} = f''_\mathrm{W}/\hat{f}''_\mathrm{W}(V_1^*/\hat{V}_1^*)$. In line with the primal shear, its adjoint complement is non-dimensionalized via an adjoint dynamic pressure ($\hat{p}^*_\infty = \rho^* \, V_1^* \, \hat{V}_1^*/2$) to obtain skin-friction coefficients, i.e.

$$\hat{c}_\mathrm{f} = \frac{\hat{\tau}^*_\mathrm{W}}{\frac{1}{2}\rho^* \, \hat{V}_1^* \, V_1^*} = \frac{2\, \hat{f}''_\mathrm{W}}{\sqrt{\mathrm{Re}_{\mathrm{a+bx_1}}}} \qquad \rightarrow \qquad \hat{c}_\mathrm{f} \approx \frac{0.369}{\sqrt{\mathrm{Re}_{\mathrm{a+bx_1}}}}\,. \tag{4.146}$$

Moreover, known adjoint shear-stress distributions allow the integration of a total adjoint shear force on the plate

$$\hat{F}^*_\mathrm{s} = \int_{\Gamma^*} \hat{\tau}^*_\mathrm{W} \mathrm{d}\Gamma^{*\mathrm{W}} = t^* \int_0^{\mathrm{L}^*} \mu^* \frac{\partial\, \hat{v}_1^*}{\partial\, x_2^*}\bigg|_{\mathrm{x}_2^*=0} \mathrm{d}x_1^* = 2\, \hat{f}''_\mathrm{W}\, t^* \, \hat{V}_1^* \sqrt{\mu^* \, \rho^* \, V_1^*} \frac{\sqrt{a^* + b\, L^*} - \sqrt{a^*}}{b}$$

$$\rightarrow \qquad \hat{F}^*_\mathrm{s} \approx 0.369\, t^* \, \hat{V}_1^* \sqrt{\mu^* \, \rho^* \, V_1^*} \frac{\sqrt{a^* + b\, L^*} - \sqrt{a^*}}{b}, \tag{4.147}$$

where t^* corresponds to the lateral expansion of the plate. As expected, the choice of the coordinate system has no influence on the forces, since $\hat{F}_\mathrm{s}^*(a^*=0,b=1) = \hat{F}_\mathrm{s}^*(a^*=L^*,b=-1) = 2\hat{f}''_\mathrm{W}\,t^*\sqrt{\mu^*\,\rho^*\,L^*\,V_1^*\,\hat{V}_1^{*2}}$. Together with Eqn. (2.129), the ratio between primal and dual shear reads $F_\mathrm{s}^*/\hat{F}_\mathrm{s}^* = f''_\mathrm{W}/\hat{f}''_\mathrm{W}(V_1^*/\hat{V}_1^*)$. The adjoint drag coefficient can be computed either from an integration of Eqn. (4.146) or from dividing Eqn. (4.147) by the dynamic adjoint pressure times the wetted surface $L^*\,t^*$, viz.

$$\hat{c}_\mathrm{d} = \frac{\hat{F}_\mathrm{s}^*}{\hat{p}_\infty^*\,t^*\,L^*} = \frac{1}{L^*}\int_0^{L^*}\hat{c}_\mathrm{f}\,\mathrm{d}x_1^* = \frac{4\,\hat{f}''_\mathrm{W}}{\sqrt{Re_\mathrm{L}}}\frac{\sqrt{a^*+b\,L^*}-\sqrt{a^*}}{b\sqrt{L^*}}$$

$$\rightarrow \qquad \hat{c}_\mathrm{d} \approx \frac{0.738}{\sqrt{Re_\mathrm{L}}}\frac{\sqrt{a^*+b\,L^*}-\sqrt{a^*}}{b\sqrt{L^*}}\,. \qquad (4.148)$$

Except different scaling, the dual quantities resemble the well known primal relationship from Eqn. (2.130).

According to Eqn. (4.44), the combination of primal and dual shear results in a sensitivity distribution along the design surface of the shape. Analogous to the simplification of the shear objective ($J^* = F_\mathrm{s}^*$), the approach also applies to its shape sensitivity, viz.

$$s^* = -\nu^*\frac{\tau_\mathrm{W}^*}{\mu^*}\frac{\hat{\tau}_\mathrm{W}^*}{\mu^*} = -\nu^*\frac{\partial\,v_1^*}{\partial\,x_2^*}\bigg|_{\mathrm{x}_2^*=0}\frac{\partial\,\hat{v}_1^*}{\partial\,x_2^*}\bigg|_{\mathrm{x}_2^*=0} = -f''_\mathrm{W}\hat{f}''_\mathrm{W}\frac{\hat{V}_1^*V_1^{*2}}{a^*+b\,x_1^*}$$

$$\rightarrow \qquad s^* \approx -0.06127\frac{\hat{V}_1^*\,V_1^{*2}}{a^*+b\,x_1^*}\,. \qquad (4.149)$$

The local shape derivative has again singularities at the leading and trailing edge of the plate. However, the intermediate behavior scales with x^{*-1} instead of $x^{*-1/2}$. Furthermore, the local sensitivity increases quadratically with the primal but only linearly with the adjoint velocity. This reminds of the quadratic character of the primal NS equations (e.g. $v_\mathrm{k}^*(\partial\,v_\mathrm{i}^*/\partial\,x_\mathrm{k}^*)$) which is opposed by the linear nature of the adjoint counterpart (e.g. $v_\mathrm{k}^*(\partial\,\hat{v}_\mathrm{i}^*/\partial\,x_\mathrm{k}^*)$). The sensitivity expression (4.149) can be non-dimensionalized towards a sensitivity-coefficient c_s via the kinematic viscosity and the primal as well as dual dynamic pressure or by combining the primal and adjoint skin-friction coefficient, viz.

$$c_\mathrm{s} = s^*\frac{\rho^{*2}\,\nu^*}{p_\infty^*\,\hat{p}_\infty^*} = s^*\frac{4\,\nu^*}{V_1^{*3}\,\hat{V}_1^*} = -c_\mathrm{f}\,\hat{c}_\mathrm{f} = -\frac{4\,f''_\mathrm{W}\,\hat{f}''_\mathrm{W}}{\mathrm{Re}_{\mathrm{a+b\,x_1}}} \qquad \rightarrow \qquad c_\mathrm{s} \approx -\frac{0.06127}{\mathrm{Re}_{\mathrm{a+b\,x_1}}}. \qquad (4.150)$$

Finally, the integration of (4.149) along the plate provides the sensitivity derivative on an integral level

$$\delta_\mathrm{u}J^* = t^*\int_0^{L^*} s^*\,\mathrm{d}x_1^* = -f''_\mathrm{W}\,\hat{f}''_\mathrm{W}\frac{t^*\,\hat{V}_1^*\,V_1^{*2}}{b}\ln\left[\frac{a^*+b\,L^*}{a^*}\right]$$

$$\rightarrow \qquad \delta_\mathrm{u}J^* \approx -0.06127\frac{t^*\,\hat{V}_1^*\,V_1^{*2}}{b}\ln\left[\frac{a^*+b\,L^*}{a}\right]. \qquad (4.151)$$

Interestingly, a singularity arises for the integral sensitivity. Owing to the proportionality $s^* \propto x^{*-1}$, a logarithmic relationship $\delta_\mathrm{u}J^* \propto \pm(\ln(L^*) - \ln(0))$ results for the integral sensitivity. The $s^* \propto x^{*-1}$ relationship originates in the definition of the similarity variable

which in turn estimates the primal interface thickness by $\delta^* \propto x^{*1/2}$ that finally yields $s^* \propto 1/\delta^{*2}$. The singularity cannot be avoided by adjusting the coordinate system, i.e. a^* and b, since the integral bounds also need to be adjusted to a^* and b. Mind that only $a^* = 0, b = 1$ or $a^* = L^*, b = -1$ are applied in this thesis. It seems that the plate has an infinite potential to reduce its flow resistance from an integral point of view. This statement seems suspicious at first. However, mind that a disappearing plate would wipe out its resistance completely. A perturbation into the plate normal affects the drag via a variation in the local shear $\delta F^* \propto \delta f''_{\mathrm{W}}$ (cf. Eqn. (2.129)) which in turn follows from a variation in the similarity variable $\delta f''_{\mathrm{W}} \rightarrow f'''_{\mathrm{W}} \delta\eta$ that finally can be estimated via $\delta\eta \propto \delta x_2^*/\sqrt{x_1^*} - 0.5(\eta/x_1^*)\delta x_1^*$ for an interface measure that employs $a^* = 0$ and $b = 1$. Thus, $\delta F^* \propto f'''_{\mathrm{W}}[\delta x_2^*/\sqrt{x_1^*} - 0.5(\eta/x_1^*)\delta x_1^*]$ becomes singular if both coordinates tend to zero. Note that the drag as well as the similarity variable become singular at the leading edge and the influence of a plate normal variation is debatable, not least because the direction of the normal is not defined at the leading edge.

The integral shape derivative can be non-dimensionalized based on the dynamic pressures and the wetted surface. An alternative approach to a global sensitivity coefficient follows from the integration over the sensitivity coefficient, viz.

$$c_{\delta_{\mathrm{u}}\mathrm{J}} = \frac{\delta_{\mathrm{u}} J^* \, \nu^*}{p_\infty^* \, \hat{p}_\infty^* \, t^* \, L^*} = -\frac{1}{L^*} \int_0^{\mathrm{L}^*} c_{\mathrm{s}} \, \mathrm{d}x_1^* = -\frac{f''_{\mathrm{W}} \, \hat{f}''_{\mathrm{W}}}{\mathrm{Re}_{\mathrm{L}}} \frac{1}{b} \ln\left[\frac{a^* + b\,L^*}{a^*}\right]$$

$$\rightarrow \qquad c_{\delta_{\mathrm{u}}\mathrm{J}} \approx -\frac{0.06127}{\mathrm{Re}_{\mathrm{L}}} \frac{1}{b} \ln\left[\frac{a^* + b\,L^*}{a^*}\right]. \tag{4.152}$$

Verification

The adjoint investigations are performed for a drag objective ($r_{\mathrm{i}} = [1, 0]^{\mathrm{T}}$) on the basis of two different formulations referred to as interior (FI) or exterior (FE) drag-force evaluation. Additionally, simulations that neglect (A0) or employ (A1) ATC are distinguished. Thus, four adjoint computations are conducted for each primal flow from Sec. 2.3.1, where the general numerical setting is defined. The convective adjoint momentum transport is approximated using the QDICK scheme.

Unified Adjoint Velocity Profile: As shown in Sec. 4.3.1, the internal and external adjoint formulation of a force functional can be unified. To illustrate this, results obtained from an exemplary adjoint simulation at $\mathrm{Re}_{\mathrm{L}} = 10^4$ are discussed in more detail. Figure 4.6 illustrates predicted adjoint tangential velocity profiles at ten equally spaced positions along the plate for both the (FI) as well as the (FE) formulation. Both sets of exemplary results incorporate ATC (A1). As outlined in Sec. 4.3.1, the FI and FE adjoint velocity profiles reveal a similarity, since they are based on different formulations that aim at answering the same engineering question. Optically visible and numerically measurable, both adjoint velocity profile sets grow out of the plate with the same gradient. The latter enters the sensitivity along the plate ($x_2^*/L^* = 0$) according to Eqn. (4.44). In addition to the adjoint velocity profiles, the 99%-b.-l. thickness $\hat{\delta}_{99}^*$ is depicted for various formulations, viz. [FI, FE] × [A0, A1]. The trend of an increased $\hat{\delta}_{99}^*$ b.-l. thickness due to the influence of ATC (A0 vs. A1) is reproduced by the simulations, though to a lesser extent.

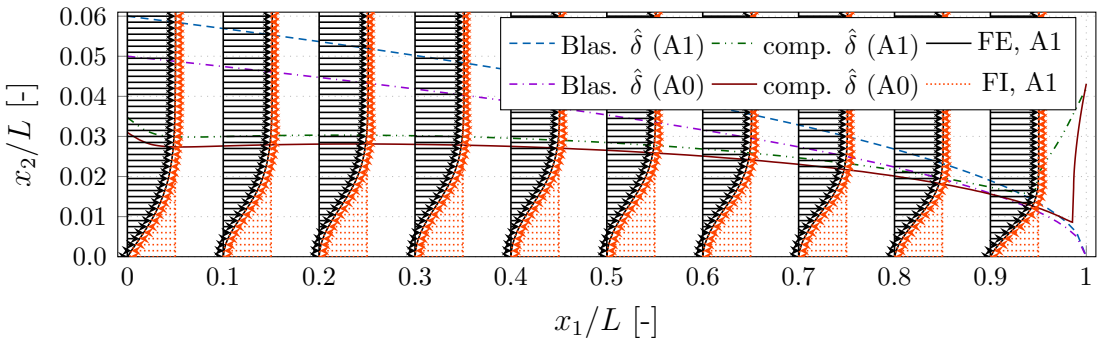

Figure 4.6: Comparison of several plate tangential adjoint velocity profiles $\hat{v}_1^*(x_2^*)$ for an external (FE, $\hat{v}_1^*(0)/\hat{V}_1^* = 0$) and internal (FI, $\hat{v}_1^*(0)/\hat{V}_1^* = -1$) drag formulation. Additionally, several adjoint 99%-b.-l. thicknesses $\hat{\delta}_{99}^*$ are depicted, augmented by the expected adjoint Blasius solutions.

Manipulated Primal Field: The investigated b.-l. contradicts the assumption of an infinitely long plate immanent to the theory, and deviations between the computed Navier-Stokes results and the Blasius solution increase towards the trailing edge of the plate. However, due to the (approximately) parabolic nature of the computed flow, deviations are primarily transported downstream and their significantly local influence documented by Fig. 2.11 has hardly any effect on an integral level, cf. Fig. 2.10. A different picture emerges for the adjoint flow. Since the adjoint solution propagates from the trailing to the leading edge, the processes reverse their direction in adjoint mode and primal flow deviations are introduced at the adjoint upstream location. Therefore, the comparison of computed and Blasius adjoint results for a plate of finite-length is afflicted by initial value deviations of the primal field and might be debatable. For this reason, the primal velocity field at $\mathrm{Re_L} = 10^4$ was manipulated by re-initialising a velocity field that follows from the similarity transformation of a computed primal velocity profile extracted at $x_1^*/L^* = 3/4$. Subsequently all four adjoint simulations were performed based on $a^* = L^*$ and $b = -1$. Figure 4.7 outlines the computed results for the normalized adjoint tangential $\hat{v}_1^*/\hat{V}_1^*$ (left) and normal $\hat{v}_2^*/\hat{V}_1^*$ (center) velocity next to the adjoint friction coefficient (right) in comparison to the Blasius solutions with (A1) and without (A0) ATC. Only minor deviations are observed when comparing the Navier-Stokes predictions for different adjoint formulations. However, an improved agreement with the Blasius solution that neglects the ATC (A0) is clearly seen. This supports the results of the similarity transformation, i.e. Eqns. (4.127)-(4.128), according to which ATC influence should disappear in laminar flat plate b.-l. flows. Analogue to the primal investigation, the plate tangential adjoint velocity profiles are closer to their companion Blasius solutions than the normal velocity profiles. However, a smaller normal velocity variation is observed between the different locations. Moreover, the manipulation of the (upstream) primal results reveals benefits for the agreement between the Blasius and the computed adjoint skin friction.

Consistent Primal Field: The final study discusses computed adjoint Navier-Stokes results based upon non-manipulated predictions of the primal flow, which are displayed in Figs. 2.10-2.11. Figure 4.8 shows the evolution of the adjoint drag-coefficient $\hat{c}_\mathrm{d}$ (left) and

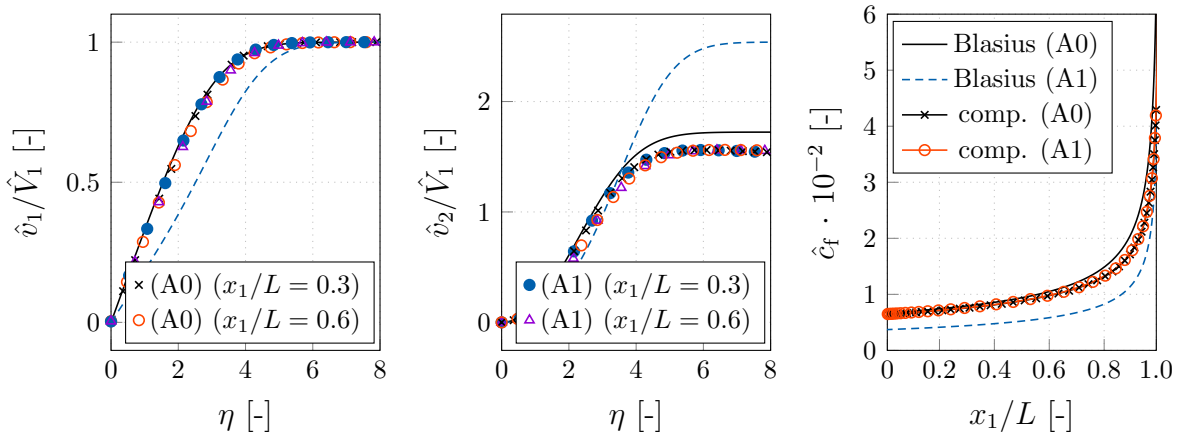

Figure 4.7: Local results for the adjoint flow over a flat plate at $\mathrm{Re_L} = 10^4$ based on a manipulated primal field: Left) tangential adjoint velocity $(\hat{v}_1^*/\hat{V}_1^*)$ against $\hat{f}'$ and center) normal adjoint velocity $(\hat{v}_2^*/\hat{V}_1^*)$ against $\hat{f}'\hat{\eta} - \hat{f}$ both over the similarity variable. Right) adjoint friction coefficient $\hat{c}_\mathrm{f}$ against the adjoint Blasius estimations based on an interface measure that employs $a^* = L^*$ and $b = -1$.

the adjoint b.-l. thickness $\hat{\delta}_{99}$ (center) over the Reynolds number for the two considered adjoint formulations (A0, A1). The adjoint b.-l. thickness is evaluated at $x_1^*/L^* = 1/4$ based on a measure that employs $a^* = L^*$ and $b = -1$. Regarding the adjoint drag coefficient, the predicted results of the formulation without ATC (A0) are again significantly closer to the corresponding Blasius results than those that include ATC (A1). As already shown in Fig. 4.6 for $\mathrm{Re_L} = 10^4$, simulations without adjoint advection result in a reduced b.-l. thickness in line with the observations of Fig. 4.5. The investigations in Sec. 4.3.1 reveal that the integral shape sensitivity scales with $1/\mathrm{Re_L}$ but approaches a singularity towards the leading edge of the plate. Therefore, no adjoint Blasius solutions are shown in Fig. 4.8 (right). Instead, the numerical results expressed by the dimensionless sensitivity coefficient are compared with two reference curves, which scale with $1/\mathrm{Re_L}$ and $1/\sqrt{\mathrm{Re_L}}$, respectively. The computed Navier-Stokes results fall in between these two reference curves, but tend to follow the inverse root relation. Due to the more singular behavior in comparison to, e.g., the adjoint drag coefficient ($\mathcal{O}(-\mathrm{Re_L^{-1}})$ vs. $\mathcal{O}(-\mathrm{Re_L^{-1/2}})$), only the range between $10^3 \leq \mathrm{Re_L} \leq 5 \cdot 10^4$ is shown. From these results, it is concluded that consistent, real (finite-length) plate investigations w.r.t. integral adjoint quantities are qualitatively in good agreement with analytical relations from Sec. 4.3.1. Quantitative discrepancies follow mainly from initial offsets due to pronounced local inaccuracies of primal results introduced in the vicinity of the (finite) end of the plate, cf. right graph of Fig. 2.11.

4.3.2 Adjoint Two-Phase Plane Couette-Flow

This section scrutinizes the adjoint of a plane Couette flow and thus continues the investigation of the primal verification study from Sec. 2.3.2. The partial access to available analytical solutions for (4.66)-(4.67) makes this case particularly interesting. This section illustrates two important aspects: a) the ill-posed nature of the adjoint VoF system and

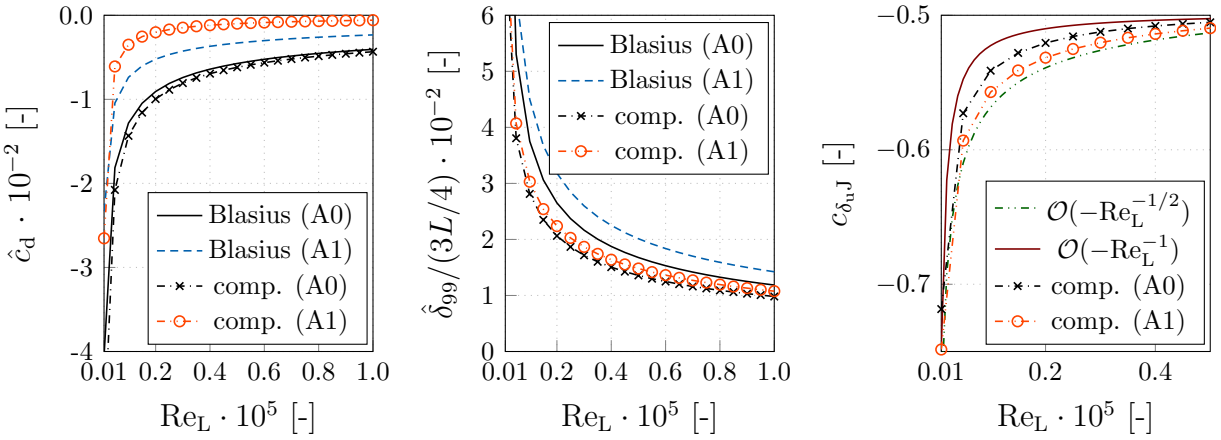

Figure 4.8: Integral results for the adjoint flow over a flat plate: Left) adjoint drag coefficient $\hat{c}_\mathrm{d}$, center) adjoint b.-l. thickness ($\hat{\delta}_{99}$) at $x/L = 1/4$ and right) integral shape sensitivity coefficient $c_{\delta_\mathrm{u}\mathrm{J}}$ over the plate length based Reynolds number $\mathrm{Re_L}$.

b) a remedy with negligible impact on the computed sensitivities that bridges towards the under-resolved adjoint CH formulation. In line with the primal verification, the Couette system is systematically divided into a sharp (VoF) and diffusive (CH) interface formulation, whereby it will become apparent that closed, non-trivial solutions are only available for the conceptual transfer of the former into the latter. The analysis is consistently performed in a dimensionless manner.

Sharp Interface (VoF) results follow from the abrupt change of fluid properties along the free surface and consistently employ $\nu^{*\mathrm{c}} = 0$ or $M^* = 0$. The corresponding adjoint Eqns. (4.67)-(4.66) belonging to a force functional can be simplified under the assumptions made for the primal flow and Eqns. (2.135)-(2.136), which resembles a *derive-and-simplify* approach. Alternatively, they can be obtained from a *simplify-and-derive* procedure via a Lagrangian based on a x_1-force objective together with (2.131)-(2.134), viz.

$$L = \int -\frac{1}{\mathrm{Re}}\mu\frac{\partial v_1}{\partial x_2}\,\mathrm{d}x_1 + \int\int \hat{v}_1\,\mathrm{R}_1^{\mathrm{v,CO}} + \hat{v}_2\,\mathrm{R}_2^{\mathrm{v,CO}} + \hat{p}\,\mathrm{R}^{\mathrm{p,CO}} + \hat{c}\,\mathrm{R}^{\mathrm{c,CO}}\,\mathrm{d}x_1\,\mathrm{d}x_2\,. \tag{4.153}$$

The application of first-order optimality conditions reveals the adjoint equations to (2.131)-(2.134). Inserting the primal Eqns. (2.131)-(2.134) finally reduces their adjoint complements to

$$\mathrm{R}_1^{\hat{\mathrm{v}},\mathrm{CO}} : -\frac{1}{\mathrm{Re}}\frac{\partial}{\partial x_2}\left[\mu\frac{\partial \hat{v}_1}{\partial x_2}\right] = 0 \tag{4.154}$$

$$\mathrm{R}_2^{\hat{\mathrm{v}},\mathrm{CO}} : \rho\,\hat{v}_1\frac{\partial v_1}{\partial x_2} - \frac{1}{\mathrm{Re}}\frac{\partial}{\partial x_2}\left[\mu\frac{\partial \hat{v}_2}{\partial x_2}\right] + \left(\frac{C}{V}\right)\frac{\partial \hat{p}}{\partial x_2} - \left(\frac{C}{V}\right)c\frac{\partial \hat{c}}{\partial x_2} = 0 \tag{4.155}$$

$$\mathrm{R}^{\hat{\mathrm{p}},\mathrm{CO}} : \mathrm{Eu}\frac{\partial \hat{v}_2}{\partial x_2} = 0 \tag{4.156}$$

$$\mathrm{R}^{\hat{\mathrm{c}},\mathrm{CO}} : \frac{\mu_\Delta}{\mathrm{Re}}\frac{\partial \hat{v}_1}{\partial x_2}\frac{\partial v_1}{\partial x_2} + \frac{\rho_\Delta}{\mathrm{Fn}^2}\left[\hat{v}_1\,g_1 + \hat{v}_2\,g_2\right] = 0\,. \tag{4.157}$$

where the product between primal and adjoint concentration is active in the upper fluid, $\alpha^{\mathrm{c}} = 0$ (cf. Eqn. (4.90)). As opposed to the primal system, additional coupling terms occur in the transverse momentum ($\hat{R}_2$) and the concentration balance ($\hat{C}$). Similar to the primal problem, the adjoint velocity and pressure could be determined from the two momentum equations provided that the adjoint concentration is known. However, the adjoint concentration equation does not support the determination of $\hat{c}$, but restricts the adjoint velocity further towards a constant. Moreover, the product between the normal gradients of the adjoint and the primal velocities refers to the sensitivity which vanishes according to Eqn. (4.66). Integration by parts of the varied concentration convection would draw the derivative from the adjoint to the primal concentration, which in this case tends toward an infinitely large [small] value along the phase transition [bulk phases]. Mind, that the adjoint equations and their solution depend on the underlying objective functional. However, a general objective does not inhere the adjoint concentration and would not meaningfully improve the r.h.s. towards an accessible solution. Using a force objective, the boundary values of the adjoint velocity are assigned to unity in the negative direction of the minimized force along the objective boundaries and zero in all other cases. This would indeed allow for a solution of the adjoint velocity and formally also $\hat{p}$, but does still not provide a solution for the adjoint concentration, which in turn might impair the solution for the pressure. The problem is admittedly motivated by the chosen unidirectional shear flow example, which, however, is fairly relevant in practical situations.

The ill-posed nature of the problem is related to the grossly simplified inter-phase physics of the VoF procedure. The vanishing substantial change of the VoF approach $\mathrm{d}\,c/\mathrm{d}\,t^* = 0$ is inherently satisfied in the underlying Couette case, so that the primal concentration field does not follow from an equation condition enclosed by boundary conditions but has only an intuitive prescribed field distribution. Related problems are inhibited by subtracting an additional adjoint diffusion term $\mathcal{D}_{\hat{c}}$ on the l.h.s. of the adjoint concentration Eqn. (4.66), viz.

$$\mathcal{D}_{\hat{c}} = \nu^{\hat{c}} \frac{\partial^2 \hat{c}}{\partial x_k^2}\,, \tag{4.158}$$

where $\nu^{\hat{c}} = \nu^{*\hat{c}}\,\rho^{*\mathrm{b}}/\mu^{*\mathrm{b}}$. The heuristic approach needs further justification and involves an artificial kinematic viscosity $\nu^{*\hat{c}}$ of dimension $[m^2/s]$ which remains a free parameter. The suggested modification essentially borrows an element of the CH model which builds the bridge towards the diffuse-interface models.

Diffuse Interface (CH) models describe the desired phase separation by the use of a nonlinear viscosity, cf. (2.57) and Fig. 2.2). In the limit of a vanishing interface thickness, the CH-VoF equation of the primal mixture fraction reads $\mathrm{d}\,c/\mathrm{d}\,t^* = \partial/\partial\, x^*_{\mathrm{k}}[\nu^{*\mathrm{c}}(\partial\, c/\partial x^*_{\mathrm{k}})]$. Here M^* is a spatially constant mobility factor of dimension $[\mathrm{m}^2/\mathrm{s}]$, which is assigned to an empirically chosen or numerically measured value, cf. Sec. 2.2.9. The gradient diffusion displays a nonlinear normalized diffusivity $\nu^{*\mathrm{c}}/M^* = 2\,(6\,c^2 - 6\,c + 1)$, which is part of a potential and exposed to sign changes. It is zero at $c = 0.5 \pm \sqrt{1/12}$, positive in outer regime and negative in between the zeros, cf. Fig. 2.2 (b). The sign change promotes the desired phase separation. This avoids the need for compressive, downwind-biased approximations of convective kinematics to separate the two fluids, which is inherent to VoF. Mind that downwinding also refers to the introduction of negative diffusion. The related CH-solution

for the mixture fraction should closely resemble the VoF solution, which is strictly speaking confined to zero or unity values. In the limit of immiscible fluids, the linearized diffusivity $\nu^{*\hat{c}}$ obtained from a frozen concentration field approach of a CH-model would be positive and identical for the two limit states of c.

The modified adjoint concentration equation for the simplified Couette flow takes the following dimensionless residual form

$$\mathrm{R}^{\hat{\mathrm{c}},\mathrm{CO}} : \frac{\mu_\Delta}{\mathrm{Re}} \frac{\partial v_1}{\partial x_2} \frac{\partial \hat{v}_1}{\partial x_2} - \frac{\rho_\Delta}{\mathrm{Fn}^2} \hat{v}_1 g_1 - \left(\frac{\mathrm{C}^*}{\mathrm{V}^*} \right) \frac{\nu^{\hat{c}}}{\mathrm{Re}} \frac{\partial^2 \hat{c}}{\partial {x_2}^2} = 0 \,. \tag{4.159}$$

The introduction of the additional diffusion term supports an analytical description of the adjoint concentration field: Due to the viscosity jump along the phase boundary, four integration constants have to be determined. Since the synthetic viscosity is constant, it is possible to achieve a smooth solution in the entire field by means of zero and first-order coupling conditions along the phase transition regime. The third unknown is computed based on a Neumann condition on the upper channel side. However, the break of dual consistency in the domain has to be continued also at the boundary: The introduction of the diffusive term in Eqn. (4.159) requires at least one Dirichlet boundary condition to determine all integration constants. This is contrary to the demand of adjoint analysis, which requires the invariable use of Neumann boundary conditions at walls (cf. Tab. 4.1). For this reason, a Dirichlet value is prescribed on the bottom of the channel for the adjoint concentration, which does not change the qualitative curve, but forces a quantitative fixation. Mind that this is also the case for the primal and adjoint pressure. It is justifiable since the adjoint concentration enters the adjoint momentum balance based on its gradient.

The solution of the adjusted adjoint system can be constructed as follows: The internal force functional (3.7) enters the adjoint system via the optimization direction that is defined in main flow direction $r_\mathrm{i} = \delta_{\mathrm{i}1}$. Thus, the boundary condition for the adjoint velocity reads $\hat{v}_{\mathrm{bottom},1} = -1$ on the lower and $\hat{v}_{\mathrm{top},1} = 0$ on the upper channel side. Likewise, adjoint pressure and adjoint concentration are prescribed on the lower channel wall, whereas Neumann conditions are imposed on top of the channel. An integration provides the following analytical solution of the entire system

$$0 \leq x_2 < \frac{1}{2} : \begin{cases} \hat{v}_1 = P_\mathrm{b} x_2 - 1 \\ \hat{p} = -\frac{V}{C} \left[\frac{1}{3} P_\mathrm{b} T_\mathrm{b} {x_2}^3 + \frac{1}{2} \left(P_\mathrm{b} C_{1\mathrm{b}} - T_\mathrm{b} \right) {x_2}^2 - C_{1\mathrm{b}} x_2 \right] + C_{6\mathrm{b}} \\ \hat{v}_2 = 0 \\ \hat{c} = L_\mathrm{b} \left[\frac{\mu_\Delta}{\mu_\mathrm{b}} \left(\frac{1}{6} T_\mathrm{b} {x_2}^3 + \frac{1}{2} C_{1\mathrm{b}} {x_2}^2 \right) + \frac{\rho_\Delta}{\rho_\mathrm{b}} T_\mathrm{b} \left(\frac{1}{6} {x_2}^3 - \frac{1}{2 P_\mathrm{b}} {x_2}^2 \right) \right] + C_{4\mathrm{b}} x_2 + C_{5\mathrm{b}} \end{cases} \tag{4.160}$$

$$\frac{1}{2} < x_2 \leq 1 : \begin{cases} \hat{v}_1 = P_\mathrm{a} \left(x_2 - 1 \right) \\ \hat{p} = \hat{c} - \frac{V}{C} \frac{\rho_\mathrm{a}}{\mu_\mathrm{a}} P_\mathrm{a} \left[\frac{1}{3} T_\mathrm{a} {x_2}^3 + \frac{1}{2} \left(C_{1\mathrm{a}} - T_\mathrm{a} \right) {x_2}^2 - C_{1\mathrm{a}} x_2 \right] + C_{6\mathrm{a}} \\ \hat{v}_2 = 0 \\ \hat{c} = L_\mathrm{a} \left[\frac{\mu_\Delta}{\mu_\mathrm{a}} \left(\frac{1}{6} T_\mathrm{a} {x_2}^3 + \frac{1}{2} C_{1\mathrm{a}} {x_2}^2 \right) + \frac{\rho_\Delta}{\rho_\mathrm{b}} T_\mathrm{b} \left(\frac{1}{6} {x_2}^3 - \frac{1}{2} {x_2}^2 \right) \right] + C_{4\mathrm{a}} x_2 + C_{5\mathrm{a}} \end{cases} \tag{4.161}$$

with the following integration constants

$$C_{4\mathrm{a}} = -L_{\mathrm{a}}\left[\frac{\mu_\Delta}{\mu_{\mathrm{a}}}\left(\frac{1}{2}T_{\mathrm{a}} + C_{1\mathrm{a}}\right) - \frac{1}{2}T_{\mathrm{b}}\rho_\Delta\right], \qquad C_{5\mathrm{b}} = 0\,, \qquad C_{6\mathrm{b}} = 0\,, \tag{4.162}$$

$$C_{4\mathrm{b}} = -L_{\mathrm{a}}\left[\frac{\mu_\Delta}{\mu_{\mathrm{a}}}\left(\frac{3}{8}T_{\mathrm{a}} + \frac{1}{2}C_{1\mathrm{a}}\right) - \frac{1}{8}T_{\mathrm{b}}\rho_\Delta\right] - L_{\mathrm{b}}\left[\frac{\mu_\Delta}{\mu_{\mathrm{b}}}\left(\frac{1}{8}T_{\mathrm{b}} + \frac{1}{2}C_{1\mathrm{b}}\right) + T_{\mathrm{b}}\rho_\Delta\left(\frac{1}{8} - \frac{1}{2P_{\mathrm{b}}}\right)\right], \tag{4.163}$$

$$C_{5\mathrm{a}} = L_{\mathrm{a}}\left[\frac{\mu_\Delta}{\mu_{\mathrm{a}}}\left(\frac{1}{24}T_{\mathrm{a}} + \frac{1}{8}C_{1\mathrm{a}}\right) - \frac{1}{12}T_{\mathrm{b}}\rho_\Delta\right] - L_{\mathrm{b}}\left[\frac{\mu_\Delta}{\mu_{\mathrm{b}}}\left(\frac{1}{24}T_{\mathrm{b}} + \frac{1}{8}C_{1\mathrm{b}}\right) - T_{\mathrm{b}}\rho_\Delta^*\left(\frac{1}{24} - \frac{1}{8P_{\mathrm{b}}}\right)\right], \tag{4.164}$$

$$C_{6\mathrm{a}} = -\frac{\mathrm{V}^*}{\mathrm{C}^*}\left[\frac{1}{24}P_{\mathrm{b}}T_{\mathrm{b}} + \frac{1}{8}\left(P_{\mathrm{b}}C_{1\mathrm{b}} - T_{\mathrm{b}}\right) - \frac{1}{2}C_{1\mathrm{a}} - \frac{\rho_{\mathrm{a}}}{\mu_{\mathrm{a}}}P_{\mathrm{a}}\left[\frac{1}{24}T_{\mathrm{a}} + \frac{1}{8}\left(C_{1\mathrm{a}} - T_{\mathrm{a}}\right) - \frac{1}{2}C_{1\mathrm{a}}\right]\right] - \hat{c}\Big|_{x_2=\frac{1}{2}} \tag{4.165}$$

as well as the upcoming abbreviations

$$P_{\mathrm{a}} = \frac{2\mu_{\mathrm{b}}}{\mu_{\mathrm{a}} + \mu_{\mathrm{b}}}, \qquad L_{\mathrm{a}} = \frac{1}{\nu^{\hat{c}}}\frac{\mathrm{V}^*}{\mathrm{C}^*}P_{\mathrm{a}}, \tag{4.166}$$

$$P_{\mathrm{b}} = \frac{2\mu_{\mathrm{a}}}{\mu_{\mathrm{a}} + \mu_{\mathrm{b}}}, \qquad L_{\mathrm{b}} = \frac{1}{\nu^{\hat{c}}}\frac{\mathrm{V}^*}{\mathrm{C}^*}P_{\mathrm{b}}\,. \tag{4.167}$$

Interestingly, the solution of the adjoint velocity and therefore also the sensitivity does not depend on L_{a} or L_{b} and is by far less tedious compared to the solution of the adjoint concentration and the adjoint pressure. Thus, the mobility parameter that scales the heuristic diffusivity $\nu^{\hat{c}}$ only governs the adjoint hydrostatic field. In the limit of vanishing diffusivity $\nu^{\hat{c}}$, one would impose a very large sink term while approaching the wall, which would challenge the numerical solution of the adjoint pressure and the adjoint concentration in the upper fluid regime, where the adjoint pressure sees the adjoint concentration abruptly. Mind that one can shift the active region of $\hat{c}$ in accordance to Eqn. (4.90). The disappearance of the constants T_{a} and T_{b} for $g_1 \to 0$ (or $\hat{v}_{\mathrm{i}}g_{\mathrm{i}} \to 0$), which strongly simplifies the solutions of adjoint concentration and adjoint pressure due to the cancellation of all cubic terms in the analytic solutions, supports the regularization characteristics of the synthetic viscosity.

Hence, manipulated adjoint VoF and consistent adjoint under-resolved CH formulations differ slightly w.r.t. the diffusivity which is inherently constant for VoF and partly spatially variable along the interface transition regime in terms of CH. If positive, the additional diffusive contribution can be treated implicitly, resulting in a positive impact on the main diagonal of the system matrix that supports the balance for vanishing Reynolds/Froude numbers or under extreme strain rates when different fluid properties occur. The minimal associated break of dual consistency provides a strongly regularized adjoint system.

Verification

The adjoint verification essentially continues the primal sharp interface study, cf. Sec. 2.3.2. The gravitational inclination refers to 10° and the same Reynolds- and Froude

number are employed. The adjoint solutions based on the primal verification cases are computed for an exemplary heuristic viscosity of $\nu^{\hat{c}} = 10^{-3}$. Again, periodic boundary conditions are used in longitudinal direction. In contrast to the primal problem, adjoint field quantities are specified on the lower channel side, where the adjoint velocity is assigned to $\hat{v}_{\text{bottom},1} = -\delta_{1,1} = -1$. Dirichlet values for adjoint pressure and concentration are set to zero at the bottom wall. The adjoint momentum equation utilizes a first-order DDS and the adjoint concentration employs the adjoint HRIC scheme (4.96) to approximate convective fluxes. Figure 4.9 verifies the implementation of the adjoint system against the analytical solutions (4.160, 4.161). The resulting adjoint concentration is smooth in the

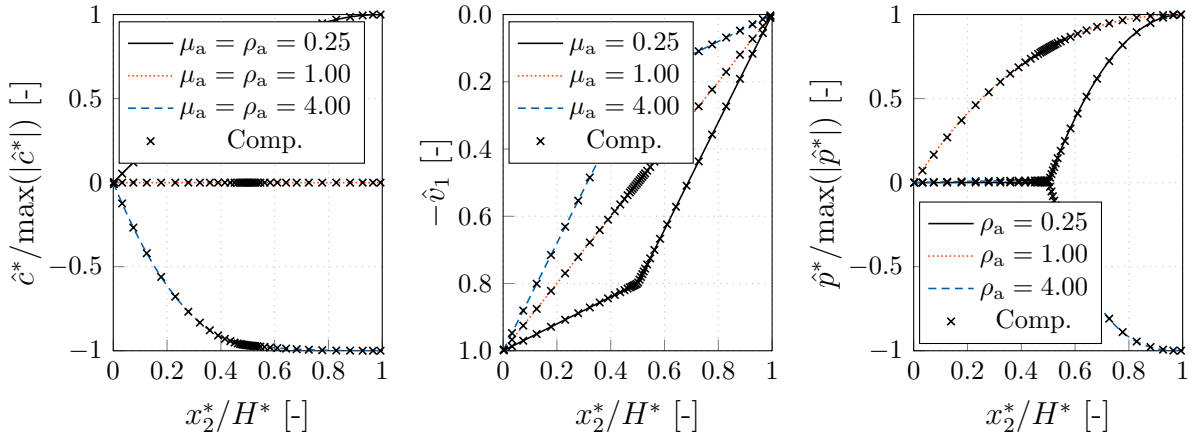

Figure 4.9: Plane Couette flow case ($\text{Re}_\text{H} = 100$, $\text{Fn} = 5$): Adjoint results of the planar Couette flow for a synthetic viscosity of $\nu^{\hat{c}} = 10^{-3}$ for Froude and Reynolds number of $\text{Fn} = 5$ and $\text{Re}_\text{H} = 100$ as well as density (viscosity) ratios of $\rho_\text{a} = \rho_\text{a}^*/\rho_\text{b}^* = 1/4$ ($\mu_\text{a} = \mu_\text{a}^*/\mu_\text{b}^* = 1/4$), $\rho_\text{a} = 1$ ($\mu_\text{a} = 1$) and $\rho_\text{a} = 4$ ($\mu_\text{a} = 4$) under a gravity angle of $\varphi = 10°$.

entire domain, whereas the adjoint pressure buckles along the free surface region. This can be attributed to the abrupt introduction of the adjoint concentration to the upper fluid domain in accordance with $\alpha^\text{c} = 0$. However, introducing a (heuristic) viscosity attenuates the adjoint concentration magnitude, thus a larger value of $\nu^{\hat{c}}$ smoothens the solution of the adjoint pressure. In Fig. 4.10, the synthetic viscosity is increased step by step to underline its regularizing characteristics w.r.t. the adjoint pressure. This is especially relevant for real world flows, in which adjoint pressure-velocity coupling is a critical aspect of the numerical stability, cf. Fig. 4.22.

4.3.3 Adjoint Universal Law of the Wall for Turbulent Flows

The last verification case studies the adjoint of the universal LoW for momentum b.-l., which is especially relevant for the consistent implementation of adjoint wall functions. The adjoint complement to the LoW (2.152) also follows the two-layer approach. In line with Sec. 4.1.8 or Eqn. (2.149), an adjoint unidirectional shear flow and a constant adjoint shear stress are obtained, viz.

$$\frac{\mathrm{d}\,\hat{\tau}^{*\text{eff}}}{\mathrm{d}\,x_2^*} = 0\,, \qquad \rightarrow \qquad \hat{\tau}^{*\text{eff}} = \hat{\tau}_\text{l}^* + \hat{\tau}_\text{t}^* = (\mu^* + \beta\mu_\text{t}^*)\frac{\mathrm{d}\,\hat{v}_1}{\mathrm{d}\,x_2^*} = \text{const.} =: \rho^*\,\hat{V}_{1,\tau}^{*2}\,. \tag{4.168}$$

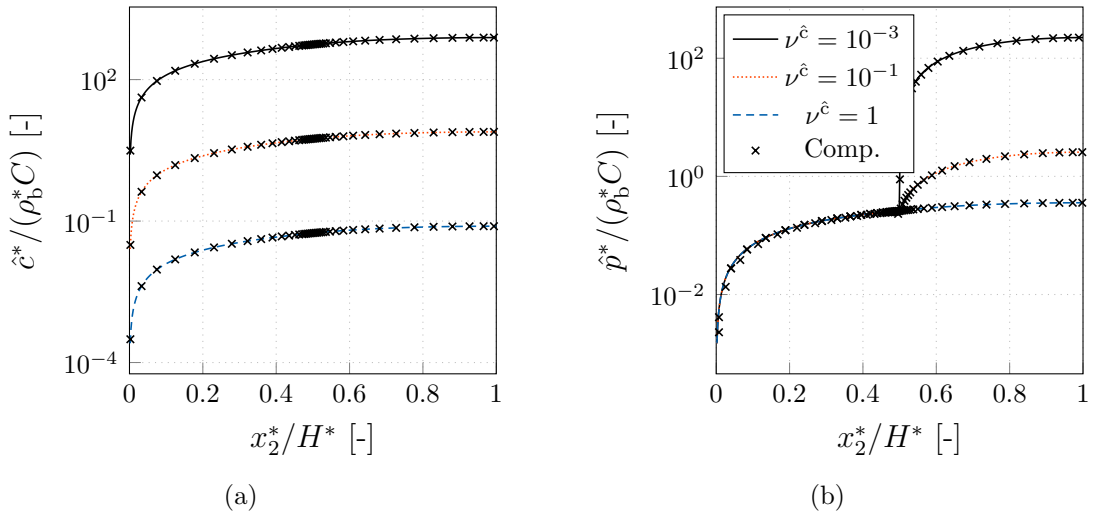

Figure 4.10: Plane Couette flow case ($\mathrm{Re_H} = 100$, $\mathrm{Fn} = 5$): Numerical and analytical results of (a) adjoint concentration and (b) adjoint pressure of the planar Couette flow for different (synthetic) viscosity magnitudes that indicates the regularization characteristics of the heuristic modification.

Equation (4.168) utilizes a coefficient β to switch between the frozen (F; $\beta = 1$) and the consistent (C; $\beta = 2$) algebraic approach, cf. (4.53). Along the route of the primal flow, the adjoint stress $\hat{\tau}^{*\mathrm{eff}}$ is assumed to be proportional to the square of an adjoint friction velocity $\hat{V}_{1,\tau}^*$. The two layer model inherited from the primal flow restricts the effective viscosity of the viscous layer ($\mu_t^*/\mu^* \to 0$) and the logarithmic layer ($\mu^*/\mu_t^* \to 0$). Analogue to the primal derivation, Eqn. (4.168) is integrated separately for both cases

$$x_2^* \leq \tilde{x}_2^* : \quad \hat{V}_{1,\tau}^{*2} = \nu^* \frac{\mathrm{d}\,\hat{v}_1^*}{\mathrm{d}\,x_2^*} \quad \to \quad \hat{v}_1^* = \frac{\hat{V}_{1,\tau}^{*2}}{\nu^*} x_2^* + \hat{C}_1^* \,, \tag{4.169}$$

$$x_2^* \geq \tilde{x}_2^* : \quad \hat{V}_{1,\tau}^{*2} = \beta\,(\kappa\, x_2^*)^2 \frac{\mathrm{d}\,v_1^*}{\mathrm{d}\,x_2^*} \frac{\mathrm{d}\,\hat{v}_1^*}{\mathrm{d}\,x_2^*} \quad \to \quad \hat{v}_1^* = \frac{1}{\beta} \left(\frac{\hat{V}_{1,\tau}^*}{V_{1,\tau}^*} \right) \frac{\hat{V}_{1,\tau}^*}{\kappa} \ln(x_2^*) + \hat{C}_2^* \,. \tag{4.170}$$

Note that the primal velocity gradient in the logarithmic regime $\mathrm{d}\,v_1^*/\mathrm{d}\,x_2^*$ is replaced by $V_{1,\tau}^*/(\kappa\, x_2^*)$ to solve for the adjoint tangential velocity. Applying a similar adjoint velocity normalization, i.e. $\hat{v}_1^+ \coloneqq \hat{v}_1^*/\hat{V}_{1,\tau}^*$, yields a compact form of the adjoint LoW similar to (2.152), viz.

$$\hat{u}^+ = \begin{cases} x_2^+ \frac{\hat{V}_{1,\tau}^*}{V_{1,\tau}^*} + \frac{\hat{v}_1^{*\mathrm{W}}}{\hat{V}_{1,\tau}^*} & \text{for } x_2^+ < \tilde{x}_2^+ \\ \frac{1}{\beta\,\kappa} \ln\left(x_2^+\right) \left(\frac{\hat{V}_{1,\tau}^*}{V_{1,\tau}^*} \right) + \hat{B} & \text{for } x_2^+ \geq \tilde{x}_2^+ \end{cases} . \tag{4.171}$$

Despite a possible shift due to non-intuitive boundary conditions, the adjoint LoW resembles the primal counterpart scaled by the friction velocity ratio ($\hat{V}_\tau^*/V_\tau^*$) and employs half the logarithmic inclination by the parameter β for the consistent approach.

Since the adjoint field quantities are mathematically motivated, their adjoint boundary conditions enter the integration constants in Eqns. (4.169)-(4.170). Depending on the objective under investigation, the adjoint velocity potentially experiences a non-zero boundary condition along no-slip walls, hence $\hat{C}_1^* = \hat{v}_1^{*\mathrm{W}}$, e.g., $\hat{C}_1 = -1$ if the internal

shear stress objective (3.7) is considered. The piece-wise continuous transition from the sub- towards the logarithmic layer is ensured by an appropriate value of $\hat{C}_2^*$. The latter is reformulated into $\hat{B}$ as an adjoint counterpart of the primal B, viz.

$$\tilde{x}_2^+ \frac{\hat{V}_{1,\tau}^*}{V_{1,\tau}^*} + \frac{\hat{v}_1^{*\mathrm{W}}}{\hat{V}_{1,\tau}^*} \stackrel{!}{=} \frac{1}{\beta\,\kappa} \ln\left(\tilde{x}_2^+\right) \frac{\hat{V}_{1,\tau}^*}{V_{1,\tau}^*} + \hat{B} \qquad \text{and} \qquad \tilde{x}_2^+ \stackrel{!}{=} \frac{1}{\kappa} \ln\left(\tilde{x}_2^+\right) + B\,. \tag{4.172}$$

Hence, the adjoint $\hat{B}$ follows from the primal B augmented by a constant shift in line with the prescribed boundary condition for the adjoint velocity

$$\hat{B} = \frac{\hat{v}_1^{*\mathrm{W}}}{\hat{V}_{1,\tau}^*} + \frac{\hat{V}_{1,\tau}^*}{V_{1,\tau}^*} \left[\frac{B}{\beta} + \tilde{x}_2^+ \left(1 - \frac{1}{\beta}\right) \right] . \tag{4.173}$$

Verification

The general numerical setup is already defined in Sec. 2.3.3. The convective term for adjoint momentum is approximated using the QDICK scheme.

Figure 4.11 depicts the result of the low-Re studies. For all investigated Reynolds numbers, the results are in fair predictive agreement with the respective LoW (2.152) and (4.171). All results feature a narrow buffer layer region triggered by the employed van-Driest term. Figure 4.12 depicts the results obtained for the high-Re simulations. It is

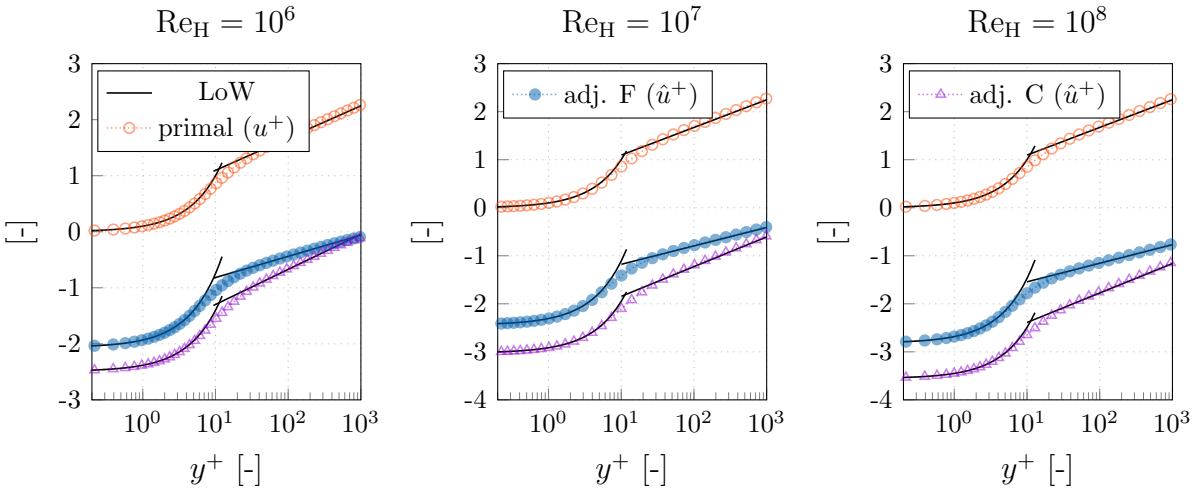

Figure 4.11: Comparison of predicted primal and adjoint velocity profiles using the frozen turbulence (F) as well as the LoW-consistent (C) approach for a turbulent channel flow at Reynolds numbers between $10^6 \leq \mathrm{Re_H} \leq 10^8$, increasing from left to right (low-Reynolds formulation).

seen, that the logarithmic layer branch of the two solutions (2.152) and (4.171) is again matched fairly accurate in combination with a $k^* - \varepsilon^*$ BVM and one can conclude, that the adjoint LoW for momentum is compatible with the above suggested approach.

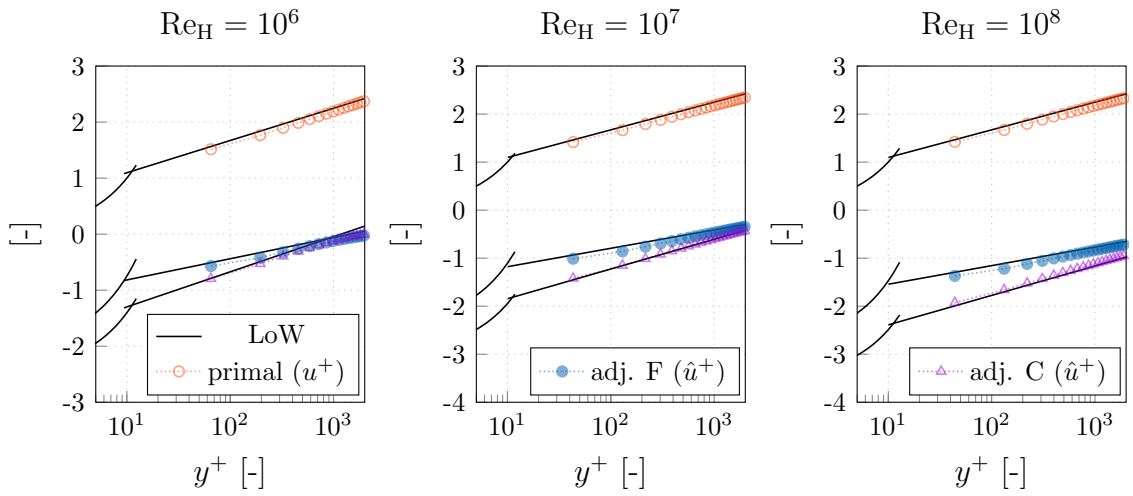

Figure 4.12: Comparison of predicted primal and adjoint velocity profiles using the frozen turbulence (F) as well as the LoW-consistent (C) approach for a turbulent channel flow at Reynolds numbers between $10^6 \leq \mathrm{Re_H} \leq 10^8$, increasing from left to right (high-Reynolds formulation).

4.4 Adjoint Flow Validation

More complex situations are investigated for validation purposes after the successful verification of the adjoint implementation. Hence, whereas the previous section showed that the *adjoint equations are solved correctly*, this section investigates if the *correct adjoint equations are solved*. The fundamental goal of the adjoint analysis in this work is to determine a shape sensitivity rule along the controlled wall region. The following studies investigate precisely Eqns. (4.44,4.53) and are distinguished based on whether the respective validation study aims at the local [global] integrand [integral] of the sensitivity derivative.

The discussion begins with a laminar single-phase flow and then steadily increases in flow complexity. In the absence of flow turbulence, the laminar single- and two-phase flows should reveal consistent adjoint-based shape derivatives, which in turn gives rise to their comparison against sensitivity derivatives based on alternative (discrete) methods, e.g. based on a FD study, cf. Eqn. (3.3). In all FD cases, the local boundary perturbations are embedded in the LB metric and transported based on the Laplacian mesh deformation Eqn. (3.29) into the (normal) interior domain as well as based on a Gaussian filter with a width of 4 times the discrete surface element width into the (tangential) neighborhood, cf. Kröger and Rung [2015], Kühl et al. [2019]. The turbulent flows of increased complexity towards the end of this section compare the adjoint-based shape sensitivity on integral level based on several complete shape optimization cycles according to Alg. 3. Each optimization employs the same surface metric and the same step size per respective geometry to ensure their reliability.

4.4.1 Laminar Boundary-Layer

The initial validation case continues the verification studies of the primal and adjoint (Blasius) b.-l. flows and thus employs the same numerical grid (Fig. 2.9) and discretization, cf. Sec. 2.3.1 and 4.3.1. The study aims at a) the agreement of the continuous adjoint shape derivative with discrete FD results and b) a deeper insight into the influence of the ATC term. The similarity solutions have shown that the neglect of the ATC term is admissible for infinitely long plates. Technical flows, however, address real, finite plates. As a consequence, their shape derivative w.r.t. a drag objective based on an adjoint formulation with and without ATC is validated against FD results.

Figure (4.13) (a) depicts the results of two adjoint sensitivity evaluations for a drag objective into the direction $r_\mathrm{i} = \delta_{1\mathrm{i}}$ where the adjoint formulations differ in their treatment of the advective adjoint momentum transport. The first approach includes the ATC term and thus corresponds to a fully consistent formulation. The second simulation leans on the results of the similarity transformation, neglects the ATC influence and therefore represents a break of the dual consistency for the considered real plate. Due to the singularity in the primal and dual shear, only the region between $0.1 \leq x_1^*/L^* \leq 0.9$ is presented. Additionally, results of 17 FD-studies are marked at the discrete positions obtained from 34 additional simulations using a perturbation size of $\epsilon^*/L^* = 10^{-5}$, cf. (3.3). The consistent adjoint sensitivity that incorporates ATC agrees almost perfectly with the discrete FD results. The linearity of the FD-analysis has been verified using a sequence of three perturbation magnitudes. An exemplary documentation of the linear system answer is displayed in Fig. 4.13 (b), which refers to an exemplary plate position $x_1^*/L^* = 1/2$.

The ATC term resembles an adjoint momentum source which flows back over the plate

due to the opposite convection direction, resulting in the quantitative difference between both formulations that disappears for infinitely long plates ($\partial\, v_\mathrm{i}^*/\partial\, x_1^* \to 0$) only. However, both shape derivatives appear qualitatively similar and therefore affine to each other. The difference resembles a quantitative shift pronounced towards the singular leading edge, which in turn can be treated based on reduced step sizes within a steepest descent optimization procedure. Although the findings are not provably valid for more complex flows, e.g., turbulent b.-l. or separated flows, they might still be indicative for attached boundary-layers and other virtually unidirectional shear flows.

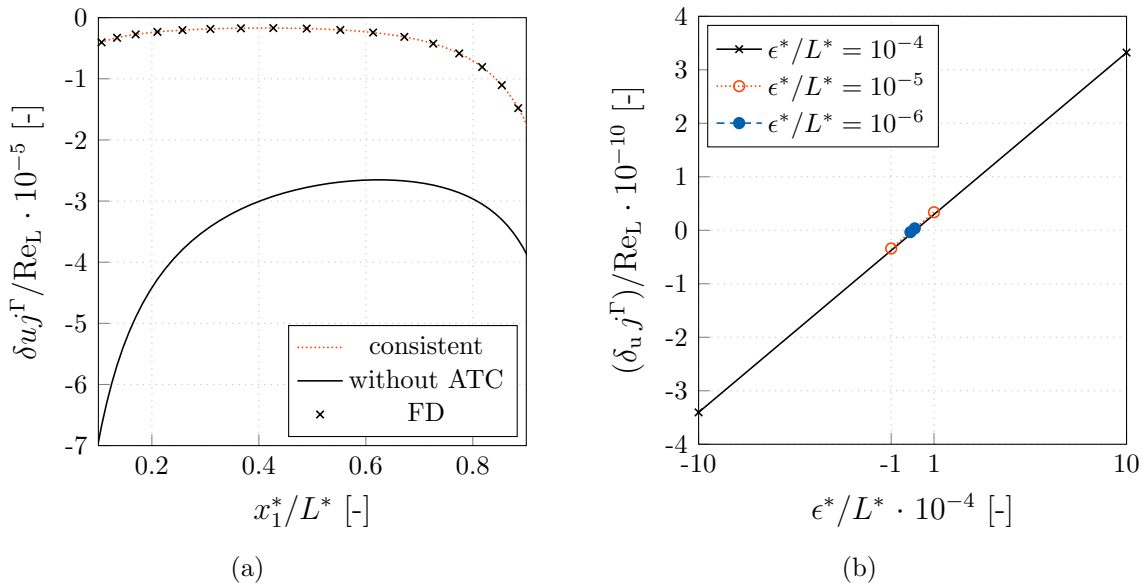

Figure 4.13: Flat plate case ($\mathrm{Re_L} = 10^4$): (a) Continuous adjoint-based drag sensitivity with and without ATC, superposed by several local finite-difference results and (b) three exemplary finite system answers at $x_1^*/L^* = 1/2$.

4.4.2 Submerged Cylinder

The second test case remains in the laminar regime but introduces a second fluid phase. The exercise aims to a) validate the correctness of the two-phase flow system against FD results for b) different values of the stabilizing apparent viscosity. In addition, the c) local and d) global influence of the different adjoint two-phase coupling terms will be systematically investigated on two different cost functionals.

A cylindrical shape is placed twice its diameter D^* below the initial free surface, cf. Fig. 4.14 (a). The study is performed at $\mathrm{Re_D} = v_1^* D^*/\nu^{*\mathrm{b}} = 20$ and $\mathrm{Fn} = v_1^*/\sqrt{G^*\, 2\, D^*} = 0.75$, based on the gravitational acceleration G^*, the inflow velocity v_1^* and the kinematic viscosity of the water $\nu^{*\mathrm{b}}$. The two-dimensional domain has a length and height of $60\, D^*$ and $30\, D^*$, where the inlet and bottom boundaries are located 20 diameters away from the origin. A dimensionless wave length of $\lambda = \lambda^*/D^* = 2\,\pi\,\mathrm{Fn}^2 = 3.534$ is expected. To ensure the independence of the objective functional w.r.t. spatial discretization, a grid study was first conducted. The utilized structured numerical grid is displayed in Fig. 4.14 (b) and consists of approximately 215 000 control volumes where the controlled

cylinder shape is discretized with 500 surface patches along the circumference. At the inlet, velocity and concentration values are prescribed, slip walls are used along the top as well as bottom boundaries and a hydrostatic pressure boundary is employed along the outlet. The convective term for primal [adjoint] momentum is approximated using the QUICK [QDICK] scheme. A compressive HRIC scheme was used to approximate the convective fluxes of the concentration equation. The wall normal distance of the first grid layer reads $x_2^+ = y^+ \approx 0.01$ and the free surface refinement employs approximately $\Delta x_1^*/\lambda^* = 1/100 = \Delta x_2^*/\lambda^*$ cells in the longitudinal as well as in the normal direction. Material properties are extracted based on a linearized hyperbolic tangent with $\gamma^{\mathrm{m},\rho} = \gamma^{\mathrm{m},\mu} = 0.6$, cf. (2.9). According to Alg. (2) the integration in pseudo-time applies an adaptive time step size based on $\mathrm{Co}^{\mathrm{tar}} = 0.2$ which is embedded in five sub-cycles.

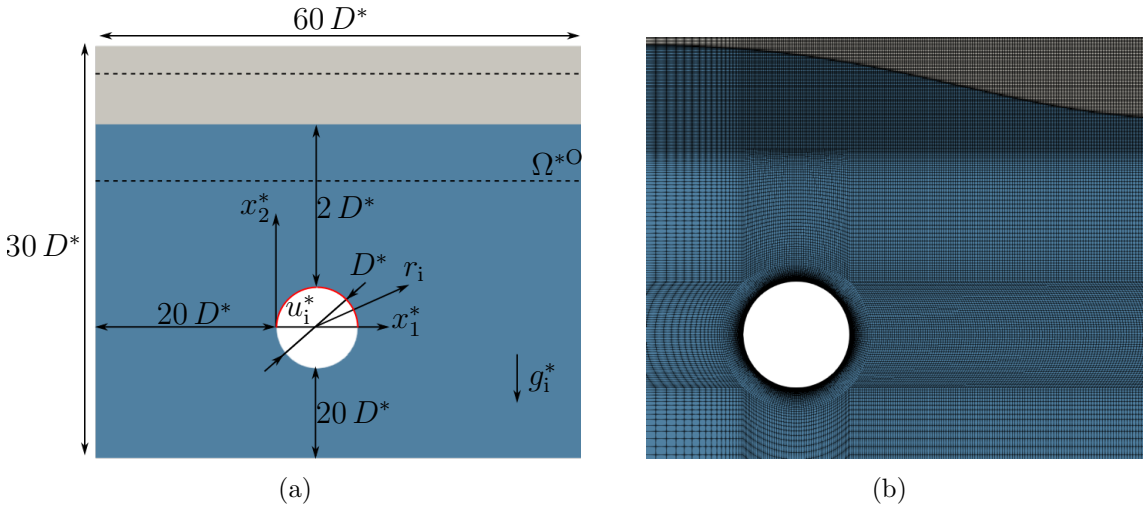

Figure 4.14: Submerged cylinder case ($\mathrm{Re_D} = 20$, $\mathrm{Fn} = 0.75$): (a) Schematic drawing of the initial configuration around the controlled cylinder shape u_i^* (red) and (b) structured numerical grid around the cylinder and the free surface.

Local Validation

Local results are depicted in Fig. 4.15 for two exemplary objectives: A boundary-based force (left) objective (3.7) into the direction $r_\mathrm{i} = [\sqrt{(2)}, \sqrt{2}]^\mathrm{T}/2$ as well as a volumetric target concentration (center) objective (3.9) with a habitat along $\Omega^{*\mathrm{O}} = [-5D^*, D^*] \times [25D^*, 5D^*]$. The force functional is constructed in such a way that the adjoint velocity sees the gravity vector already along the cylinder, i.e. $r_\mathrm{i}\, g_\mathrm{i}^* \neq 0$. Only the upper half of the cylinder is investigated for different magnitudes of the perturbation $\epsilon^*/D^* \in [10^{-4}, 10^{-5}, 10^{-6}]$.

First, the influence of the adjoint apparent viscosity on the local shape derivative is investigated. For each functional, two adjoint systems are constructed employing either no ($\nu^{*\hat{\mathrm{c}}} = 0$) or a moderate non-zero and spatially constant ($\nu^{*\hat{\mathrm{c}}} = M^*$) synthetic viscosity, where M^* refers to an estimated mobility value, cf. (2.53). It should be noted that the magnitude of the CH mobility is only roughly estimated for under-resolved flows. The first case corresponds to a pure adjoint VoF procedure and the second case to an adjoint CH-VoF approach with an estimated spatially constant (positive) diffusivity. The latter represents an, albeit small, break in dual consistency, since the consistent CH-VoF viscosity

becomes partly negative along the phase transition regime and only the former approach can be deemed fully consistent. The results for several FD-studies are marked at 21 discrete positions obtained from 42 additional (forward) simulations using the intermediate perturbation size $\epsilon^*/D^* = 10^{-5}$. The consistent adjoint sensitivities agree almost perfectly with the discrete FD results. However, a break of dual consistency due to a non-zero synthetic viscosity $\nu^{*\hat{c}}$ causes the sensitivity results to deviate for the concentration-based objective, especially in regions of high sensitivity. Since the volume functional depends exclusively on the primal concentration distribution, a manipulation of the dual concentration field is much more critical compared to the boundary-based force objective. This is an important finding for practical marine engineering applications, which often refer to the minimization of boundary-based force objectives. Mind that the linearity of the FD-analysis has been verified using a sequence of three perturbation magnitudes for both functionals. An exemplary documentation of the systems linear answer is displayed in the right graph of Fig. 4.15, which refers to an exemplary surface position $x_1^*/D^* = 1/4$ for the force functional.

Subsequently, nine additional adjoint studies investigate the influence of all adjoint cross-coupling terms. The results are documented in Fig. 4.16 (drag functional) and 4.17 (inverse concentration objective) based on the adjoint systems defined in Tab. 4.3. Formulations A1-A3 neglect either all four source terms (A1), only the ATC term due to the nonlinear momentum convection (A2) or all coupling terms due to the differentiation of the material properties (A3), respectively. The neglect of adjoint concentration sources (A3) can be motivated by a consistently differentiated (too) sharp density and viscosity EoS ($\gamma^\rho \rightarrow 0$, $\gamma^\mu \rightarrow 0$), cf. Sec. 4.1.3. The benefit of different adjoint concentrations sources in combination with the ATC term are investigated in A4-A6. The individual concentration sources are exclusively activated in A7-A9.

$S^{\hat{\varphi}}$	$\hat{v}_\mathrm{k}^* \frac{\partial v_\mathrm{k}^*}{\partial x_\mathrm{i}^*}$	$\rho^{*\Delta}\, \hat{v}_\mathrm{i}^*\, v_\mathrm{k}^* \frac{\partial v_\mathrm{i}^*}{\partial x_\mathrm{k}^*}$	$\frac{2\,\mu^{*\Delta}}{\mathrm{Re}} S_\mathrm{ik}^* \frac{\partial \hat{v}_\mathrm{i}^*}{\partial x_\mathrm{k}^*}$	$\frac{\rho^{*\Delta}}{\mathrm{Fn}^2} \hat{v}_\mathrm{i}^*\, g_\mathrm{i}^*$
A1	-	-	-	-
A2	-	x	x	x
A3	x	-	-	-
A4	x	-	x	x
A5	x	x	-	x
A6	x	x	x	-
A7	-	x	-	-
A8	-	-	x	-
A9	-	-	-	x

Table 4.3: Adjoint source term configurations for the submerged cylinder case ($\mathrm{Re_D} = 20$, $\mathrm{Fn} = 0.75$) where '-' represents a neglect of the respective contribution.

The scenarios A1-A3 study the influences of the advective momentum (a.k.a. ATC) or advective concentration transport to the adjoint momentum balance. Their influence w.r.t. the total resistance objective resembles an overall sound influence while maintaining the qualitative characteristics. In line with the flat plate b.-l. study from Fig. 4.13, an amplification of the shape derivative is obtained in its most sensitive region if the ATC term

is neglected, which in turn can be treated based on reduced step size within a steepest descent optimization procedure. The situation becomes more crucial in the case of the inverse concentration objective. Already the neglect of the ATC term (A2) shifts the roots of the shape derivative. The manipulation of the sensitivity is significantly increased by neglecting the adjoint concentration sources (A3). The quantitative differences are anticipated to have sound influence on the final gradient-based optimization process by employing, e.g., an adaptive step size. The qualitative differences indicate the absence of a descent direction, as shown in later global validation studies.

A more detailed insight into the influence of the adjoint concentration sources is obtained by freezing only selected terms (A4-A6). The resulting shape sensitivities are depicted in the central figures. The sensitivity deviations from the consistent formulation appear to be largest when the contributions due to a variation of the density are neglected, where the variation of the Froude term seems to have the largest influence. While a quantitative shift is observed in the case of the surface-based functional, the deviations w.r.t. the volume-based cost functional are noticeably increased.

Finally, the previous situation is reversed by consequently neglecting all adjoint concentration sources except for selective contributions (A7-A9). Considering only the Froude term (A9) underlines its major relevance by driving the shape sensitivity of the inverse concentration objective comparably close to the consistent result or towards the results of A2.

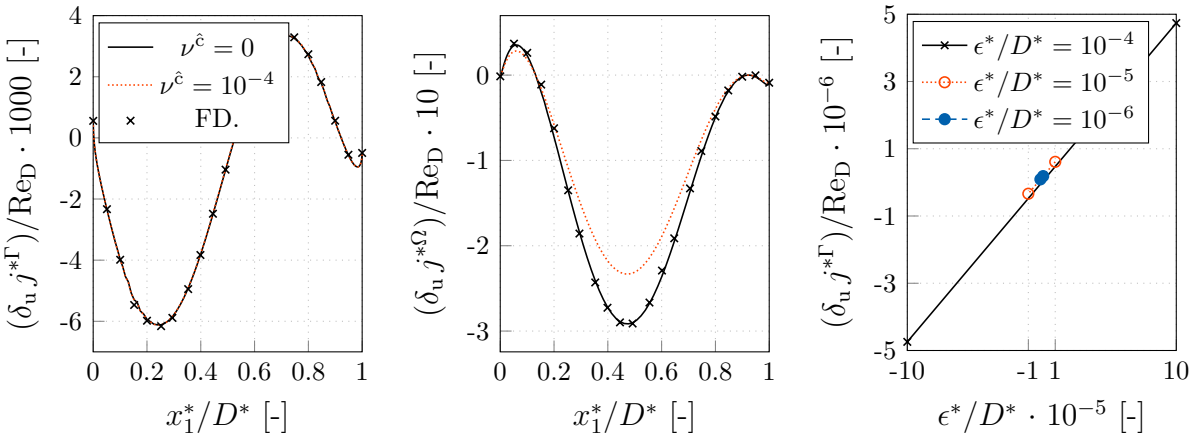

Figure 4.15: Submerged cylinder case ($\mathrm{Re_D} = 20$, $\mathrm{Fn} = 0.75$): Continuous as well as discrete finite-difference (FD) based sensitivity derivative along the upper cylinder side for (left) a drift functional ($r_\mathrm{i} = [\sqrt{(2)}, \sqrt{2}]^\mathrm{T}/2$), (center) the target concentration objective ($\Omega^{*\mathrm{O}} = [-5D^*, D^*] \times [25D^*, 5D^*]$) as well as (right) three exemplary finite (force functional) system answers at $x_1^*/D^* = 1/4$.

Global Validation

Global validation studies aim at an integral comparison in a relative fashion, e.g., comparing $(J^* - J^{*\mathrm{ini}})/J^{*\mathrm{ini}}$ over an optimization for different adjoint systems, cf. Alg. 3. Provided that a fully consistent adjoint formulation is employed, the previously presented studies in this thesis have demonstrated local agreement between the adjoint-based shape derivatives and FD results. Manipulations of the adjoint formulation to obtain increased numerical

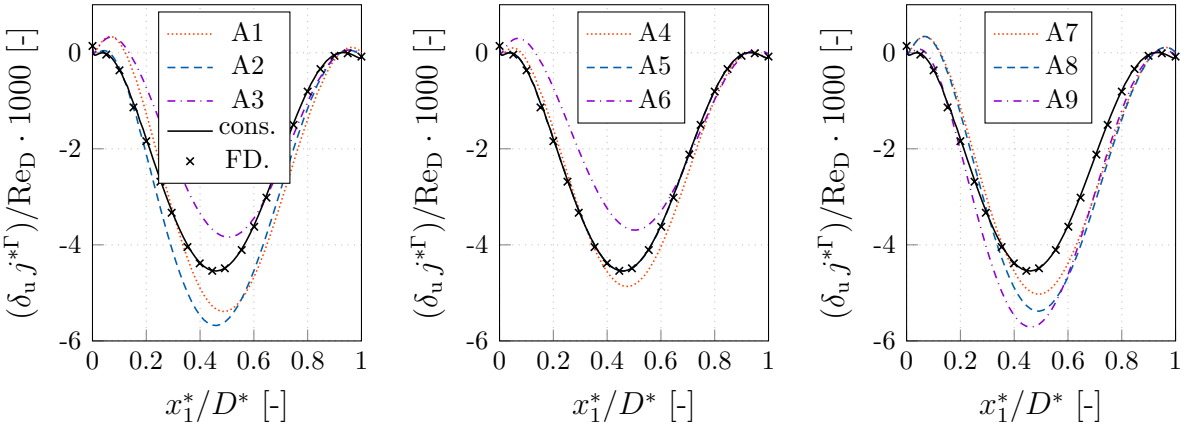

Figure 4.16: Submerged cylinder case ($\mathrm{Re_D} = 20$, $\mathrm{Fn} = 0.75$): Continuous sensitivity derivative along the upper cylinder side for a drag functional ($r_\mathrm{i} = [1, 0]^\mathrm{T}$) based on different adjoint systems that break the dual consistency via a modification of adjoint sources, cf. Tab. 4.3.

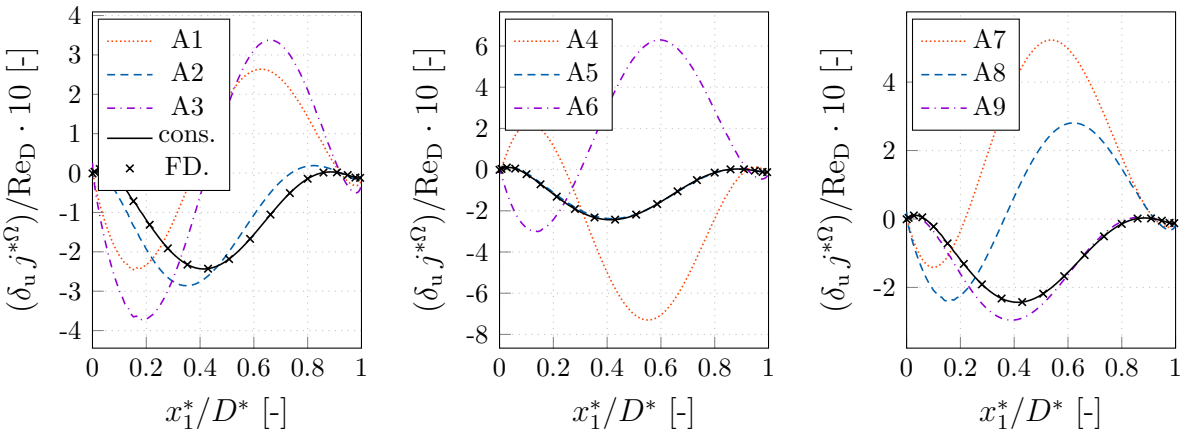

Figure 4.17: Submerged cylinder case ($\mathrm{Re_D} = 20$, $\mathrm{Fn} = 0.75$): Continuous sensitivity derivative along the upper cylinder side for an inverse concentration objective ($\Omega_\mathrm{O}^* = [-5D^*, D^*] \times [25D^*, 5D^*]$) based on different adjoint systems that break the dual consistency via a modification of adjoint sources, cf. Tab. 4.3.

stability based on, e.g., too large apparent viscosities or a neglect of adjoint coupling terms reveal both qualitative and quantitative influences on the desired shape derivatives. The influence of the different consistency violations on a complete gradient-based optimization will be assessed in the following. A total of ten (consistent + A1-A9) optimizations are performed for each cost functional together with an explicitly evaluated LB metric based on a filter width of $\mu^{*\tilde{\mathrm{g}}_\mathrm{i}}/D^* = 1/10$ in Eqn. (3.28) as well as equal step sizes. All studies employ $\nu^{\hat{\mathrm{c}}} = 0$ and the optimization results are depicted in Figs. 4.18-4.19. Studies on the influence of the apparent viscosity are conducted in the subsequent section. The different adjoint formulations result in similar drag values, where the Froude term provides the most relevant contribution. The optimization gain w.r.t. drag is maximized if the fully consistent adjoint formulation is employed. However, neglecting all four adjoint source terms (A1) decreases the drag gain by $\approx 1\%$ only. The difference arises within the last 20-30%

of the optimization, at the beginning of the optimization the value of the cost functional is almost identical. In addition, a descent direction is determined in all cases which is no longer the case if the concentration-based volumetric objective is considered. All adjoint systems that neglect the Froude term (A1-A2, A6-A8) perform a step into a direction of ascent and the optimization algorithm terminates immediately, cf. Alg. 3. From a global perspective, the influence of the variation of the molecular viscosity (A5) appears to have a negligible impact.

Although the transfer of the results to a turbulent marine engineering flow seems questionable, they are at least indicative.

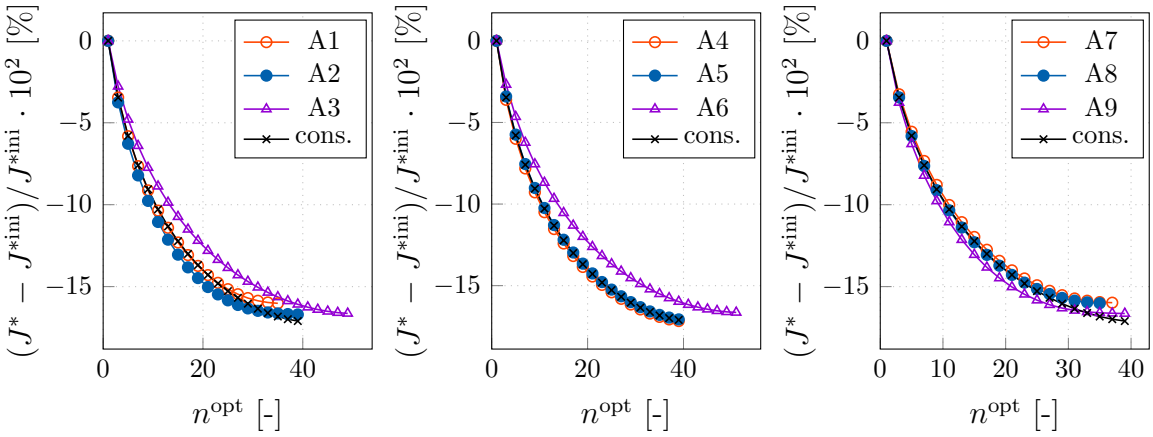

Figure 4.18: Submerged cylinder case ($\mathrm{Re_D} = 20$, $\mathrm{Fn} = 0.75$): Drag objective ($r_\mathrm{i} = [1, 0]^\mathrm{T}$) convergence based on different adjoint systems that break the dual consistency via a modification of adjoint sources, cf. Tab. 4.3.

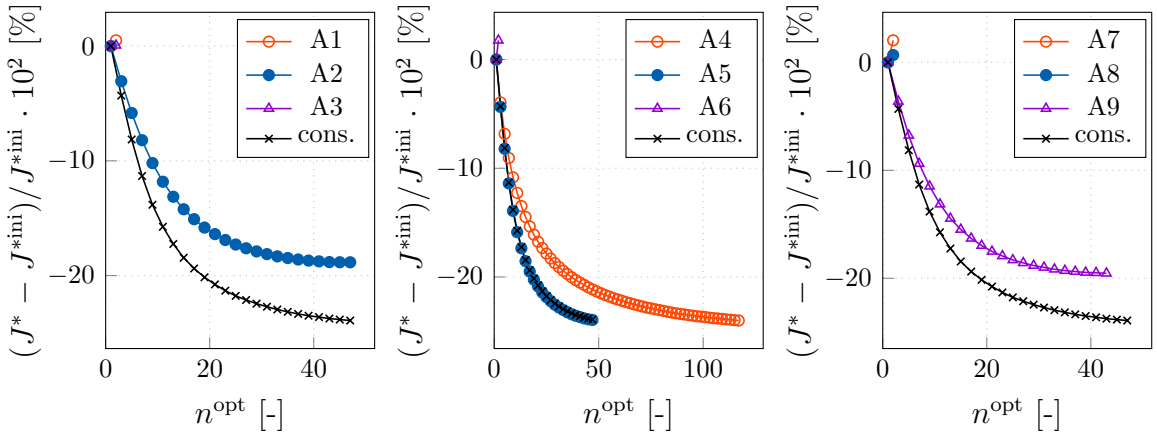

Figure 4.19: Submerged cylinder case ($\mathrm{Re_D} = 20$, $\mathrm{Fn} = 0.75$): Inverse concentration objective ($\Omega^{*\mathrm{O}} = [-5D^*, D^*] \times [25D^*, 5D^*]$) convergence based on different adjoint systems that break the dual consistency via a modification of adjoint sources, cf. Tab. 4.3.

4.4.3 Hydrofoil

This section examines the adjoint two-phase system on the submerged NACA0012 hydrofoil at $\mathrm{Re_L} = 144\,855$ and $\mathrm{Fn} = 0.567$. The test case refers to the Duncan (cf. Duncan [1981, 1983]) foil case which was already introduced during the primal validation, cf. Sec. 2.4.4 and Fig. 2.22, and aims at a systematic investigation of the influence of the apparent viscosity of the CH-VoF approach on the shape sensitivity (4.44) on local level. The convective term for adjoint momentum is approximated using the QDICK scheme and a frozen (F) turbulence wall function approach is employed. The adjoint system is solved

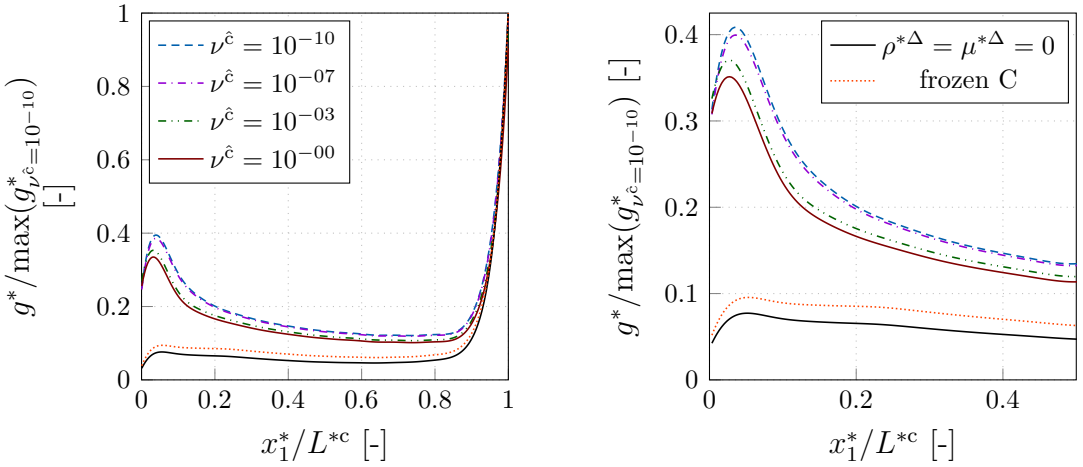

Figure 4.20: Submerged hydrofoil case ($\mathrm{Re_L} = 144\,855$, $\mathrm{Fn} = 0.567$): Normalized filtered ($\mu^{*\tilde{g}_i}/L^{*c} = 1/30$) shape gradients for a 45° drift force objective along the complete (left) and front half (right) suction side for various adjoint concentration models ranging from identical fluid properties ($\rho^{\Delta} = 0 = \mu^{\Delta}$), over a frozen concentration approach to different apparent viscosities.

for a force and inverse concentration criterion considering a steady primal solution. The test case barely converges for $\nu^{*\hat{c}} \to 0$ and the adjoint time step size $\Delta t^{*\mathrm{adj}}$ is significantly reduced by a factor $\Delta t^{*\mathrm{adj}}/\Delta t^{*\mathrm{pri}} = 1/100$ compared to the primal time step size $\Delta t^{*\mathrm{pri}}$. During the simulations it is noticed that the numerical stability is mainly affected by the Froude term in Eqn. (4.65) which in turn is particularly relevant for a consistent sensitivity as shown in the previous section.

First, the foil is investigated for its optimization potential w.r.t. a drift functional, i.e. 50% drag, 50% lift, or $r_i = \sqrt{2}/2$ in (3.7). According to Tab. 4.1, the adjoint velocity is prescribed to $\hat{v}_i = -r_i$ along the foil. Thus, the adjoint velocity sees the gravitational vector $\hat{v}_i\, g_i \neq 0$ in the foil vicinity and the Froude term is therefore forced to be active in the sensitive region. Moreover, the noisy shape derivative (sensitivity) is explicitly transformed into the shape gradient based on the LB metric. The filter-width reads $\mu^{*\tilde{g}_i}/L^{*c} = 1/30$ and various adjoint systems are constructed for the HRIC solution: Starting from a consistent ($\nu^{\hat{c}} = 0$) system, the synthetic viscosity $\nu^{\hat{c}}$ is carefully increased. Finally, simulations are performed for a frozen concentration approach and an approach based on identical fluid properties ($\rho^{*\Delta} = 0 = \mu^{*\Delta}$) to better understand and assess the results. The resulting normalized shape gradients are depicted by Fig. 4.20 (a) along the suction side of the

foil. Small qualitative differences are recognized and no changes in sign are observed for the different levels of adjoint concentration viscosity. Only a neglect of the two-phase information within the adjoint momentum equation results in significant distortions of the shape gradient. Although no sign change is observed, the shape gradients of the frozen concentration approach fall close to the results of a single-phase flow. The latter is obtained based on a primal/dual flow for $\rho^{*\Delta} = 0$ and $\mu^{*\Delta} = 0$. Results of the force objective study indicate, that the impact of the synthetic viscosity on the predicted sensitivity is negligible, whilst the robustness of the procedure is significantly improved.

A possibly more crucial objective w.r.t. consistency issues might be the inverse concentration objective (3.9). In this case, the objective functional exclusively speaks through the adjoint concentration and enters the adjoint system (only) on the r.h.s. of $\mathrm{R}^{*\hat{c}}$ which makes the frozen concentration approach obsolete. The habitat of $j^{*\Omega}$ reads $\Omega^{*\mathrm{O}} = [-L^{*\mathrm{c}}, L^{*\mathrm{c}}] \times [20L^{*\mathrm{c}}, 2L^{*\mathrm{c}}]$, where the 2D coordinate system originates in the leading edge. Again, various adjoint systems are constructed, which differ only in the amplitude of the

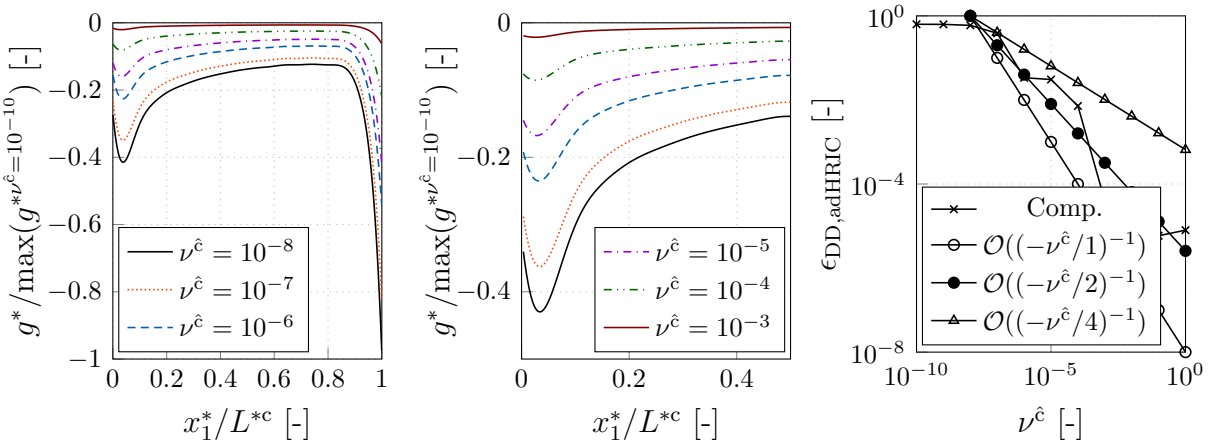

Figure 4.21: Submerged hydrofoil case ($\mathrm{Re_L} = 144\,855$, $\mathrm{Fn} = 0.567$): Normalized filtered ($\mu^{*\tilde{g}_i}/L^{*\mathrm{c}} = 1/30$) shape gradients for an inverse concentration objective along the complete (left) and front half (middle) suction side as well as the error (right) between a consistent adjoint HRIC and a pure DDS approximation of the adjoint convection of $\hat{c}$ based on the maximum norm ($\epsilon^{\mathrm{DD,adHRIC}} = \max(|(g^{*\mathrm{DD}} - g^{*\mathrm{adHRIC}})/g^{*\mathrm{adHRIC}}|)$) for different magnitudes of the apparent adjoint concentration viscosity.

apparent adjoint concentration viscosity and result in the normalized shape gradients depicted on the left [center] part in Fig. 4.21 along the complete [front half] suction side. Analogous to the force functional, the increase in synthetic viscosity only leads to an attenuation of the gradient, which in turn could be treated by an appropriate step size within a gradient-based optimization procedure.

When attention is directed to practical marine engineering applications, the computational effort associated with time stepping of compressive primal approximations is substantial. As outlined above, the related efforts increase for an adjoint system. Means to reduce this effort whilst still retaining reliable sensitivity information are appreciated. To address this aspect, simulations were repeated using simple DDS approximations of the

convective transport in the adjoint concentration equation, instead of swapping from DDS to UDS along the interface region in line with the adjoint HRIC approach. This approach was formerly suggested by Kröger et al. [2018] and circumvents the time step size dependency of the adjoint system (4.109), which would basically allow steady adjoint simulations. However, for the current investigation the integration within the pseudo-time remains unchanged in order to support the comparison of results. The respective shape gradients differ only quantitatively. Hence, their deviation w.r.t. a consistent adjoint HRIC approximation is estimated in terms of the maximum norm $\epsilon^{\mathrm{DD,adHRIC}} = \max(|(g^{*\mathrm{DD}} - g^{*\mathrm{adHRIC}})/g^{*\mathrm{adHRIC}}|)$ and plotted in Fig. 4.21 (right) over the employed apparent viscosity. The deviation is large for a small synthetic viscosity $\nu^{\hat{\mathrm{c}}}$ and drops significantly for larger values of $\nu^{\hat{\mathrm{c}}}$. Its evolution is located in a corridor limited by $\mathcal{O}(-1/\nu^{\hat{\mathrm{c}}})$ and $\mathcal{O}(-4/\nu^{\hat{\mathrm{c}}})$, which results from $\nu^{\hat{\mathrm{c}}}$ exceeding the numerical viscosity inherent to any dual [primal] downwind [upwind] biased interpolation method. The diffusive influence of synthetic viscosity on the adjoint concentration field is plotted in Fig. 4.22 (a) for different magnitudes of the synthetic viscosity. Increasing values smear the initially parabolic into an elliptical field. Furthermore, Fig. 4.22 (b) confirms the observations of the 1D Couette model from Sec. 4.3.2, according to which increased apparent viscosity suppresses the jump of adjoint pressure along the free surface and thus stabilizes the numerical procedure, cf. Fig. 4.10 (b).

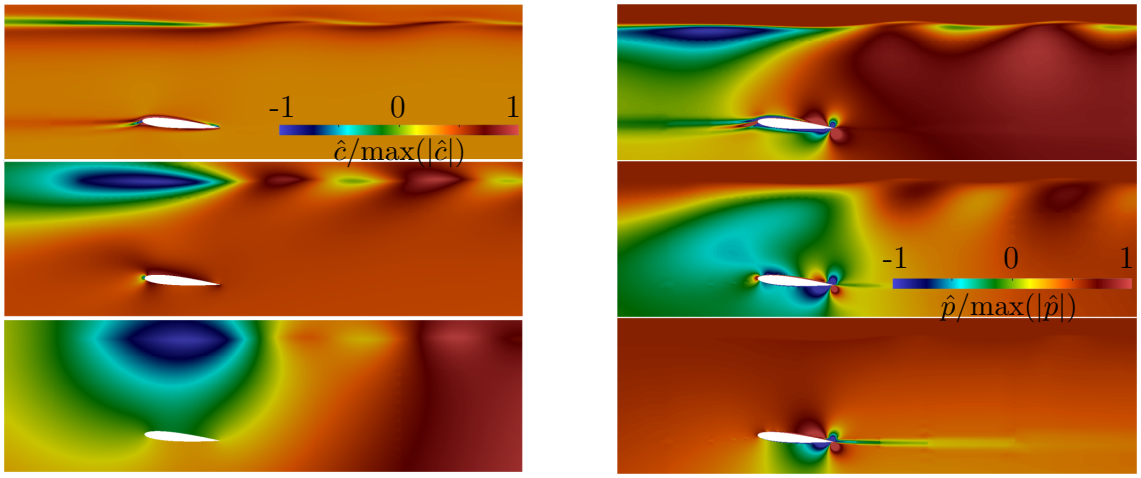

(a) (b)

Figure 4.22: Submerged hydrofoil case ($\mathrm{Re_L} = 144\,855$, $\mathrm{Fn} = 0.567$): Normalized (left) adjoint concentration and (right) adjoint pressure distribution for the inverse concentration objective around the foil for synthetic viscosity increasing from $\nu^{\hat{\mathrm{c}}} = 10^{-4}$ (top) over $\nu^{\hat{\mathrm{c}}} = 1$ (middle) to $\nu^{\hat{\mathrm{c}}} = 10^{4}$ (bottom).

4.4.4 Pointed Oval

The fourth validation case examines a two-dimensional elliptic, pointed oval geometry of length [height] L^* [$L^*/2$] under a Reynolds number of $\mathrm{Re_L} = V_1^* L^*/\nu^* = 10^6$ where V_1^* and ν^* refer to the bulk velocity and kinematic viscosity, respectively, cf. Fig. 4.23 (a) and 4.24 (left). Hence, the investigated oval employs a height h^* to length ratio of $h^*/L^* = 1/2$. The focal point of interest refers to a comparison of initial shape sensitivities

predicted by the adjoint frozen (F) and the LoW-consistent (C) adjoint turbulence closure. Their influence on a complete, gradient- (steepest descent) based shape optimization will be considered also in terms of global validation. The structured numerical grid consists of 11 600 control volumes and the obstacle is discretized with 200 surface elements as depicted in Fig. 4.23 (b). A homogeneous velocity is imposed along the inlet, a zero

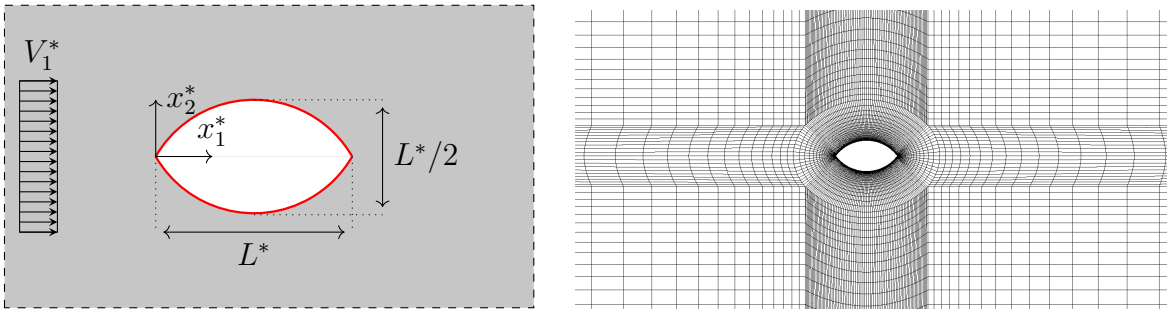

(a) (b)

Figure 4.23: Pointed oval case ($\mathrm{Re_L} = 10^6$): Illustration of the considered geometry (a) and computational grid (b) where red lines indicate the design region.

pressure value is prescribed at the outlet and slip-walls are employed along the top and bottom boundary. The obstacle is examined with respect to its optimization potential in terms of total resistance. In line with the habitat of the internal force objective, the adjoint velocity reads $\hat{v}_\mathrm{i} = -r_\mathrm{i} = -\delta_{1\mathrm{i}}$ along the design surface. The initial shape sensitivities along the upper side resulting from both employed adjoint formulations (F vs. C) are shown in Fig. 4.24 (center). Notable quantitative differences are observed in the maximum absolute sensitivity. Moreover, qualitative differences occur due to the deviating signs in the vicinity of the leading and trailing edge. While the former should primarily result in an accelerated optimization, the latter points to possibly different optimal solutions. For this reason, two optimizations were performed, i.e. one for a convex problem, that should exclusively reveal convergence speed differences, and one for a non-convex problem.

The first study uses an identical step size in combination with the LB surface metric. The utilized filter-width reads $\mu^{*\tilde{\mathrm{g}}_\mathrm{i}}/L^* = 1/10$ and the step size was chosen to ensure a maximum first displacement d_i^* of $d_\mathrm{i}^*/L^* = 1/1000$ for the consistent optimization. The mathematically convex problem should physically converge to a flat plate b.-l. flow. The convergence of the drag objective is documented in Fig. 4.24 (right) where both strategies yield almost the same optimal value that drops by approximately 85%. However, the LoW-consistent approach converges approximately 30% faster compared to the frozen turbulence approach. The optimized shapes are depicted in Fig. 4.24 (left) and the deviation of their optimal drag value is below 2% w.r.t. the non-dimensional drag coefficient of a turbulent flat plate b.-l., e.g. $c^\mathrm{d} \approx 0.074\,\mathrm{Re_L}^{(-1/5)} = 4.7 \cdot 10^{-3}$, cf. Hucho [2002]. Subsequently, an additional optimization study was carried out, whereby the sensitivity is modified in such that the flow displacement of the initial shape is conserved using the projection method (3.33). Analogous to the previous optimization, the same constant step size was specified for both optimizations, which was chosen to ensure a maximum first displacement of $d_\mathrm{i}^*/L^* = 1/1000$ for the consistent optimization. The convergence of the objective functional is documented in the right graph of Fig. 4.25. Again, the LoW-consistent approach converges almost 30% faster, while absolute [relative] improvements of ≈3% [≈10%] are

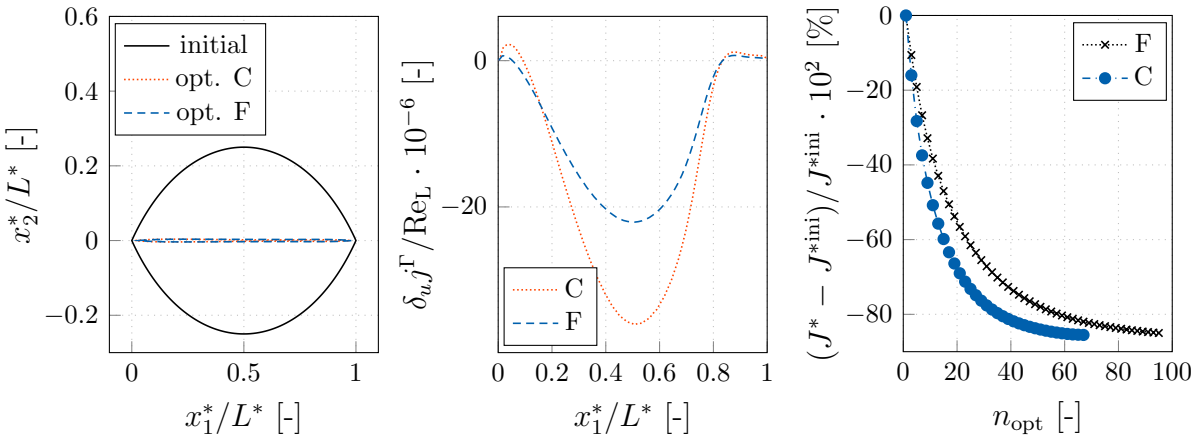

Figure 4.24: Pointed oval case ($\mathrm{Re_L} = 10^6$): Initial and optimized shapes (left), initial upper wall shape sensitivities predicted by the frozen (F) and consistent (C) approach (center), as well as drag objective convergence (right) for the geometrically unconstrained optimization.

observed for the resistance reduction compared to the frozen turbulence approach. The profit follows mainly from the slightly more bulbous [slimmer] front [rear] region (cf. Fig. 4.25).

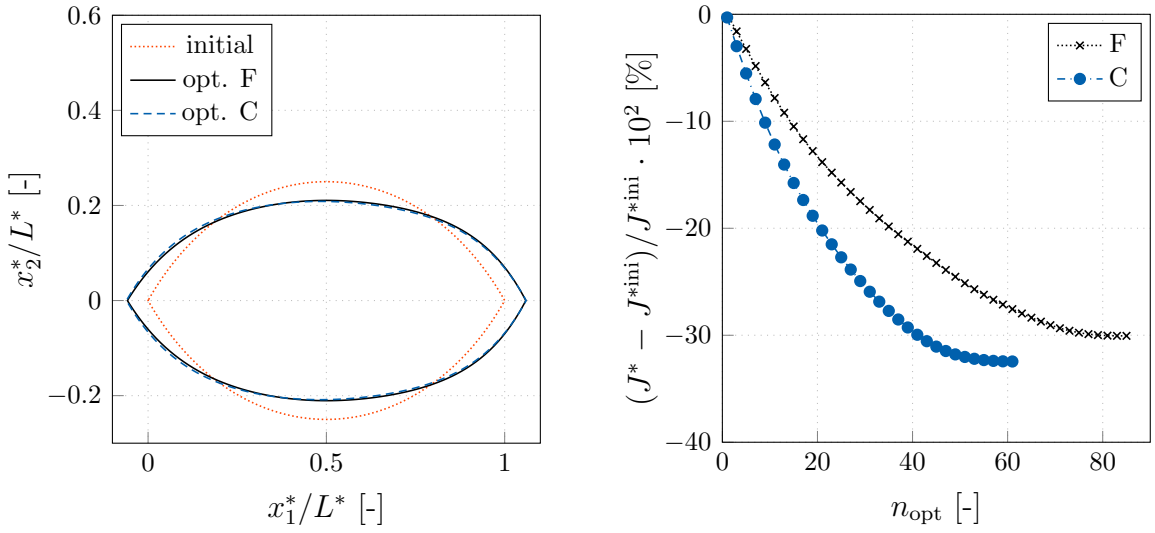

Figure 4.25: Pointed oval case ($\mathrm{Re_L} = 10^6$): Initial and optimized shapes (a) as well as drag objective convergence (b) predicted by the frozen (F) and the LoW-consistent (C) approaches for the volume conserving optimization.

Further studies of the LoW-consistent adjoint framework w.r.t. two- and three-dimensional internal flows are available in Kühl et al. [2021c].

5 Application Studies

This chapter applies the previously presented primal/adjoint CH-VoF RANS procedure to three maritime two-phase flow test-cases on industrial level. Examples included involve a generic underwater vehicle, a double ended ferry and an offshore supply vessel. Attention is given to a) the attainable robustness returned by the adjoint formulation and its level of consistency, b) the obedience to geometrical constraints – such as plane transoms or symmetry requirements – and c) the consideration of a varying floatation. All optimizations employ the SP metric from Sec. 3.5.2 to extract the gradient out of the sensitivity derivative. A spatially constant (positive) adjoint apparent viscosity is determined according to the estimation rule from Sec. 2.2.9 and the first application employs the linearized EoS (2.9), while the second and third use the algebraic adjoint turbulence model.

5.1 Generic Underwater Vehicle

This first application investigates a submerged generic DARPA (Defense Advanced Research Projects Agency) SUBOFF geometry as described in Groves et al. [1989] without appendages. The test case is frequently used during studies that focus on the propulsion and manoeuvring of deeply submerged submarines or in the vicinity of the free surface, e.g. Wang et al. [2020], Daum et al. [2017], Chase and Carrica [2013]. The present study is focused on the near surface operation. When operating close to the free surface, the wave field induced by the interaction of the dynamic pressure field with the free surface is unfavorable in terms of wave resistance as well as the signature of the submarine.

As illustrated in Fig. 5.1, the hull consists of three sections: A bow section ($0 \leq x_1^* \leq 2D^*$), a middle body ($2D^* \leq x_1^* \leq 0.745L^{*\mathrm{S}}$) as well as an aft section including cap ($0.745L^{*\mathrm{S}} \leq x_1^* \leq L^{*\mathrm{S}}$). The origin of the coordinate system is located at the front tip. Here, $L^{*\mathrm{S}}$ and D^* represent the length of the submarine and the maximum body diameter.

The present study is performed for a turbulent flow at $\mathrm{Re}_\mathrm{L} = V_1^* L^{*\mathrm{S}}/\nu^{*\mathrm{b}} = 8.54 \cdot 10^6$ and $\mathrm{Fn} = V_1^*/\sqrt{G^* L^{*\mathrm{S}}} = 0.3$, based on the gravitational acceleration G^*, the inflow velocity V_1^* and the kinematic viscosity of the water $\nu^{*\mathrm{b}}$. The non-dimensional submergence reads $L^*/D^* = 1.1$.

The three-dimensional domain has a length, height and width of $20\,L^{*\mathrm{S}}$, $10\,L^{*\mathrm{S}}$ as well as $5\,L^{*\mathrm{S}}$, where the inlet, bottom and outer boundaries are located five geometry-lengths away from the origin. A dimensionless wave length of $\lambda = \lambda^*/L^* = 2\,\pi\,\mathrm{Fn}^2 = 4.4$ is expected and the wave elevation w.r.t. still water should be minimized, viz. $\Omega^{*\mathrm{O}} = [-L^{*\mathrm{S}}, L^{*\mathrm{S}}/10, 0] \times [5\,L^{*\mathrm{S}}, 1.5\,L^{*\mathrm{S}}, 5\,L^{*\mathrm{S}}]$, by modifying only the middle body of the underwater vehicle while conserving its displacement. The utilized unstructured numerical grid is displayed in Fig. 5.1 (b) and consists of approximately $4 \cdot 10^6$ control volumes. Due to symmetry, only half of the geometry is modeled in the lateral direction.

The fully turbulent simulations employ a wall function-based $k^* - \omega^*$ SST model and convective terms for momentum and turbulence are approximated using the QUICK scheme.

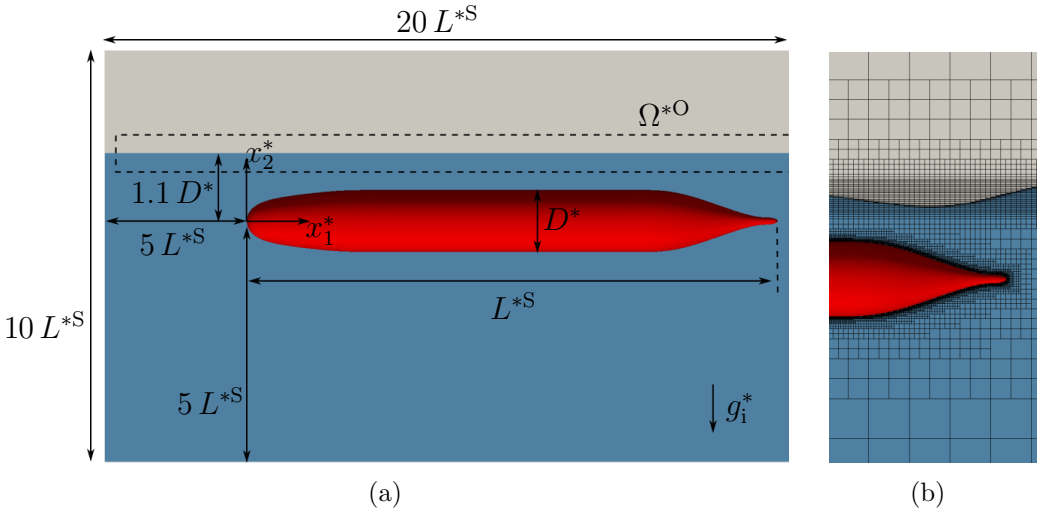

Figure 5.1: Submerged DARPA SUBOFF case ($\mathrm{Re_L} = 8.54 \cdot 10^6$, $\mathrm{Fn} = 0.3$): (a) Schematic drawing of the initial configuration and (b) unstructured numerical grid around the generic underwater vehicle and the free surface.

The CICSAM scheme is used for the compressive concentration transport. In contrast, the adjoint equations employ the QDICK and adCICSAM procedure. At the inlet, velocity and concentration values are prescribed, slip walls are used along the top, bottom as well as outer boundaries and a hydrostatic pressure boundary is employed along the outlet. Along the mid ship plane a symmetry condition is declared. The dimensionless wall normal distance of the first grid layer reads $x_2^+ = y^+ \approx 30$ and the free surface refinement employs approximately $\delta x_1^*/\lambda^* = \delta x_3^*/\lambda^* = 1/50$ cells in the longitudinal as well as lateral and $\delta x_2^*/\lambda^* = 1/500$ cells in the normal direction. The tangential resolution of the free surface region is refined within a Kelvin-wedge to capture the wave field generated by the submerged geometry, cf. Fig. 5.2. According to Alg. (2) the integration in pseudo-time applies a time step size based on $\mathrm{Co}^{\mathrm{tar}} = 0.4$ embedded in five sub-cycles. The employed steepest descent approach uses a step size based on a prescribed maximum deformation for the initial design, viz. $\alpha^{*\mathrm{d_i}} = L^{*S}/1000$ based on one per mil of the reference length as maximum initial deformation, cf. Alg. 3. The step size is kept constant over the optimization, leading to a smooth convergence of the objective functional. Five optimizations are performed: Four of them carefully increase the adjoint apparent viscosity from $\nu^{\hat{c}}\,\rho^{*b}/\mu^{*b} = 1$ to $\nu^{\hat{c}}\,\rho^{*b}/\mu^{*b} = 1000$. The relative decrease of the cost functional is depicted over the number of gradient steps (performance evaluations) in Fig. 5.3. The fifth optimization employs the smallest apparent viscosity but neglects all three source terms scaling with the density and viscosity difference within the adjoint concentration equation and thus resembles a frozen material property approach. These source/sink terms are a strong motivation for the introduction of an apparent viscosity, as they drastically increase the coupling of the adjoint equation system and by that decrease the numerical stability. Except for the optimization with frozen fluid properties, all optimizations achieve a similar order of magnitude for the minimization of the cost functional. The adjoint coupling terms resulting from a variation of the fluid properties seem to have a much stronger influence on the shape derivative than the adjoint apparent viscosity. An increase of the latter results in a deviating convergence behavior and a somewhat smaller reduction of the cost

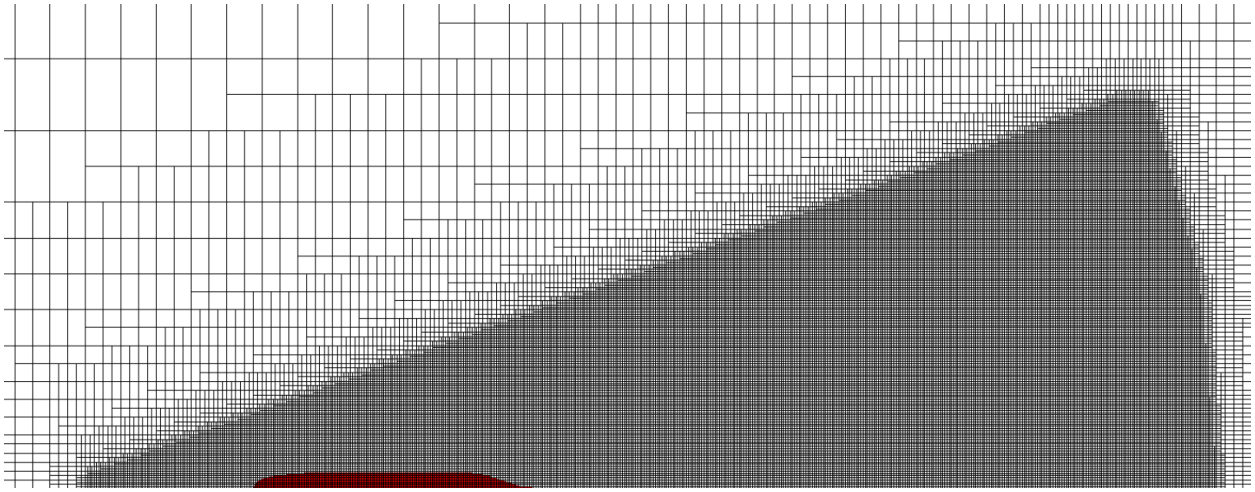

Figure 5.2: Submerged DARPA SUBOFF case ($\mathrm{Re_L} = 8.54 \cdot 10^6$, $\mathrm{Fn} = 0.3$): Numerical grid in the still water plane.

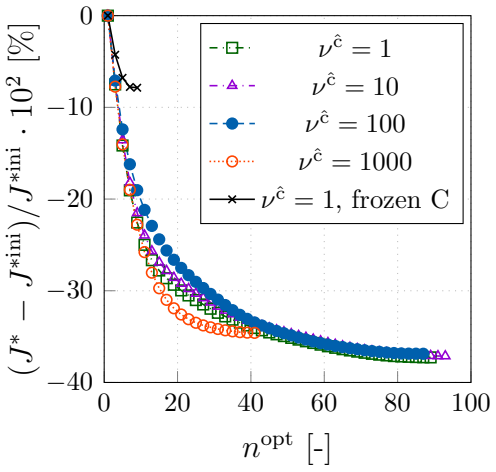

Figure 5.3: Submerged DARPA SUBOFF at $\mathrm{Re_L} = 8.54 \cdot 10^6$, $\mathrm{Fn} = 0.3$: Inverse concentration objective decrease over the number of performed shape updates during a steepest descent procedure. Four optimizations differ in the amplitude of the apparent viscosity and one optimization neglects all adjoint coupling terms that originate from the derivative of material properties.

functional. Interestingly, the fastest convergence is achieved with the highest apparent viscosity. The inferior influence of the apparent viscosity compared to the coupling terms is also demonstrated by the wave patterns displayed in Fig. 5.4. The three graphs are extracted at three different lateral positions, viz. $x_3^*/D^* = 0$ (left), $x_3^*/D^* = 2$ (middle) and $x_3^*/D^* = 4$ (right) as indicated in Fig. 5.5. This observation is confirmed by the resulting hull geometries. Figures 5.6 and 5.7 present water lines and buttocks of the initial and the optimized geometry with $\nu^{\hat{c}} = 1$ against the optimization with frozen material properties (top) and the final shape resulting from $\nu^{\hat{c}} = 1000$ (bottom). The slices underline the local character of the optimization approach as well as the strength of the proposed method wr.t. large shape and mesh deformations.

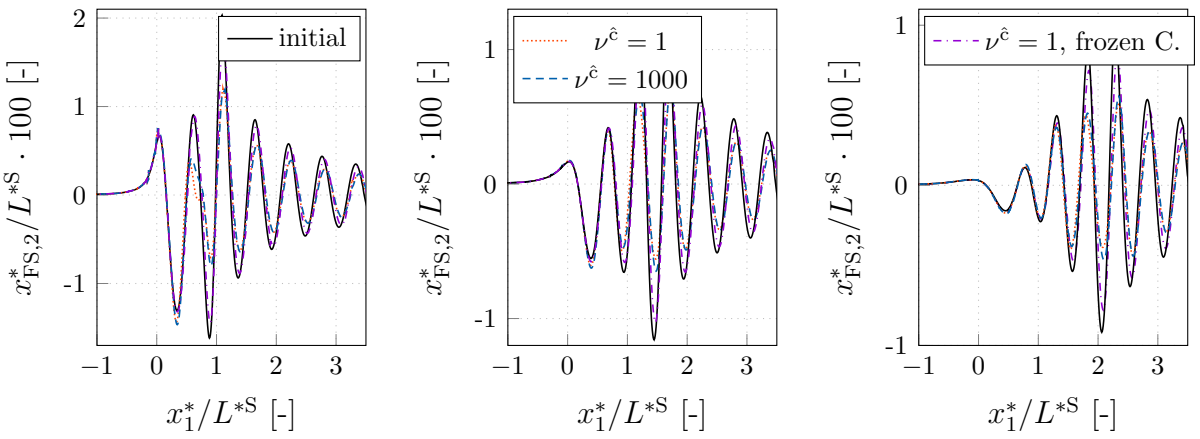

Figure 5.4: Submerged DARPA SUBOFF case ($\mathrm{Re_L} = 8.54 \cdot 10^6$, $\mathrm{Fn} = 0.3$): Wave elevation for the initial and for three optimized shapes with $\nu^{\hat{c}} = 1$ (with and without adjoint two-phase coupling terms) as well as $\nu^{\hat{c}} = 1000$ along the main flow direction (x^*_1) at three different lateral positions, viz. (left) $x^*_3/D^* = 0$, (center) $x^*_3/D^* = 2$ and (right) $x^*_3/D^* = 4$.

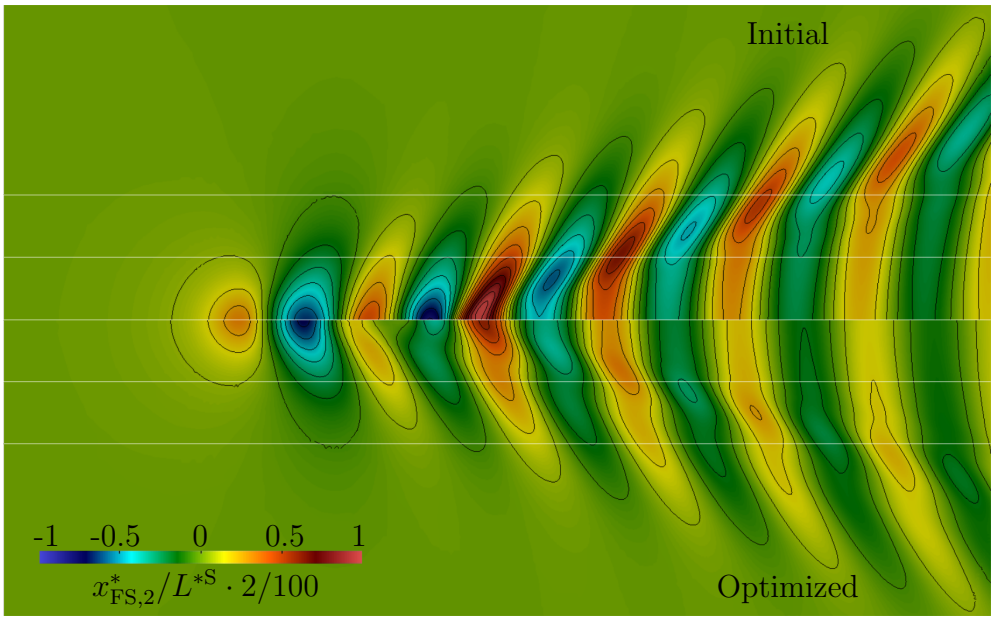

Figure 5.5: Submerged DARPA SUBOFF case ($\mathrm{Re_L} = 8.54 \cdot 10^6$, $\mathrm{Fn} = 0.3$): Normalized wave elevation for top) the initial geometry and bottom) the optimized hull resulting from an optimization with $\nu^{\hat{c}} = 1$.

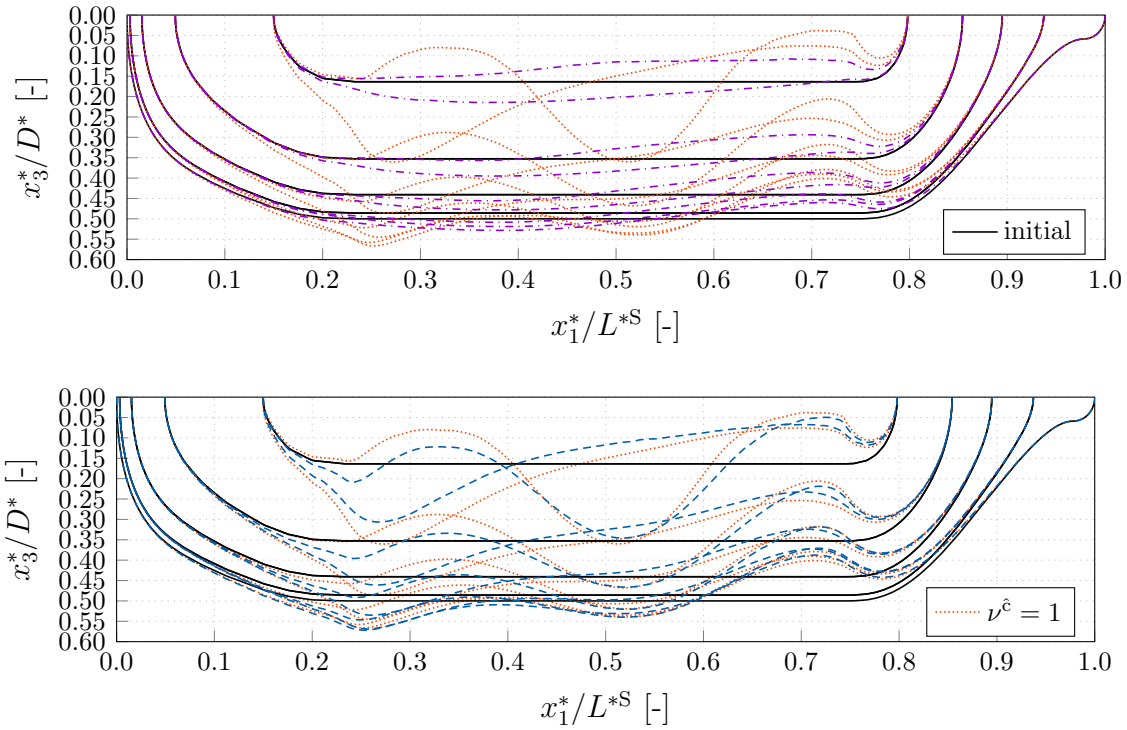

Figure 5.6: Submerged DARPA SUBOFF case ($\mathrm{Re_L} = 8.54 \cdot 10^6$, $\mathrm{Fn} = 0.3$): Water lines for the initial geometry (black), two optimized geometries based on $\nu^{\hat{c}} = 1$ (orange) and $\nu^{\hat{c}} = 1000$ (blue) as well as the resulting slices for an optimization that employs $\nu^{\hat{c}} = 1$ with a frozen material property approach (purple).

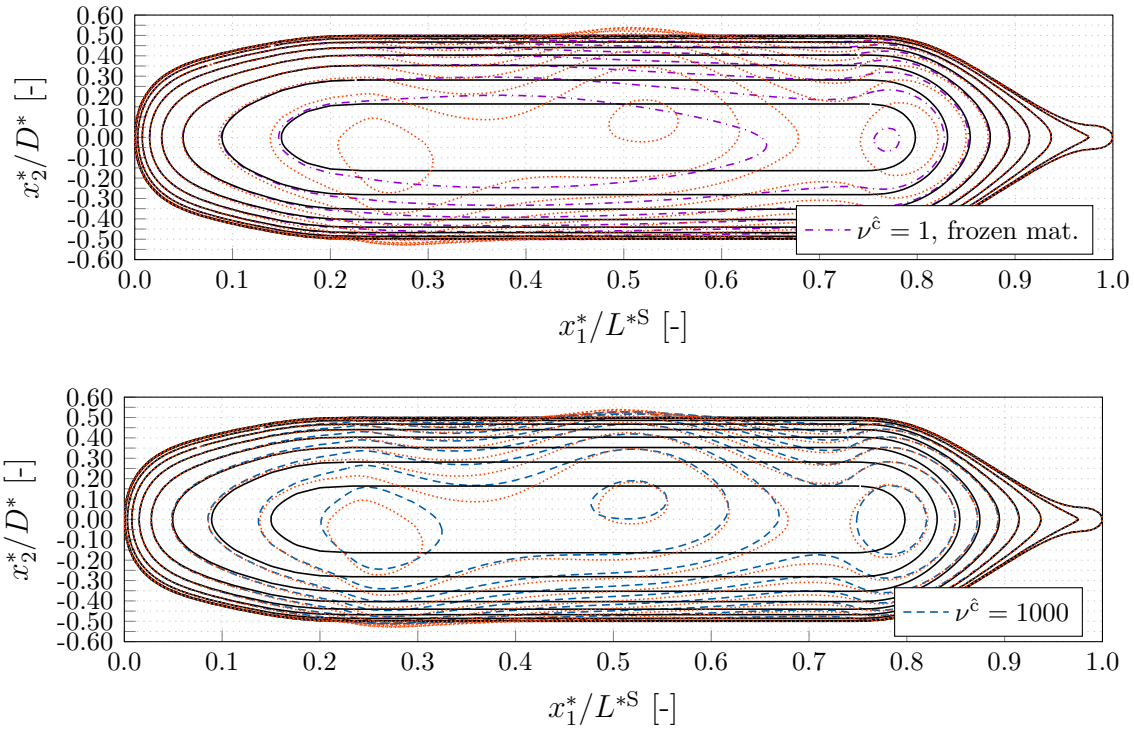

Figure 5.7: Submerged DARPA SUBOFF case ($\mathrm{Re_L} = 8.54 \cdot 10^6$, $\mathrm{Fn} = 0.3$): Buttocks for the initial geometry (black), two optimized geometries based on $\nu^{\hat{c}} = 1$ (orange) and $\nu^{\hat{c}} = 1000$ (blue) as well as the resulting slices for an optimization that employs $\nu^{\hat{c}} = 1$ with a frozen material property approach (purple).

5.2 Double Ended Ferry

The second application refers to a Double Ended Ferry (DEF), as depicted in Figs. 5.8 and 5.9. The hull is optimized w.r.t. total drag for a scale 1:8.75 model. Since a double ended ferry moves both forward ($V_1^* < 0$) and backward ($V_1^* > 0$), the performance optimization must mimic this symmetry and preserve the longitudinal symmetry along the central $x_2^* - x_3^*$ plane (mid ship section) of the initial hull, cf. Fig. 5.9 (a). Floatation is

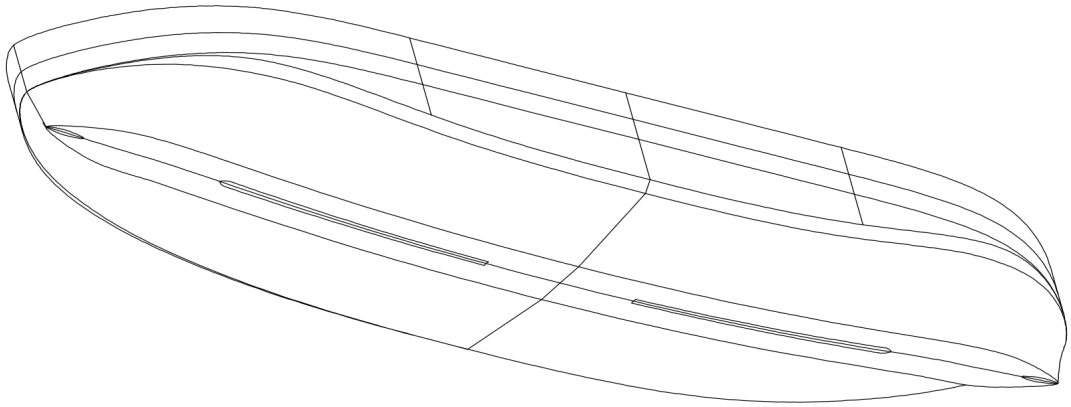

Figure 5.8: Double Ended Ferry (DEF): Perspective 3D representation of the initial geometry.

not considered, and geometrical constraints aim to preserve the initial main dimensions, to maintain the displacement, and to guarantee the symmetry of the hull w.r.t. an identical forward and backward cruise performance. Simply speaking, the latter requires the reformulation of the force objective from Sec. 3.2, in which the forces of the forward (J^{*+}) and backward (J^{*-}) cruise need to be evaluated separately to subsequently form an equally weighted sum, viz. $J^{*+,-} = 0.5\,J^{*+} + 0.5\,J^{*-}$. However, in case of a perfectly symmetric initial geometry and domain, the determination of the sensitivity for one cruise direction, e.g. J^{*+}, using an unmirrored geometry is sufficient, if the sensitivity is subsequently mirrored around the mid ship plane. The mirrored sensitivity should precisely correspond to the reversed flow sensitivity, e.g. J^{*-}, and thus to the opposite travel direction. Both sensitivity distributions are combined to guide the gradient-based optimization. A perfectly mirrored grid with an identical control volume distribution on both sides of the mid ship symmetry plane is therefore much appreciated. In this situation, an interpolation of mirrored sensitivities could be bypassed by a simple injection, and the optimized shape naturally remains symmetric throughout the optimization.

The DEF consists of a hull, bulkwark and deck as conceptually sketched in Fig. 5.9, where the coordinate system is placed at the bottom of the hull in the mid ship section and the free surface is initialized in the $x_1^* - x_2^*$ plane at $x_3^*/L^{*\mathrm{D}} = 5/146$ based on the DEF length $L^{*\mathrm{D}}$. The study is performed for a turbulent flow at $\mathrm{Re_L} = V_1^* L^{*\mathrm{D}}/\nu^{*\mathrm{b}} = 6.26 \cdot 10^6$ and $\mathrm{Fn} = V_1^*/\sqrt{G^* L^{*\mathrm{D}}} = 0.25$, based on the gravitational acceleration G^*, the inflow velocity V_1^* and the kinematic viscosity of the water $\nu^{*\mathrm{b}}$. A dimensionless wave length of $\lambda = \lambda^*/L^{*\mathrm{D}} = 2\,\pi\,\mathrm{Fn}^2 = 4.4$ is expected. The three-dimensional domain has a length, height and width of $10\,L^{*\mathrm{D}}$, $4\,L^{*\mathrm{D}}$ as well as $4\,L^{*\mathrm{D}}$. The geometry is symmetric around the $x_1^* - x_3^*$ and $x_2^* - x_3^*$ plane. Therefore only half of the lateral x_2^*-extend is considered and the numerical grid is mirrored around the mid ship $x_2^* - x_3^*$ plane by construction. The inlet and

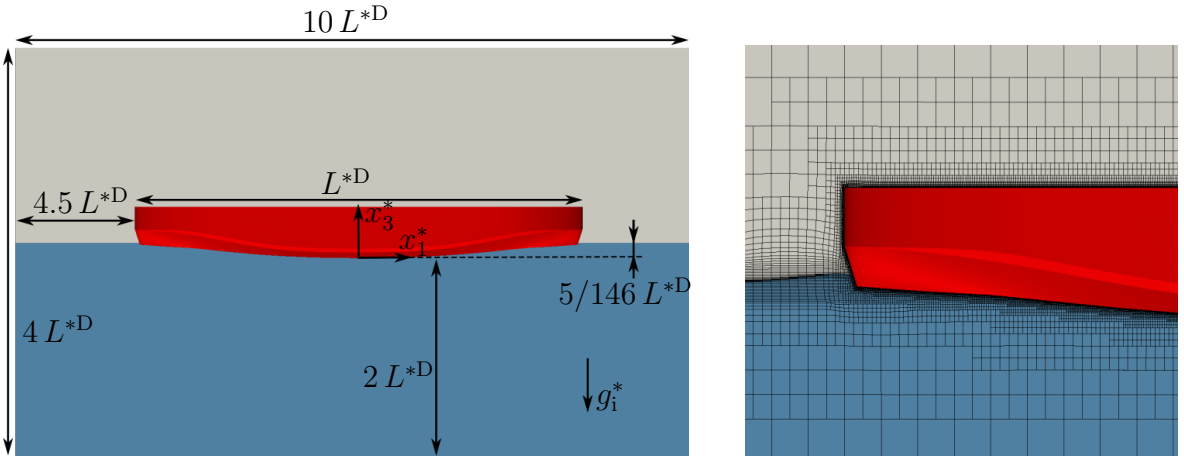

(a) (b)

Figure 5.9: Double Ended Ferry (DEF) case ($\mathrm{Re_L} = 6.26 \cdot 10^6$ and $\mathrm{Fn} = 0.25$): (a) Schematic drawing of the initial configuration and (b) unstructured numerical grid around the stern and the free surface.

outlet boundaries are located 4.5 geometry-lengths away from the origin. The symmetric unstructured numerical grid is displayed in Fig. 5.9 (b) and consists of approximately $5 \cdot 10^6$ control volumes. The fully turbulent simulations employ a wall-function-based $k^* - \omega^*$ SST model and convective terms for momentum and turbulence are approximated using the QUICK scheme. The HRIC scheme is used for the compressive concentration transport. The simulation applies a main flow against the x_1^*-axis. Velocity and concentration values are prescribed at the inlet and slip walls are used along the top, bottom as well as remote lateral planes. A hydrostatic pressure boundary is employed along the outlet located at the minimum x_1^*-position. A symmetry condition is imposed along the central lateral plane. The dimensionless wall normal distance of the first grid layer reads $x_2^+ = y^+ \approx 50$ and the free surface refinement employs approximately $\delta x_1^*/\lambda^* = \delta x_3^*/\lambda^* = 1/50$ cells in the longitudinal as well as lateral and $\delta x_2^*/\lambda^* = 1/500$ cells in the normal direction. The tangential resolution of the free surface region is refined within a Kelvin-wedge to capture the wave field generated by the DEF geometry. To ensure a symmetric mesh update, the utilized numerical mesh and thus the Kelvin-wedge is mirrored, cf. Fig. 5.10. According to Alg. (2) the integration in pseudo-time applies a time step size based on $\mathrm{Co}^{\mathrm{tar}} = 0.35$ embedded in five sub-cycles.

Adjoint simulations employ a pure DDS approximation of the convective adjoint concentration transport and use an apparent viscosity based on the primal estimation from (2.53) together with an adjoint time step size $\Delta t^{*\mathrm{adj}}$ that is significantly reduced by a factor $\Delta t^{*\mathrm{adj}}/\Delta t^{*\mathrm{pri}} = 1/100$ compared to the primal time step size $\Delta t^{*\mathrm{pri}}$.

During a first series of computations, the symmetry condition is not considered for the formulation of the objective functional and only the forward cruise (J^{*+}) force on the hull is minimized for three different step sizes. The cost functional convergence is shown in Fig. 5.11 (a). All optimizations minimize the force by about $(J^{*+} - J^{*+,\mathrm{ini}})/J^{*+,\mathrm{ini}} \approx 2.75\%$. The normalized initial deformation field is shown in Fig. 5.12 (top). Due to the asymmetric shape update, the forces of the forward (J^{*+}) and rearward (J^{*-}) cruise diverge for the optimized shape. To validate this, the inlet and outlet boundary conditions are reversed

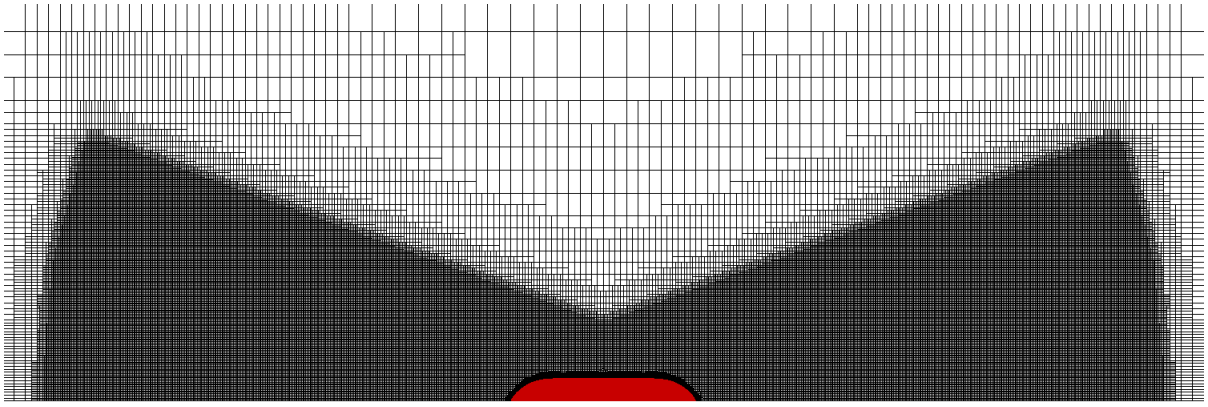

Figure 5.10: Double Ended Ferry (DEF) case ($\mathrm{Re_L} = 6.26 \cdot 10^6$ and $\mathrm{Fn} = 0.25$): Symmetric numerical grid in the still water plane.

on both the initial as well as the optimized grid, so that the DEF now effectively travels in the reverse direction that offers access to the J^{*-} performance. The resulting normalized drag force is shown in Fig. 5.11 (b) for a certain time period, where the solid [dashed] lines correspond to the total resistance from forward (J^{*+}) [backward (J^{*-})] travel. In line with the expectation, the initial grid provides an identical resistance for both cases (i.e. $J^{*+,\mathrm{ini}} = J^{*-,\mathrm{ini}}$). Nonetheless, the drag convergence as well as the final value of the optimized shape differ significantly (i.e. $J^{*+,\mathrm{opt}} \neq J^{*-,\mathrm{opt}}$) and the optimized resistance of the backward travel even exceeds that of the initial forward cruise, i.e. $J^{*-,\mathrm{opt}} > J^{*-,\mathrm{ini}}$ ($= J^{*+,\mathrm{ini}}$).

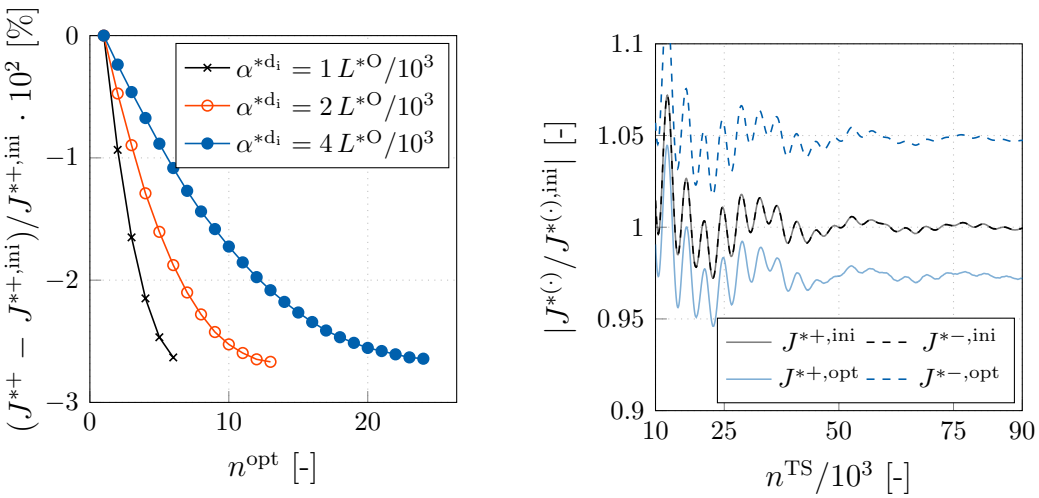

(a) (b)

Figure 5.11: Double Ended Ferry (DEF) case ($\mathrm{Re_L} = 6.26 \cdot 10^6$ and $\mathrm{Fn} = 0.25$) with unsymmetric shape update: (a) Relative objective convergences and (b) comparison of initial and optimized shape based on forward and backward cruise.

Subsequently, three additional optimizations are performed, which mirror the sensitiv-

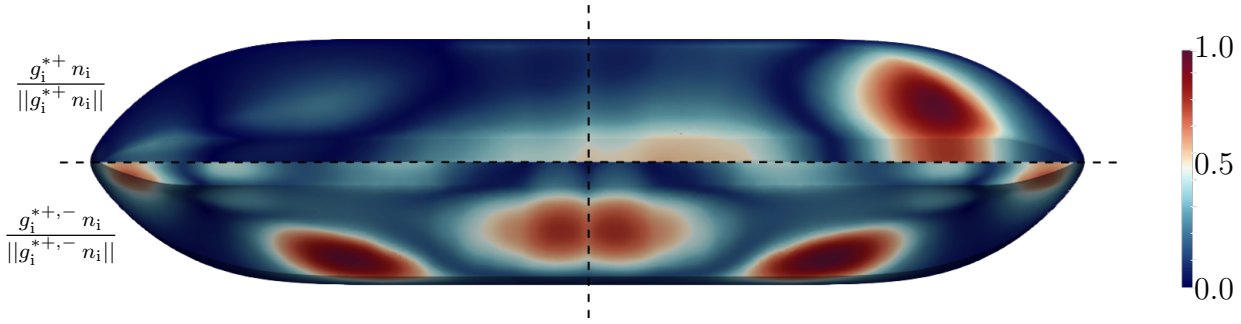

Figure 5.12: Double Ended Ferry (DEF) case ($\mathrm{Re_L} = 6.26 \cdot 10^6$ and $\mathrm{Fn} = 0.25$): Normalized initial deformation field along the hull for (top) the straight forward drag minimization and (bottom) its symmetrized analogue.

ity derivative around the mid ship after each adjoint simulation in order to minimize $J^{*+,-} = 0.5\, J^{*+} + 0.5\, J^{*-}$. An exemplary normalized deformation field is shown in Fig. 5.12 (bottom) and indicates the symmetrized character in contrast to the former, non-symmetric approach. For all three step sizes used, the cost functional convergence is plotted in Fig. 5.13 (a). Again, all optimizations converge to nearly the same gain of $(J^{*+,-} - J^{*+,-,\mathrm{ini}})/J^{*+,-,\mathrm{ini}} \approx 3.7\%$, which is, interestingly, below that of the non-symmetric optimization. To emulate the reverse travel, the optimized shape based on the smallest step size is simulated with reversed inlet and outlet boundary conditions. The resulting total resistance force convergence over an exclusive time period is shown in Fig. 5.13 (b), where the solid [dashed] lines correspond to the total resistance from forward (J^{*+}) [backward (J^{*-})] cruise. As for the initial shape, the symmetrically optimized shape has an identical cost functional convergence for both forward and backward travel, i.e. $J^{*+,\mathrm{opt}} = J^{*-,\mathrm{opt}} < J^{*-,\mathrm{ini}} = J^{*+,\mathrm{ini}}$ and thus $J^{*+,-,\mathrm{opt}} < J^{*+,\mathrm{ini}} = J^{*-,\mathrm{ini}}$. To summarize: The mirroring of the shape sensitivity derivative after an adjoint simulation of the DEF forward cruise allows a symmetry preservation of the shape optimization for the purpose of an equivalent backward traveling performance. For the optimizations based on the smallest step size, slices of the optimized shapes with and without symmetrization are depicted in Fig. 5.14.

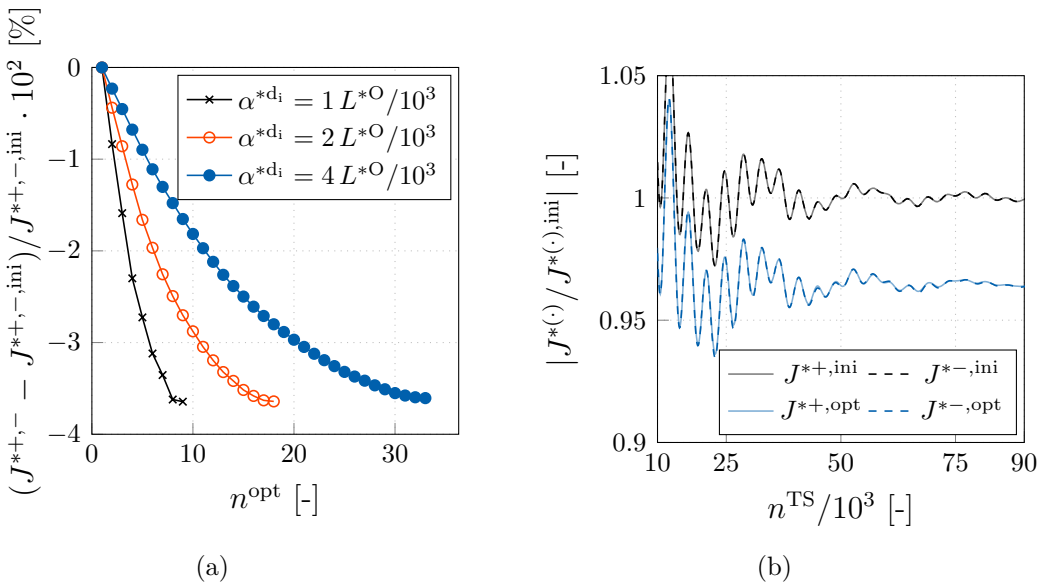

Figure 5.13: Double Ended Ferry (DEF) case ($\mathrm{Re_L} = 6.26 \cdot 10^6$ and $\mathrm{Fn} = 0.25$) with symmetric shape update: (a) Relative objective convergence and (b) comparison of initial and optimized shape based on forward and backward cruise.

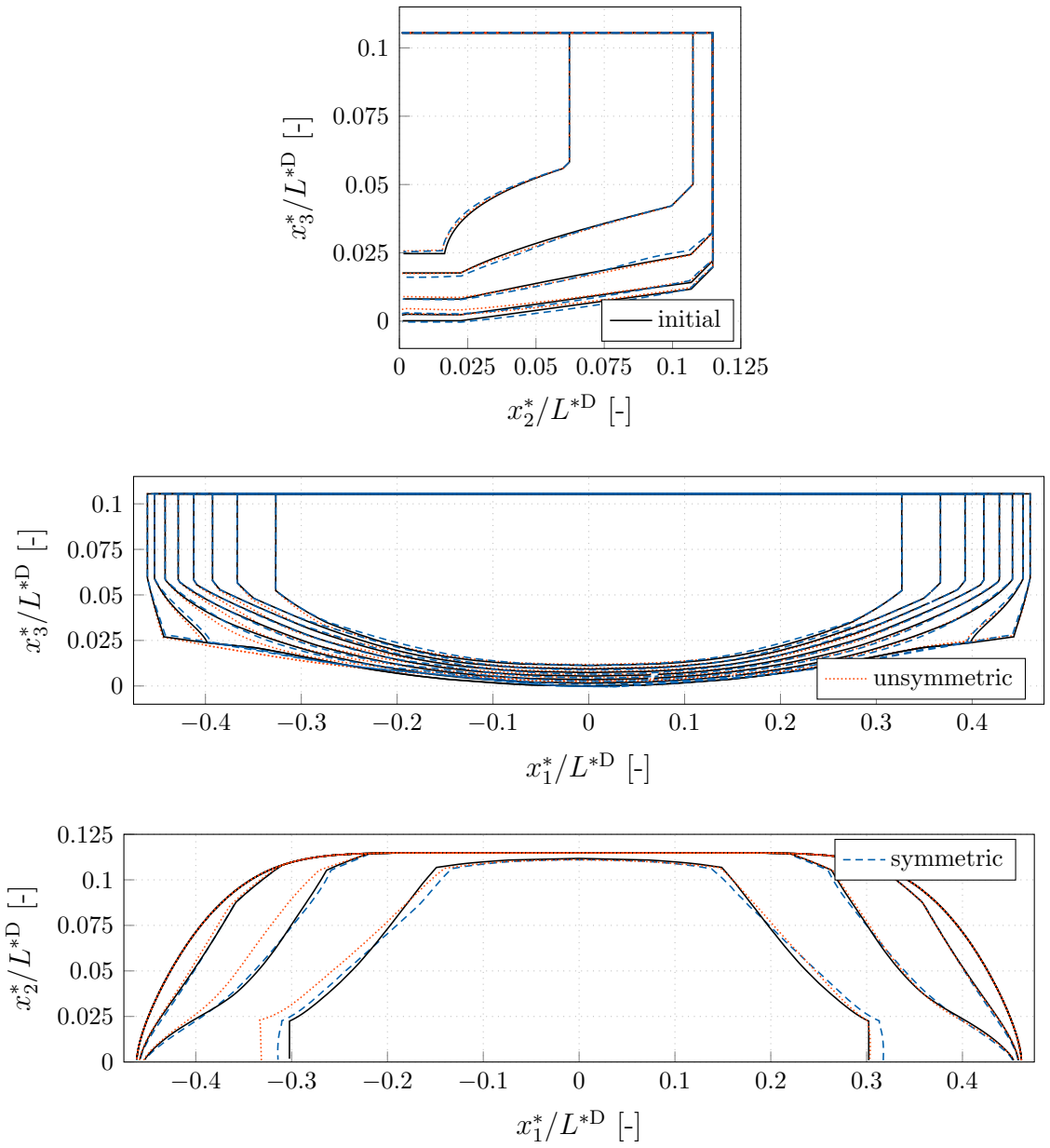

Figure 5.14: Double Ended Ferry (DEF) case ($\mathrm{Re_L} = 6.26 \cdot 10^6$ and $\mathrm{Fn} = 0.25$): (Top) Frames, (center) waterlines and (bottom) buttocks for the initial (black) and symmetric (blue, dashed) as well as unsymmetric optimized (orange, dotted) geometry.

5.3 Offshore Supply Vessel

This final application refers to an Offshore Supply Vessel (OSV) in both 1:9 model-scale (MS) and full-scale (FS), where the hull length is small compared to the cruising speed. Hence, the supply vessel operates at comparably large Froude numbers ($\mathrm{Fn} > 0.3$) and therefore experiences high wave resistances based on, e.g., braking waves. A modification of the latter might trigger a change of the floatation and therefore the OSV represents a competitive test case for the presented adjoint-based two-phase shape optimization framework under free floatation. The geometry features a transom which allows for geometrical constraints based on a robust mesh deformation process. The considered geometrical constraints refer to the conservation of a plane transom that allows tangential-only deformation, the conservation of the displacement, and the adherence to a prescribed maximum vessel length.

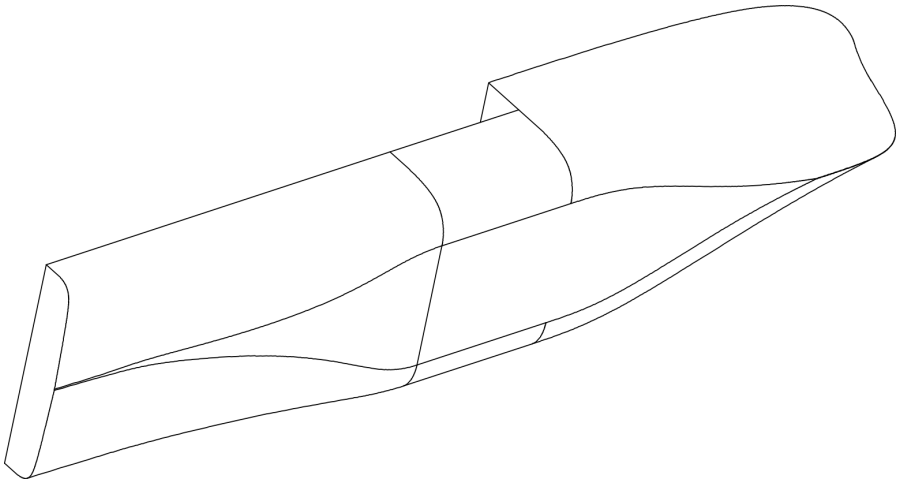

Figure 5.15: Perspective 3D representation of the initial Offshore Suplly Vessel (OSV) geometry. Numerical studies simplify the deck region and minimize the step, cf. Fig. 5.16.

The OSV consists of a hull, transom, bulkwark and deck as conceptually sketched in Figs. 5.15,5.16, where the coordinate system is placed at the bottom of the stern and the free surface is initialized in the $x_1^* - x_2^*$ plane at $x_3^*/L^{*\mathrm{O}} = 1/16$ based on the OSV length $L^{*\mathrm{O}}$. To emphasize the industrial applicability of the optimization method, the geometry is optimized in both MS and FS, with Reynolds and Froude numbers of $\mathrm{Re}_{\mathrm{L}}^{\mathrm{MS}} = 8.92 \cdot 10^6$, $\mathrm{Fn}^{\mathrm{MS}} = 0.32$ [$\mathrm{Re}_{\mathrm{L}}^{\mathrm{FS}} = 2.81 \cdot 10^8$, $\mathrm{Fn}^{\mathrm{FS}} = 0.37$] for the MS [FS] configuration. In both cases, the three-dimensional domain has a length, height and width of $8\,L^{*\mathrm{O}}$, $6\,L^{*\mathrm{O}}$ as well as $4\,L^{*\mathrm{O}}$, where the outlet [bottom] boundaries are located four [two] OSV-lengths away from the origin. A dimensionless wave length of $\lambda^{\mathrm{MS}} = \lambda^*/L^{*\mathrm{O}} = 2\,\pi\,\mathrm{Fn}^2 = 0.626$ and $\lambda^{\mathrm{FS}} = 0.852$ is expected and the total drag of the OSV should be minimized, viz. $r_{\mathrm{i}} = -\delta_{\mathrm{i}1}$ in Eqn. (3.8), by modifying the hull and transom while conserving the displaced water. The utilized unstructured numerical grid around the MS transom is displayed in Fig. 5.16 (b) and consists of approximately $3 \cdot 10^6$ control volumes. Due to symmetry, only half of the geometry is modeled in lateral direction. The fully turbulent simulations employ a wall-function-based $k^* - \omega^*$ SST model and convective terms for primal and adjoint momentum as well as primal turbulence are approximated using the QUICK scheme. The HRIC

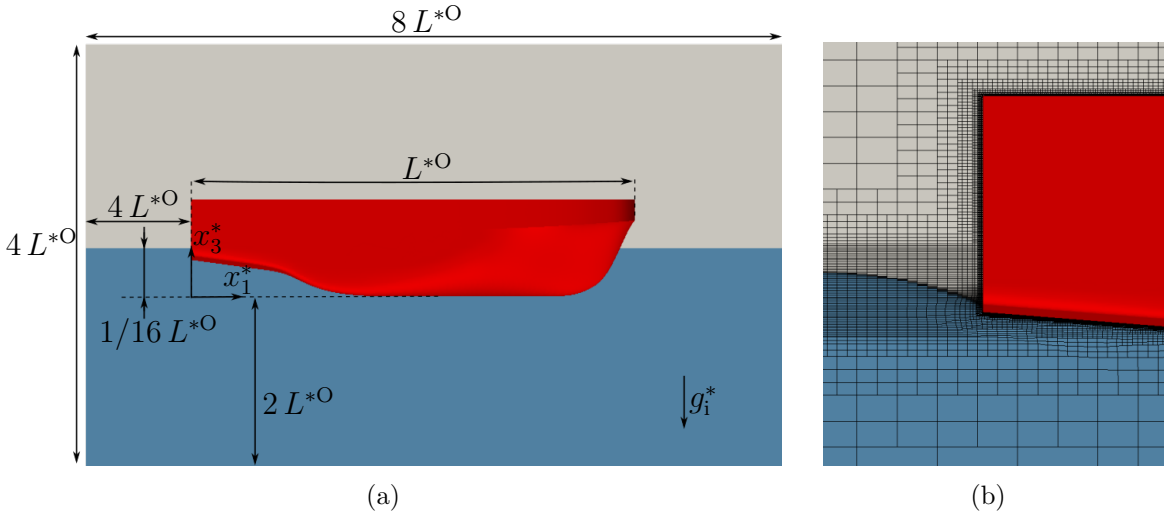

Figure 5.16: (a) Schematic drawing of the initial configuration and (b) unstructured numerical grid around the stern and the free surface for a model scale configuration of the Offshore Supply Vessel (OSV).

scheme is used for the compressive concentration transport. The adjoint concentration equation features a DDS approximation together with an apparent viscosity based on the CH-VoF estimation from (2.53) and the algebraic adjoint turbulence closure is employed. At the inlet, velocity and concentration values are prescribed, slip walls are used along the top, bottom as well as outer boundaries and a hydrostatic pressure boundary is employed along the outlet. Along the mid ship plane a symmetry condition is declared. The dimensionless wall normal distance of the first grid layer reads $x_2^+ = y^+ \approx 50$ and the free surface refinement employs approximately $\delta x_1^*/\lambda^* = \delta x_2^*/\lambda^* = 1/50$ cells in the longitudinal as well as lateral direction and $\delta x_3^*/\lambda^* = 1/500$ cells in the normal direction. The tangential resolution of the free surface region is refined within a Kelvin-wedge to capture the wave field generated by the vessel, cf. Fig. 5.17 for the FS grid. According to Alg. (2) the integration in pseudo time applies a time step size based on $\mathrm{Co}^{\mathrm{tar}} = 0.4$ embedded in five sub-cycles. The adjoint time step size $\Delta t^{*\mathrm{adj}}$ is significantly reduced by a factor $\Delta t^{*\mathrm{adj}}/\Delta t^{*\mathrm{pri}} = 1/100$ compared to the primal time step size $\Delta t^{*\mathrm{pri}}$. All MS [FS] optimizations permit [allow for] a tangential deformation of the symmetry cross-section while maintaining the initial main dimensions of the OSV. The optimized geometries are re-meshed after the cost functional convergence based on the –initially scripted– HEXPRESS (cf. NUMECA [2018]) grid generator and re-simulated from scratch. The predicted performance of the re-meshed geometries match the morphed grid-based counterparts in all cases. The discussion starts with the presentation of MS results.

Model Scale

Model scale studies refer to three different simulation series, i.e. using prescribed floatation, fixed floatation computed for the initial configuration and updated floatation which accompanies each primal flow simulation of the optimization procedure.

First, a series of three optimizations with fixed floating position but variable step size is considered. The tangential deformation along the symmetry plane is suppressed to keep

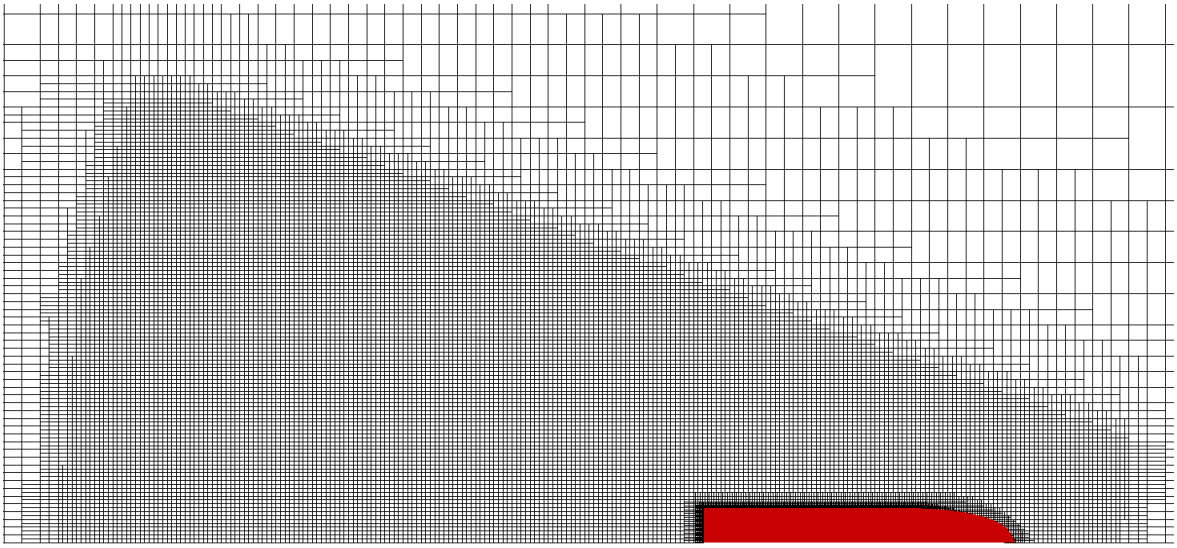

Figure 5.17: Numerical grid in the still water plane for a full scale configuration of the Offshore Supply Vessel (OSV).

the ship's main cross section constant. The modification of the transom is prohibited in the normal direction. The three optimizations vary in their initial displacement based on one, two and four per mile of the total vessel length ($\alpha^{*\mathrm{d_i}} = L^{*\mathrm{O}}/1000$, $\alpha^{*\mathrm{d_i}} = 2\,L^{*\mathrm{O}}/1000$, $\alpha^{*\mathrm{d_i}} = 4\,L^{*\mathrm{O}}/1000$) and the convergences are documented in Fig. 5.18 (left). All optimizations converge to a similar drag objective of $(J^* - J^{*\mathrm{ini}})/J^{*\mathrm{ini}} \approx 8\%$. However, the convergence is partially non-smooth, e.g. the objective drops significantly from $\approx 4\%$ to $\approx 6\%$ after the 17'th gradient step for the smallest step size. Figure 5.19 shows the $c = 0.5$ contour around the front ship region for shape 17 (left) and 20 (right) based on two additional simulations from scratch to ensure compatibility. Hence, the erratic objective behavior follows from a decreased breaking wave amplitude which in turn represents a strong nonlinearity in the design space. The detection of this nonlinearity, despite the necessity of possibly smaller step sizes, underlines the robustness of the method. Mind that a descent direction along nonlinearities is usually associated with small step sizes. The optimized geometry obtained in combination with the smallest step size is depicted by Fig. 5.20. The figure displays the frames (top), waterlines (middle) and buttocks (bottom). Essentially, the S-twist at the transition from the mid- to the aft ship is reduced and the bow becomes fuller. Both increased displacements follow from a shifted volume from the transom region towards the deck as well as an overall slimming of the wetted region.

The subsequent studies refer to a free floating initial vessel, where the trim and sinkage is adjusted every 5000th time step. The evolution of the drag coefficient of the initial geometry at run time is shown in Fig. 5.18 (center). The adjustment of the floatation becomes apparent by the fluctuating values of the total drag force. On the r.h.s., trim $T^{*\mathrm{O}}$ as well as dimensionless sinkage $S^{*\mathrm{O}}/L^{*\mathrm{O}}$ are plotted over the number of pseudo-time steps. After an initial overestimation of the trim, both curves converge. The converged shape is employed by the optimization process but no adjustment of the floatation is performed during the optimization process, i.e. fixed floatation. Again three optimization studies are performed with different step sizes ($\alpha^{*\mathrm{d_i}} = L^{*\mathrm{O}}/1000$, $\alpha^{*\mathrm{d_i}} = 2\,L^{*\mathrm{O}}/1000$,

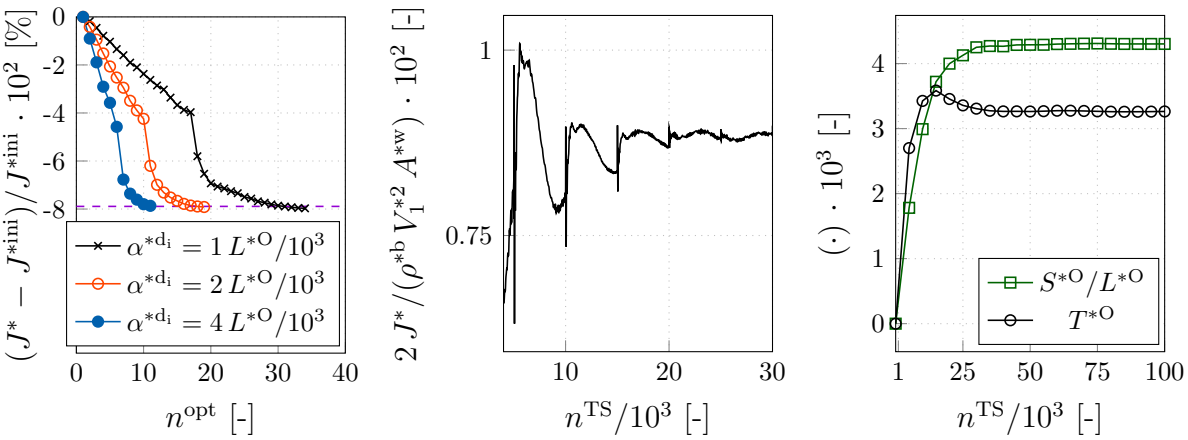

Figure 5.18: Offshore Supply Vessel (OSV) at model scale ($\mathrm{Re_L^{MS}} = 8.92 \cdot 10^6$, $\mathrm{Fn^{MS}} = 0.32$): (Left) relative objective convergence for fixed floatation, (center) drag coefficient for initial shape with adaptive trim sinkage and (right) respective dimensionless sinkage and trim angle. The dashed purple horizontal lines on the l.h.s. indicate the final total resistance value after re-meshing of the final designs.

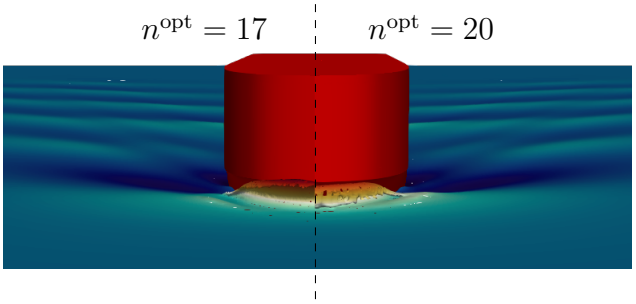

Figure 5.19: Offshore Supply Vessel (OSV) MS case ($\mathrm{Re_L^{MS}} = 8.92 \cdot 10^6$, $\mathrm{Fn^{MS}} = 0.32$): Wave field ($c = 0.5$ contour) around the front ship for shape 17 (left) and 20 (right).

$\alpha^{*\mathrm{d_i}} = 4\,L^{*\mathrm{O}}/1000$). The convergence behavior is documented in Fig. 5.21 (left). Similar to the previous fixed floatation studies, all optimizations converge to a similar value of $(J^* - J^{*\mathrm{ini}})/J^{*\mathrm{ini}} \approx 13.5\%$ but the nonlinearity of the breaking wave is much less pronounced than in the initially computed fixed flotation series, cf. from Fig. 5.18 (left). Based on the initial hydrostatic data, the optimized shapes were released for floating and three simulations from scratch are performed for the three optimized shapes. Again, all ships provide a similar value, which is incorporated as a horizontal dashed purple line in Fig. 5.21 (left). The total resistance increases drastically and two thirds of the predicted $\approx 13.5\%$ optimization improvement are lost due to the neglected trim/sinkage adjustment during the optimization.

Due to the collapse of the predicted improvements when neglecting the change of floatation during the optimization, the latter is now determined in the sense of a *frozen floatation* strategy during each primal flow simulation. The effort per primal (forward) simulation

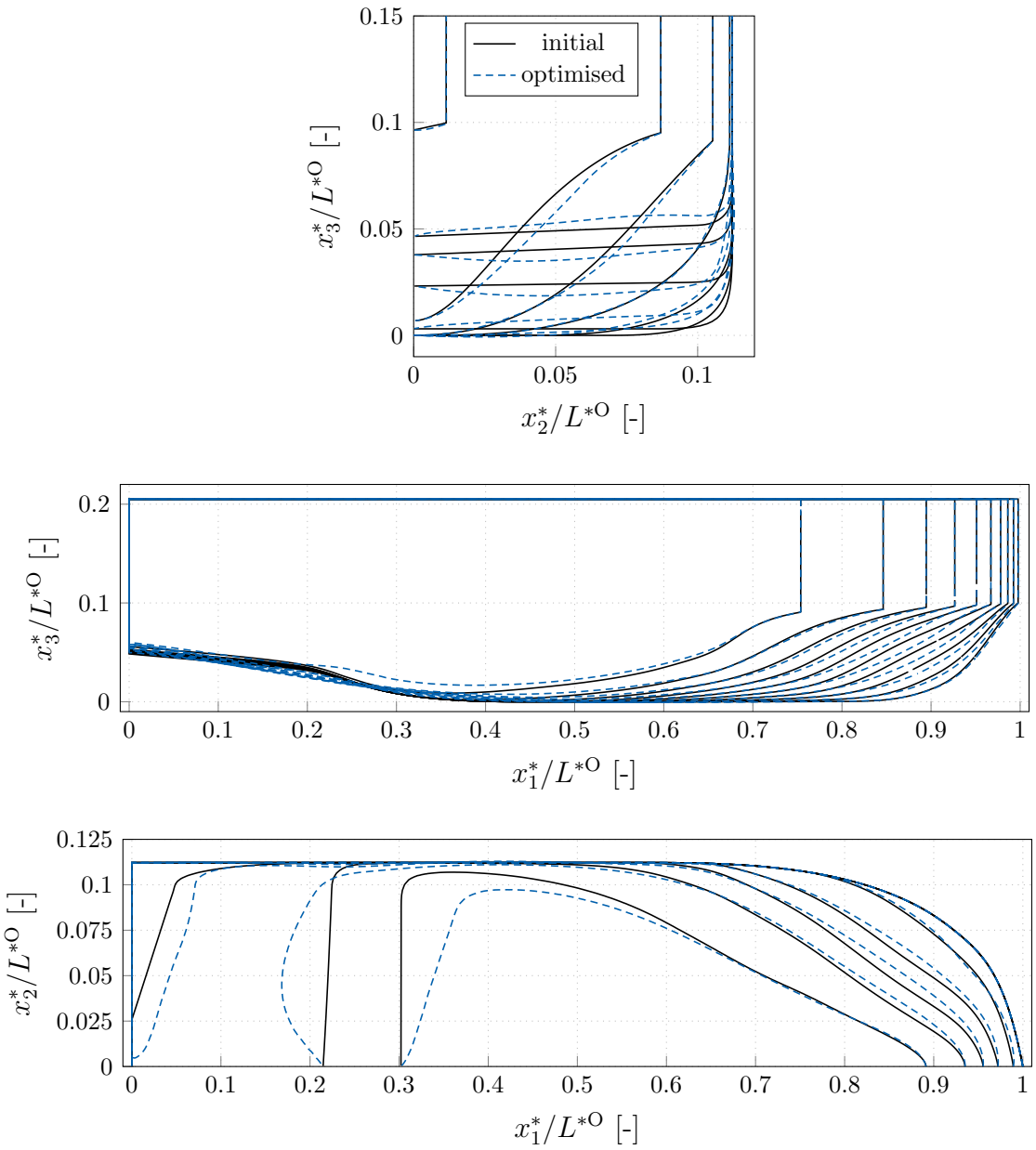

Figure 5.20: Offshore Supply Vessel (OSV) model scale case ($\mathrm{Re}_\mathrm{L}^\mathrm{MS} = 8.92 \cdot 10^6$, $\mathrm{Fn}^\mathrm{MS} = 0.32$): (Top) Frames, (center) waterlines and (bottom) buttocks for the initial (black) and optimized (blue, dotted) geometry obtained with an optimization without the adaption of trim and sinkage.

is increased by a factor of five. The adjoint (backward) calculation effort is not affected. The relative objective convergences are depicted in Fig. 5.21 (center) over the number of performed gradient steps. Again, all optimizations converge to the same final value of $(J^* - J^{*\mathrm{ini}})/J^{*\mathrm{ini}} \approx 11.75\%$ and the optimization with the smallest step size indicates two abrupt changes in the cost functional. The gain of the optimization is reduced in comparison with the fixed floatation studies, but inheres a more precise modeling of realistic floatation. The optimized shapes are re-meshed and the objective is re-evaluated from scratch with the initial hydrostatic data. The resulting cost functional value is indi-

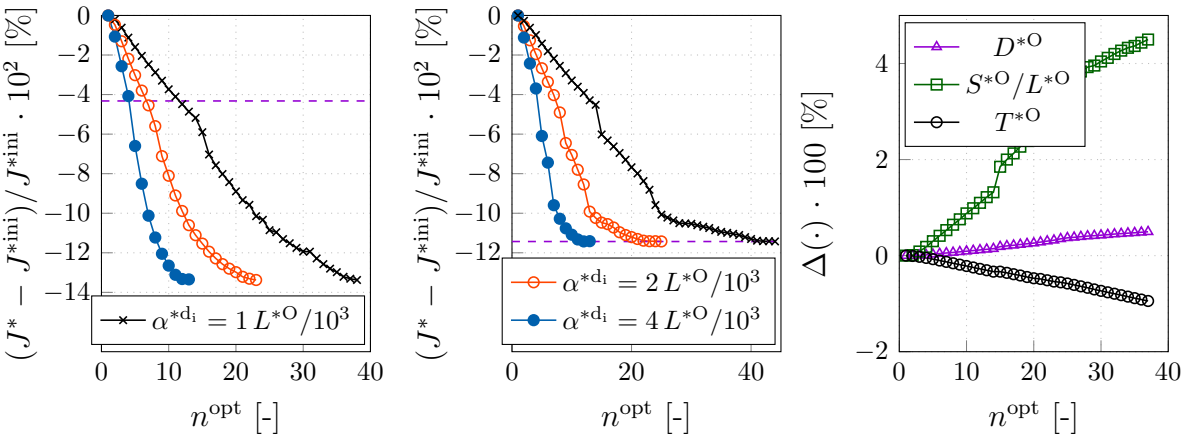

Figure 5.21: Offshore Supply Vessel (OSV) model scale case ($\mathrm{Re}_{\mathrm{L}}^{\mathrm{MS}} = 8.92 \cdot 10^6$, $\mathrm{Fn}^{\mathrm{MS}} = 0.32$): Relative objective convergences for (left) no adaptive trim sinkage and (center) frozen adaptive trim sinkage during the optimization. The dashed purple horizontal lines indicate the final total resistance value with adaptive trim and sinkage adjustment based on the initial hydrostatic data after a re-mesh and re-simulation from scratch of the final designs. Right) Relative hydrostatic data for the optimization with the smallest step size from the center figure.

cated as a dashed purple horizontal that serves to validate the gained reduction in total resistance. In addition, the evolution of the trim, sinkage and displacement are observed with the gradient steps for the smallest step size. None of the floatation quantities reaches convergence and the ship sinkage ($(S^{*\mathrm{O}} - S^{*\mathrm{O,ini}})/S^{*\mathrm{O,ini}} \approx 4\%$) is increased while the OSV trims back ($(T^{*\mathrm{O}} - T^{*\mathrm{O,ini}})/T^{*\mathrm{O,ini}} \approx 0.75\%$). In relation to the total ship length, however, the additional sinkage is comparatively small, i.e. ($(S^{*\mathrm{O,fin}} - S^{*\mathrm{O,ini}})/L^{*\mathrm{O}} \approx 2 \cdot 10^{-5}$), and the trim has a greater influence on the overall performance. Interestingly, the displacement $D^{*\mathrm{O}}$ even increases slightly by a value of $(D^{*\mathrm{O}} - D^{*\mathrm{O,ini}})/D^{*\mathrm{O,ini}} \approx 0.5\%$.

Full Scale

To further test the industrial capabilities, the previous investigations are repeated for a FS configuration. Due to the higher Reynolds number and the associated thinner boundary layers, FS simulations are more sensitive to disturbances in the wall normal direction. As a consequence, the simulation times of restart cases during an optimization are only halved and no longer decreased by one order. Optimizations are carried out with two instead of three different step sizes. In contrast to the MS optimizations, symmetry plane tangential deformation is now allowed.

Two optimization series are performed, which both start from a converged initial floation. The corresponding initial drag coefficient is plotted in Fig. 5.22 (left) for an initial simulation period, where the floatation adjustment according to Sec. 2.2.11 is performed every 10.000 time steps. The first two optimization studies neglect a floatation adjustment during the optimization and reduce the cost functional by approx. $(J^* - J^{*\mathrm{ini}})/J^{*\mathrm{ini}} \approx 5.75\%$ as shown in Fig. 5.22 (center). In line with the MS studies, the convergence is not constant

and experiences a kink after $\approx 0.75\%$ drag reduction, but reaches a similar, minimized value for both step sizes. The converged shape based on the smaller step size is re-meshed and re-simulated, where an adjustment of the floating position based on the hydrostatic data of the first shape is activated. The result is indicated as a horizontal dashed purple line in the center Fig. 5.22. Although not as drastic as in the MS case, a considerable part of the optimization gain is lost due to the neglected floatation during the optimization. Figure 5.23 presents frames (top), water lines (middle) and buttocks (bottom) of the initial and the optimized geometry without the adaption of trim and sinkage. Above all, the S-twist is reduced and the displacement in the bow area is increased.

In two further optimization studies, the floating position is adjusted during each primal simulation that resembles a *frozen floatation* approach. The additional iterative effort increases the simulation time and the resulting cost functional convergences are documented in Fig. 5.22 (right). The objective is minimized by $(J^* - J^{*\mathrm{ini}})/J^{*\mathrm{ini}} \approx 4\%$ for both step sizes. Again, a kink occurs in the convergences of the objectives, but now earlier at $\approx 0.4\%$ drag reduction. However, a re-meshing and subsequent re-simulation of the optimal shape obtained from the smaller step size display almost no change of cost functional value, which is, albeit minimal, above the value of the previous study with neglected floatation.

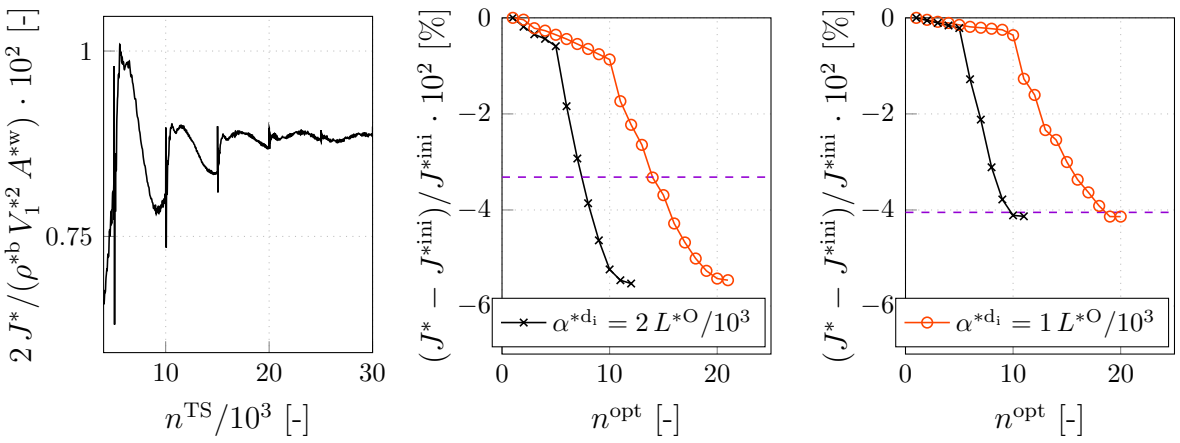

Figure 5.22: Offshore Supply Vessel (OSV) full scale case ($\mathrm{Re_L^{FS}} = 2.81 \cdot 10^8$, $\mathrm{Fn^{FS}} = 0.37$): (Left) drag coefficient for the initial shape with adaptive trim sinkage and relative cost functional convergences for (center) fixed and (right) free adaptive trim and sinkage. The dashed purple horizontal lines indicate the final total resistance value with adaptive trim and sinkage adjustment based on the initial hydrostatic data after a re-mesh and re-simulation from scratch of the final designs.

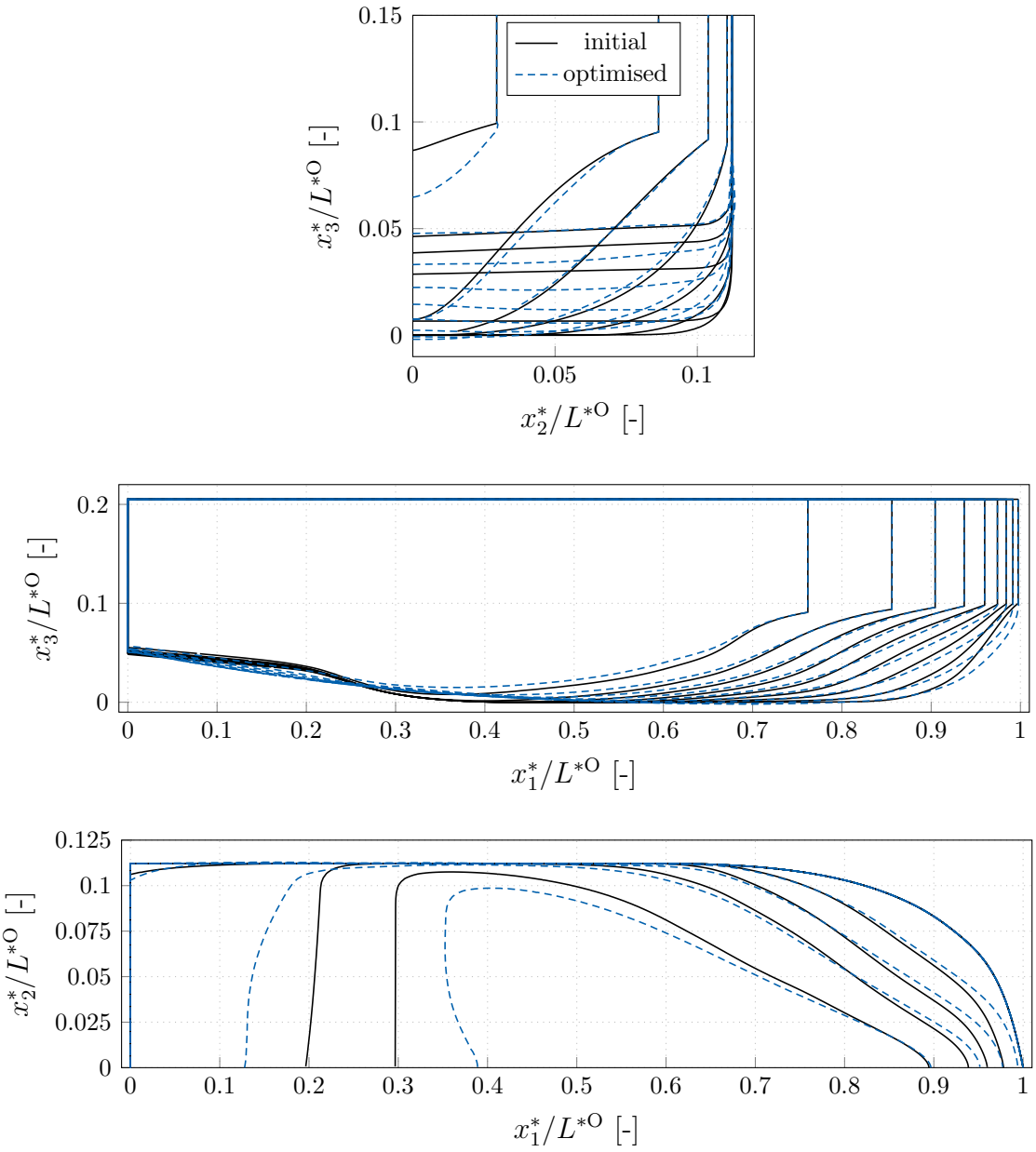

Figure 5.23: Offshore Supply Vessel (OSV) full scale case ($\mathrm{Re}_{\mathrm{L}}^{\mathrm{FS}} = 2.81 \cdot 10^8$, $\mathrm{Fn}^{\mathrm{FS}} = 0.37$): (Top) Frames, (center) waterlines and (bottom) buttocks for the initial (black) and optimized (blue, dotted) geometry obtained with an optimization without the adaption of trim and sinkage.

6 Summary and Outlook

The thesis presented gradient-based optimization methods for CAD-free and thus non-parametrized shapes exposed to immiscible two-phase flows using an adjoint Cahn-Hilliard Volume-of-Fluid Reynolds-Averaged Navier-Stokes (CH-VoF-RANS) approach. Attention was given to the trade-off between adjoint consistency and industrial process capability. The efforts have been structured into four building blocks (I-IV): Compatible fully turbulent (I) primal (physical) and (II) dual (mathematical, adjoint) relationships together with appropriate objective functional formulations (III) have been analysed with curiosity and scepticism at the same time, in order to attain the required accuracy, robustness and efficiency. A volume-based geometry engine (IV), which translates the computed sensitivities into shape deformations and grid adjustments, has been employed. The volume-based formulation is beneficial for the efficiency of the process, the technical usability of the optimization result and the HPC capability. Different aspects of the simulation-driven shape optimization process have been addressed. This research's common ground was to analyse potential issues in greater depth rather than to formulate ad-hoc measures. The guiding principle frequently followed the concept of "Learning from the Adjoints". It was seen that potential weaknesses displayed by an adjoint approach –e.g. when developing (continuous) analytical solutions, in conjunction with (discrete) convergence problems, or enhanced iterative efforts– are often attributable to weaknesses of the primal formulation and a twist of the research question led to fruitful insights.

Contributions to (I) refer to the derivation, implementation, verification and validation of an efficient engineering CH-VoF branch. In line with analytical considerations for a model problem, a nonlinear equation of state has been derived to relate an indicator function (a.k.a. concentration) with the fluid properties. Building block (II) covered the derivation of discrete adjoint VoF formulations and the implementation of an adjoint VoF sub-cycling strategy. The suggestion of a discretely differentiable equation of state, together with a novel combination of an inconsistent adjoint VoF method and the CH-VoF approach, allowed for a robust and flexible consistent adjoint two-phase formulation. Another major part was concerned with a continuous adjoint complement to 2D, incompressible, first-order boundary-layer (b.-l.) equations. The findings support the heuristic neglect of the adjoint transposed convection term used by many authors of continuous adjoint optimization studies in complex engineering shear flows and offer analytical expressions for adjoint laminar b.-l. parameters. Next to the analysis of laminar b.-l. flows, the thesis has been also concerned with improving adjoint investigations of turbulent flows. A unified algebraic adjoint momentum equation has been derived using mixing-length arguments for the frozen turbulence strategy and a Law of the Wall consistent (differentiated) approach. A simple algebraic expression provides a consistent closure of the adjoint momentum equation in the logarithmic layer. Spatial decoupling of the control from the objective (III) affected the formulation of boundary conditions and reduced the iterative efforts when the design surface does not cover the entire wetted surface. Additionally, an implicit surface metric approach was presented to extract the inherently smooth gradient (IV) out of the possible

rough sensitivity derivative. Attention was devoted to compliance with geometrical constraints, e.g. constant volume, maximum outer dimensions or a plane transom. Finally, an adaptive floatation module has been added to the gradient-based optimization procedure. The floating model was not differentiated and considered frozen during the adjoint simulation. Examples included underlined the capability of the *frozen floatation* approach and provide partially drastically improved ship hull shapes. It was also demonstrated that fixed floatation can lead to optimization losses when the final shape is released.

Practical applications referred to maritime two-phase flows at the industrial level, namely a Kriso container ship (KCS), a generic submarine (DARPA), a double-ended ferry (DEF), and an offshore-supply vessel (OSV). Selected studies have been conducted even in full-scale.

Future studies of the primal CH-VoF system could focus on a temporally and spatially variable mobility parameter. Based on the demonstrated stability limits of the convection-diffusion concentration equation, the local interface quality should improve by preventing potential overdamping (under damping) due to local overestimation (underestimation) of the numerical viscosity. Regarding the flexible adjoint CH-VoF system, laminar validation studies of this work show a considerable influence of the adjoint coupling terms in the case of inverse concentration objectives. When a force functional is considered, the stability-impeding adjoint cross-coupling terms seem to have a subordinate influence. Hence, the global (integral) influence of adjoint coupling terms should also be investigated term-wise in more detail for other geometries of practical relevance. E.g., conceptual studies on generic ship types are conceivable so that a statement can be made as to which coupling term is possibly negligible for which application. An enormously process-relevant step refers to the extraction of the inherent smooth shape gradient from the possibly rough shape derivative. The technique developed in this thesis based on a spatially operating Steklov-Poincaré metric should be further investigated and extended to include nonlinear aspects. Conceivable are structural mechanics analogies in the sense of a nonlinear material law which prevents the overtaking of material points, so that the quality of the numerical grid is maintained over a longer optimization period. Other self-similar adjoint flows should be developed, e.g., adjoint Falkner-Skan solutions for wedged geometries, an adjoint solution for compressible or even three-dimensional boundary-layers can be considered. Volume-based objective functionals could be investigated, e.g., to account for variations in the primal flow field, which potentially build a bridge towards the stability crisis immanent to flow transition. Research toward turbulent b.-l. flows might be fruitful, whereby one could follow both the continuous and discrete adjoint approaches in parallel. Since the state of research in adjoint turbulence modelling in particular still has some gaps, both strategies *derive-and-simplify* and *simplify-and-derive* should be pursued. In this context, the investigations on adjoint turbulence closure models close to the wall should be continued into the field. It may be possible to derive reduced but still significantly more consistent algebraic adjoint turbulence closure models. Finally, means to reduce the effort of unsteady multi-continua adjoint approaches are welcome, e.g., incremental model order reduction techniques that can be evaluated at runtime.

A Boundary-Layer Scaling Analysis

A.1 Primal Scaling Analysis

Performing a non-dimensionalization of the laminar Eqns. (2.43)-(2.45) –devided by density and considered to be free of gravitational and surface tensional body forces– with the reference data given in Tab. 2.3 results in:

$$\mathrm{R}_1^{*\mathrm{v,BL}}: v_1\frac{\partial v_1}{\partial x_1}\frac{V_1^* V_1^*}{L^*} + v_2\frac{\partial v_1}{\partial x_2}\frac{V_2^* V_1^*}{\delta^*} + \frac{P^*}{L^*\rho^*}\frac{\partial p}{\partial x_1} - \nu^*\frac{V_1^*}{L^{2*}}\left[\frac{\partial^2 v_1}{\partial x_1^{*2}} - \frac{L^{2*}}{\delta^{2*}}\frac{\partial^2 v_1}{\partial x_2^2}\right] = 0 \quad \text{(A.1)}$$

$$\mathrm{R}_2^{*\mathrm{v,BL}}: v_1\frac{\partial v_2}{\partial x_1}\frac{V_1^* V_2^*}{L^*} + v_2\frac{\partial v_2}{\partial x_2}\frac{V_2^* V_2^*}{\delta^*} + \frac{P^*}{\delta^*\rho^*}\frac{\partial p}{\partial x_2} - \nu^*\frac{V_2^*}{L^{2*}}\left[\frac{\partial^2 v_2}{\partial x_1^2} + \frac{L^{2*}}{\delta^{2*}}\frac{\partial^2 v_2}{\partial x_2^2}\right] = 0 \quad \text{(A.2)}$$

$$\mathrm{R}^{*\mathrm{p,BL}}: -\frac{\partial v_1}{\partial x_1}\frac{V_1^*}{L^*} - \frac{\partial v_2}{\partial x_2}\frac{V_2^*}{\delta^*} = 0. \quad \text{(A.3)}$$

The relations can be simplified towards:

$$\mathrm{R}_1^{\mathrm{v,BL}}: v_1\frac{\partial v_1}{\partial x_1} + v_2\frac{\partial v_1}{\partial x_2} + \mathrm{Eu}\frac{\partial p}{\partial x_1} - \frac{1}{\mathrm{Re_L}}\left[\frac{\partial^2 v_1}{\partial x_1^2} + \frac{\partial^2 v_1}{\partial x_2^2}\frac{L^{2*}}{\delta^{2*}}\right] = 0 \quad \text{(A.4)}$$

$$\mathrm{R}_2^{\mathrm{v,BL}}: v_1\frac{\partial v_2}{\partial x_1} + v_2\frac{\partial v_2}{\partial x_2} + \mathrm{Eu}\frac{L^{2*}}{\delta^{2*}}\frac{\partial p}{\partial x_2} - \frac{1}{\mathrm{Re_L}}\left[\frac{\partial^2 v_2}{\partial x_1^2} + \frac{\partial^2 v_2}{\partial x_2^2}\frac{L^{2*}}{\delta^{2*}}\right] = 0 \quad \text{(A.5)}$$

$$\mathrm{R}^{\mathrm{p,BL}}: -\frac{\partial v_1}{\partial x_1} - \frac{\partial v_2}{\partial x_2} = 0 \quad \text{(A.6)}$$

by assuming $V_2^* \propto V_1^*\delta^*/L^*$.

A.2 Adjoint Scaling Analysis

Performing a non-dimensionalization of Eqn. (4.16)-(4.18) with the reference data given in Tab. 4.2 results in:

$$\begin{aligned}\mathrm{R}_1^{*\hat{\mathrm{v}},\mathrm{BL}}: &- v_1\frac{\partial \hat{v}_1}{\partial x_1}\frac{V_1\hat{V}_1}{L} - v_2\frac{\partial \hat{v}_1}{\partial x_2}\frac{V_2\hat{V}_1}{\hat{\delta}} + \hat{v}_1\frac{\partial v_1}{\partial x_1}\frac{\hat{V}_1 V_1}{L} \\ &+ \hat{v}_2\frac{\partial v_2}{\partial x_1}\frac{\hat{V}_2 V_2}{L} + \frac{\hat{P}}{L}\frac{\partial \hat{p}}{\partial x_1} - \nu\frac{\hat{V}_1}{L^2}\left[\frac{\partial^2 \hat{v}_1}{\partial x_1^2} + \frac{L}{\hat{\delta}}\frac{\partial^2 \hat{v}_1}{\partial x_2^2}\right] = -\frac{\partial j_\Omega}{\partial v_1}\frac{J_\Omega}{V_1}\end{aligned} \quad \text{(A.7)}$$

$$\begin{aligned}\mathrm{R}_2^{*\hat{\mathrm{v}},\mathrm{BL}}: &- v_1\frac{\partial \hat{v}_2}{\partial x_1}\frac{V_1\hat{V}_2}{L} - v_2\frac{\partial \hat{v}_2}{\partial x_2}\frac{V_2\hat{V}_2}{\hat{\delta}} + \hat{v}_1\frac{\partial v_1}{\partial x_2}\frac{\hat{V}_1 V_1}{\delta} \\ &+ \hat{v}_2\frac{\partial v_2}{\partial x_2}\frac{\hat{V}_2 V_2}{\delta} + \frac{\hat{P}}{\hat{\delta}}\frac{\partial \hat{p}}{\partial x_2} - \nu\frac{\hat{V}_2}{L^2}\left[\frac{\partial^2 \hat{v}_2}{\partial x_1^2} + \frac{L}{\hat{\delta}}\frac{\partial^2 \hat{v}_2}{\partial x_2^2}\right] = -\frac{\partial j_\Omega}{\partial v_2}\frac{J_\Omega}{V_2}\end{aligned} \quad \text{(A.8)}$$

$$\mathrm{R}^{*\hat{\mathrm{p}},\mathrm{BL}}: -\frac{1}{\rho}\frac{\partial \hat{v}_1}{\partial x_1}\frac{\hat{V}_1}{L} - \frac{1}{\rho}\frac{\partial \hat{v}_2}{\partial x_2}\frac{\hat{V}_2}{\hat{\delta}} = 0 \quad \text{(A.9)}$$

pri. quantity / operator	v_1	v_2	$\partial v_1/\partial x_1$	$\partial v_1/\partial x_2$	$\partial^2 v_1/\partial x_2^2$
sim. transf.	$V_1 f'$	$\frac{1}{2}\sqrt{\frac{\nu b^2 V_1}{a+bx_1}}\,[f'\eta - f]$	$-\frac{1}{2}\frac{V_1 b}{a+bx_1} f''\eta$	$V_1\sqrt{\frac{V_1}{\nu(a+bx_1)}} f''$	$V_1\frac{V_1}{\nu(a+bx_1)} f'''$
adj. quantity / operator	$\hat{v}_1$	$\hat{v}_2$	$\partial \hat{v}_1/\partial x_1$	$\partial \hat{v}_1/\partial x_2$	$\partial^2 \hat{v}_1/\partial x_2^2$
sim. transf.	$\hat{V}_1 \hat{f}'$	$\frac{1}{2}\sqrt{\frac{\nu b^2 V_1}{a+bx_1}}\left[\hat{f}'\hat{\eta} - \hat{f}\right]$	$-\frac{1}{2}\frac{\hat{V}_1 b}{a+bx_1}\hat{f}''\hat{\eta}$	$\hat{V}_1\sqrt{\frac{V_1}{\nu(a+bx_1)}}\hat{f}''$	$\hat{V}_1\frac{V_1}{\nu(a+bx_1)}\hat{f}'''$

Table A.1: Similarity relations for the primal and the adjoint boundary-layer equations.

that can be simplified towards:

$$\begin{aligned}
\mathrm{R}_1^{\hat{\mathrm{v}},\mathrm{BL}} :& -v_1\frac{\partial \hat{v}_1}{\partial x_1} - v_2\frac{\partial \hat{v}_1}{\partial x_2}\frac{\delta}{\hat{\delta}} + \hat{v}_1\frac{\partial v_1}{\partial x_1} \\
&+ \hat{v}_2\frac{\partial v_2}{\partial x_1}\frac{\hat{\delta}^2}{L^2} + \frac{\hat{P}}{V_1\hat{V}_1}\frac{\partial \hat{p}}{\partial x_1} - \frac{1}{\mathrm{Re}_\mathrm{L}}\left[\frac{\partial^2 \hat{v}_1}{\partial x_1^2} + \frac{\partial^2 \hat{v}_1}{\partial x_2^2}\frac{L^2}{\hat{\delta}^2}\right] = -\frac{\partial j_\Omega}{\partial v_1}\frac{J_\Omega L}{V_1^2 \hat{V}_1} \qquad \text{(A.10)} \\
\mathrm{R}_2^{\hat{\mathrm{v}},\mathrm{BL}} :& -v_1\frac{\partial \hat{v}_2}{\partial x_1} - v_2\frac{\partial \hat{v}_2}{\partial x_2}\frac{\delta}{\hat{\delta}} + \hat{v}_1\frac{\partial v_1}{\partial x_2}\frac{L^2}{\delta\hat{\delta}} \\
&+ \hat{v}_2\frac{\partial v_2}{\partial x_2} + \frac{\partial \hat{p}}{\partial x_2}\frac{\hat{P}}{\hat{V}_1 V_1}\frac{L^2}{\hat{\delta}^2} - \frac{1}{\mathrm{Re}_\mathrm{L}}\left[\frac{\partial^2 \hat{v}_2}{\partial x_1^2} + \frac{L^2}{\hat{\delta}^2}\frac{\partial^2 \hat{v}_2}{\partial x_2^2}\right] = -\frac{\partial j_\Omega}{\partial v_2}\frac{J_\Omega L^3}{V_1^2 \hat{V}_1 \delta\hat{\delta}} \qquad \text{(A.11)} \\
\mathrm{R}^{\hat{\mathrm{p}},\mathrm{BL}} :& -\frac{\partial \hat{v}_1}{\partial x_1} - \frac{\partial \hat{v}_2}{\partial x_2} = 0 \qquad \text{(A.12)}
\end{aligned}$$

by assuming $\hat{V}_2 \propto \hat{V}_1\hat{\delta}/L$.

A.3 Primal and Adjoint Similarity Relations

The relations in Tab. A.1 simplify the tangential primal and the tangential as well as normal adjoint b.-l. equations.

B Shape Calculus

B.1 Shape Tangential Calculus

Fundamental shape tangential operators refer to the tangential

- gradient

$$\underline{\nabla}^*_\Gamma j^* = \underline{\nabla}^* j^* - (\underline{n} \cdot \underline{\nabla}^* j^*)\, \underline{n} = \frac{\partial j^*}{\partial x^*_\mathrm{i}} - \frac{\partial j^*}{\partial x^*_\mathrm{k}} n_\mathrm{k}\, n_\mathrm{i}\,, \tag{B.1}$$

- divergence

$$\underline{\nabla}^*_\Gamma \cdot \underline{V}^* = \underline{\nabla}^* \cdot \underline{V}^* - \underline{n} \cdot (\underline{\nabla}^* \underline{V}^*) \cdot \underline{n} = \frac{\partial V^*_\mathrm{i}}{\partial x^*_\mathrm{i}} - n_\mathrm{k} \frac{\partial V^*_\mathrm{i}}{\partial x^*_\mathrm{k}} n_\mathrm{i}\,, \tag{B.2}$$

- and Laplacian (a.k.a. Laplace-Beltrami) operator

$$\Delta^*_\Gamma j^* = \underline{\nabla}^*_\Gamma \cdot \underline{\nabla}^*_\Gamma j^* = \Delta^* j^* - \underline{n} \cdot (\underline{\nabla}^* (\underline{\nabla}^* j^*)) \cdot \underline{n} = \frac{\partial^2 j^*}{\partial x^{*2}_\mathrm{i}} - n_\mathrm{k} \frac{\partial^2 j^*}{\partial x^*_\mathrm{k} \partial x^*_\mathrm{i}} n_\mathrm{i}\,. \tag{B.3}$$

B.2 General Shape Derivatives

In line with the boundary variation method of hadamard (Hadamard [1968], Delfour and Zolésio [2011], Delfour and Zolésio [2011], Sokolowski and Zolésio [1992], Allaire et al. [2021]), the considered shape optimizations are governed by a design velocity field V^*_i. The derivative of a cost functional w.r.t. the design velocity is frequently denoted as $J^{*\Omega,\prime}(\Omega^*)[V^*_\mathrm{i}]$ for a volume and $J^{*\Gamma,\prime}(\Omega^*)[V^*_\mathrm{i}]$ for a surface objective. The notation indicates the dependence of $J^{*\prime}$ w.r.t. the domain Ω^* in the direction of the design velocity. For the sake of compact notation, the brackets are omitted and the derivative of the volume-based objective in the direction of V^*_i reads

$$J^{*\Omega} = \int j^{*\Omega}\, \mathrm{d}\Omega^* \qquad \rightarrow \qquad \frac{\mathrm{d}}{\mathrm{d}\tau^*} J^{*\Omega}\bigg|_{\tau^*=0} = J^{*\Omega,\prime} = \int j^{*\Omega}\, V^*_\mathrm{i}\, n_\mathrm{i}\, \mathrm{d}\Gamma^*\,. \tag{B.4}$$

In the case of a surface functional, additional terms arise due to the tangential calculus from B.1, viz.

$$J^{*\Gamma} = \int j^{*\Gamma}\, \mathrm{d}\Omega^* \qquad \rightarrow \qquad \frac{\mathrm{d}}{\mathrm{d}\tau^*} J^{*\Gamma}\bigg|_{\tau^*=0} = J^{*\Gamma,\prime} = \int \left[\frac{\partial j^{*\Gamma}}{\partial n^*} + \kappa^*\, j^{*\Gamma}\right] V^*_\mathrm{i}\, n_\mathrm{i}\, \mathrm{d}\Gamma^* \tag{B.5}$$

An additional contribution accounts for local mean curvature κ^*. Accoding to the proposition 4.3 in Allaire et al. [2021], the mean curvature follows from the tangential relation $\kappa^*\, j^*\, \underline{V}^* \cdot \underline{n} = \underline{\nabla}^*_\Gamma j^* \cdot \underline{V}^* + j^*\, \underline{\nabla}^*_\Gamma \cdot \underline{V}^*$, i.e.

$$\kappa^*\, j^{*\Gamma}\, V^*_\mathrm{i}\, n_\mathrm{i} = \left[\frac{\partial j^*}{\partial x^*_\mathrm{i}} - \frac{\partial j^*}{\partial x^*_\mathrm{k}} n_\mathrm{k}\, n_\mathrm{i}\right] V^*_\mathrm{i} + j^* \left[\frac{\partial V^*_\mathrm{i}}{\partial x^*_\mathrm{i}} - \frac{\partial V^*_\mathrm{i}}{\partial x^*_\mathrm{k}} n_\mathrm{k}\, n_\mathrm{i}\right] \tag{B.6}$$

The relations hold for augmented objectives also.

B.3 Specific (Constraint) Shape Derivatives

The discussion originates by defining a cost functional J^* that is constraint by a laminar single-phase flow as well as four generic boundary conditions that refer to an inlet (I), outlet (O), symmetry (S) and wall (D) condition, respectively. The optimization problem reads

$$\text{min.} \quad J^* \quad \text{s.t.} \quad \rho^* \, v_\mathrm{k}^* \frac{\partial \, v_\mathrm{i}^*}{\partial \, x_\mathrm{k}^*} + \frac{\partial}{\partial \, x_\mathrm{k}^*} \left[p^* \, \delta_\mathrm{ik} - 2 \, \mu^* \, S_\mathrm{ik}^* \right] = 0 \qquad \text{in} \quad \Omega^* \tag{B.7}$$

$$- \frac{\partial \, v_\mathrm{i}^*}{\partial \, x_\mathrm{i}^*} = 0 \qquad \text{in} \quad \Omega^* \tag{B.8}$$

$$v_\mathrm{i}^* - v_\mathrm{i}^{*\mathrm{I}} = 0, \frac{\partial \, p^*}{\partial \, n^*} = 0 \qquad \text{on} \quad \Gamma^{*\mathrm{I}} \tag{B.9}$$

$$\left[p^* \delta_\mathrm{ik} - 2 \, \mu^* \, S_\mathrm{ik}^* \right] n_\mathrm{k} \, n_\mathrm{i} = 0, \frac{\partial \, v_\mathrm{i}^*}{\partial \, n^*} = 0 \qquad \text{on} \quad \Gamma^{*\mathrm{O}} \tag{B.10}$$

$$v_\mathrm{i}^* \, n_\mathrm{i} = 0, \left[p^* \delta_\mathrm{ik} - 2 \, \mu^* \, S_\mathrm{ik}^* \right] n_\mathrm{k} \, t_\mathrm{i} = 0, \frac{\partial \, p^*}{\partial \, n^*} = 0 \qquad \text{on} \quad \Gamma^{*\mathrm{S}} \tag{B.11}$$

$$v_\mathrm{i}^* = 0, \frac{\partial \, p^*}{\partial \, n^*} = 0 \qquad \text{on} \quad \Gamma^{*\mathrm{D}} \, . \tag{B.12}$$

Boundary-based objectives refer to force objectives in this thesis. The investigations consistently define several Lagrangians based on the primal (v_i^*, p^*) and adjoint $(\hat{v}_\mathrm{i}^*, \hat{p}^*)$ state as well as complementary variable λ_i^* along the controlled design wall. In order to ensure a compact notation, the entire exposed body is released for design.

B.3.1 Internal Force Evaluation

The projected force can be determined by integrating the stress components along the body surface and then projecting them into the direction of the objective force component

$$J^{*\Gamma,\mathrm{I}} = \int_{\Gamma^{*\mathrm{D}}} j^{*\Gamma,\mathrm{I}} \, \mathrm{d}\Gamma^* \qquad \text{with} \qquad j^{*\Gamma,\mathrm{I}} = \left[p^* \, \delta_\mathrm{ik} - 2 \, \mu^* \, S_\mathrm{ik}^* \right] n_\mathrm{k} \, r_\mathrm{i} \, . \tag{B.13}$$

The respective Lagrangian reads

$$\begin{aligned} L^{*\Gamma,\mathrm{I}} = & \int_{\Gamma^{*\mathrm{O}}} \left[p^* \, \delta_\mathrm{ik} - 2 \, \mu^* \, S_\mathrm{ik}^* \right] n_\mathrm{k} \, r_\mathrm{i} \, \mathrm{d}\Gamma^* + \int_{\Gamma^{*\mathrm{D}}} \lambda_\mathrm{i}^* \, v_\mathrm{i}^* \, \mathrm{d}\Gamma^* \\ & + \int \hat{v}_\mathrm{i} \left[\rho^* \, v_\mathrm{k}^* \frac{\partial \, v_\mathrm{i}^*}{\partial \, x_\mathrm{k}^*} + \frac{\partial}{\partial \, x_\mathrm{k}^*} \left[p^* \, \delta_\mathrm{ik} - 2 \, \mu^* \, S_\mathrm{ik}^* \right] \right] + \hat{p}^* \left[- \frac{\partial \, v_\mathrm{i}^*}{\partial \, x_\mathrm{i}^*} \right] \mathrm{d}\Omega^* \, . \end{aligned} \tag{B.14}$$

The corresponding adjoint state reads

$$\rho^* \left[\hat{v}_\mathrm{k} \frac{\partial v_\mathrm{k}^*}{\partial x_\mathrm{i}^*} - v_\mathrm{k}^* \frac{\partial \hat{v}_\mathrm{i}}{\partial x_\mathrm{k}^*} \right] + \frac{\partial}{\partial x_\mathrm{k}^*} \left[\hat{p}\, \delta_\mathrm{ik} - 2\,\mu^*\, \hat{S}_\mathrm{ik}^* \right] = 0 \qquad \text{in} \quad \Omega^* \tag{B.15}$$

$$-\frac{\partial \hat{v}_\mathrm{i}^*}{\partial x_\mathrm{i}^*} = 0 \qquad \text{in} \quad \Omega^* \tag{B.16}$$

$$\hat{v}_\mathrm{i} = 0, \frac{\partial \hat{p}^*}{\partial n^*} = 0 \qquad \text{on} \quad \Gamma^{*\mathrm{I}} \tag{B.17}$$

$$\left[\hat{p}^* \delta_\mathrm{ik} - 2\,\mu^*\, \hat{S}_\mathrm{ik}^* \right] n_\mathrm{k}\, n_\mathrm{i} - \rho^*\, v_\mathrm{k}^*\, \hat{v}_\mathrm{i}\, n_\mathrm{k}\, n_\mathrm{i} = 0, \frac{\partial \hat{v}_\mathrm{i}}{\partial n^*} = 0 \qquad \text{on} \quad \Gamma^{*\mathrm{O}} \tag{B.18}$$

$$\left[\hat{p}^* \delta_\mathrm{ik} - 2\,\mu^*\, \hat{S}_\mathrm{ik}^* \right] n_\mathrm{k}\, t_\mathrm{i} = 0, \hat{v}_\mathrm{i}\, n_\mathrm{i} = 0, \frac{\partial \hat{p}^*}{\partial n^*} = 0 \qquad \text{on} \quad \Gamma^{*\mathrm{S}} \tag{B.19}$$

$$\lambda_\mathrm{i}^* - \hat{p}^*\, n_\mathrm{i} + 2\,\mu^*\, \hat{S}_\mathrm{ik}^*\, n_\mathrm{k} = 0, \hat{v}_\mathrm{i} + r_\mathrm{i} = 0, \frac{\partial \hat{p}^*}{\partial n^*} = 0 \qquad \text{on} \quad \Gamma^{*\mathrm{D}}\,. \tag{B.20}$$

Application of the shape calculus from B.2 yields

$$\begin{aligned} \frac{\mathrm{d}}{\mathrm{d}\tau^*} L^{*\Gamma,\mathrm{I}} \bigg|_{\tau^*=0} = & \int_{\Gamma^{*\mathrm{D}}} \left[\frac{\partial\, j^{*\Gamma,\mathrm{I}}}{\partial\, n^*} + \kappa^*\, j^{*\Gamma,\mathrm{I}} + \frac{\partial\, \lambda_\mathrm{i}^*\, v_\mathrm{i}^*}{\partial\, n^*} + \kappa^*\, \lambda_\mathrm{i}^*\, v_\mathrm{i}^* \right] V_\mathrm{m}^{*0}\, n_\mathrm{m} \mathrm{d}\Gamma^* \\ & + \int \left[\hat{v}_\mathrm{i} \left[\rho^*\, v_\mathrm{k}^* \frac{\partial\, v_\mathrm{i}^*}{\partial\, x_\mathrm{k}^*} + \frac{\partial}{\partial\, x_\mathrm{k}^*} \left[p^*\, \delta_\mathrm{ik} - 2\,\mu^*\, S_\mathrm{ik}^* \right] \right] \right. \\ & \left. + \hat{p}^* \left[- \frac{\partial\, v_\mathrm{i}^*}{\partial\, x_\mathrm{i}^*} \right] \right] V_\mathrm{m}^{*0}\, n_\mathrm{m}\, \mathrm{d}\Gamma^*\,. \end{aligned} \tag{B.21}$$

The design [fluid] velocity V_k^* [v_i^*] is non-zero [zero] along the design surface and (B.21) simplifies to

$$\begin{aligned} \frac{\mathrm{d}}{\mathrm{d}\tau^*} L^{*\Gamma,\mathrm{I}} \bigg|_{\tau^*=0} = & \int_{\Gamma^{*\mathrm{D}}} \left[\frac{\partial\, j^{*\Gamma,\mathrm{I}}}{\partial\, n^*} + \kappa^*\, j^{*\Gamma,\mathrm{I}} + \left[\hat{p}^*\, n_\mathrm{i} - 2\,\mu^*\, \hat{S}_\mathrm{ik}^*\, n_\mathrm{k} \right] \frac{\partial\, v_\mathrm{i}^*}{\partial\, n^*} - \frac{\partial\, j^{*\Gamma,\mathrm{I}}}{\partial\, n^*} \right. \\ & \left. + \hat{p}^* \left[- \frac{\partial\, v_\mathrm{i}^*}{\partial\, x_\mathrm{i}^*} \right] \right] V_\mathrm{m}^{*0}\, n_\mathrm{m}\, \mathrm{d}\Gamma^*\,. \end{aligned} \tag{B.22}$$

based on the boundary condition for the adjoint velocity, i.e. $\hat{v}_\mathrm{i} = -r_\mathrm{i}$. Adjoint pressure as well as normal objective gradient cancel and one arrives at

$$\frac{\mathrm{d}}{\mathrm{d}\tau^*} L^{*\Gamma,\mathrm{I}} \bigg|_{\tau^*=0} = \int_{\Gamma^{*\mathrm{D}}} \left[\kappa^*\, j^{*\Gamma,\mathrm{I}} - \mu^* \frac{\partial\, \hat{v}_\mathrm{i}^*}{\partial\, n^*} \frac{\partial\, v_\mathrm{i}^*}{\partial\, n^*} \right] V_\mathrm{m}^{*0}\, n_\mathrm{m}\, \mathrm{d}\Gamma^*\,. \tag{B.23}$$

B.3.2 External Force Evaluation

The force objective can also be examined by the momentum loss inside the computational domain. The latter is reformulated via integration by parts and evaluated along the far field boundaries, namely

$$J^{*\Gamma,\mathrm{E}} = \int_{\Gamma^{*\mathrm{I}} \cap \Gamma^{*\mathrm{O}}} j^{*\Gamma,\mathrm{E}}\, \mathrm{d}\Gamma^* \qquad \text{with} \qquad j^{*\Gamma,\mathrm{E}} = \left[2\,\mu^*\, S_\mathrm{ik}^* - v_\mathrm{i}^*\, \rho^*\, v_\mathrm{k}^* - p^*\, \delta_\mathrm{ik} \right] n_\mathrm{k}\, r_\mathrm{i}\,. \tag{B.24}$$

The respective Lagrangian reads

$$L^{*\Gamma,\mathrm{E}} = \int_{\Gamma^{*\mathrm{I}}\cap\Gamma^{*\mathrm{O}}} \left[2\,\mu^*\,S^*_{\mathrm{ik}} - v^*_{\mathrm{i}}\,\rho^*\,v^*_{\mathrm{k}} - p^*\,\delta_{\mathrm{ik}}\right] n_{\mathrm{k}}\,r_{\mathrm{i}}\,\mathrm{d}\Gamma^* + \int_{\Gamma^{*\mathrm{D}}} \lambda^*_{\mathrm{i}}\,v^*_{\mathrm{i}}\,\mathrm{d}\Gamma^* + \int \hat{v}_{\mathrm{i}}\left[\rho^*\,v^*_{\mathrm{k}}\frac{\partial\,v^*_{\mathrm{i}}}{\partial\,x^*_{\mathrm{k}}} + \frac{\partial}{\partial\,x^*_{\mathrm{k}}}\left[p^*\,\delta_{\mathrm{ik}} - 2\,\mu^*\,S^*_{\mathrm{ik}}\right]\right] + \hat{p}^*\left[-\frac{\partial\,v^*_{\mathrm{i}}}{\partial\,x^*_{\mathrm{i}}}\right]\mathrm{d}\Omega^*\,. \tag{B.25}$$

The corresponding adjoint state reads

$$\rho^*\left[\hat{v}_{\mathrm{k}}\frac{\partial\,v^*_{\mathrm{k}}}{\partial\,x^*_{\mathrm{i}}} - v^*_{\mathrm{k}}\frac{\partial\,\hat{v}_{\mathrm{i}}}{\partial\,x^*_{\mathrm{k}}}\right] + \frac{\partial}{\partial\,x^*_{\mathrm{k}}}\left[\hat{p}\,\delta_{\mathrm{ik}} - 2\,\mu^*\,\hat{S}^*_{\mathrm{ik}}\right] = 0 \qquad \text{in} \quad \Omega^* \tag{B.26}$$

$$-\frac{\partial\,\hat{v}^*_{\mathrm{i}}}{\partial\,x^*_{\mathrm{i}}} = 0 \qquad \text{in} \quad \Omega^* \tag{B.27}$$

$$\hat{v}_{\mathrm{i}} - r_{\mathrm{i}} = 0, \frac{\partial\,\hat{p}^*}{\partial\,n^*} = 0 \qquad \text{on} \quad \Gamma^{*\mathrm{I}} \tag{B.28}$$

$$\left[\hat{p}^*\delta_{\mathrm{ik}} - 2\,\mu^*\,\hat{S}^*_{\mathrm{ik}}\right] n_{\mathrm{k}}\,n_{\mathrm{i}} - \rho^*\,v^*_{\mathrm{k}}\left[\hat{v}_{\mathrm{i}}\,n_{\mathrm{k}} - r_{\mathrm{i}}\,n_{\mathrm{k}} - r_{\mathrm{k}}\,n_{\mathrm{i}}\right] n_{\mathrm{i}} = 0, \frac{\partial\,\hat{v}_{\mathrm{i}}}{\partial\,n^*} = 0 \qquad \text{on} \quad \Gamma^{*\mathrm{O}} \tag{B.29}$$

$$\left[\hat{p}^*\delta_{\mathrm{ik}} - 2\,\mu^*\,\hat{S}^*_{\mathrm{ik}}\right] n_{\mathrm{k}}\,t_{\mathrm{i}} = 0, \hat{v}_{\mathrm{i}}\,n_{\mathrm{i}} = 0, \frac{\partial\,\hat{p}^*}{\partial\,n^*} = 0 \qquad \text{on} \quad \Gamma^{*\mathrm{S}} \tag{B.30}$$

$$\lambda^*_{\mathrm{i}} - \hat{p}^*\,n_{\mathrm{i}} + 2\,\mu^*\,\hat{S}^*_{\mathrm{ik}}\,n_{\mathrm{k}} = 0, \hat{v}_{\mathrm{i}} = 0, \frac{\partial\,\hat{p}^*}{\partial\,n^*} = 0 \qquad \text{on} \quad \Gamma^{*\mathrm{D}}\,. \tag{B.31}$$

Application of the shape calculus from B.2 yields

$$\begin{aligned}\frac{\mathrm{d}}{\mathrm{d}\tau^*}L^{*\Gamma,\mathrm{E}}\bigg|_{\tau^*=0} &= \int_{\Gamma^{*\mathrm{I}}\cap\Gamma^{*\mathrm{O}}}\left[\frac{\partial\,j^{*\Gamma,\mathrm{E}}}{\partial\,n^*} + \kappa^*\,j^{*\Gamma,\mathrm{E}}\right] V^{*0}_{\mathrm{m}}\,n_{\mathrm{m}}\mathrm{d}\Gamma^* \\ &+ \int_{\Gamma^{*\mathrm{D}}}\left[\frac{\partial\,\lambda^*_{\mathrm{i}}\,v^*_{\mathrm{i}}}{\partial\,n^*} + \kappa^*\,\lambda^*_{\mathrm{i}}\,v^*_{\mathrm{i}}\right] V^{*0}_{\mathrm{m}}\,n_{\mathrm{m}}\mathrm{d}\Gamma^* \\ &+ \int\left[\hat{v}_{\mathrm{i}}\left[\rho^*\,v^*_{\mathrm{k}}\frac{\partial\,v^*_{\mathrm{i}}}{\partial\,x^*_{\mathrm{k}}} + \frac{\partial}{\partial\,x^*_{\mathrm{k}}}\left[p^*\,\delta_{\mathrm{ik}} - 2\,\mu^*\,S^*_{\mathrm{ik}}\right]\right] + \hat{p}^*\left[-\frac{\partial\,v^*_{\mathrm{i}}}{\partial\,x^*_{\mathrm{i}}}\right]\right] V^{*0}_{\mathrm{m}}\,n_{\mathrm{m}}\,\mathrm{d}\Gamma^*\,.\end{aligned} \tag{B.32}$$

The design [primal and adjoint fluid] velocity V^*_{k} [v^*_{i} and $\hat{v}^*_{\mathrm{i}}$] is non-zero [zero] along the design surface and (B.32) simplifies to

$$\frac{\mathrm{d}}{\mathrm{d}\tau^*}L^{*\Gamma,\mathrm{E}}\bigg|_{\tau^*=0} = \int_{\Gamma^{*\mathrm{D}}}\left[\left[\hat{p}^*\,n_{\mathrm{i}} - 2\,\mu^*\,\hat{S}^*_{\mathrm{ik}}\,n_{\mathrm{k}}\right]\frac{\partial\,v^*_{\mathrm{i}}}{\partial\,n^*} + \hat{p}^*\left[-\frac{\partial\,v^*_{\mathrm{i}}}{\partial\,x^*_{\mathrm{i}}}\right]\right] V^{*0}_{\mathrm{m}}\,n_{\mathrm{m}}\,\mathrm{d}\Gamma^*\,. \tag{B.33}$$

The adjoint pressure cancels and one arrives at

$$\frac{\mathrm{d}}{\mathrm{d}\tau^*}L^{*\Gamma,\mathrm{E}}\bigg|_{\tau^*=0} = \int_{\Gamma^{*\mathrm{D}}}\left[-\mu^*\frac{\partial\,\hat{v}^*_{\mathrm{i}}}{\partial\,n^*}\frac{\partial\,v^*_{\mathrm{i}}}{\partial\,n^*}\right] V^{*0}_{\mathrm{m}}\,n_{\mathrm{m}}\,\mathrm{d}\Gamma^*\,. \tag{B.34}$$

Note that the design velocity is set to zero along the habitat of J^*. As a consequence, no further further variations arise in the total shape derivative that can be generalized: Whenever control and objective are decoupled, only local variational contributions remain.

C Geometrical Variation of a Circular Cylinder

The definition of the hydrostatic portion of the objective reads $j^{*\Gamma,\mathrm{I}} = \rho^* \, g_\mathrm{k}^* \, x_\mathrm{k}^* \, n_\mathrm{i} \, r_\mathrm{i}$. Its derivative can be obtained by

$$\frac{\partial j^{*\Gamma,\mathrm{I}}}{\partial x_\mathrm{m}} n_\mathrm{m} = \rho^* \, g_\mathrm{k}^* \, r_\mathrm{i} (\underbrace{\frac{\partial \, x_\mathrm{k}^*}{\partial \, x_\mathrm{m}^*}}_{\delta_\mathrm{km}} \, n_\mathrm{i} + x_\mathrm{k}^* \frac{\partial \, n_\mathrm{i}}{\partial \, x_\mathrm{m}^*}) n_\mathrm{m} \, , \tag{C.1}$$

where spatially homogeneous g_k^*, r_i and ρ^* are assumed. The second r.h.s. contribution vanishes for a simple cylinder geometry (e.g. polar-coordinates: $x_\mathrm{i}^* = [\cos(\varphi) d^*/2, \sin(\varphi) d^*/2]^\mathrm{T}$; $n_\mathrm{i} = (\partial \, x_\mathrm{i}^* / \partial \, d^*)/2 = [\cos(\varphi), \sin(\varphi)]^\mathrm{T}$ with d^* beeing the cylinder diameter and φ a measure of the angle) due to $(\partial \, n_\mathrm{i} / \partial \, x_\mathrm{m}^*) n_\mathrm{m} = \partial \, n_\mathrm{i} / \partial \, x_\mathrm{n}^* = \partial \, n_\mathrm{i} / \partial \, d^* = 0$. The first r.h.s. term can be rewritten based on the definition of the Kronecker delta and afterwards rearranged into a constant and a φ-dependent part, viz:

$$\rho^* \, g_\mathrm{k}^* \, n_\mathrm{k} \, n_\mathrm{i} \, r_\mathrm{i} = \rho^* \left[\underbrace{g_1^* \, r_1 + g_2^* \, r_2}_{=\text{const.}} + \underbrace{(g_1^* \, r_2 + g_2^* \, r_1) n_1 \, n_2 - g_1^* \, r_1 \, n_2^2 - g_2^* \, r_2 \, n_1^2}_{:=C(\varphi)} \right] , \tag{C.2}$$

where only the first part is constant along the cylinder shape. The second part is of variable sign, not everywhere active in the presented example (since $g_1 = 0$) and mostly vanishes after integrating over the complete cylinder due to the symmetric setting.

D Adjoint Derivation

D.1 Derive-And-Simplify Strategy

A general *derive-and-simplify* approach augments the cost functional with the very basic, non-simplified primal relationships based on Eqns. (2.3), (2.14) and (2.31), viz.

$$L^* = J^* + \int\int \hat{\rho}^* \left[\frac{\mathrm{D}\,\rho^*}{\mathrm{D}\,t^*} - s^{*\rho} \right] + \hat{c}^* \left[\frac{\mathrm{d}\,c}{\mathrm{d}\,t^*} - s^{*\mathrm{c}} \right] + \hat{v}_\mathrm{i}^* \left[\frac{\mathrm{D}\,\rho^*\,v_\mathrm{i}^*}{\mathrm{D}\,t^*} - s^{*\rho\,\mathrm{v_i}} \right] + \sum_{\mathrm{n}=1}^{2} \hat{q}_\mathrm{n}^* \left[\frac{\mathrm{D}\,q_\mathrm{n}^*}{\mathrm{D}\,t^*} - s^{*\mathrm{q_n}} \right] \mathrm{d}\Omega^*\,\mathrm{d}t^* \,. \tag{D.1}$$

Here, q_1 and q_2 refer to the TKE k^* as well as ε^* or ω^* dependent on what kind of turbulent closure is employed. Note that no adjoint pressure is introduced but four different types of adjoint variables arise, which follow the respective primal conservation of

1. Mass: Without directly making anticipatory simplifications and assumptions, an adjoint mass variable is generally introduced. Since the density appears in a variety of terms, it is to be expected that a comparatively large number of coupling terms arise that are associated with the density variation. As shown in the primal derivation part, the density field is directly connected to an indicator function or concentration field via an EoS, cf. Eqn. (2.6). A variation of the density therefore attaches to the variation of the concentration. Analogous to the primal relation between mass conservation and pressure determination, the Lagrange multiplier of density conservation is anticipated to merge into an adjoint pressure variable, e.g. $\hat{\rho}^* \rightarrow \hat{p}^*$.

2. Concentration: The primal conservation of concentration is connected to an adjoint concentration variable $\hat{c}^*$. Although the primal concentration is dimensionless, this is not necessarily true for its adjoint counterpart.

3. Momentum: The primal conservation of momentum is based on two field quantities, viz. $\delta(\rho^*\,v_\mathrm{i}^*) \rightarrow \delta\rho^* v_\mathrm{i}^* + \rho^*\,\delta v_\mathrm{i}^*$. Additional contributions further constitute the variation of the density. The second contribution of the momentum variation is attached to a Lagrangian multiplier for the velocity, denoted as $\hat{v}_\mathrm{i}^*$.

4. Turbulence: The primal RANS model treats flow turbulence based on statistical averaging which finally results in the conservation of two additional turbulent field quantities, generalized in the variable q_i^*. The immense complexity of the turbulence modeling –especially w.r.t. its discrete implementation that features several nonlinear near-wall manipulations– is therefore neglected in the adjoint calculus of this thesis in line with the frozen turbulence approach, cf. Dwight and Brézillon [2006], Othmer [2008], Stück and Rung [2013]. Hence, the associated adjoint variables are set to zero, e.g. $\hat{q}_\mathrm{i}^* = 0$.

In the absence of adjoint turbulence due to $\hat{q}_\mathrm{n}^* = 0$, a total variation of the generalized Lagrangian (D.1) takes the following form

$$\delta L^* = \delta J^* + \int\int \delta\rho^* \left[-\frac{\mathrm{d}\,\hat{\rho}^*}{\mathrm{d}\,t^*} - s^{*\hat{\rho}} \right] + \delta c \left[-\frac{\mathrm{D}\,\hat{c}^*}{\mathrm{D}\,t^*} - s^{*\hat{\mathrm{c}}} \right] + \delta v_\mathrm{i}^* \left[-\rho^* \frac{\mathrm{d}\,\hat{v}_\mathrm{i}^*}{\mathrm{d}\,t^*} - s^{*\hat{\mathrm{v}}_\mathrm{i}} \right] \mathrm{d}\Omega^*\,\mathrm{d}t^*\,, \tag{D.2}$$

where the sign of the conservative / substantial derivatives are consistently flipped. The adjoint balance equations are given in the parenthesized expressions. For an exemplary laminar VoF system, the respective source terms are populated as follows

$$s^{*\hat{\rho}} = v_\mathrm{i}^* \frac{\mathrm{D}\,\hat{v}_\mathrm{i}^*}{\mathrm{D}\,t^*} + \hat{v}_\mathrm{i}^*\, g_\mathrm{i}^* \tag{D.3}$$

$$s^{*\hat{\mathrm{c}}} = \mu^{*\Delta}\, m^{\mu\prime}\, \frac{\partial\,\hat{v}_\mathrm{i}^*}{\partial\,x_\mathrm{k}^*} \left[\frac{2}{3} \frac{\partial\,v_\mathrm{m}^*}{\partial\,x_\mathrm{m}^*} \delta_\mathrm{ik} - 2\,S_\mathrm{ik}^* \right] \tag{D.4}$$

$$s^{*\hat{\mathrm{v}}_\mathrm{i}} = \rho^* \frac{\partial\,\hat{\rho}^*}{\partial\,x_\mathrm{i}^*} - \hat{c}^* \frac{\partial\,c}{\partial\,x_\mathrm{i}^*} + \rho^*\, v_\mathrm{k}^* \frac{\partial\,\hat{v}_\mathrm{k}^*}{\partial\,x_\mathrm{i}^*} + \frac{\partial}{\partial\,x_\mathrm{k}^*} \left[2\mu^* \hat{S}_\mathrm{ik}^* - \frac{2}{3}\mu^* \frac{\partial\,\hat{v}_\mathrm{m}^*}{\partial\,x_\mathrm{m}^*} \delta_\mathrm{ik} \right], \tag{D.5}$$

where $2\,\hat{S}_\mathrm{ik}^* = \partial\,\hat{v}_\mathrm{i}^*/\partial\,x_\mathrm{k}^* + \partial\,\hat{v}_\mathrm{k}^*/\partial\,x_\mathrm{i}^*$ represents an adjoint shear strain tensor.

D.2 Low-Re Variation

The total variation of (4.55) reads

$$\delta L^* = -\left[\nu^* \frac{\mathrm{d}\delta v_1^*}{\mathrm{d}\,x_2^*} \right]_\mathrm{W} - \int \left[\hat{v}_1 \frac{\mathrm{d}}{\mathrm{d}\,x_2^*} \left[\nu^* \left(\frac{\mathrm{d}\delta v_1^*}{\mathrm{d}\,x_2^*} \right) \right] - \hat{k}^* \left[\delta k^* \right] - \hat{\epsilon}^* \left[\delta\epsilon^* - 2\nu^* \frac{\delta k^*}{x_2^{*2}} \right] \right] \mathrm{d}\,x_2^* \tag{D.6}$$

and can be rearranged to apply first-order optimality conditions, viz.

$$\begin{aligned} \delta L^* = &- \left[\nu^* \frac{\mathrm{d}\delta v_1^*}{\mathrm{d}\,x_2^*} \right]_\mathrm{W} - \nu^* \left[\hat{v}_1 \frac{\mathrm{d}\delta v_1^*}{\mathrm{d}\,x_2^*} - \frac{\mathrm{d}\hat{v}_1}{\mathrm{d}\,x_2^*} \delta v_1^* \right]_\mathrm{w}^\Delta \\ &- \int \left[\delta v_1^* \frac{\mathrm{d}}{\mathrm{d}\,x_2^*} \left[\nu^* \frac{\mathrm{d}\hat{v}_1}{\mathrm{d}\,x_2^*} \right] - \delta k \left[\hat{k}^* - \hat{\epsilon}\, \frac{2\nu^*}{x_2^2} \right] - \delta\epsilon^* \left[\hat{\epsilon}^* \right] \right] \mathrm{d}\,x_2^* \\ &\overset{!}{=} 0 \quad \forall\,(\delta v_1^*, \delta k^*, \delta\epsilon^*)\,. \end{aligned} \tag{D.7}$$

The adjoint low-Re formulation follows from the integral in (D.7) and yields

$$\hat{\epsilon}^* = 0 \quad \text{and} \quad \hat{k}^* = 0 \qquad \rightarrow \qquad \int \left[\frac{\mathrm{d}}{\mathrm{d}\,x_2^*} \left[\nu^* \frac{\mathrm{d}\,\hat{v}_1}{\mathrm{d}\,x_2^*} \right] \right] \mathrm{d}\,x_2^* = 0\,. \tag{D.8}$$

Mind that (D.7) is also fulfilled if $\partial k^*/\partial x_2^*$ is employed, hence $\partial\,\delta k^*/\partial x_2^* = 0 \rightarrow \partial\hat{k}^*/\partial x_2^* = 0$. The boundary conditions for the low-Re formulation follow from the remaining terms

in (D.7) that can be collected in a compact form and subsequently eliminated, viz.

$$x_2^* = \Delta^* : \quad \left[\hat{v}_1 \frac{\mathrm{d}\,\delta v_1^*}{\mathrm{d}\,x_2^*} - \frac{\mathrm{d}\hat{v}_1}{\mathrm{d}\,x_2^*}\delta v_1^*\right] \\ \text{with} \quad \delta\left(\frac{\mathrm{d}\,v_1^*}{\mathrm{d}\,x_2^*}\right) = \frac{\mathrm{d}\,\delta v_1^*}{\mathrm{d}\,x_2^*} = 0 \quad \rightarrow \quad \left.\frac{\mathrm{d}\hat{v}_1}{\mathrm{d}\,x_2^*}\right|_\Delta = 0 \tag{D.9}$$

$$x_2^* = 0 : \quad \left[(1+\hat{v}_1)\frac{\mathrm{d}\,\delta v_1^*}{\mathrm{d}\,x_2^*} - \frac{\mathrm{d}\hat{v}_1}{\mathrm{d}\,x_2^*}\delta v_1^*\right] \\ \text{with} \quad \delta v_1^* = 0 \quad \rightarrow \quad \hat{v}_1\big|_\mathrm{W} = -1\,. \tag{D.10}$$

Eqn. (D.10) is fulfilled if either

$$\delta v_1^* = 0 \quad \text{or} \quad \delta v_1^* = -\frac{\mathrm{d}\,v_1^*}{\mathrm{d}\,x_2^*}\delta u^* \quad \rightarrow \quad \delta_\mathrm{u} L^{*\mathrm{LR}} = -\nu^* \left.\frac{\mathrm{d}\hat{v}_1}{\mathrm{d}\,x_2^*}\right|_\mathrm{W} \left.\frac{\mathrm{d}\,v_1^*}{\mathrm{d}\,x_2^*}\right|_\mathrm{W} \tag{D.11}$$

holds that allows for a low-Re (LR) shape derivative expression if a linear development of the local flow w.r.t. a perturbation in wall normal direction is applied, cf. Sec. 3.3.

D.3 High-Re Variation

The total variation of (4.61) reads

$$\begin{aligned}\delta L^* = &-\left[\delta V_{1,\tau}^*(\kappa\, x_2^*)\frac{\mathrm{d}\,v_1^*}{\mathrm{d}\,x_2^*} + (V_{1,\tau}^*\kappa\, x_2^*)\frac{\mathrm{d}\,\delta v_1^*}{\mathrm{d}\,x_2^*}\right]_\mathrm{W} \\ &- \int \left[\hat{v}_1 \frac{\mathrm{d}}{\mathrm{d}\,x_2^*}\left[(\kappa\, x_2^*)\left(\frac{\mathrm{d}\delta v_1^*}{\mathrm{d}\,x_2^*}\right)\cdot(k^*\sqrt{C^\mu})^{1/2} + (\kappa\, x_2^*)\left(\frac{\mathrm{d}\,v_1^*}{\mathrm{d}\,x_2^*}\right)\delta k^* \frac{\sqrt[4]{C^\mu}}{2\sqrt{k^*}}\right]\right. \\ &\left. - \hat{k}^*\left[\delta k^* - 2\frac{V_{1,\tau}^*}{\sqrt{C^\mu}}\delta V_{1,\tau}^*\right] - \hat{\epsilon}^*\left[\delta\epsilon^* - \delta k^* \frac{3\sqrt{k^*}\sqrt[4]{C^\mu}}{2\,\kappa\, x_2^*}\right]\right]\mathrm{d}\,x_2^*.\end{aligned} \tag{D.12}$$

The variations of primal velocity and the TKE are isolated to

$$\begin{aligned}\delta L^* = &-\left[\delta V_{1,\tau}^*(\kappa\, x_2^*)\frac{\mathrm{d}\,v_1^*}{\mathrm{d}\,x_2^*} + (V_{1,\tau}^*\,\kappa\, x_2^*)\frac{\mathrm{d}\delta v_1^*}{\mathrm{d}\,x_2^*}\right]_\mathrm{W} \\ &- \left[\hat{v}_1\left(\frac{\mathrm{d}\delta v_1^*}{\mathrm{d}\,x_2^*}(\kappa\, x_2^*)(k^*\sqrt{C^\mu})^{1/2} + \delta k^* \frac{\kappa\, x_2^*}{2}\frac{\mathrm{d}\,v_1^*}{\mathrm{d}\,x_2^*}\frac{\sqrt[4]{C^\mu}}{\sqrt{k^*}}\right)\right. \\ &\left. \quad - \delta v_1^*\left(\frac{\mathrm{d}\hat{v}_1}{\mathrm{d}\,x_2^*}(\kappa\, x_2^*)(k^*\sqrt{C^\mu})^{1/2} + 2\,\hat{k}^* \frac{V_{1,\tau}^*\,\kappa\, x_2^*}{\sqrt{C^\mu}}\right)\right]_\mathrm{W}^\Delta \\ &- \int \left[\delta v_1^* \frac{\mathrm{d}}{\mathrm{d}\,x_2^*}\left[\left(\frac{\mathrm{d}\hat{v}_1}{\mathrm{d}\,x_2^*}\right)(\kappa\, x_2^*)\cdot(k^*\sqrt{C^\mu})^{1/2} + 2\,\hat{k}^*\,\frac{V_{1,\tau}^*\,\kappa\, x_2^*}{\sqrt{C^\mu}}\right]\right. \\ &\quad - \delta k^*\left[\hat{k}^* - \hat{\epsilon}^* \frac{3\sqrt{k^*}\sqrt[4]{C^\mu}}{2\,\kappa\, x_2^*} - \frac{\sqrt[4]{C^\mu}}{2\sqrt{k^*}}(\kappa\, x_2^*)\left(\frac{\mathrm{d}v_1^*}{\mathrm{d}\,x_2^*}\right)\left(\frac{\mathrm{d}\,\hat{v}_1}{\mathrm{d}\,x_2^*}\right)\right] \\ &\left. \quad - \delta\varepsilon^*\,[\hat{\varepsilon}^*]\right]\mathrm{d}\,x_2^*\,.\end{aligned} \tag{D.13}$$

Rewriting (D.13) by expressing everything in terms of the primal friction velocity $V_{1\tau}^*$ yields

$$\begin{aligned}\delta L^* = &-\left[\delta V_{1,\tau}^*(\kappa\, x_2^*)\frac{\mathrm{d}\, v_1^*}{\mathrm{d}\, x_2^*} + (V_{1,\tau}^*\,\kappa\, x_2^*)\frac{\mathrm{d}\,\delta v_1^*}{\mathrm{d}\, x_2^*}\right]_{\mathrm{W}} \\ &- \left[\hat{v}_1\left(\frac{\mathrm{d}\delta v_1^*}{\mathrm{d}\, x_2^*}(V_{1,\tau}^*\,\kappa\, x_2^*) + \delta k^*\frac{\sqrt{C^\mu}}{2}\right) - \delta v_1^*\left(V_{1\tau}^*\,\kappa\, x_2^*\left(\frac{\mathrm{d}\hat{v}_1}{\mathrm{d}\, x_2^*} + \frac{2\,\hat{k}^*}{\sqrt{C^\mu}}\right)\right)\right]_{\mathrm{W}}^{\Delta} \\ &- \int \delta v_1^*\,\frac{\mathrm{d}}{\mathrm{d}\, x_2^*}\left[V_{1,\tau}^*\,\kappa\, x_2^*\left(\frac{\mathrm{d}\hat{v}_1}{\mathrm{d}\, x_2^*} + \frac{2\,\hat{k}^*}{\sqrt{C^\mu}}\right)\right] - \delta k^*\left[\hat{k}^* - \hat{\epsilon}^*\frac{3\,V_{1,\tau}^*}{2\,\kappa\, x_2^*} - \frac{\sqrt{C^\mu}}{2}\left(\frac{\mathrm{d}\hat{v}_1}{\mathrm{d}\, x_2^*}\right)\right] \\ &\quad - \delta\epsilon^*\left[\hat{\epsilon}^*\right]\mathrm{d}\, x_2^* \\ \overset{!}{=}\, &0 \quad \forall\,(\delta v_1^*, \delta k^*, \delta\epsilon^*)\,. \end{aligned} \tag{D.14}$$

Ensuring a vanishing Lagrangian for all possible variations finally yields the adjoint wall functions, viz.

$$\begin{aligned}&\hat{\epsilon}^* = 0 \qquad \text{and} \qquad \hat{k}^* = \frac{\sqrt{C^\mu}}{2}\frac{\mathrm{d}\hat{v}_1}{\mathrm{d}\, x_2^*} \\ &\quad\rightarrow \qquad \int\left[\frac{\mathrm{d}}{\mathrm{d}\, x_2^*}\left[2(V_{1,\tau}^*\,\kappa\, x_2^*)\frac{\mathrm{d}\hat{v}_1}{\mathrm{d}\, x_2^*}\right]\right]\mathrm{d}x_2^* = 0 \qquad \text{with} \qquad V_{1,\tau}^*\,\kappa\, x_2^* = \nu^{*\mathrm{t}}\,. \end{aligned} \tag{D.15}$$

Interestingly, the adjoint dissipation rate is identical zero whereas the adjoint TKE remains as a passive scalar that enters the adjoint shear based on a doubled turbulent viscosity. The boundary conditions for the high-Re formulation follow from the remaining terms in (D.14) that can be collected in a compact form and subsequently eliminated, viz.

$$\begin{aligned}x_2^* = \Delta^*: \quad &\delta k^*\frac{\sqrt{C^\mu}}{2}\frac{(\kappa\, x_2^*)}{V_{1,\tau}^*}\frac{\mathrm{d}\, v_1^*}{\mathrm{d}\, x_2^*}\hat{v}_1 + \frac{\mathrm{d}\delta v_1^*}{\mathrm{d}\, x_2^*}V_{1,\tau}^*(\kappa\, x_2^*)\hat{v}_1 \\ &\qquad - \delta v_1^*\left[2(\kappa\, x_2^*)V_{1,\tau}^*\frac{\mathrm{d}\hat{v}_1}{\mathrm{d}\, x_2^*}\right] \qquad \overset{!}{=} 0 \quad \forall\,(\delta k^*, \delta v_1^*) \\ &\text{with} \qquad \delta k^* = 0 \qquad \text{and} \qquad \frac{\mathrm{d}\delta v_1^*}{\mathrm{d}\, x_2^*} = 0 \qquad \rightarrow \qquad \left.\frac{\mathrm{d}\hat{v}_1}{\mathrm{d}\, x_2^*}\right|_{\Delta} = 0 \end{aligned} \tag{D.16}$$

$$\begin{aligned}x_2^* = 0: \quad &\delta k^*\left[\frac{\sqrt{C^\mu}}{2}\frac{(\kappa\, x_2^*)}{V_{1,\tau}^*}\frac{\mathrm{d}\, v_1^*}{\mathrm{d}\, x_2^*}\left[1+\hat{v}_1\right]\right] + \frac{\mathrm{d}\delta v_1^*}{\mathrm{d}\, x_2^*}\left[V_{1,\tau}^*(\kappa\, x_2^*)\left[1+\hat{v}_1\right]\right] \\ &\qquad - \delta v_1^*\left[2(\kappa\, x_2^*)V_{1,\tau}^*\frac{\mathrm{d}\hat{v}_1}{\mathrm{d}\, x_2^*}\right] \qquad \overset{!}{=} 0 \quad \forall\,(\delta k^*, \delta v_1^*) \\ &\text{with} \qquad \delta k^* = 0 \qquad \text{and} \qquad \delta v_1^* = 0 \qquad \rightarrow \qquad \hat{v}_1\big|_{\mathrm{W}} = -1\,. \end{aligned} \tag{D.17}$$

Similar to the low-Re formulation, Eqn. (D.17) is again fulfilled if either

$$\begin{aligned}\delta v_1^* = 0 \quad \text{or} \quad \delta v_1^* = -\frac{\mathrm{d}\, v_1^*}{\mathrm{d}\, x_2^*}\delta u^* \quad \rightarrow \quad \delta_{\mathrm{u}} L^{*\mathrm{HR}} &= -2(\kappa\, x_2^*)V_{1\tau}^*\left.\frac{\mathrm{d}\hat{v}_1}{\mathrm{d}\, x_2^*}\right|_{\mathrm{W}}\left.\frac{\mathrm{d}\, v_1^*}{\mathrm{d}\, x_2^*}\right|_{\mathrm{W}} \\ &= -2\nu^{*\mathrm{t}}\left.\frac{\mathrm{d}\hat{v}_1}{\mathrm{d}\, x_2^*}\right|_{\mathrm{W}}\left.\frac{\mathrm{d}\, v_1^*}{\mathrm{d}\, x_2^*}\right|_{\mathrm{W}} \end{aligned} \tag{D.18}$$

holds that allows for a high-Re (HR) shape derivative expression based on twice the turbulent viscosity.

Bibliography

H. Abels, H. Garcke, and G. Grün. Thermodynamically Consistent, Frame Indifferent Diffuse Interface Models for Incompressible Two-Phase Flows with Different Densities. *Mathematical Models and Methods in Applied Sciences*, 22(03):1150013, 2012. doi: 10.1142/S0218202511500138.

D. Agarwal, T.T. Robinson, C.G. Armstrong, S. Marques, I. Vasilopoulos, and M. Meyer. Parametric Design Velocity Computation for CAD-Based Design Optimization Using Adjoint Methods. *Engineering with Computers*, 34(2):225–239, 2018. doi: 10.1007/s00366-017-0534-x.

AIAA. *AIAA Guide for the Verification and Validation of Computational Fluid Dynamics Simulations*. American Institute of Aeronautics and Astronautics, 1998.

E. Akervik and M. Vartdal. Simulation of Two-Phase Interface Flows. Technical Report 16/00822, Norwegian Defence Research Establishment (FFI), 2016.

G. Allaire, F. Jouve, and A.M. Toader. StructuralOoptimization Using Sensitivity Analysis and a Level-Set Method. *Journal of Computational Physics*, 194(1):363–393, 2004. doi: 10.1016/j.jcp.2003.09.032.

G. Allaire, C. Dapogny, and F. Jouve. Chapter 1 - shape and topology optimization. In *Geometric Partial Differential Equations - Part II*, volume 22 of *Handbook of Numerical Analysis*, pages 1 – 132. Elsevier, 2021. doi: 10.1016/bs.hna.2020.10.004.

W.K. Anderson and D.L. Bonhaus. Airfoil Design on Unstructured Grids for Turbulent Flows. *AIAA Journal*, 37(2):185–191, 1999. doi: 10.2514/2.712.

R. Andreani, E.G. Birgin, J.M. Martínez, and M.L. Schuverdt. On Augmented Lagrangian Methods with General Lower-evel Constraints. *SIAM Journal on Optimization*, 18(4):1286–1309, 2008. doi: 10.1137/060654797.

T. Back. *Evolutionary Algorithms in Theory and Practice: Evolution Strategies, Evolutionary Programming, Genetic Algorithms*. Oxford University Press, 1996.

A.K. Bagheri and A. Da Ronch. Adjoint-Based Surrogate Modelling of Spalart-Allmaras Turbulence Model Using Gradient Enhanced Kriging. In *AIAA AVIATION 2020 FORUM*, 2020. doi: 10.2514/6.2020-2991.

S. Balay, S. Abhyankar, M.F. Adams, J. Brown, P. Brune, K. Buschelman, L. Dalcin, A. Dener, V. Eijkhout, W.D. Gropp, D. Karpeyev, D. Kaushik, M.G. Knepley, D.A. May, L.C. McInnes, R.T. Mills, T. Munson, K. Rupp, Sanan. P., B.F. Smith, S. Zampini, H. Zhang, and H. Zhang. PETSc Web page. `https://www.mcs.anl.gov/petsc`, 2019. URL `https://www.mcs.anl.gov/petsc`.

J. Banks, A. Phillips, and S. Turnock. Free Surface CFD Prediction of Components of Ship Resistance for KCS. In *13th Numerical Towing Tank Symposium, Duisburg, Germany*, page 6 pp, 2010.

S. Beckers, J. Behrens, and W. Wollner. Duality Based Error Estimation in the Presence of Discontinuities. *Applied Numerical Mathematics*, 144:83–99, 2019. doi: 10.1016/j.apnum.2019.05.016.

H. Blasius. *Grenzschichten in Flüssigkeiten mit Kleiner Reibung.* Druck von BG Teubner, 1907.

G. Bletsos, N. Kühl, and T. Rung. Adjoint-Based Shape Optimization for the Minimization of Flow-Induced Hemolysis in Biomedical Applications. *Engineering Applications of Computational Fluid Mechanics*, 15(1):1095–1112, 2021. doi: 10.1080/19942060.2021.1943532.

K.-U. Bletzinger. A consistent frame for sensitivity filtering and the vertex assigned morphing of optimal shape. *Structural and Multidisciplinary Optimization*, 49(6):873–895, 2014. doi: 10.1007/s00158-013-1031-5.

J.U. Brackbill, D.B. Kothe, and C. Zemach. A Continuum Method For Modeling Surface Tension. *Journal of Computational Physics*, 100(2):335–354, 1992. doi: 10.1016/0021-9991(92)90240-Y.

P. Bradshaw, D.H. Ferriss, and N.P. Atwell. Calculation of Boundary-Layer Development Using the Turbulent Energy Equation. *Journal of Fluid Mechanics*, 28(3):593–616, 1967. doi: 10.1017/S0022112067002319.

A. Bueno-Orovio, C. Castro, F. Palacios, and E. Zuazua. Continuous Adjoint Approach for the Spalart-Allmaras Model in Aerodynamic Optimization. *AIAA Journal*, 50(3):631–646, 2012. doi: 10.2514/1.J051307.

J.W. Cahn and J.E. Hilliard. Free Energy of a Nonuniform System. I. Interfacial Free Energy. *The Journal of Chemical Physics*, 28(2):258–267, 1958. doi: 10.1063/1.1744102.

N. Chase and P. M. Carrica. Submarine Propeller Computations and Application to Self-Propulsion of DARPA Suboff. *Ocean Engineering*, 60:68–80, 2013. doi: 10.1016/j.oceaneng.2012.12.029.

A. J. Chorin. Numerical Solution of the Navier-Stokes Equations. *Mathematics of computation*, 22(104):745–762, 1968.

P.I. Crumpton and M.B. Giles. Implicit Time–Accurate Solutions on Unstructured Dynamic Grids. *International Journal for Numerical Methods in Fluids*, 25(11):1285–1300, 1997.

S. Daum, M. Greve, and R. Skejic. Effective Power and Speed Loss of Underwater Vehicles in Close Proximity to Regular Waves. In *International Conference on Offshore Mechanics and Arctic Engineering*, volume 57731, page V07AT06A024. American Society of Mechanical Engineers, 2017. doi: 10.1115/OMAE2017-62056.

K. Deb. Multi-Objective Optimisation Using Evolutionary Algorithms: An Introduction. In *Multi-Objective Evolutionary Optimisation for Product Design and Manufacturing*, pages 3–34. Springer, 2011. doi: 10.1007/978-0-85729-652-8_1.

M. C. Delfour and J.-P. Zolésio. Shapes and Geometries, 2011. In: Advances in Design and Control, 22, SIAM, Philadelphia.

M.C. Delfour and J.-P. Zolésio. *Shapes and Geometries: Metrics, Analysis, Differential Calculus, and Optimization*. Society for Industrial and Applied Mathematics, 2011.

H. Ding, P. D.M. Spelt, and C. Shu. Diffuse Interface Model for Incompressible Two–Phase Flows with Large Density Ratios. *Journal of Computational Physics*, 226:2078–2095, 2007. doi: 10.1016/j.jcp.2007.06.028.

J.H. Duncan. An Experimental Investigation of Breaking Waves Produced by a Towed Hydrofoil. *Proceedings of the Royal Society of London A*, 377(1770):331–348, 1981. doi: 10.1098/rspa.1981.0127.

J.H. Duncan. The Breaking and Non-Breaking Wave Resistance of a Two-Dimensional Hydrofoil. *Journal of Fluid Mechanics*, 126:507–520, 1983. doi: 10.1017/S0022112083000294.

R. Duvigneau. *Adaptive Parameterization Using Free-Form Deformation for Aerodynamic Shape Optimization*. PhD thesis, INRIA, 2006.

R. Dwight and J. Brézillon. Effects of Various Approximations of the Discrete Adjoint on Gradient-Based Optimization. *AIAA paper 2006*, 690, 2006. doi: 10.2514/1.21744.

J. Elliott and J. Peraire. Practical 3D Aerodynamic Design and Optimization using Unstructured Meshes. *AIAA Journal*, 35(9):1479–1485, 1997. doi: 10.2514/2.271.

J.H. Ferziger and M. Peric. *Computational Methods for Fluid Dynamics*. Springer Science & Business Media, 2012.

H. Garcke, M. Hinze, and C. Kahle. Optimal Control of Time-Discrete Two-Phase Flow Driven by a Diffuse-Interface Model. *ESAIM: Control, Optimisation and Calculus of Variations*, 25:13, 2019. doi: 10.1051/cocv/2018006.

I. Gatin, H. Jasak, and V. Vukčević. Validation and Verification of Steady Resistance KCS Simulations with Sinkage and Trim using Embedded Free Surface Method. In *Proceedings, Tokyo 2015 Workshop on CFD in Ship Hydrodynamics*, pages 431–436. National Maritime Research Institute, 2015.

N.R. Gauger, A. Walther, C. Moldenhauer, and M. Widhalm. Automatic Differentiation of an Entire Design Chain for Aerodynamic Shape Optimization. In *New Results in Numerical and Experimental Fluid Mechanics VI*, pages 454–461. Springer, 2008. doi: 10.1007/978-3-540-74460-3_56.

I. Gherman and V. Schulz. Preconditioning of One-Shot Pseudo-Timestepping Methods for Shape Optimization. *PAMM*, 5(1):741–742, 2005. doi: 10.1002/pamm.200510345.

K.C. Giannakoglou. Design of Optimal Aerodynamic Shapes Using Stochastic Optimization Methods and Computational Intelligence. *Progress in Aerospace Sciences*, 38(1): 43–76, 2002. doi: 10.1016/S0376-0421(01)00019-7.

K.C. Giannakoglou and D.I. Papadimitriou. Adjoint Methods for Shape Optimization. In *Optimization and Computational Fluid Dynamics*, pages 79–108. Springer, 2008. doi: 10.1007/978-3-540-72153-6_4.

R. Giering and T. Kaminski. Recipes for Adjoint Code Construction. *ACM Transactions on Mathematical Software*, 24(4):437–474, 1998. doi: 10.1145/293686.293695.

M.B. Giles and N.A. Pierce. Adjoint Equations in CFD: Duality, Boundary Conditions and Solution Behaviour. *AIAA Paper*, 1997. doi: 10.2514/6.1997-1850. AIAA–97–1850.

M.B. Giles and N.A. Pierce. An Introduction to the Adjoint Approach to Design. *Flow, Turbulence and Combustion*, 65(3):393–415, 2000. doi: 10.1023/A:1011430410075.

M.B. Giles and S. Ulbrich. Convergence of Linearized and Adjoint Approximations for Discontinuous Solutions of Conservation Laws. part 1: Linearized Approximations and Linearized Output Functionals. *SIAM Journal on Numerical Analysis*, 48(3):882–904, 2010. doi: 10.1137/080727646.

M.B. Giles, M.C. Duta, J.D. Müller, and N.A. Pierce. Algorithm Developments for Discrete Adjoint Methods. *AIAA journal*, 41(2):198–205, 2003. doi: 10.2514/2.1961.

S.K. Godunov. *Different Methods for Shock Waves*. PhD thesis, Moscow State University, 1954.

S.K. Godunov. A Difference Scheme for Numerical Solution of Discontinuous Solution of Hydrodynamic Equations. *Math. Sbornik*, 47:271–306, 1959.

A. Griewank. On Automatic Differentiation. In *Mathematical Programming, Applications*, pages 83–108. Kluwer Academic publishers, 1989.

A. Griewank and A. Walther. Revolve - Reverse or Adjoint Mode of Computational Differentiation. *Transaction on Mathematical Software*, 26(1):19–45, 2000.

A. Griewank and A. Walther. *Evaluating Derivatives, Principles and Techniques of Algorithmic Differentiation, second edition*. Society for Industrial and Applied Mathematics, 2008.

N. C. Groves, T. T. Huang, and M. S. Chang. Geometric Characteristics of DARPA (Defense Advanced Research Projects Agency) SUBOFF Models (DTRC Model Numbers 5470 and 5471). Technical report, David Taylor Research Center Bethesda MD Ship Hydromechanics Dept, 1989.

J. Hadamard. Memoire sur le probleme d' analyse relatif a l' equilibre des plaques elastiques, 1968. In: Memoire des savants etrangers, 33, 1907, Oeuvres de Jaques Hadamard, p. 515-641, Edition du CNRS, Paris.

S. Harries, C. Abt, and M. Brenner. Upfront CADParametric Modeling Techniques for Shape Optimization. In *Advances in Evolutionary and Deterministic Methods for Design, Optimization and Control in Engineering and Sciences*, pages 191–211. Springer, 2019. doi: 0.1007/978-3-319-89988-6_12.

A. Harten. High Resolution Schemes for Hyperbolic Conservation Laws. *Journal of Computational Physics*, 135(2):260–278, 1997. doi: 10.1016/0021-9991(83)90136-5.

R. Hartmann, J. Held, and T. Leicht. Adjoint-Based Error Estimation and Adaptive Mesh Refinement for the RANS and k-ω Turbulence Model Equations. *Journal of Computational Physics*, 230(11):4268–4284, 2011. doi: 10.1016/j.jcp.2010.10.026.

J. Haubner, M. Siebenborn, and M. Ulbrich. A Continuous Perspective on Modeling of Shape Optimal Design Problems. *SIAM Journal on Scientific Computing*, 43(3):A1997–A2018, 2021. doi: 10.1137/20M1332050.

J.P. Heners, L. Radtke, M. Hinze, and A. Düster. Adjoint Shape Optimization for Fluid-Structure Interaction of Ducted Flows. *Computational Mechanics*, pages 1–18, 2017. doi: 10.1007/s00466-017-1465-5.

J.A. Heyns, A.G. Malan, T.M. Harms, and O.F. Oxtoby. Development of a Compressive Surface Capturing Formulation for Modelling Free-Surface Flow by Using the Volume-of-Fluid Approach. *International Journal for Numerical Methods in Fluids*, 71(6):788–804, 2013. doi: 10.1002/fld.3694.

R.M. Hicks and P.A. Henne. Wing design by numerical optimization. *Journal of Aircraft*, 15(7):407–412, 1978. doi: 10.2514/3.58379.

M. Hinze and C. Kahle. A Nonlinear Model Predictive Concept for Control of Two-Phase Flows Governed by the Cahn-Hilliard Navier-Stokes System. In *System Modelling and Optimization*, pages 348–357. Springer, 2011. doi: 10.1007/978-3-642-36062-6_35.

M. Hinze and J. Sternberg. A-Revolve: An Adaptive Memory-and Run-Time-Reduced Procedure for Calculating Adjoints; With an Application to the Instationary Navier–Stokes System. *Optimization Methods Software*, 20(6):645–663, 2005. doi: 10.1080/10556780410001684158.

M. Hinze, A. Walther, and J. Sternberg. An Optimal Memory-Reduced Procedure for Calculating Adjoints of the Instationary Navier-Stokes Equations. *Optimal Control Applications and Methods*, 27(1):19–40, 2006. doi: 10.1002/oca.771.

C.W. Hirt and B.D. Nichols. Volume of Fluid (VoF) Method for the Dynamics of Free Boundaries. *Journal of Computational Physics*, 39(1):201–225, 1981. doi: 10.1016/0021-9991(81)90145-5.

P.C. Hohenberg and B.I. Halperin. Theory of Dynamic Critical Phenomena. *Reviews of Modern Physics*, 49(3):435, 1977. doi: 10.1103/RevModPhys.49.435.

W.H. Hucho. *Aerodynamik der Stumpfen Körper*. Springer, 2002.

D. Jacqmin. Calculation of Two-Phase Navier–Stokes Flows Using Phase-Field Modeling. *Journal of Computational Physics*, 155(1):96–127, 1999. doi: 10.1006/jcph.1999.6332.

D. Jacqmin. Contact-Line Dynamics of a Diffuse Fluid Interface. *Journal of Fluid Mechanics*, 402:57–88, 2000. doi: 10.1017/S0022112099006874.

A. Jameson. Aerodynamic Design via Control Theory. *Journal of Scientific Computing*, 3 (3):233–260, 1988. doi: 10.1007/BF01061285.

A. Jameson. Optimum Aerodynamic Design Using CFD and Control Theory. *AIAA Paper*, 1995. doi: 10.2514/6.1995-1729. AIAA–95–1729–CP.

A. Jameson and J.C. Vassberg. Studies of Alternative Numerical Optimization Methods Applied to the Brachistochrone Problem. *International Journal of Computational Fluid Dynamics*, 9(3):281–296, 2000.

A. Jameson, L. Martinelli, and N.A. Pierce. Optimum Aerodynamic Design Using the Navier-Stokes Equations. *Theoretical and Computational Fluid Dynamics*, 10(1):213–237, 1998. doi: 10.1007/s001620050060.

H. Jasak and Ž. Tuković. Automatic mesh motion for the unstructured finite volume method. *Transactions of FAMENA*, 30(2):1–20, 2006.

W.P. Jones and B.E. Launder. The Prediction of Laminarization with a Two-Equation Model of Turbulence. *International Journal of Heat and Mass Transfer*, 15(2):301–314, 1972. doi: 10.1016/0017-9310(72)90076-2.

C.S. Kapellos, E.M. Papoutsis-Kiachagias, K.C. Giannakoglou, and M. Hartmann. The Unsteady Continuous Adjoint Method for Minimizing Flow-Induced Sound Radiation. *Journal of Computational Physics*, 392:368–384, 2019. doi: 10.1016/j.jcp.2019.04.056.

G.K. Karpouzas, E. M. Papoutsis-Kiachagias, T. Schumacher, E. Villiers, K. C. Giannakoglou, and Othmer C. Adjoint Optimization for Vehicle External Aerodynamics. *International Journal of Automotive Engineering*, 7(1):1–7, 2016.

I.S. Kavvadias, E.M. Papoutsis-Kiachagias, G. Dimitrakopoulos, and K.C. Giannakoglou. The Continuous Adjoint Approach to the k–ω SST Turbulence Model with Applications in Shape Optimization. *Engineering Optimization*, 47(11):1523–1542, 2015a. doi: 10.1080/0305215X.2014.979816.

I.S. Kavvadias, E.M. Papoutsis-Kiachagias, and K.C. Giannakoglou. On The Proper Treatment of Grid Sensitivities in Continuous Adjoint Methods for Shape Optimization. *Journal of Computational Physics*, 301:1–18, 2015b. doi: 10.1016/j.jcp.2015.08.012.

M.A. Khanwale, A.D. Lofquist, Sundar H., J.A. Rossmanith, and Ganapathysubramaniana B. Simulating Two-Phase Flows with Thermodynamically Consistent Energy Stable Cahn-Hilliard Navier-Stokes Equations on Parallel Adaptive Octree Based Meshes. *Journal of Computational Physics*, 419, 2020a. doi: 10.1016/j.jcp.2020.109674.

M.A. Khanwale, K. Saurabh, M. Fernando, V.M. Calo, J.A. Rossmanith, H. Sundar, and B. Ganapathysubramanian. A Fully-Coupled Framework for Solving Cahn-Hilliard Navier-Stokes Equations: Second-Order, Energy-Stable Numerical Methods on Adaptive Octree Based Meshes. *arXiv preprint arXiv:2009.06628*, 2020b.

W.J. Kim, S.H. Van, and D.H. Kim. Measurement of Flows Around Modern Commercial Ship Models. *Experiments in Fluids*, 31(5):567–578, 2001. doi: 10.1007/s003480100332.

J. Kröger. *A Numerical Process for the Hydrodynamic Optimisation of Ships*. PhD thesis, Hamburg University of Technology, 2016.

J. Kröger and T. Rung. CAD-Free Hydrodynamic Optimisation Using Consistent Kernel-Based Sensitivity Filtering. *Ship Technology Research*, 62(3):111–130, 2015. doi: 10.1080/09377255.2015.1109872.

J. Kröger, N. Kühl, and T. Rung. Adjoint Volume-of-Fluid Approaches for the Hydrodynamic Optimisation of Ships. *Ship Technology Research*, 65(1):47–68, January 2018. doi: 10.1080/09377255.2017.1411001.

N. Kühl. *Numerical Approximation of the Adjoint Blasius Equation*. MATLAB Central File Exchange, 2020. URL `https://www.mathworks.com/matlabcentral/fileexchange/82525-numerical-approximation-of-the-adjoint-blasius-equation`. Retrieved November 8, 2020.

N. Kühl, P. M. Müller, A. Stück, M. Hinze, and T. Rung. Decoupling of Control and Force Objective in Adjoint-Based Fluid Dynamic Shape Optimization. *AIAA journal*, 57(9):4110–4114, 2019. doi: 10.2514/1.J058376.

N. Kühl, M. Hinze, and T. Rung. Cahn-Hilliard Navier-Stokes Simulations for Marine Free-Surface Flows. *Experimental and Computational Multiphase Flow*, 2021a. doi: 10.1007/s42757-020-0101-3.

N. Kühl, J. Kröger, M. Siebenborn, M. Hinze, and T. Rung. Adjoint Complement to the Volume-of-Fluid Method for Immiscible Flows. *Journal of Computational Physics*, 440:110411, 2021b. doi: 10.1016/j.jcp.2021.110411.

N. Kühl, P. M. Müller, and T. Rung. Adjoint Complement to the Universal Momentum Law of the Wall. *Flow, Turbulence and Combustion*, 2021c. doi: 10.1007/s10494-021-00286-7.

N. Kühl, P.M. Müller, and T. Rung. Continuous Adjoint Complement to the Blasius Equation. *Physics of Fluids*, 33(3):033608, 2021d. doi: 10.1063/5.0037779.

G. Kuruvila, S. Ta'asan, and M.D. Salas. Airfoil Optimization by the One-Shot Method. In *Optimim Design Methods in Aerodynamics*. NASA Langley Technical Report Server, 1994. AGARD-FDP-VKI Special Course.

B. Lafaurie, C. Nardone, R. Scardovelli, S. Zaleski, and G. Zanetti. Modelling Merging and Fragmentation in Multiphase Flows with SURFER. *Journal of Computational Physics*, 113(1):134–147, 1994. doi: 10.1006/jcph.1994.1123.

L. Larsson, F. Stern, and V. Bertram. Benchmarking of Computational Fluid Dynamics for Ship Flows: The Gothenburg 2000 Workshop. *Journal of Ship Research*, 47(1):63–81, 2003. doi: 10.5957/jsr.2003.47.1.63.

L. Larsson, F. Stern, and M. Visonneau. *Numerical Ship Hydrodynamics: An Assessment of the Gothenburg 2010 Workshop*. Springer, 2013.

B.P. Leonard. A Stable and Accurate Convective Modelling Procedure Based on Quadratic Upstream Interpolation. *Computer Methods in Applied Mechanics and Engineering*, 19 (1):59–98, 1979. doi: 10.1016/0045-7825(79)90034-3.

B.P. Leonard. The ULTIMATE Conservative Difference Scheme Applied to Unsteady One-Dimensional Advection. *Computer Methods in Applied Mechanics and Engineering*, 88 (1):17–74, 1991. doi: 10.1016/0045-7825(91)90232-U.

F.S. Lien and M.A. Leschziner. A General Non-Orthogonal Collocated Finite Volume Algorithm for Turbulent Flow at All Speeds Incorporating Second-Moment Turbulence-Transport Closure, Part 1: Computational Implementation. *Computer Methods in Applied Mechanics and Engineering*, 114(1-2):123–148, 1994a. doi: 10.1016/0045-7825(94)90165-1.

F.S. Lien and M.A. Leschziner. Upstream Monotonic Interpolation for Scalar Transport with Application to Complex Turbulent Flows. *International Journal for Numerical Methods in Fluids*, 19(6):527–548, 1994b. doi: 10.1002/fld.1650190606.

R. Löhner. *Applied Computational Fluid Dynamics Techniques: An Introduction Based on Finite Element Methods*. John Wiley & Sons, 2008.

R. Löhner and C. Yang. Improved ALE Mesh Velocities for Moving Bodies. *Communications in Numerical Methods in Engineering*, 12(10):599–608, 1996. doi: 10.1002/(SICI)1099-0887(199610)12:10⟨599::AID-CNM1⟩3.0.CO;2-Q.

J. Lowengrub and L. Truskinovsky. Quasi–Incompressible Cahn–Hilliard Fluids and Topological Transitions. In *Proceedings of the Royal Society of London A: Mathematical, Physical and Engineering Sciences*, volume 454, pages 2617–2654. The Royal Society, 1998. doi: 10.1098/rspa.1998.0273.

D.G. Luenberger, Y. Ye, et al. *Linear and Nonlinear Programming*, volume 2. Springer, 1984.

X. Luo-Theilen and T. Rung. Computation of Mechanically Coupled Bodies in a Seaway. *Ship Technology Research*, 64(3):129–143, 2017. doi: 10.1080/09377255.2017.1348654.

X. Luo-Theilen and T. Rung. Numerical Analysis of the Installation Procedures of Offshore Structures. *Ocean Engineering*, 179:116–127, 2019. doi: 10.1016/j.oceaneng.2019.03.004.

C.A. Mader, J.R.R.A. Martins, J.J. Alonso, and E. Van Der Weide. ADjoint: An Approach for the Rapid Development of Discrete Adjoint Solvers. *AIAA journal*, 46(4):863–873, 2008. doi: 10.2514/1.29123.

F. Magaletti, F. Picano, M. Chinappi, L. Marino, and C. M. Casciola. The Sharp-Interface Limit of the Cahn–Hilliard/Navier–Stokes Model for Binary Fluids. *Journal of Fluid Mechanics*, 714:95–126, 2013. doi: 10.1017/jfm.2012.461.

S. Manservisi and F. Menghini. Numerical Simulations of Optimal Control Problems for the Reynolds Averaged Navier-Stokes System Closed with a Two-Equation Turbulence Model. *Computers & Fluids*, 125:130–143, 2016a. doi: 10.1016/j.compfluid.2015.11.007.

S. Manservisi and F. Menghini. Optimal Control Problems for the Navier–Stokes System Coupled with the k-ω Turbulence Model. *Computers & Mathematics with Applications*, 71(11):2389–2406, 2016b. doi: 10.1016/j.camwa.2015.10.003.

M. Manzke. *Development of a Scalable Method for the Efficient Simulation of Flows using Dynamic Goal-Orientated Local Grid-Adaption.* PhD thesis, Hamburg University of Technology, 2018.

M. Manzke, J.P. Voss, and T. Rung. Sub-Cycling Strategies for Maritime Two-Phase Flows. In *Notes on Numerical Fluid Mechanics and Multidisciplinary Design*, volume 120, pages 237–251. Springer, 2012. doi: 10.1007/978-3-642-33221-0_14.

A.C. Marta and S. Shankaran. On the Handling of Turbulence Equations in RANS Adjoint Solvers. *Computers & Fluids*, 74:102–113, 2013. doi: 10.1016/j.compfluid.2013.01.012.

L. Martinelli and A. Jameson. An Adjoint Method for Design Optimization of Ship Hulls. In *Proc. of the 9th International Conference on Numerical Ship Hydrodynamics, Ann Arbor, Michigan*, 2007.

J.R.R.A. Martins and J.T. Hwang. Review and Unification of Methods for Computing Derivatives of Multidisciplinary Computational Models. *AIAA journal*, 51(11):2582–2599, 2013. doi: 10.2514/1.J052184.

F.R. Menter. Two-Equation Eddy-Viscosity Turbulence Models for Engineering Applications. *AIAA Journal*, 32(8):1598–1605, 1994. doi: 10.2514/3.12149.

F.R. Menter, M. Kuntz, and R. Langtry. Ten Years of Industrial Experience with the SST Turbulence Model. *Turbulence, heat and mass transfer*, 4(1):625–632, 2003.

B. Mohammadi and O. Pironneau. *Applied Shape Optimization for Fluids.* Oxford University Press, 2010.

S.N. Morkovin. Effects of Compressibility on Turbulent Flows. In *Mechanique de la Turbulence*, pages 367–380. CNRS (ed.: A. Favre), Gordon Breach, 1962.

P. M. Müller, N. Kühl, M. Siebenborn, K. Deckelnick, M. Hinze, and T. Rung. A Novel p-Harmonic Descent Approach Applied to Fluid Dynamic Shape Optimization. *Structural and Multidisciplinary Optimization*, 2021. doi: 10.1007/s00158-021-03030-x.

S. Muzaferija and M. Peric. Computation of Free-Surface Flows Using Interface Tracking and Interface-Capturing Methods. In *Nonlinear Water Wave Interaction*, pages 59–100. Wessex Institute of Technology Press, Southampton, 1999. doi: 10.1080/10407799708915014.

S. K. Nadarajah. *The Discrete Adjoint Approach to Aerodynamic Shape Optimization*. PhD thesis, Stanford University, 2003.

S. K. Nadarajah and A. Jameson. A Comparison of the Continuous and Discrete Adjoint Approach to Automatic Aerodynamic Optimization. In *38th Aerospace Sciences Meeting and Exhibit, Reno, Nevada*, AIAA–2000–0667, 2000. doi: 10.2514/6.2000-667.

S. K. Nadarajah, P. Castonguay, and A. Mousavi. Survey of Shape Parameterization Techniques and Its Effect on Three-Dimensional Aerodynamic Shape Optimization. In *18th AIAA Computational Fluid Dynamics Conference*, AIAA–2007–3837, 2007. doi: 10.2514/6.2007-3837.

E.J. Nielsen and B. Diskin. Discrete Adjoint-Based Design for Unsteady Turbulent Flows on Dynamic Overset Unstructured Grids. *AIAA journal*, 51(6):1355–1373, 2013. doi: 10.2514/1.J050035.

E.J. Nielsen, J. Lu, M.A. Park, and D.L. Darmofal. An Implicit, Exact Dual Adjoint Solution Method for Turbulent Flows on Unstructured Grids. *Computers & Fluids*, 33 (9):1131–1155, 2004. doi: 10.1016/j.compfluid.2003.09.005.

E.J. Nielsen, B. Diskin, and N.K. Yamaleev. Discrete Adjoint-Based Design Optimization of Unsteady Turbulent Flows on Dynamic Unstructured Grids. *AIAA journal*, 48(6): 1195–1206, 2010. doi: 10.2514/1.J051859.

W.F. Noh and P. Woodward. SLIC (Simple Line Interface Calculation). In *Proceedings of the fifth International Conference on Numerical Methods in Fluid Dynamics, June 28–July 2, 1976 Twente University, Enschede*, pages 330–340. Springer, 1976. doi: 10.1007/3-540-08004-X_336.

NUMECA. *HEXPRESS*. Brussels, Belgium, 2018. URL `www.numeca.com`.

E. Olsson and G. Kreiss. A Conservative Level Set Method for Two Phase Flow. *Journal of Computational Physics*, 210(1):225–246, 2005. doi: 10.1016/j.jcp.2005.04.007.

E. Olsson, G. Kreiss, and S. Zahedi. A Conservative Level Set Method for Two Phase Flow II. *Journal of Computational Physics*, 225(1):785–807, 2007. doi: 10.1016/j.jcp.2006.12.027.

S. Osher and J.A. Sethian. Fronts Propagating with Curvature-Dependent Speed: Algorithms Based on Hamilton-Jacobi Formulations. *Journal of Computational Physics*, 79 (1):12–49, 1988. doi: 10.1016/0021-9991(88)90002-2.

C. Othmer. A Continuous Adjoint Formulation for the Computation of Topological and Surface Sensitivities of Ducted Flows. *International Journal for Numerical Methods in Fluids*, 58(8):861–877, 2008. doi: 10.1002/fld.1770.

C. Othmer. Adjoint Methods for Car Aerodynamics. *Journal of Mathematics in Industry*, 4(1):6, 2014. doi: 10.1186/2190-5983-4-6.

E. Özkaya and N.R. Gauger. Single-Step One-shot Aerodynamic Shape Optimization. In *Optimal Control of Coupled Systems of Partial Differential Equations*, pages 191–204. Birkhäuser Basel, 2009. doi: 10.1007/978-3-7643-8923-9_11.

F. Palacios, J.J. Alonso, and A. Jameson. Shape Sensitivity of Free-Surface Interfaces Using a Level Set Methodology. In *42nd AIAA Computational Fluid Dynamics Conference and Exhibit, New Orleans, Louisiana*, AIAA–2012–3341, 2012. doi: 10.2514/6.2012-3341.

F. Palacios, J.J. Alonso, and A. Jameson. Design of Free-Surface Interfaces using RANS Equations. In *43rd AIAA Computational Fluid Dynamics Conference, San Diego, California*, AIAA–2013–3210, 2013. doi: 10.2514/6.2013-3210.

E.M. Papoutsis-Kiachagias and K.C. Giannakoglou. Continuous Adjoint Methods for Turbulent Flows, Applied to Shape and Topology Optimization: Industrial Applications. *Archives of Computational Methods in Engineering*, 23(2):255, 2016. doi: 10.1007/s11831-014-9141-9.

E.M. Papoutsis-Kiachagias, A.S. Zymaris, I.S. Kavvadias, D.I. Papadimitriou, and K.C. Giannakoglou. The Continuous Adjoint Approach to the k-ϵ Turbulence Model for Shape Optimization and Optimal Active Control of Turbulent Flows. *Engineering Optimization*, 47(3):370–389, 2015. doi: 10.1080/0305215X.2014.892595.

I.R. Park, K.S. Kim, J. Kim, and S.H. Van. A Volume-of-Fluid Method for Incompressible Free Surface Flows. *International Journal for Numerical Methods in Fluids*, 61(12): 1331–1362, 2009. doi: 10.1002/fld.2000.

S.V. Patankar and D.B. Spalding. A Calculation Procedure for Heat, Mass and Momentum Transfer in Three-Dimensional Parabolic Flows. *International Journal of Heat and Mass Transfer*, 15:1787–1806, 1972. doi: 10.1016/B978-0-08-030937-8.50013-1.

J.E.V. Peter and R.P. Dwight. Numerical Sensitivity Analysis for Aerodynamic Optimization: A Survey of Approaches. *Computers & Fluids*, 39(3):373–391, 2010. doi: 10.1016/j.compfluid.2009.09.013.

J.E. Pilliod Jr. and E.G. Puckett. Second-Order Accurate Volume-of-Fluid Algorithms for Tracking Material Interfaces. *Journal of Computational Physics*, 199(2):465–502, 2004. doi: 10.1016/j.jcp.2003.12.023.

O. Pironneau. On Optimum Design in Fluid Mechanics. *Journal of Fluid Mechanics*, 64 (1):97–110, 1974. doi: 10.1017/S0022112074002023.

S.B. Pope. *Turbulent Flows*. Cambridge University Press, 2001.

L. Prandtl. Bericht über die Entstehung der Turbulenz. *Zeitschrift für Angewandte Mathematik und Mechanik*, 5:136–139, 1925.

A. Prosperetti. Motion of Two Superposed Viscous Fluids. *The Physics of Fluids*, 24(7): 1217–1223, 1981. doi: 10.1063/1.863522.

S.A. Ragab. An Adjoint Formulation for Shape Optimization in Free-Surface Potential Flow. *Journal of Ship Research*, 45(4):269–278, 2001a. doi: 10.5957/jsr.2001.45.4.269.

S.A. Ragab. Shape Optimization in Free Surface Potential Flow Using an Adjoint Formulation. In *31st AIAA Computational Fluid Dynamics Conference and Exhibit, Anaheim, California*, AIAA–2001–3042, 2001b. doi: 10.2514/6.2001-3042.

O. Reynolds. On the Dynamical Theory of Incompressible Viscous Fluids and the Determination of the Criterion. In *Philosophical Transactions of the Royal Society of London.*, A 186-I, pages 123–164. The Royal Society London, 1895. doi: 10.1098/rsta.1895.0004.

C.M. Rhie and W. L. Chow. Numerical Study of the Turbulent Flow Past an Airfoil with Trailing Edge Separation. *AIAA Journal*, 21(11):1525–1532, 1983. doi: 10.2514/3.8284.

W.J. Rider and D.B. Kothe. Reconstructing Volume Tracking. *Journal of Computational Physics*, 141(2):112–152, 1998. doi: 10.1006/jcph.1998.5906.

A. Ronzheimer. Shape Parametrization Using Free-Form Deformation. In *MEGAFLOW-Numerical Flow Simulation for Aircraft Design*, pages 211–222. Springer, 2005. doi: 10.1007/3-540-32382-1_15.

T. Rung, K. Wöckner, M. Manzke, J. Brunswig, C. Ulrich, and A. Stück. Challenges and Perspectives for Maritime CFD Applications. *Jahrbuch der Schiffbautechnischen Gesellschaft*, 103:127–39, 2009.

J.A. Samareh. A Survey of Shape Parameterization Techniques. In *NASA Conference Publication*, pages 333–344. Citeseer, 1999.

J.A. Samareh. Survey of Shape Parameterization Techniques for High-Fidelity Multidisciplinary Shape Optimization. *AIAA journal*, 39(5):877–884, 2001. doi: 10.2514/2.1391.

H. Schlichting and K. Gersten. *Grenzschicht-Theorie*. Springer-Verlag, 2006.

S. Schmidt. *Efficient Large Scale Aerodynamic Design Based on Shape Calculus*. PhD thesis, University of Trier, 2010.

S. Schmidt and V. Schulz. Impulse Response Approximations of Discrete Shape Hessians with Application in CFD. *SIAM Journal on Control and Optimization*, 48(4):2562–2580, 2009. doi: 10.1137/080719844.

S. Schmidt, C. Ilic, V. Schulz, and N.R. Gauger. Three-Dimensional Large-Scale Aerodynamic Shape Optimization Based on Shape Calculus. *AIAA Journal*, 51(11):2615–2627, 2013. doi: 10.2514/1.J052245.

S. Schubert. *Analysis of Coupling Techniques for Overset-Grid Finite-Volume Methods*. PhD thesis, Hamburg University of Technology, 2019.

S. Schubert and T. Rung. On the Relation of Added Mass and Added Resistance Due to Wall Interference. *Ship Technology Research*, 66(2):117–134, 2019. doi: 10.1080/09377255.2018.1556496.

V. Schulz and M. Siebenborn. Computational Comparison of Surface Metrics for PDE Constrained Shape Optimization. *Computational Methods in Applied Mathematics*, 16 (3):485–496, 2016. doi: 10.1515/cmam-2016-0009.

T.W. Sederberg and S.R. Parry. Free-Form Deformation of Solid Geometric Models. In *Proceedings of the 13th annual conference on Computer graphics and interactive techniques*, pages 151–160, 1986. doi: 10.1145/15886.15903.

Z. Shen, D. Wan, and P.M. Carrica. Dynamic Overset Grids in OpenFOAM with Application to KCS Self-Propulsion and Maneuvering. *Ocean Engineering*, 108:287–306, 2015. doi: 10.1016/j.oceaneng.2015.07.035.

K.K. So, X. Hu, and N.A. Adams. Anti-Diffusion Method for Interface Steepening in Two-Phase Incompressible Flow. *Journal of Computational Physics*, 230(13):5155–5177, 2011. doi: 10.1016/j.jcp.2011.03.011.

H. Söding. Hull Shape Design for Reduced Resistance. *Ship Technology Research-Schiffstechnik*, 48(3):134–144, 2001a.

H. Söding. Practical Hull Shape Design for Reduced Resistance. In *Hydronav 2001, September 27–29, Szczecin, Poland*, 2001b.

H. Söding. Resistance Decrease by Computer-Aided Hull Shape Improvements. In *HIPER 2001, May 2–5, Hamburg, Germany*, 2001c.

J. Sokolowski and J.-P. Zolésio. *Introduction to Shape Optimization: Shape Sensitivity Analysis*, volume 16. Springer Series in Computational Mathematics, 1992.

B. Song, C.M. Lopez, and M. Avila. Phase–Field Simulation of Core–Annular Pipe Flow. *International Journal of Multiphase Flow*, 117:14–24, 2019. doi: 10.1016/j.ijmultiphaseflow.2019.04.027.

O. Soto and R. Löhner. CFD Shape Optimization Using an Incomplete-Gradient Adjoint Formulation. *International Journal for Numerical Methods in Engineering*, 51(6):735–753, 2001. doi: 10.1002/nme.207.

O. Soto and R. Löhner. On the Computation of Flow Sensitivities from Boundary Integrals. In *42nd AIAA Aerospace Sciences Meeting and Exhibit, Reno, Nevada*, AIAA–2004–0112, 2004.

O. Soto, R. Löhner, and C. Yang. A Stabilized Pseudo-Shell Approach for Surface Parametrization in CFD Design Problems. *Communications in Numerical Methods in Engineering*, 18(4):251–258, 2002. doi: 10.1002/cnm.490.

O. Soto, R. Löhner, and C. Yang. An Adjoint-Based Design Methodology for CFD Problems. *International Journal of Numerical Methods for Heat & Fluid Flow*, 14(6):734–759, 2004. doi: 10.1108/09615530410544292.

P. Spalart and S. Allmaras. A One-Equation Turbulence Model for Aerodynamic Flows. In *30th AIAA Aerospace Sciences Meeting and Exhibit, Rena, Nevada*, page 439, 1992. doi: 10.2514/6.1992-439.

J. Springer. *Multiphase Adjoint Optimization for Efficient Calculation of Rigid Body Positions in Navier-Stokes Flow*. PhD thesis, University of Ulm, 2014.

J. Springer and K. Urban. Adjoint-Based Optimization for Rigid Body Motion in Multiphase Navier-Stokes Flow. *SIAM Journal on Scientific Computing*, 37(2):B185–B214, 2015. doi: 10.1137/140974511.

E. Stavropoulou, M. Hojjat, and K.-U. Bletzinger. In-Plane Mesh Regularization for Node-Based Shape Optimization Problems. *Computer Methods in Applied Mechanics and Engineering*, 275:39–54, 2014. doi: 10.1016/j.cma.2014.02.013.

A. Stück. *Adjoint Navier-Stokes Methods for Hydrodynamic Shape Optimisation.* PhD thesis, Hamburg University of Technology, 2012.

A. Stück and T. Rung. Adjoint RANS with Filtered Shape Derivatives for Hydrodynamic Optimisation. *Computers & Fluids*, 47(1):22–32, 2011. doi: 10.1016/j.compfluid.2011.01.041.

A. Stück and T. Rung. Adjoint Complement to Viscous Finite-Volume Pressure-Correction Methods. *Journal of Computational Physics*, 248:402–419, 2013. doi: 10.1016/j.jcp.2013.01.002.

M. Sussman. *A Level Set Approach for Computing Solutions to Incompressible Two-Phase Flow.* PhD thesis, University of California Los Angeles, 1994.

M. Sussman, E. Fatemi, P. Smereka, and S. Osher. An Improved Level Set Method for Incompressible Two-Phase Flows. *Computers & Fluids*, 27(5-6):663–680, 1998. doi: 10.1016/S0045-7930(97)00053-4.

E. Theilen. *Numerical Modelling of Multi-Body Hydrodynamics in Multi-Phase Simulations.* PhD thesis, Hamburg University of Technology, 2020.

D. Thévenin and G. Janiga. *Optimization and Computational Fluid dynamics.* Springer Science & Business Media, 2008.

O. Ubbink and R. Issa. A Method for Capturing Sharp Fluid Interfaces on Arbitrary Meshes. *Journal of Computational Physics*, 153(1):26–50, 1999. doi: 10.1006/jcph.1999.6276.

S. Ulbrich. A Sensitivity and Adjoint Calculus for Discontinuous Solutions of Hyperbolic Conservation Laws with Source Terms. *SIAM Journal on Control and Optimization*, 41 (3):740–797, 2002. doi: 10.1137/S0363012900370764.

S. Ulbrich. Adjoint-Based Derivative Computations for the Optimal Control of Discontinuous Solutions of Hyperbolic Conservation Laws. *Systems & Control Letters*, 48(3): 313–328, 2003. doi: 10.1016/S0167-6911(02)00275-X.

E.R. Van Driest. On Turbulent Flow Near a Wall. *Journal of the Aeronautical Sciences*, 23(11):1007–1011, 1956. doi: 10.2514/8.3713.

B. Van Leer. Towards the Ultimate Conservative Difference Scheme. v. a Second-Order Sequel to Godunov's Method. *Journal of Computational Physics*, 32(1):101–136, 1979. doi: 10.1016/0021-9991(79)90145-1.

J. Vassberg and A. Jameson. Aerodynamic Shape Optimization Part I: Theoretical Background, 2006a. Introduction to Optimization and Multidisciplinary Design, Von Karman Inst. for Fluid Dynamics Brussels.

J. Vassberg and A. Jameson. Aerodynamic Shape Optimization Part 2: Sample Applications, 2006b. Introduction to Optimization and Multidisciplinary Design, Von Karman Inst. for Fluid Dynamics Brussels.

H. Veelken. *Hotspot Cooling Using Phase Change Materials*. PhD thesis, Hamburg University of Technology, 2020.

S. Völkner, J. Brunswig, and T. Rung. Analysis of Non-Conservative Interpolation Techniques in Overset Grid Finite-Volume Methods. *Computers & Fluids*, 148:39–55, 2017. doi: 10.1016/j.compfluid.2017.02.010.

J. Wackers, B. Koren, H. C. Raven, A. Van der Ploeg, A.R. Starke, G.B. Deng, P. Queutey, M. Visonneau, T. Hino, and K. Ohashi. Free-Surface Viscous Flow Solution Methods for Ship Hydrodynamics. *Archives of Computational Methods in Engineering*, 18(1):1–41, 2011. doi: 10.1007/s11831-011-9059-4.

L. Wang, J. E. Martin, M. Felli, and P. M. Carrica. Experiments and CFD for the Propeller Wake of a Generic Submarine Operating Near the Surface. *Ocean Engineering*, 206: 107304, 2020. doi: 10.1016/j.oceaneng.2020.107304.

D.C. Wilcox. *Turbulence Modeling for CFD*, volume 2. DCW Industries La Canada, 1998.

S. Xu, W. Jahn, and J.D. Müller. CAD-Based Shape Optimisation with CFD Using a Discrete Adjoint. *International Journal for Numerical Methods in Fluids*, 74(3):153–168, 2014. doi: 10.1002/fld.3844.

VS. Yakhot, S.A. Orszag, S. Thangam, T.B. Gatski, and C.G. Speziale. Development of Turbulence Models for Shear Flows by a Double Expansion Technique. *Physics of Fluids A: Fluid Dynamics*, 4(7):1510–1520, 1992. doi: 10.1063/1.858424.

S. Yakubov, T. Maquil, and T. Rung. Experience Using Pressure-Based CFD Methods for Euler-Euler Simulations of Cavitating Flows. *Computers & Fluids*, 111:91–104, 2015. doi: 10.1016/j.compfluid.2015.01.008.

C. Yang and R. Löhner. Calculation of Ship Sinkage and Trim using a Finite Element Method and Unstructured Grids. *International Journal of Computational Fluid Dynamics*, 16(3):217–227, 2002. doi: 10.1080/10618560290034690.

G. Yu, J.D. Müller, D. Jones, and F. Christakopoulos. CAD-Based Shape Optimisation Using Adjoint Sensitivities. *Computers & Fluids*, 46(1):512–516, 2011. doi: 10.1016/j.compfluid.2011.01.043.

Z. Zhang. Verification and Validation for RANS Simulation of KCS Container Ship without/with ropeller. *Journal of Hydrodynamics*, 22(1):932–939, 2010. doi: 10.1016/S1001-6058(10)60055-8.

A.S. Zymaris, D.I. Papadimitriou, K.C. Giannakoglou, and C. Othmer. Continuous Adjoint Approach to the Spalart-Allmaras Turbulence Model for Incompressible Flows. *Computers & Fluids*, 38(8):1528–1538, 2009. doi: 10.1016/j.compfluid.2008.12.006.

A.S. Zymaris, D.I. Papadimitriou, K.C. Giannakoglou, and C. Othmer. Adjoint Wall Functions: A New Concept for Use in Aerodynamic Shape Optimization. *Journal of Computational Physics*, 229(13):5228–5245, 2010. doi: 10.1016/j.jcp.2010.03.037.